High Entropy Materials as Air Cathodes for Robust Zinc-Air Batteries

Ren He

ADVERTIMENT. La consulta d'aquesta tesi queda condicionada a l'acceptació de les següents condicions d'ús: La difusió d'aquesta tesi per mitjà del servei TDX (**www.tdx.cat**) i a través del Dipòsit Digital de la UB (**diposit.ub.edu**) ha estat autoritzada pels titulars dels drets de propietat intel·lectual únicament per a usos privats emmarcats en activitats d'investigació i docència. No s'autoritza la seva reproducció amb finalitats de lucre ni la seva difusió i posada a disposició des d'un lloc aliè al servei TDX ni al Dipòsit Digital de la UB. No s'autoritza la presentació del seu contingut en una finestra o marc aliè a TDX o al Dipòsit Digital de la UB (framing). Aquesta reserva de drets afecta tant al resum de presentació de la tesi com als seus continguts. En la utilització o cita de parts de la tesi és obligat indicar el nom de la persona autora.

ADVERTENCIA. La consulta de esta tesis queda condicionada a la aceptación de las siguientes condiciones de uso: La difusión de esta tesis por medio del servicio TDR (**www.tdx.cat**) y a través del Repositorio Digital de la UB (**diposit.ub.edu**) ha sido autorizada por los titulares de los derechos de propiedad intelectual únicamente para usos privados enmarcados en actividades de investigación y docencia. No se autoriza su reproducción con finalidades de lucro ni su difusión y puesta a disposición desde un sitio ajeno al servicio TDR o al Repositorio Digital de la UB. No se autoriza la presentación de su contenido en una ventana o marco ajeno a TDR o al Repositorio Digital de la UB (framing). Esta reserva de derechos afecta tanto al resumen de presentación de la tesis como a sus contenidos. En la utilización o cita de partes de la tesis es obligado indicar el nombre de la persona autora.

WARNING. On having consulted this thesis you're accepting the following use conditions: Spreading this thesis by the TDX (**www.tdx.cat**) service and by the UB Digital Repository (**diposit.ub.edu**) has been authorized by the titular of the intellectual property rights only for private uses placed in investigation and teaching activities. Reproduction with lucrative aims is not authorized nor its spreading and availability from a site foreign to the TDX service or to the UB Digital Repository. Introducing its content in a window or frame foreign to the TDX service or to the UB Digital Repository is not authorized (framing). Those rights affect to the presentation summary of the thesis as well as to its contents. In the using or citation of parts of the thesis it's obliged to indicate the name of the author.

Doctoral thesis

High Entropy Materials as Air Cathodes for Robust Zinc-Air Batteries

Author:

Ren He

Director:

Andreu Cabot

UNIVERSITAT DE BARCELONA

High Entropy Materials as Air Cathodes for Robust Zinc-Air Batteries

Programa de doctorat en Nanociències

Autor:

Ren He

Director:

Andreu Cabot

Tutor:

Frank Güell

Institut de Recerca en Energia de Catalunya (IREC)

UNIVERSITAT DE BARCELONA

Contents

Abstract/Keywords

High Entropy Materials as Air Cathodes for Robust Zinc-Air Batteries

Abstract:This thesis focuses on the development of high-entropy materials (HEMs) as advanced bifunctional catalysts for oxygen evolution reaction (OER) and oxygen reduction reaction (ORR). The study systematically investigates the synthesis methods, structural properties, and catalytic performance of these materials, with particular emphasis on their application in zinc-air batteries (ZABs). Through the incorporation of transition metals and experiencing surface reconstruction processes, these materials exhibit remarkable catalytic efficiencies and stability. Density functional theory (DFT) calculations provide further insights into the active sites and mechanisms driving the enhanced catalytic activity. This research highlights the potential of high entropy alloys (HEAs) and high-entropy phosphides (HEPs) as next-generation catalysts, paving the way for future advancements in energy storage and conversion technologies.

In Chapter 2, I detail the development a low-temperature colloidal method to synthesize CrMnFeCoNi and CuMnFeCoNi HEAs, along with quaternary and ternary alloys. CrMnFeCoNi displays superior bifunctional catalytic performance for both OER and ORR, outperforming CuMnFeCoNi, quaternary alloys, and commercial catalysts like RuO_2 and Pt/C. DFT calculations reveal that the incorporation of Cr into the MnFeCoNi matrix lowered the energy barriers for OER and optimized ORR intermediate steps. This material exhibits high power density, specific capacity, and excellent long-term cycling stability when applied as a bifunctional catalyst in ZABs, underscoring its potential for energy storage applications. This work was published in *Energy Storage Materials* in 2023.

Chapter 3 presents the synthesis of FeCoNiMoW HEA by incorporating 4d Mo and 5d W into a 3d FeCoNi matrix using a low-temperature solution-based method. The resulting alloy demonstrates a highly distorted lattice and strong electronic coupling effects. The FeCoNiMoW HEA exhibits excellent catalytic performance for OER with low overpotentials and great bifunctional properties, surpassing commercial catalysts like Pt/C and RuO_2. DFT calculations identify Ni as the active site for OER, with Mo and W enhancing oxygen intermediate interactions. The FeCoNiMoW-based ZABs show high power density, specific capacity, and exceptional long-term stability, even in flexible applications, making them a promising candidate for wearable energy devices. This work was published in *Advanced Materials* in 2023.

In Chapter 4, I detail the synthesis of FeCoNiPdWP HEPs via a mild colloidal method, resulting in a homogeneous nanostructure. These HEPs demonstrate exceptional bifunctional catalytic performance for both OER and ORR, with a low overpotential of 227 mV for OER and a half-wave potential of 0.81 V for ORR. The outstanding OER performance is attributed to the reconstructed FeCoNiPdWOOH surface, enriched with high-oxidation-state Fe, Co, and Ni. Pd facilitates OH^- adsorption, while W modulates the electronic structure for better oxygen intermediate adsorption. For ORR, surface reconstruction into FeCoNiPdWPOH further enhances performance, with Pd and W maintaining their phosphide environments and Pd as the main active site for ORR. The small energy gap between OER and ORR enables FeCoNiPdWP HEPs to achieve over 700 h of stable operation in ZABs, showcasing their potential for long-term and highly efficient bifunctional catalysis. This work was published in *Energy & Environmental Science* in 2024.

The main conclusions of this thesis and some perspectives for future work are presented in the last. .

Keywords: *High Entropy Materials, High Entropy Alloys, Oxygen Evolution Reaction，Oxygen Reduction Reaction, Zinc-Air Batteries, Colloidal Method*

Resumen/Palabras clave

Materiales de alta entropía como cátodos de aire para baterías de zinc-aire robustas

Resumen:Esta tesis se centra en el desarrollo de materiales de alta entropía (HEMs) como catalizadores bifuncionales avanzados para la reacción de evolución de oxígeno (OER) y la reacción de reducción de oxígeno (ORR). El estudio investiga sistemáticamente los métodos de síntesis, las propiedades estructurales y el rendimiento catalítico de estos materiales, con un énfasis particular en su aplicación en baterías de aire-zinc (ZABs). A través de la incorporación de metales de transición y procesos de reconstrucción superficial, estos materiales exhiben notables eficiencias catalíticas y estabilidad. Los cálculos de teoría del funcional de la densidad (DFT) proporcionan más información sobre los sitios activos y los mecanismos que impulsan la actividad catalítica mejorada. Esta investigación destaca el potencial de las aleaciones de alta entropía (HEAs) y los fosfuros de alta entropía (HEPs) como catalizadores de próxima generación, allanando el camino para futuros avances en tecnologías de almacenamiento y conversión de energía.

En el Capítulo 2, desarrollo un método coloidal a baja temperatura para sintetizar HEAs de CrMnFeCoNi y CuMnFeCoNi, junto con aleaciones cuaternarias y ternarias. El CrMnFeCoNi muestra un rendimiento catalítico bifuncional superior tanto para OER como para ORR, superando al CuMnFeCoNi, las aleaciones cuaternarias y los catalizadores comerciales como RuO_2 y Pt/C. Los cálculos de DFT revelan que la incorporación de Cr en la matriz de MnFeCoNi reduce las barreras energéticas para la OER y optimiza los pasos intermedios de la ORR. Este material exhibe una alta densidad de potencia, capacidad específica y una excelente estabilidad en ciclos prolongados cuando se aplica como catalizador bifuncional en baterías de aire-zinc, subrayando su potencial para aplicaciones de almacenamiento de energía. Este trabajo fue publicado en *Energy Storage Materials* en 2023.

El Capítulo 3 introduce la síntesis de una HEA de FeCoNiMoW mediante la incorporación de Mo 4d y W 5d en una matriz de FeCoNi 3d utilizando un método basado en soluciones a baja temperatura. La aleación resultante muestra una red altamente distorsionada y fuertes efectos de acoplamiento electrónico. La HEA de FeCoNiMoW demuestra un excelente rendimiento catalítico para OER con bajos sobrepotenciales y un pequeño E_{gap} de 0,75 V, superando a los catalizadores comerciales como Pt/C y RuO_2. Los cálculos de DFT identifican el Ni como el sitio activo para la OER, con Mo y W mejorando las interacciones de los intermedios de oxígeno. Las ZABs basadas en FeCoNiMoW muestran una alta densidad de potencia, capacidad específica y una estabilidad excepcional a largo plazo, incluso en aplicaciones flexibles, lo que la convierte en una candidata prometedora para dispositivos energéticos portátiles. Este trabajo fue publicado en *Advanced Materials* en 2023.

En el Capítulo 4, detallo la sintesis de HEPs de FeCoNiPdWP mediante un método coloidal suave, lo que resulta en una nanostructura homogénea. Estos HEPs demuestran un rendimiento catalítico bifuncional excepcional tanto para OER como para ORR, con un bajo sobrepotencial de 227 mV para OER y un potencial a media onda de 0,81 V para ORR. El rendimiento sobresaliente en OER se atribuye a la reconstrucción superficial de FeCoNiPdWOOH, enriquecida con Fe, Co y Ni en estados de oxidación elevados. El Pd facilita la adsorción de OH^-, mientras que W modula la estructura electrónica para mejorar la adsorción de intermedios de oxígeno. Para ORR, la reconstrucción superficial en FeCoNiPdWPOH mejora aún más el rendimiento, con Pd y W manteniendo sus entornos fosforados y Pd como los principales sitios activos para ORR. El pequeño E_{gap} de 0,65 V permite que los HEPs de FeCoNiPdWP logren más de 700 horas de operación estable en ZABs, lo que demuestra su potencial para la catálisis bifuncional a largo plazo y altamente eficiente. Este trabajo fue publicado en *Energy & Environmental Science* en 2024.

Las principales conclusiones de esta tesis y algunas perspectivas para trabajos futuros se presentan en el último capítulo.

Palabras clave: *Materiales de alta entropía, Aleaciones de alta entropía, Reacción de evolución de oxígeno, Reacción de reducción de oxígeno, Baterías de zinc-aire, Método coloidal*

Resum/Paraules clau

Materials d'alta entropia com a càtodes d'aire per a bateries de zinc-aire robustes

Resum: Aquesta tesi se centra en el desenvolupament de materials d’alta entropia (HEMs) com a catalitzadors bifuncionals avançats per a la reacció d'evolució d'oxigen (OER) i la reacció de reducció d'oxigen (ORR). L'estudi investiga de manera sistemàtica els mètodes de síntesi, les propietats estructurals i el rendiment catalític d’aquests materials, amb un èmfasi especial en la seva aplicació en bateries de zinc-aire (ZABs). Mitjançant la incorporació de metalls de transició i els processos de reconstrucció superficial, aquests materials mostren eficiències catalítiques i estabilitats notables. Els càlculs de la teoria del funcional de la densitat (DFT) proporcionen més informació sobre els llocs actius i els mecanismes que impulsen l'activitat catalítica millorada. Aquesta recerca destaca el potencial dels aliatges d'alta entropia (HEAs) i els fosfurs d'alta entropia (HEPs) com a catalitzadors de nova generació, obrint el camí per a futurs avenços en tecnologies d’emmagatzematge i conversió d’energia.

Al Capítol 2, detallo el desenvolupament d’un mètode col·loidal a baixa temperatura per sintetitzar HEAs com CrMnFeCoNi i CuMnFeCoNi, juntament amb aliatges quaternaris i ternaris. CrMnFeCoNi demostra un rendiment catalític bifuncional superior tant per a l’OER com per a l’ORR, superant CuMnFeCoNi, els aliatges quaternaris i els catalitzadors comercials com RuO_2 i Pt/C. Els càlculs DFT revelen que la incorporació de Cr a la matriu MnFeCoNi redueix les barreres energètiques per a l’OER i optimitza els passos intermedis de l’ORR. Aquest material presenta una alta densitat de potència, capacitat específica i una excel·lent estabilitat a llarg termini quan s’aplica com a catalitzador bifuncional en ZABs, destacant el seu potencial per a aplicacions d’emmagatzematge d’energia. Aquest treball va ser publicat a *Energy Storage Materials* el 2023.

El Capítol 3 presenta la síntesi de l’HEA FeCoNiMoW mitjançant la incorporació de Mo de les sèries 4d i W de les sèries 5d en una matriu FeCoNi de les sèries 3d utilitzant un mètode de solució a baixa temperatura. L’aliatge resultant demostra una xarxa fortament distorsionada i efectes de fort acoblament electrònic. L’HEA FeCoNiMoW mostra un excel·lent rendiment catalític per a l’OER amb baixos sobrepotencials i grans propietats bifuncionals, superant els catalitzadors comercials com Pt/C i RuO_2. Els

càlculs DFT identifiquen Ni com el lloc actiu per a l'OER, amb Mo i W millorant les interaccions amb els intermedis d'oxigen. Les ZABs basades en FeCoNiMoW presenten una alta densitat de potència, capacitat específica i una estabilitat excepcional a llarg termini, fins i tot en aplicacions flexibles, fet que les fa candidates prometedores per a dispositius d'energia portàtils. Aquest treball va ser publicat a *Advanced Materials* el 2023.

Al Capítol 4, detallo la síntesi dels HEPs FeCoNiPdWP mitjançant un mètode col·loidal suau, resultant en una nanostructura homogènia. Aquests HEPs demostren un rendiment catalític bifuncional excepcional tant per a l'OER com per a l'ORR, amb un sobrepotencial baix de 227 mV per a l'OER i un potencial de mig onada de 0.81 V per a l'ORR. El rendiment excepcional de l'OER s'atribueix a la superfície reconstruïda de FeCoNiPdWOOH, enriquida amb Fe, Co i Ni en estat d'oxidació alt. Pd facilita l'adsorció d'OH^-, mentre que W modula l'estructura electrònica per a una millor adsorció d'intermedis d'oxigen. Per a l'ORR, la reconstrucció superficial en FeCoNiPdWPOH millora encara més el rendiment, amb Pd i W mantenint els seus entorns de fosfur, i Pd com a principal lloc actiu per a l'ORR. El petit gap d'energia entre l'OER i l'ORR permet que els HEPs FeCoNiPdWP aconsegueixin més de 700 hores d'operació estable en ZABs, mostrant el seu potencial per a una catàlisi bifuncional a llarg termini i d'alta eficiència. Aquest treball va ser publicat a *Energy & Environmental Science* el 2024.

Les principals conclusions d'aquesta tesi i algunes perspectives de treball futur es presenten al final.

Paraules clau: *Materials d'alta entropia, Aliatges d'alta entropia, Reacció d'evolució de l'oxigen, Reacció de reducció d'oxigen, Bateries de zinc-aire, Mètode col·loïdal*

Acknowledgments

As the thesis goes here, my Ph.D. career is coming to an end. Looking back on these three more years, I felt both excited and tearful. It’s been a journey filled with challenges, growth, and countless moments of uncertainty, but also one of immense fulfillment and discovery. The path has not always been smooth, with long nights, failed experiments, and the constant pressure to push boundaries, but each obstacle has shaped me into the researcher and individual I am today. Now, as I prepare to close this chapter and step into the next, I am filled with gratitude—for the knowledge gained, the friendships formed, and the personal resilience developed. There’s a deep sense of satisfaction in knowing that all the hard work, the highs and lows, have led me to this moment, and although the future is uncertain, I look forward to the new opportunities and challenges that lie ahead with optimism and confidence.

First and foremost, I would like to express my deepest gratitude to my supervisor, Prof. Andreu Cabot, for his unwavering support, insightful guidance, and constant encouragement throughout the course of my PhD journey. Your expertise, patience and competitive spirit have been invaluable to me, and I am deeply grateful for the opportunity to learn from you. Meanwhile, I will never forget every time I competed with you on the basketball court, wanting to win every game we played against each other without succeeding. I will also never forget every mountain we conquered together, just like the difficulties we overcame in our academic research. In the days ahead, I will keep competing and striving to be a strong person under your influence.

I would also like to extend my heartfelt thanks to the members of my thesis committee at the University of Barcelona, Maria Lourdes Mestres Vila, M. Elena Xuriguera Martin, and Narciso Homs Marti, for their constructive feedback, critical insights, and continuous encouragement, which have greatly contributed to the quality and direction of my research.

Special thanks to my colleagues and lab mates at the Catalonia Institute for Energy Research, especially Peter Zhang, for creating such a collaborative and intellectually stimulating environment. Meanwhile, as a guide, he took me into the palace of chemical synthesis. Thanks to Xiang Wang, who brought me into a new field of electrochemical research and carry forward this research direction. My sincere thanks also go to our friendly members in IREC: Alberto, Pablo, Jordi Jacas, Marti Biset Peiro, Albert

Tarancon Rubio, Marc Nuñez Eroles, Victor Izquierdo-Roca, Maxim Guc, Robert Fonoll Rubio, Dioulde Huguette Sylla. Also thanks for Functional Nanomaterials group members: Congcong, Mengyao, Ruifeng, Zhifu, Chaoqi, Jesus, Guillem, Ke, Bingfei, Xuan, Guifang, Lili, Paulina, Karol, Chaoyue, Canhuang, Ao, Xingqi, Xueqiang, Chen, Jing, Cristhyan, Nicolas, Qian Xue, Xuede, Jiali, Yuchuan, Xiaoyu, Shengnan, Armando, Xinyuan, Ye, Ning. All of you contributed to my happy and fulfilling years in IREC, and wish you all the best in the future. I also need to thank the IREC staff Francesc Torregrosa Mora, Victor Senero, Carlos Bardí, Yolanda Lara Bejar, Raquel Fontana Vinelli, Jesica Emperador Year, Francesc Valls Mariscal, Miguel Angel Collado Borrull and Amadou Diallo. Without your warm help and patient guidance, I could not have successfully completed many purchases, complicated experiments and instruments. I will never forget the time I worked until 7:30 pm and Amadou came to urge me, and we were the last two to leave IREC. I will never forget that Miguel was the first person I saw every morning at IREC. Thanks again to Amadou and Miguel.

Next, I want to express my deepest gratitude to my parents. Mom and Dad, none of this would have been possible without your unwavering love, support, and belief in me. From the very beginning, you have been my greatest source of strength, always encouraging me to pursue my dreams and standing by me through every challenge. Your sacrifices, guidance, and constant reassurance have been the foundation upon which I've built not only this academic journey but also my personal growth. I am forever grateful for the values you've instilled in me, the perseverance you've taught me, and the unconditional love you've always shown. Thank you for being my rock and my inspiration every step of the way.

As I conclude this important chapter of my life, I want to express my deepest gratitude to my wife, Linlin Yang. Your love, support, and understanding have been my anchor throughout this entire Ph.D. journey. You have stood by my side through the long hours, late nights, and countless moments of frustration, always offering encouragement and reminding me to keep going when things felt overwhelming. Your patience, unwavering belief in me, and the sacrifices you’ve made have meant the world to me. I remember that we worked together on countless sleepless nights, solved experimental problems together, faced the pain of paper rejection together, and prepared for our doctoral dissertation defense together. This achievement is not just mine—it is ours. I am forever grateful to have you in my life, and I couldn’t have done this without you.

Thank you for being my partner, my best friend, and my greatest source of strength.

As I reach the end of this PhD journey, I want to take a moment to thank myself for the perseverance and determination that have brought me this far. It has not always been easy—there were many moments of doubt, frustration, and exhaustion. But through it all, I continued to move forward, step by step, refusing to give up when things got tough. I have learned to trust in my abilities, to adapt to challenges, and to grow both personally and professionally. Completing this work is a reminder of my strength and resilience, and I am proud of the commitment and hard work I have put into every stage of this process. Today, I acknowledge my own efforts, my dedication, and the courage it took to pursue this dream.

Lastly, I gratefully acknowledge the financial support from IREC that made my research possible and the resources provided by the University of Barcelona, which were essential to the success of this work.

You never know how strong you are until you try. You never realize the depth of your resilience until you're pushed to your limits. This journey has shown me that we often underestimate our own potential, and that only by daring to take the first step can we discover the strength within ourselves. The challenges, the moments of doubt, and the countless hours of effort have all led to a deeper understanding of my own capabilities. Through it all, I have learned that staying passionate and facing every hurdle with unwavering determination is what keeps us truly alive.

As I stand at the threshold of this new chapter, I carry with me the lessons learned, the friendships forged, and the unwavering belief that we can achieve more than we ever thought possible. And through it all, I hold on to the idea of staying forever young—forever curious, forever resilient, and forever moved by the beauty of this journey. Because in the end, it is not just about reaching the goal; it is about embracing every step along the way, with eyes wide open and hearts full of hope. O ever youthful, O ever weeping.

Barcelona, Spain

October 2024

Ren He

List of publications

My PhD research work includes three manuscripts, which have already been published in peer-reviewed journals. A full copy of each of the publications can be found in the Annex part. The following is the list of publications included in this thesis:

1. **R. He**$^{\#}$, L. L. Yang$^{\#}$, Y. Zhang, X. Wang, S. Lee, T. Zhang, L. X. Li, Z. F. Liang, J. W. Chen, J. S. Li, A. O. Moghaddam, J. Llorca, M. Ibáñez, J. Arbiol, Y. Xu, A. Cabot, A CrMnFeCoNi high entropy alloy boosting oxygen evolution/reduction reactions and zinc-air battery performance, *Energy Storage Mater.*, **2023**, 287-298.

2. **R. He**, L. L. Yang, Y. Zhang, D. C. Jiang, S. Lee, S. Horta, Z. F. Liang, X. Lu, A. O. Moghaddam, J. S. Li, M. Ibáñez, Y. Xu, Y. T. Zhou, A. Cabot, A 3d-4d-5d High Entropy Alloy as a Bifunctional Oxygen Catalyst for Robust Aqueous Zinc-Air Batteries, *Adv. Mater.*, **2023**, 2303719.

3. **R. He**$^{\#}$, S. Q. Wang$^{\#}$, L. L. Yang$^{\#}$, S. Horta, Y. Ding, C. Di, X. S. Zhang, Y. Xu, M. Ibáñezd, Y. T. Zhou, S. Mebs, H. Dau, J. N. Hausmann, W. Y. Huo, P. W. Menezes, and Andreu Cabot, Active site switching on high entropy phosphides as bifunctional oxygen electrocatalysts for rechargeable/robust Zn-Air battery, *Energy Environ. Sci.*, **2024**, 17, 7193-7208.

Authors' contributions

The work presented in this thesis was performed at the Catalonia Institute for Energy Research (IREC). The PhD student, **Ren He**, has a primary contribution to all experimental work, data processing, and manuscript writing for each of the publications included in this thesis. The contributions of co-authors corresponding to each paper are specifically mentioned in the paragraph below. The impact factor in 2023 and 2024 of the journals where the manuscripts were published is provided. All of the publications belong to the 1st quartile according to the Science Citation Index. None of these papers has been previously presented in any other PhD thesis.

Chapter 2:

R. He[#], L. L. Yang[#], Y. Zhang, X. Wang, S. Lee, T. Zhang, L. X. Li, Z. F. Liang, J. W. Chen, J. S. Li, A. O. Moghaddam, J. Llorca, M. Ibáñez, J. Arbiol, Y. Xu, A. Cabot, A CrMnFeCoNi high entropy alloy boosting oxygen evolution/reduction reactions and zinc-air battery performance, *Energy Storage Mater.*, **2023**, 287-298.

Impact factor 2023: **20.4**

R. He, and L. L. Yang participated in experiment design, material synthesis, electrochemical performance measurements, zinc-air batteries measurements and analysis, and the first draft writing. Y. Zhang participated in material synthesis. X. Wang participated in electrochemical performance measurements. S. Lee, T. Zhang, M. Ibáñez, and J. Arbiol participated in HRTEM characterization. L. X. Li and Y. Xu did the DFT calculations. J. W. Chen, J. Llorca and Y. Xu participated in XPS measurement. Z. F. Liang, J. S. Li, and A. O. Moghaddam helped to do the data analysis. A. Cabot revised the manuscript and was responsible for the manuscript submission.

Chapter 3:

R. He, L. L. Yang, Y. Zhang, D. C. Jiang, S. Lee, S. Horta, Z. F. Liang, X. Lu, A. O. Moghaddam, J. S. Li, M. Ibáñez, Y. Xu, Y. T. Zhou, A. Cabot, A 3d-4d-5d High Entropy Alloy as a Bifunctional Oxygen Catalyst for Robust Aqueous Zinc-Air Batteries, *Adv. Mater.*, **2023**, 2303719.

Impact factor 2018: **29.4**

R. He participated in experiment design, material synthesis, electrochemical performance measurements, zinc-air batteries measurements and analysis, and the first draft writing. L. L. Yang participated in experiment design and writing the first draft. D. C. Jiang and Y. T. Zhou did the DFT calculations. S. Lee, S. Horta and M. Ibáñez participated in HRTEM characterization. X. Lu participated in ICP measurements. Y. Zhang, Z. F. Liang, A. O. Moghaddam, and J. S. Li participated in data discussion. A. Cabot revised the manuscript and was responsible for the manuscript submission.

Chapter 4:

R. He[#], S. Q. Wang[#], L. L. Yang[#], S. Horta, Y. Ding, C. Di, X. S. Zhang, Y. Xu, M. Ibáñezd, Y. T. Zhou, S. Mebs, H. Dau, J. N. Hausmann, W. Y. Huo, P. W. Menezes, and Andreu Cabot, Active site switching on high entropy phosphides as bifunctional oxygen electrocatalysts for rechargeable/robust Zn-Air battery, *Energy Environ. Sci.*, **2024**, 17, 7193-7208.

Impact factor 2024: **32.4**

R. He and L. L. Yang participated in experiment design, material synthesis, electrochemical performance measurements, zinc-air batteries measurements and analysis, and did the first draft writing. S. Horta and Y. Ding, X. S. Zhang, M. Ibáñezd participated in HRTEM characterization. Y. Ding, C. Di and Y Xu participated in XPS and UPS measurements. Y. T. Zhou participated in data analysis. S. Mebs, H. Dau, J. N. Hausmann, and P. W. Menezes did the XAS measurements and analysis. S. Q. Wang and W. Y. Huo did the DFT calculations. A. Cabot revised the manuscript and were responsible for the manuscript submission.

Prof. Andreu Cabot
Certify the information provided above is true.
Barcelona,
October, 2024

List of abbreviations

ACTEM	Aberration corrected transmission electron microscopy
AC-HRTEM	Aberration corrected-high resolution transmission electron microscopy
AIMD	Ab initio molecular dynamics
T	Absolute temperature
E_{ads}	Adsorption energy
$E_{ad/sub}$	Adsorption energy of optimized adsorbate/substrate system
E_{ad}	Adsorption energy of adsorbate in the structure
E_{sub}	Adsorption energy of the clean substrate
R_0	Adsorption resistance
c_i	Atomic percentage
δ	Atomic size difference
γ	Average surface atomic energy
$\bar{r}$	Average atomic radius
E_{gap}	Bifunctional oxygen catalytic potential gap
BCC	Body-centered cubic
C_0	Bulk concentration of O_2
CTAC	(1-hexadecyl) trimethylammonium chloride
C_s	Capacitance coefficient
CC	Carbon cloth
CP	Carbon paper
CDD	Charge density difference
R_{ct}	Charge transfer resistance
μ	Chemical potential
CA	Chronoamperometry
J	Current density
I_D	Current on the disk electrode
I_R	Current on the ring electrode
j_p	Current density in positive scan
j_n	Current density in negative scan
CV	Cyclic voltammetry
r_c	Critical radius

COHP	Crystal orbital Hamilton population
d_c	d-band center
DI	Deionized
DFT	Density functional theory
DOS	Density of states
D_0	Diffusion coefficient of O_2
R_D	Distance between two atoms
C_{dl}	Double-layer capacitance
EIS	Electrochemical impedance spectroscopy
ELF	Electron localization function
ECSA	Electrochemical surface area
A	Electrode surface area
n	Electron transfer number
n_{OER}	Electron transfer number during OER process
EDS	Energy-dispersive X-ray spectroscopy
H_{SOL}	Enthalpy of the constituent solvated ions
ΔS	Entropy difference
S_{SOL}	Entropy of the constituent solvated ions
J_0	Exchange current density
EXAFS	Extended X-ray absorption fine structure
F	Faraday constant
FFT	Fast Fourier transformation
FCC	Face-centered cubic
E_F	Fermi level
R_f	Fit error sm in % in the range 0-3.5 Å
GPA	Geometric phase analysis
ΔG	Gibbs free energy change
HDA	Hexadecylamine
HCP	Hexagonal close-packed
HAADF	High angle annular dark-field
HEA	High entropy alloy
HEB	High entropy boride
HEM	High entropy material

H_{HEML}	High entropy materials lattice enthalpy
H_{HEMS}	High entropy materials surface enthalpy
S_{HEML}	High entropy materials lattice entropy
S_{HEMS}	High entropy materials surface entropy
HEN	High entropy nitride
HEO	High entropy oxide
HEP	High entropy phosphide
HES	High entropy sulfide
HRTEM	High resolution transmission electron microscopy
HER	Hydrogen evolution reaction
ICPMS	Inductively coupled plasma mass spectrometry
ICP-OES	Inductively coupled plasma-optical emission spectroscopy
ICOHP	Integral projected crystal orbital Hamilton population
IFFT	Inverse fast Fourier transform
IL	Ionic liquid
R	Gas constant
GDL	Gas diffusion layer
GPE	Gel polymer electrolyte
GGA	Generalized gradient approximation
GC	Glassy carbon
GCE	Glassy carbon electrode
$E_{1/2}$	Half-wave potential
K-L	Koutecky-Levich
ρ	Lattice atomic density
u	Lattice atomic energy
LED	Light emitting diode
LIB	Lithium-ion batterie
LSV	Linear sweep voltammetry
LBFGS	Liner Broyden-Fletcher-Goldfarb-Shannon
α	Local atomic distortion
MAB	Metal-air battery
MOF	Metal-organic framework
MOR	Methanol oxidation reaction

H_{mix}	Mixng enthalpies
S_{mix}	Mixng entropies
G_{mix}	Mixng free energy
NPs	Nanoparticles
N_A	Number of active site
ODE	1-Octadecene
OAm	Oleylamine
OCP	Open-circuit potential
OER	Oxygen evolution reaction
ORR	Oxygen reduction reaction
η	Overpotential
PBE	Perdew-Burke-Ernzerhof
PBS	Phosphate-buffered saline
PE	Polyethylene
PP	Polypropylene
PVA	Poly(vinyl alcohol)
N	Population of the shell
PDS	Potential determination step
PC	Porous carbon
$E_{j=10}$	Poetntial for OER to dirve 10 mA cm^{-2}
PAW	Projected augmented wave
pCOHP	Projected COHP
PDOS	Projected DOS
QSS	Quasi-solid-state
r	Radius
RDS	Rate-determining step
RHE	Reversible hydrogen electrode
RDE	Rotating disk electrode
RRDE	Rotating ring-disk electrode
SEM	Scanning electron microscopy
STEM	Scanning transmission electron microscopy
SAED	Selected area electron diffraction
σ	Surface atomic density

TDOS	Total density of state
ΔE	Total energy difference before and after intermediates adsorption
TEM	Transmission electron microscopy
TPP	Triphenylphosphite
TOF	Turnover frequency
R_s	Uncompensated solution resistance
VEC	Valence electron concentration
vdW	Van der Waals
VASP	Vienna ab-initio simulation package
XAS	X-ray absorption spectroscopy
XANES	X-ray absorption near edge structure
XRD	X-ray diffraction
XPS	X-ray photoelectron spectroscopy
ZPC	Zinc-air pouch cell
ZAB	Zinc-air battery
ΔE_{ZPE}	Zero-point energy difference

Preface

The 4 chapters incorporated in the PhD thesis cover the work performed by the PhD candidate Ren He at the Catalonia Institute for Energy Research (IREC) in Sant Adrià de Besòs, Barcelona, in the period 2021-2024. The thesis focuses on designing advanced high entropy materials as oxygen bifunctional catalysts for air cathode in zinc-air batteries.

Chapter 1 presents a fundamental introduction to basic concepts of zinc-air batteries (ZABs) and high entropy materials (HEM). The state-of-the-art development and the challenges for HEM and ZABs are also discussed. Chapter 2 to Chapter 4 present the experimental work on the synthesis of transition metal HEMs and their application in ZABs. Chapter 2 states a low-temperature colloid method for the synthesis of CrMnFeCoNi and CuMnFeCoNi high entropy alloy (HEA) nanoparticles, identifying CrMnFeCoNi as a highly efficient bifunctional catalyst for oxygen evolution reaction (OER) and oxygen reduction reaction (ORR), outperforming other alloys and commercial catalysts, and demonstrating superior performance in ZABs. Chapter 3 focuses on the synthesis of FeCoNiMoW HEA by introducing 4d Mo and 5d W into a 3d FeCoNi alloy system. This HEA shows strong lattice distortion and modulated electronic structure resulting in a catalyst with excellent OER performance and superior bifunctional oxygen activity, demonstrating high efficiency and stability in both aqueous and solid flexible ZABs. Chapter 4 demonstrates that FeCoNiPdWP high entropy phosphides synthesized via a mild colloidal method have exceptional bifunctional catalytic performance for OER and ORR, and outstanding long-term stability in ZABs. The crucial roles of surface reconstruction and individual element contributions to catalytic activity are also discussed. After these experimental chapters, I include a discussion of the results, the thesis conclusions, and future work. Finally, I provide my curriculum vitae and publications.

Chapter 1

General Introduction

1.1 Metal air batteries (MABs)

Renewable energy plays a critical role in fostering a sustainable economy, driven by global efforts to achieve carbon neutrality and mitigate climate change.[1-3] Although fossil fuels are expected to remain a significant energy source until at least 2050, their declining net energy efficiency due to the increasing demands of extraction and processing underscores the need for alternatives.[4] Renewable technologies, particularly solar photovoltaics and wind turbines, have achieved remarkable advancements in efficiency and cost reduction, supported by technological progress and economies of scale.[5, 6] Moreover, advancements in grid-scale energy storage systems have enabled the integration of intermittent renewable energy sources, ensuring a stable power supply and facilitating the growth of electric vehicles.[7]

Lithium-ion batteries (LIBs), based on lithium-ion intercalation, have dominated portable electronics due to their superior performance over traditional batteries.[8] However, their broader adoption in energy storage is constrained by moderate energy density (~400 Wh kg^{-1}), high production costs, resource limitations, and safety concerns. These challenges have driven research into alternative rechargeable battery technologies with improved performance and sustainability.

Aqueous MABs, utilizing metals such as zinc, aluminum, magnesium, and iron, have gained attention as high-energy-density energy storage solutions for mobile and electronic applications. These systems offer advantages such as low cost, abundant resources, environmental sustainability, and improved safety.[9] Their half-open configuration enables oxygen uptake from the ambient air, contributing to their superior theoretical energy densities compared to LIBs (**Figure 1a**).[10-12] Typically, aqueous MABs consist of a metal anode, an alkaline electrolyte, and a composite air cathode comprising a catalyst layer, current collector, and gas diffusion layer (GDL). During discharge, the oxygen reduction reaction (ORR) occurs at the air cathode, while metal dissolution takes place at the anode. Conversely, the charging process involves the oxygen evolution reaction (OER) at the cathode and metal deposition at the anode (**Figure 1b**).[13] These processes, alongside their high theoretical specific and volumetric energy densities, make aqueous MABs promising candidates for next-generation energy storage systems.

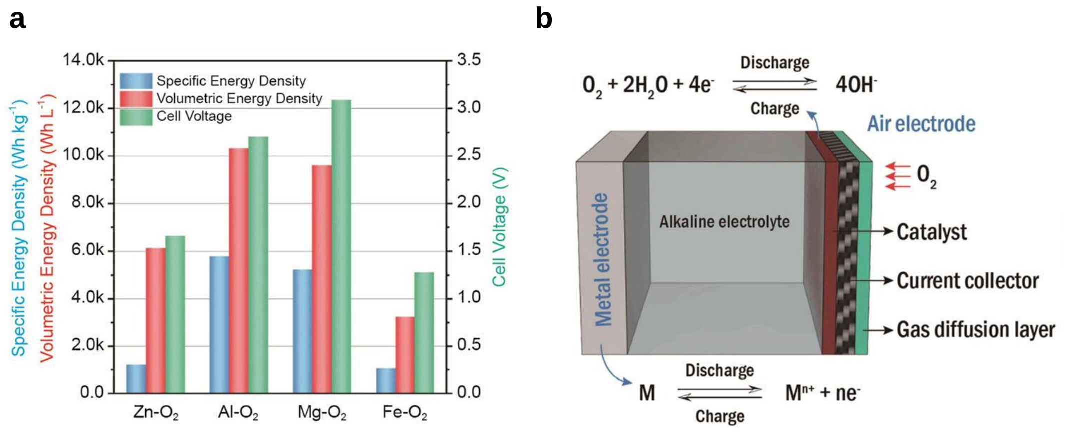

Figure 1. (a) Theoretical energy densities and cell working voltages of various aqueous MABs.[10-12] (b) Schematic operation principles of aqueous MABs.[14]

1.1.1 Zinc-air batteries (ZABs)

Among aqueous MABs, ZABs are particularly promising, offering a high theoretical specific energy density (~1218 Wh kg^{-1}) and a working voltage of ~1.66 V. With zinc being abundant and cost-effective, ZABs are positioned as a scalable, low-cost energy storage solution, potentially achieving costs below \$10 kWh^{-1}, making them attractive for applications like electric vehicles.[15] Additionally, zinc electrodes demonstrate stable and rechargeable performance in alkaline electrolytes. While aluminum-air and magnesium-air batteries exhibit higher theoretical energy densities, their practical applications are hindered by low working voltages and severe polarization in alkaline media.[11] Similarly, iron-air batteries are primarily limited to primary applications due to hydrogen evolution during charging.[16] As a result, ZABs stand out as the most economically viable and practical candidate for future large-scale energy storage systems.

ZABs have a long history, originating in 1868 as primary batteries utilizing NH_4Cl electrolytes.[17] Early designs faced challenges such as low working voltage and poor stability, which were partially addressed in 1932 when Heiser and Schumacher introduced alkaline electrolytes, significantly enhancing performance.[18] Further advancements, including improved packaging technologies and the development of gel electrolytes in 2006, expanded ZAB applications to devices like hearing aids and signaling systems while improving durability.[19]

In recent decades, advances in nanotechnology and catalytic science have driven the evolution of rechargeable ZABs. However, major challenges remain, including (i) high polarization and degradation of the air cathode, (ii) low stability and compatibility of the electrolyte, and (iii) poor electrochemical reversibility of the zinc anode. Addressing these issues requires optimizing electrocatalysts for ORR/OER at the air cathode, improving zinc anode stability, and enhancing the electrolyte-electrode interface. Achieving long-term interface stability is critical to ensuring reliable operation and unlocking the full potential of ZABs as sustainable energy storage systems.

ZABs consist of an air cathode, zinc anode, electrolyte, and separator, operating through reversible ORR/OER at the cathode and zinc dissolution/deposition at the anode (**Figure 2**). Despite a theoretical equilibrium voltage of 1.66 V (vs. reversible hydrogen electrode (RHE)), internal losses from activation, ohmic, and concentration polarization result in significantly lower practical operating voltages, limiting overall efficiency. During discharge, ZABs couple cathodic ORR with anodic zinc oxidation. Oxygen diffuses into the air cathode, where it is reduced to form hydroxide (OH^-) ions. These ions migrate to the zinc anode, where zinc oxidizes to form zincate ions ($Zn(OH)_4^{2-}$), which precipitate as zinc oxide (ZnO) upon saturation. During charging, Zn^{2+} in the electrolyte are reduced and deposited as metallic Zn on the anode, while OH^- ions at the cathode are oxidized to generate O_2.

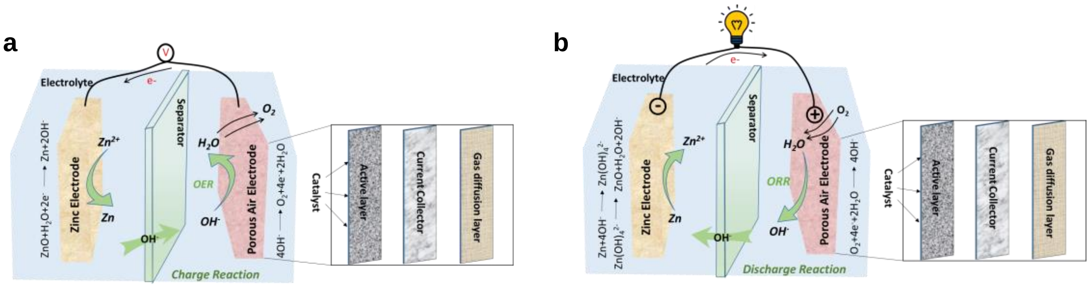

Figure 2. The schematic diagram of the mechanism for ZABs during (a) charge and (b) discharge process.

The charging-discharging performance and energy efficiency of ZABs are generally limited by the sluggish kinetics of ORR and OER at the cathode.[21] In practical applications, overcoming the thermodynamic and kinetic barriers of this process requires a certain overpotential (η). The role of oxygen electrocatalysts is critical in accelerating the ORR and OER, both of which are essential for sustainable ZAB operation. In alkaline media, oxygen electrocatalysis must ideally proceed via a four-electron pathway, as the alternative two-electron pathway generates peroxide ions (HO_2^-), which can poison the catalyst's active sites and degrade both catalytic activity and stability. The binding energies of key reaction intermediates (OOH*, O*, and OH*) during each elementary step of the reaction cannot be independently optimized, resulting in distinct rate-determining steps (RDSs). The ORR and OER proceed through different mechanisms, necessitating distinct active sites for each, as achieving an ideal oxygen binding strength for both reactions simultaneously is challenging.[22]

Commercial noble metal catalysts, such as Pt/C for ORR and Ru/Ir-based catalysts for OER, are known for their high performance. However, their limited availability and poor long-term stability pose challenges for large-scale applications. Therefore, the development of cost-effective, durable, and efficient bifunctional oxygen catalysts as alternatives to noble metals has become a key focus in both scientific research and practical applications.

Aqueous ZABs typically consist of a Zn anode, liquid electrolyte, and air cathode, with the electrolyte also serving as a separator to prevent short-circuiting (**Figure 3a**).[23] The distance between the anode and cathode influences internal resistance and redox reaction rates, with shorter distances generally enhancing performance.[24] During charging, gas bubbles form on the air cathode's active sites, negatively affecting cycling performance. The stability of the electrolyte is crucial for charge-discharge efficiency and battery lifespan. Flowing electrolytes improve electrochemical performance by reducing concentration polarization, enhancing rechargeability, and providing better stability at high current densities.[25-27] However, aqueous ZABs are susceptible to leakage, raising safety concerns.

To overcome the limitations of aqueous electrolytes, quasi-solid-state (QSS) gel polymer electrolytes (GPEs) have been introduced in ZABs, enabling flexible and stretchable designs suitable for wearable devices and robotics. QSS ZABs are available in two main configurations: sandwich-type (**Figure 3b**) and cable-type (**Figure 3c**).[10, 28] In sandwich-type ZABs, the GPE is placed between the Zn anode and air cathode, maintaining the structure of conventional aqueous ZABs and ensuring stable voltage under bending and twisting. Cable-type ZABs feature a coiled design, with the Zn anode at the center, surrounded by GPEs and the air cathode, making them ideal for applications subject to complex mechanical forces.[29] For long-term stability, it is essential to match the mechanical strength of materials and ensure good interfacial contact.[30] Performance can be further enhanced by configuring battery packs in series or parallel.[31,32]

The use of aqueous electrolytes in ZABs generally requires bulky, rigid structures and additional packaging materials, complicating structural design and limiting the potential for size reduction. Therefore, to advance the practical applications of ZABs, it is crucial to develop more compact forms such as pouch cells and coin cells.

One notable advancement is the development of 1-Ah-scale zinc-air pouch cells (ZPCs), which were achieved by simultaneously optimizing the cathode, electrolyte, and anode components (**Figure 3d**).[33] These ZPCs demonstrated exceptionally high cell-level energy densities, extended cycle life, and the ability to function across a wide range of operating temperatures, making them promising for larger-scale applications.

Coin-type ZABs, characterized by their small size and simple structure, are particularly convenient for batch assembly and industrial-scale production. [34] As shown in **Figure 3e**, coin-type ZABs maximize specific energy by filling the cell with Zn powder to the maximum allowable limit, with the metallic shell acting as the current collector. The cover of the battery contains numerous holes to facilitate oxygen input. To prevent electrolyte evaporation and extend the shelf life during storage, the coin-type ZAB is sealed with a layer of sticky gypsum.

Additionally, Schmidt and colleagues developed a micro-sized ZAB, measuring just 3×3 mm^2, using micro-imprint fabrication techniques compatible with microelectronic manufacturing processes (**Figure 3f**).[35] This chip-based ZAB exhibited excellent volumetric power density and volumetric energy density, further pushing the boundaries of ZAB miniaturization and integration with microelectronic devices.

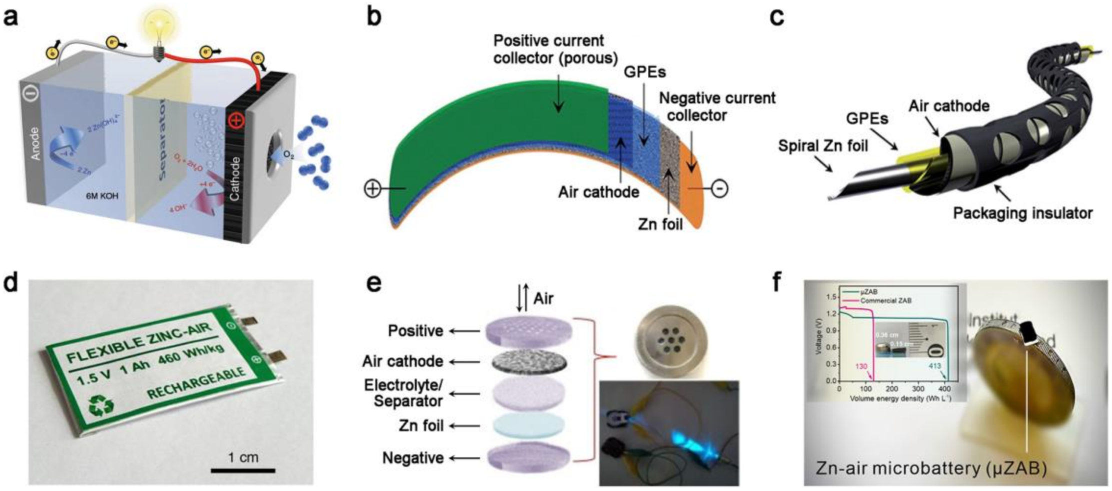

Figure 3. (a) Schematic illustration of aqueous ZABs.[23] (b) Schematic illustration of sandwich-type ZABs.[10](c) Schematic illustration of cable-type ZABs.[36] (d) Photograph of an all-solid-state ZPCs.[37] (e) Schematic illustration of coin-cell ZABs.[34] (f) Volumetric energy density of the μZAB and commercial ZAB.[35]

ZABs can be broadly categorized into alkaline and neutral types based on the pH of the electrolyte used. Alkaline ZABs, which rely on a well-established 4-electron ($4e^-$) oxygen redox mechanism, typically utilize alkali hydroxides as electrolytes. In these systems, the stable transition between Zn and ZnO is recognized as the primary reaction mechanism. Alkaline ZABs generally outperform neutral ZABs due to the stronger redox activity of oxygen and the higher ionic conductivity of alkaline environments.[38] However, alkaline ZABs face significant challenges in terms of air cathode degradation, electrolyte stability, and Zn anode reversibility in the strongly alkaline medium.

In contrast, neutral electrolytes offer improved stability by avoiding reactions with carbon dioxide (CO_2) that form carbonates, thus preserving the electrolyte's long-term stability. The reaction mechanisms in neutral ZABs are highly dependent on the specific electrolyte used. Reported neutral electrolytes include ammonium chloride (NH_4Cl) solutions, phosphate-buffered saline (PBS) solutions, and soluble zinc salt solutions.[39-42]

1.1.2 Evaluation parameters

1.1.2.1 OER evaluation parameters

i) η. The η refers to the additional potential beyond the thermodynamic potential (1.23 V vs. RHE for water splitting) required to drive the OER. Lower η s indicate higher catalytic efficiency. η is measured by finding the potential at a specific current density (e.g., 10 mA cm^{-2}) and subtracting the thermodynamic potential: $\eta = E_{measurement} - 1.23$ V (vs. RHE)

ii) Tafel slope. The Tafel slope gives insight into the kinetics of the OER process by describing how the η changes with current density. A lower Tafel slope indicates faster reaction kinetics and better catalytic performance. The Tafel slope is determined from the linear region of a plot, where the η is plotted against the logarithm of the current density (J). It is calculated as:

$$\eta = a + b\log J$$

$$a = \frac{2.303RTlogj0}{n_{OER}\mathrm{F}}$$

$$b = \frac{2.303}{n_{OER}\mathrm{F}}$$

where R is gas constant, T is absolute temperature, j_0 is the exchange current density, n_{OER} is the electron transfer number during the OER process, and F is Faraday constant (96485.3 C mol^{-1}).

iii) Faradaic efficiency. Faradaic efficiency refers to the percentage of the total charge that is used for the desired OER rather than side reactions. Faradaic efficiency is calculated by measuring the amount of oxygen evolved and comparing it to the theoretically expected oxygen based on the total charge passed:

$$\text{Faradaic efficiency (\%)} = \frac{\mathrm{E}xperimental\ O_2\ produced}{\mathrm{T}heorectical\ O_2\ produced} \times 100$$

The theoretical O_2 amount can be calculated by the integral charge content of chronoamperometry (CA) analysis or chronopotentiometry. The experimental O_2 amount by water splitting can be measured by traditional water-gas displacement method, gas chromatography, or fluorescence spectrometry.

iv) Turnover frequency (TOF). TOF represents the number of oxygen molecules evolved per active site per second. Higher TOF values indicate a more efficient catalyst in terms of the number of reactions occurring at each active site. TOF is calculated as:

$$TOF = \frac{\mathrm{J}A}{4AN_AF}$$

Where A is the electrode surface area and N_A is the number of active site.

v) Mass activity. Mass activity measures the current generated per unit mass of catalyst. It is particularly important for evaluating the efficiency of precious-metal-based catalysts. Mass activity is calculated as:

$$Mass\ activity = \frac{Current\ (A)}{\mathrm{M}ass\ of\ Catalyst\ (mg)}$$

vi) Electrochemical surface area (ECSA). The ECSA refers to the active surface area of the catalyst that is accessible for the OER. A larger ECSA usually means more active sites are available, which can enhance the reaction rate. ECSA is often evaluated using capacitance measurements from cyclic voltammetry (CV) in a non-Faradaic region, and estimating from the double-layer capacitance (C_{dl}) by using the equation:

$$ECSA = \frac{C_{dl}}{\mathrm{C}_s}$$

where C_s is the capacitance coefficient of the catalysts.

vii) Stability. The stability of an OER catalyst is critical for long-term applications. A good catalyst should be able to maintain its activity over extended periods. CA or chronopotentiometry tests are often used to measure the stability of an OER catalyst by holding it at a constant potential or current for several hours or days. Another method is repeating cycling the catalysts in a certain potential range to evaluate catalyst durability and loss in activity.

1.1.2.2 ORR evaluation parameters

i) Onset potential. The onset potential refers to the potential at which the ORR begins to occur, usually at the current density of 0.1 mA cm^{-2}. A higher onset potential, closer to the theoretical value (1.23 V vs. RHE), indicates better catalytic activity.

ii) Half-wave potential ($E_{1/2}$). The $E_{1/2}$ is defined as the potential at which the current density reaches half of the maximum value in the polarization curve. It is an important measure of the catalyst’s activity, with a higher $E_{1/2}$ indicating stronger ORR activity. This value is commonly compared among different catalysts to determine their relative performance.

iii) Limiting diffusion current density. The limiting diffusion current density represents the maximum current density achievable, which is limited by the diffusion rate of oxygen to the catalyst surface. A higher limiting diffusion current density indicates that the catalyst facilitates efficient oxygen transport and has high ORR performance, especially under mass-transfer-limited conditions.

iv) Electron transfer number (n). The ORR can proceed via a two-electron pathway (leading to the production of hydrogen peroxide) or a four-electron pathway (leading to the production of water). A higher number of electrons transferred, ideally close to four, suggests that the catalyst favors the more efficient four-electron pathway, leading to fewer unwanted by-products and higher efficiency. n can be calculated by the rotating disk electrode (RDE) method by using Koutecky-Levich (K-L) or the rotating ring-disk electrode (RRDE) method.

K-L equation:

$$\frac{1}{J}=\frac{1}{J_L}+\frac{1}{J_K}=\frac{1}{B\omega^{\frac{1}{2}}}+\frac{1}{J_K}$$

$$B=0.62\text{nF}C_0D_0^{\frac{2}{3}}V^{-\frac{1}{6}}$$

where J_K is the measured current density, J_L is the limiting current density, ω is the angular velocity of the disk, C_0 is 1.2×10^{-6} mol cm^{-3}, representing the bulk concentration of O_2, D_0 is 1.9×10^{-5} cm^2 s^{-1}, representing the diffusion coefficient of O_2 in 0.1 M KOH, V is 0.01 cm^2 s^{-1}, representing the kinematic viscosity of the electrolyte. Thus, n can be deduced from the slope of the linear plot of J^{-1} versus $\omega^{-1/2}$.

The RRDE method directly measures the amount of hydrogen peroxide produced during the ORR and uses this information to determine the number of electrons transferred. By simultaneously measuring the current on the disk electrode (I_D) and the ring electrode (I_R), the following formula can be used to calculate the n:

$$n = 4 \times \frac{I_D}{I_D + I_R/N}$$

N is the collection efficiency of the ring (typically provided by the instrument, usually between 0.2 and 0.4)

v) Hydrogen peroxide yield. The hydrogen peroxide yield is typically calculated using the data obtained from the RRDE. The H_2O_2 yield is calculated as:

$$H_2O_2(\%) = 200 \times \frac{\frac{I_R}{N}}{I_D + \frac{I_R}{N}}$$

vi) Stability. Stability is a critical metric, particularly for long-term applications. It can be evaluated through prolonged cycling tests or by holding the catalyst at a constant potential over time while monitoring any loss in activity. A stable catalyst will maintain its performance with minimal degradation over extended periods of use, which is essential for practical applications.

1.1.2.3 Bifunctional properties evaluation parameters

The bifunctional oxygen catalytic potential gap (E_{gap}) between the poetntial for OER to dirve 10 mA cm^{-2} ($E_{j=10}$) and the $E_{1/2}$ for ORR. The lower E_{gap} value implies better bifunctional catalytic properties.

1.1.2.4 ZAB evaluation parameters

i) Open-circuit potential (OCP). OCP is the voltage of a ZAB is in an open-circuit state. It reflects the thermodynamic driving force for the electrochemical reaction occurring in the cell and represents the maximum voltage the battery can provide.

ii) Energy density. Energy density refers to the amount of energy a battery can store relative to its weight (gravimetric energy density, Wh kg^{-1}) or its volume (volumetric energy density, Wh L^{-1}). It is calculated as:

$$\begin{aligned} Energy\ density &= \frac{\mathrm{t}otal\ energy\ output\ (Wh)}{\mathrm{M}ass\ (Kg)\ or\ volume\ (L) of\ the\ battery} \\ &= \frac{average\ discharg\ volyage\ (V) \times capacity(Ah)}{\mathrm{M}ass\ (Kg)\ or\ volume\ (L) of\ the\ battery} \end{aligned}$$

iii) Power density. Power density refers to the rate at which a battery can deliver energy relative to its weight or volume, often expressed as W kg^{-1} (gravimetric) or W L^{-1} (volumetric). It reflects the battery's ability to provide high power output over a short period. It is calculated as:

$$Power\ density = \frac{\mathrm{d}ischarge\ power\ (W)}{\mathrm{M}ass\ (Kg)\ or\ volume\ (L) of\ the\ battery}$$

$$= \frac{Voltage\ (V) \times current\ density\ (A\, m^{-2})}{\mathrm{M}ass\ (Kg)\ or\ volume\ (L) of\ the\ battery}$$

iv) Specific capacity. Specific capacity refers to the total charge a battery can store per unit mass of the active material (typically the zinc anode in a ZAB), usually expressed in mAh g^{-1}. It is a measure of the battery's ability to hold charge relative to the amount of zinc used. It is calculated as:

$$Specific\ capacity\ (mAh\ g^{-1}) = \frac{\mathrm{T}otal\ charge\ (mAh)}{\mathrm{M}ass\ of\ zinc\ (g)}$$

v) Stability and durability. The ZABs can cycle for long-term cycling without significant capacity degradation.

1.1.3 Challenges and progress on ZABs

ZAB technology faces significant challenges that must be addressed before it can achieve commercial viability. One of the primary obstacles is the short operational lifespan of ZABs due to the deactivation leading to low current density and high η. Additionally, the porous air electrode is structurally fragile resulting in mechanical degradation and loss of catalytic activity, which ultimately shortens the battery's lifespan. Another critical issue is the formation of zinc dendrites and unwanted parasitic reactions, such as hydrogen evolution reactions (HER). Furthermore, the electrolyte itself presents several technical challenges, including inadequate ionic conductivity, increased zinc solubility (which diminishes the available active surface area of the zinc anode), and evaporation, all of which reduce the practical usability of rechargeable ZABs. To overcome these challenges, further research is necessary. This includes exploring new catalytically active materials, optimizing electrode structures, improving electrolyte compositions, and developing more stable zinc anode materials.[43, 44]

In terms of Zn anode, enhancing the reversibility of the Zn anode and addressing challenges like dendrite formation, passivation, side reactions (such as HER), and corrosion are key to improving the operational lifespan of ZABs. Traditional Zn electrodes are typically made from plates, foil, or compressed particles. 3D porous structures have been investigated to be a good solution to increase surface area and reduce dendrite formation by enhancing contact with the electrolyte. For example, Parker et al. achieved a Zn utilization rate of nearly 90% in a primary ZAB by using a 3D Zn electrode with interconnected Zn domains and a monolithic void space.[45] Another study showed that 3D Zn electrodes exhibited uniform ZnO deposition within voids.[46] Another strategy is using coatings or composite structures through alloying or chemical deposition as the Zn anode. [47, 48] Sun et al. created a Cu/Zn composite anode using a displacement reaction, which improved the corrosion resistance by forming a CuZn/Zn composite layer during cycling. [49] Chen et al. deposited a Cu_xZn_y alloy layer on a Zn foil anode, which inhibited dendrite growth and enhanced electrochemical performance.[50] Aremu et al. achieved a high-capacity ZAB with a long cycling performance with a Zn anode coated with bismuth oxide, potassium sulfide, and lead(II) oxide.[51] Furthermore, metal coatings like Al_2O_3, CuO, and TiO_2 have shown promise in improving ZAB performance.[52-55]

For electrolytes, ZABs usually use KOH or NaOH mixed with Zn salts. Since KOH has superior ionic conductivity, higher oxygen diffusion coefficient, and lower viscosity than NaOH, it is more commonly used.[56] Additionally, KOH helps mitigate carbonate precipitation, a common issue in ZABs, by forming more soluble products, such as potassium carbonate (K_2CO_3) and potassium bicarbonate ($KHCO_3$), compared to sodium-based compounds. Additionally, the volatilization and toxicity of alkaline electrolytes, particularly from CO_2 interaction, limit charge-discharge efficiency and lifespan. To overcome these issues, acidic and neutral electrolytes have been explored to improve the reversibility of zinc anodes. [57, 58] Non-aqueous ionic liquids (ILs) have emerged as promising alternatives. Studies have shown that IL-based electrolytes can suppress HER and dendrite growth, improving ZAB efficiency. For example, Ma et al. demonstrated that using $[EMIm]BF_4$-$Zn(BF_4)_2$ as an electrolyte with a cobalt hexacyanoferrate cathode led to significant improvements in ZAB performance, including a capacity retention of 98% over 40,000 cycles.[62]

In ZABs, separators act as barriers to prevent short circuits between the Zn and air electrodes while allowing ion transport. These separators need to be electrically resistant, ionically conductive, and mechanically robust to avoid issues like zinc dendrite formation. Common materials include polyethylene (PE), polyamide, and polypropylene (PP), which retain electrolytes and support OH^- transport. [63] To improve separator performance, surface functionalization techniques, such as sulfonation and surfactant treatments, enhance hydrophilicity and ionic conductivity. For example, sulfonated PP/PE separators showed improved conductivity and doubled ionic conductivity, achieving power densities of 27 to 38 mW cm^{-2}.[64,65] Inorganic polymer-based separators, offer superior thermal stability compared to organic counterparts. For example, a ZAB using a 5-µm MCM-41 membrane on the zinc electrode demonstrated a power density of 32 mW cm^{-2} and an energy density of 300 Wh L^{-1}, comparable to commercial zinc-air button cells.[66] Other strategies include PP membrane coatings with copolymers for anionic exchange and Nafion impregnated with anion-repelling agents.[67,68]

The air electrode is pivotal in determining ZAB performance, as it influences the kinetics of oxygen reactions. Slow kinetics during ORR and OER contribute to high polarization and poor reversibility, motivating the development of efficient bifunctional oxygen catalysts. Active layer, GDL, and the current collector are the three main components in air cathode. Porous carbon materials with a wet-proofing binder (such as polytetrafluoroethylene) are usually used to support the active layer, which provides a hydrophobic surface for the active layer to have better contact with electrolyte.[69] The active layer is used to catalytic the oxygen to finish the charge and discharge process[70-72-75] Effective catalysts, with high activity and stability, are essential for practical ZAB use.[76-79] Oxygen electrocatalysis occurs at the three-phase interface (gas, liquid, and solid), where catalyst activity depends on unsaturated coordination sites. Thus, optimizing the electronic structure and surface properties of the catalyst is crucial to enhance adsorption, desorption, and reduce energy barriers, improving reaction kinetics. Materials such as metal oxides, hydroxides, sulfides, and carbon composites have been extensively studied for their potential as bifunctional oxygen electrocatalysts, with ongoing efforts to enhance ZAB performance.[80-83]

1.2 High entropy materials (HEMs)

HEMs are an emerging and distinct class of compounds typically characterized by the presence of five or more principal elements randomly distributed within the structure. The term 'high entropy alloy' (HEA) was introduced by Yeh et al. in 2004 when rationalizing the potential stabilization of a solid solution through the entropic contribution to the system’s total free energy.[84] The authors postulated that in a solid solution with a sufficient number of elements, the entropy term could be large enough to counterbalance the enthalpy of formation for all possible intermetallic phases. They estimated that combining five elements in equiatomic ratios would be sufficient to overcome the enthalpy of formation for most intermetallic phases. This condition, which was from the beginning relaxed to at least 5 elements with ratios in the range between 5 and 35 at.%, has been empirically observed not to consistently result in the formation of a solid solution. Nevertheless, this criterion has been widely accepted and adopted as the definition for HEAs and later HEMs.

HEAs challenged conventional alloy design principles and thus experienced slow development in the early 2000s. However, during the mid-2010s, the field of HEAs experienced a surge in recognition and attention. This was marked by the development of multiple novel alloy compositions, the comprehensive characterization of their properties, and the identification of new applications. Beyond HEAs, other high-entropy compounds began to attract interest, including high entropy oxides (HEOs),[85-89] high entropy phosphides (HEPs),[90] high entropy sulfides (HESs),[91, 92] high entropy nitrides (HENs),[93, 94] and high entropy borides (HEBs),[95, 96] among many others.[97-101] Simultaneously, significant theoretical and experimental efforts have been dedicated to the investigation of the fundamental science behind HEMs, focused on elucidating their formation and stabilization mechanisms,[102-107] as well as identifying the factors that contribute to their distinctive functional properties.[108-113]

HEMs provide exceptional flexibility in tailoring their composition, enabling optimization for diverse applications. Initially recognized for their superior mechanical properties, HEMs have gained significant attention as structural materials. More recently, their potential has been recognized in supporting the transition to renewable energy, as they contribute to the development of various key technologies based on electrochemical processes. These include catalysis, electrocatalysis, photocatalysis, batteries, supercapacitors, and photovoltaics. Additionally, HEMs have promising applications in memory devices, biomedical fields such as bone implants and coatings, thermoelectrics, aerospace, surface treatments, and even nuclear reactors, among others.[114-131]

1.2.1 The core effect of HEMs

The unique design principles of HEA materials enable the creation of a large number of catalytically active sites, effectively addressing the limitations typically associated with the relationship between catalyst structure and activity.[132,133] In addition to the broad tunability achieved through composition control, the remarkable catalytic performance of HEAs can be attributed to four key effects (**Figure 4**): the high entropy effect in thermodynamics, the significant lattice distortion in structure, the slow diffusion in dynamics, and the "cocktail" effect in performance.[134, 135]

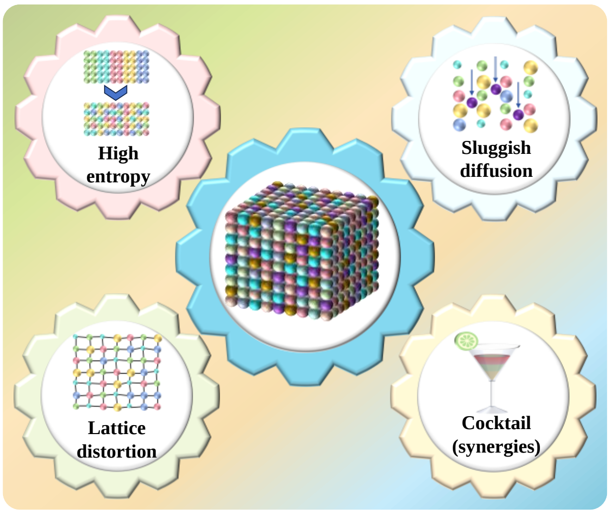

Figure 4. Schematic illustration of the four core effects of HEMs.

The high configurational entropy of HEMs was the first and most prominent characteristic identified in these materials. This high entropy promotes a homogeneous atomic arrangement with a single solid crystal structure, such as body-centered cubic (BCC), face-centered cubic (FCC), or hexagonal close-packed (HCP),[136-138] reducing the thermodynamic driving force for phase segregation. HEMs are also characterized by sluggish atomic diffusion, contributing to their exceptional mechanical, structural, and chemical stability. The atomic size mismatch among different elements and the resulting local disorder in the crystal cause subtle lattice distortions, which are influenced by the specific composition and proportions of elements. These lattice distortions impede the movement of dislocations, leading to solid solution strengthening.[139, 140] Additionally, lattice distortion affects the material's response to stress and strain, significantly influencing its mechanical behavior.[115, 141-144] Moreover, the lattice distortion impacts the electronic properties, particularly the density of states (DOS) near the Fermi level (E_F) and the degree of electron localization/delocalization. Lattice distortion can also introduce defects that act as a source or trap of charge carriers, thereby affecting the overall electronic behavior. Beyond these factors, within the socalled 'cocktail effect' a wide range of properties arising from the virtually unlimited potential combinations of elements in HEMs have been encompassed. As a result, these materials exhibit enhanced functional properties, including relatively low thermal conductivity,[127, 128] resistance to wear and corrosion,[145, 146] and unique magnetic,[147-149] electronic,[150, 151] and catalytic performance.[115]

1.2.2 Synthesis methods of HEMs

In several of these applications, high surface area materials are essential to maximize interactions with the surrounding media. Additionally, the availability of the HEMs in the form of small particles is particularly advantageous for processing. As a result, the development of HEM nanoparticles (NPs) has become a major focus in advanced materials science and engineering communities.[152-156] However, producing HEM particles with dimensions in the nanometer-scale regime is a challenging task. Typically, high temperatures are required to maximize the entropic contribution, which is considered essential for stabilizing the multi-component mixtures in HEMs. On the other hand, high temperatures also enhance atomic diffusion and crystal growth, which is detrimental to the synthesis of NPs with controlled parameters. As a result, some of the conventional methods for synthesizing NPs may not be suitable for producing HEM NPs or may require significant optimization, particularly when aiming for precise control over the size, shape, phase, and composition of the HEM NPs.

As shown in **Figure 5**, the synthesis method could be divided into two main categories: top-down and bottom-up approaches.

Figure 5. Schematic overview of the different approaches for synthesizing HEM NPs.

1.2.2.1 Top-down strategies

A straightforward strategy to obtain HEM NPs, when bulk HEMs produced by conventional high-temperature solid-state reaction strategies are available, is to break down the bulk material into smaller pieces or disintegrate and reconstruct it into NPs. The composition and crystal structure of the HEM NPs produced through these top-down approaches generally remain similar to the original bulk material, although some variations may occur, particularly due to chemical contamination and structural defects introduced during the processing. Additionally, certain elements might be lost during the disintegration process. Top-down methods generally allow high NP production throughput and yields. As a drawback, top-down approaches rely on the use of high-temperature processes to produce the precursor bulk HEM and require additional energy input to break it, which strongly reduces the overall energy efficiency of the process. All top-down methods for producing HEM NPs begin with the synthesis of a bulk HEM target or precursor. From this common starting point, two main pathways emerge for reducing the particle size to the nanoscale. The first pathway involves the direct physical or chemical fragmentation of the bulk HEM into smaller particles, which typically preserves the material's original crystal structure and composition. The second pathway involves the ablation or disintegration of the bulk HEM, followed by its rapid reconstruction into smaller particles, often in a high-energy environment, to maintain the random distribution of elements characteristic of HEMs.

The simplest strategy to produce HEM NPs from bulk HEMs is to fragment the material into smaller pieces. This can be achieved through various methods (**Figure 6**): grinding or milling, which breaks the material without controlling the fragmentation planes; exfoliating along specific weak planes to produce NPs with a nanoplate or nanosheet morphology; or selectively dealloying or etching the HEM. Ablation strategies involve disintegrating a target bulk HEM into atoms or clusters by applying a physical shock, and then rapidly reconstructing it into a nanostructured HEM with the same or similar composition as the target material. Ablation strategies are widely recognized as a promising method to synthesize HEM NPs because of their high energy density and rapid heating/cooling process, which can effectively prevent phase separation during bulk HEM processing. These strategies include electrical discharge ablation using an electric arc, laser ablation that uses an electromagnetic pulse, and sputtering or ion beam ablation using ions to break the precursor bulk HEM into little pieces (**Figure 6**). The process must maintain the random element distribution characteristic of the HEM. Therefore, either moderate energies should be used to avoid generating secondary phases, or high temperatures should be reached to preserve the high entropic term that a priori stabilizes the HEM phase.

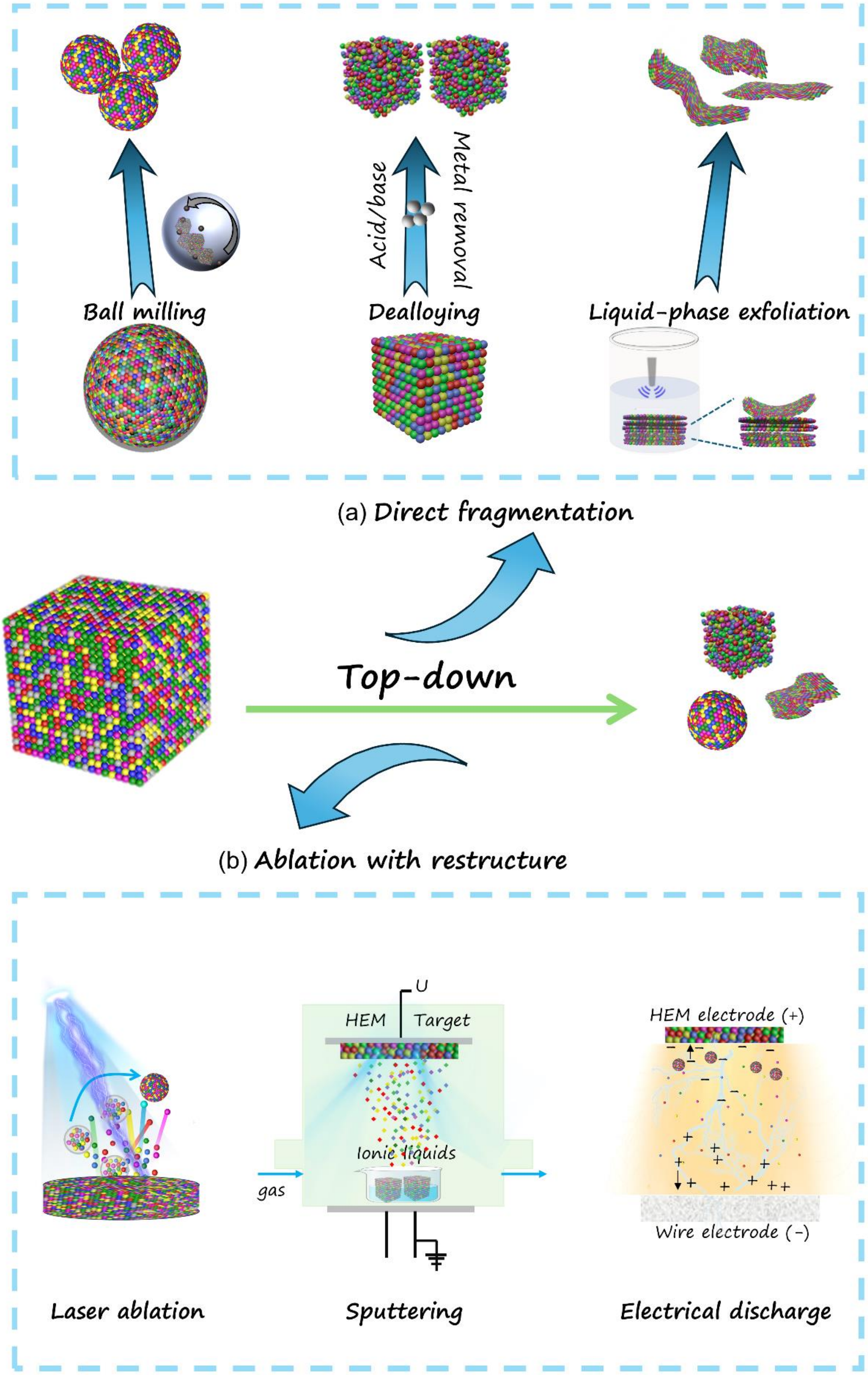

Figure 6. The synthesis approaches for HEM NPs with top-down strategies.

1.2.2.2 Bottom-up strategies

Bottom-up methods directly produce HEM NPs through the reaction of ionic, atomic, or molecular species. These approaches are generally more energy efficient than top-down methods, as they usually involve fewer steps and leverage the shorter-range atomic order inherent in NPs, thus avoiding the substantial energy required to produce and subsequently break down bulk materials.

However, a key challenge in the bottom-up synthesis of HEM NPs lies in balancing the a priori conflicting requirements for HEM phase formation and NP size stabilization. Achieving a stable HEM phase often requires high temperatures to maximize the entropic contribution, while producing NPs with tuned particle size demands moderate temperatures to restrict atomic diffusion and limit crystal growth. Indeed, NPs are inherently metastable: they are susceptible to dissolution when their radii fall below a critical size, yet are prone to grow uncontrollably when they exceed that threshold. To restrict such growth, it is essential to manage the supply of reactants to the NPs, minimize Ostwald ripening by limiting atomic diffusion, and prevent NP aggregation and coalescence by inhibiting particle interactions. Therefore, selecting the appropriate high-temperature conditions that promote HEM phase formation while simultaneously restricting NP growth requires a delicate balance.

Beyond high-temperature processes that focus on entropy-driven formation and stabilization of HEM phases, the synthesis of HEM NPs can also be kinetically driven at lower temperatures. These kinetically driven NPs are stabilized by the high energy barrier required for full redistribution of the constituent atoms. Additionally, the high energy cost of generating the additional surfaces and interfaces associated with the segregation of multiple phases may play a significant role in both the synthesis and stabilization of HEM NPs. Therefore, three general bottom-up strategies can be distinguished for producing HEM NPs, depending on whether HEM phase formation is governed by entropy, kinetics, or enthalpy (**Figure 7**).

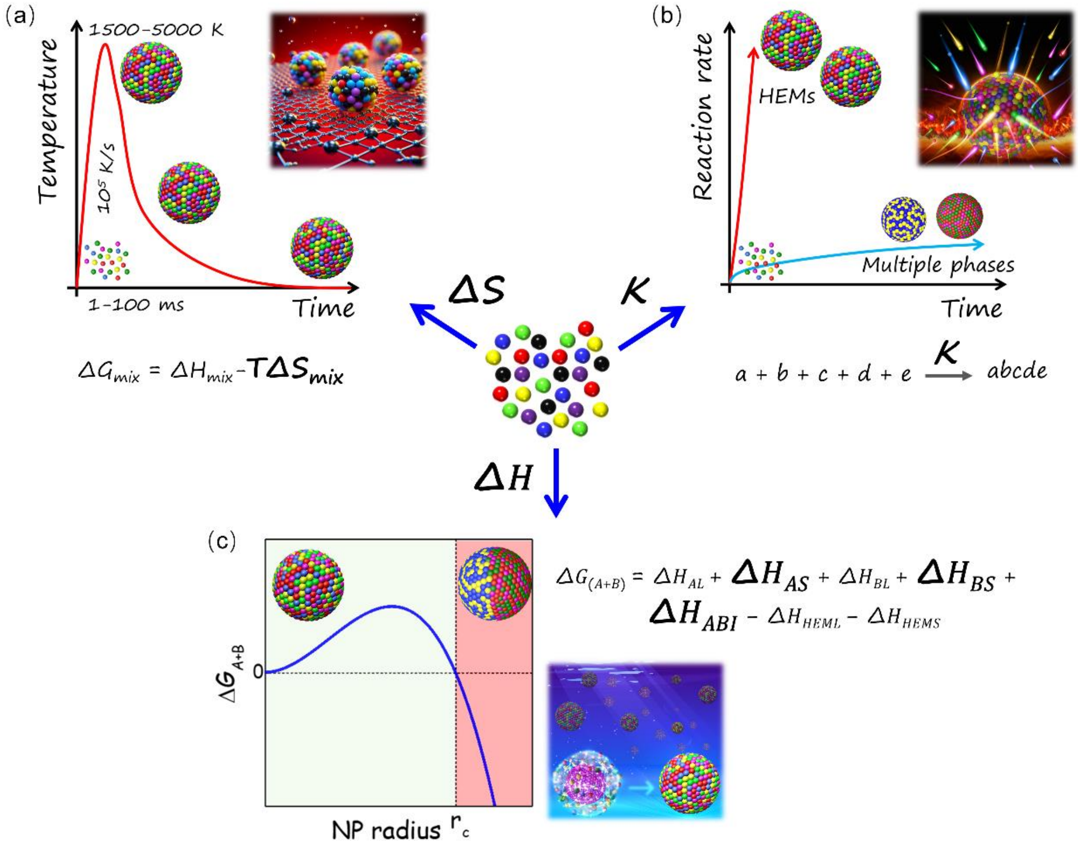

Figure 7. Scheme of the three main bottom-up strategies to directly produce HEM NPs from a mixture of atomic, ionic, or molecular precursors: (a) entropy-driven; (b) kinetics-driven; and (c) enthalpy-driven.

The first strategy employs the high-temperature conditions commonly used in bulk HEM synthesis while controlling particle size by limiting reactant availability and preventing NP Ostwald ripening and coalescence. This size limitation can be achieved in several ways: (i) shortening the reaction time to reduce diffusion distances; (ii) restricting precursor mobility by dispersing atomic/ionic/molecular precursors onto high-surface-area supports, within polymers, templates, or solvent droplets before initiating high-temperature crystallization; (iii) localizing the energy input to confine the reaction volume; and (iv) combining high-energy HEM formation with milling processes to disrupt large crystal growth.

The second strategy relies on kinetically driving HEM NP production, where atoms are prevented from arranging into their thermodynamically preferred configurations due to insufficient time or energy. This approach avoids the need for a significant entropic contribution, i.e. high temperatures. It requires a homogeneous dispersion of reactants, achievable using a suitable medium such as a solvent where precursors are dissolved, a gas where gaseous or ionic reactants are combined, or a solid with simultaneous milling to overcome mass transport limitations. Three main approaches can be used for this strategy: (i) preassembling different components at low temperatures, followed by annealing at moderate temperatures that are sufficient for precursor reaction and HEM formation while remaining low enough to prevent phase segregation; (ii) simultaneous assembly and reaction of precursors via rapid, concurrent reduction or reaction of a homogeneous distribution of primary elements, achieved by rapid heating, the addition of a strong chemical reductant/reactant or injecting charge at a proper potential; and iii) using highly diluted solutions to minimize collisions and interactions between species that have the highest affinity for one another, thereby reducing phase segregation and promoting uniform element distribution.

A third strategy involves the enthalpy-driven formation of HEM NPs, which capitalizes on the significant contribution of surface and interface energies to the total energy of a NP. As particle size decreases, the influence of these energies becomes increasingly dominant, leading to a critical radius (r_c) below which the formation of a single-phase HEM NP becomes more favorable than the formation of multiple phases, which would involve larger cumulative surface and interface energies. In such cases, the reduction of interfacial energy can drive the merging of phases into a homogenous HEM structure, stabilizing the NP. While pinpointing the precise mechanism behind HEM phase formation is highly challenging, and reports of enthalpy-driven synthesis schemes for HEM NPs are very rare, there are clear examples where enthalpy seems to play a dominant role. These include processes involving the sequential addition of elements into pre-formed nuclei, the transformation of heterostructured or binary NPs into HEM phases through phase merging, or the integration of additional elements via ion exchange or galvanic replacement, typically at or near ambient temperatures. These cases highlight the role of enthalpy in driving HEM NP formation, even under conditions where high-temperature entropic stabilization is not feasible.

The first bottom-up strategy designed for producing HEM NPs mirrors the methods initially developed for bulk HEMs, where entropy is considered the primary driver for HEM phase formation. In this approach, high temperatures are employed to maximize the mixing entropy in the Gibbs free energy equation. However, to prevent excessive particle growth, strategies must be implemented to restrict reactant supply and minimize particle interactions. These strategies include ultrafast processing to limit growth time, highly dispersing or confining reactants to control the available material for NP growth, localizing energy input, and combining HEM formation with particle fragmentation to maintain nanoscale dimensions (**Figure 8**).

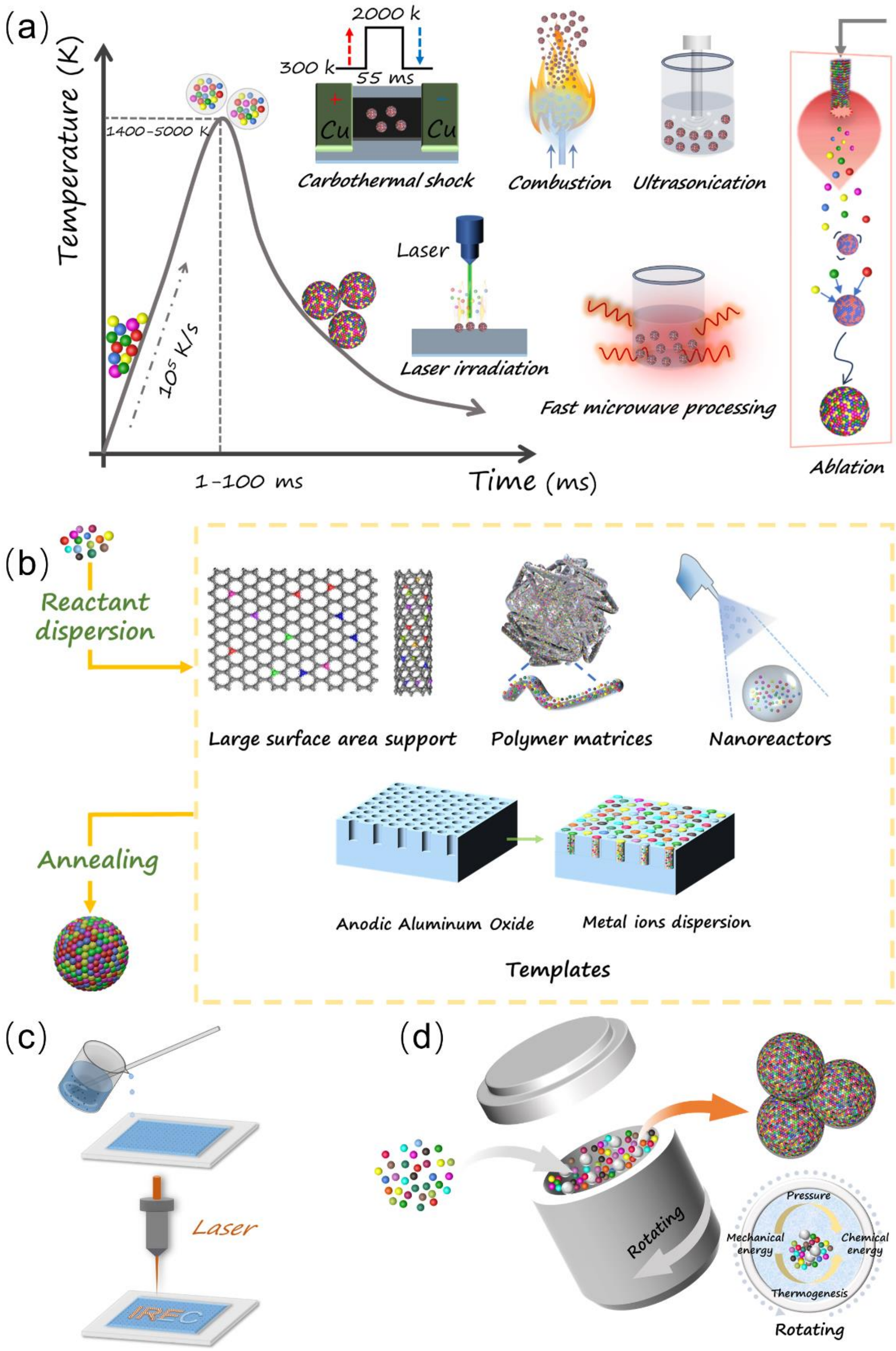

Figure 8. Scheme of the high-temperature processing strategies used to produce HEM NPs limiting NP growth (a) using ultrafast thermal processing, (b) dispersing the reactants, (c) localizing energy input, and (d) mechanochemical method.

An alternative to the high-temperature processing typically used to enhance the entropic term for thermodynamically driven HEM growth is to kinetically drive the process. Kinetically driven approaches focus on rapidly reacting different elements to prevent the system from settling into more thermodynamically stable phases. For successful HEM NP formation, it is crucial that all reagents encounter each other and react simultaneously, enabling the direct formation of the HEM phase while bypassing unwanted intermediate phases. Kinetic control of HEM NP formation can be achieved through three main approaches: i) pre-condensing a random element dispersion into precursor particles followed by crystallization at moderate temperatures; ii) fast triggering the reaction of a homogeneous dispersion of elements through high reaction temperatures, rapid addition of a highly reactive precursor or strong reducing agent, applying a reducing plasma, or injecting charge at a suitable potential; iii) using a highly diluted precursor solution to minimize the probability of interaction of affine species. Specifically, it will touch on the rapid heating rates achievable through fast-moving bed pyrolysis, but the main emphasis will be on solution-based strategies. The most evident examples of kinetically-driven HEM formation involve synthesizing HEM NPs in solution, where NP growth is constrained by moderate temperatures and the natural phase separation between evolving nuclei in the liquid phase (**Figure 9**). These conditions allow for controlled, simultaneous reactions that favor the formation of HEM NPs without the need for high entropic contributions. The primary challenge, instead, lies in balancing the reactivity and interaction of the different precursors.[157]

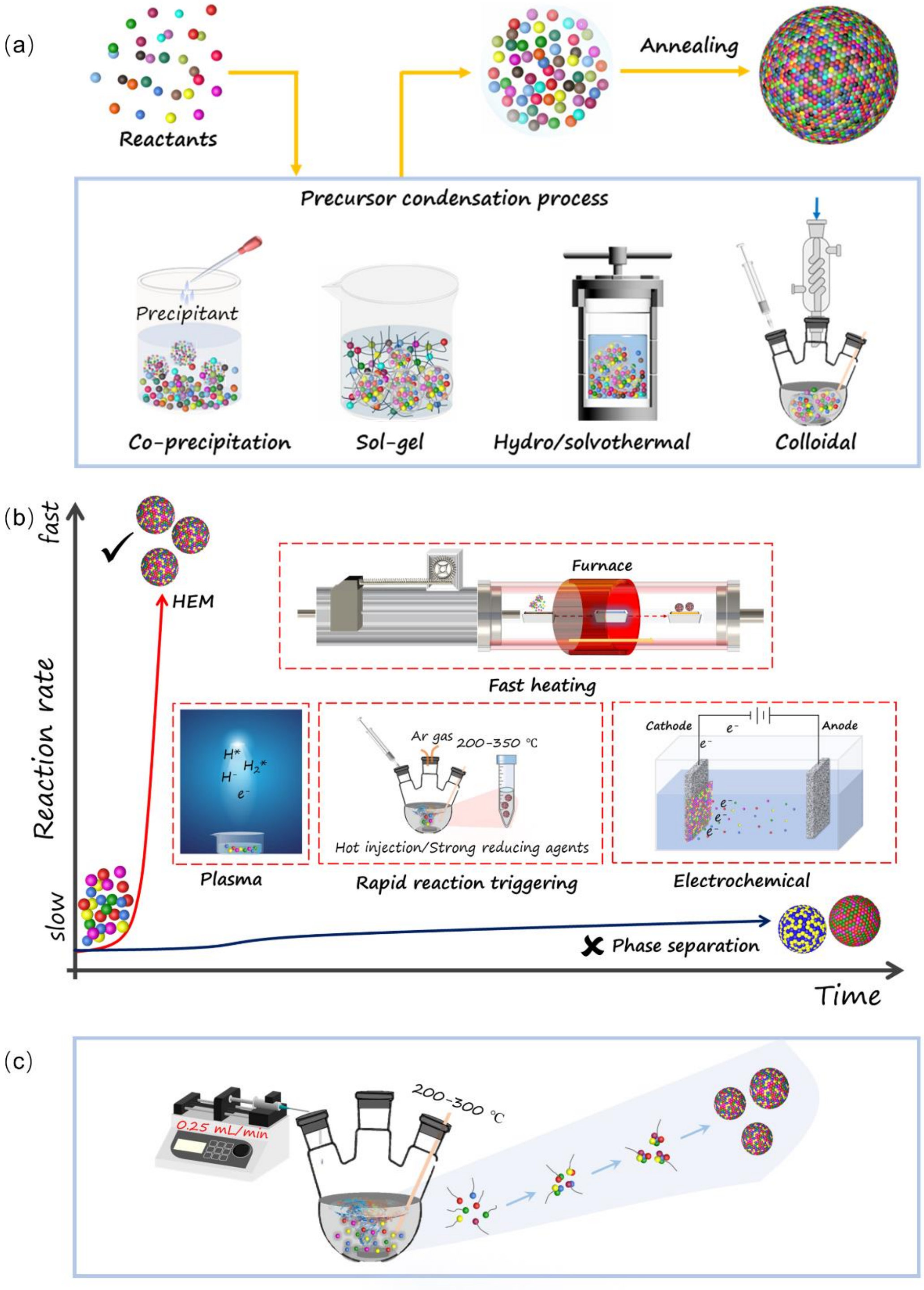

Figure 9. HEM NPs produced strategy by kinetic-driven process. (a) Condensing the different elements into precursor NPs with different methods, followed by a crystallization treatment at a moderate temperature, preventing NP growth and phase separation. (b) Fast reaction at moderate temperature. (c) Using a highly diluted solution to minimize precursor collisions.

Initial attempts to synthesize HEM NPs directly from atomic/ionic/molecular precursors (bottom-up) closely followed the methodologies used for bulk HEMs, based on the assumption that the high entropic contribution would stabilize the multielement phase against potentially more thermodynamically stable phases with lower formation enthalpies. However, unlike bulk synthesis, these NP-focused approaches incorporated additional strategies specifically aimed at preventing excessive growth. A subsequent common approach aimed at kinetically driving HEM NP formation aided by the preorganization of a homogeneous mixture of the elements, triggering a rapid reaction, or minimizing interactions between affine elements.

Over the past two decades, numerous studies have suggested that thermodynamically driven HEM formation can occur with minimal contribution from entropy. Indeed, the enthalpy change associated with forming a HEM from a homogenous mixture of elements can be significantly lower than the energy required to form multiple segregated phases in NP form, where surface, interphase, and solvation energies are substantial. Additionally, enthalpy may play a critical role not only in driving the formation process but also in ensuring stability at ambient temperature, where the contribution of entropy is secondary, for HEM NPs produced at higher temperatures.

In contrast to the synthesis of bulk HEMs where the free energy of mixing, derived from the enthalpy and entropy of mixing ($\Delta G_{mix} = \Delta H_{mix} - T\Delta S_{mix}$), has traditionally been considered the key factor in determining the HEM phase formation, the growth of HEM NPs from a homogeneous mixture of precursors requires consideration of additional factors. In the growth of a HEM NP from a uniform metal ion solution:

$$\Delta G_{HEM} = \Delta H_{HEML} + \Delta H_{HEMS} - \Delta H_{SOL} - T(\Delta S_{HEML} + \Delta S_{HEMS} - \Delta S_{SOL})$$

Where ΔH_{HEML} and ΔH_{HEMS} are the HEM lattice and surface enthalpies, ΔH_{SOL} is the enthalpy of the constituent solvated ions, and ΔS_{HEML}, ΔS_{HEMS}, and ΔS_{SOL} are the corresponding entropies. The change of entropy associated with the formation of a HEM from a uniform metal ion solution at ambient temperature is negligible. Thus, considering the growth of a spherical HEM NP with radius r, lattice atomic density ρ, surface atomic density σ, average surface atomic energy γ, and lattice atomic energy u, from a metal ion solution with average ionic energy, i.e. chemical potential, μ, the total energy of the system can be expressed as follows:

$$\Delta G_{HEM} = 4\pi r^2\sigma\gamma + \frac{4}{3}\pi r^3\rho u - \left(4\pi r^2\sigma + \frac{4}{3}\pi r^3\rho\right)\mu$$
$$= 4\pi r^2\sigma(\gamma - \mu) + \frac{4}{3}\pi r^3\rho(u - \mu)$$

As expected, the growth of a HEM can be energetically favored ($\Delta G_{HEM} < 0$) only when $u < \mu$, i.e. when the energy per atom within the HEM lattice is lower than within the solution. In this case, when $u < \mu$, the growth of a bulk HEM, i.e. $r\rightarrow\infty$, is always energetically favored. However, if the surface energy per atom is higher than the μ, as is often the case, a r$_c$ exists below which the formed nuclei are unstable against dissolution (**Figure 10a**). This r$_c$ is determined by the balance between the surface energy, which favors dissolution, and the bulk energy, which favors growth:

$$r_c = \frac{3\sigma(\gamma - \mu)}{\rho(\mu - u)}$$

To evaluate the energetically more favorable scenario, either the growth of a homogeneous HEM or the formation of multiple phases, we compare the Gibbs free energy of a spherical HEM NP with that of a similar NP containing two distinct phases, A+B. This comparison also determines the stability of an already formed HEM NP against phase segregation. Assuming the entropy change is negligible at ambient temperature, the difference in Gibbs free energy can be expressed as:

$$\Delta G_{A+B} = \Delta H_{AL} + \Delta H_{AS} + \Delta H_{BL} + \Delta H_{BS} + \Delta H_{ABI} - \Delta H_{HEML} - \Delta H_{HEMS}$$

Assuming an interphase energy lower than the surface energy, the most energetically favorable scenario for the formation of A+B is when the two phases maintain the spherical morphology, so the overall surface area remains constant, and only an interphase is created between the two materials. In this case, assuming the simplified case of equal volumes for the two phases and similar surface and bulk atomic densities, the change in Gibbs free energy for segregation can be expressed as:

$$\Delta G_{A+B} = 2\pi r^2\sigma\left(\gamma_A + \gamma_B + \frac{\gamma_I}{2} - 2\gamma_{HEM}\right) + \frac{2}{3}\pi r^3\rho(u_A + u_B - 2u_{HEM})$$

As expected, for a bulk HEM ($r\rightarrow\infty$), the segregation of the two phases is energetically favorable when the average lattice energy of the segregated phases is lower than that of the HEM ($u_A + u_B < 2u_{HEM}$). However, in HEM NPs, surface and interface energies become significant, leading to a r below which the HEM NP remains stable against phase segregation even if $u_A + u_B < 2u_{HEM}$ (**Figure 10b**). In this simplified case, the r_c is given by:

$$r_c = \frac{3\sigma\left(\gamma_A + \gamma_B + \frac{\gamma_I}{2} - 2\gamma_{HEM}\right)}{\rho(2u_{HEM} - u_A - u_B)}$$

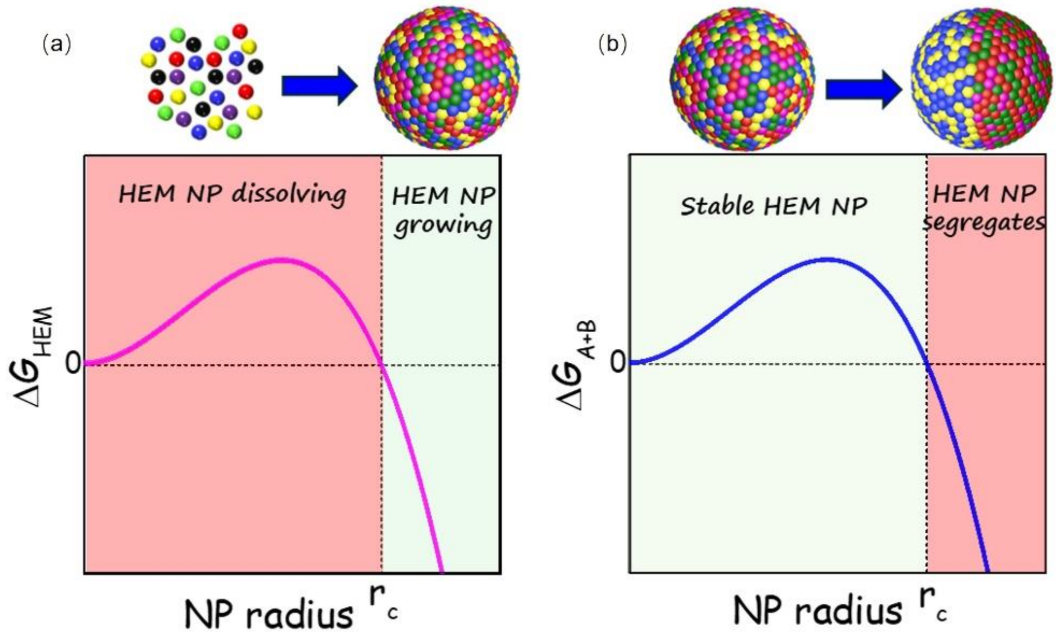

Figure 10. Gibbs free energy change (ΔG) as a function of NP r for the formation of a spherical HEM NP from a metal ion solution (a) and for the phase segregation of a spherical HEM NP in two hemispherical phases A+B (b).

As anticipated, high interphase energies stabilize the HEM NP against the formation of segregated phases. Additionally, an increase in surface energy with phase formation (not considered in this example) also favors HEM stability. On the other hand, a high HEM surface energy can contribute to destabilizing the HEM structure. However, due to the shorter diffusion lengths and fewer atoms involved, the energy barrier for atomic organization at the HEM surface to minimize surface energy is significantly lower than the energy required to reorganize the entire particle into different phases. In fact, while analyzing the atomic distribution within HEM NPs remains challenging, careful studies of this aspect have revealed that the composition is often far from homogeneous, with certain afine atoms showing preferential organization, particularly at the surface.[103, 158] In this context, the use of specific ligands could also contribute to stabilizing the HEM NP. Moreover, for a given composition, the average atomic surface energy of smaller

NPs tends to be higher than that of larger particles, due to the formation of additional defects and a relatively smaller area of energy-favorable surfaces or facets. This effect further stabilizes smaller HEM NPs against segregation into smaller entities. Nevertheless, in some compositions, lattice energy may be significantly increased by the presence of atoms that differ considerably in terms of charge and/or size, promoting segregation. However, the introduction of additional elements into the HEM can reduce lattice stresses, thereby lowering the lattice energy and stabilizing the HEM through a mechanism different from the commonly cited entropy-driven stabilization.

Determining the exact mechanisms that stabilize HEM compositions remains challenging; however, numerous studies suggest enthalpy-driven HEM NP formation and stabilization. Particularly illustrative are cases where colloidal NPs evolve compositionally towards a HEM phase, the production of HEM NPs through sequential incorporation of additional elements via galvanic replacement or ion exchange reactions, and the merging of heterostructured NPs into a single-phase HEM (**Figure 11**). These particle-to-particle conversion approaches offer an additional, effective synthesis strategy beyond conventional top-down and bottom-up methods for producing HEM NPs, where the mixing entropy contribution to the HEM's stability is secondary due to the low processing temperatures involved. The atomic diffusion process at the core of this conversion can occur either in one step during NP synthesis or in a two-step process and can be driven by several factors, including entropy increase of the system, reduction of surface or interface energy, decrease in solvation energy, and differences in the redox potentials of the elements. As a common starting point, these strategies use NPs as seeds or templates for growing new NPs with a HEM composition. By carefully controlling the size, shape, and composition of the initial template, these methods allow precise control over the properties of the resulting HEM NPs. This provides a pathway to engineer HEM NPs with tailored functionalities for various applications.

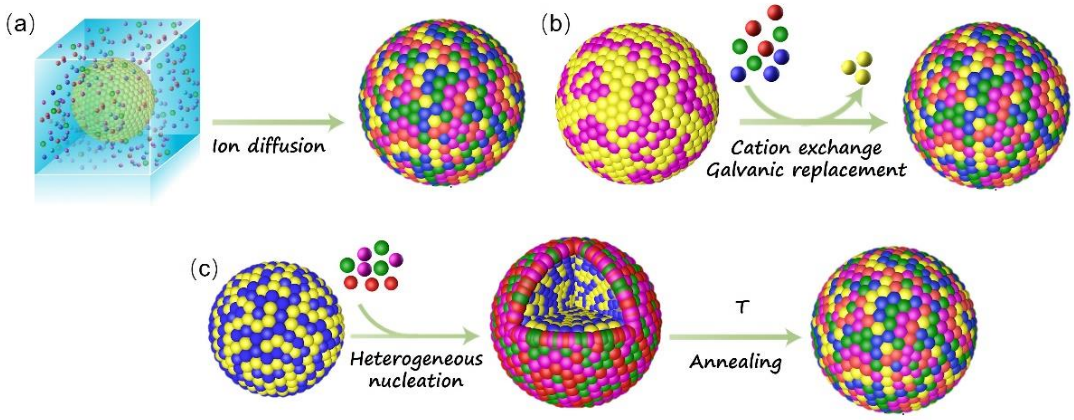

Figure 11. HEM synthesis process by thermodynamic-driven strategies. (a) Ion diffusion during NP synthesis. (b) Ion exchange and galvanic replacement of a pre-prepared NP. (c) Merging of a heterostructured NP during a post-annealing process.

1.2.3 HEMs electrocatalysts for OER/ORR/ZABs

HEAs could precisely tune their surface electronic structures by selecting suitable elements, controlling elemental proportions, morphology, crystal structure, etc, thus adjusting adsorption energies of reactants and intermediates. This versatility makes HEAs ideal for facilitating multi-product reactions and heterogeneous catalysis by improved activity and stability.. Consequently, HEAs hold significant promise for enhancing the efficiency and performance of electrocatalytic reactions, such as OER, ORR, and in applications like ZABs.[160-162]

Although noble metal catalysts like RuO_2 and IrO_2 are highly effective for OER, their high cost and instability hinder their widespread use.[163-166] HEAs offer a promising alternative due to the synergistic effects of multi-element mixtures. For example, Fang et al. synthesized CoNiCuMnAl@C HEA-based nanocatalysts with a metal@carbon core-shell structure, which exhibited excellent OER activity with a low overpotential (η = 215 mV at 10 mA cm^{-2}) and excellent stability due to the high entropy effect and carbon shell protection. *In situ* Raman spectroscopy revealed that there was a active Ni(Co)OOH layer formed on the surface, which reduced the RDS reaction barrier for O* transfer to OOH* in the OER process, as confirmed by density functional theory (DFT) calculations [167] Further advancements include the development of FeCoNiMnCr HEA/HEO heterocatalysts, which showed enhanced OER performance with low overpotentials and long-term stability. The formation of heterojunctions in these catalysts optimized the electronic structure, improving the binding energy to OH* and enhancing activity.[168] Similarly, Cheng et al. developed a HEA catalyst (HEA@Ir-MEO) with a core-shell structure with a particle size of 2 nm, which demonstrated excellent OER performance and stability under acidic conditions due to lattice distortion and suppression of transition metal dissolution.[169] The high-entropy effect enhances the stability of catalysts by promoting a single-phase solid solution structure, while the synergy between elements and surface reconstruction during OER significantly improves activity.[170,171] However, despite the promising potential of HEAs, more research is needed to actively control surface reconstruction processes to optimize catalyst performance, particularly in multi-step catalytic reactions.[172,173]

The electrocatalytic ORR is crucial for the discharge process in ZABs. Although Pt/Pd-based materials remain the primary catalysts for ORR, their high cost and limited stability, particularly due to the formation of H_2O_2 during the $2e^-$ ORR, pose significant challenges. Thus, the development of highly active, selective, and durable electrocatalysts at a moderate cost is essential for improving ORR performance and enhancing ZAB stability. Fu et al. synthesized PtPdFeCoNi HEA NPs via a high-temperature injection method, achieving an ORR $E_{1/2}$ of 0.920 V, with mass and specific activities 6.2 and 4.9 times higher than commercial Pt/C, respectively.[174] This approach improved the utilization of Pt, reducing costs while maintaining excellent stability over 50,000 cycles. Pt-based HEAs can enhance electrocatalytic performance through high entropy and synergistic effects.[175,176] Li et al. developed Pt alloy nanocrystals (HENCs) with six elements, encapsulated in ordered mesoporous carbon.[177] These catalysts exhibited the highest $E_{1/2}$ (0.898 V) and mass activity 3.8-6.3 times greater than other alloy samples and commercial Pt/C. The stability of 6-HENCs/PC was also remarkable, retaining nearly 98% of its initial mass activity after 5000 cycles. This durability was attributed to the high entropy effect, lattice strain, and electron density enhancement around Pt atoms, which improved the adsorption of oxygenated species and stabilized the catalyst interface, preventing metal migration and aggregation during the ORR process.

MABs face challenges on the cathode side, particularly due to the slow kinetics of both the ORR and OER. HEMs), with their broad electronic band gaps and localized electronic states, offer significant advantages over traditional alloys due to their superior catalytic activity and stability. HEAs, with unique atomic compositions and distributions, allow precise modulation of the d_c position and intensity. This enables the optimization of surface adsorption properties and activation energies, leading to improved catalytic performance. By adjusting elemental compositions and inducing lattice distortion, HEMs can significantly enhance catalytic activity and stability, providing novel solutions to the limitations of conventional catalysts in ZABs. For example, Gao et al. prepared $Fe_6Ni_{20}Co_2Mn_2Cu_{1.5}$@rGO using Joule heating, which positively shifted the d_c of Ni metal in the HEA, improving adsorption and electron transfer for reaction intermediates.[178] The catalyst demonstrated excellent stability without structural collapse during cycling. Similarly, Cao et al. synthesized FeNiCrCoMn HEAs, with $Fe_{12}Ni_{23}Cr_{10}Co_{30}Mn_{25}$ exhibiting the lowest d_c position, leading to stronger adsorption for oxygen intermediates.[179] This catalyst powered a ZAB with a specific capacity of 760 mAh g^{-1} and specific energy of 865.5 Wh kg^{-1}. Additionally, FeCoNiMnCu nanoparticles encapsulated in N-doped carbon tubes showed excellent stability in ZABs, with a specific capacity of 630 mAh g^{-1}.[180] FeCoNiMnV HEAs, with enhanced d-band hybridization, exhibited a continuous and broad binding energy distribution, improving reaction rates and catalyst durability. These catalysts achieved a OCP of 1.482 V and outstanding stability for approximately 2000 cycles.[181] Furthermore, Jin et al. synthesized eight-component AlNiCoRuMoCrFeTi HEO catalysts, which enhanced the electronic structure of active sites, leading to high-performance ZABs with a power density of 123.5 mW cm^{-2}.[182] These advancements highlight the potential of HEAs in improving MAB performance, offering efficient, cost-effective, and durable solutions for energy storage systems.

1.3 Challenges for HEMs bifunctional air oxygen catalysts for ZABs

Achieving optimal catalytic activity for both OER and ORR within a single material requires a delicate balance between adsorption energies for reaction intermediates. Designing HEMs with bifunctional catalytic activity for OER and ORR presents several significant challenges due to the complex nature of these reactions with different binding energy requirements, and structural and electronic requirements for the catalysts.

1.3.1 Synthesis of nanostructured HEMs

The synthesis of nanostructured HEMs with uniform morphology, homogeneous elemental distribution, and large specific surface area presents several challenges. Achieving nanostructured morphology requires precise control over nucleation and growth processes, often complicated by the diverse chemical and physical properties of the constituent elements. Ensuring homogeneous elemental distribution is difficult due to the varying atomic sizes and affinities, which can lead to phase separation or elemental segregation during synthesis. Additionally, maximizing the specific surface area while maintaining structural stability at the nanoscale is a delicate balance, as high surface areas increase the risk of agglomeration and surface reconstruction, which may degrade catalytic performance.

1.3.2 Monitor the reconstruction behavior for HEMs during catalytic process

Catalysts undergoing OER and ORR often experience complex surface reconstruction. This phenomenon not only plays a decisive role in the stability and activity of the catalyst but also leads to the formation of distinct active sites under varying reaction conditions. In the case of HEMs, this issue is particularly pronounced. Due to the multi-element composition and structural complexity, the reconstruction behavior exhibits high dynamism and heterogeneity, potentially differing between the OER and ORR processes and impacting the overall catalytic performance. Therefore, understanding the reconstruction behavior of high-entropy catalysts during these reactions is critical for elucidating their catalytic mechanisms and optimizing performance.

However, identifying and monitoring the reconstruction behavior of high-entropy catalysts during OER and ORR presents several challenges. First, the surface reconstruction that occurs during the reactions is often dynamic and involves the synergistic interactions of multiple elements, resulting in complex structural changes at the nanoscale. This complexity makes it difficult for conventional characterization methods to capture the intricate details of the reconstruction process in real time. Furthermore, the inherent complexity of high-entropy catalysts, with their multicomponent compositions, can lead to diverse reconstruction pathways, causing both surface and bulk structures to evolve differently under reaction conditions. This complicates the task of determining the nature of the active sites and enhancing catalytic performance.

In this context, *in situ* characterization techniques have become essential tools for elucidating the reconstruction behavior of high-entropy catalysts. For example, *in situ*

X-ray absorption spectroscopy (XAS) can provide real-time insights into changes in the oxidation states and local structures of metal centers during the reactions. *In situ* Raman spectroscopy offers information on the vibrational modes of surface molecules to help to identify the absorbed oxygen intermediates. The integration of these techniques holds promise for unveiling the structural reconstruction pathways of high-entropy catalysts under different electrochemical conditions.

1.3.3 Identify the role of element in HEMs during catalytic process

Determining the role of individual elements in HEMs during electrocatalysis presents significant challenges due to their complex, disordered structures. Multiple elements interact in ways that alter the electronic structure, making it difficult to isolate the contribution of a single element. Surface segregation and dynamic rearrangements under electrochemical conditions further complicate the identification of active sites, as elements may migrate or oxidize during reactions. Additionally, the synergistic effects between elements make it challenging to pinpoint individual contributions. Advanced *in situ* techniques and computational models are essential but remain limited in capturing the full complexity of HEMs in catalytic processes.

1.4 Objectives

The work in this thesis aims to develop advanced HEM NPs bifunctional catalysts targeted at OER/ORR process and applications in ZAB.

i) For synthesizing HEM NPs, I aim to achieve uniform elemental distribution by carefully selecting elements and utilizing a simple, low-temperature colloidal synthesis method. Through detailed material characterization, I aim to construct a relationship between the material structure with the resulting catalytic performance.

ii) I aim to evaluate the performance of the HEM NPs for their catalytic applications in OER, ORR, and ZABs, targeting efficiency that surpasses that of commercial noble metal catalysts. I aim to find some HEM NPs that could be applied in practical applications in energy conversion and storage.

iii) I aim to utilize *in situ* characterization techniques to monitor the reconstruction behavior of HEM NPs during various reactions to understand the underlying oxygen redox catalytic mechanisms. By identifying the true active sites, I seek to link the observed catalytic performance with specific structural features.

1.5 References

[1] R. J. Leicester, V. G. Newman, J. K. Wright, *Nature*, **1978**, 275,518.

[2] J. M. Morales, A. J. Conejo, H. Madsen, P. Pinson and M. Zugno, *Integrating renewables in electricity markets: operational problems*, Springer Science & Business Media, **2013**.

[3] D. E. H. J. Gernaat, H. S. de Boer, V. Daioglou, S. G. Yalew, C. Müller and D. P. van Vuuren, Nat Clim Change, **2021**, 11, 119-125.

[4] L. C. King and J. C. Van Den Bergh, *Nat. Energy*, **2018**, 3, 334-340.

[5] R. A. Badwawi, M. Abusara, T. Mallic, *Smart Science*, **2015**, 3, 127.

[6] K. Barnham, K. Knorr and M. Mazzer, *Nat. Mater.*, **2016**, 15, 115-116.

[7] B. Dunn, H. Kamath and J.-M. Tarascon, Science, **2011**, 334, 928-935.

[8] J. W. Choi and D. Aurbach, *Nat. Rev. Mater.*, **2016**, 1, 1-16.

[9] X. B. Zhang, *Metal-Air Batteries:Fundamentals and Applications*, John Wiley & Sons, **2018**.

[10] J. Fu, Z. P. Cano, M. G. Park, A. Yu, M. Fowler and Z. Chen, *Adv. Mater.*, **2017**, 29, 1604685.

[11] P. Tan, B. Chen, H. Xu, H. Zhang, W. Cai, M. Ni, M. Liu and Z. Shao, *Energ Environ Sci*, **2017**, 10, 2056-2080.

[12] J. Zhou, J. Cheng, B. Wang, H. Peng and J. Lu, *Energ Environ Sci*, **2020**, 13, 1933-1970.

[13] H. F. Wang and Q. Xu, *Matter*, **2019**, 1, 565-595.

[14] L. Jiang, X. Luo and D. W. Wang, *Carbon Energy*, **2022**, 5, e284.

[15] W. Tahil, *Meridian International Research*, **2007**, 1-9.

[16] A. Inoishi, S. Ida, S. Uratani, T. Okano and T. Ishihara, *Phys Chem Chem Phys*, **2012**, 14, 12818-12822.

[17] G. X. Zhang, *ECS Trans.*, **2009,** 16, 47.

[18] J. Jindra, J. Mrha and M. Musilová, J. Appl. Electrochem, **1973**, 3, 297-301.

[19] A. A. Mohamad, *J. Power Sources*, **2006**, 159, 752-757.

[20] Y. Li, M. Gong, Y. Liang, J. Feng, J. E. Kim, H. Wang, G. Hong, B. Zhang and H. Dai, *Nat. Commun.*, **2013**, 4, 1805.

[21] C. X. Zhao, J. N. Liu, B. Q. Li, D. Ren, X. Chen, J. Yu and Q. Zhang, *Adv. Funct. Mater.*, **2020**, 30, 2003619.

[22] F. Shi, X. Zhu and W. Yang, *Chin. J. Catal.*, **2020**, 41, 390-403.

[23] H. Shang, X. Zhou, J. Dong, A. Li, X. Zhao, Q. Liu, Y. Lin, J. Pei, Z. Li, Z. Jiang, D. Zhou, L. Zheng, Y. Wang, J. Zhou, Z. Yang, R. Cao, R. Sarangi, T. Sun, X. Yang, X. Zheng, W. Yan, Z. Zhuang, J. Li, W. Chen, D. Wang, J. Zhang and Y. Li, *Nat. Commun.*, **2020**, 11, 3049.

[24] D. Jiao, Z. Ma, J. Li, Y. Han, J. Mao, T. Ling and S. Qiao, *J Energy Chem*, **2020**, 44, 1-7.

[25] K. Wu, L. Zhang, Y. Yuan, L. Zhong, Z. Chen, X. Chi, H. Lu, Z. Chen, R. Zou, T. Li, C. Jiang, Y. Chen, X. Peng and J. Lu, *Adv. Mater.*, **2020**, 32, e2002292.

[26] Z. Zhao, Y. He, W. Yu, W. Shang, Y. Ma, Z. Zhang and P. Tan, *J. Electrochem. Soc.*, **2022**, 169, 100551.

[27] W. Yu, W. Shang, X. Xiao, Y. Ma, Z. Chen, B. Chen, H. Xu, M. Ni and P. Tan, *J. Energy Storage*, **2021**, 40, 102779,

[28] J. Park, M. Park, G. Nam, J. Lee and J. Cho, *Adv. Mater.*, **2014**, 27, 1396-1401.

[29] J. Liu, M. Wang, C. Gu, J. Li, Y. Liang, H. Wang, Y. Cui and C. S. Liu, *Adv. Sci.*, **2022**, 9, e2200753.

[30] T. Deng, X. Ji, L. Zou, O. Chiekezi, L. Cao, X. Fan, T. R. Adebisi, H.-J. Chang, H. Wang and B. Li, *Nat. Nanotechnol.*,**2022**, 17, 269-277.

[31] S. Qu, Z. Song, J. Liu, Y. Li, Y. Kou, C. Ma, X. Han, Y. Deng, N. Zhao, W. Hu and C. Zhong, *Nano Energy*, **2017**, 39, 101-110.

[32] Z. Cao, H. Hu, M. Wu, K. Tang and T. Jiang, *J. Mater. Chem. A*, **2019**, 7, 17581-17593.

[33] S. S. Shinde, J. Y. Jung, N. K. Wagh, C. H. Lee, D.-H. Kim, S.-H. Kim, S. U. Lee and J. H. Lee, *Energy Environ. Sci.*,**2021**, 6, 592-604.

[34] C. C. Hou, L. Zou, Y. Wang and Q. Xu, *Angew Chem Int Edit*, **2020**, 59, 21360-21366.

[35] H. Zhang, Z. Qu, H. Tang, X. Wang, R. Koehler, M. Yu, C. Gerhard, Y. Yin, M. Zhu, K. Zhang and O. G. Schmidt, *ACS Energy Lett.*, **2021**, 6, 2491-2498.

[36] J. Park, M. Park, G. Nam, J. S. Lee and J. Cho, *Adv. Mater.*, **2015**, 27, 1396-1401.

[37] S. S. Shinde, C. H. Lee, J.-Y. Jung, N. K. Wagh, S.-H. Kim, D.-H. Kim, C. Lin, S. U. Lee and J.-H. Lee, *Energy Environ. Sci.*, **2019**, 12, 727-738.

[38] C. Wang, J. Li, Z. Zhou, Y. Pan, Z. Yu, Z. Pei, S. Zhao, L. Wei and Y. Chen, *EnergyChem*, **2021**, 3, 100055.

[39] W. F. Wu, X. Yan and Y. Zhan, *Chem. Eng. J.*, **2023**, 451, 138608.

[40] W. Zhang, J. W. Zhang, N. Wang, K. R. Zhu, C. C. Yang, Y. Ai, F. M. Wang, Y. Tian, Y. Z. Ma, Y. Ma, X. M. Zhang, L. L. Duan, D. L. Chao, F. Wang, D. Y. Zhao, W. Li, *Nat. Sustain.*, **2024**, 7, 463.

[41] L. An, Z. Zhang, J. Feng, F. Lv, Y. Li, R. Wang, M. Lu, R. B. Gupta, P. Xi and S. Zhang, *J Am Chem Soc*, **2018**, 140, 17624-17631.

[42] W. Sun, F. Wang, B. Zhang, M. Zhang, V. Küpers, X. Ji, C. Theile, P. Bieker, K. Xu and C. Wang, Science, **2021**, 371, 46-51.

[43] K. W. Leong, Y. Wang, M. Ni, W. Pan, S. Luo and D. Y. C. Leung, *Renew Sust Energ Rev*, **2022**, 154,111771.

[44] A. Iqbal, O. M. El-Kadri and N. M. Hamdan, *J. Energy Storage*, **2023**, 62，106926.

[45] J. F. Parker, C. N. Chervin, E. S. Nelson, D. R. Rolison and J. W. Long, *Energ Environ Sci*, **2014**, 7, 1117-1124.

[46] J. F. Parker, C. N. Chervin, I. R. Pala, M. Machler, M. F. Burz, J. W. Long and D. R. Rolison, Science, **2017**, 356, 415-418.

[47] Y. N. Jo, K. Prasanna, S. H. Kang, P. R. Ilango, H. S. Kim, S. W. Eom and C. W. Lee, *J Ind Eng Chem*, **2017**, 53, 247-252.

[48] R. Li, Y. Du, Y. Li, Z. He, L. Dai, L. Wang, X. Wu, j. Zhang and J. Yi, *ACS Energy Lett.*, **2022**, 8, 457-476.

[49] Z. Cai, Y. Ou, J. Wang, R. Xiao, L. Fu, Z. Yuan, R. Zhan and Y. Sun, *Energy Storage Mater.*, **2020**, 27, 205-211.

[50] Y. Chen, Q. Zhao, Y. Wang, W. Liu, P. Qing and L. Chen, *Electrochimica Acta*, **2021**, 399, 139334.

[51] E. O. Aremu, D.-J. Park and K.-S. Ryu, *Ionics*, **2019**, 25, 4197-4207.

[52] S.-M. Lee, Y.-J. Kim, S.-W. Eom, N.-S. Choi, K.-W. Kim and S.-B. Cho, *J. Power Sources*, **2013**, 227, 177-184.

[53] Z. Li, H. Wang, Y. Zhong, L. Yuan, Y. Huang and Z. Li, *ACS Appl. Mater. Interfaces*, **2022**, 14, 9097-9105.

[54] K. Wang, P. Pei, Y. Wang, C. Liao, W. Wang and S. Huang, *Appl Energ*, **2018**, 225, 848-856.

[55] Z. Zhao, X. Fan, J. Ding, W. Hu, C. Zhong and J. Lu, *ACS Energy Lett.*, **2019**, 4, 2259-2270.

[56] D. M. See, R. E. White, *J. Chem. Eng. Data*, **1997**, 42, 1266.

[57] C. Xu, B. Li, H. Du and F. Kang, *Angew Chem Int Edit*, **2012**, 51, 933-935.

[58] A. Naveed, T. Rasheed, B. Raza, J. Chen, J. Yang, N. Yanna and J. Wang, *Energy Storage Mater.*, **2022**, 44, 206-230.

[59] N. Zhang, X. Chen, M. Yu, Z. Niu, F. Cheng and J. Chen, *Chem Soc Rev*, **2020**, 49, 4203-4219.

[60] Z. Yi, G. Chen, F. Hou, L. Wang and J. Liang, *Adv. Energy Mater.*, **2020**, 11, 2003065.

[61] F. Ilyas, M. Ishaq, M. Jabeen, M. Saeed, A. Ihsan and M. Ahmed, *J Mol Liq*, **2021**, 343, 117606.

[62] L. Ma, S. Chen, N. Li, Z. Liu, Z. Tang, J. A. Zapien, S. Chen, J. Fan and C. Zhi,

Adv. Mater., **2020**, 32, e1908121.

[63] A. Abbasi, Y. Xu, R. Khezri, M. Etesami, C. Lin, S. Kheawhom and Y. Lu, *Mater Today Sustain*, **2022**, 18, 100126.

[64] G. M. Wu, S. J. Lin and C. C. Yang, *J Membrane Sci*, **2006**, 284, 120-127.

[65] G. M. Wu, S. J. Lin, J. H. You and C. C. Yang, *Mater. Chem. Phys.*, **2008**, 112, 798-804.

[66] H. Saputra, R. Othman, A. G. E. Sutjipto and R. Muhida, *J Membrane Sci*, **2011**, 367, 152-157.

[67] H. J. Hwang, W. S. Chi, O. Kwon, J. G. Lee, J. H. Kim and Y. G. Shul, *ACS Appl. Mater. Interfaces*, **2016**, **8**, 26298-26308.

[68] H.-W. Kim, J.-M. Lim, H.-J. Lee, S.-W. Eom, Y. T. Hong and S.-Y. Lee, *J. Mater. Chem. A*, **2016**, 4, 3711-3720.

[69] Y. Li and H. Dai, *Chem Soc Rev,* **2014,** 43, 5257-5275.

[70] F. Cheng, J. Shen, B. Peng, Y. Pan, Z. Tao and J. J. N. c. Chen, **2011**, 3, 79-84.

[71] F. Bidault, D. J. L. Brett, P. H. Middleton and N. P. Brandon, *J. Power Sources*, **2009**, 187, 39-48.

[72] J. S. Lee, S. Tai Kim, R. Cao, N. S. Choi, M. Liu, K. T. Lee and J. Cho, *Adv. Energy Mater.*, **2010**, 1, 34-50.

[73] S. B. Park and Y.-i. Park, *Int. J. Precis. Eng. Manuf.*, **2012**, 13, 1145-1151.

[74] Y.-C. Lu, D. G. Kwabi, K. P. C. Yao, J. R. Harding, J. Zhou, L. Zuin and Y. Shao-Horn, *Energy Environ. Sci.*, **2011**, 4, 2999-3007.

[75] J. Pan, Y. Y. Xu, H. Yang, Z. Dong, H. Liu and B. Y. Xia, *Adv. Sci.*, **2018**, 5, 1700691.

[76] Y. Liu, P. He and H. Zhou, *Adv. Energy Mater.*, **2017**, 8, 1701602.

[77] Y. Liu, J. Li, W. Li, Y. Li, Q. Chen and Y. Liu, *Int. J. Hydrogen Energy.*, **2015**, 40, 9225-9234.

[78] H. Ma and B. Wang, *RSC Adv.*, **2014**, 4, 46084-46092.

[79] R. Zhao, L. Huan, P. Gu, R. Guo, M. Chen and G. Diao, *J. Power Sources*, **2016**, 331, 527-534.

[80] G. Yang, J. Zhu, P. Yuan, Y. Hu, G. Qu, B. A. Lu, X. Xue, H. Yin, W. Cheng, J. Cheng, W. Xu, J. Li, J. Hu, S. Mu and J. N. Zhang, *Nat. Commun.*, **2021**, 12, 1734.

[81] X. Li, H. Zhang, Y. Wang, H. Wang, J. Wang, J. Zhang, L. Qiu, Y. Deng, X. Han and W. Hu, *Sci. China Mater.*, **2022**, 65, 3479-3489.

[82] Y. Dai, J. Yu, C. Cheng, P. Tan and M. Ni, *J. Chem. Eng.*, **2020**, 397, 125516.

[83] Q. Wang, S. Kaushik, X. Xiao and Q. Xu, *Chem Soc Rev,* **2023**, 52, 6139-6190.

[84] Y.-C. Qin, F.-Q. Wang, X.-M. Wang, M.-W. Wang, W.-L. Zhang, W.-K. An, X.-

P. Wang, Y.-L. Ren, X. Zheng, D.-C. Lv and A. Ahmad, *Rare Metals*, **2021**, 40, 2354-2368.

[85] S. S. Aamlid, M. Oudah, J. Rottler and A. M. Hallas, *J. Am. Chem. Soc.*, **2023**, 145, 5991-6006.

[86] A. Sarkar, Q. Wang, A. Schiele, M. R. Chellali, S. S. Bhattacharya, D. Wang, T. Brezesinski, H. Hahn, L. Velasco and B. Breitung, *Adv. Mater.*, **2019**, 31, e1806236.

[87] L. Su, J. Ren, T. Lu, K. Chen, J. Ouyang, Y. Zhang, X. Zhu, L. Wang, H. Min, W. Luo, Z. Sun, Q. Zhang, Y. Wu, L. Sun, L. Mai and F. Xu, *Adv. Mater.*, **2023**, 35, e2205751.

[88] A. Abdelhafiz, B. Wang, A. R. Harutyunyan and J. Li, *Adv. Energy Mater.*, **2022**, 12, 2200742.

[89] J. L. Rowell, M. Kang, D. Yoon, K. Z. Jiang, Y. Jia, H. D. Abruna, D. A. Muller and R. D. Robinson, *J. Am. Chem. Soc.*, **2024**, 146, 17613-17617.

[90] P.-W. Chien, C.-B. Chang and H.-Y. Tuan, *Energy Storage Mater.*, **2023**, 61, 102853.

[91] M. Cui, C. Yang, B. Li, Q. Dong, M. Wu, S. Hwang, H. Xie, X. Wang, G. Wang and L. Hu, *Adv. Energy Mater.*, **2020**, 11, 2002887.

[92] M. J. Theibault, C. R. McCormick, S. Lang, R. E. Schaak and H. D. Abruna, *ACS Nano*, **2023**, 17,18402–18410.

[93] Y. Li, Y. Y. Tay, P. J. S. Buenconsejo, W. Manalastas, W. H. Tu, H. K. Lim, T. Salim, M. O. Thompson, S. Madhavi, C. Y. Tay and K. W. Tan, *Adv. Funct. Mater.*, **2023**, 33, 2211279.

[94] P. Wu, C. Deng, P. Liu, F. Liu, L. Chen, B. Wang, W. Zhu and C. Xu, *J. Chem. Eng.*, **2023**, 474, 145850.

[95] S. Dong, H. Zhou, X. Hu, J. Zhang, Y. Li, W. Shang, Z. Liu, L. Wan and H. Zhao, *Int. J. Hydrogen Energy.*, **2023**, 48, 18233-18244.

[96] X. Wang, Y. Zuo, S. Horta, R. He, L. Yang, A. Ostovari Moghaddam, M. Ibanez, X. Qi and A. Cabot, *ACS Appl. Mater. Interfaces*, **2022**, 14, 48212-48219.

[97] X. Lei, Q. Tang, Y. Zheng, P. Kidkhunthod, X. Zhou, B. Ji and Y. Tang, *Nat. Sustain*, **2023**, 6, 816-826.

[98] Y. Zhang, *High entropy materials*, Springer, **2023**.

[99] C. Oses, C. Toher and S. Curtarolo, *Nat. Rev. Mater.*, **2020**, 5, 295-309.

[100] Y. Ma, Y. Ma, Q. Wang, S. Schweidler, M. Botros, T. Fu, H. Hahn, T. Brezesinski and B. Breitung, *Energy Environ. Sci.*, **2021**, 14, 2883-2905.

[101] M. C. Gao, D. B. Miracle, D. Maurice, X. Yan, Y. Zhang and J. A. Hawk, *J. Mater. Res.*, **2018**, 33, 3138-3155.

[102] B. Wang, C. Wang, X. Yu, Y. Cao, L. Gao, C. Wu, Y. Yao, Z. Lin and Z. Zou, *Nat. Synth.*, **2022**, 1, 138-146.

[103] R. K. Pittkowski, C. M. Clausen, Q. Chen, D. Stoian, W. van Beek, J. Bucher, R. L. Welten, N. Schlegel, J. K. Mathiesen, T. M. Nielsen, J. Du, A. W. Rosenkranz, E. D. Bøjesen, J. Rossmeisl, K. M. Ø. Jensen and M. Arenz, *EES Catal.*, **2023**, 1, 950-960.

[104] A. Barbero, C. Moreira Da Silva, N. Ortiz Pena, N. Kefane, A. Jaafar, M. Thorey, H. Bouaia, J. Nelayah, G. Wang, H. Amara, C. Ricolleau, V. Huc and D. Alloyeau, *Faraday Discuss*, **2023**, 242, 129-143.

[105] S. S. Soliman, G. R. Dey, C. R. McCormick and R. E. Schaak, *ACS Nano*, **2023**, 17, 16147-16159.

[106] S. L. A. Bueno, A. Leonardi, N. Kar, K. Chatterjee, X. Zhan, C. Chen, Z. Wang, M. Engel, V. Fung and S. E. Skrabalak, *ACS Nano*, **2022**, 16, 18873-18885.

[107] A. V. Saghir, S. M. Beidokhti, J. V. Khaki and A. Salimi, *J. Eur. Ceram. Soc.*, **2021**, 41, 563-579.

[108] B. Han, J. Wei, F. He, D. Chen, Z. J. Wang, A. Hu, W. Zhou and J. J. Kai, *Entropy*, **2018**, 20, 910.

[109] B. Han, J. Wei, Y. Tong, D. Chen, Y. Zhao, J. Wang, F. He, T. Yang, C. Zhao, Y. Shimizu, K. Inoue, Y. Nagai, A. Hu, C. T. Liu and J. J. Kai, *Scr. Mater.*, **2018**, 148, 42-46.

[110] Z. Zeng, J. Zhao, X. Zhou, J. Li and B. Liang, *Chem. Phys.*, **2019**, 517, 126-130.

[111] S.-P. Ju, I. J. Lee and H.-Y. Chen, *J. Alloys Compd.*, **2021**, 858, 157681.

[112] M.-H. Tsai and J.-W. Yeh, *Mater. Res. Lett.*, **2014**, 2, 107-123.

[113] J.-W. Yeh, *Ann. Chim.: Sci. Mater.*, **2006**, 31, 633-648.

[114] N. Kumar Katiyar, K. Biswas, J.-W. Yeh, S. Sharma and C. Sekhar Tiwary, *Nano Energy*, **2021**, 88, 106261.

[115] B. Wang, Y. Yao, X. Yu, C. Wang, C. Wu and Z. Zou, *J. Mater. Chem. A*, **2021**, 9, 19410-19438.

[116] S. Jo, M. C. Kim, K. B. Lee, H. Choi, L. Zhang and J. I. Sohn, *Adv. Energy Mater.*, **2023**, 13, 2301420.

[117] S. Wang, G. Zeng, Q. Sun, Y. Feng, X. Wang, X. Ma, J. Li, H. Zhang, J. Wen, J. Feng, L. Ci, A. Cabot and Y. Tian, *ACS Nano*, **2023**, 17, 13256-13268.

[118] H. Huang, J. Zhao, H. Guo, B. Weng, H. Zhang, R. A. Saha, M. Zhang, F. Lai, Y. Zhou, R. Z. Juan, P. C. Chen, S. Wang, J. A. Steele, F. Zhong, T. Liu, J. Hofkens, Y. M. Zheng, J. Long and M. B. J. Roeffaers, *Adv. Mater.*, **2024**, 36, e2313209.

[119] S. Qi, K. Zhu, T. Xu, H. Zhang, X. Guo, J. Wang, F. Zhang and X. Zong, *Adv. Mater.*, **2024**, 36, e2403328.

[120] Q. Wang, A. Sarkar, D. Wang, L. Velasco, R. Azmi, S. S. Bhattacharya, T. Bergfeldt, A. Düvel, P. Heitjans, T. Brezesinski, H. Hahn and B. Breitung, *Energy Environ. Sci.*, **2019**, 12, 2433-2442.

[121] Y. Ma, Y. Ma, S. L. Dreyer, Q. Wang, K. Wang, D. Goonetilleke, A. Omar, D.

Mikhailova, H. Hahn, B. Breitung and T. Brezesinski, *Adv. Mater.*, **2021**, 33, e2101342.

[122] Y. Wang and Y. Wang, *Nano Energy*, **2022**, 104, 107958.

[123] A. D. Mendaza, A. Melianas, S. Rossbauer, O. Backe, L. Nordstierna, P. Erhart, E. Olsson, T. D. Anthopoulos, O. Inganas and C. Muller, *Adv. Mater.*, **2015**, 27, 7325-7331.

[124] M. Ahn, Y. Park, S. H. Lee, S. Chae, J. Lee, J. T. Heron, E. Kioupakis, W. D. Lu and J. D. Phillips, *Adv. Electron. Mater.*, **2021**, 7, 2001258.

[125] D. Castro, P. Jaeger, A. C. Baptista and J. P. Oliveira, *Metals*, **2021**, 11, 648.

[126] F. Cemin, S. R. S. de Mello, C. A. Figueroa and F. Alvarez, *Surf. Coat. Technol.*, **2021**, 421, 127357.

[127] Z. Ma, T. Xu, W. Li, Y. Cheng, J. Li, D. Zhang, Q. Jiang, Y. Luo and J. Yang, *Adv. Funct. Mater.*, **2021**, 31, 2103197.

[128] Y. Luo, S. Hao, S. Cai, T. J. Slade, Z. Z. Luo, V. P. Dravid, C. Wolverton, Q. Yan and M. G. Kanatzidis, *J. Am. Chem. Soc.*, **2020**, 142, 15187-15198.

[129] S. Dixit, S. Rodriguez, M. R. Jones, P. Buzby, R. Dixit, N. Argibay, F. W. DelRio, H. H. Lim and D. Fleming, *J. Therm. Spray Technol.*, **2022**, 31, 1021-1031.

[130] J. Li, Y. Huang, X. Meng and Y. Xie, *Adv. Eng. Mater.*, **2019**, 21, 1800841.

[131] A. Kareer, J. C. Waite, B. Li, A. Couet, D. E. J. Armstrong and A. J. Wilkinson, *J. Nucl. Mater.*, **2019**, 526, 151744.

[132] F. He, B. Han, Z. Yang, D. Chen, G. Yeli, Y. Tong, D. Wei, J. Li, Z. Wang, J. Wang and J.-j. Kai, *J. Mater. Sci. Technol.*, **2021**, 72, 52-60.

[133] R. Feng, C. Zhang, M. C. Gao, Z. Pei, F. Zhang, Y. Chen, D. Ma, K. An, J. D. Poplawsky, L. Ouyang, Y. Ren, J. A. Hawk, M. Widom and P. K. Liaw, *Nat. Commun.*, **2021**, 12, 4329.

[134] L. Xiao, Z. Wang and J. Guan, *Chem. Sci.*, **2023**, 14, 12850-12868.

[135] W. L. Hsu, C. W. Tsai, A. C. Yeh and J. W. Yeh, *Nat. Rev. Chem.*, **2024**, 8, 471-485.

[136] S. Guo, C. Ng, J. Lu and C. T. Liu, *J. Appl. Phys.*, **2011**, 109, 103505.

[137] S. Guo, *Mater. Sci. Technol.*, **2015**, 31, 1223-1230.

[138] X. Chang, M. Zeng, K. Liu and L. Fu, *Adv. Mater.*, **2020**, 32, e1907226.

[139] C. Lee, Y. Chou, G. Kim, M. C. Gao, K. An, J. Brechtl, C. Zhang, W. Chen, J. D. Poplawsky, G. Song, Y. Ren, Y. C. Chou and P. K. Liaw, *Adv. Mater.*, **2020**, 32, e2004029.

[140] R. K. Nutor, Q. Cao, X. Wang, D. Zhang, Y. Fang, Y. Zhang and J.-Z. Jiang, *Adv. Eng. Mater.*, **2020**, 22, 2000466.

[141] H. Wang, Q. He, X. Gao, Y. Shang, W. Zhu, W. Zhao, Z. Chen, H. Gong and

Y. Yang, *Adv. Mater.*, **2024**, 36, 2305453.

[142] Q. Chen, X. Han, Z. Xu, Q. Chen, Q. Wu, T. Zheng, P. Wang, Z. Wang, J. Wang, H. Li, Z. Xia and J. Hao, *Nano Energy*, **2023**, 110, 108380.

[143] J. Ren, Y. Zhang, D. Zhao, Y. Chen, S. Guan, Y. Liu, L. Liu, S. Peng, F. Kong, J. D. Poplawsky, G. Gao, T. Voisin, K. An, Y. M. Wang, K. Y. Xie, T. Zhu and W. Chen, *Nature*, **2022**, 608, 62-68.

[144] Z. Li, S. Zhao, R. O. Ritchie and M. A. Meyers, *Prog. Mater. Sci.*, **2019**, 102, 296-345.

[145] L. Zendejas Medina, L. Mølmen, E. M. Paschalidou, O. Donzel-Gargand, P. Leisner, U. Jansson and L. Nyholm, *Adv. Funct. Mater.*, **2023**, 33, 2307897.

[146] Z. Chen, Z. Tian, L. Zheng, K. Ming, X. Ren, J. Wang and B. Li, *Journal of Adv. Ceram*, **2022**, 11, 1279-1293.

[147] A. R. Mazza, E. Skoropata, Y. Sharma, J. Lapano, T. W. Heitmann, B. L. Musico, V. Keppens, Z. Gai, J. W. Freeland, T. R. Charlton, M. Brahlek, A. Moreo, E. Dagotto and T. Z. Ward, *Adv. Sci.*, **2022**, 9, e2200391.

[148] Z. Rao, B. Dutta, F. Körmann, W. Lu, X. Zhou, C. Liu, A. K. da Silva, U. Wiedwald, M. Spasova, M. Farle, D. Ponge, B. Gault, J. Neugebauer, D. Raabe and Z. Li, *Adv. Funct. Mater.*, **2020**, 31, 2007668.

[149] V. Chaudhary, R. Chaudhary, R. Banerjee and R. V. Ramanujan, *Materials Today*, **2021**, 49, 231-252.

[150] J. Kwon, S. Sun, S. Choi, K. Lee, S. Jo, K. Park, Y. K. Kim, H. B. Park, H. Y. Park, J. H. Jang, H. Han, U. Paik and T. Song, *Adv. Mater.*, **2023**, 35, e2300091.

[151] T. X. Nguyen, Y. H. Su, C. C. Lin, J. Ruan and J. M. Ting, *Adv. Sci.*, **2021**, 8, 2002446.

[152] Y.-B. Lu, G.-X. Zhang, F.-Y. Yang, M.-Q. Yao, L.-Y. Liu and H. Pang, *Rare Metals*, **2023**, 42, 3212-3245.

[153] G. R. Dey, S. S. Soliman, C. R. McCormick, C. H. Wood, R. R. Katzbaer and R. E. Schaak, *ACS Nanosci. Au*, **2024**, 4, 3-20.

[154] W. Al Zoubi, R. A. K. Putri, M. R. Abukhadra and Y. G. Ko, *Nano Energy*, **2023**, 110, 108362.

[155] Y. Yao, Q. Dong, A. Brozena, J. Luo, J. Miao, M. Chi, C. Wang, I. G. Kevrekidis, Z. J. Ren, J. Greeley, G. Wang, A. Anapolsky and L. Hu, *Science*, **2022**, 376, eabn3103.

[156] G. Pacchioni, *Nat. Rev. Mater.*, **2022**, 7, 156-156.

[157] G. R. Dey, C. R. McCormick, S. S. Soliman, A. J. Darling and R. E. Schaak, *ACS Nano*, **2023**, 17, 5943-5955.

[158] F. Calvo, *Phys. Chem. Chem. Phys.*, **2023**, 25, 18439-18453.

[159] X.-J. Hua, P. Hu, H.-R. Xing, J.-Y. Han, S.-W. Ge, S.-L. Li, C.-J. He, K.-S. Wang and C.-J. Cui, *Acta Metall. Sin.*, **2022**, 35, 1231-1265.

[160] W. Xiong, A. X. Y. Guo, S. Zhan, C.-T. Liu and S. C. Cao, *J. Mater. Sci.*, **2023**, 142, 196-215.

[161] T. A. A. Batchelor, J. K. Pedersen, S. H. Winther, I. E. Castelli, K. W. Jacobsen and J. Rossmeisl, *Joule*, **2019**, 3, 834-845.

[162] H. Li, J. Lai, Z. Li and L. Wang, *Adv. Funct. Mater.*, **2021**, 31, 2106715.

[163] X. Wang, S. Xi, P. Huang, Y. Du, H. Zhong, Q. Wang, A. Borgna, Y. W. Zhang, Z. Wang, H. Wang, Z. G. Yu, W. S. V. Lee and J. Xue, *Nature*, **2022**, 611, 702-708.

[164] A. Malek, Y. Xue and X. Lu, *Angew Chem Int Edit*, **2023**, 62, e202309854.

[165] G. Li, S. Li, J. Ge, C. Liu and W. Xing, *J. Mater. Chem. A*, **2017**, 5, 17221-17229.

[166] T. X. Nguyen, Y. H. Su, C. C. Lin and J. M. Ting, *Adv. Funct. Mater.*, **2021**, 31, 2106229.

[167] S. Wang, W. Huo, F. Fang, Z. Xie, J. K. Shang and J. Jiang, *J. Chem. Eng.*, **2022**, 429, 132410.

[168] J. Hu, T. Guo, X. Zhong, J. Li, Y. Mei, C. Zhang, Y. Feng, M. Sun, L. Meng, Z. Wang, B. Huang, L. Zhang and Z. Wang, *Adv. Mater.*, **2024**, 36, e2310918.

[169] L. Yao, F. Zhang, S. Yang, H. Zhang, Y. Li, C. Yang, H. Yang and Q. Cheng, *Adv. Mater.*, **2024**, 36, 2314049.

[170] T. Wu, E. Song, S. Zhang, M. Luo, C. Zhao, W. Zhao, J. Liu and F. Huang, *Adv. Mater.*, **2022**, 34, e2108505.

[171] M. Jiang, H. Zhai, L. Chen, L. Mei, P. Tan, K. Yang and J. Pan, *Adv. Funct. Mater.*, **2023**, 33, 2302621.

[172] H. Lei, L. Ma, Q. Wan, S. Tan, B. Yang, Z. Wang, W. Mai and H. J. Fan, *Adv. Energy Mater.*, **2022**, 12, 2202522.

[173] Y. Sun, J. Wang, S. Xi, J. Shen, S. Luo, J. Ge, S. Sun, Y. Chen, J. V. Hanna, S. Li, X. Wang and Z. J. Xu, *Nat. Commun.*, **2023**, 14, 2467.

[174] Y. Yu, F. Xia, C. Wang, J. Wu, X. Fu, D. Ma, B. Lin, J. Wang, Q. Yue and Y. Kang, *Nano Res.*, **2022**, 15, 7868-7876.

[175] P. Xie, Y. Yao, Z. Huang, Z. Liu, J. Zhang, T. Li, G. Wang, R. Shahbazian-Yassar, L. Hu and C. Wang, *Nat. Commun.*, **2019**, 10, 4011.

[176] Z. Jia, T. Yang, L. Sun, Y. Zhao, W. Li, J. Luan, F. Lyu, L. C. Zhang, J. J. Kruzic, J. J. Kai, J. C. Huang, J. Lu and C. T. Liu, *Adv. Mater.*, **2020**, 32, e2000385.

[177] W. Zhang, X. Feng, Z. X. Mao, J. Li and Z. Wei, *Adv. Funct. Mater.*, **2022**, 32, 2204110.

[178] L. Gao, X. Zhong, Z. Li, J. Hu, S. Cui, X. Wang and B. Xu, *Chem Commun*, **2024**, 60, 1269-1272.

[179] X. Cao, Y. Gao, Z. Wang, H. Zeng, Y. Song, S. Tang, L. Luo and S. Gong, *ACS Appl. Mater. Interfaces*, **2023**, 15, 32365-32375.

[180] Y. Yao, Z. Li, Y. Dou, T. Jiang, J. Zou, S. Y. Lim, P. Norby, E. Stamate, J. O. Jensen and W. Zhang, *Dalton Trans.*, **2023**, 52, 4142-4151.

[181] D. H. Wu, M. Ul Haq, L. Zhang, J. J. Feng, F. Yang and A. J. Wang, *J. Colloid Interface Sci.*, **2024**, 662, 149-159.

[182] Z. Jin, J. Lyu, K. Hu, Z. Chen, G. Xie, X. Liu, X. Lin and H. J. Qiu, *Small*, **2022**, 18, e2107207.

Chapter 2

A CrMnFeCoNi HEA Boosting OER/ORR and ZAB Performance

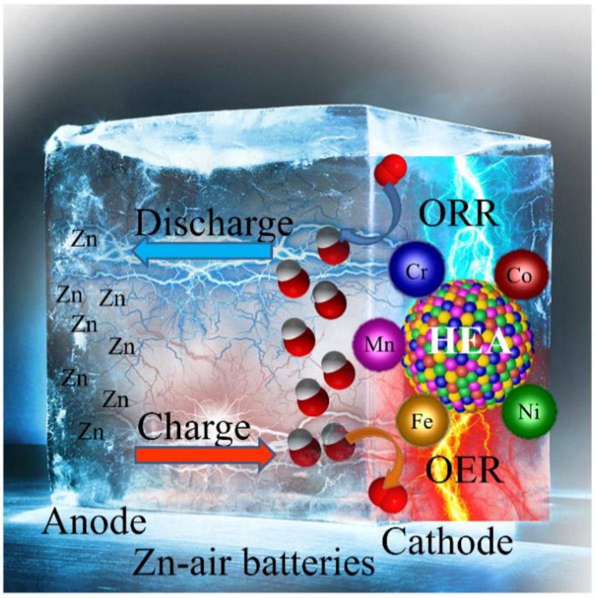

2.1 Abstract

The development of cost-effective, high-activity and stable bifunctional catalysts for ORR and OER is essential for ZABs to reach the market. Such catalysts must contain multiple adsorption/reaction sites to cope with the high demands of reversible oxygen electrodes. Herein, we propose a HEA based on relatively abundant elements as a bifunctional ORR/OER catalyst. More specifically, we detail the synthesis of a CrMnFeCoNi HEA through a low-temperature solution-based approach. Such HEA displays superior OER performance with an η of 265 mV at a current density of 10 mA cm^{-2}, and a 37.9 mV dec^{-1} Tafel slope, well above the properties of a standard commercial catalyst based on RuO_2. This high performance is partially explained by the presence of twinned defects, the incidence of large lattice distortions, and the electronic synergy between the different components, being Cr key to decreasing the energy barrier of the OER RDS. CrMnFeCoNi also displays superior ORR performance with a half-potential of 0.78 V and an onset potential of 0.88 V, comparable with commercial Pt/C. The E_{gap} of CrMnFeCoNi is just 0.734 V. Taking advantage of these outstanding properties, ZABs are assembled using the CrMnFeCoNi HEA as air cathode and a zinc foil as the anode. The assembled cells provide an OCP of 1.489 V, i.e. 90% of its theoretical limit (1.66 V), a peak power density of 116.5 mW cm^{-2}, and

a specific capacity of 836 mAh/g that stays stable for more than 10 days of continuous cycling, i.e. 720 cycles @ 8 mA cm^{-2} and 16.6 days of continuous cycling, i.e. 1200 cycles @ 5 mA cm^{-2}.

2.2 Introduction

Oxygen electrocatalysts play a fundamental role in several energy conversion and storage technologies [1,2]. Oxygen catalysts are required to facilitate the OER at the anode of water electrolyzers [3,4], the ORR at the cathode of fuel cells [5,6], and both OER and ORR at the cathode of rechargeable MABs, among others [7]. A particularly interesting case in the latter field is that of rechargeable aqueous ZABs [8,9]. While ZABs offer appealing advantages over competing technologies, such as high specific energy (1,218 Wh kg^{-1}) [10], safety [11], potential for low cost [12], and suitability for smart-grid energy storage, their cost-effectiveness relies on finding a durable and low-cost bifunctional OER/ORR catalyst that enables an energy-efficient charge/discharge process [13,14]. In this direction, despite the huge efforts dedicated, the most effective oxygen catalysts proposed to date are usually based on noble metals [15–17], which hinders the large-scale practical application of this battery technology.

A particular limitation of the OER and especially ORR is their sluggish reaction kinetics associated with complex multiple-step processes that involve the transference of 4 electrons and several intermediates. Besides, a major difficulty in developing bifunctional oxygen catalysts as ZABs cathode is the difference in binding strengths of the OER and ORR intermediates. Thus, high-performance OER catalysts are not necessarily suitable for ORR and vice versa. Generally, complex functional systems such as the reversible dual oxygen oxidation and reduction processes require equally elaborated catalysts to provide the multiple surface sites required for the adsorption, activation, and reaction of the several involved species [18–29].

HEAs are solid solutions of five or more elements with high thermodynamic and kinetic stability associated with the high activation energy for atomic diffusion [30]. This hampered diffusion is related to lattice distortions associated with the different sizes of the atoms within the HEA. Such lattice distortions play also a notable role in defining the HEA electronic structure, thus leading to unique structural, physical, and chemical properties [31]. HEAs have recently attracted increasing attention in several areas, particularly in catalysis [32–34]. In the catalysis field, HEAs offer advantages in terms of stability, diversity of adsorption/reaction sites, and design and engineering flexibility [35,36]. Owing to their intricate composition, HEAs contain diverse active sites. Besides, the interaction between the different atoms within the HEA may result in favorable synergistic effects [37]. Additionally, such complex compositions provide additional degrees of freedom to fine-tune the material structural, electronic, and catalytic properties [38]. Thus, overall, HEAs are highly promising candidates as bifunctional oxygen catalysts compared with elemental particles and binary or ternary alloys that are generally optimized for a single oxygen reaction due to the limited degrees of freedom available for their design and engineering.

Despite the high potential of HEAs as multifunctional catalysts and the significant efforts devoted to the production of HEA-based oxygen electrocatalysts, the developed catalysts have usually targeted just a single oxygen reaction, either OER or ORR. At the same time, little work has been done on the application of no-noble metal HEA bifunctional electrocatalysts in ZABs. A notable exception is a work by Qiu et al. detailing a dealloying method to synthesize the bifunctional electrocatalysts AlFeCoNiCr that provides a specific capacity of 799.8 mAh g^{-1} [39].

The most studied HEAs are based on 3d transition metals. As a representative HEA, CrMnFeCoNi can be synthesized by sputtering [40], arc-melting [41], and plasma sintering [42], which involve either high temperatures or expensive and low production throughput equipment, that do not meet the demands for cost-efficiency. Besides, most previous works on this material have focused on studying the crystal formation mechanism [43,44], mechanical strength [45,46], anti-radiation performance [47,48], and corrosion resistance [49,50].

Here, we detail the synthesis of the noble metal-free CrMnFeCoNi HEA using a solution-based approach. The final composition was optimized after screening several combinations of elements based on the system Mn-Fe-Co-Ni. Cr or Cu was afterward introduced into the optimized quaternary composition to further tune its morphology, lattice and electronic structure, and overall catalytic properties. The resulting HEAs were tested both for OER and ORR, and as bifunctional OER/ORR catalysts within reversible ZABs. The outstanding performances obtained, well above state-of-the-art commercial catalysts, are rationalized using DFT calculations.

2.3 Experimental section

2.3.1 Materials and reagents

Manganese(II) acetylacetonate (Mn(acac)$_2$), nickel(II) acetylacetonate (Ni(acac)$_2$), cobalt(II) acetylacetonate (Co(acac)$_2$), iron(II) acetylacetonate (Fe(acac)$_2$), copper(II) acetylacetonate (Cu(acac)$_2$), chromium(III) acetylacetonate (Cr(acac)$_3$), oleylamine (OAm, >70 %) and D(+)-glucose (99.5 %) were bought from Sigma-Aldrich. Methanol (99 %), cyclohexane (99 %), potassium hydroxide (87 %), (1-hexadecyl) trimethylammonium chloride (CTAC, 96 %), and Nafion solution (5 wt %) were supplied by Alfa Aesar. Ethanol (96 %) and isopropanol (99.7 %) were purchased from Solvech. All chemicals were used as received without further purification. Deionized (DI) water ($\geq$18.2 MΩ cm^{-1}) was obtained by an ultra-pure purification system (Aqua Solutions).

2.3.2 Synthesis of catalysts

Preparation of MnFeCoNi, CrMnFeCoNi, and CuMnFeCoNi NPs. All syntheses were carried out using standard vacuum/argon Schlenk lines. In a typical preparation of MnFeCoNi particles, 240 mg glucose and 400 mg CTAC were dissolved in 10 mL OAm, followed by ultrasonication for 2 h. Then, 0.1 mmol Mn(acac)$_2$, Fe(acac)$_2$, Co(acac)$_2$, and Ni(acac)$_2$ were added into the mixture, followed by ultrasonication for 2 h and magnetic stirring for 30 min to form a homogeneous solution. The mixture was then vacuumed for 1 h at 90 °C to remove oxygen and low boinging point impurities. Then the temperature was increased to 260 °C in an argon atmosphere and the mixture was allowed to react for 2 h. Afterward, the flask was allowed to cool down to 200 °C by removing the heating mantle and then cooled rapidly down to room temperature with a water bath. The black product was collected by centrifugation and washed three times with a cyclohexane/ethanol mixture. CrMnFeCoNi and CuMnFeCoNi particles were produced following the exact same procedure but adding 0.1 mmol of the additional metal precursor (Cr (acac)$_3$ or Cu(acac)$_2$) in the initial reaction mixture.

2.3.3 Material characterization

Scanning electron microscopy (SEM) images were obtained in a Zeiss Auriga field emission-SEM operating at 5 kV. Transmission electron microscopy (TEM) micrographs were obtained in a Tecnai F20 field emission gun microscope with a 0.19

nm point-to-point resolution at 200 kV. Images were analyzed using Gatan Digital Micrograph software. High angle annular dark-field (HAADF)-scanning transmission electron microscopy (STEM) images and elemental mapping were measured in a spherical aberration-corrected transmission electron microscope FEI Titan G2 80-200 ChemiSTEM with four energy-dispersive X-ray spectroscopy (EDS) detectors and operated at 80 and 200 keV. The crystal structure was characterized by means of powder X-ray diffraction (XRD) measured in a Bruker AXS D8 Advance X-ray diffractometer. (Cu-Kα radiation, λ =1.5418 Å, 40 kV and 40 mA; Bruker, Germany). Inductively coupled plasma-optical emission spectroscopy (ICP-OES) and laser-ablation ICP-OES (LA-ICP-OES) were conducted on an ICPE-9820 system. X-ray photoelectron spectroscopy (XPS) was performed with an Al anode XR50 source on a Specs system equipped with a Phoibos 150 MCD-9 detector (150 W).

2.3.4 Electrochemical measurements

All the electrochemical measurements were carried out on a Chi760E electrochemical workstation (Shanghai Chenhua, China) at room temperature using a standard three-electrode setup system with iR compensation. A platinum grid, a glassy carbon electrode (GCE) with a 5 mm diameter, and a Hg/HgO electrode were used as the counter electrode, working electrode, and reference electrode, respectively. To prepare the working electrode, 4 mg catalyst, 2 mg carbon black, and 30 μL 5 wt% Nafion solution were added to 750 μL isopropanol and 220 μL DI water. The obtained solution was sonicated for 1 h to obtain a homogeneous catalyst ink. 5 μL of the mixture solution was dropped on the GCE electrode and dried before the electrochemical tests.

For OER, linear sweep voltammetry (LSV) measurements were conducted in 1.0 M KOH at room temperature with a scan rate of 5 mV s^{-1}. Electrochemical impedance spectroscopy (EIS) measurements were recorded under alternating current voltage with frequencies from 0.01 to 105 Hz. The C_{dl} value was measured from CV curves at different scan rates (20, 40, 80, 120, 160, 200 mV s^{-1}) within the non-faradaic potential range of 0.91–1.01 V vs. RHE, and by plotting $j= (j_p - j_n)/2$ at 0.96 V vs. RHE as a function of the scan rate, j_p and j_n represent the current density in positive scan and negative scan at 0.96 V, respectively. The slope of the linear fit corresponds to the C_{dl} value. *In situ* Raman spectra were collected by a Raman microscope (iHR320 monochromator, HORIBA) using an *in situ* Raman cell. The excitation source was a frequency-doubled Nd: YAG laser, emitting 532 nm laser, and the spectra were collected using a grating of 1800 lines mm^{-1}. The electrode was first subjected to CA measurements at a particular applied voltage (1.1-1.6 V vs. RHE) for 5 min, then we started acquiring Raman spectra while keep running the CA measurements.

The ORR was conducted in 0.1 M KOH. A RRDE was used as the substrate for the working electrode. Before tests, O_2 was flowed through the electrolyte for about 30 min to achieve an O_2- saturated solution. CV curves were measured in O_2-saturated or Ar-saturated 0.1 M KOH solution with a scan rate of 10 mV s^{-1}. LSV tests were conducted in O_2-saturated 0.1 M KOH at different rotation rates with a sweep rate of 10 mV s^{-1} at room temperature.

2.3.5 ZAB measurements

10 mg catalyst was dispersed in 1 mL solution containing 750 μL isopropyl alcohol, 220 μL DI water, and 30 μL 5 wt% Nafion solution. Then, the ink was sprayed on the hydrophobic carbon paper (CP) uniformly with a mass loading of 0.5 mg cm^{-2}. This CP was used as the air cathode while a polished Zn foil was used as the anode. The two electrodes were assembled into a ZAB, while a 6 M KOH and 0.2 M zinc acetate aqueous solution was used as the electrolyte.

Solid flexible ZABs based on the HEA catalyst were produced using an electrolyte gel. The poly(vinyl alcohol) (PVA)-KOH-H_2O gel was prepared as follows: 2 g PVA was dissolved in 16 mL DI water at 98 °C under magnetic stirring. Then 2 g KOH dissolved in 4 mL DI water was introduced until the liquid turned viscous and pale-yellow. After that, the gel was introduced into the container and frozen for 2 h, then thawed at room temperature. ZABs were assembled following a stack-type cell configuration. The air electrode was fabricated by dropping 50 μL catalyst ink on a clean CP and then dried at room temperature for 24 h. The polished Zn plate electrode was used as the anode, and the PVA-KOH-H_2O gel was used as the electrolyte.

Charge-discharge polarization curves and OCP measurements were determined utilizing an electrochemical workstation (Chi760E, Chenhua). The galvanostatic test was performed using a Neware BTS4008 battery test system at room temperature. The specific capacities were determined using the galvanostatic discharge profiles standardized to the consumed mass of Zn.

2.3.6 DFT calculations

The plane-wave code Vienna ab-initio simulation package (VASP) program [51-52] was used to perform all the spin-polarized DFT calculations within the generalized gradient approximation (GGA) using the Perdew-Burke-Ernzerhof (PBE) [53] formulation. Projected augmented wave (PAW) potentials [54-55] were chosen to describe the ionic cores, valence electrons were used a plane wave basis set with a kinetic energy cutoff of 500 eV. The valence electron configurations applied in this work are $4S_13d_5$ (Cr), $4S_23d_5$ (Mn), $4S_23d_6$ (Fe), $4S_23d_7$ (Co), $4S_23d_8$ (Ni), $4S_13d_{10}$ (Cu), $2S_22P_4$ (O), and $1S_1$ (H), respectively. Partial occupancies of the Kohn-Sham orbitals were allowed to use the Gaussian smearing method and a width of 0.02 eV. The electronic energy was considered self-consistent when the energy change was smaller than 10^{-6} eV.

The overall OER process includes four elementary steps that follow:

$$H_2O + * \rightarrow *OH + H^+ + e^- \quad (1)$$

$$*OH + H_2O \rightarrow *O + H_2O + H^+ + e^- \quad (2)$$

$$*O + H_2O \rightarrow *OOH + H^+ + e^- \quad (3)$$

$$*OOH + H_2O \rightarrow * + O_2 + H_2O + H^+ + e^- \quad (4)$$

The ΔG are calculated as follows:

$$\Delta G_1 = G(*OH) + G(H_2) - G(*) - G(H_2O)$$

$$\Delta G_2 = G(*O) + 1/2\, G(H_2) - G(*OH)$$

$$\Delta G_3 = G(*OOH) + 1/2\, G(H_2) - G(*O) - G(H_2O)$$

$$\Delta G_4 = 4.92(\text{eV}) - \Delta G_1 - \Delta G_2 - \Delta G_3$$

The ΔG values are calculated by:

$$\Delta G = \Delta E + \Delta E_{ZPE} - T\Delta S$$

ΔE is the total energy difference before and after intermidiattes adsoption. ΔE_{ZPE} is the zero-point energy difference, ΔS is the entropy difference.

.

2.4 Results and discussion

2.4.1 Catalyst structural and chemical characterization

As schematized in **Figure 1**, ternary and quaternary particles within the Mn-Fe-Co-Ni system, and CrMnFeCoNi and CuMnFeCoNi alloys were produced from the simultaneous reduction of the metal salts at 260 °C in the presence of OAm as a solvent and reducing agent, glucose as an additional reducing agent, and CTAC as a surfactant.

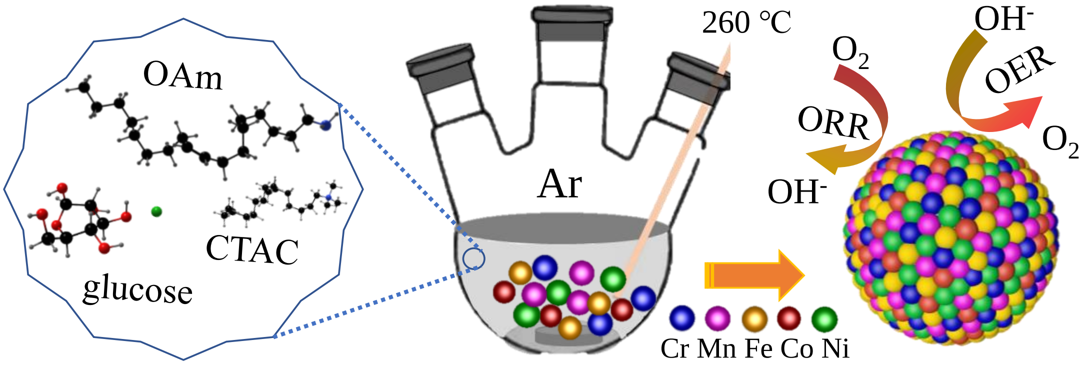

Figure 1. Schematic diagram of a HEA synthesis process.

The ternary alloys, FeCoNi, MnFeNi, MnCoNi, and MnFeCo were initially produced to determine the possible range of reaction parameters and as a reference for electrochemical measurements. The results from their composition and structural analysis are shown in **Figures 2 and 3**. All the ternary alloys show an amorphous or weak crystalline phase.

a

Element	Weight%	Atomic%
Fe K	26.9	27.9
Co K	19.3	19.1
Ni K	53.8	53.0

b

Element	Weight%	Atomic%
Mn K	36.4	37.3
Fe K	35.4	35.7
Ni K	28.2	27.0

c

Element	Weight%	Atomic%
Mn K	35.4	36.9
Co K	29.1	28.4
Ni K	35.5	34.7

d

Element	Weight%	Atomic%
Mn K	36.1	37.0
Fe K	34.7	35.1
Co K	29.2	27.9

Figure 2. EDS composition of the ternary alloys: FeCoNi, MnFeNi, MnCoNi, and

MnFeCo

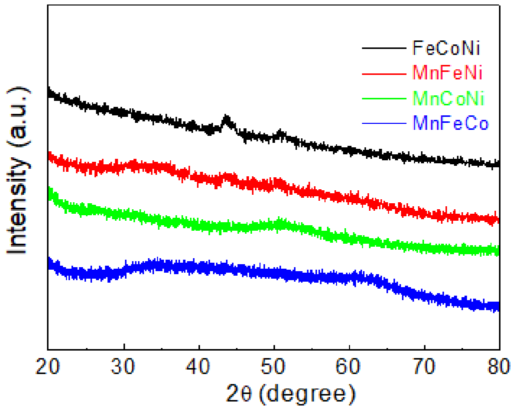

Figure 3. XRD pattern of the ternary alloys: FeCoNi, MnFeNi, MnCoNi, and MnFeCo.

According to ICP-OES analysis, the quaternary MnFeCoNi particles were characterized by a metal ratio of Mn:Fe:Co:Ni = 28:29:19:24 (**Figure 4a**). As displayed in **Figure 4b**, the XRD pattern shows the MnFeCoNi alloy to be characterized by a FCC structure with a lattice constant of 3.543 Å, resembling that of cubic CoNi (3.530 Å). As observed by TEM analysis, MnFeCoNi particles showed a large dispersion in size and morphology (**Figure 4c**). The high-resolution TEM (HRTEM) micrograph shown in **Figure 4d** displays a cubic crystal phase in agreement with XRD analysis with a lattice fringe distance of 0.211 nm along the (111) zone axis, which is similar to that of CoNi phase (0.204 nm). As shown in **Figure 4d**, no significant lattice distortions were observed in the MnFeCoNi quaternary alloy.

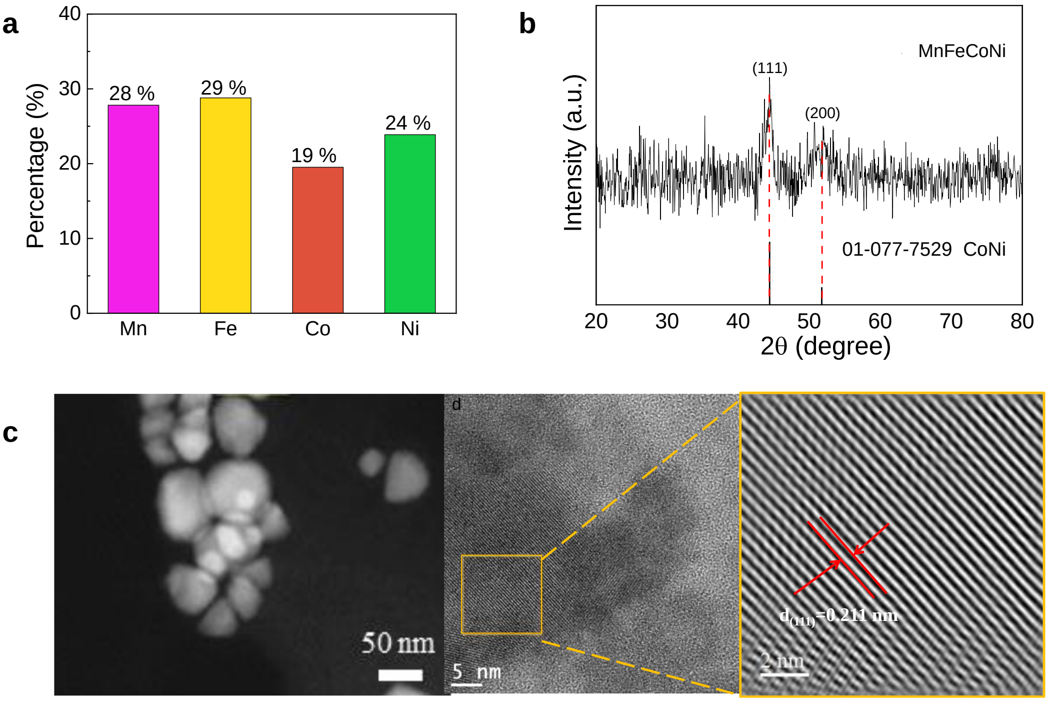

Figure 4. (a) ICP-OES composition, (b) XRD pattern, (c) TEM image, and (d) HRTEM images of a MnFeCoNi quaternary alloy.

Cr was introduced into the MnFeCoNi system to form the CrMnFeCoNi quinary alloy. **Figure 5a** shows a representative TEM image of the produced CrMnFeCoNi particles that display an average size of 170 nm and octahedral morphology. EDS composition maps show a homogeneous distribution of Cr, Mn, Fe, Co, and Ni within each particle. XRD peaks of CrMnFeCoNi were detected at 43.60°, 50.85° and 74.39°, as shown in **Figure 5b**, pointing at an FCC structure, resembling that of the cubic FeCoNi phase, but with a lattice constant of 3.559 Å. The slightly larger lattice constant measured, compared with that of the FeCoNi phase (3.545 Å), is consistent with the slightly larger atomic r of Cr and Mn compared with Fe, Co, and Ni (see details in **Table 1**). ICP-OES showed the Cr:Mn:Fe:Co:Ni ratio to be 12:24:31:16:17 (**Figure 5c**).

Table 1. Atomic r and electronegativity of different elements.

	Cr	Mn	Fe	Co	Ni	Cu
atomic r	128 pm	127 pm	126 pm	125 pm	124 pm	128 pm

Electronegativity (Pauling scale)	1.66	1.55	1.83	1.88	1.91	1.9

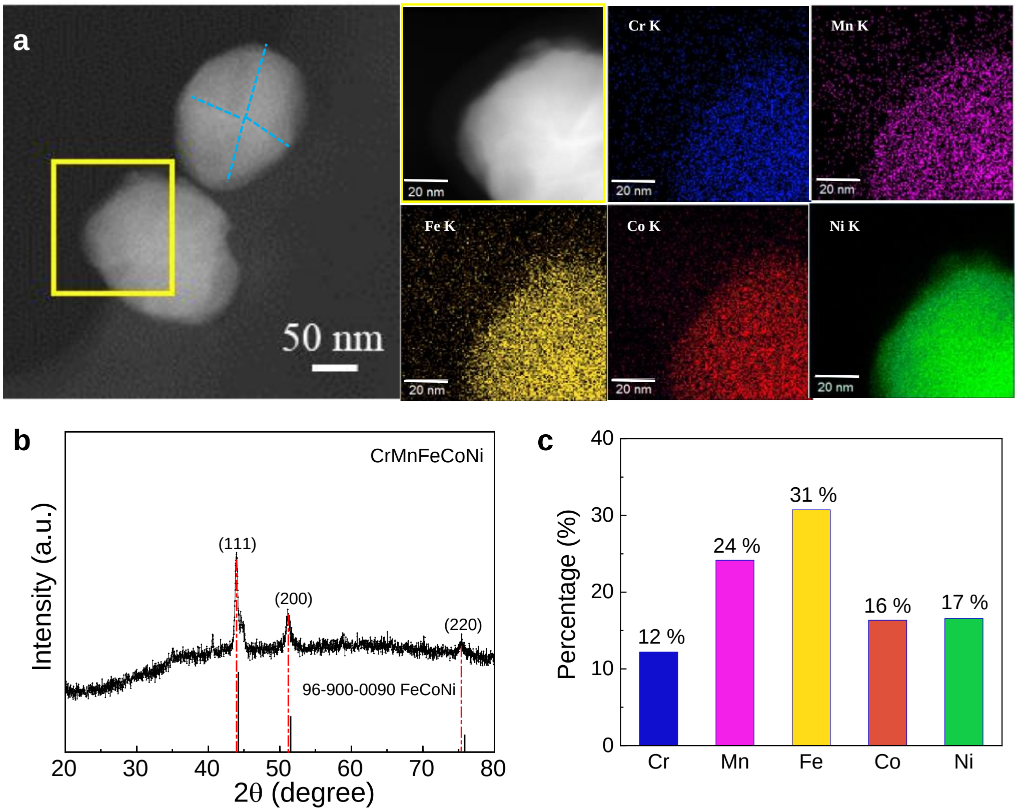

Figure 5. (a) TEM image and EDS chemical composition maps. (b) XRD pattern and (c) ICP-OES composition of a CrMnFeCoNi HEAs.

The mixing entropy of CrMnFeCoNi was calculated to be 1.55R[56]. According to the entropy concept, HEAs are quantitatively defined as having a configurational entropy larger than 1.5R in their random solution state, Therefore, taking into account the single crystal phase observed, the large atomic percentage (C_i) of each element, and the high entropy calculated, the CrMnFeCoNi produced here is probed to be a HEA.

Unlike the quaternary compounds, CrMnFeCoNi HEAs were characterized by a large density of defects, including lattice distortions and dislocations. As observed in the representative HRTEM image shown in **Figure 6a**, the region marked by a yellow square and amplified in **Figure 6b** shows a large number of dislocations indicated by T-shape symbols. The red-squared area in **Figure 6c** shows a twin structure with an interface composed of a (111) coherent boundary (**Figure 6c**). The lattice fringes observed here have double hump shape dislocations. The fast Fourier transformation (FFT) of this region is shown in **Figure 6d**. The two overlapping patterns from the two observed crystallites are indicated by the indexation of the FCC phases with two different colors. For the growth of the CrMnFeCoNi HEA FCC structure, the segregation of metal atoms on the (111) crystallographic plane proceeds with a twin fault packing sequence (-'A-B-C'-D-'C-B-A'), where A, B, and C represent different kinds of atomic stacking sites, in which the twin faulted plane "D" separates the twinned lattice "-C-B-A".

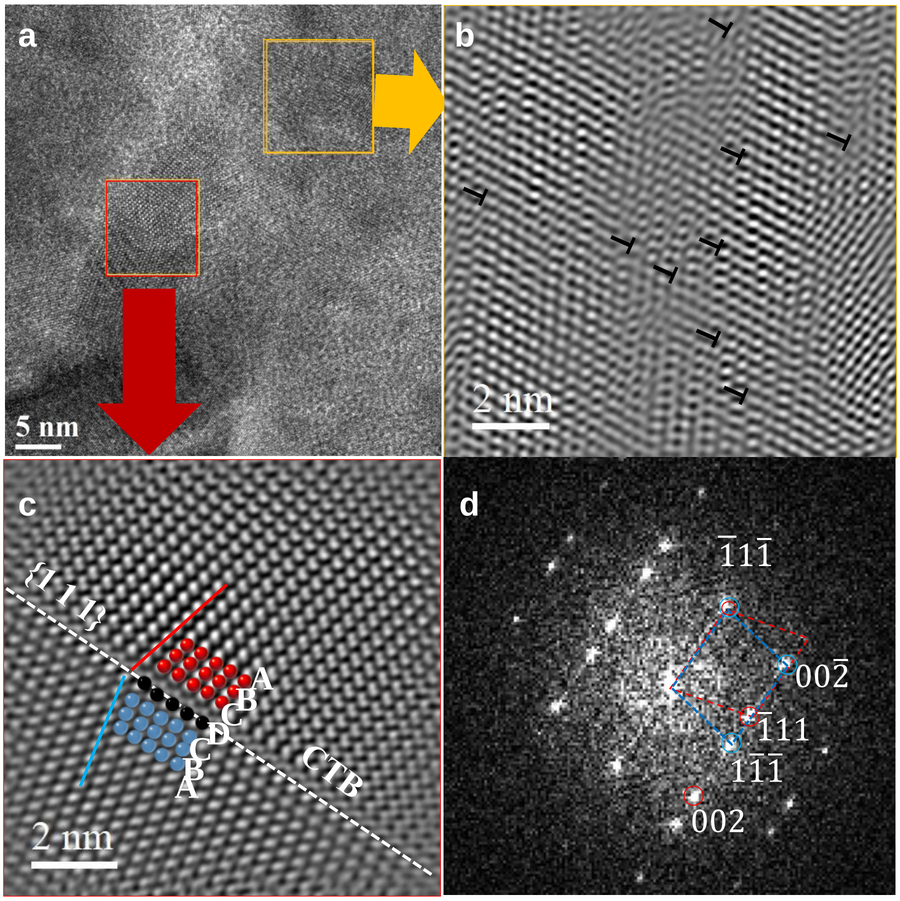

Figure 6. (a) HRTEM image of CrMnFeCoNi particles. (b) HRTEM image of the magnified right yellow square in (a). (c) HRTEM image of the magnified red square in (a). (d) FFT pattern of (c).

CuMnFeCoNi particles were produced by introducing Cu instead of Cr into the quaternary MnFeCoNi system. ICP-OES analysis showed the CuMnFeCoNi particles to have a metal ratio Cu:Mn:Fe:Co:Ni of 21:20:16:21:22 (**Figure 7a**). Their XRD pattern (**Figure 7b**) showed the CuMnFeCoNi particles to be characterized by an FCC structure with a lattice constant of 3.54 Å, resembling that of the cubic CuNi phase (3.60 Å). The mixing entropy of CuMnFeCoNi was calculated to be 1.60R, thus confirming this alloy as a HEA. CuMnFeCoNi particles displayed a non-uniform geometry and a broad size distribution centered at around 120 nm (**Figure 7c**). All the particles contained the five elements according to EDS maps (**Figure 7c**). HRTEM micrographs displayed numerous lattice dislocations with a lattice fringe distance of 0.206 nm along the (111) zone axis, which is similar to the 0.208 nm of CuNi (**Figure 7d**).

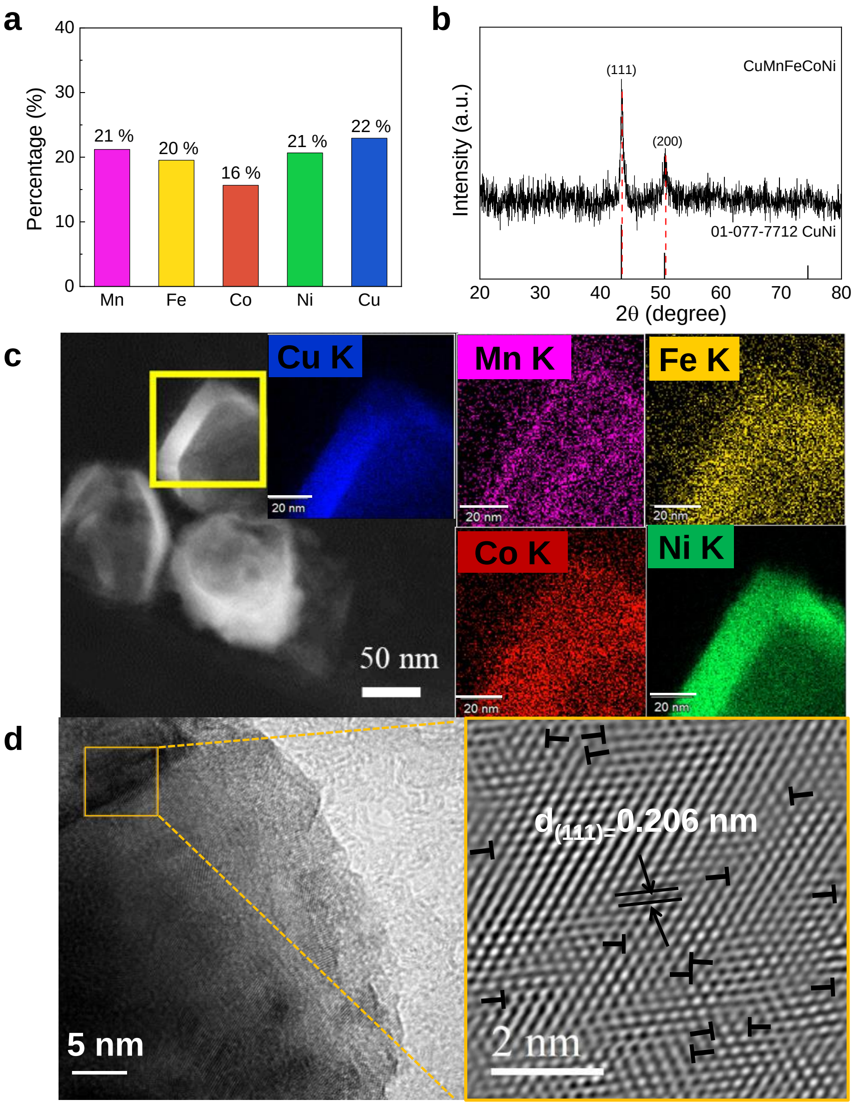

Figure 7. (a) ICP-OES composition, (b) XRD pattern, (c) TEM image and EDS chemical composition maps, and (d) HRTEM images of a CuMnFeCoNi HEA.

Overall, it was experimentally observed that when Cr or Cu was introduced into the MnFeCoNi system, a significant change in the crystal structure took place, distorting the lattice and creating dislocations and particularly twins. We associate this distortion with the slightly different atomic r, electronegativity, and oxidation state of Cr and Cu. Particularly, electronic differences between the several distinct atoms generate a local charge unbalance and an associated electric field that affects the atomic organization and particle morphology [57], which could explain the lattice dislocations and twin structures observed by HRTEM.

The high-resolution Cr 2p, Mn 2p, Fe 2p, Co 2p, and Ni 2p XPS spectra of the MnFeCoNi, CrMnFeCoNi, and CuMnFeCoNi particles are shown in **Figure 8**. All elements display two chemical states, a metallic component assigned to the particle core and an oxidized component associated with the formation of a thin oxide layer at the particle surface. As shown in **Figure 8a**, the Mn 2p XPS spectrum of MnFeCoNi displays a doublet at 638.36 eV (Mn 2p3/2) assigned to Mn^0 and a second doublet at 642.48 eV (Mn 2p3/2) assigned to Mn^{4+}. The Fe 2p XPS spectrum of MnFeCoNi displays a doublet at 706.79 eV (Fe 2p3/2) assigned to Fe^0 and a second doublet at 710.22 eV (Fe 2p3/2) assigned to Fe^{3+}, accompanied by two satellite peaks (**Figure 8b**). The Co 2p XPS spectrum (**Figure 8c**) displays a Co^0 valence state at 777.88 eV (Co 2p3/2), and a Co^{2+} state at 781.81 eV (Co 2p3/2). The Ni 2p XPS spectrum of MnFeCoNi shows two doublets, assigned to Ni^0 at 852.84 eV (Ni 2p3/2), and Ni^{2+} at 856.45 eV (Ni 2p3/2), and two satellite peaks (**Figure 8d**). For the CrMnFeCoNi HEA, the Cr 2p XPS spectrum displays two chemical states, Cr^0 at 574.38 eV (Cr 2p3/2) and Cr^{3+} at 576.56 eV (Cr 2p3/2) (**Figure 8e**). In comparison with the MnFeCoNi quaternary alloy, the introduction of Cr significantly changed the local chemical environment of the different elements. When introducing Cr, the Co 2p electronic states shifted to lower binding energies, which implies some electron transfer towards this element [58]. Meanwhile, the binding energy of Mn 2p, Fe 2p, and Ni 2p electrons were positively shifted, implying electron transfer from these elements to the surrounding atoms. The detailed peak positions obtained from the fitting of the spectra are shown in **Table 2**. For the CuMnFeCoNi HEA, the Cu 2p XPS spectrum displays two chemical states, Cu^0 at 932.47 eV (Cu 2p3/2) and Cu^{2+} at 934.50 eV (Cu 2p3/2) (**Figure 8e**). In comparison with the MnFeCoNi quaternary alloy, in the CuMnFeCoNi HEA, the Mn 2p and Co 2p electronic states shifted to lower binding energies, while Fe 2p and Ni 2p shifted to higher binding energies, indicating that Mn and Co attract electrons, while Fe and Ni lose them. **Figure 8f** and **Figures 9-10** show the slices of the electron density difference of CrMnFeCoNi and CuMnFeCoNi obtained from DFT calculations, which further indicates the interaction of electrons in each atom of the HEAs.

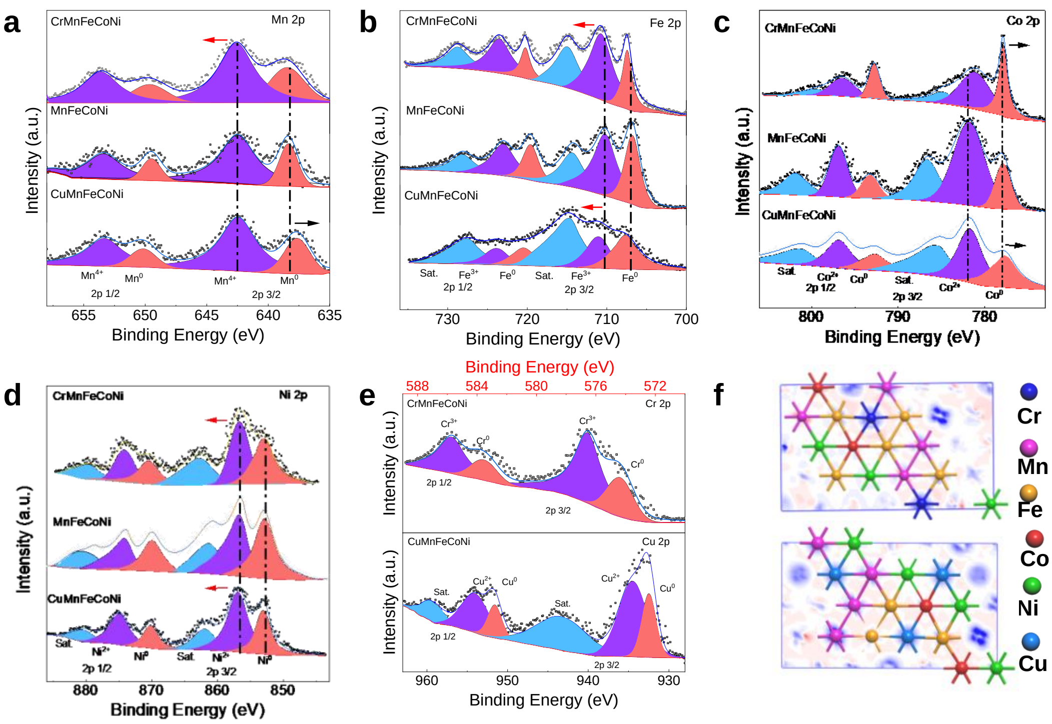

Figure 8. High resolution (a) Mn 2p, (b) Fe 2p, (c) Co 2p, (d) Ni 2p, and (e) Cr 2p and Cu 2p XPS spectra of MnFeCoNi, CrMnFeCoNi, and CuMnFeCoNi particles. (f) Slices of electron density difference of CrMnFeCoNi and CuMnFeCoNi. The contour around the atoms represents electron accumulation (red) or electron depletion (blue).

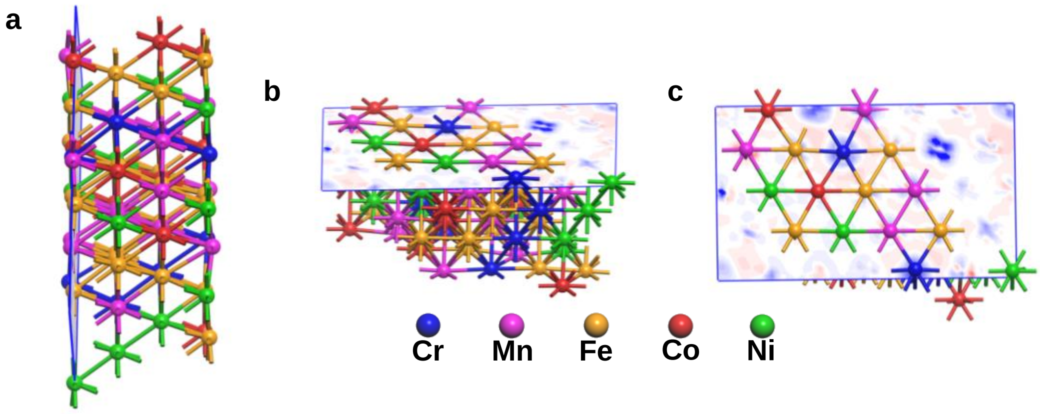

Figure 9. Slices of electron density difference of CrMnFeCoNi in (a) side view, (b)

front view, and (c) top view. The contour around the atoms represents electron accumulation (red) or electron depletion (blue).

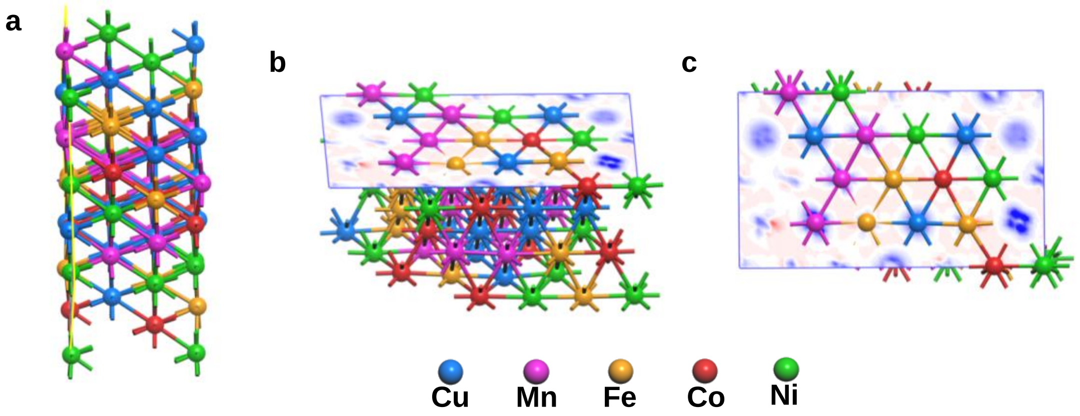

Figure 10. Slices of electron density difference of CuMnFeCoNi in (a) side view, (b) front view, and (c) top view. The contour around the atoms represents electron accumulation (red) or electron depletion (blue).

Table 2. Mn 2p, Fe 2p, Co 2p and Ni 2p XPS binding energies of MnFeCoNi, CrMnFeCoNi, and CuMnFeCoNi.

		MnFeCoNi (eV)	CrMnFeCoNi (eV)	CuMnFeCoNi (eV)
Cr $2p_{3/2}$	Cr^0	-	574.38	-
	Cr^{3+}	-	576.56	-
Cu $2p_{3/2}$	Cu^0	-	-	932.47
	Cu^{2+}	-	-	934.50
Mn $2p_{3/2}$	Mn^0	638.36	638.47↑	637.65↓
	Mn^{4+}	642.48	642.60↑	642.45↓
Fe $2p_{3/2}$	Fe^0	706.79	707.44 ↑	707.68 ↑
	Fe^{3+}	710.22	710.72↑	711.07↑
Co $2p_{3/2}$	Co^0	777.88	776.43↓	777.67↓
	Co^{2+}	781.81	781.10↓	781.69↓
Ni $2p_{3/2}$	Ni^0	852.84	852.96 ↑	852.94↑
	Ni^{2+}	856.45	856.66↑	856.81↑

2.4.2 Electrocatalytic OER performance

LSV in 1.0 M KOH electrolyte was initially used to evaluate the OER activity of the catalysts. **Figure 11a** shows the LSV curves of the four ternary alloys based on Mn, Fe, Co, and Ni. The η at 10 mA cm^{-2} of FeCoNi, MnFeNi, MnCoNi, and MnFeCo particles was 295 mV, 323 mV, 345 mV, and 331 mV, respectively (**Figure 11b**). As shown in **Figure 11c** and **11d**, among the ternary compounds, FeCoNi displays the smallest Tafel slope and charge transfer resistance (R_{ct}), as measured by EIS. We generally observed the performance of the ternary alloys containing Fe to be better than that of MnCoNi, indicating that Fe plays an essential role in the OER.

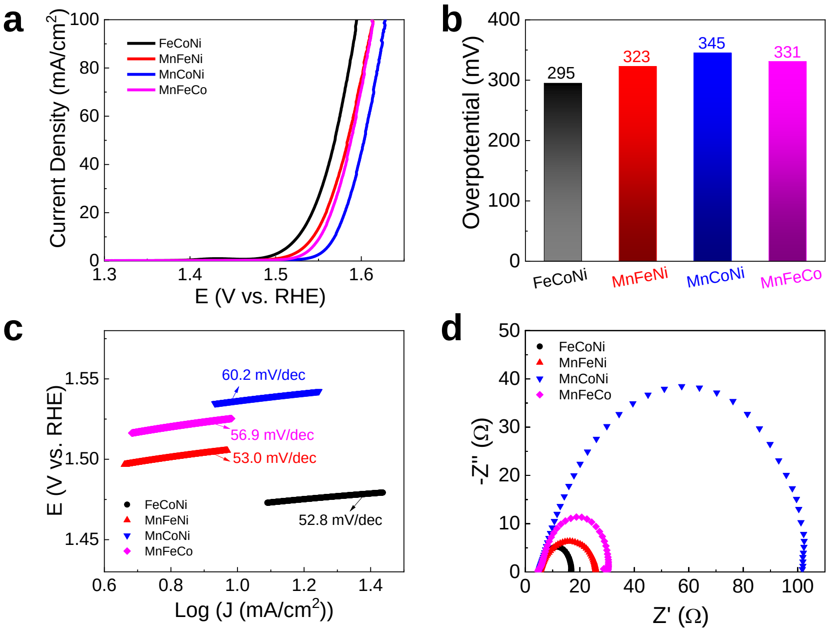

Figure 11. OER performance of the ternary alloys. (a) LSV curves, (b) corresponding η at 10 mA cm^{-2}, (c) corresponding Tafel plots, and (d) EIS spectra.

The LSV curve of the MnFeCoNi alloy is displayed in **Figure 12a**. It shows that the combination of the four elements results in an even lower η, 282 mV, at 10 mA cm^{-2}. Subsequently, we tested the performance of the HEAs obtained by adding Cr or Cu into the Mn-Fe-Co-Ni precursor solution. These two additional elements were selected taking into account their low cost, high abundance, non-toxic nature, and potential OER and ORR performance [59–62]. **Figure 12a** shows the LSV curves obtained from CrMnFeCoNi, CuMnFeCoNi, and a commercial RuO_2 catalyst used as a reference. As displayed in **Figure 12b**, CrMnFeCoNi displays the best OER performance with an η at 10 mA cm^{-2} of 265 mV, well below that of MnFeCoNi (282 mV), CuMnFeCoNi (298 mV), and RuO_2 (293 mV). The Tafel slopes calculated from LSV curves are displayed in **Figure 12c**. CrMnFeCoNi is characterized by the fastest OER kinetics, with the smallest Tafel slope at 37.9 mV dec^{-1}, significantly below that of MnFeCoNi (46.8 mV dec^{-1}), CuMnFeCoNi (49.1 mV dec^{-1}), and RuO_2 (90 mV dec^{-1}).

CrMnFeCoNi also displayed the smallest R_{ct} among the tested electrocatalysts, as measured by EIS (**Figure 12d**). On the other hand, similar C_{dl} and thus ECSA were obtained for all the catalysts, as analyzed through CV at different scan rates (**Figure 13**). Thus, the higher catalytic performance of CrMnFeCoNi needs to be attributed to an intrinsically higher activity of its active sites rather than to a higher surface area [63]. Overall, CrMnFeCoNi showed an improved OER performance over the tested materials and most previously reported alloy catalysts, as shown in **Figure 12e** and **Table 3**. The CrMnFeCoNi stability under OER conditions was analyzed using CA. As shown in **Figure 12f**, after a 30 h measurement at 1.5 V vs. RHE, 99 % of the initial current density was maintained.

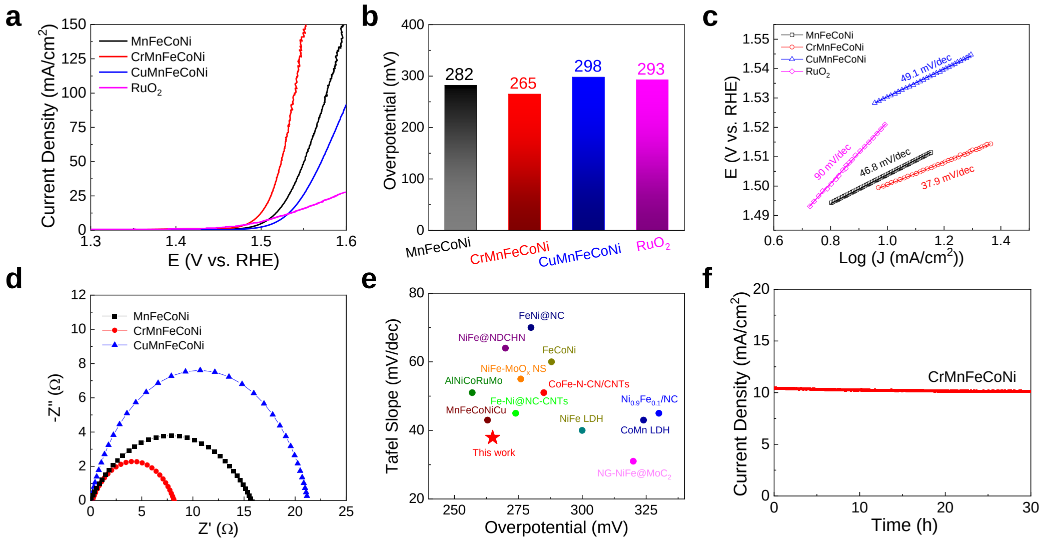

Figure 12. OER performance. (a) LSV curves, (b) η at 10 mA cm^{-2}, and (c) Tafel slopes of CrMnFeCoNi, MnFeCoNi, CuMnFeCoNi, and RuO_2 electrodes. (d) EIS spectra of CrMnFeCoNi, MnFeCoNi, and CuMnFeCoNi electrodes. (e) Comparisons of the OER performance of CrMnFeCoNi with recently reported catalysts. (f) Chronoamperometric curves of CrMnFeCoNi HEA during OER.

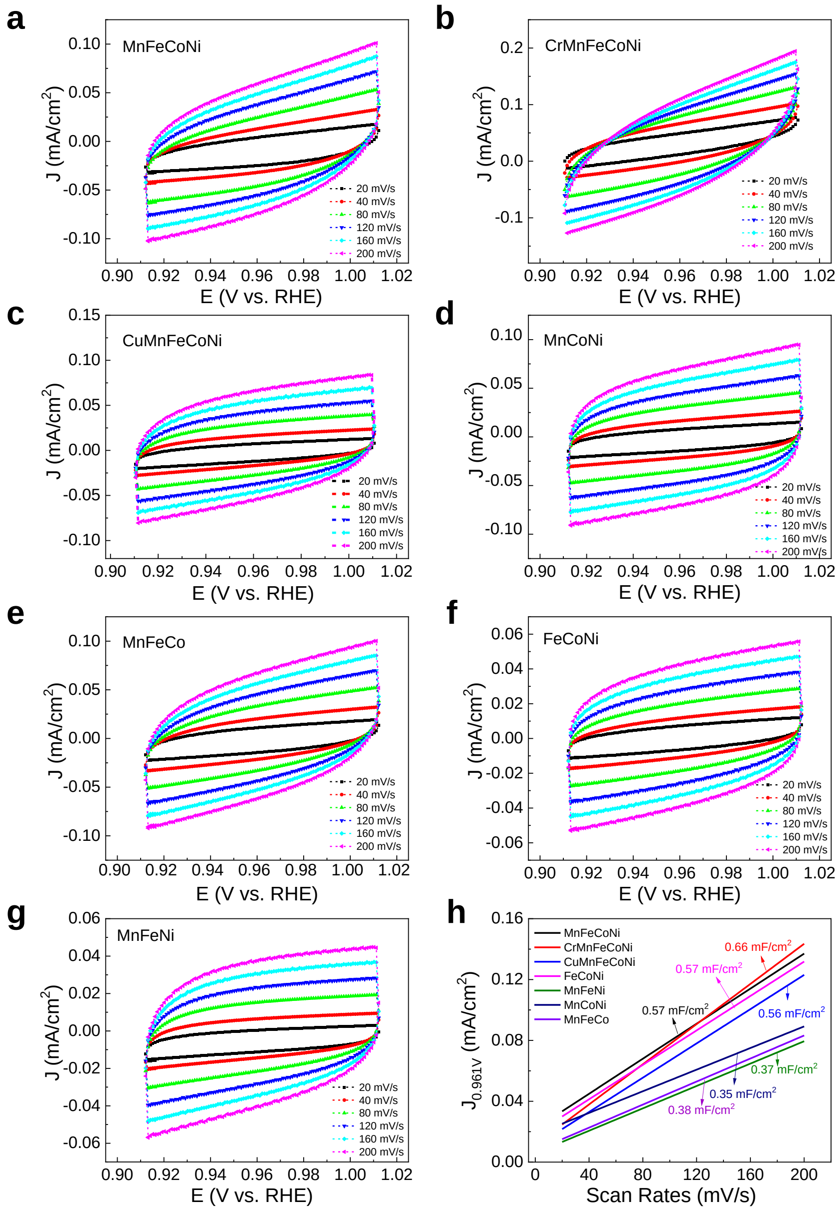

Figure 13. (a-g) CV curves with different scan rates of different HEA, quaternary alloy, and ternary alloys in 1.0 M KOH showing the C_{dl} without electrochemical reactions. (h) Current density at 0.961V vs. RHE plotted against the scan rate and fitted to a linear region to estimate the capacitance.

Table 3. Comparison of the OER performance of the CrMnFeCoNi HEA with recently reported HEA catalysts.

Catalyst	Substrate	η@10 mA cm^{-2}(mV)	Tafel slope (mV dec^{-1})	Ref.
MnFeCoNi-MO_x	CP	302	83.7	*J. Power Sources*, **2019**, 430, 104-

				111.
CoCrFeNiMo	Mg-holder	220	59	*J. Mater. Sci. Technol.*, **2021**, 79, 171-177.
CoFeGaNiZn	GCE	370	71	*Nano Res.*, **2021**, 4799–4806.
FeCoNiCuZn	GCE	304	-	*J. Mater. Sci. Technol.*, **2021**, 93, 110-118.
AlNiCoFeMo	GCE	240	46	*ACS Mater. Lett.*, **2019**, 1, 526-533.
AlNiCoRuMo	GCE	245	54.5	*ACS Mater. Lett.*, **2020**, 2, 1698-1706.
Mo$_{51}$Ni$_{40}$Fe$_{9}$	GCE	257	51	*Acs Appl. Mater. Inter.*, **2017**, 9, 7059-7067.
NiFe LDH	Ni-Foam	300	40	*Nat. Commun.*, **2014**, 5, 4477.
CoMn LDH	GCE	324	43	*J. Am. Chem. Soc.*, **2014**, 136, 16481-16484.
FeCoNi alloy	GCE	400	72	*ChemistrySelect*, **2017**, 2, 1630-1636.
CoFeLaNiPt	GCE	377	150	*Nat. Commun.*, **2019**, 10, 2650.
Fe-Ni@NC-CNTs	GCE	274	45	*Angew Chem. Int. Ed.*, **2018**, 57, 8921-8926.
CoFe-N-CN/CNTs	GCE	285	51	*ChemSusChem*, **2018**, 11, 2358-2366.
Mo$_{0.6}$Ni$_{0.4}$	GCE	290	115	*Adv. Mater. Interfaces*, **2018**, 5, 1800359.
FeNi@NC	GCE	280	70	*Energy Environ. Sci.*, **2016**, 9, 123-129.
FeCoNi	GCE	288	60	*ACS Catal.*, **2016**, 7, 469-479.
NiFe@NDCHN	GCE	270	64	*Nano Energy*, **2018**, 48, 489-499.
MnFeCoNiCu	CC	263	43	*J. Mater. Chem. A*, **2020**, 8, 11938-11947
AlFeCoNiCr	GCE	270	52	*Appl. Catal. B-*

				environ., **2020**, 268, 118431.
CrMnFeCoNi	**GCE**	**265**	**37.9**	**In this work**

CC: carbon cloth.

Besides, after long-term OER, the composition of the HEA, as measured by ICP-OES analysis, was relatively similar to the original one, with an atomic ratio Cr:Mn:Fe:Co:Ni = 17:21:26:17:19 (**Figure 14**). The metal content in the electrolyte after long-term OER was also analyzed and it is displayed in **Table 4**. After a 30 h reaction, negligible amounts of metal were dissolved in the KOH electrolyte, which indicates HEAs to be very stable and resistant to alkaline corrosion. The high stability of HEAs is generally associated with a high entropy effect [64]. XRD analysis showed the crystal structure of the materials to be maintained (**Figure 15**). Besides, HRTEM characterization confirmed that, after the OER stability test, CrMnFeCoNi conserved the cubic FeCoNi phase in the particle core, while a thin amorphous layer attributed to the metal (oxyhydr)oxide had formed on their surface (**Figure 16**).

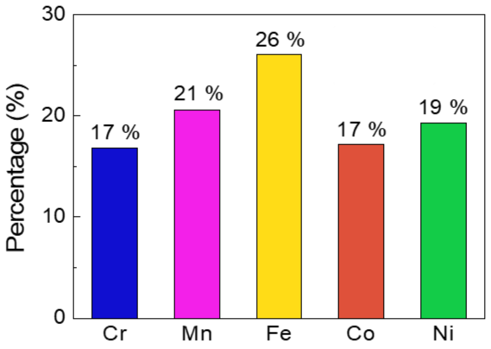

Figure 14. ICP-OES composition of a CrMnFeCoNi HEA after stability test.

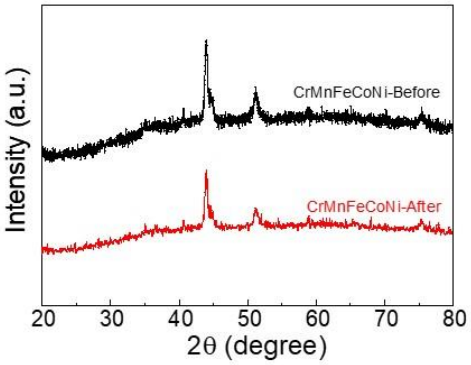

Figure 15. XRD pattern of CrMnFeCoNi before and after OER stability measurements.

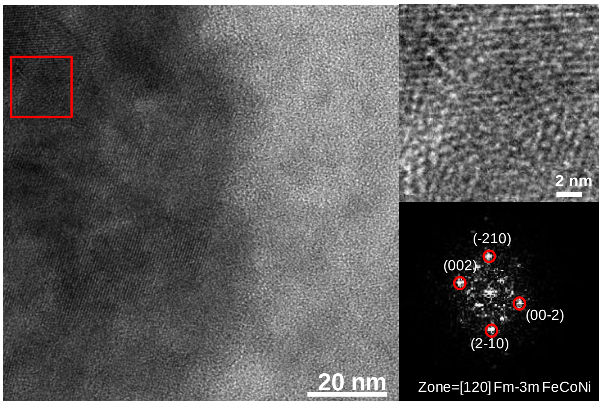

Figure 16. HRTEM image of CrMnFeCoNi after OER measurements.

Table 4. ICP-OES results of the amount of metallic elements in the electrolyte after long-term tests.

Elements Content (ppb, parts per billion)	Cr	Mn	Fe	Co	Ni
0.5 h	3.72	2.92	8.9	2.22	3.83
2 h	4.31	3.36	9.5	2.43	4.29
5 h	4.75	3.88	10.8	2.6	4.66
10 h	8.91	5.51	13.56	3.5	5.15
30 h	11.32	8.25	20.27	5.3	7.83

In situ Raman spectroscopy was used to determine the evolution of CrMnFeCoNi (**Figure 17**). While no Raman signal was obtained from CrMnFeCoNi at the OCP, as the potential increased to 1.1 and 1.2 V vs. RHE, two peaks at 452 and 479 cm^{-1} were observed. These two peaks were indexed as the A_{1g} stretching $Ni(OH)_2$ [65] and FeOH asymmetric stretching [66] Raman modes, respectively. With the potential further increasing to 1.3-1.6 V, i.e. above 1.23 V vs. RHE, three additional peaks at 524, 562, and 609 cm^{-1} were detected and indexed as the FeOOH [67], A_{1g} stretching of NiOOH [67], and E_g of FeOOH [68] Raman modes, respectively. Overall, *in situ* Raman data showed that CrMnFeCoNi was first transformed to metal hydroxide and then to metal oxyhydroxide under OER conditions. XPS characterization of the materials after long-term OER showed the surface of the CrMnFeCoNi particles to be completely oxidized (**Figure 18**), further verifying the evolution of the catalysts.

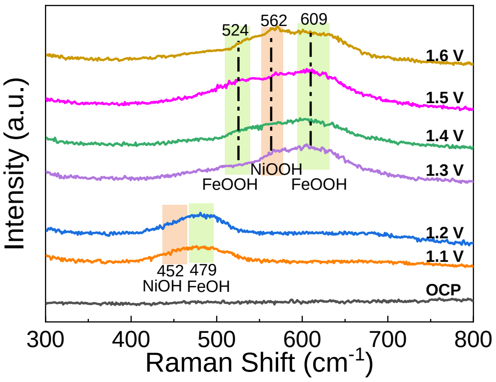

Figure 17. *In situ* Raman spectra of CrMnFeCoNi during OER measurements.

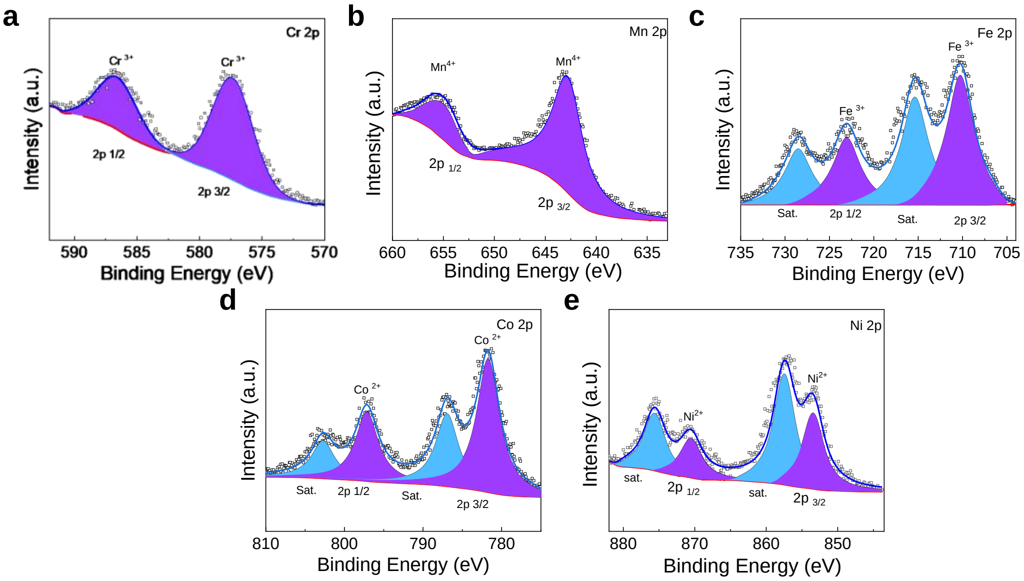

Figure 18. High-resolution XPS spectra of CrMnFeCoNi HEA after OER stability measurements.

2.4.3 Electrocatalytic ORR performance

Towards obtaining a high-performance bifunctional catalyst, the two HEAs and the quaternary catalyst, CrMnFeCoNi, CuMnFeCONi, and MnFeCoNi, were further characterized towards the ORR in 0.1 M KOH using an RRDE electrode. **Figure 19a** shows the CV curves measured from CrMnFeCoNi both in Ar and O_2 saturated electrolytes. Beyond the non-Faradic current characteristic of a double-layer charge-discharge, no obvious electrochemical feature was obtained for the CrMnFeCoNi catalyst within an Ar-saturated electrolyte. In contrast, a noticeable cathodic peak was observed when the electrolyte was saturated with O_2, pointing at a good electrocatalytic activity toward ORR.

Figure 19b shows the LSV curves measured with a rotation speed of 1600 rpm from CrMnFeCoNi, CuMnFeCONi, MnFeCoNi, and a commercial Pt/C catalyst. Among the quaternary and quinary alloys, the CrMnFeCoNi electrode provided the highest current densities, comparable with those of Pt/C. **Figure 19c** shows the LSV curves obtained from the CrMnFeCoNi electrode at different rotation speeds in the range from 400 rpm to 2500 rpm. At 1600 rpm, the $E_{1/2}$ of the CrMnFeCoNi electrode was 0.78 V, and its onset potential was 0.88 V. From the LSV data, the kinetics of the CrMnFeCoNi electrode was investigated using the K-L plots of the inverse current density with the square root of the rotation speed (**Figure 19d**). The excellent linearity of the plots indicates a first-order reaction kinetics with the oxygen concentration [69]. The overlapping of the curves obtained at different voltages pointed to a potential-independent n for ORR, which was estimated at 3.95. Thus, CrMnFeCoNi electrodes showed high selectivity toward a total oxygen reduction dominated by a one-step 4-electron oxygen reduction pathway. This result was corroborated by analyzing the H_2O_2 yield. As determined by RRDE tests, the H_2O_2 average selectivity of the CrMnFeCoNi electrode was just 0.2 % (**Figure 20**), confirming the dominant 4-electron ORR pathway [70]. **Figure 19e** displays the LSV curves measured from the CrMnFeCoNi electrode before and after 1000, 2000, and 5000 CV cycles. LSV curves showed no significant variation in the maximum current density and the onset potential, demonstrating the excellent stability of the CrMnFeCoNi electrode.

The first quantitative measurement of the potential performance of the bifunctional catalyst towards oxygen reactions was evaluated from the E_{gap}[71]. As shown in **Figure 19f**, CrMnFeCoNi electrodes exhibit an outstanding low E_{gap} value of 0.734 V in 0.1 M KOH, well below that of Pt/C and RuO_2 (0.760 V) and most state-of-the-art ORR and OER bifunctional electrocatalysts reported recently (**Table 5**).

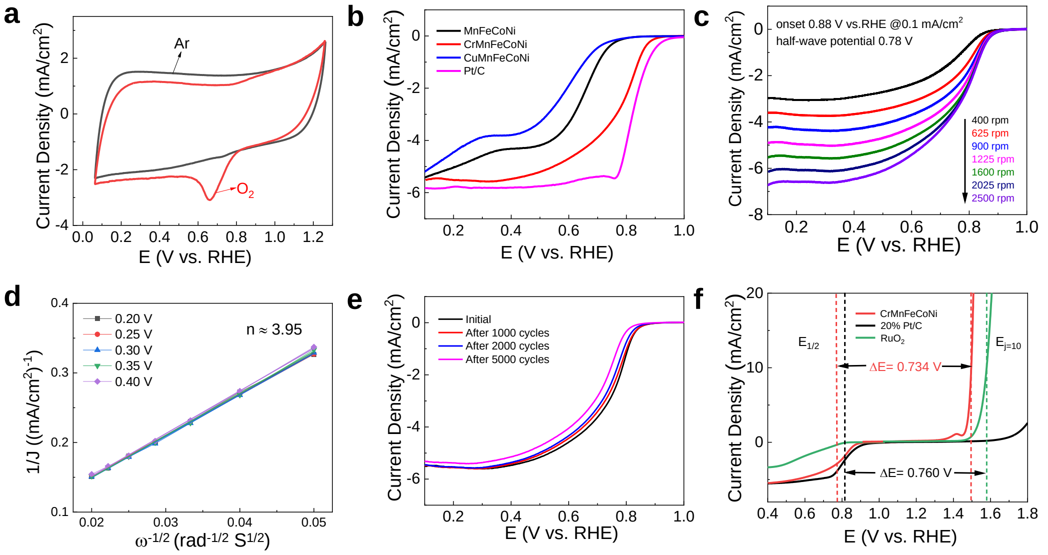

Figure 19. ORR and bifunctional catalytic performance of the CrMnFeCoNi electrode. (a) CV curves measured in Ar and O_2 saturated electrolytes. (b) ORR polarization curves of different electrodes. (c) LSV curves with different rotation rates. (d) K-L plots. (e) LSV curves before and after stability tests of 1000, 2000, and 5000 cycles. (f) ORR/OER bifunctional LSV curves of different electrodes.

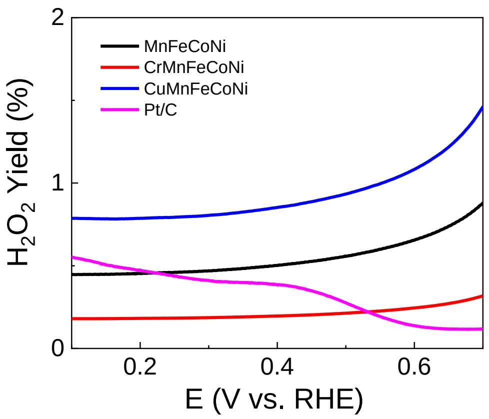

Figure 20. H_2O_2 yield vs. potential from MnFeCoNi, CrMnFeCoNi, CuMnFeCoNi, and Pt/C.

Table 5. Comparison of the bifunctional activities of various state-of-the-art electrocatalysts for OER and ORR.

Catalyst	$E_{j=10}$ (V vs. RHE)	$E_{1/2}$ (V vs. RHE)	E_{gap}（V）	Ref.
AlNiCoRuMo	1.475	0.875	0.6	*ACS Mater. Lett.*,

				2019, 1, 526-533.
AlFeCoNiCr	1.5	0.71	0.79	*Appl. Catal. B-environ.*, **2020**, 268, 118431.
CoO	1.594	0.857	0.737	*Adv. Funct. Mater.*, **2021**, 31, 2101239.
Co_2Fe_1@NC	1.65	0.85	0.8	*J. Am. Chem. Soc.*, **2020**, 142, 7116-7127.
CoDNG900	1.613	0.864	0.75	*Appl. Catal. B-environ.*, **2021**, 281, 119514.
Co@hNCTs-800	1.63	0.87	0.76	*Nano Energy*, **2020**, 71, 104592.
Ni-MnO/rGO	1.6	0.78	0.82	*Adv. Mater.*, **2018**, 30, 1704609.
NiFe-LDH	1.54	0.79	0.75	*Adv. Energy Mater.*, **2017**, 7, 1700467.
Ni_3Fe/C	1.6	0.78	0.82	*Adv. Energy Mater.*, **2017**, 7, 1601172.
NiFe-LDH	1.53	0.91	0.62	*Nano Res.*, **2020**, 14, 1175-1186.
NiFe@NCX	1.55	0.86	0.69	*ACS Catal.*, **2016**, 6, 6335-6342.
FeCo/N-GCNT	1.73	0.92	0.81	*Adv. Energy Mater.*, **2017**, 7, 1602420.
FeCo/N-DNC	1.62	0.81	0.81	*Nanoscale*, **2018**, 10, 19937-19944.
Pt/C	1.91	0.81	1.1	*Adv. Energy Mater.*, **2018**, 8, 1701642.
Pt/C	**1.90**	**0.82**	**1.08**	**This work**
RuO_2	**1.58**	**0.61**	**0.97**	**This work**
Pt/C&RuO_2	**1.58**	**0.82**	**0.76**	**This work**
CrMnFeCoNi	**1.514**	**0.78**	**0.734**	**This work**

OER and ORR of this work in Table 5 were tested in 0.1 M KOH.

2.4.4 DFT calculations

DFT calculations were used to evaluate the Gibbs free energy for each of the four OER elementary steps [72] on the MnFeCoNi (111), CrMnFeCoNi (111), and CuMnFeCoNi

(111) surfaces. A 15 Å vacuum layer in the z-direction was considered between the slab and its periodic images. During structural optimizations of the (111) surface models, a 3×3×1 γ-point centered k-point grid for Brillouin zone was used. All the atomic layers were allowed to fully relax. **Figure 21** shows the relaxed molecular configuration of the four fundamental steps of the OER/ORR for CrMnFeCoNi, CuMnFeCoNi, and MnFeCoNi.

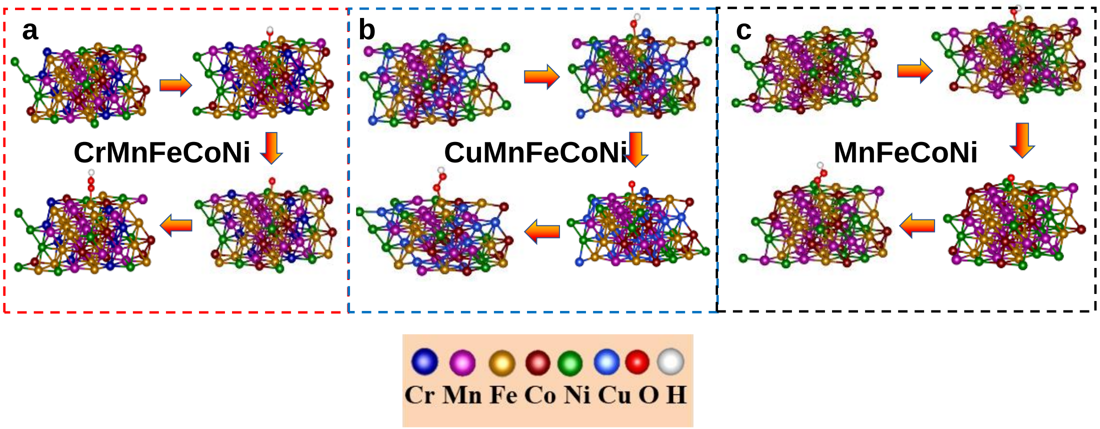

Figure 21. Relaxed atomic configuration of the four fundamental steps of OER/ORR for the (a) CrMnFeCoNi, (b) CuMnFeCoNi, and (c) MnFeCoNi structure.

Figure 22 shows the Gibbs free energies calculated for the three materials. For OER, the *O reaction with the electrolyte to generate *OOH is the RDS as it is the one involving the largest energy barrier. [73] CrMnFeCoNi displayed a significantly lower energy barrier for the OER RDS step (1.48 eV) compared with MnFeCoNi (1.74 eV), and CuMnFeCoNi (1.95 eV). For ORR, **Figure 23** shows a plot of the free energy of the oxygen intermediates for the associative mechanism at both 0 V and 1.23 V vs. RHE. Comparing the free energy diagram at 0 V and 1.23 V, two uphill steps appear, the O* to OH* and especially the OH* to H_2O, which is considered the RDS for ORR. According to DFT results, CrMnFeCoNi displayed the smallest RDS energy step, 0.28 eV, when compared with MnFeCoNi,0.65eV, and CuMnFeCoNi, 0.8 eV. The lower OER/ORR energy barriers are consistent with the best OER and ORR performance experimentally obtained with CrMnFeCoNi. The larger OER/ORR energy barriers obtained for CuMnFeCoNi are also consistent with experimental evidence showing that Cu deteriorated the OER and ORR performances.

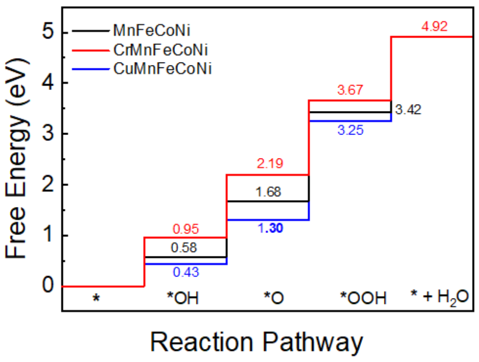

Figure 22. ΔG change diagrams of the OER process.

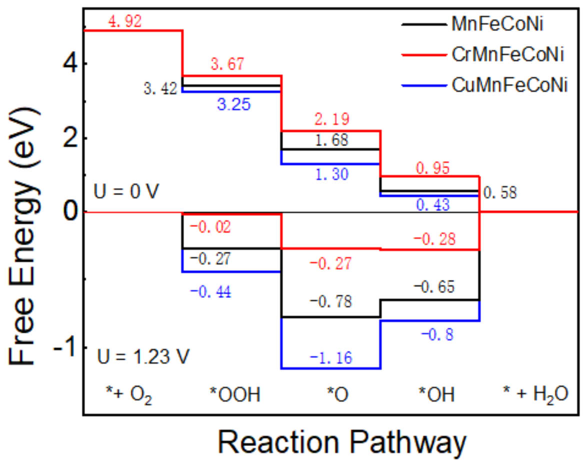

Figure 23. ΔG diagrams of the ORR process.

Beyond composition, the experimentally-observed lattice distortions can notably impact the physical and chemical properties of the HEA. HEAs are already often characterized by severe strain associated with atomic size mismatches, which potentially affect the binding modes of intermediates as well as the catalytic selectivity [74]. Lattice distortion in HEAs can promote a higher density of active electrons around the E_F, resulting in faster electron transfer [75]. Furthermore, twinning is demonstrated to be an effective way of enhancing the performance of metallic catalysts [76].

The adsorption properties of CrMnFeCoNi and CuMnFeCoNi with/without lattice distortions were analyzed using the d_c as a descriptor of the adsorbate-metal interaction. The higher the d_c energy, i.e. the closer to the E_F, the stronger the binding between the metal atoms and the intermediates. According to the Sabatier principle, a moderate adsorption value usually gives rise to the highest catalytic activity. As displayed with black lines in **Figure 24**, the d_c of CrMnFeCoNi and CuMnFeCoNi with distortions is downward displaced when compared with those calculated without distortions, indicating a weaker interaction between metal atoms and intermediates in the distorted lattices. The d_c value of MnFeCoNi, CrMnFeCoNi with lattice distortions, and CuMnFeCoNi with lattice distortions are -1.92 eV, -2.52 eV, and -2.62 eV, respectively. Interestingly, the reduced binding energies can facilitate the final reaction step, the release of O_2, which energy barrier is comparable to that of the RDS in CrMnFeCoNi.

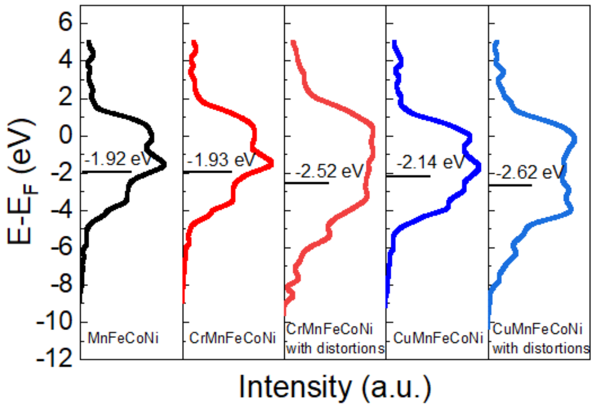

Figure 24. d band spectra of MnFeCoNi, CrMnFeCoNi, and CuMnFeCoNi with/without lattice distortions. The black lines represent the corresponding d_c position.

2.4.5 ZAB performance

Owing to the excellent OER and ORR activity of the CrMnFeCoNi HEA, this catalyst was tested as the oxygen electrode in reversible ZABs. ZABs were assembled using the CrMnFeCoNi HEA as the air cathode and zinc foil as the anode (**Figure 25a**). A 20 wt% Pt/C was also tested as a reference air cathode. As shown in **Figure 25b**, the ZAB based on a CrMnFeCoNi cathode exhibited an OCP of 1.489 V, i.e. 90% of its theoretical limit (1.66 V) [11], slightly above that of the Pt/C-based ZAB (1.472 V). The peak power density of the CrMnFeCoNi-based ZAB was 116.5 mW cm^{-2}, slightly higher than that of the Pt/C ZAB (114.1 mW cm^{-2}, **Figure 25c**). Besides, at a current density of 8 mA cm^{-2}, the CrMnFeCoNi-based ZAB delivered a specific capacity of 836 mAh g^{-1}, significantly larger than that of the Pt/C ZAB, 788 mAh g^{-1} (**Figure 25d**). A comparison of the outstanding performance of the CrMnFeCoNi-based ZAB with previously reported devices is provided in **Table 6**. As shown in **Figure 25d**, the CrMnFeCoNi-based ZAB can power a 1.4 V red light emitting diode (LED) screen. Most important, as shown in **Figure 25e**, the CrMnFeCoNi-based ZAB is not only characterized by a lower charge-discharge η, i.e. a higher energy efficiency, compared with the Pt/C-based ZAB, but also much higher durability. Unlike the Pt/C-based ZAB with an obvious η increase after 60 h of charging/discharging cycles, the CrMnFeCoNi-based ZAB exhibits a negligible variation in voltage even after 240 h, i.e. 10 days and 720 cycles, of continuous operation with charge/discharge cycles at a current density of 8 mAcm^{-2}, which suggests outstanding long-term durability. The stability of CrMnFeCoNi-based ZAB operating at different current densities was also investigated. As shown in **Figures 26-27**, the CrMnFeCoNi-based ZAB exhibits excellent durability even after 400 h (1200 cycles) and 240 h (720 cycles) of continuous charge/discharge operation at a current density of 5 mA cm^{-2} and 12 mA cm^{-2}, further proving its excellent stability.

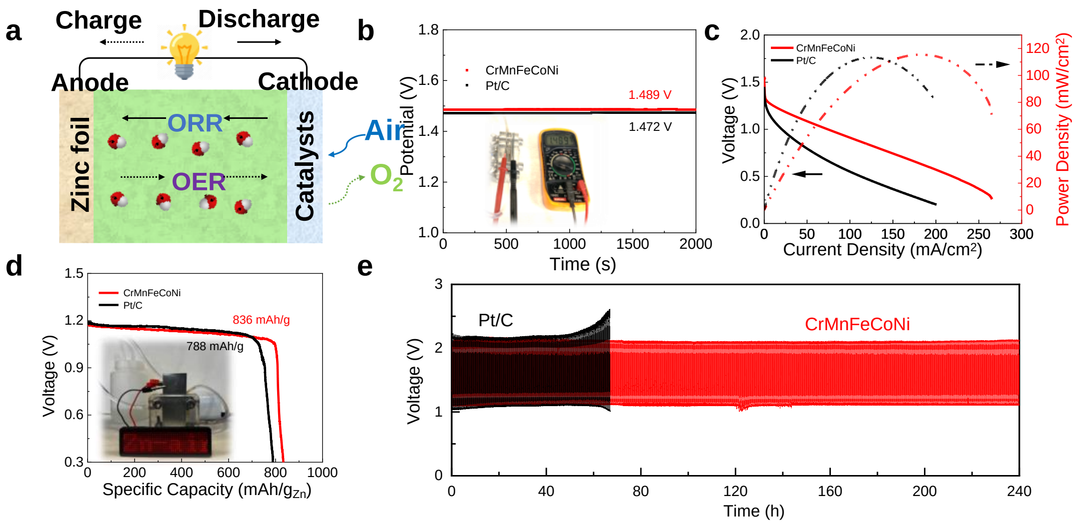

Figure 25. (a) ZAB schematic diagram. (b) OCP measurements and photograph of the assembled ZAB. (c) Power density plots. (d) Specific capacity comparisons between a CrMnFeCoNi- and a Pt/C-based ZAB. A photograph of a red LED screen powered by a CrMnFeCoNi-based ZAB is also shown. (e) Galvanostatic discharge-charge curves with 10 min discharge and 10 min charge cycles at a current density of 8 mA cm^{-2}.

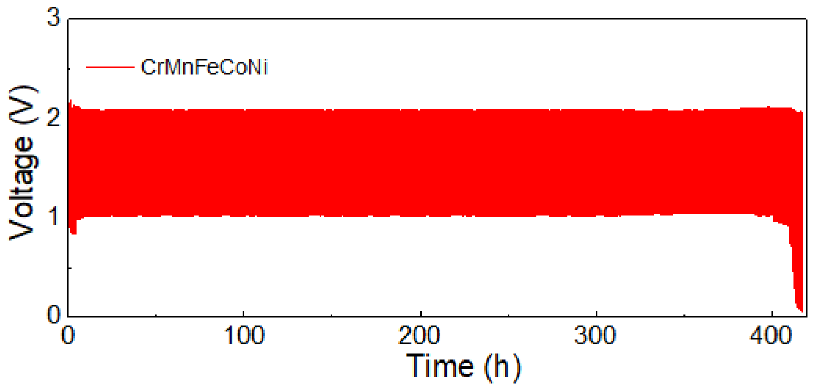

Figure 26. Galvanostatic discharge-charge curves with 10 min discharge and 10 min charge cycles at a current density of 5 mA cm^{-2}.

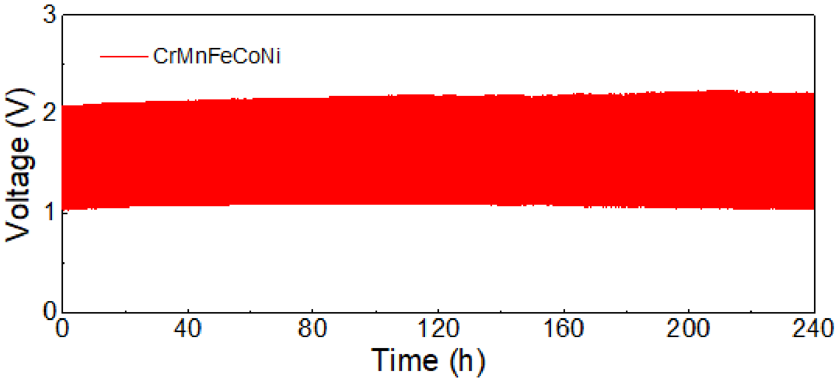

Figure 27. Galvanostatic discharge-charge curves with 10 min discharge and 10 min charge cycles at a current density of 12 mA cm^{-2}.

Table 6. Comparison of the ZAB performances obtained using state-of-the-art air cathodes.

Catalyst	OCP (V)	Power density (mW cm^{-2})	Specific capacity (mAh g_{Zn}^{-1})@J (mA cm^{-2})	Cycling condition and stability (h)	Ref.
AlNiCoRuMo	1.48	146.5	-	2 mA cm^{-2}, 720 cycles for 120 h	*ACS Mater. Lett.*, **2019**, 1, 526-533.
AlFeCoNiCr	-	125	800@20	2 mA cm^{-2}, 360 cycles for 60 h	*Appl. Catal. B-environ.*, **2020**, 268, 118431.
Pt/C+IrO_2	1.41	87	732@20	2 mA cm^{-2}, 168 cycles for 28 h	*Appl. Catal. B-environ.*, **2020**, 268, 118431.
ODAC-CoO	1.45	81	706@20	5 mA cm^{-2}, 450 cycles for 150 h	*Adv. Funct. Mater.*, **2021**, 31, 2101239.
Co_2Fe_1@NC	1.454	423.7	813@20	2 mA cm^{-2}, 750 cycles for 250 h	*J. Am. Chem. Soc.*, **2020**, 142, 7116-7127.
Ni-MnO/rGO	-	123	758@5	10 mA cm^{-2}, 100 cycles for 33.3 h	*Nano Energy*, **2020**, 71, 104592.
Co@hNCTs	1.45	149	746@10	5 mA cm^{-2}, 3000 cycles for 500 h	*Nano Energy*, **2020**, 71, 104592.
AlCuNiPtMn	-	-	831@20	-	*J. Catal.*, **2020**, 383,

					164-171.
FeNi@NCNT	1.551	200	788@10	10 mA cm^{-2}, 250 cycles for 250 h	*Small*, **2021**, 17, e2006183.
Pt/C	**1.472**	**114.1**	**788@8**	**8 mA cm^{-2}, 180 cycles for 60 h**	**This work**
CrMnFeCoNi	**1.489**	**116.5**	**836@8**	**5/8/12 mA cm^{-2}, 1200/720/720 cycles for 400/240/240 h**	**This work**

Flexible ZABs based on a CrMnFeCoNi oxygen catalyst were also assembled using a gel electrolyte. **Figure 28a** shows the structure diagram of the flexible solid ZABs, where a polished Zn plate is used as the anode, a hydrophilic CP with catalysts is used as the cathode, and the PVA-KOH-H_2O gel is used as the electrolyte. CrMnFeCoNi-based ZABs could light a red LED while bent at different angles, proving their flexibility upon operation (**Figure 28b**). The solid CrMnFeCoNi-based ZAB displayed a higher OCP value of 1.254 V than that of Pt/C-based ZAB of 1.204 V (**Figure 28c**). The peak power density of the solid CrMnFeCoNi-based ZAB was 25.5 mW cm^{-2}, higher than the 23.7 mW cm^{-2} of the Pt/C-based ZAB (**Figure 28d**). As shown in **Figure 28e**, the solid CrMnFeCoNi-based ZAB exhibits good stability at the current densities of 2, 4, 6, and 8 mA cm^{-2} with continuous cycling. Long-time charge-discharge cycling is shown in **Figure 28f**. The solid CrMnFeCoNi-based ZAB was stable for 50 h of continuous 10 min discharge and 10 min charge cycles, i.e. 150 cycles, at a current density of 5 mA cm^{-2}.

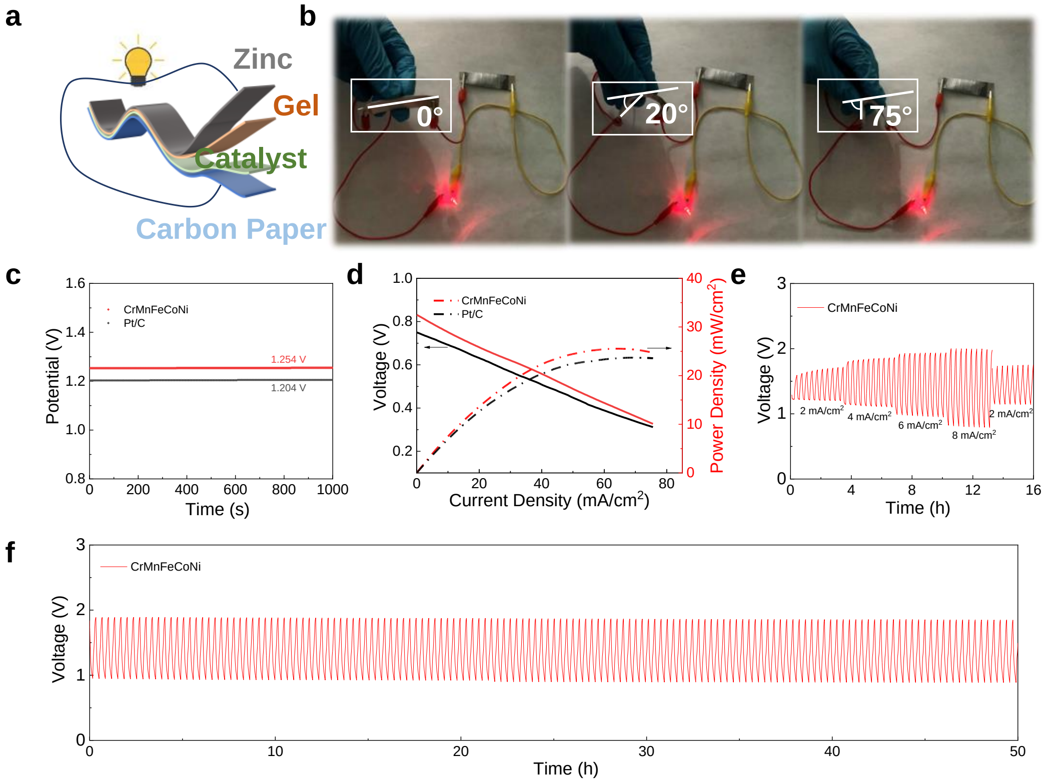

Figure 28. (a) Solid and flexible ZAB schematic diagram. (b) Optical images of a red LED lighted by a CrMnFeCoNi-based ZABs while bended at different angles. (c) OCP measurements, and (d) power density plots of a CrMnFeCoNi- and a Pt/C-based flexible ZAB. (e) Galvanostatic discharge-charge curves of a CrMnFeCoNi-based ZAB with 10 min discharge and 10 min charge cycles at a current density of 2, 4, 6, and 8 mA cm^{-2}. (f) Galvanostatic discharge-charge curves of a CrMnFeCoNi-based ZAB with 10 min discharge and 10 min charge cycles at a current density of 5 mA cm^{-2}.

2.5 Conclusions

In summary, we detailed a solution-based synthetic procedure to produce CrMnFeCoNi and CuMnFeCoNi HEAs, the MnFeCoNi quaternary alloy, and the different ternary alloys at a moderate reaction temperature. The CrMnFeCoNi HEA, characterized by a strongly distorted lattice and modulated surface electronic states, showed an outstanding OER and ORR catalytic performance, significantly above that of quaternary alloys, CuMnFeCoNi, and commercial RuO_2 and Pt/C catalysts. DFT calculations showed the incorporation of Cr within the quaternary MnFeCoNi and the defective HEA structure to reduce the energy barrier for the generation of *OOH from *O and the release of O_2, respectively, which were identified as the RDS of the OER process. DFT calculations also showed the CrMnFeCoNi to present more favorable ORR intermediate energy steps. Owing to the small E_{gap} value of CrMnFeCoNi, 0.734 V, this HEA was used bifunctional catalyst at the air cathode of a rechargeable ZAB. The CrMnFeCoNi-based ZAB showed an OCP of 1.489 V, a peak power density of 116.5 mW cm^{-2}, and a specific capacity of 836 mAh g^{-1} at a current density of 8 mA cm^{-2}. Besides, CrMnFeCoNi-based ZABs displayed excellent stability for more than 240 h and 400 h of continuous charge/discharge cycling at a current density of 8 mA cm^{-2} and 5 mA cm^{-2}.

2.6 References

[1] B. Wei, Z. Fu, D. Legut, T. C. Germann, S. Du, H. Zhang, J. S. Francisco, R. Zhang, *Adv. Mater.*, **2021**, 33, e2102595.

[2] J. Yan, Y. Wang, Y. Zhang, S. Xia, J. Yu, B. Ding, *Adv. Mater.*, **2021**, 33, e2007525.

[3] Y. Wang, X. Li, M. Zhang, J. Zhang, Z. Chen, X. Zheng, Z. Tian, N. Zhao, X. Han, K. Zaghib, Y. Wang, Y. Deng, W. Hu, *Adv. Mater.*, **2022**, e2107053.

[4] H. Song, J. Yu, Z. Tang, B. Yang, S. Lu, *Adv. Energy Mater.*, **2022**, 2102573.

[5] L. Gong, X. Y. E. Chng, Y. Du, S. Xi, B. S. Yeo, *ACS Catal.*, **2017**, 8, 807-814.

[6] Y. Chen, S. Ji, S. Zhao, W. Chen, J. Dong, W. C. Cheong, R. Shen, X. Wen, L. Zheng, A. I. Rykov, S. Cai, H. Tang, Z. Zhuang, C. Chen, Q. Peng, D. Wang, Y. Li, *Nat. Commun.*, **2018**, 9, 5422.

[7] H. Li, Q. Li, P. Wen, T. B. Williams, S. Adhikari, C. Dun, C. Lu, D. Itanze, L. Jiang, D. L. Carroll, G. L. Donati, P. M. Lundin, Y. Qiu, S. M. Geyer, *Adv. Mater.*, **2018**, 30, 1705796.

[8] S. Chen, T. Wang, L. Ma, B. Zhou, J. Wu, D. Zhu, Y. Y. Li, J. Fan, C. Zhi, *Chem*, **2022**, 9, 497-510.

[9] T. Gu, D. Zhang, Y. Yang, C. Peng, D. Xue, C. Zhi, M. Zhu, J. Liu, *Adv. Funct. Mater.*, **2022**, 2212299.

[10] J. Han, X. Meng, L. Lu, J. Bian, Z. Li, C. Sun, *Adv. Funct. Mater.*, **2019**, 29, 1808872.

[11] J. Fu, Z. P. Cano, M. G. Park, A. Yu, M. Fowler, Z. Chen, *Adv. Mater.*, **2017**, 29, 1604685.

[12] P. Tan, B. Chen, H. Xu, H. Zhang, W. Cai, M. Ni, M. Liu, Z. Shao, *Energy Environ. Sci.*, **2017**, 10, 2056-2080.

[13] Z. Li, W. Niu, Z. Yang, N. Zaman, W. Samarakoon, M. Wang, A. Kara, M. Lucero, M. V. Vyas, H. Cao, H. Zhou, G. E. Sterbinsky, Z. Feng, Y. Du, Y. Yang, *Energy Environ. Sci.*, **2020**, 13, 884-895.

[14] Y. Tian, X. Liu, L. Xu, D. Yuan, Y. Dou, J. Qiu, H. Li, J. Ma, Y. Wang, D. Su, S. Zhang, *Adv. Funct. Mater.*, **2021**, 31, 2101239.

[15] L. Zhuang, Y. Jia, H. Liu, X. Wang, R. K. Hocking, H. Liu, J. Chen, L. Ge, L. Zhang, M. Li, C. L. Dong, Y. C. Huang, S. Shen, D. Yang, Z. Zhu, X. Yao, *Adv. Mater.*, **2019**, 31, e1805581.

[16] Y. Chang, P. Zhai, J. Hou, J. Zhao, J. Gao, *Adv. Energy Mater.*, **2021**, 12, 2102359.

[17] W. Zhang, J. Chang, G. Wang, Z. Li, M. Wang, Y. Zhu, B. Li, H. Zhou, G. Wang, M. Gu, Z. Feng, Y. Yang, *Energy Environ. Sci.*, **2022**, 1573-1584.

[18] Y. Lin, H. Cui, C. Liu, R. Li, S. Wang, G. Qu, Z. Wei, Y. Yang, Y. Wang, Z. Tang, H. Li, H. Zhang, C. Zhi, H. Lv, *Angew Chem. Int. Ed.*, **2023**, e202218745.

[19] X. Wang, X. Han, R. Du, Z. Liang, Y. Zuo, P. Guardia, J. Li, J. Llorca, J. Arbiol, R. Zheng, A. Cabot, *Appl. Catal. B-environ*, **2023**, 320, 121988.

[20] R. Du, K. Xiao, B. Li, X. Han, C. Zhang, X. Wang, Y. Zuo, P. Guardia, J. Li, J. Chen, J. Arbiol, A. Cabot, *Chem. Eng. J.*, **2022**, 441, 135999.

[21] X. Wang, J. Li, Q. Xue, X. Han, C. Xing, Z. Liang, P. Guardia, Y. Zuo, R. Du, L. Balcells, J. Arbiol, J. Llorca, X. Qi, A. Cabot, *ACS Nano*, **2023**, 17, 825-836.

[22] S. Chen, X. Liang, S. Hu, X. Li, G. Zhang, S. Wang, L. Ma, C.L. Wu, C. Zhi, J.A. Zapien, *Nanomicro Lett.*, **2023**, 15, 47.

[23] S. S. Shinde, C. H. Lee, J.-Y. Jung, N. K. Wagh, S.-H. Kim, D.-H. Kim, C. Lin, S.U. Lee, J.-H. Lee, *Energy Environ. Sci.*, **2019**, 12, 727-738.

[24] T. Berestok, J. Chacon-Borrero, J. Li, P. Guardia, A. Cabot, *Langmuir*, **2023**, 39, 3692-3698.

[25] M. Li, D. Yang, J. J. Biendicho, X. Han, C. Zhang, K. Liu, J. Diao, J. Li, J. Wang, M. Heggen, R. E. Dunin-Borkowski, J. Wang, G. Henkelman, J. R. Morante, J. Arbiol, S. L. Chou, A. Cabot, *Adv. Funct. Mater.*, **2022**, 32, 2200529.

[26] C. Zhang, B. Fei, D. Yang, H. Zhan, J. Wang, J. Diao, J. Li, G. Henkelman, D. Cai, J. J. Biendicho, J. R. Morante, A. Cabot, *Adv. Funct. Mater.*, **2022**, 32, 2201322.

[27] D. Yang, Z. Liang, P. Tang, C. Zhang, M. Tang, Q. Li, J. J. Biendicho, J. Li, M. Heggen, R. E. Dunin-Borkowski, M. Xu, J. Llorca, J. Arbiol, J. R. Morante, S. L. Chou, A. Cabot, *Adv. Mater.*, **2022**, 34, e2108835.

[28] X. Wang, X. Han, R. Du, C. Xing, X. Qi, Z. Liang, P. Guardia, J. Arbiol, A. Cabot, J. Li, *ACS Appl. Mater. Interfaces*, **2022**, 14, 41924-41933.

[29] D. Yang, M. Li, X. Zheng, X. Han, C. Zhang, J. Jacas Biendicho, J. Llorca, J. Wang, H. Hao, J. Li, G. Henkelman, J. Arbiol, J.R. Morante, D. Mitlin, S. Chou, A. Cabot, *ACS Nano*, **2022**, 16, 11102-11114.

[30] Q. Ding, Y. Zhang, X. Chen, X. Fu, D. Chen, S. Chen, L. Gu, F. Wei, H. Bei, Y. Gao, M. Wen, J. Li, Z. Zhang, T. Zhu, R. O. Ritchie, Q. Yu, *Nature*, **2019**, 574, 223-227.

[31] M.-H. Tsai, *Entrop*y, **2013**, 15, 5338-5345.

[32] D. B. Miracle, O. N. Senkov, *Acta Mater.*, **2017**, 122, 448-511.

[33] A. Ostovari Moghaddam, A. Cabot, E. A. Trofimov, *Int. J. Refract. Hard Met.*, **2021**, 97, 105504.

[34] M.-H. Tsai, J.-W. Yeh, *Mater. Res. Lett.*, **2014**, 2, 107-123.

[35] N. Kumar Katiyar, K. Biswas, J.-W. Yeh, S. Sharma, C. Sekhar Tiwary, *Nano Energy*, **2021**, 88, 106261.

[36] C. S. Tiwary, P. Pandey, S. Sarkar, R. Das, S. Samal, K. Biswas, K. Chattopadhyay, *Prog. Mater. Sci.*, **2022**, 123 100793.

[37] G. M. Tomboc, T. Kwon, J. Joo, K. Lee, *J. Mater. Chem. A*, **2020**, 8, 14844-14862.

[38] M. Fu, X. Ma, K. Zhao, X. Li, D. Su, *iScience*, **2021**, 24, 102177.

[39] G. Fang, J. Gao, J. Lv, H. Jia, H. Li, W. Liu, G. Xie, Z. Chen, Y. Huang, Q. Yuan, X. Liu, X. Lin, S. Sun, H.-J. Qiu, *Appl. Catal. B-environ.*, **2020**, 268, 118431.

[40] L. Zendejas Medina, L. Riekehr, U. Jansson, *Surf. Coat. Technol.*, **2020**, 403, 126323.

[41] T. Lindner, M. Löbel, E. Saborowski, L.-M. Rymer, T. Lampke, *Crystals*, **2020**, 10, 110.

[42] Z. Li, S. Zhao, S.M. Alotaibi, Y. Liu, B. Wang, M.A. Meyers, **2018**, 151, 424-431.

[43] Z. Li, K. G. Pradeep, Y. Deng, D. Raabe, C. C. Tasan, *Nature*, **2016**, 534, 227-230.

[44] B. Cantor, I. T. H. Chang, P. Knight, A. J. B. Vincent, *Mater. Sci. Eng. A*, **2004**, 375-377, 213-218.

[45] H. Cheng, W. Chen, X. Liu, Q. Tang, Y. Xie, P. Dai, *Mater. Sci. Eng. A*, 2018, 719, 192-198.

[46] S. Xiang, J. Li, H. Luan, A. Amar, S. Lu, K. Li, L. Zhang, X. Liu, G. Le, X. Wang, F. Qu, W. Zhang, D. Wang, Q. Li, *Mater. Sci. Eng. A*, **2019**, 743, 412-417.

[47] F. Granberg, K. Nordlund, M. W. Ullah, K. Jin, C. Lu, H. Bei, L. M. Wang, F. Djurabekova, W.J. Weber, Y. Zhang, *Phys. Rev. Lett.*, **2016**, 116, 135504.

[48] C. Lu, L. Niu, N. Chen, K. Jin, T. Yang, P. Xiu, Y. Zhang, F. Gao, H. Bei, S. Shi, M. R. He, I. M. Robertson, W. J. Weber, L. Wang, *Nat. Commun.*, **2016**, 7, 13564.

[49] Y. Tian, C. Lu, Y. Shen, X. Feng, *Surf. Interfaces*, **2019**, 15, 135-140.

[50] C. Wang, J. Yu, Y. Yu, Y. Zhao, Y. Zhang, X. Han, *J. Mater. Res. Technol.*, **2020**, 9, 8482-8496.

[51] G.-L. Chai, K. Qiu, M. Qiao, M.-M. Titirici, C. Shang, Z. Guo, *Energy Environ. Sci.*, **2017**, 10, 1186-1195.

[52] J. Yan, Y. Wang, Y. Zhang, S. Xia, J. Yu, B. Ding, *Adv. Mater.*, **2021**, 33, e2007525.

[53] B. Wei, Z. Fu, D. Legut, T. C. Germann, S. Du, H. Zhang, J. S. Francisco, R. Zhang, *Adv. Mater.*, 2021, 33, e2102595.

[54] J. Diao, Y. Qiu, S. Liu, W. Wang, K. Chen, H. Li, W. Yuan, Y. Qu, X. Guo, *Adv. Mater.*, **2020**, 32, e1905679.

[55] P. E. Blochl, *Phys. Rev. B Condens Matter.*, **1994**, 50, 17953-17979.

[56] Z. P. Lu, H. Wang, M. W. Chen, I. Baker, J. W. Yeh, C. T. Liu, T. G. Nieh, *Intermetallics*, **2015**, 66, 67-76.

[57] K. Zhang, G. Zhang, J. Qu, H. Liu, *Small*, **2020**, 16, e1907001.

[58] F. A. Stevie, C. L. Donley, *Journal of Vacuum Science & Technology A*, **2020**, 38.

[59] Q. Zhou, Z. Zhang, J. Cai, B. Liu, Y. Zhang, X. Gong, X. Sui, A. Yu, L. Zhao, Z. Wang, Z. Chen, *Nano Energy*, **2020**, 71, 104592.

[60] E. Luo, H. Zhang, X. Wang, L. Gao, L. Gong, T. Zhao, Z. Jin, J. Ge, Z. Jiang, C. Liu, W. Xing, *Angew Chem. Int. Ed.*, **2019**, 58, 12469-12475.

[61] J. Su, R. Ge, K. Jiang, Y. Dong, F. Hao, Z. Tian, G. Chen, L. Chen, *Adv. Mater.*, **2018**, e1801351.

[62] H. Wu, H. Li, X. Zhao, Q. Liu, J. Wang, J. Xiao, S. Xie, R. Si, F. Yang, S. Miao, X. Guo, G. Wang, X. Bao, *Energy Environ. Sci.*, **2016**, 9, 3736-3745.

[63] H.-J. Qiu, G. Fang, J. Gao, Y. Wen, J. Lv, H. Li, G. Xie, X. Liu, S. Sun, *ACS Mater. Lett.*, **2019**, 1, 526-533.

[64] J. W. Yeh, S. K. Chen, S. J. Lin, J-Y. Gan, T-S. Chin, T-T.Shun, C-H. Tsau, S-Y. Chang, *Adv. Eng. Mater.*, **2004**, 6, 299-30.

[65] J. Li, L. Jiang, S. He, L. Wei, R. Zhou, J. Zhang, D. Yuan, S. P. Jiang, E*nerg. Fuels*, **2019**, 33, 12052-12062.

[66] J. H. Kwon, L. D. Wilson, R. Sammynaiken, *Synth. Met.*, **2014**, 197, 8-17.

[67] L. Bai, S. lee, X. Hu, *Angew Chem. Int. Ed.*, **2021**, 60, 3095-3103.

[68] M. Sendova, B.D. Hosterman, A. Grebe, *J, Raman Spectrosc.*, **2017**, 48, 618-622.

[69] J. Liu, X. Yu, R. Du, C. Zhang, T. Zhang, J. Llorca, J. Arbiol, Y. Wang, M. Meyns, A. Cabot, *Appl. Catal. B-environ.*, **2019**, 256, 117846.

[70] H. Tan, Y. Li, J. Kim, T. Takei, Z. Wang, X. Xu, J. Wang, Y. Bando, Y.M. Kang, J. Tang, Y. Yamauchi, *Adv. Sci.*, **2018**, 5, 1800120.

[71] X. Zheng, X. Cao, K. Zeng, J. Yan, Z. Sun, M. H. Rummeli, R. Yang, *Small*, **2021**, 17, e2006183.

[72] J. Du, F. Li, L. Sun, *Chem. Soc. Rev.*, **2021**, 50, 2663-2695.

[73] J. Lee, A. Kumar, T. Yang, X. Liu, A.R. Jadhav, G. H. Park, Y. Hwang, J. Yu, C. T. K. Nguyen, Y. Liu, S. Ajmal, M. G. Kim, H. Lee, *Energy Environ. Sci.*, **2020**, 13, 5152-5164.

[74] M. Luo, S. Guo, *Nat. Rev.Mater.*, **2017**, 2, 17059.

[75] K. Chen, S. Kim, R. Rajendiran, K. Prabakar, G. Li, Z. Shi, C. Jeong, J. Kang, O. L. Li, *J. Colloid Interface Sci.*, **2021**, 582, 977-990.

[76] C. L. Huang, K. Sasaki, D. Senthil Raja, C. T. Hsieh, Y.J. Wu, J. T. Su, C.C. Cheng, P. Y. Cheng, S. H. Lin, Y. Choi, S. Y. Lu, *Adv. Energy Mater.*, **2021**, 11, 2101827.

Chapter 3

A 3d-4d-5d HEA as a Bifunctional Oxygen Catalyst for Robust Aqueous ZABs

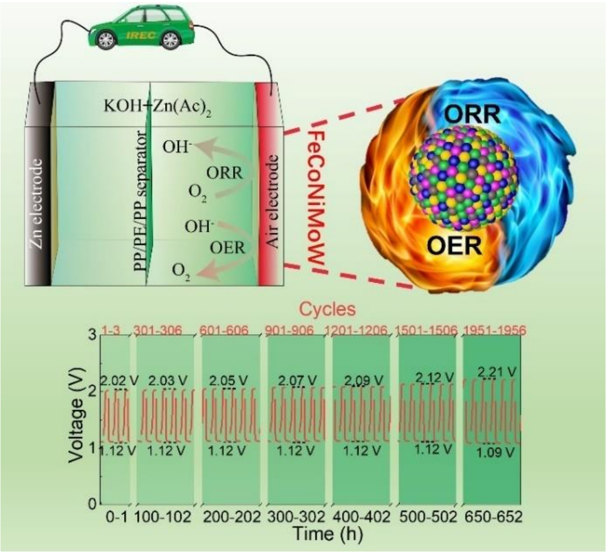

3.1 Abstract

HEAs are highly suitable candidate catalysts for OER/ORR as they offer numerous parameters for optimizing the electronic structure and catalytic sites. Herein, FeCoNiMoW HEA NPs are synthesized using a solution-based low-temperature approach. Such FeCoNiMoW NPs show high entropy properties, subtle lattice distortions, and modulated electronic structure, leading to superior OER performance with an η of 233 mV at 10 mA cm^{-2} and 276 mV at 100 mA cm^{-2}. DFT calculations reveal the electronic structures of the FeCoNiMoW active sites with an optimized d_c position that enables suitable adsorption of OOH* intermediates and reduces the Gibbs free energy barrier in the OER process. Aqueous ZABs based on this HEA demonstrate a high OCP of 1.59 V, a peak power density of 116.9 mW cm^{-2}, a specific capacity of 857 mAh g Zn^{-1}, and excellent stability for over 660 h of continuous charge-discharge cycles. Flexible and solid ZABs are also assembled and tested, displaying excellent charge-discharge performance at different bending angles. This work shows the significance of 4d/5d metal-modulated electronic structure and optimized adsorption ability to improve the performance of OER/ORR, ZABs, and beyond.

3.2 Introduction

Aqueous ZABs, offering considerable energy density at a low cost as well as minimal safety concerns and environmental impact, are deemed to be a key component in the future energy storage mix, particularly for the integration of renewables and the transport sector.[1-2] Themain advantages but also limitations of secondary ZABs come from their unique air cathode, which requires highly active, stable, and cost-effective materials able to catalyze the OER/ORR.[3-5] Currently, to speed up the sluggish kinetics of the oxygen reactions, state-of-theart electrocatalysts are based on IrO_2/RuO_2 for OER and Pt for ORR, which compromises the cost-effectiveness of ZABs.[6-8] Besides their scarcity and high cost, these noble metals are also characterized by moderate long-term stability thus further hindering their practical application. In this scenario, alloys based on more abundant 3d metals such as Fe, Co, and Ni, are widely investigated as alternative oxygen catalysts aiming at finding materials providing optimum binding energies for OER and ORR intermediates.[8-15] While alloying allows tuning of the electronic properties, the main drawbacks of conventional binary and ternary compositions based on Fe, Co, and Ni are their poor corrosion resistance and moderate catalytic stability associated with their large miscibility gap.[16]

In contrast to 3d orbitals, 4d and 5d orbitals have a larger spatial extent allowing stronger hybridization with neighboring ligand orbitals. Thus the electronic bandwidths in 4d/5d metal are considerably larger than in 3dmetals, which allows a wider range of adjustment of the electronic structure.[17] Besides, 4d/5d metals have additional orbital degrees of freedom to tailor the electronic band structure and the adsorption and desorption energy of the intermediates. Recently, 4d and 5d high-valence metals, such as Mo and W, have been demonstrated effective in modulating the electronic structure of catalysts, which could adjust the adsorption and desorption performance of the oxygen intermediates and extend durability.[16,18-20] Lu et al. showed the presence of Mo within a PtFeMo alloy to alleviate the adsorption energy (E_{ads}) of the intermediate on the surface of the Pt active site thus promoting ORR performance.[21] Xu et al. successfully incorporated Mo into Co-MOF to promote catalyst stability and OER performance.[22] Besides, Zhang et al. incorporated W^{6+} into amorphous FeCo oxyhydroxide gels to achieve near-optimal *OH adsorption energies for OER intermediates.[23]

HEAs are solid solutions of five or more elements with high thermodynamic and kinetic stability, hold great promise as bifunctional catalysts owing to their high configurational entropy, distorted atomic arrangement, altered electronic densities, and potentially strong synergistic effects to optimize the adsorption energies and electrical conductivity.[24-32] The high configurational entropy associated with the mixing of several different elements in similar proportions stabilizes the solid solutions and improves their corrosion resistance. Besides, the lattice distortions related to the different atomic sizes of the combined elements result in significant variations in the electronic structure of the alloy. HEAs also offer numerous additional degrees of freedom to fine-tune the material structural, electronic, and catalytic properties.[33-36] Overall, the design and engineering of HEA is a powerful strategy to optimize the surface adsorption properties, catalytic active centers, electronic structures,[37] and consequently the OER and ORR catalytic activity and ZAB performance.[38-39]

Beyond composition, the performance of an electrocatalyst strongly depends on its architectural parameters. To maximize activity, the transport of both electrons and reactant/product and the catalyst/electrolyte interphase area must be maximized. Despite the multiple advantages of HEAs, the synthesis of nanostructured HEAs remains a major challenge.[40] HEAs are generally produced in the form of bulk solids using high-temperature processes or thin films using low throughput vacuum-based technologies, which do not meet the demands of large-scale applications requiring huge 3D surfaces. Besides, while some HEAs have been applied in the electrochemistry field, most of them are based on costly and scarce noble metals.[41-44]

Herein, noble-metal-free nano-structured HEAs are synthesized using a simple colloidal-based approach at a low temperature and used in aqueous and flexible ZABs. Specifically, transition metals from the 3d series, including Fe, Co, and Ni, along with the 4d metal Mo and 5d metal W, were chosen for synthesizing ternary, quaternary, and quinary compositions. Fe, Co, and Ni exhibit inherent activity in both the OER and ORR. Furthermore, their alloys have been demonstrated to function as bifunctional oxygen catalysts, making them ideal candidates as the primary metal constituents. 4d Mo and 5d W, exhibiting noble metal-like behavior without toxicity, were selected to be introduced within FeCoNi 3d ternary alloys to form FeCoNiMo and FeCoNiW quaternary alloys, and FeCoNiMoW HEAs in the form of NPs. The high entropy properties, lattice distortions, and electron modulations of FeCoNiMoW are thoroughly investigated and discussed. Besides, FeCoNiMoW is explored as OER/ORR bifunctional oxygen catalysts, and *in situ* Raman spectroscopy is used to track its evolution during the OER. The excellent performances obtained are rationalized with the use of DFT calculations of the electronic synergy, d-band position, and E_{ads} of the oxygen intermediates. Additionally, robust aqueous and flexible ZABs containing FeCoNiMoW-based cathodes are produced and investigated.

3.3 Experimental section

3.3.1 Materials and reagents

Iron(II) acetylacetonate ($Fe(acac)_2$, 99.5%), cobalt(II) acetylacetonate ($Co(acac)_2$, 99%), nickel(II) acetylacetonate ($Ni(acac)_2$, 96%), molybdenum hexacarbonyl ($Mo(CO)_6$, 98%), tungsten hexacarbonyl ($Mo(CO)_6$, 97%), OAm, >70 %， D-(+)-glucose (99.5%) Nafion solution (5 wt%), PVA, 99+% were bought from Sigma-Aldrich. Methanol (99%), potassium hydroxide (KOH, 87%), CTAC, 96 %, and cyclohexane (95%) were supplied by Alfa Aesar. DI water (≥18.2 MΩ/cm) was purified by an ultra-pure purification system (Aqua Solutions).

3.3.2 Synthesis of catalysts

Synthesis of FeCoNi, FeCoNiMo, FeCoNiW and FeCoNiMoW NPs. All synthesis processes were carried out by using a standard vacuum/argon Schlenk line. In a typical preparation of FeCoNiMoW NPs, 270 mg of glucose and 200 mg of CTAC were dissolved in 20 mL of OAm to get a homogeneous solution by ultrasonication for 2 h. Then, 0.1 mmol of $Fe(acac)_2$, $Co(acac)_2$, and $Ni(acac)_2$, 0.15 mmol $Mo(CO)_6$, and $W(CO)_6$ precursors were added into the mixture, followed by another long-time ultrasonication. Then the mixture homogeneous solution was transferred into a three-neck flask, which was firstly vacuumed for 1h at 70 ℃ to remove oxygen and impurities with a low boiling point, and then the temperature was increased to 260 ºC in an argon atmosphere under magnetic stirring. The homogeneous mixture was allowed to react at 260 ºC for 2 h. Afterward, the flask was cooled down to 220 ℃ by removing the heating mantle and then cooled rapidly down to room temperature with a water bath. The black product was collected by centrifugation and washed three times with a cyclohexane/ethanol mixture. FeCoNi, FeCoNiMo, and FeCoNiW particles were synthesized using the same procedure as the FeCoNiMoW but using the proper metal combinations.

3.3.3 Material characterization

SEM images and EDS spectra were obtained in a Zeiss Auriga field emission scanning electron microscope. TEM micrographs were obtained in a Tecnai F20 field emission gun microscope with a 0.19 nm point-to-point resolution at 200 kV. Images were analyzed using Gatan Digital Micrograph software. HAADF-STEM images and elemental mapping were measured in a spherical aberration-corrected transmission electron microscope FEI Titan G2 80-200 ChemiSTEM with four EDS detectors were operated at 80 and 200 keV. The crystal structure was characterized by powder XRD measurement in a Bruker AXS D8 Advance X-ray diffractometer. (Cu-Kα radiation, λ =1.5418 Å, 40 kV and 40 mA; Bruker, Germany). ICP-OES was conducted on an ICPE-9820 system. XPS was performed with an Al anode XR50 source on a Specs system equipped with a Phoibos 150 MCD-9 detector (150 W). *In situ* Raman spectra were collected by a Raman microscope (iHR320 monochromator, HORIBA) using an *in situ* Raman cell. The excitation source was a frequency-doubled Nd: YAG laser, 532 nm laser, and the spectra were collected using a grating of 1800 lines mm^{-1}. The electrode was first subjected to CA measurements at a set applied voltage (0-1.7 V vs. RHE) for 5 min, then we started acquiring Raman spectra while keeping the CA measurements running. The Raman spectra were obtained with an acquisition time of 20 s and accumulation of 8 times from the range of 200-1000 cm^{-1}.

3.3.4 Electrochemical measurements

All the electrochemical measurements were carried out on a Chi760E electrochemical workstation (Shanghai Chenhua, China) at room temperature using a standard three-electrode setup system with a platinum grid as the counter electrode, a Hg/HgO electrode as the reference electrode, and a glassy carbon (GC) as the working electrode. The catalytic ink was prepared with 4 mg of catalyst, 2 mg carbon black, and 30 µL of 5 wt% Nafion solution dispersion in 750 µL isopropanol and 220 µL DI water with a continuous sonication until getting a homogeneous solution. Then, 10 µL catalyst ink was uniformly loaded on the surface of the polished GC electrode, and dried at room temperature. All measured potentials ($E_{Hg/Hgo}$) were converted to the RHE potential through the Nernst equation ($E_{RHE} = E_{Hg/Hgo} + 0.0591 \times pH + 0.098$), in which the PH value obtained by a PH meter (pH & Ion-metro GLP 22-Crison Instruments) is 13.85 for 1.0 M KOH electrolyte and 12.96 for 0.1 M KOH electrolyte.

The OER measurements were conducted in a 1.0 M KOH electrolyte. LSV measurements were conducted at a scan rate of 5 mV s^{-1}. EIS measurements were recorded at 1.5 V vs. RHE with frequencies from 0.01 to 10^5 Hz. The C_{dl} value was measured from CV curves at different scan rates (20, 40, 80, 120, 160, 200 mV s^{-1}) within the non-faradaic potential range of 1.06–1.16 V vs. RHE. The stability was measured by CA with CP as the working electrode.

The ORR measurements were conducted in 0.1 M KOH electrolyte. A RRDE was used as the substrate for the working electrode. CV curves were measured in an O_2-saturated or Ar-saturated electrolyte at a scan rate of 10 mV s^{-1}. LSV curves were conducted in an O_2-saturated electrolyte at different rotation rates from 400-2500 rpm at a scan rate of 10 mV s^{-1}.

3.3.5 ZAB measurements

Aqueous ZABs were assembled with a hydrophobic CP with a catalytic mass loading of 0.5 mg cm^{-2} as the air cathode, a polished Zn foil as the anode, and 6 M KOH and 0.2 M zinc acetate aqueous solution as the electrolyte. The flexible ZABs were assembled with a hydrophobic CC with a catalytic mass loading of 0.5 mg cm^{-2} as the air cathode, a polished Zn foil as the anode, and the PVA-KOH-H_2O gel as the electrolyte. The preparation of PVA-KOH-H_2O gel polymer was as follows. 2 g PVA was dissolved in 16 mL DI water at 98°C under magnetic stirring, then 2 g KOH was dissolved in 4 ml DI water, which was introduced into PVA solution until the liquid turned viscous. During this process, the color of the liquid gradually changed to pale-yellow. After that, the gel was introduced into the container and froze for 2 h, then it was thawed at room temperature.

The electrochemical measurement of ZABs was carried out on a CHi760E electrochemical station (Shanghai Chenhua, China). The galvanostatic test was performed using a Neware BTS4008 battery test system at room temperature. The specific capacities were determined using the galvanostatic discharge profiles standardized to the consumed mass of Zn.

3.3.6 DFT calculations

First principle calculations were performed by the VASP using the GGA and PBE method based on DFT.[45] The PAW was used to describe ions and electron interaction. The kinetic energy cutoff was set at 450 eV.

FeCoNi, FeCoNiMo and FeCoNiMoW were employed as the models to further determine the mechanisms behind the obtained catalytic activity. The FeCoNiMoW model construction process is as follows: firstly, creating a 5x5x5 supercell of FCC-Fe. Then, we proportionally replace iron atoms and obtain a FeCoNiMoW HEA with equal atomic compositions. Since the lattice atomic configurations of HEAs are disordered, we had to generate a large number of models, which is a total of 1000 models, and select the one with the lowest energy. When generating a new model, we used a different set of random numbers to replace the Fe atoms, ensuring that each configuration is unique. Additionally, we performed optimization on each model using conjugate gradient and fast descent methods to obtain the energy of their optimized structures. In the vertical direction, a vacuum layer of about 15 Å thickness was introduced to avoid the interaction between neighboring image structures.

In all the calculations, we used 3×2×1 for the Monkhorst-Pack k-point for periodic crystal structure and surface model. The convergence threshold for energy was set at 10^{-5} eV.[46] The equilibrium lattice constants were optimized with maximum stress on each atom within 0.05 eV $Å^{-1}$. To precisely reflect the calculations, the DFT+U corrections for 3d transition metal (Fe: 2.5eV, Co: 2.5 eV and Ni: 2.5 eV) and 4d transition metal (Mo: 3.5 eV) and 5d transition metal (W:4.0 eV) were employed.[47,48]

The E_{ads} is defined as follows：$E_{ads}= E_{ad/sub}- E_{ad}- E_{sub}$, where $E_{ad/sub}$, E_{ad} and E_{sub} are the optimized adsorbate/substrate system, the adsorbate in the structure and the clean substrate respectively. Usually, a more negative E_{ads} value reflects stronger adsorption.

3.4 Results and discussion

3.4.1 Catalyst structural and chemical characterization

Ternary alloy FeCoNi, quaternary alloys FeCoNiMo and FeCoNiW, and FeCoNiMoW HEA NPs were synthesized through a colloidal synthesis method and schematized in **Figure 1**. Briefly, the NPs were produced in an oxygenfree atmosphere from the simultaneous reduction of the corresponding metal salts at 260 °C in the presence of OAm as the solvent and reducing agent, glucose as an additional reducing agent, and CTAC as surfactant.

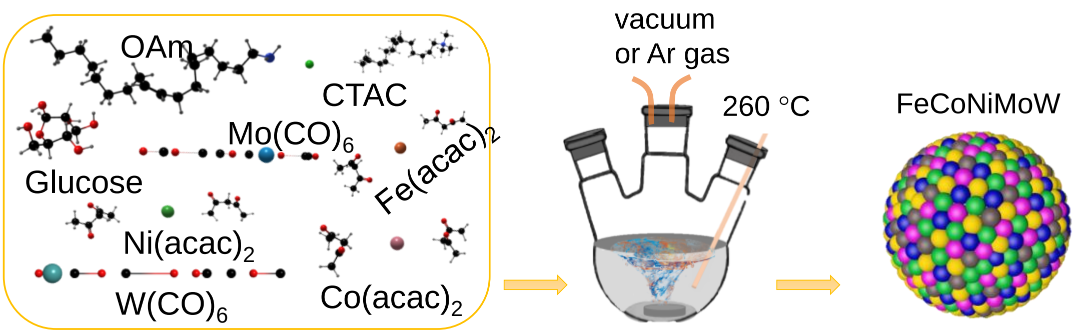

Figure 1. Schematic diagram of the colloidal synthesis process used to produce FeCoNiMoW NPs.

The results from the elemental composition and crystal structure analyses of the ternary alloy (FeCoNi) and the quaternary alloys (FeCoNiMo and FeCoNiW) are displayed in **Figures 2-4**. As shown from the SEM and EDS data, the three samples show relatively similar amounts of different metals. According to the XRD pattern (**Figure 5**), FeCoNi shows good crystallinity with the cubic Fm-3m FeCoNi phase and a lattice constant of 3.537 Å. With the introduction of Mo or W, FeCoNiMo and FeCoNiW still exhibit the FeCoNi phase, with wider XRD peaks slightly shifted to lower angles due to the relatively large atomic r of Mo and W.

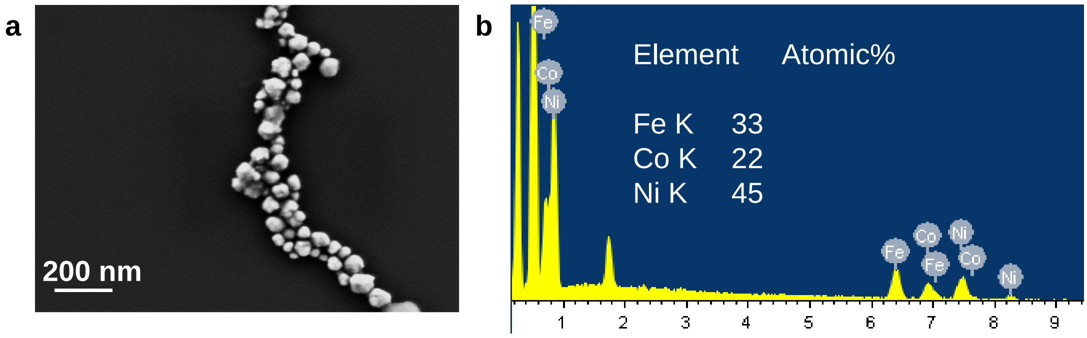

Element	Atomic%
Fe K	33
Co K	22
Ni K	45

Figure 2. (a) SEM and (b) EDS spectra of FeCoNi NPs. Insets show the calculated elemental composition.

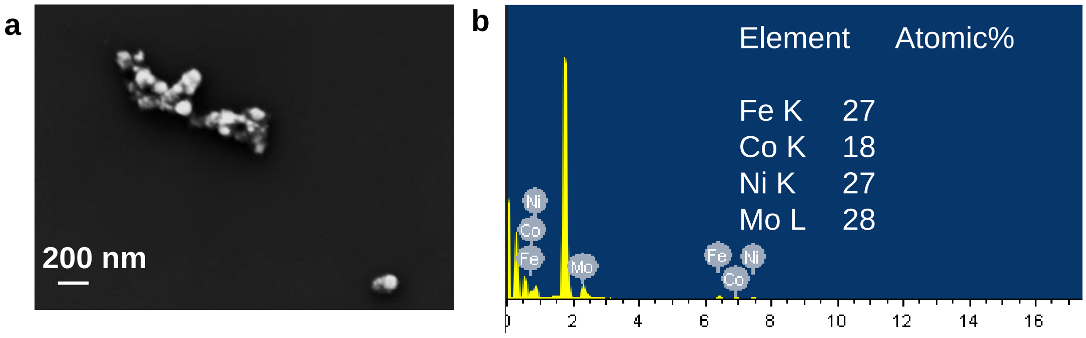

Figure 3. (a) SEM and (b) EDS spectra of FeCoNiMo NPs. Insets show the calculated elemental composition.

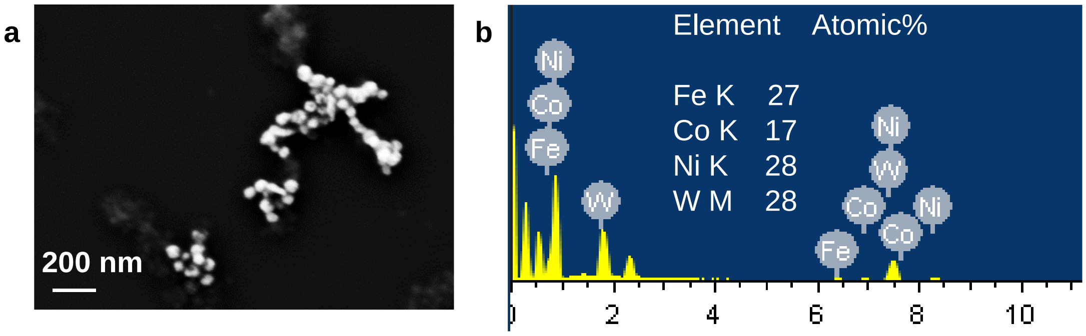

Figure 4. (a) SEM and (b) EDS spectra of FeCoNiW NPs. Insets show the calculated elemental composition.

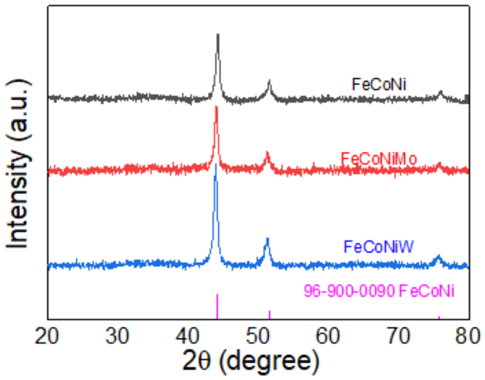

Figure 5. XRD pattern of FeCoNi, FeCoNiMo, and FeCoNiW NPs.

Figure 6a shows a representative TEM image of the FeCoNiMoW particles displaying an average size of 35 ± 20 nm. TEM-EDS composition maps and line scanning profiles demonstrate a homogeneous distribution of the five elements within each particle and a relatively uniform composition from particle to particle with moderate C_i deviations from particle to particle (**Figure 6 b-d**). Surrounding the particles, a large concentration of oxygen is detected and associated with the presence of oxygen-containing species/ligands adsorbed/bonded to the particle surface and potentially a metal oxide layer formed at the particle surface. The XRD pattern of FeCoNiMoW displays a FCC structure, resembling that of the cubic FeCoNi phase (**Figure 7**). The lattice constant was calculated at 3.552 Å, that is, slightly larger than that of FeCoNi (3.545 Å), which is again consistent with the slightly larger atomic r of Mo and W compared with Fe, Co, and Ni. The overall elemental ratio of FeCoNiMoW was determined by ICP-OES at Fe:Co:Ni:Mo: W = 18:16:21:22:23 (**Figure 8**).

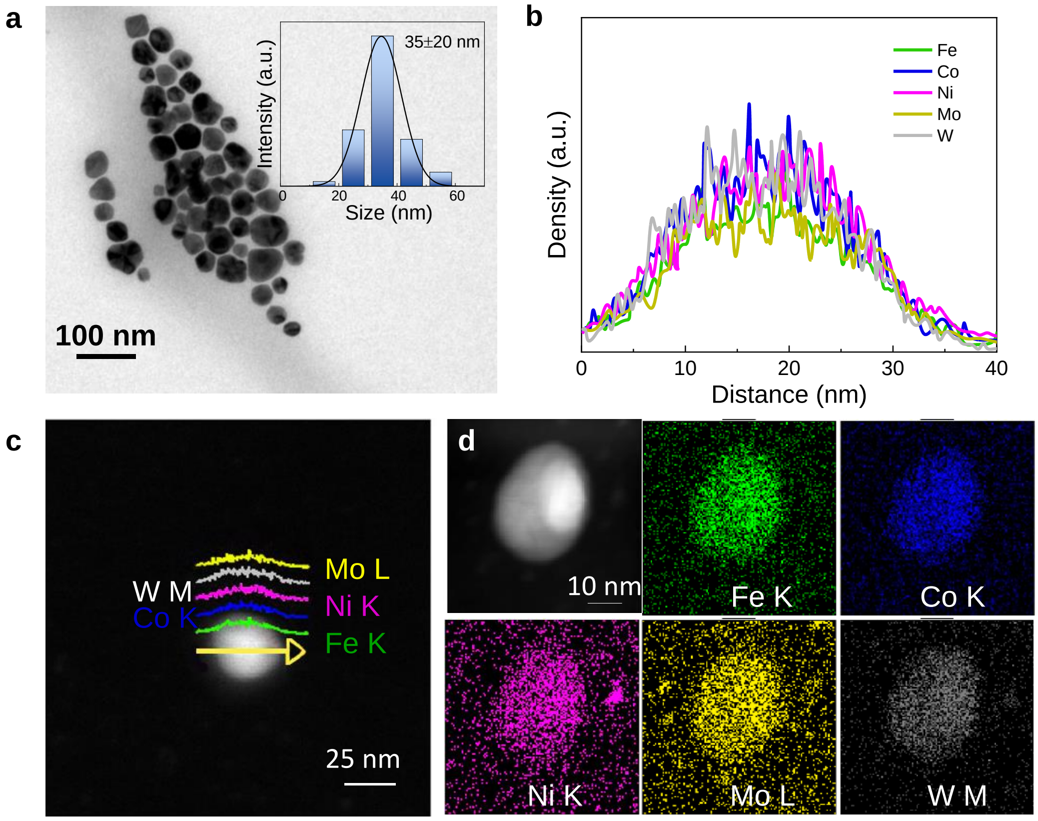

Figure 6. (a) TEM micrograph and size distribution histogram (inset). (b) Compositional line profile for each element. (c, d) HAADF-STEM micrograph and EDS compositional maps for each element.

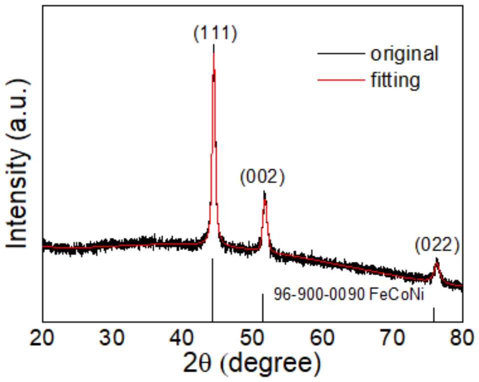

Figure 7. XRD pattern for FeCoNiMoW NPs.

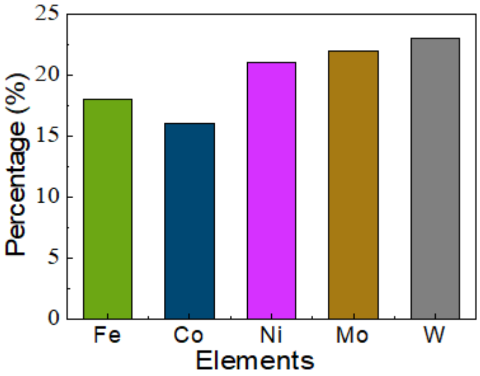

Figure 8. ICP-OES composition for FeCoNiMoW NPs.

According to the measured metal content, the mixing entropy of FeCoNiMoW was calculated using equation (1).[49,50]

$$\Delta S_{mix} = -R \sum_{i=1}^{n} c_i \, lnc_i \tag{1}$$

FeCoNiMoW particles were characterized by a mixing entropy of 1.60 R, which demonstrates its HEA character.[51] The mixing entropy of FeCoNiMo and FeCoNiW was calculated at 1.37 R, proving its middle entropy properties. The valence electron concentration (VEC) plays a decisive role in determining the crystal solid solution in HEAs.[50] In particular, a large VEC ($\geqslant 8$) favors the formation of FCC-type solid solutions, while a small VEC (<6.87) favors the formation of BCC phases.[49] The VEC of the ternary, quaternary, and quinary alloys was calculated using equation (2).[49]

$$\text{VEC} = \sum_{i=1}^{n} C_i VEC_i \tag{2}$$

where VEC_i is the VEC of each element. The VEC, atomic radii, and Pauling electronegativity of each of the different elements are shown in **Table 1**. From these values, FeCoNi, FeCoNiMo, FeCoNiW, and FeCoNiMoW were calculated to be characterized by VEC values of 9.12, 8.16, 8.17, and 7.68, respectively, which satisfy the statistical law for the formation of the FCC phase, consistently with the measured XRD patterns. The calculated VEC and ΔS_{mix} of the different alloys are summarized in **Table 2**.

Table 1. Atomic r, Pauling electronegativity and VEC for the different elements.

Element	r/Å	Pauling electronegativity	VEC
Fe	1.241	1.83	8
Co	1.251	1.88	9
Ni	1.246	1.91	10
Mo	1.363	2.16	6
W	1.367	2.36	6

Table 2. The physical parameters calculation results of FeCoNi, FeCoNiMo, FeCoNiW, and FeCoNiMoW.

Alloy	S_{mix}	**α**	δ	VEC	Phase
FeCoNi	1.0R/8.80	0.05%	0.29	9.12	FCC
FeCoNiMo	1.37R/11.37	0.89 %	4.14	8.16	FCC
FeCoNiW	1.37R/11.37	0.89 %	4.27	8.17	FCC
FeCoNiMoW	1.6R/13.28	0.78 %	4.57	7.68	FCC

α: local atomic distortion; δ: atomic size difference

A representative HRTEM micrograph of one of the FeCoNiMoW NPs and its selected area electron diffraction (SAED) pattern are shown in **Figure 9a**. **Figure 10a,b** shows the inverse fast Fourier transform (IFFT) lattice fringes of spot (1 1 1) and (−2 0 0) from the SAED pattern of the FeCoNiMoW NP. As regular fringes, without lattice distortion, we selected those having the FeCoNi lattice spacing, that is, 0.206 and 0.177 nm for the (1 1 1) and (−2 0 0) planes, respectively (**Figure 10c,d**). A geometric phase analysis (GPA) was carried out to image the internal distortions and strain distribution of the FeCoNiMoW NPs. **Figure 11a,b** exhibits the quantitative lattice distortions maps and **Figure 11c,d** displays the internal strain maps of (1 1 1) and (−2 0 0) zone axis in the FeCoNiMoW NP. A large number of lattice distortions and drastic internal tensile and compressive stresses are ubiquitously observed inside the HEA NP, which can be reasonably attributed to the different atomic r and electronegativity of the constituent elements, Fe, Co, Ni, Mo, and W.

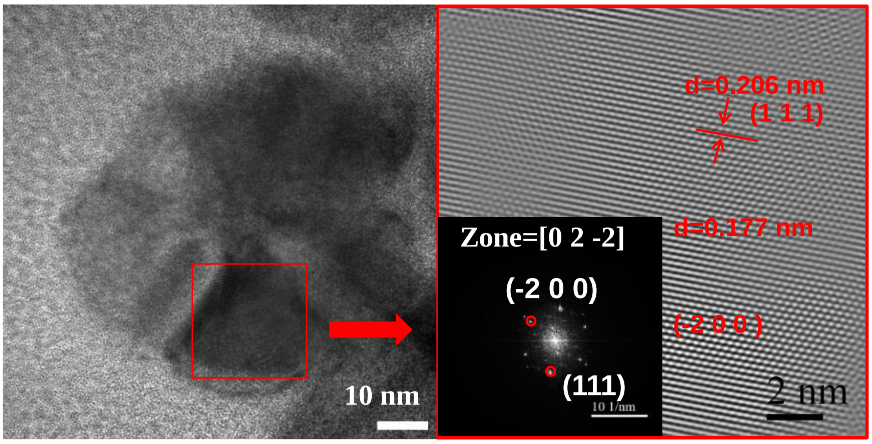

Figure 9. HRTEM micrograph and magnified image of the red square. Inset is the corresponding SAED pattern.

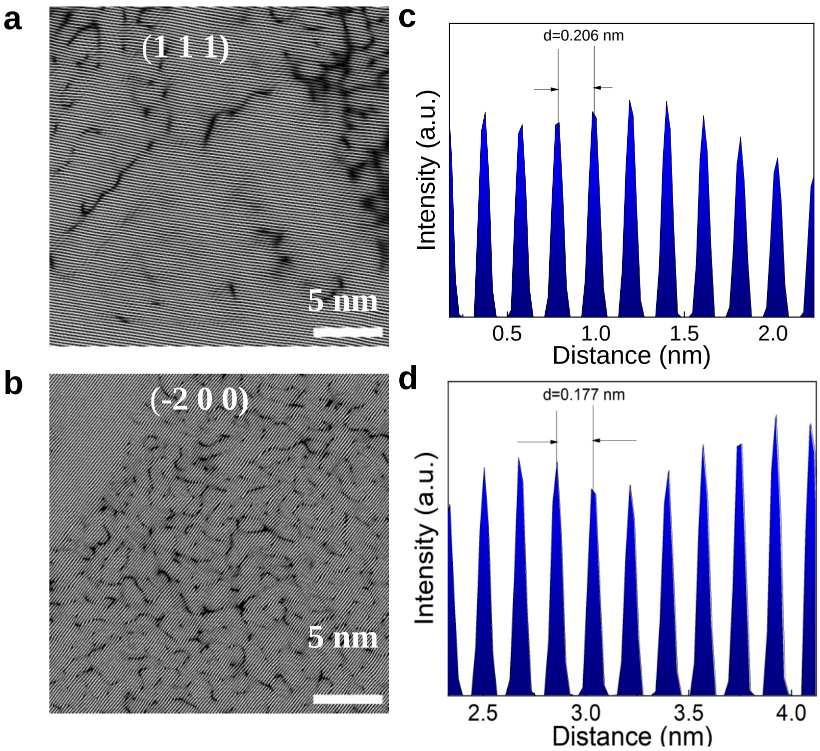

Figure 10. (a, b) IFFT patterns of crystal planes (111) and (−200) of the FeCoNiMoW NPs. (c, d) Lattice distance plots along the blue lines in (a) and (b), respectively.

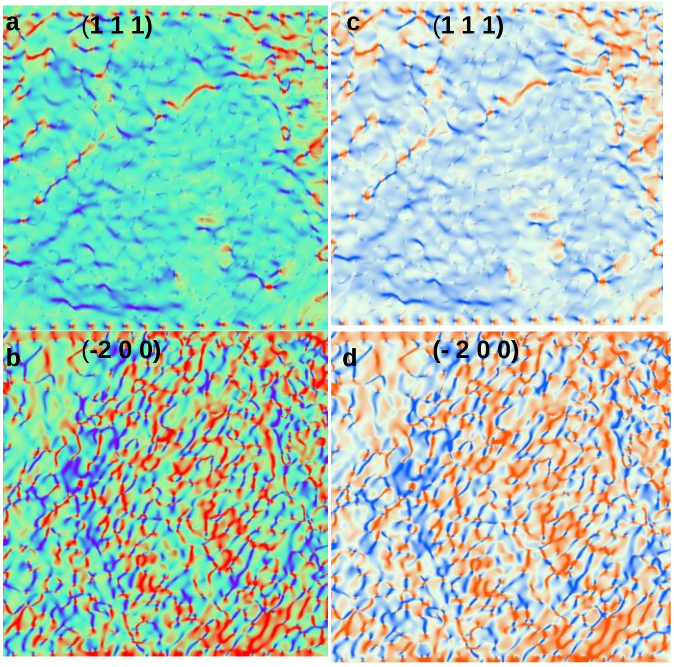

Figure 11. (a, b) Lattice distortion distribution maps and (c, d) internal strain maps of the crystal planes (111) and (-200) zone axis of the FeCoNiMoW NPs based on GPA analysis.

The δ and the α were used to evaluate the lattice distortion within the HEA particles. δ and α were calculated using equations (3) and (4), respectively.[52]

$$\delta = 100\sqrt{\sum_{i=1}^{n} c_i (1 - r_i/\bar{r})^2} \tag{3}$$

$$\alpha = \sum_{j \geqslant i}^{n} \frac{c_i c_j |r_i + r_j - 2\bar{r}|}{2\bar{r}} \tag{4}$$

where $\bar{r}$ is the average atomic r and calculated using equation (5).[52]

$$\bar{r} = \sum_{i}^{n} C_i r_i \tag{5}$$

The calculated α and δ of the different alloys are included in **Table 2**. FeCoNiMoW shows the largest δ between the five elements. Besides, FeCoNiMoW shows an α value of 0.78%, higher than that of the other alloys, for example, FeCoNi at 0.05%. These large δ and α, in large part related to the presence of Mo and W, explain the obvious lattice distortions experimental observed in the FeCoNiMoW HEA NPs.

XPS analyses were used to investigate the metal valences and electronic distribution within the HEA surface. The high-resolution Fe 2p, Co 2p, Ni 2p, and W 4f XPS spectra of FeCoNiW and FeCoNiMoW NPs are shown in **Figure 12**. Additionally, the high-resolution Mo 3d XPS spectrum of FeCoNiMoWis displayed in **Figure 13**. The high-resolution Fe 2p, Co 2p, Ni 2p, and Mo 3d XPS spectra of the FeCoNiMo NPs are shown in **Figure 14**. The detailed information on the peaks and metal content are summarized in **Tables 3-5**. Besides the satellite peaks, all the spectra display two doublets for each of the elements, which are associated with two different chemical states; a metallic component assigned to the particle core and an oxidized component related to the presence of a thin oxide layer at the particle surface. For the FeCoNiMoW HEA, the Fe 2p spectrum displays a doublet at 706.87 eV (Fe 2p3/2) assigned to Fe^0 and a second doublet at 710.79 eV (Fe 2p3/2) assigned to a Fe^{3+} chemical environment (**Figure 12a**).[53] Co displays a Co^0 valence state at 778.12 eV (Co 2p3/2), and a Co^{2+} state at 781.61 eV (Co 2p3/2) **(Figure 12b**).[53] The Ni 2p spectrum shows a doublet assigned to Ni^0 at 852.60 eV (Ni 2p3/2) and another one to Ni^{2+} at 855.82 eV (Ni 2p3/2) (**Figure 12c**).[53] The W 4f spectrum also displays two chemical states, W^0 at 31.47 eV (W 4f7/2) and W^{6+} at 35.45 eV (W 4f7/2) (**Figure 12d**).[53] Finally, the Mo 3d spectrum also displays two chemical states, Mo^0 at 227.59 eV (Mo 3d5/2) and Mo^{6+} at 232.68 eV (Mo 3d5/2) (**Figure 13**).[53]

Compared with the FeCoNiW and FeCoNiMo quaternary alloys, the binding energy of each element within FeCoNiMoW appears slightly shifted (**Tables 3,4**). Specifically, the Co 2p and Ni 2p electronic states shift to lower binding energies, implying a higher electron density. On the other hand, the binding energies of the Fe 2p are positively shifted, implying a lower electron density. The Mo 3d spectrum shifts to lower binding energies when introducing W into FeCoNiMo while theW4f spectrum shifts to higher binding energies when introducing Mo into FeCoNiW. These shifts are in part consistent with the different electronegativity of the elements: Fe < Co < Ni << Mo < W (**Table 1**) but are probably also influenced by a shift of the E_F used as zero energy reference to plot the XPS data. In any case, the presence of the 4d and 5d high valence elements, Mo and W, clearly affects the electronic distribution within the FeCoNiMoW HEA. In terms of composition, XPS analyses (**Table 5**) show the surface of the HEA to be slightly Fe-rich and Mo-poor compared with the overall HEA composition obtained by ICP. The variation in surface composition observed may have arisen from the differential oxidation of the various metals during the partial oxidation of the HEA surface when exposed to air.[54]

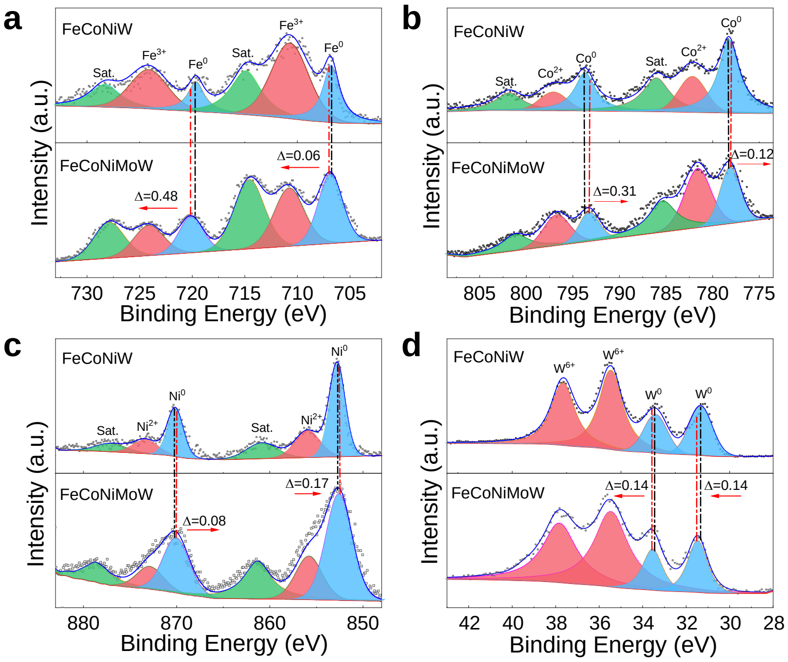

Figure 12. Surface electronic state analysis. High-resolution a) Fe 2p, b) Co 2p, c) Ni 2p, and d) W 4f XPS spectra of FeCoNiW (upper spectra) and FeCoNiMoW (bottom spectra).

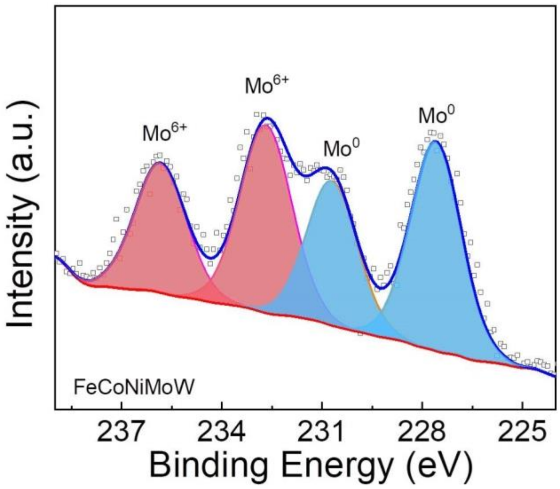

Figure 13. High-resolution Mo 3d XPS spectra of FeCoNiMoW NPs.

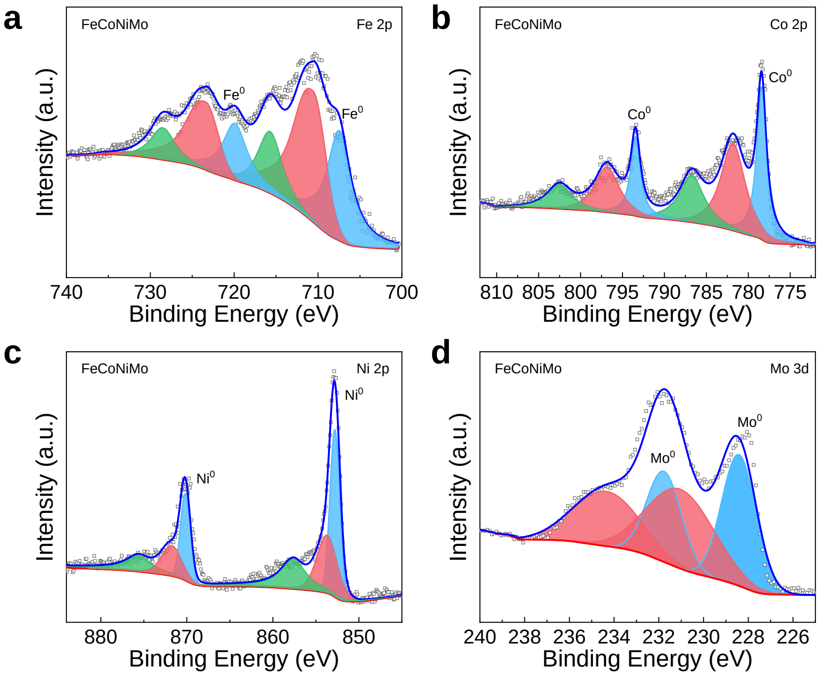

Figure 14. High-resolution XPS spectra of FeCoNiMo NPs for (a) Fe 2p, (b) Co 2p, (c) Ni 2p and (d) Mo 3d.

Table 3. Binding energies of Fe 2p, Co 2p, Ni 2p, Mo 3d and W 4f of FeCoNiMoW and FeCoNiW.

Elements	FeCoNiMoW		FeCoNiW	
	2p 3/2	2p 1/2	2p 3/2	2p 1/2
Fe^0	706.87↑	720.12↑	706.81	719.64
	2p 3/2	2p 1/2	2p 3/2	2p 1/2
Co^0	778.12↓	793.38↓	778.24	793.69
	2p 3/2	2p 1/2	2p 3/2	2p 1/2
Ni^0	852.60↓	870.06↓	852.77	870.14
	4f 7/2	4f 5/2	4f 7/2	4f 5/2
W^0	31.47↑	33.54↑	31.33	33.40
	3d 5/2	3d 3/2	3d 5/2	3d 3/2

Mo^0	227.59	230.70	/	/

Table 4. Binding energies of Fe 2p, Co 2p, Ni 2p, Mo 3d and W 4f of FeCoNiMoW and FeCoNiMo.

Elements	FeCoNiMoW		FeCoNiMo	
	2p 3/2	2p 1/2	2p 3/2	2p 1/2
Fe^0	706.87↑	720.12↑	706.48	719.90
	2p 3/2	2p 1/2	2p 3/2	2p 1/2
Co^0	778.12↓	793.38↓	778.42	793.39
	2p 3/2	2p 1/2	2p 3/2	2p 1/2
Ni^0	852.60↓	870.06↓	852.79	870.17
	4f 7/2	4f 5/2	4f 7/2	4f 5/2
W^0	31.47	33.54	/	/
	3d 5/2	3d 3/2	3d 5/2	3d 3/2
Mo^0	227.59↓	230.70↓	228.42	231.77

Table 5. Metal content of FeCoNiMo, FeCoNiW, and FeCoNiMoW by XPS technique.

Element	FeCoNiMo	FeCoNiW	FeCoNiMoW
Fe	44%	28%	29%
Co	22%	17%	15%
Ni	21%	18%	19%
Mo	13%	/	14%
W	/	37%	21%

3.4.2 Electrocatalytic OER performance

LSV in 1 M KOH electrolyte was used for a preliminary evaluation of the OER activities of electrodes based on FeCoNi, FeCoNiMo, FeCoNiW, FeCoNiMoW, and a commercial RuO_2 catalyst used as a reference (**Figure 15a**). FeCoNiMoW displays the best OER performance with a low η of 233 mV at 10 mA cm^{-2}, well below that of

FeCoNi (304 mV), FeCoNiMo (294 mV), FeCoNiW (283 mV), and RuO_2 (327 mV) (**Figure 15b**). Even at a higher current density of 100 mA cm^{-2}, FeCoNiMoW displays an exceptionally low η of 276 mV, significantly below that of FeCoNi (400 mV), FeCoNiMo (364 mV), FeCoNiW (361 mV), and RuO_2 (484 mV). The Tafel slopes calculated from LSV curves and the CA data are displayed in **Figure 16** and **Figures 17-20**. FeCoNiMoW shows the smallest Tafel slope among the tested catalysts, at 36.7 mV dec^{-1} from the LSV curves and 52.73 mV dec^{-1} using CA data, thus reflecting the fastest OER kinetics. The Tafel slope obtained from the CA data is higher than that of the LSV curves as it has a lower contribution of the double-layer charging and the catalyst's self-oxidation current.[55]

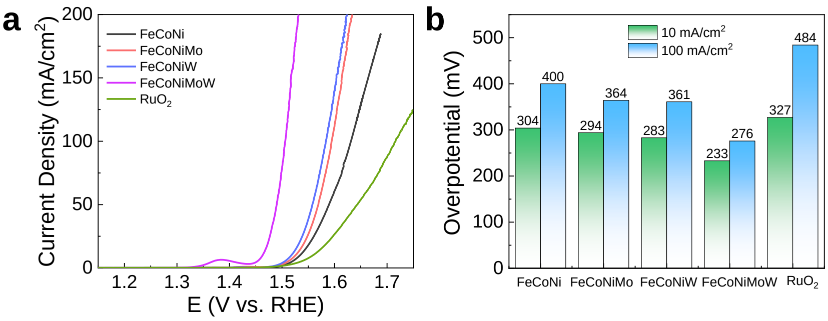

Figure 15. (a) LSV curves measured in 1.0 m KOH electrolyte. (b) OER η comparison at 10 and 100 mA cm^{-2}.

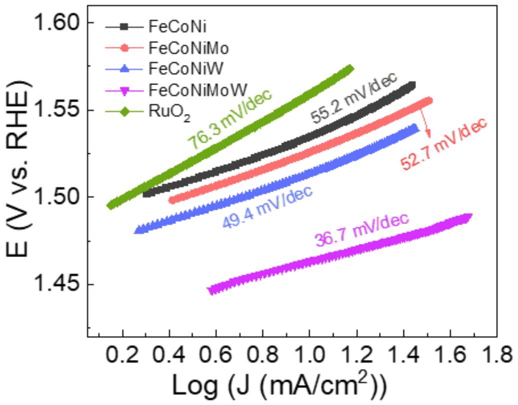

Figure 16. Tafel slopes of different catalysts.

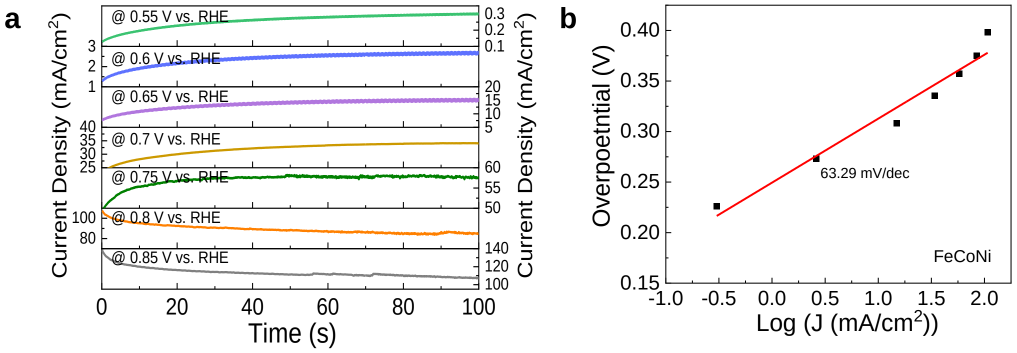

Figure 17. (a) CA responses of activity stabilized FeCoNi in 1.0 M KOH in the catalytic turnover region. (b) True steady-state polarization curve (Tafel plot) constructed from OER current densities sampled from steady-state CA responses.

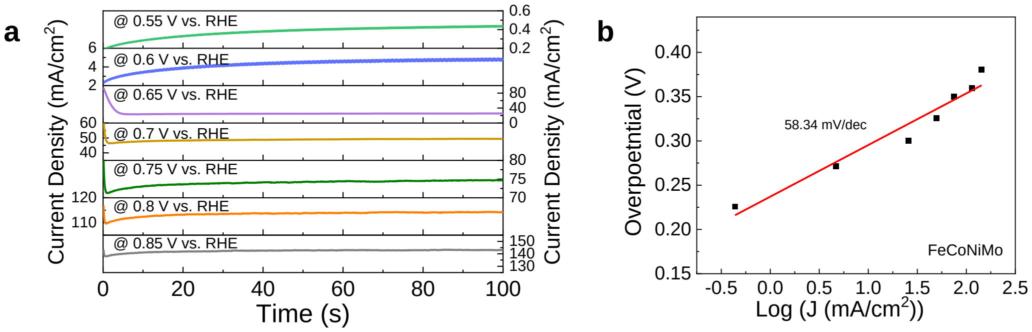

Figure 18. (a) CA responses of activity stabilized FeCoNiMo in 1.0 M KOH in the catalytic turnover region. (b) True steady-state polarization curve (Tafel plot) constructed from OER current densities sampled from steady-state CA responses.

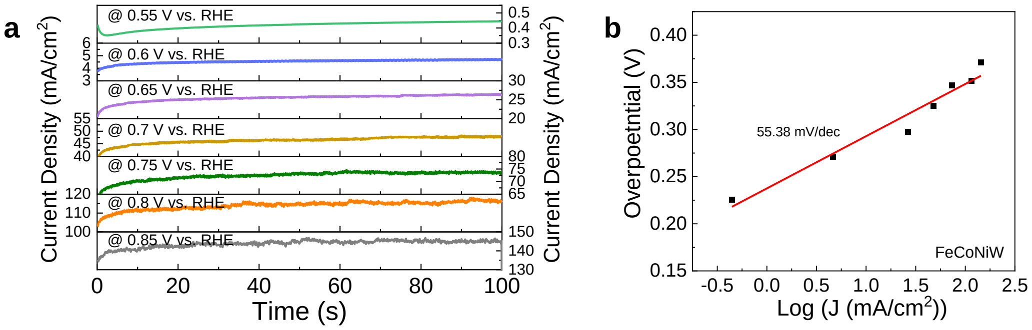

Figure 19. (a) CA responses of activity stabilized FeCoNiW in 1.0 M KOH in the catalytic turnover region. (b) True steady-state polarization curve (Tafel plot) constructed from OER current densities sampled from steady-state CA responses.

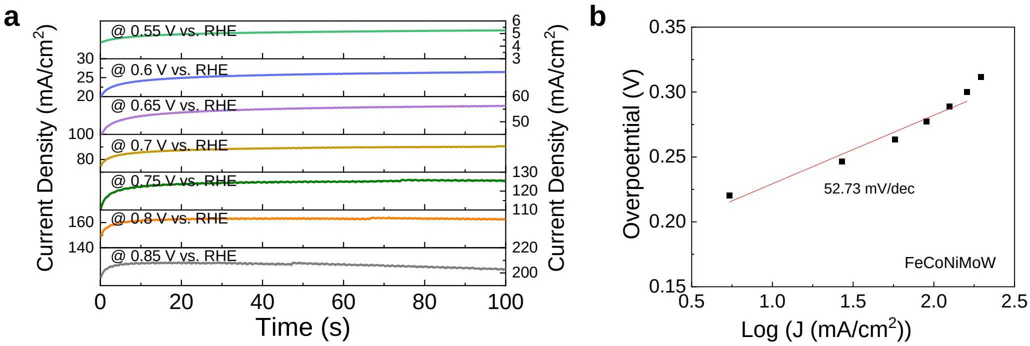

Figure 20. (a) CA responses of activity stabilized FeCoNiMoW in 1.0 M KOH in the catalytic turnover region. (b) True steady-state polarization curve (Tafel plot) constructed from OER current densities sampled from steady-state CA responses.

This result was further verified using EIS. **Figure 21** shows the Nyquist plot of the EIS spectra of the different electrodes at 1.5 V versus RHE and the equivalent circuit used for the fittings. The fitting results are listed in **Table 6**. The electrode based on FeCoNiMoW displays the smallest R_{ct} among the tested electrocatalysts, consistent with its fastest reaction kinetics. Besides, the electrochemical active surface area was determined from the C_{dl} calculated using CV scans in a non-Faradaic region (**Figure 22**). As shown in **Figure 23**, FeCoNiMoW shows the largest C_{dl} value among the tested catalysts, indicating the largest active surface area. Overall, FeCoNiMoW displayed excellent OER performance when compared not only with the reference materials here tested but also with previously reported catalysts, as shown in **Figure 24** and **Table 7**.

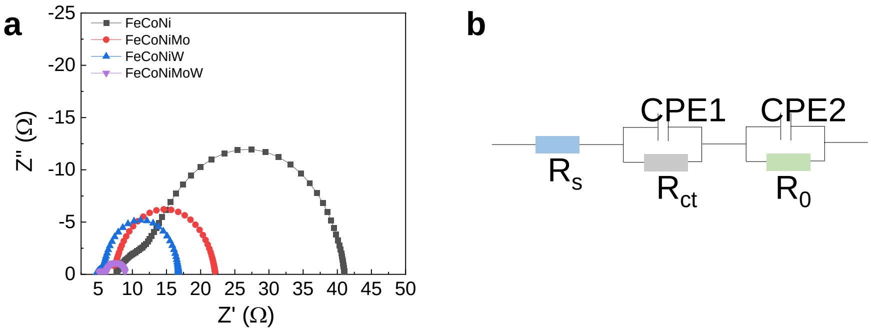

Figure 21. (a) EIS spectra of FeCoNi, FeCoNiMo, FeCoNiW, and FeCoNiMoW NPs. (b) The equivalent circuit model. For the equivalent circuit used for the Nyquist plot fitting, R_s is the uncompensated solution resistance, R_o represents adsorption resistance.

Table 6. Resistances obtained from the fitting of the EIS spectra by the equivalent circuit for the different catalysts.

Catalysts	R_s (Ω)	R_{ct} (Ω)	R_0 (Ω)
FeCoNi	7.54	6.16	27.40
FeCoNiMo	5.37	2.10	14.70
FeCoNiW	4.72	1.22	10.84
FeCoNiMoW	5.18	0.96	2.84

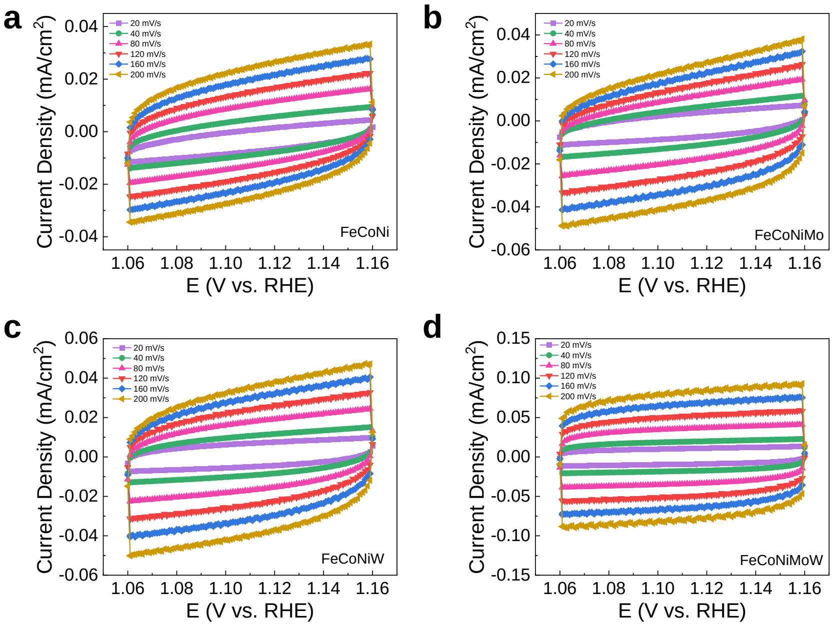

Figure 22. (a-d) CV curves at different scan rates of FeCoNi, FeCoNiMo, FeCoNiW, and FeCoNiMoW.

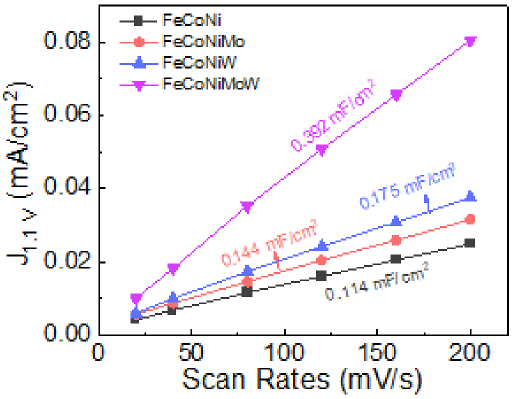

Figure 23. C_{dl} plots obtained from CV curves for different catalysts.

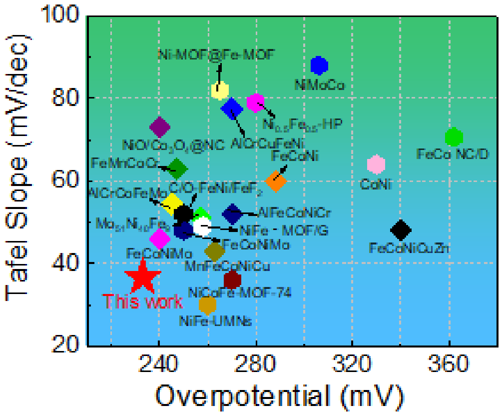

Figure 24. Comparisons of the OER performance of FeCoNiMoW with other recently reported catalysts.

Table 7. OER performance comparison of FeCoNiMoW with recently reported catalysts.

Catalyst	Substrate	η@10 mA cm^{-2} (mV)	Tafel slope (mV dec^{-1})	Stability (h)	Ref.
AlNiCoFeMo	GCE	240	46	50	*ACS Mater. Lett.*, **2019**, 1, 526-533
AlNiCoRuMo	GCE	245	54.5	100	*ACS Mater. Lett.*, **2020**, 2, 1698-1706
$Mo_{51}Ni_{40}Fe_9$	GCE	257	51	14	*ACS Appl. Mater. Inter.*, **2017**, 9, 7059-7067
AlCrCuFeNi	GCE	270	77.5	35	*Rare Met.*, **2022**, 41,125-131
FeCoNiCuZn	GCE	340	48	24	*J. Mater. Sci. Technol.*, **2021**, 93, 110-118
FeMnCoCr	GCE	247	63	60	*J. Mater. Sci. Technol.*, **2022**, 109, 267-275
FeCoNi	GCE	288	60	10	*ACS Catal.*, **2016**, 7, 469-479
MnFeCoNiCu	CC	263	43	24	*J. Mater. Chem. A*, **2020**, 8, 11938-11947
AlFeCoNiCr	GCE	270	52	-	*Appl Catal B-environ.*, **2020**, 268, 118431
FeCoNiMo	GCE	250	48	65	*ACS Catal.*, **2020**, 12, 10808-10817
NiO/Co_3O_4 @NC	GCE	240	73	48	*ACS Energy Lett.*, **2017**, 2, 2177-2182
FeCo NC/D	GCE	362	70.6	100	*Appl Catal B-environ.*, **2022**, 315, 121501
CoNi	CC	330	64	16	*Appl Catal B-environ.*, **2022**, 317, 121764
NiMoCo	GCE	306	88	12	*Electrochim. Acta*, **2022**, 424, 140613
C/O-FeNi/FeF_2	GCE	250	52	16	*Chem. Eng. J.*, **2022**, 442,

					136165
$Ni_{0.5}Fe_{0.5}$-HP	GCE	280	79	24	*Electrochim. Acta*, **2019**, 318, 430-439
NiFe-MOF/G	GCE	258	49	32	*Adv. Energy Mater.*, **2021**, 11, 2003759
NiFe-UMNs	GCE	260	30	3	*Nano Energy*, **2018**, 44, 345
Ni- MOF@Fe-MOF	GCE	265	82	5	*Adv. Funct Mater*, **2018**, 28, 1801554
NiCoFe-MOF-74	GCE	270	36	8	*J Am Chem Soc*, **2018**, 140, 15336
FeCoNiMoW	***GCE***	***233***	***36.7***	***40***	***This work***

The structural evolution of FeCoNiMoW during the OER was investigated using *in situ* Raman spectroscopy. A fixed voltage in the range from 0 to 1.7 V versus RHE was applied to the electrode and the CA was measured for 5 min, then the Raman spectra started to be acquired while maintaining the CA measurement running at the set voltage. The Raman spectra were obtained with an acquisition time of 20 s and the accumulation of 8 spectra in the range of 200-1000 cm^{-1}. **Figure 25** displays an image of the *in situ* cell coupled with the Raman system and the electrochemical workstation. **Figure 26a** displays the *in situ* Raman spectra measured for the FeCoNi electrode. A wide peak at ≈450 cm^{-1} is attributed to Ni and potentially also Fe and/or Co hydroxides, as all these metal hydroxides have Raman modes at a similar position (425 cm^{-1} for $Fe(OH)_2$,[56] 452 cm^{-1} for $Ni(OH)_2$,[57] 473 cm^{-1} for $Co(OH)_2$ [58]). These hydroxides are the common intermediate formed at the first OER step. The peaks at ≈530–560 cm^{-1} with wide shoulders could be related to the metal oxyhydroxide (538 cm^{-1} for CoOOH,[59] 543 cm^{-1} for FeOOH,[60] and 556 cm^{-1} for NiOOH[61]), which are the common intermediates during the OER at the third step. Besides, as CA progresses, the intensity of the metal hydroxide peak decreases while the intensity of the metal oxyhydroxide peaks increases, proving the surface evolution from hydroxide to oxyhydroxide during the OER. Similar results are obtained for the FeCoNiMo electrode (**Figure 26b**). At 1.3 V versus RHE, the broadband at ≈420–485 cm^{-1} should be related to the presence of the different Fe/Co/Ni hydroxides, and the wide peak at ≈550 cm^{-1} is attributed to the Fe/Co/Ni metal oxyhydroxide. The *in situ* Raman spectra of the FeCoNiMoW electrode are shown in **Figure 26c**. Already at 1.2 V versus RHE, that is, at a slightly lower voltage than the ternary and quaternary alloys, the Raman peaks associated with metal hydroxide and oxyhydroxide were clearly observed. Besides, at 1.3 V versus RHE, a new Raman peak at 678 cm^{-1} is attributed to the Fe-O stretching mode in iron oxide.[62,63] The observation of the hydroxide Raman peaks at lower potential indicates that Fe/Co/Ni sites in FeCoNiMoW are more active than in FeCoNiMo and FeCoNi.We will return to the discussion on active sites when presenting the results of DFT calculations below.

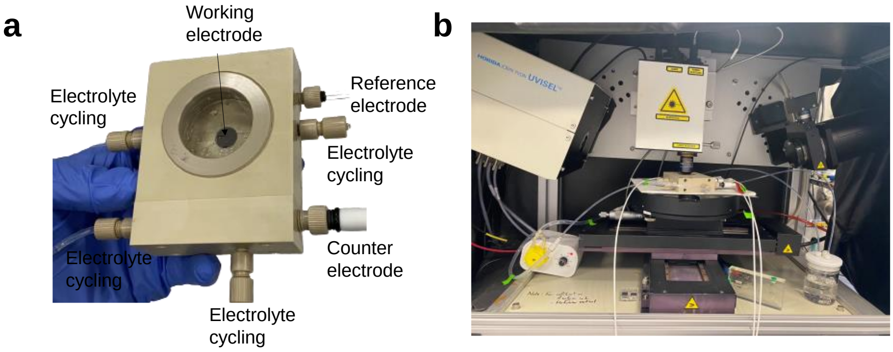

Figure 25. (a) Photograph of the *in situ* Raman cell. (b) Photograph of *in situ* Raman cell coupled with Raman set-up and workstation.

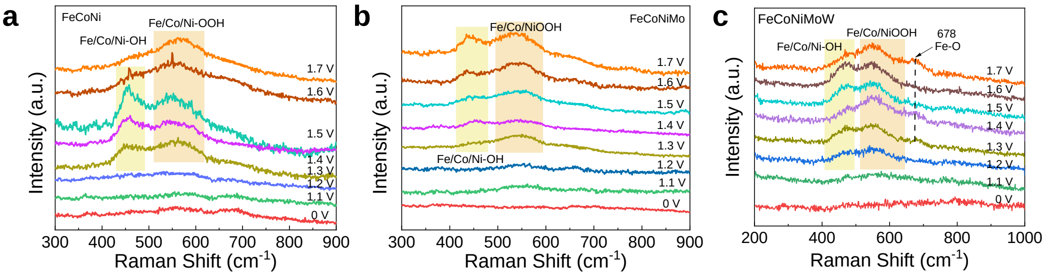

Figure 26. *In situ* Raman spectra of (a) FeCoNi, (b) FeCoNiMo, and (c) FeCoNiMoW at different applied potentials.

The stability of FeCoNiMoW under OER conditions was analyzed using CA. As shown in **Figure 27**, the FeCoNiMoW-based electrode shows a current density decrease of 7.5% after 100 h of continuous operation at 1.47 V versus RHE. At higher current densities, the FeCoNiMoW electrode maintained 88.8% of the initial current after 115 h at 1.49 V versus RHE (50 mA cm^{-2}) and 83.7% after 104 h at 1.51 V versus RHE (100 mA cm^{-2}). The reduction in current density at higher operation voltages is in large part related to the generation of numerous bubbles, which caused the catalysts to slightly peel off from the CP support. To determine a possible metal leaching during OER, the metal composition of the KOH electrolyte and the metal content reduction of FeCoNiMoW after 20, 50, and 100 h long-term OER tests were analyzed by inductively coupled plasma mass spectrometry (ICPMS). As shown in **Tables 8,9**, small metal amounts, especially of Fe, Ni, and Co, were detected in the KOH, representing a minor HEA compositional change. Interestingly the leaching of Ni but particularly Mo and W was accentuated under ORR conditions, up to 12% for Mo after 50 h ORR, while that of Fe and Co was slightly higher under OER operation.

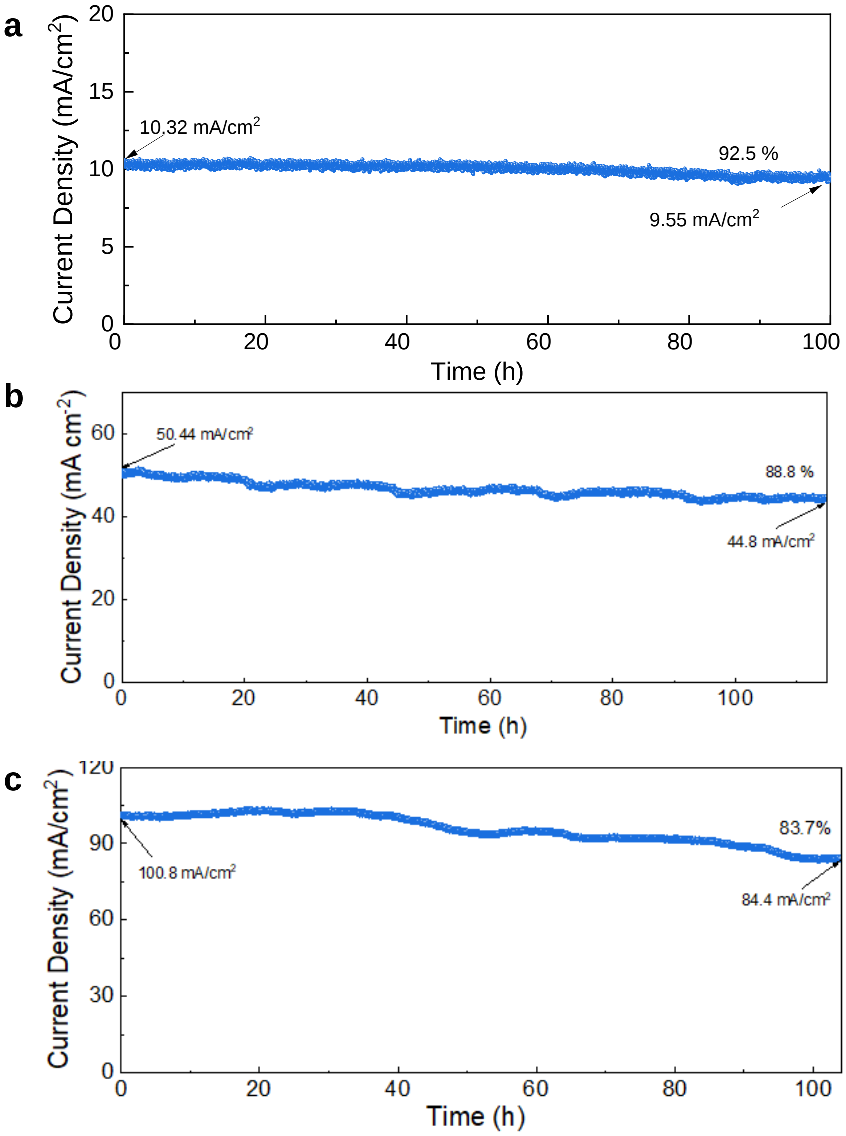

Figure 27. CA curve of FeCoNiMoW during OER at the potential of (a) 1.47 V vs. RHE, (b) 1.49 V vs. RHE, and (c) 1.51 V vs. RHE.

Table 8. ICPMS results of the content of metallic elements in the electrolyte after long-term tests.

Elements Content (ppb, parts per billion)	Fe	Co	Ni	Mo	W
20 h (OER)	3.3	1.7	0.5	22	14
50 h (OER)	5.2	1.9	0.8	42	33
100 h (OER)	8.6	3.2	1.5	67	45
2 h (ORR)	1.3	1.5	3.6	62	54
50 h (ORR)	2.1	1.3	2.3	97	72

Table 9. Percentage of each metal of the initial FeCoNiMoW find in the electrolyte solution after different OER/ORR operating time, as measured by ICPMS.

	Fe (%)	Co (%)	Ni (%)	Mo (%)	W (%)
20 h (OER)	0.41	0.21	0.06	2.75	1.75
50 h (OER)	0.65	0.24	0.1	5.25	4.12
100 h (OER)	1.08	0.4	0.18	8.37	5.62
2 h (ORR)	0.16	0.18	0.45	7.75	6.75
50 h (ORR)	0.26	0.16	0.28	12.12	9.00

XPS characterization of the FeCoNiMoW HEAs after long-term OER measurements shows the surface of FeCoNiMoW to be completely oxidized (**Figure 28**). The O 1s spectrum displays at least three contributions at 530.0, 532.3, and 533.9 eV, which are assigned to oxygen within a metal oxide chemical environment, and additional O-H and O-O bonds that could be associated with adsorbed oxygen-containing species and/or the formation of a hydroxide or oxyhydroxide surface layer.[64] XRD analysis shows the FeCoNiMoW crystal phase does not change after the OER process. However, the XRD peak intensity decreased after long-term OER, which we correlate with the formation of an amorphous oxide or oxyhydroxide surface layer (**Figure 29**). From the width of the XRD peaks, the HEA crystal domain size before and after OER measurements is 13.8 and 12.7 nm, implying the growth of an additional ≈0.5 nm-thick amorphous oxide/oxyhydroxide shell on the particle surface. Notice the small crystal domain size obtained from the fitting of the XRD patterns is notably influenced by the highly distorted lattice, which contributes to the XRD peak broadening. HRTEM images of FeCoNiMoW HEAs after the stability test further confirmed the existence of an amorphous layer on the surface, while the crystal core still displays the cubic FeCoNi phase (**Figure 30**).

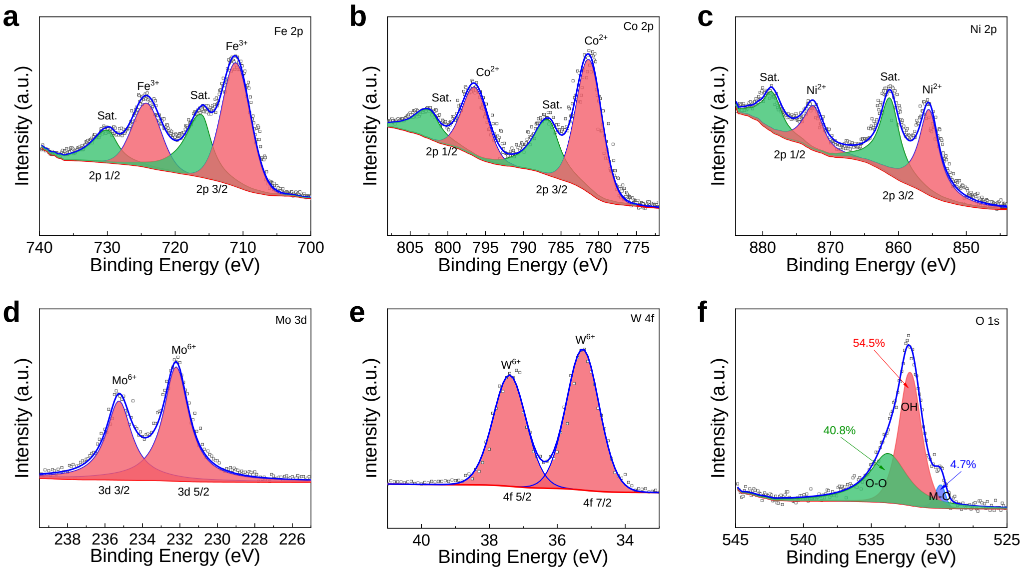

Figure 28. High-resolution XPS spectra of FeCoNiMoW after long-term OER measurements (a) Fe 2p, (b) Co 2p, (c) Ni 2p, (d) Mo 3d, (e) W 4f, and (f) O 1s.

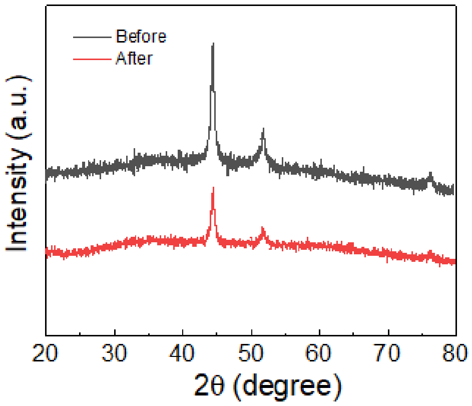

Figure 29. XRD pattern of FeCoNiMoW after long-term OER measurements.

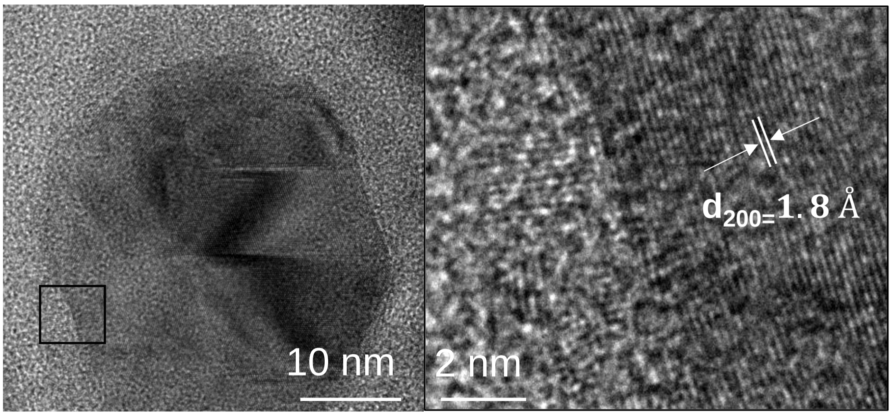

Figure 30. HRTEM images of a polycrystalline FeCoNiMoW NP after OER stability measurements.

3.4.3 Electrocatalytic ORR performance

FeCoNiMoW was further tested as an ORR electrocatalyst in 0.1 M KOH using a RRDE. **Figure 31a** shows the CV curves measured from electrolytes saturated in Ar and O_2. Beyond the characteristic double-layer charge-discharge profile, no obvious ORR cathodic peak is obtained for the FeCoNiMoW catalyst within an Ar-saturated electrolyte. In contrast, a large cathodic peak is observed when the electrolyte is saturated with O_2, pointing at a notable ORR electrochemical activity. **Figure 31b** shows the LSV curves obtained from FeCoNiMoW at different rotation speeds in the range from 400 to 2500 rpm. At 1600 rpm, the $E_{1/2}$ of FeCoNiMoW is 0.71 V and its onset potential is 0.83 V. The CV and LSV curves with rotation speeds in the range from 400 to 2500 rpm of FeCoNi, FeCoNiMo, and FeCoNiW are shown in **Figure 32**.

Besides, **Figure 33** shows the LSV curves at 1600 rpm and the n of the different alloys. Among the tested alloys, FeCoNiMoW shows the highest current density, largest onset and $E_{1/2}$, and highest n, proving an enhanced ORR performance with the HEA formation. In the same measurement conditions, the 20 wt.% Pt/C catalyst showed slightly higher halfwave and onset potentials, at 0.82 and 0.95 V, respectively (**Figure 34**). The Pt/C catalyst also shows an n of 3.95 at 0.5 V versus RHE indicating a direct $4e^-$ pathway. On the other hand, FeCoNiMoW shows an n of 3.12 at 0.5 V versus RHE, indicating that ORR does not follow either the $2e^-$ or $4e^-$ pathway (**Figure 35**). For FeCoNiMoW, the average n calculated by K-L plots is 2.66 (**Figure 36**), consistent with the coexistence of both the 2e- and 4e- ORR pathways. As shown in **Figure 35b**, FeCoNiMoW shows a higher ring disk current density than Pt/C, indicating a relatively higher yield of H_2O_2. The H_2O_2 average selectivity of the FeCoNiMoW electrode is calculated to be 27% at 0.5 V versus RHE (**Figure 35c**), further confirming the existence of a 2e⁻ pathway during the ORR. FeCoNiMoW shows good stability under ORR conditions with 5000 cycles and long-term CA measurements with 92% current density retention for 65 h (**Figure37**) without modifying its morphology, crystal phase, and composition (**Figures 38,39** and **Tables 8,9**).

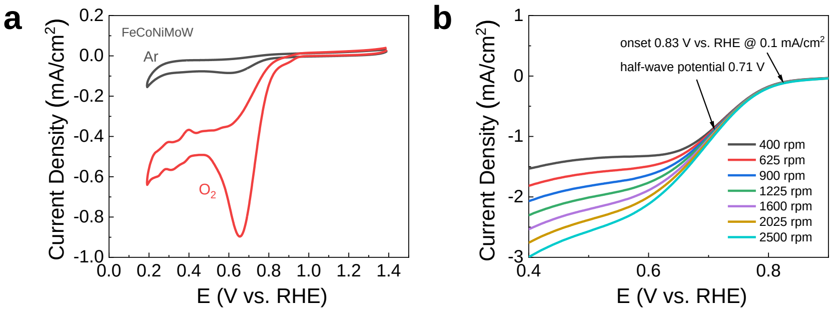

Figure 31. (a) CV curves measured in Ar and O_2 saturated 0.1 M KOH electrolytes. (b) LSV curves at different rotation speeds in the range from 400 to 2500 rpm.

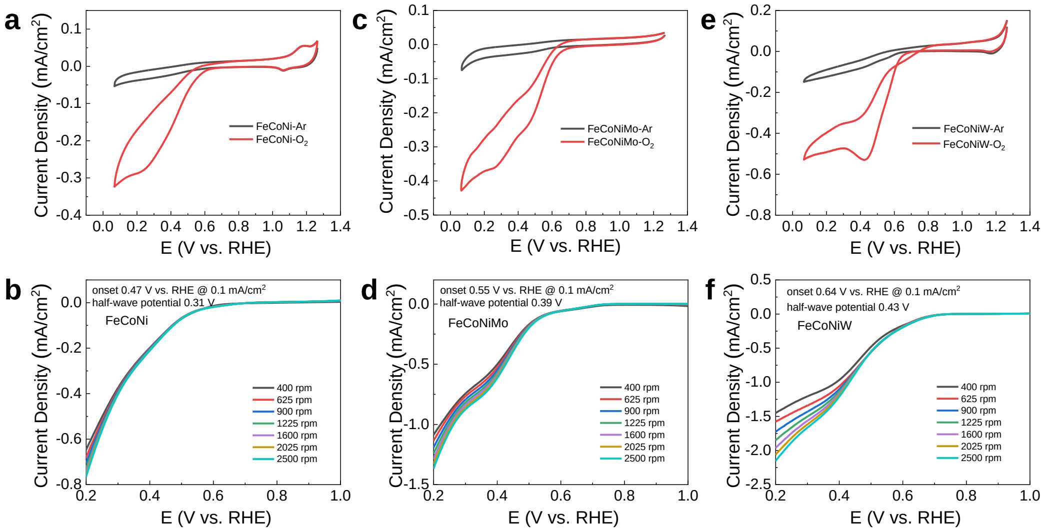

Figure 32. (a, c, e) CV curves measured in Ar and O_2 saturated 0.1 M KOH electrolytes and (b, d, f) LSV curves at different rotation speeds in the range from 400 rpm to 2500 rpm of FeCoNi, FeCoNiMo, and FeCoNiW.

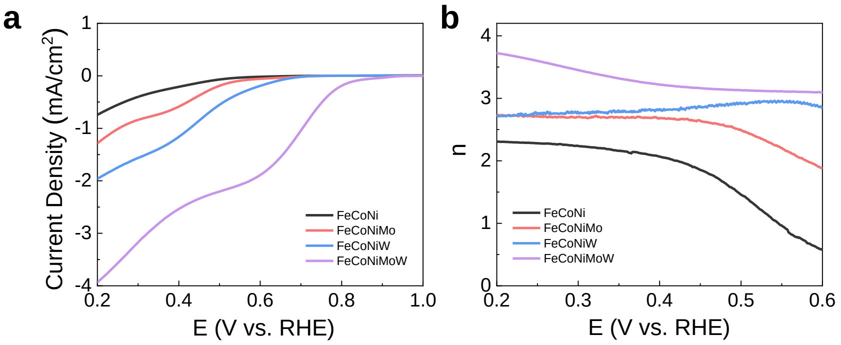

Figure 33. (a) LSV curves at the rotation speeds of 1600 rpm of different catalysts. (b) n of different catalysts.

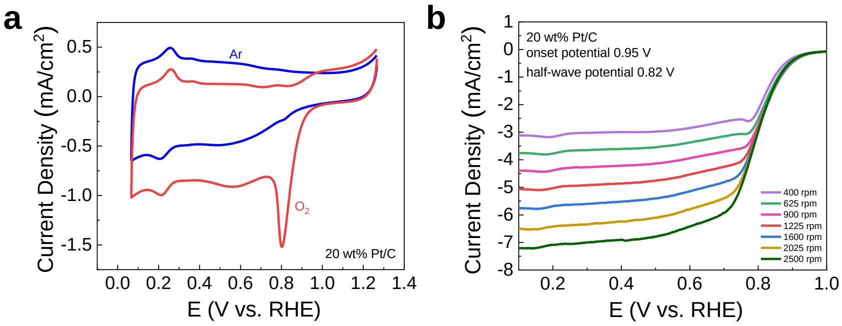

Figure 34. (a) CV curves of 20 wt% Pt/C measured in Ar and O_2 saturated 0.1 M KOH electrolytes. (b) LSV curves at different rotation speeds in the range from 400 rpm to 2500 rpm of 20 wt% Pt/C.

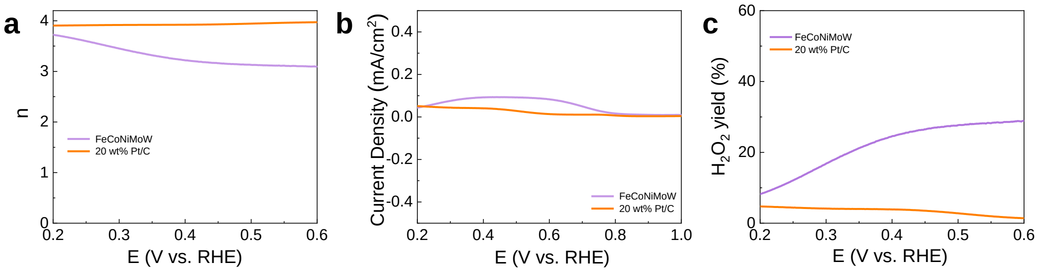

Figure 35. (a) Calculated n, (b) ring current density, and (c) H_2O_2 yield of FeCoNiMoW and 20 wt% Pt/C during the ORR process.

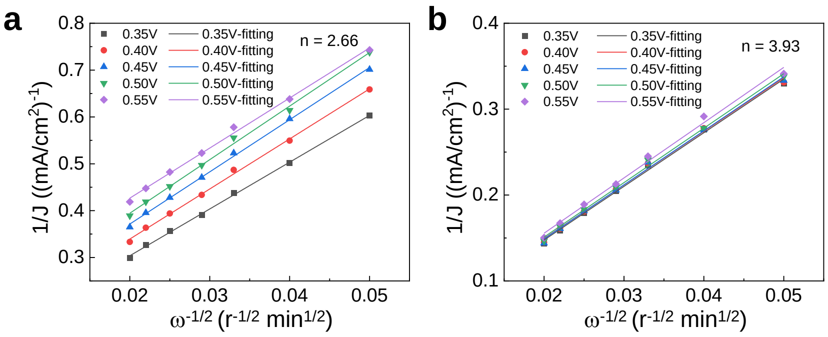

Figure 36. Calculated n from K-L plots of (a) FeCoNiMoW and (b) 20 wt % Pt/C.

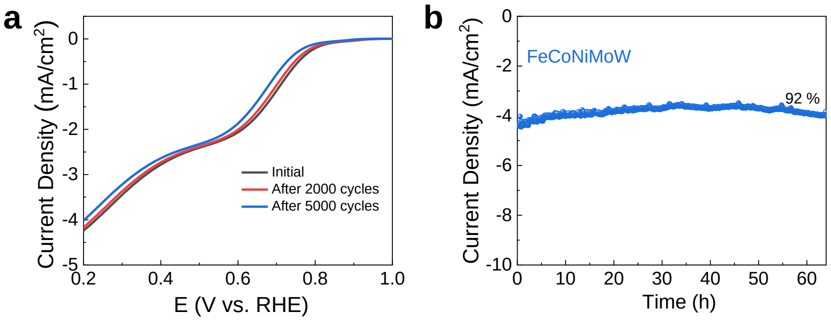

Figure 37. Stability of FeCoNiMoW HEAs for ORR. (a) LSV curves and (b) CA curves for 65 h.

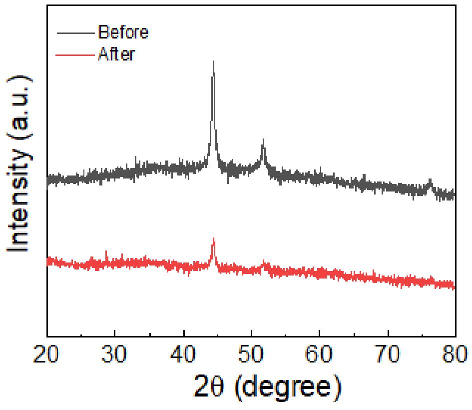

Figure 38. XRD pattern of FeCoNiMoW after long-term ORR measurements.

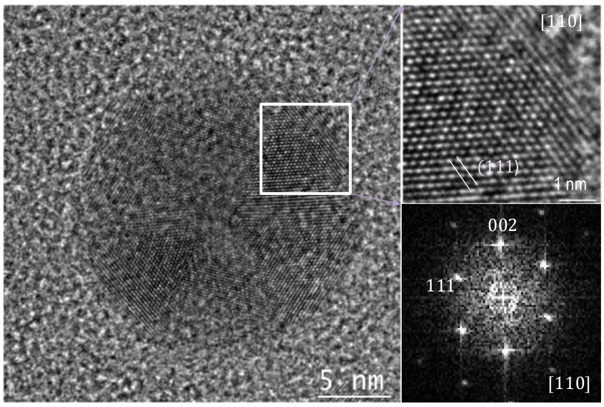

Figure 39. HRTEM images of a FeCoNiMoW NP after ORR stability measurements. HRTEM image magnified image from white squared region shown right up and corresponding FFT pattern given right below.

Overall, a key performance parameter of a bifunctional oxygen catalyst is the E_{gap}. Compared with the noble metal-based RuO_2 and Pt/C couple with an E_{gap} of 0.76 V in 0.1 M KOH, the FeCoNiMoW electrode exhibits a slightly improved performance with an E_{gap} of 0.75 V (**Figure 40**).

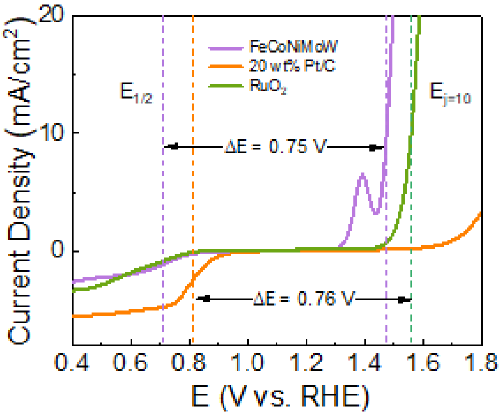

Figure 40. ORR/OER bifunctional LSV curves of different electrodes measured in 0.1 M KOH electrolyte.

3.4.4 DFT calculations

DFT was used to calculate the orbital hybridization η and Gibbs energy barrier to gain inside from the active sites, electronic structure, and catalytic ability of the catalysts during the OER. The DFT models of the FeCoNi, FeCoNiMo, and FeCoNiMoW particles were constructed based on the experimental results of the structural and chemical analysis of the HEA and are shown in **Figures 41-43**.

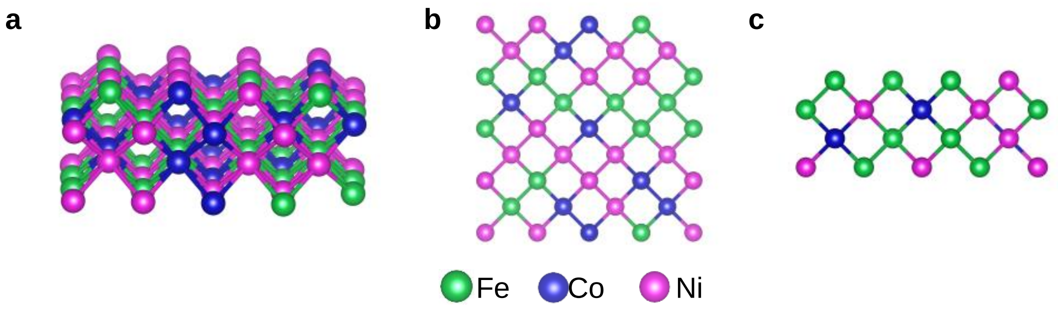

Figure 41. Schematic diagram of the optimized structure of FeCoNi, (a) overall, (b) top, and (c) side view.

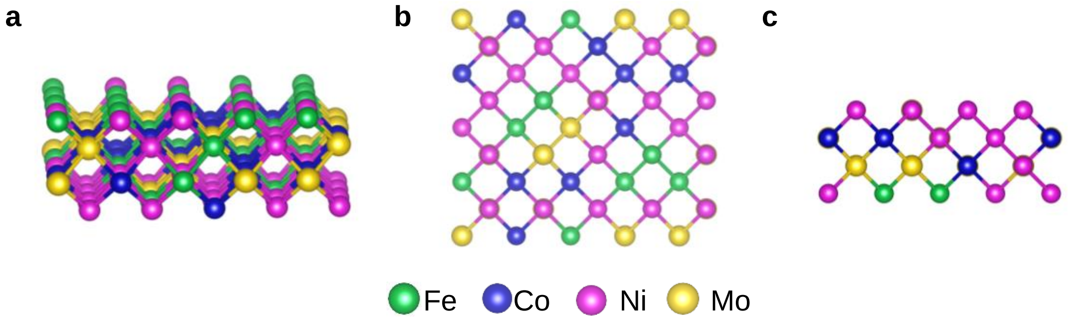

Figure 42. Schematic diagram of the optimized structure of FeCoNiMo, (a) overall, (b) top, and (c) side view.

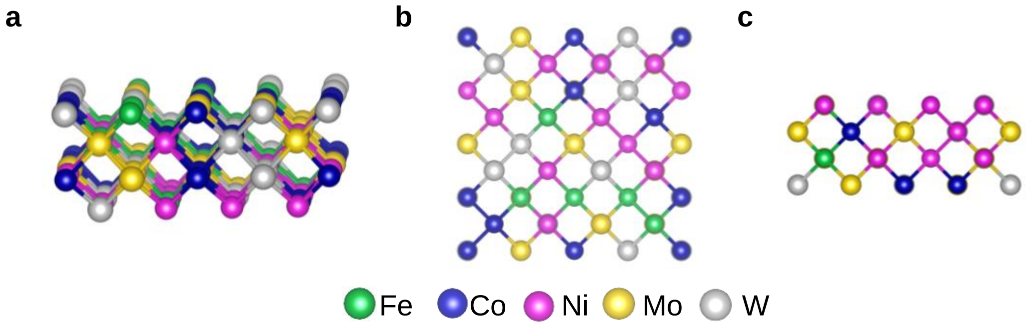

Figure 43. Schematic diagram of the optimized structure of FeCoNiMoW, (a) overall, (b) top, and (c) side view.

The first OER step is the H_2O adsorption on the catalytic surface. The H_2O E_{ads} for different active sites in FeCoNiMoW is shown in **Figure 44a**. The Ni atoms on the FeCoNiMoW surface show the largest H_2O E_{ads}. Generally, the d_c is an indicator of the binding strength between the metal active center and reactants/intermediates/products. The closer the d_c level is to the E_F, the stronger the adsorption ability.[65] The project

DOS (PDOS) of Ni atoms is displayed in **Figure 44b**. Compared with FeCoNi and FeCoNiMo, within FeCoNiMoW the d_c of Ni is shifted to higher energy, which strengthens the adsorption of intermediate species, thus enabling higher reaction rates.

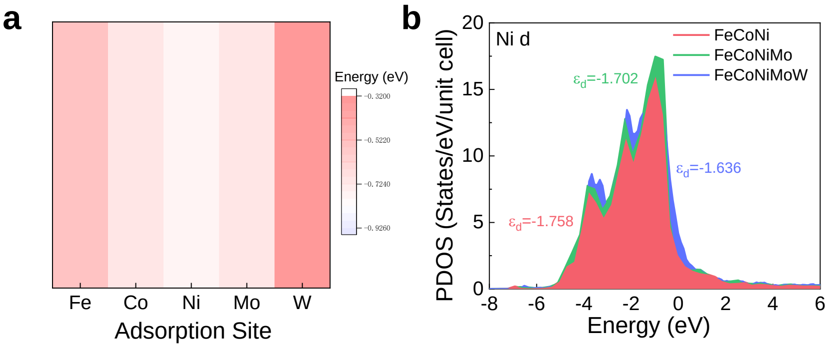

Figure 44. (a) E_{ads} between different active sites in FeCoNiMoW and H_2O molecules. (b) d_c position of Ni atoms in FeCoNi, FeCoNiMo, and FeCoNiMoW.

The electron localization function (ELF) was employed to visualize the chemical bond between Ni active sites of different catalysts and OOH* intermediate species. As shown in **Figure 45**, the lengths of the Ni-O bond for FeCoNi, FeCoNiMo, and FeCoNiMoW are 1.85, 1.82, and 1.71 Å, respectively, proving their covalent nature. Besides, the Ni-O bond length for FeCoNiMoW is the shortest among the three catalysts, implying that Ni atoms in FeCoNiMoWprovide the largest bond strength with O in OOH*, which is consistent with the d_c analysis.

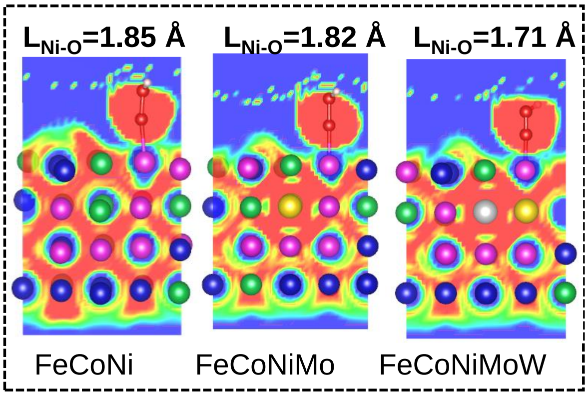

Figure 45. ELF calculations of Ni-O bond for FeCoNi, FeCoNiMo, and FeCoNiMoW.

The crystal orbital Hamilton population (COHP) of Ni-O bond analysis, which is the DOS weighted by the corresponding Hamiltonian matrix element, was further used to analyze the strength and nature of the bonding states of FeCoNi, FeCoNiMo, and FeCoNiMoW. As shown in **Figure 46**, the calculated absolute integrated COHP value of FeCoNi, FeCoNiMo, and FeCoNiMoW are 2.453, 2.677, and 2.985 eV, respectively, implying more Ni metal active sites bonding with O atoms in the FeCoNiMoW.[66]

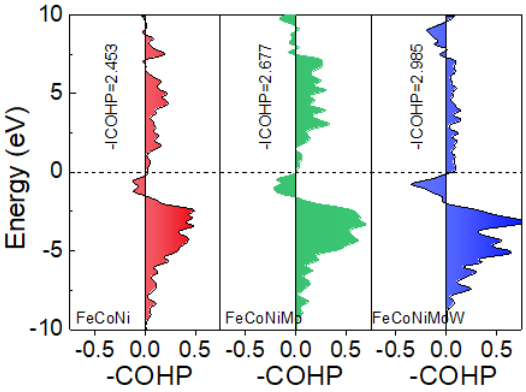

Figure 46. COHP analysis of Ni-O bond for FeCoNi, FeCoNiMo, and FeCoNiMoW.

The electrons in the d orbital of Ni atoms in FeCoNiMoW are hybridized with the p orbital of the O atom in H_2O, forming bonding and anti-bonding orbitals. Since the d_c in FeCoNiMoW is closer to the E_F than in the other catalysts, the anti-bonding orbital of FeCoNiMoW is higher, then the occupation degree of electrons on the antibonding orbital is reduced and that of the bonding orbital is larger. The diagram of the hybridizing between FeCoNi and FeCoNiMoW catalysts and O atoms is shown in **Figure 47**.

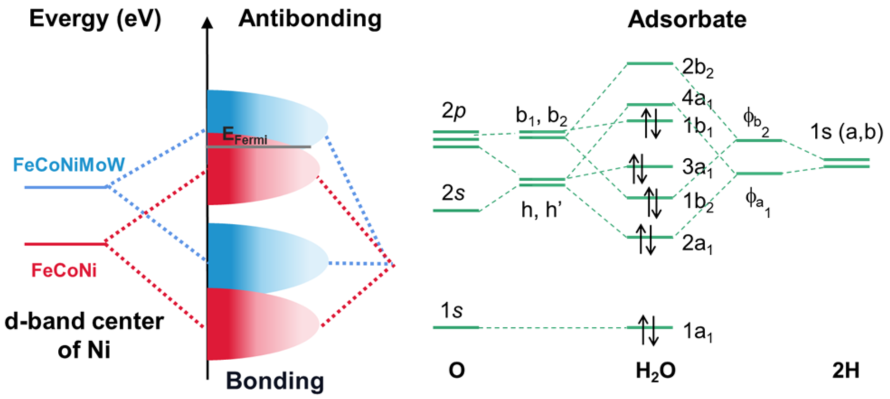

Figure 47. Diagram of the hybridizing between catalysts of FeCoNi and FeCoNiMoW and O atoms of H_2O molecule.

The catalytic activity of each atom within FeCoNi, FeCoNiMo, and FeCoNiMoW was further investigated. **Figure 48** shows a volcano-shaped curve where the *x*-axis is the difference in Gibbs free energy between OH* and O*, and the *y*-axis is the theoretical η during OER. As observed in the graph, the Ni active sites in FeCoNiMoW have the lowest η and a moderate Gibbs free energy difference, which is consistent with Ni being the active site and FeCoNiMoW being the most active OER catalyst. Besides, Fe in FeCoNiMoW shows a larger η than Ni, demonstrating Ni sites are much more efficient than Fe, which is consistent with the adsorption energies of H_2O on different active sites obtained by DFT and the appearance of the NiOOH fingerprint in the *in situ* Raman spectra.

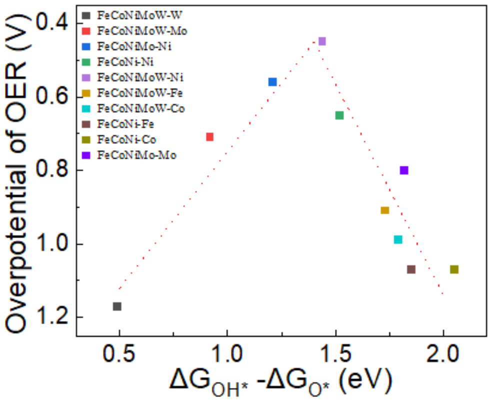

Figure 48. OER catalytic activity of each atom for FeCoNi, FeCoNiMo, and FeCoNiMoW.

The free energy step diagram of the OER process is shown in **Figure 49**. Regardless of whether the applied voltage is 0 or 1.23 V, the Gibbs free energy barrier of the OER potential determination step (PDS) that needs to be overcome is smaller for FeCoNiMoW than for FeCoNi and FeCoNiMo, thus the OER is more favorable to occur in the former. Specifically, when the applied voltage is 0 V, the positive ΔG changes of the PDS for FeCoNi, FeCoNiMo, and FeCoNiMoW are 1.87, 1.81, and 1.65 eV, respectively. In addition, the catalytic OER efficiencies of FeCoNi, FeCoNiMo, and FeCoNiMoW show a trend of FeCoNi < FeCoNiMo < FeCoNiMoW, and the theoretical η are 0.64, 0.58, and 0.42 eV, respectively, which is consistent with the experimental results, indicating that the introduction of 4d Mo and 5d W atoms improves the overall activity of the catalyst. Overall, the proposed OER mechanism on FeCoNiMoW is depicted in **Figure 50**.

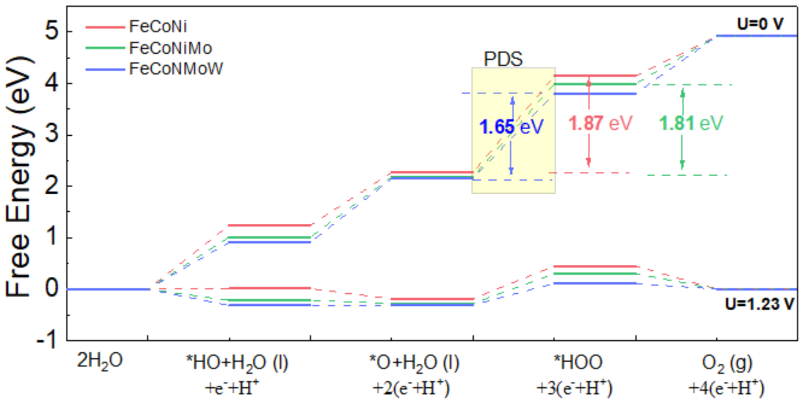

Figure 49. Free energy step diagram during the OER process of FeCoNi, FeCoNiMo, and FeCoNiMoW.

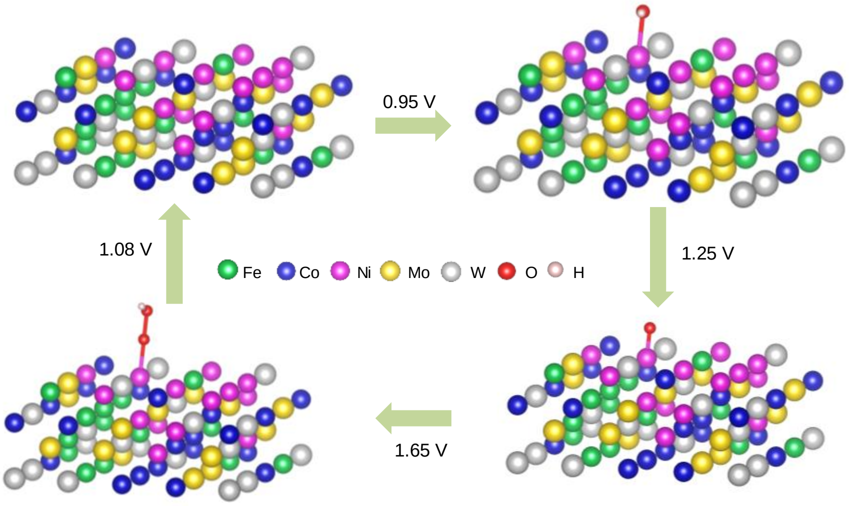

Figure 50. OER reaction mechanism on FeCoNiMoW catalysts.

The free energy step diagram of the ORR process is shown in **Figure 51**. There are two PDS, the O_2 molecule transfer to *HOO at the first step, and *O transfer to *HO at the third step. For the first step, the Gibbs free energy barrier of the FeCoNiMoW is 0.11 eV, which is smaller than that of FeCoNi at 0.45 eV and FeCoNiMo at 0.30 eV. The third step involves no energy barrier for the FeCoNiMoW catalyst, while in FeCoNi and FeCoNiMo energy barriers of 0.20 and 0.06 eV, respectively, need to be overcome. Therefore, DFT calculations show the catalytic ORR performance should follow the trend FeCoNi < FeCoNiMo < FeCoNiMoW, which is consistent with the experimental data.

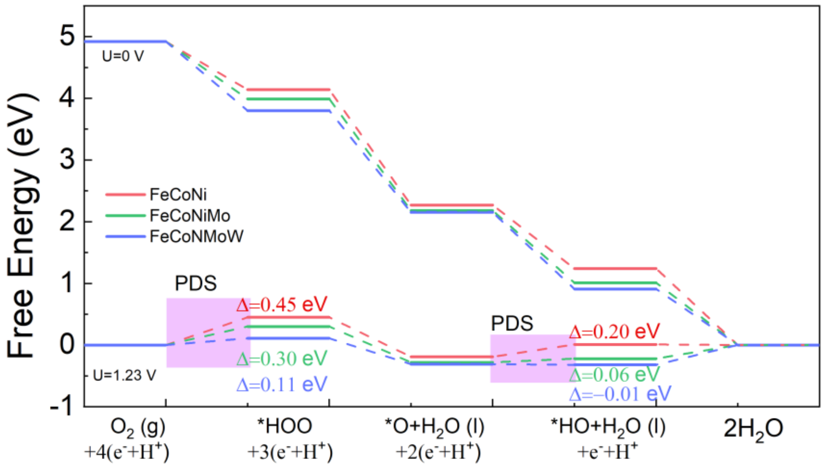

Figure 51. Free energy step diagram during the ORR process of FeCoNi, FeCoNiMo, and FeCoNiMoW.

Ab initio molecular dynamics (AIMD) simulations using a canonical ensemble with a Nosé-Hoover heat bath scheme were employed to investigate the thermal stability of the FeCoNiMoW.[67] As shown in **Figure 52**, the free energy of the FeCoNiMoW fluctuates in a narrow range in all cases at 300, 500, and 700 K, indicating that the FeCoNiMoWstructure is thermally stable during the OER/ORR process, which is consistent with the long-term catalytic stability for OER/ORR.

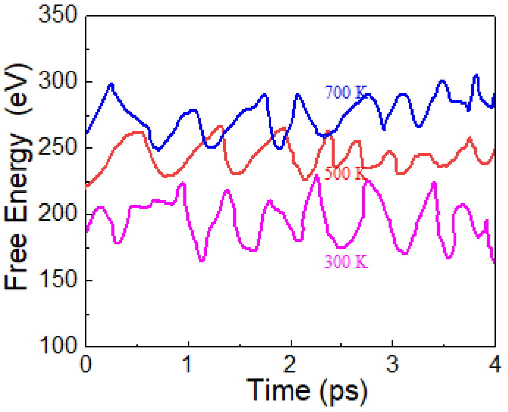

Figure 52. AIMD-calculated free energy differences of the FeCoNiMoW structure at 300, 500 and 700 K.

We further evaluated the impact of the observed partial surface oxidation of the HEA on OER and ORR using DFT calculations using a model consisting of 5% oxygen doping into the surface of FeCoNiMoW (**Figure 53**). Our results show that the presence of oxygen increases the E_{ads} of water and reduces that of oxygen on the various metal elements (**Figure 54**). Thus, partial oxidation of FeCoNiMoW enhances OER performance but degrades ORR performance. As shown in **Figure 55**, after introducing 5% oxygen doping, the d-band of Ni shifts from -1.636 to -1.582 eV for FeCoNiMoW, -1.702 to -1.686 eV for FeCoNiMo, -1.758 to -1.705 eV for FeCoNi. While the presence of oxygen on the surface of the alloy clearly alters adsorption energies and electronic properties, the overall trends observed with the pure metal surfaces, in terms of the role of each element and the comparative performance of the different alloys, remain unchanged and consistent with the experimental results.

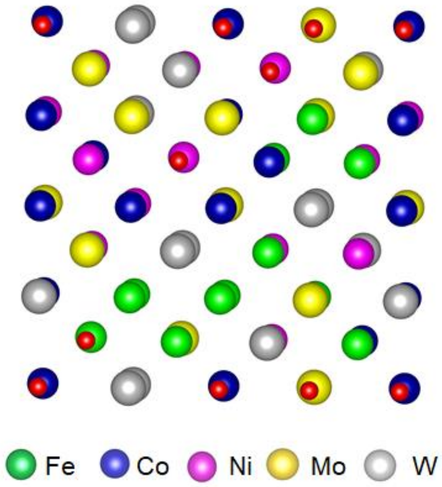

Figure 53. The top view of the 5 % FeCoNiMoWO HEA.

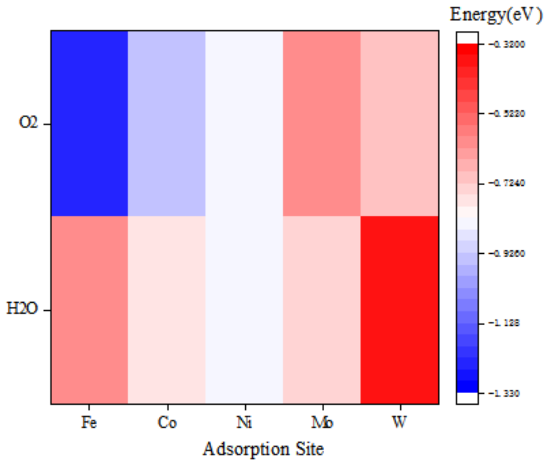

Figure 54. E_{ads} between different active sites O_2 and H_2O molecules in FeCoNiMoWO

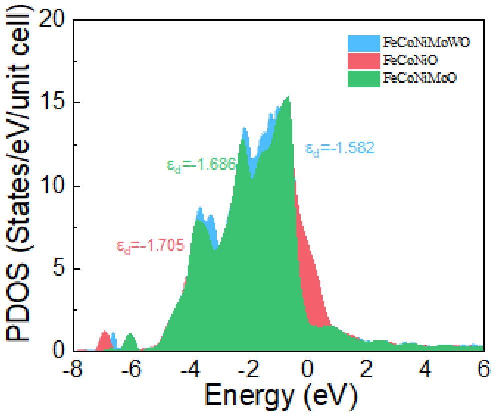

Figure 55. d_c position of Ni atoms in FeCoNiO, FeCoNiMoO, and FeCoNiMoWO.

Since catalysts restructure during the OER/ORR process, DFT calculations were further performed based on the alloy model reconstructed with OH. The reconstructed models of FeCoNiOH, FeCoNiMoOH, and FeCoNiMoWOH are shown in **Figures 56-58**. **Figures 59-60** show the detailed analysis of the E_{ads}, d_c analysis, ELF, COHP, the catalytic ability of different active sites, and the free energy step diagram for all the catalysts. Compared with the pre-catalyst metal models, all the reconstructed catalysts show improved performances and the same trends both among the different elements, with Ni as the most active site, and the different materials, with FeCoNiMoW outperforming FeCoNiMo and FeCoNi.

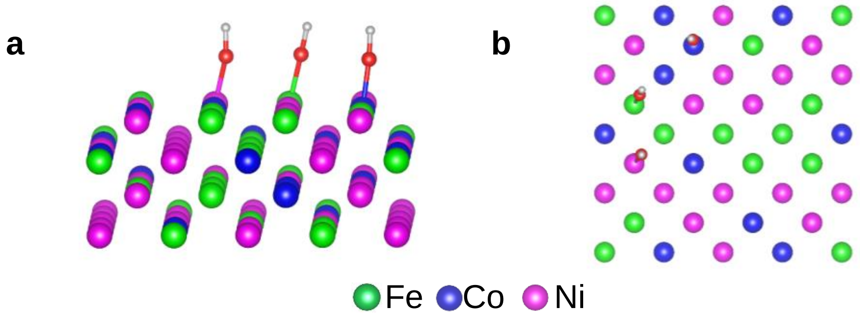

Figure 56. Schematic diagram of the optimized structure of FeCoNiOH, (a) side, and (b) top view.

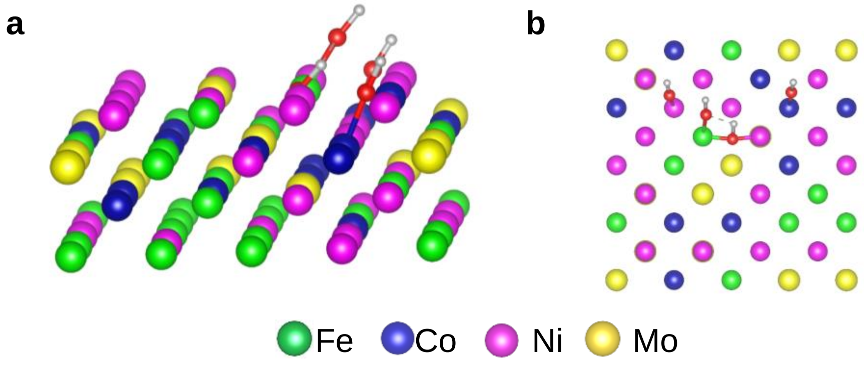

Figure 57. Schematic diagram of the optimized structure of FeCoNiMoOH, (a) side, and (b) top view.

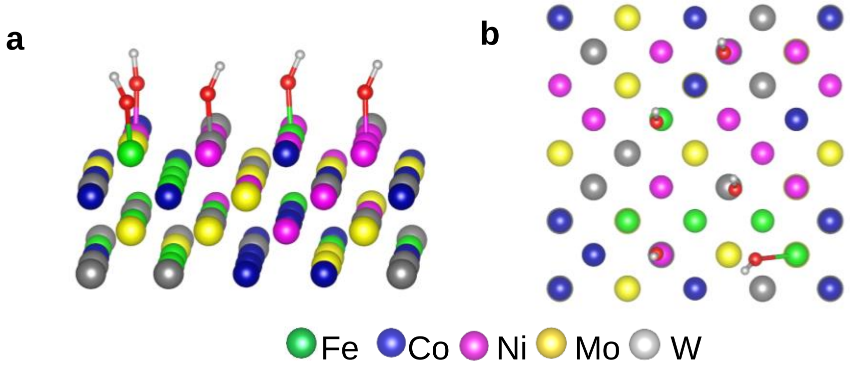

Figure 58. Schematic diagram of the optimized structure of FeCoNiMoWOH, (a) side, and (b) top view.

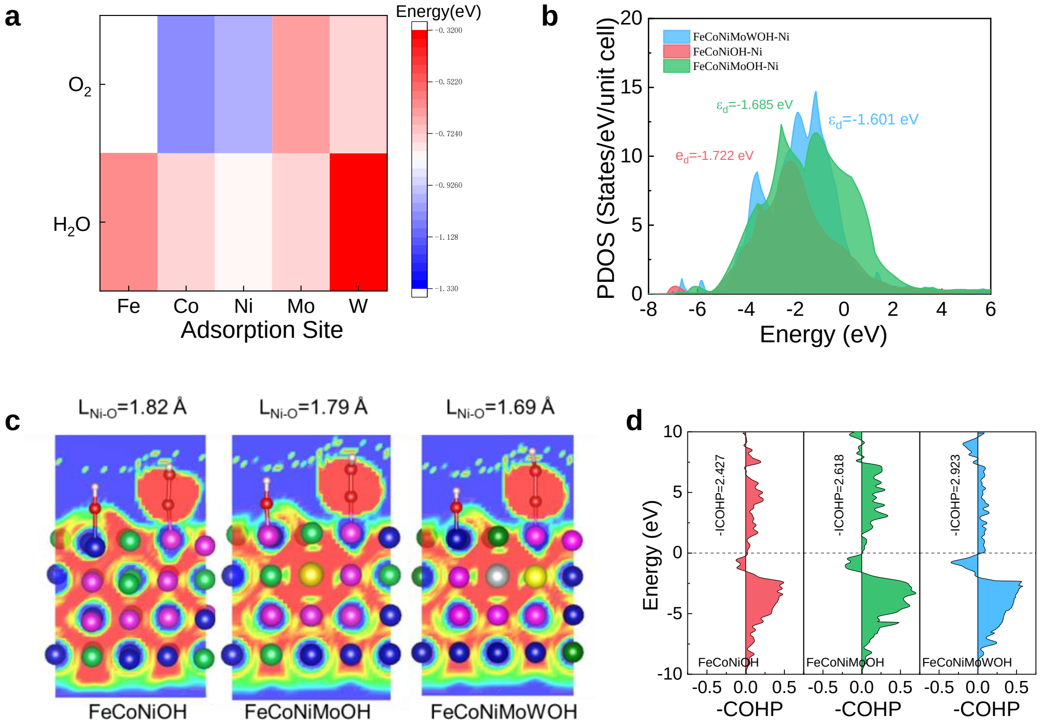

Figure 59. (a) E_{ads} between different active sites in FeCoNiMoWOH and O_2/H_2O molecules. (b) d_c position of Ni atoms in FeCoNiOH, FeCoNiMoOH, and FeCoNiMoWOH. (c) ELF calculations and (d) COHP analysis of Ni-O bond for FeCoNiOH, FeCoNiMoOH, and FeCoNiMoWOH.

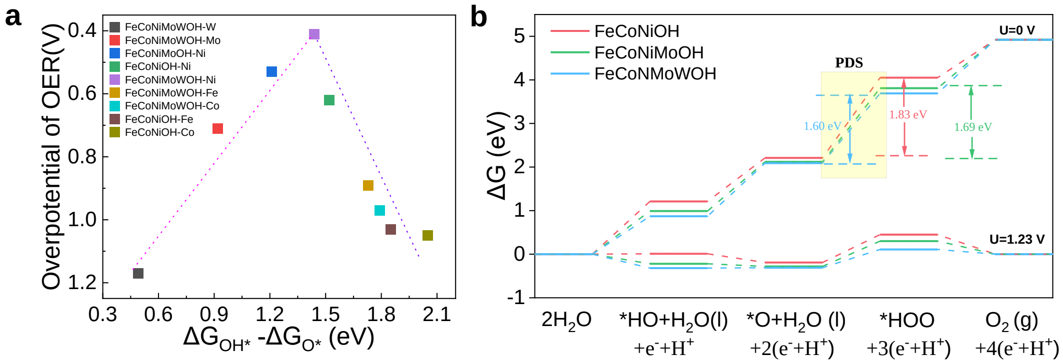

Figure 60. (a) OER catalytic activity of each atom for FeCoNiOH, FeCoNiMoOH, and FeCoNiMoWOH. (b) Free energy step diagram during the OER process of FeCoNiOH, FeCoNiMoOH, and FeCoNiMoWOH.

3.4.5 ZAB performance

FeCoNiMoW was used as the oxygen cathode in aqueous ZABs. The 20 wt.% Pt/C and

RuO_2 couple were used to produce reference ZABs. **Figure 61a** shows a schematic of the ZAB architecture, with a polished 0.5 mm-thick Zn plate as the anode, a PP/PE/PP three-layer composite film as the separator, hydrophilic CP with the catalyst as the cathode, and a KOH and zinc acetate solution as the electrolyte. The ZAB containing the FeCoNiMoW-based air cathode can light a red LED screen (**Figure 61b**) and exhibits an OCP of 1.59 V, that is, 95.8% of the theoretical limit (1.66 V),[68] significantly above that of the Pt/C and RuO_2-based ZAB (1.56 V) (**Figure 61c**).

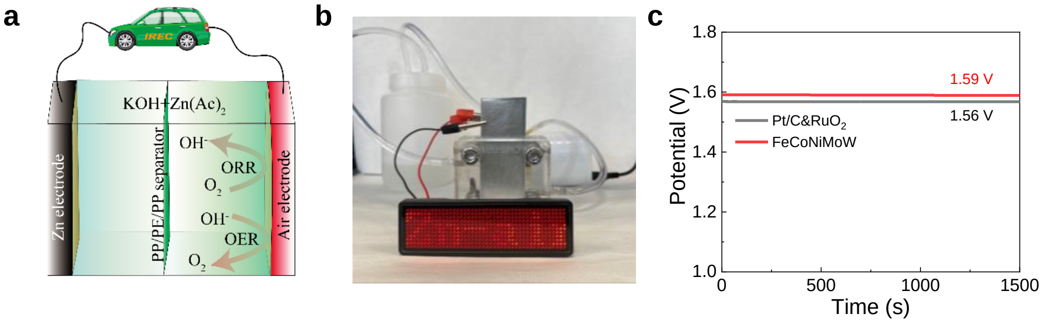

Figure 61. (a) ZAB schematic diagram. A picture of a red LED screen powered by a FeCoNiMoW-based aqueous ZAB. (b) OCP for ZABs.

The peak power density of the FeCoNiMoW-based ZAB was 116.9 mW cm^{-2}, sensible above that of the Pt/C and RuO_2-based ZAB at 112.4 mW cm^{-2} (**Figure 62a**). Besides, at a current density of 8 mA cm^{-2}, the FeCoNiMoW-based ZAB delivered a specific capacity of 857 mAh gZn^{-1}, also well above that of the Pt/C and RuO_2 ZAB (793 mAh gZn^{-1}) (**Figure 62b**). Overall, the FeCoNiMoW-based ZAB displayed an outstanding OCP and specific capacity compared not only with the reference Pt/C and RuO_2 ZAB but also with previously reported devices (**Figure 62c**, **Table 10**).

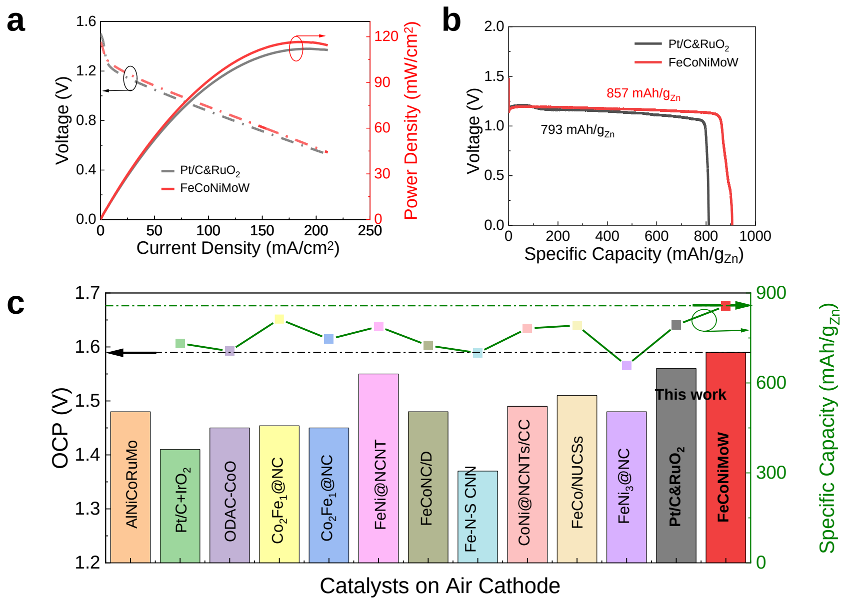

Figure 62. (a) Power density plots, and (b) specific capacity curves of a FeCoNiMoW- and a Pt/C and RuO_2-based ZAB. (c) Comparison of OCP and specific capacity of FeCoNiMoW-based ZAB with state-of-the-art ZABs.

Table 10. Comparison of the ZAB performances obtained using state-of-the-art air cathodes.

Catalyst	OCP (V)	Peak power density (mW cm^{-2})	Specific capacity (mAh g_{Zn}^{-1}) @ (mA cm^{-2})	Charge-discharge cycling durability (h)	References
AlNiCoRuMo	1.48	146.5	-	120	*ACS Mater. Lett.*, **2019**, 1, 526-533
AlFeCoNiCr	-	125	800@20	120	*Appl Catal B-environ.*, **2020**, 268, 118431
Pt/C+IrO_2	1.41	87	732@20	28	*Appl Catal B-environ.*, **2020**, 268, 118431
ODAC-CoO	1.45	81	706@20	150	*Adv. Funct. Mater.*, **2021**, 31, 2101239
Co_2Fe_1@NC	1.454	423.7	813@20	250	*J. Am. Chem. Soc.*, **2020**, 142, 7116-7127
Ni-MnO/rGO	-	123	758@5	100	*Adv. Mater.*, **2018**, 30, 1704609

Co@hNCTs	1.45	149	746@10	500	*Nano Energy*, ***2020***, 71, *104592*
AlCuNiPtMn	-	-	831@20	-	*J. Catal.*, **2020**, 383, 164-171
FeNi@NCNT	1.55	200	788@10	250	*Small*, **2021**, 17, e2006183.
FeCoNC/D	1.48	157	725@10	40	*Appl Catal B-environ.*, **2022**, 315, 121501
Fe-N-S CNN	1.37	132	700@20	-	*Appl. Catal. B- environ.*, **2019**, 250, 143-149
CoZn-NC	-	152	578@10	32	*Adv. Funct. Mater.*, **2017**, 27, 1700795
CoNi@NCNTs/CC	1.49	138	782@10	370	*Appl Catal B-environ.*, **2022**, 317, 121764
FeCo/NUCSs	1.51	152.38	791.86@10	102	*Appl Catal B-environ.*, **2022**, 316, 121687
$FeNi_3$@NC	1.48	149.7	658@10	280	*Chem. Eng. J.*, **2023**, 452, 139253
Pt/C& RuO_2	***1.56***	***112.4***	***793@8***	***100***	***This work***
FeCoNiMoW	***1.59***	***116.9***	***857@8***	***660***	***This work***

As shown in **Figure 63a**, the FeCoNiMoW-based ZAB is not only characterized by a lower charge-discharge potential, implying a higher energy efficiency, compared with the Pt/C and RuO_2-based ZAB, but also much higher durability. Unlike the Pt/C and RuO_2-based ZAB with an obvious potential gap increase of 35.6% from 0.87 to 1.18 V after just 100 h of charging/discharging cycles at 8 mA cm^{-2}, the FeCoNiMoW-based ZAB exhibits a much lower voltage variation, ≈24.4% from 0.90 to 1.12 V, even after 660 h (≈28 days) of continuous cycling, that is, after ≈2000 charge/discharge cycles at 8 mA cm^{-2}. **Figure 63b** exhibits the enlarged cycles at the specific time of 0-1, 100-102, 200-202, 300-302, 400-402, 500-502, and 650-652 h of the FeCoNiMoW-based ZAB. The charging and discharging potentials at the first cycle are 2.02 and 1.12 V, respectively, that is, the discharging-charging potential gap was 0.90 V. The potential gap increased 5.5% to 0.95 V at the 900th cycle, 11.1% to 1 V at the 1500th cycle, and 24.4% to 1.12 V at the 1950th cycle. The corresponding voltaic efficiency (discharge end voltage divided by charge end voltage) slightly decreases from the initial 55.4% to 54.1% at the 900th cycle, 52.8% at the 1500th cycle, and 49.3% at the 1950th cycle, indicating an excellent rechargeability and stability (**Figure 64a**). Furthermore, **Figure 64b** shows the charge/discharge curves at the specific cycles, first, 100th, 500th, 1000th, 1500th, and 1950th of the FeCoNiMoW-based ZAB, showing a minor evolution, further proving the outstanding long-term durability of the battery. SEM characterization of the Zn anode shows urchin shaped ZnO structures at the anode surface after long-term charging/discharging in both the Pt/C and RuO_2-based and FeCoNiMoW-based ZABs, which could explain the slight deterioration of the ZAB performance (**Figure 65**).

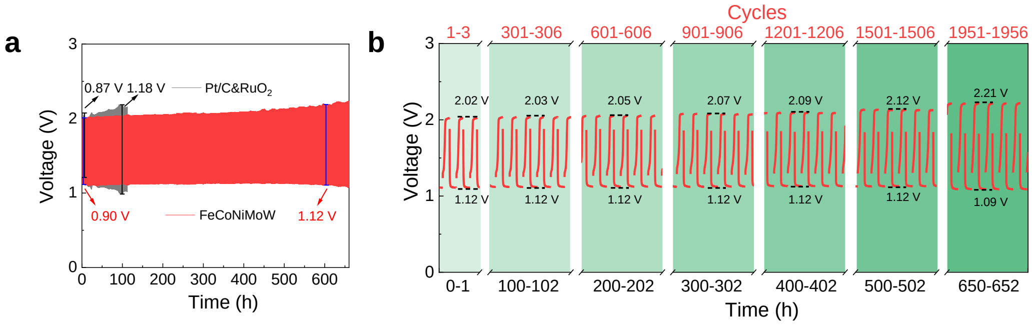

Figure 63. (a) Galvanostatic discharge-charge curves with 10 min discharge and 10 min charge cycles at a current density of 8 mA cm^{-2}. (b) Enlarged galvanostatic discharge-charge cycles at the specific cycling time of the FeCoNiMoW-based ZAB.

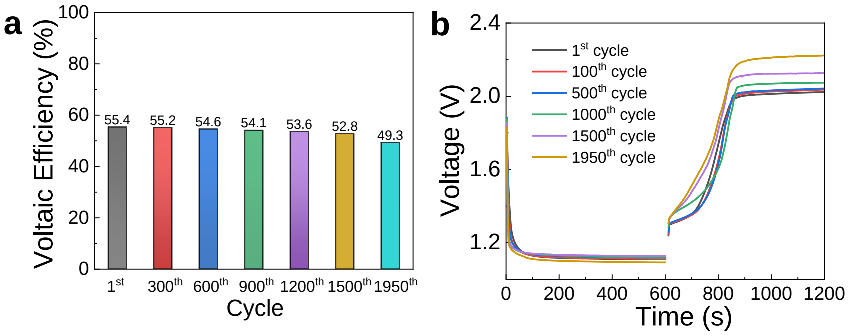

Figure 64. (a) Voltaic efficiency of FeCoNiMoW-based aqueous ZABs at different specific cycles. (b) Charge and discharge curves at different specific cycles of FeCoNiMoW-based aqueous ZABs with 10 min discharge and 10 min charge cycles at

the current density of 8 mA/cm^2.

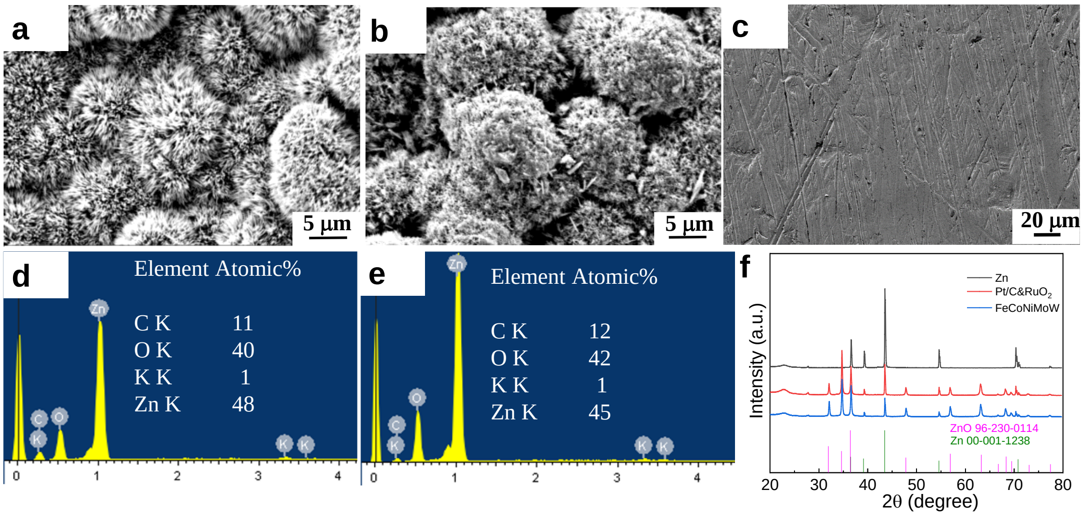

d

Element	Atomic%
C K	11
O K	40
K K	1
Zn K	48

e

Element	Atomic%
C K	12
O K	42
K K	1
Zn K	45

Figure 65. (a-b) SEM images and (d-e) EDS spectra of Zn anode after long-term cycling for (a, d) Pt/C&RuO$_2$-based and (b, e) FeCoNiMoW-based aqueous ZABs. Inset is the table of elemental composition. (c) SEM image of Zn plate. (f) XRD pattern of initial Zn plate and Zn anode after long-term cycling for Pt/C&RuO$_2$-based and FeCoNiMoW-based aqueous ZABs.

Besides capacity, flexibility and miniaturization potential are two additional battery characteristics frequently targeted in the field of energy storage. Thus, we also manufactured and tested prototypes of solid and flexible ZABs based on a gel electrolyte and the FeCoNiMoW catalyst. **Figure 66a** shows a schematic of the ZAB architecture, where a polished 0.08 mm-thick Zn foil is used as the anode, a PP/PE/PP three-layer composite film as the separator, a hydrophilic CP with the catalysts is used as the cathode, and a PVA-KOH-gel as the electrolyte. A reference ZAB was produced using the combination of Pt/C and RuO$_2$ catalysts. The solid FeCoNiMoW based ZAB displayed a higher OCP, at 1.34 V than the Pt/C and RuO$_2$-based ZAB, at 1.30 V. As shown in **Figure 66b**, two ZABs in series were able to light a green LED bulb (2.2 V). The peak power density of the solid FeCoNiMoW-based ZAB was 42.05 mW cm^{-2}, slightly above the 40.12 mW cm^{-2} obtained for the Pt/C and RuO$_2$-based ZAB (**Figure 66c**), and comparable with state-of-the-art solid ZABs (**Table 11**).

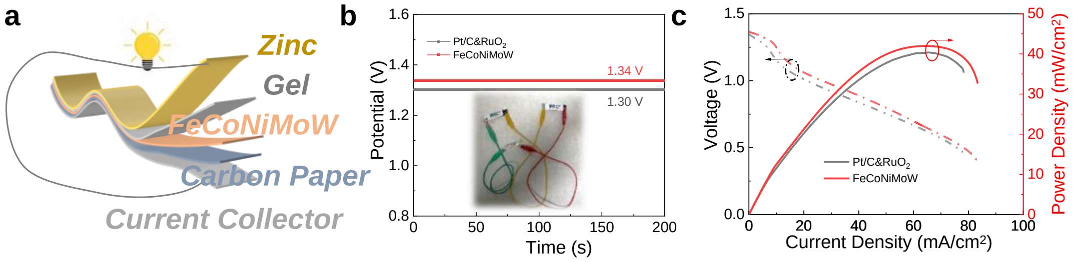

Figure 66. (a) Solid ZAB schematic diagram. (b) OCP measurements. The inset shows an optical image of a green LED bulb (2.2 V) lighted with two FeCoNiMoW-based ZABs. (c) Power density plots of a FeCoNiMoW- and a Pt/C and RuO_2-based ZAB.

Table 11. Comparison of the flexible ZAB performances obtained using state-of-the-art air cathodes.

Catalyst	OCP(V)	Peak power density (mW cm^{-2})	Cycle Time (h) @J (mA cm^{-2})	References
FeMn-DSAC	1.45	180	*80@2*	*Angew. Chem. Int. Ed.*, **2022**, 61, e202115219
AlFeCoNiCr	1.38	100	*60@2*	*Appl Catal B-environ.*, **2020**, 268, 118431
Co-N_x-C	1.439	29	*60@1*	*Adv. Mater.*, **2017**, 29, 1703185
CoFe/N-GCT	1.48	-	*16@2*	*Angew. Chem.*, **2018**, 130, 16398-16402
NC-Co_3O_4-90	1.44	82	20@1	*Adv. Mater.*, **2017**, 29, 1704117
ODAC-CoO	1.41	42	*12@2*	*Adv. Funct. Mater.*, **2021**, 31, 2101239
Co/MnO@N,S-C	1.34	62.5	*15@1*	*Appl. Catal. B- Environ.*, **2021**, 295, 120281
FeP/Fe_2O_3@ NPCA	1.42	40.8	*8.3@5*	*Adv. Mater.*, **2020**, 32, 2002292
NC-Co SA	1.41	31	*41.6@1*	*ACS Catal.*, **2018**, 8, 8961-8969
Pt/C&RuO_2	***1.30***	***40.12***	***9@5***	***This Work***
FeCoNiMoW	***1.34***	***42.05***	***30@5***	***This Work***

The charge-discharge curves at different current densities and the corresponding voltaic efficiency in each cycle of the FeCoNiMoW-based ZAB are displayed in **Figure 67**. The average voltaic efficiency at 2, 4, 6, and 8 mA cm^{-2} is 80.67%, 71.63%, 64.61%, and 58.86%, respectively, demonstrating a notable rate performance. On the other hand, the average voltaic efficiency at 2 mA cm^{-2} increases to 86.43% after undergoing several charging and discharging processes at different current densities, from 2 to 8 mA cm^{-2}. Galvanostatic discharge-charge measurements for 5 h at bending angles of 0, 30°, 50°, and 70° are shown in **Figure 68**. Notably, the battery maintains constant charging (1.88 V) and discharging (0.86 V) platforms at 5mA cm^{-2} during and after bending, suggesting that the technology has potential in flexible electronics and wearable markets. Finally, **Figure 68** also shows that the FeCoNiMoW-based ZAB could maintain a good cycling performance even after 30 h of operation. In contrast, the Pt/C and RuO_2-based ZAB failed after ≈9 h (**Figure 69**).

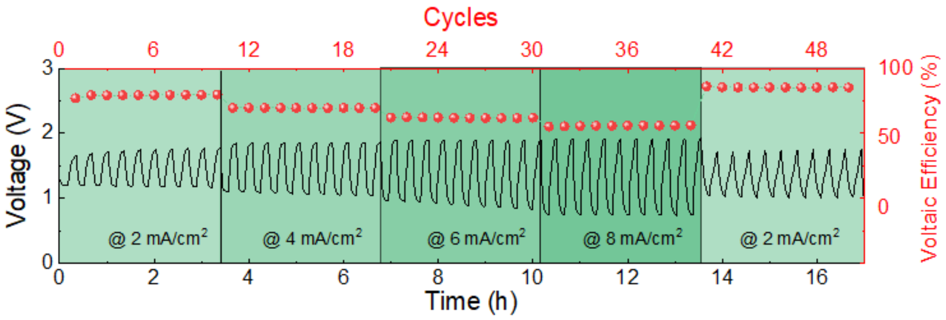

Figure 67. discharge-charge curves of a FeCoNiMoW-based ZAB with 10 min discharge and 10 min charge cycles at a current density of 2, 4, 6, and 8 mA cm^{-2}.

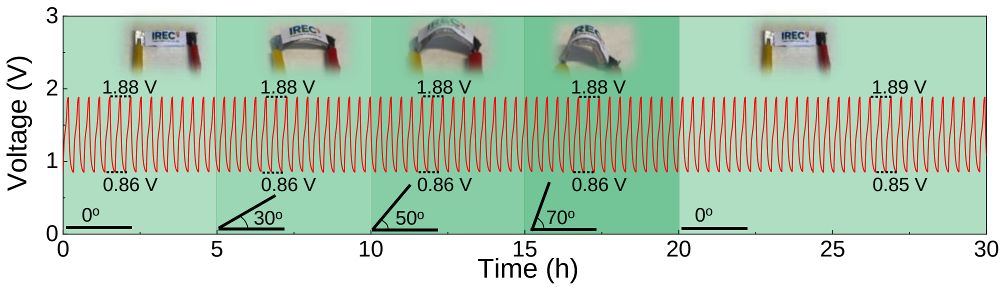

Figure 68. Galvanostatic discharge-charge curves with 10 min discharge and 10 min charge cycles at a current density of 5 mA cm^{-2} of the FeCoNiMoW-based ZAB with

different bending angles.

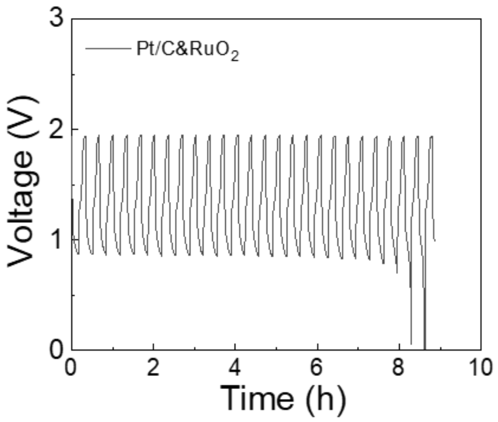

Figure 69. Galvanostatic discharge-charge curves of a Pt/C&RuO_2-based flexible ZAB with 10 min discharge and 10 min charge cycles at a current density of 5 mA cm^{-2}.

3.5 Conclusions

A solution-based synthetic procedure to produce a FeCoNiMoW HEA at a low reaction temperature was detailed. With the introduction of 4d Mo and 5d W into 3d FeCoNi, FeCoNiMoW was characterized by an extensively distorted lattice, and synergistic electronic coupling effects, which resulted in an outstanding OER catalytic performance with a low η of 233 mV at 10 mA cm^{-2} and 276 mV at 100 mA cm^{-2}. Besides, FeCoNiMoW was demonstrated to be an efficient bifunctional oxygen catalyst with a low E_{gap} value of 0.75 V, even a little better than commercial noble catalysts of Pt/C and RuO_2 (0.76 V). DFT calculations showed the Ni atoms in FeCoNiMoW as the active sites to react with the oxygen intermediates. FeCoNiMoW had the highest d_c energy and shortest Ni-O bond, proving its strongest interaction ability with oxygen intermediates. Much more d orbital of Ni atoms in FeCoNiMoW is hybridized with 2p orbital of O atoms in H_2O in the bonding states due to 3d metal FeCoNi combined with 4d Mo atom and 5d W atom, which is the reason for the highest active ability of FeCoNiMoW compared with FeCoNi and FeCoNiMo. Overall, combining experimental results and DFT calculations, Fe, Co, and especially Ni are shown to be the OER and ORR active sites, while Mo and W play a role in adjusting the electronic structure of the alloy and its individual elements. The 3d-4d-5d FeCoNiMoW-based ZAB showed an OCP of 1.59 V, 95.8% of its theoretical limit, a peak power density of 116.90 $mWcm^{-2}$, and a specific capacity of 857 mAh g Zn^{-1} at a current density of 8 mA cm^{-2}, which displayed excellent stability for more than 660 h of continuous charge/discharge cycling. Furthermore, the 3d-4d-5d FeCoNiMoW also had outstanding catalytic performance in flexible ZABs, which could retain good performance at different bending angles, thus having the potential to be integrated into wearable devices as electrical power. This work has significance for 4d/5d high-valence metal modulated electronic structure and optimized the adsorption ability of the oxygen intermediates.

3.6 References

[1] X. Zhu, C. Hu, R. Amal, L. Dai, X. Lu, *Energy Environ. Sci.,* **2020**, 13, 4536.

[2] M. Yang, X. Shu, W. Pan, J. Zhang, *Small*, **2021**, 17, e2006773.

[3] Q. Liu, L. Wang, H. Fu, *J. Mater. Chem. A*, **2023**, 11, 4400.

[4] G. Yasin, S. Ali, S. Ibraheem, A. Kumar, M. Tabish, M. A. Mushtaq, S. Ajmal, M. Arif, M. A. Khan, A. Saad, L. Qiao, W. Zhao, *ACS Catal.*, **2023**, 13, 2313.

[5] X. Zhao, J. Chen, Z. Bi, S. Chen, L. Feng, X. Zhou, H. Zhang, Y. Zhou, T. Wagberg, G. Hu, *Adv. Sci.*, **2023**, 10, e2205889.

[6] D. Böhm, M. Beetz, M. Schuster, K. Peters, A. G. Hufnagel, M. Döblinger, B. Böller, T. Bein, D. Fattakhova-Rohlfing, *Adv. Funct. Mater.* **2019**, 30, 1906670.

[7] L. Zhang, H. Jang, H. Liu, M. G. Kim, D. Yang, S. Liu, X. Liu, J. Cho, *Angew. Chem. Int. Ed.*, **2021**, 60, 18821.

[8] M. Liu, Z. Zhao, X. Duan, Y. Huang, *Adv. Mater.*, **2019**, 31, e1802234.

[9] K. Kim, K. Min, Y. Go, Y. Lee, S. E. Shim, D. Lim, S.-H. Baeck, *Appl Catal. B-environ.*, **2022**, 315, 121501.

[10] Z. Wang, J. Ang, J. Liu, X. Y. D. Ma, J. Kong, Y. Zhang, T. Yan, X. Lu, *Appl Catal. B-environ.*, **2020**, 263, 118344.

[11] W.-W. Tian, J.-T. Ren, Z.-Y. Yuan, *Appl Catal. B-environ.*, **2022**, 317, 121764.

[12] Z. Li, M. Chen, L. Zhang, R. Xing, J. Hu, X. Huang, C. Zhou, Y. Zhou, T. Wågberg, G. Hu, *J. Mater. Chem. A*, **2023**, 11, 2155.

[13] X. Wang, X. Han, R. Du, C. Xing, X. Qi, Z. Liang, P. Guardia, J. Arbiol, A. Cabot, J. Li, *ACS Appl. Mater. Inter.*, **2022**, 14, 41924.

[14] R. Du, K. Xiao, B. Li, X. Han, C. Zhang, X. Wang, Y. Zuo, P. Guardia, J. Li, J. Chen, J. Arbiol, A. Cabot, *Chem. Eng. J.*, **2022**, 441, 135999.

[15] X. Wang, J. Li, Q. Xue, X. Han, C. Xing, Z. Liang, P. Guardia, Y. Zuo, R. Du, L. Balcells, J. Arbiol, J. Llorca, X. Qi, A. Cabot, *ACS Nano*, **2023**, 17, 825.

[16] X. Wang, X. Han, R. Du, Z. Liang, Y. Zuo, P. Guardia, J. Li, J. Llorca, J. Arbiol, R. Zheng, A. Cabot, *Appl Catal B-environ.*, **2023**, 320, 121988.

[17] Y. Mei, Y. Feng, C. Zhang, Y. Zhang, Q. Qi, J. Hu, *ACS Catal.*, **2022**, 12, 10808.

[18] B. J. Kim, J. Yu, H. Koh, I. Nagai, S. I. Ikeda, S. J. Oh, C. Kim, *Phys. Rev. Lett.*, **2006**, 97, 106401.

[19] J. Zhang, K. Wang, L. Fan, H. Liu, H. Zhu, S. Yan, *J. Alloys Compd.*, **2023**, 933, 167613.

[20] G. Ke, F. Duan, B. Liu, X. Liu, J. Wen, B. Jia, X. Liu, H. He, Y. Zhou, *J. Alloys Compd.*, **2023**, 934, 167883.

[21] H. Li, C. Zhang, W. Xiang, M. A. Amin, J. Na, S. Wang, J. Yu, Y. Yamauchi, *Chem. Eng. J.* **2023**, 452, 139104.

[22] J. Lu, L. Luo, S. Yin, S. W. Hasan, P. Tsiakaras, *ACS Sustain. Chem. Eng.*, **2019**, 7, 16209.

[23] Y. T. Xu, Z. M. Ye, J. W. Ye, L. M. Cao, R. K. Huang, J. X. Wu, D. D. Zhou, X. F. Zhang, C. T. He, J. P. Zhang, X. M. Chen, *Angew. Chem. Int. Ed.*, **2019**, 58, 139.

[24] M. Yuan, J. Chen, Y. Bai, Z. Liu, J. Zhang, T. Zhao, Q. Shi, S. Li, X. Wang, G. Zhang, *Chem. Sci.*, **2021**, 12, 6048.

[25] X. Huang, G. Yang, S. Li, H. Wang, Y. Cao, F. Peng, H. Yu, *J. Energy Chem.*, **2022**, 68, 721.

[26] G. Yan, H. Tan, Y. Wang, Y. Li, *Appl. Surf. Sci.*, **2019**, 489, 519.

[27] H. Wu, Z. Li, Z. Wang, Y. Ma, S. Huang, F. Ding, F. Li, Q. Zhai, Y. Ren, X. Zheng, Y. Yang, S. Tang, Y. Deng, X. Meng, *Appl Catal B-environ.*, **2023**, 325, 122356.

[28] D. Feng, Y. Dong, P. Nie, L. Zhang, Z.-A. Qiao, *Chem. Eng. J.*, **2022**, 430, 132883.

[29] A. Ostovari Moghaddam, A. Cabot, E. A. Trofimov, *Int. J. Refract. Hard. Met.*, **2021**, 97.

[30] Z. Jin, J. Lyu, K. Hu, Z. Chen, G. Xie, X. Liu, X. Lin, H. J. Qiu, *Small*, **2022**, 18, e2107207;

[31] T. Yu, Y. Zhang, Y. Hu, K. Hu, X. Lin, G. Xie, X. Liu, K. M. Reddy, Y. Ito, H.-J. Qiu, *ACS Mater. Lett.*, **2021**, 4, 181.

[32] Z. Jin, X. Zhou, Y. Hu, X. Tang, K. Hu, K. M. Reddy, X. Lin, H. J. Qiu, *Chem. Sci.*, **2022**, 13, 12056.

[33] R. He, L. Yang, Y. Zhang, X. Wang, S. Lee, T. Zhang, L. Li, Z. Liang, J. Chen, J. Li, A. Ostovari Moghaddam, J. Llorca, M. Ibáñez, J. Arbiol, Y. Xu, A. Cabot, *Energy Stor. Mater.*, **2023**, 58, 287.

[34] Q. Ding, Y. Zhang, X. Chen, X. Fu, D. Chen, S. Chen, L. Gu, F. Wei, H. Bei, Y. Gao, M. Wen, J. Li, Z. Zhang, T. Zhu, R. O. Ritchie, Q. Yu, *Nature*, **2019**, 574, 223.

[35] H. Li, J. Lai, Z. Li, L. Wang, *Adv. Funct. Mater.*, **2021**, 31, 2106715.

[36] W. J. Liu, Z. Xu, D. Zhao, X. Q. Pan, H. C. Li, X. Hu, Z. Y. Fan, W. K. Wang, G. H. Zhao, S. Jin, G. W. Huber, H. Q. Yu, *Nat. Commun.*, **2020**, 11, 265.

[37] W. Ling, H. Wang, Z. Chen, Z. Ji, J. Wang, J. Wei, Y. Huang, *Adv. Funct. Mater.*, **2020**, 31, 2006855.

[38] K. Zhang, G. Zhang, J. Qu, H. Liu, *Small*, **2020**, 16, e1907001.

[39] M. A. Ahsan, A. R. Puente Santiago, Y. Hong, N. Zhang, M. Cano, E. Rodriguez-Castellon, L. Echegoyen, S. T. Sreenivasan, J. C. Noveron, *J. Am. Chem. Soc.*, **2020**, 142, 14688.

[40] Z. Xia, S. Guo, *Chem. Soc. Rev.*, **2019**, 48, 3265.

[41] H. Zhou, F. Yu, Y. Liu, J. Sun, Z. Zhu, R. He, J. Bao, W. A. Goddard, S. Chen, Z. Ren, *Energy Environ. Sci.*, **2017**, 10, 1487.

[42] M. W. Glasscott, A. D. Pendergast, S. Goines, A. R. Bishop, A. T. Hoang, C. Renault, J. E. Dick, *Nat. Commun.*, **2019**, 10, 2650.

[43] D. Zhang, H. Zhao, X. Wu, Y. Deng, Z. Wang, Y. Han, H. Li, Y. Shi, X. Chen, S. Li, J. Lai, B. Huang, L. Wang, *Adv. Funct. Mater.*, **2020**, 31, 2006939.

[44] Z. Chen, J. Wen, C. Wang, X. Kang, Small 2022, 18, e2204255; d)P. Zhang, X. Hui, Y. Nie, R. Wang, C. Wang, Z. Zhang, L. Yin, *Small*, **2023**, 19, e2206742.

[45] G. Kresse, *Phys. Rev. B*, **1996**, 54, 11169.

[46] L. Han, F. Jing, J. Zhang, X.-Z. Luo, Y.-L. Zhong, K. Wang, S.-H. Zang, D.-H. Teng, Y. Liu, J. Chen, C. Yang and Y.-T. Zhou, *Appl Catal. B-environ*, **2021**, 282, 119602.

[47] X. Zhao, J. Chen, Z. Bi, S. Chen, L. Feng, X. Zhou, H. Zhang, Y. Zhou, T. Wagberg and G. Hu, *Adv. Sci.*, **2023**, e2205889.

[48] P. P. González-Borrero, F. Sato, A. N. Medina, M. L. Baesso, A. C. Bento, G. Baldissera, C. Persson, G. A. Niklasson, C. G. Granqvist and A. Ferreira da Silva, *Appl. Phys. Lett.*, **2010**, 96, 061909.

[49] S. Guo, C. T. Liu, *Prog. Nat. Sci.*, **2011**, 21, 433.

[50] A. Ostovari Moghaddam, R. Fereidonnejad, A. Cabot, *J. Alloy Compd.*, **2023**, 960, 170802.

[51] Z. P. Lu, H. Wang, M. W. Chen, I. Baker, J. W. Yeh, C. T. Liu, T. G. Nieh, *Intermetallics*, **2015**, 66, 67.

[52] Z. Wang, W. Qiu, Y. Yang, C. T. Liu, *Intermetallics*, **2015**, 64, 63.

[53] J. Chastain, RC King Jr. Handbook of X-ray photoelectron spectroscopy, *Perkin-Elmer Corporation*, **1992**, 40, 221.

[54] R. Nafria, A. Genc, M. Ibanez, J. Arbiol, P. R. de la Piscina, N. Homs, A. Cabot, *Langmuir*, **2016**, 32, 2267.

[55] S. Anantharaj, S. Noda, M. Driess, P. W. Menezes, *ACS Energy Lett.*, **2021**, 6, 1607.

[56] N. Boucherit, A. Hugot-Le Goff, S. Joiret, *Corros. Sci.*, **1991**, 32, 497-507.

[57] D. S. Hall, D. J. Lockwood, C. Bock, B. R. MacDougall, *Proc. Math. Phys. Eng. Sci.*, **2015**, 471, 20140792.

[58] D. Shi, L. Zhang, N. Zhang, Y. W. Zhang, Z. G. Yu, H. Gong, *Nanoscale*, **2018**, 10, 10554.

[59] Y. Zhang, H. Guo, P. Yuan, K. Pang, B. Cao, X. Wu, L. Zheng, R. Song, *J. Power Sources*, **2019**, 442, 227252.

[60] V. Ciobotă, W. Salama, N. Tarcea, P. Rösch, M. E. Aref, R. Gaupp, J. Popp, *J. Raman Spectrosc.*, **2012**, 43, 405.

[61] B. S. Yeo, A. T. Bell, *J. Phys.Chem. C*, **2012**, 116, 8394.

[62] X. Yin, H. Li, L. Han, J. Meng, J. Lu, Q. Song, *Small*, **2021**, 17, e2008056.

[63] Y. Sang, G. Ding, Z. Guo, Y. Xue, G. Li, R. Zhang, *J. Alloys Compd.*, **2022**, 919, 165855.

[64] D. Zhou, S. Wang, Y. Jia, X. Xiong, H. Yang, S. Liu, J. Tang, J. Zhang, D. Liu, L. Zheng, Y. Kuang, X. Sun, B. Liu, *Angew. Chem. Int. Ed.*, **2019**, 58, 736.

[65] E. Santos, W. Schmickler, *Chemphyschem*, **2006**, 7, 2282.

[66] M. Ha, A. Hajibabaei, D. Y. Kim, A. N. Singh, J. Yun, C. W. Myung, K. S. Kim, *Adv. Energy Mater.*, **2022**, 12, 2201497.

[67] N. Wang, H. Gong, Z. Sun, C. Shen, B. Li, H. Xiao, X. Zu, D. Tang, Z. Yin, X. Wu, H. Zhang, L. Qiao, *ACS App. Energy Mater.*, **2021**, 4, 12163.

[68] J. Fu, Z. P. Cano, M. G. Park, A. Yu, M. Fowler, Z. Chen, *Adv. Mater.*, **2017**, 2, 1604685.

Chapter 4

Active Site Switching on HEPs as Bifunctional Oxygen Electrocatalysts for Rechargeable/Robust ZAB

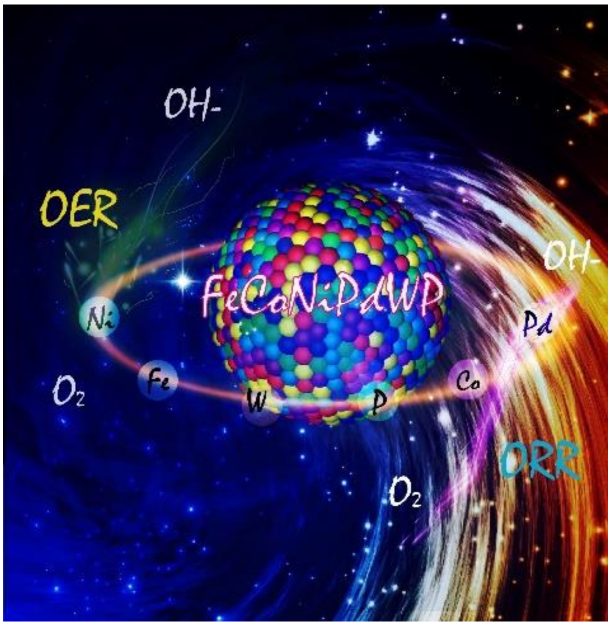

4.1 Abstract

HEMs offer a quasi-continuous spectrum of active sites and have generated great expectations in fields such as electrocatalysis and energy storage. Despite their potential, the complex composition and associated surface phenomena of HEMs pose challenges to their rational design and development. In this context, we have synthesized FeCoNiPdWP HEPs NPs using a low-temperature colloidal method, and explored their application as bifunctional electrocatalysts for OER/ORR. Our analysis provides a detailed understanding of the individual roles and transformations of each element during OER/ORR operation. Notably, the HEPs exhibit an exceptionally low OER η of 227 mV at 10 mA cm^{-2}, attributed to the reconstructed HEP surface into a FeCoNiPdW high entropy oxyhydroxide with high oxidation states of Fe, Co, and Ni serving as the active sites. Additionally, Pd and W play crucial roles in modulating the electronic structure to optimize the E_{ads} of oxygen intermediates. For the ORR, Pd emerges as the most active component. In the reconstructed catalyst, the strong d–d orbital coupling of especially Pd, Co, and W fine-tunes ORR electron transfer pathways, delivering an ORR $E_{1/2}$ of 0.81 V with a pure four-electron reduction mechanism. The practicality of these HEPs catalysts is showcased through the assembly of aqueous ZABs. These

batteries demonstrate a superior specific capacity of 886 mA h gZn^{-1} and maintain excellent stability over more than 700 h of continuous operation. Overall, this study not only elucidates the role of each element in HEMs but also establishes a foundational framework for the design and development of next-generation bifunctional oxygen catalysts, broadening the potential applications of these complex materials in advanced energy systems.

4.2 Introduction

Rechargeable aqueous ZABs are recognized for their exceptional energy densities, inherent safety, sustainability, and potential for cost-effectiveness across various applications, including electric vehicles and large-scale stationary energy storage systems.[1] However, the performance of ZABs strongly relies on the activity, stability, and cost of the oxygen catalyst used at the cathode side to boost the OER/ORR during battery charging and discharging, respectively.[2-4]

For decades, significant efforts have been directed toward developing high-performance bifunctional oxygen electrocatalysts. Traditionally, a physical mixture of noble metal catalysts, e.g. Pt/C for ORR and Ir/C for OER, has been used to accelerate the kinetics of the two reactions. Despite their relative effectiveness, the high cost, the scarcity of these noble metals, and the need to double the catalyst amount—since each material facilitates only one type of reaction—pose substantial barriers to the commercial viability of ZABs.[5-8] To address this limitation, alternative bifunctional oxygen catalysts based on layered double hydroxides,[9] perovskites,[10] metallic alloys,[11] sulfides,[12] nitrides,[13] phosphides,[14] and their composites[15-17] are intensively investigated.

Electrocatalysts based on HEMs have emerged as particularly promising due to their vast compositional versatility and the ability to finely tune their surface properties to optimize performance. Their complex composition and a huge amount of different potential surface configurations also result in quasi-continuous surface energy levels able to suit the adsorption of reactants, intermediates, and products, facilitating enhanced catalytic activities across various reactions. [18-23] The diverse range of surface sites provided by HEMs makes them ideal for catalyzing complex reactions and especially valuable as bifunctional catalysts. Despite these advantages, achieving a single HEM that excels in both OER and ORR remains a formidable challenge, primarily due to the divergent pathways and distinct intermediate adsorption energies required by these reactions.[24-25]

The vast range of potential HEM compositions makes trial-and-error processes hopeless to optimize them as dual-functional catalysts. Thus, to avoid a futile odyssey across the boundless expanse of HEMs, an educated selection of the HEMs characteristics leading to optimized catalytic performance is fundamental. This rational design must be supported by reliable structure-activity relationships and precise information on the distinct roles of each element in the OER and ORR mechanisms. However, gathering this information is especially difficult for HEMs having hundreds of thousands of possible atomic configurations. Besides, further complications arise with inevitable surface reconstructions caused by the strongly alkaline reaction conditions used.[26,27] Therefore, it is essential to delve into the catalyst reconstruction and explore the unique contributions of each metal involved. This approach is crucial for a holistic comprehension of the intricate dynamics at play within HEMs during catalysis.

Herein, FeCoNiPdWP HEP NPs are synthesized using a mild colloidal method. Subsequently, their OER and ORR performance is compared with a series of control phosphides and commercial reference catalysts. To gain deeper insights into the oxygen redox reaction mechanisms, the distinct roles played by each metal in HEPs are analyzed using electrochemical measurements, XAS, and DFT calculations. Furthermore, the HEP surface reconstruction and the real active species are explored and identified. Last, rechargeable ZABs based on FeCoNiPdWP HEPs bifunctional oxygen catalysts as the air cathodes are assembled and tested.

4.3 Experimental section

4.3.1 Materials and reagents

Hexadecylamine (HDA, 90%, technical grade), triphenylphosphite (TPP, 97%), iron pentacarbonyl ($Fe(CO)_5$, ≥99.99% trace metals basis), cobalt carbonyl ($Co_2(CO)_8$, ≥90% (Co)), tungsten hexacarbonyl ($W(CO)_6$, 97%), palladium(II) acetylacetonate ($Pd(acac)_2$, 96%), ammonium chloride (NH_4Cl, ≥99.5%), ammonium thiocyanate (NH_4SCN, ≥99%) OAm, >70%, and Nafion solution (Sigma， 5 wt%) were bought from Sigma-Aldrich. Methanol (99%), 1-octadecene (ODE, 90%), nickel(II) acetylacetonate

(Ni(acac)$_2$, 96%), potassium hydroxide (KOH, 85%), and cyclohexane (99%) were supplied by Alfa Aesar. DI water (≥18.2 MΩ/cm) was purified by an ultra-pure purification system (Aqua Solutions).

4.3.2 Synthesis of catalysts

Preparation of FeCoNiPdWP, FeCoNiPdP FeCoNiWP, FeCoPdWP, FeNiPdWP, and CoNiPdWP NPs: All synthesis processes were conducted using a standard vacuum/argon Schlenk line. In a typical preparation of FeCoNiPdWP NPs, 2.4 g of HDA as a surfactant was combined with 10.0 mL of ODE and 2.6 mL of TPP in a 100 mL three-neck flask. The system was degassed and heated to 150 °C, maintained at this temperature for 1 h to remove low-boiling-point impurities, moisture, and oxygen. Subsequently, 102.8 mg (0.4 mmol) of Ni(acac)$_2$, 0.2 mmol of Co$_2$(CO)$_8$, 98 mg (0.5 mmol) of Fe(CO)$_5$, 140.8 mg (0.4 mmol) of W(CO)$_6$, 122 mg (0.4 mmol) of Pd(acac)$_2$, and 65 mg (1.2 mmol) of NH$_4$Cl were dissolved in 8 mL of ODE and 8 mL of OAm to create a homogeneous solution through ultrasonication for 1 h, followed by degassing with argon for another hour. Afterward, the degassed homogeneous solution was transferred into a three-neck flask. It was first vacuumed for 20 min at 70 ºC and then the temperature was increased to 290 ºC in 15 min under an argon atmosphere while being stirred magnetically. The mixture was allowed to react at 290 ºC for 1 h. Subsequently, the mixture was cooled down to 220 °C by removing the heating mantle and then rapidly cooled to room temperature with a water bath. The black product was isolated by precipitation with acetone. To remove as many organic compounds as possible, three cycles of redispersion and precipitation were carried out using chloroform and ethanol. To further eliminate the organic ligands, the crude FeCoNiPdWP NPs dispersion in 20 mL of hexane. Then, 5 mL of NH$_4$SCN solution in methanol (50 mmol/L) was added to form a two-phase mixture, which was agitated for 5 min until the NPs completely mixed with the ammonium thiocyanide solution. The surface-modified NPs were washed with ethanol three times and dried in a vacuum oven for 12 h at 60 °C.

4.3.3 Material characterization

SEM images and EDS spectra were obtained in a Zeiss Auriga field emission scanning electron microscope. TEM micrographs were obtained in a Tecnai F20 field emission gun microscope with a 0.19 nm point-to-point resolution at 200 kV. Images were analyzed using Gatan Digital Micrograph software. HAADF-STEM images and elemental mapping were measured in a spherical aberration-corrected transmission electron microscope FEI Titan G2 80-200 ChemiSTEM with four EDS detectors were operated at 80 and 200 keV. The spherical aberration corrected HRTEM (AC-HRTEM) image was obtained by spherical aberration corrected transmission electron microscope: ACTEM (EM-ARM200F, Japan). The crystal structure was characterized by powder XRD measurement in a Bruker AXS D8 Advance X-ray diffractometer. (Cu-Kα radiation, λ =1.5418 Å, 40 kV and 40 mA; Bruker, Germany). ICP-OES was conducted on an ICPE-9820 system. XPS was performed with an Al anode XR50 source on a Specs system equipped with a Phoibos 150 MCD-9 detector (150 W).

In situ Raman spectra were collected by a Raman microscope (iHR320 monochromator, HORIBA) using an *in situ* Raman cell. The excitation source was a frequency-doubled Nd: YAG laser, 532 nm laser, and the spectra were collected using a grating of 1800 lines/ mm. The electrode was first subjected to CA measurements at a set applied voltage (1.0-1.6 V vs. RHE) for 5 min, then we started acquiring Raman spectra while keeping the CA measurements running. The Raman spectra were obtained with an acquisition time of 20 s and accumulation of 8 times from the range of 200-900 cm^{-1}.

The (quasi *in situ*) X-ray absorption near edge structure (XANES) and extended X-ray absorption fine structure (EXAFS) spectra were collected at the BESSY II synchrotron radiation source of the Helmholtz-Zentrum Berlin. The experiments were performed at the KMC-3 bending-magnet beamline at 20 K in a closed-cycle helium cryostat (Oxford). A Si(111) double-crystal monochromator was utilized to select the incident beam energy. Iron, cobalt, and nickel K-edge XAS spectra were collected in fluorescence mode using a 13-element energy-resolving silicon-drift detector (RaySpec). The K-edge energy was determined using the integral method.[28,29] The obtained spectra were weighted by k^3 and simulated in k-space (E_0(Fe) = 7112 eV, E_0(Co) = 7709 eV, E_0(Ni) = 8333 eV). EXAFS simulations were performed with in-house software after calculating the phase functions with the FEFF program (version 8.4).[30,31] The EXAFS simulations were optimized by minimization of the error sum acquired by summation of the squared deviations between experimental Fourier backtransforms in a 1-3.5 Å range of reduced distances and simulated spectra (least-squares fit using the Levenberg-Marquardt algorithm). Further details are given elsewhere.[32,33] Binder-free films (1×1 cm^2, 0.1 mg cm^{-2} loading) for XAS experiments were prepared on fluorine-doped tin oxide glass substrates using electrophoretic deposition. Electrophoretic deposition was performed in a two-electrode setup (both fluorine-doped tin oxide glass) at 10 V for 1 min. The electrolyte was 8 mL acetone solution with 2 mg iodine and 30 mg sample that was sonicated before for 2 h together. Through keto-enol tautomerisation and subsequent reaction, the acetone and iodine form protons that create a surface charge on the HEP NPs. These charge particles move and deposit on the cathode during the electrophoretic deposition. This procedure has previously been described in more detail.[34-36]

4.3.4 Electrochemical measurements

All the electrochemical measurements were carried out on a Chi760E electrochemical workstation (Shanghai Chenhua, China) at room temperature using a standard three-electrode setup system with a platinum grid as the counter electrode, a Hg/HgO electrode as the reference electrode, and a GC as the working electrode. The catalytic ink was prepared with 4 mg of catalyst, 2 mg carbon black, and 30 µL of 5 wt% Nafion solution dispersion in 750 µL isopropanol and 220 µL DI water with a continuous sonication until a homogeneous solution. Then, 10 µL catalyst ink was uniformly loaded on the surface of the polished GCE, and dried at room temperature. All measured potentials ($E_{Hg/Hgo}$) were converted to the RHE potential through the Nernst equation ($E_{RHE} = E_{Hg/Hgo} + 0.0591 \times pH + 0.098$), in which the PH value obtained by a PH meter (pH & Ion-metro GLP 22-Crison Instruments) is 13.85 for 1.0 M KOH electrolyte and 12.96 for 0.1 M KOH electrolyte. These values are close to the theoretically expected ones.[37]

The OER measurements were conducted in a 1.0 M KOH electrolyte. LSV measurements were conducted at a scan rate of 5 mV s^{-1}, and then the Tafel slopes were calculated from the LSV curves. EIS measurements were recorded at 1.5 V vs. RHE with frequencies from 0.01 to 10^5 Hz. The C_{dl} value was measured from CV curves at different scan rates (20, 40, 80, 120, 160, 200 mV s^{-1}) within the non-faradaic potential range of 1.01-1.11 V vs. RHE. The stability was measured by CA with CP as the working electrode.

The ORR measurements were conducted in 0.1 M KOH electrolyte. A RRDE was used as the substrate for the working electrode. CV curves were measured in an O_2-saturated or Ar-saturated electrolyte at a scan rate of 10 mV s^{-1}. LSV curves were conducted in an O_2-saturated electrolyte at different rotation rates from 400-2500 rpm at a scan rate of 10 mV s^{-1}.

4.3.5 ZAB measurments

Aqueous ZABs were assembled with a hydrophobic CP with a catalytic mass loading of 0.5 mg cm^{-2} as the air cathode, a polished Zn foil as the anode, and 6 M KOH and 0.2 M zinc acetate aqueous solution as the electrolyte. The electrochemical measurement of ZABs was carried out on a CHi760E electrochemical station (Shanghai Chenhua, China). The galvanostatic test was performed using a Neware BTS4008 battery test system at room temperature. The specific capacities were determined using the galvanostatic discharge profiles standardized to the consumed mass of Zn.

4.3.6 DFT calculations

DFT calculations were performed using the CASTEP packages.[38] The GGA exchange-correlation functionals were used to describe the electronic exchange and correlation effects.[39] We selected the ultrasoft pseudopotentials and set the plane-wave basis cutoff energy to 380 eV for all the geometry optimizations. The empirical dispersion correction in Grimme's scheme was employed to consider the van der Waals (vdW) interaction. The Liner Broyden-Fletcher-Goldfarb-Shannon (LBFGS) algorithm with the medium quality setting of k-points has been used for all the energy minimizations in this work. The geometry optimization within the conjugate gradient method was performed with forces on each atom less than 0.05 eV $Å^{-1}$. An energy tolerance of 5.0×10^{-5} eV per atom and a maximum displacement of 0.005Å were considered.

To understand the role of the oxyhydroxide over the reconstructed surface during the OER cycles, a FeOOH structure with (101) lattice plane was chosen as the pristine host matrix to perform DFT simulations. It is reasonable to choose the oxyhydroxide matrix due to the above HRTEM/*in situ* Raman/XAS results and because it has been reported to be the active phase for OER catalysis. In addition, the (101) terminated surface (with H) was reported to be a more stable and active catalytic surface. In brief, the FeCoNiPdWOOH, FeCoNiPdOOH, FeCoNiWPOOH, FeCoPdWOOH, FeNiPdWOOH, and CoNiPdWOOH (built on the FeOOH model in which Co/Ni/Pd/W atoms were doped on the surface to substitute for Fe atoms) were chosen as the local configurations. As for the theoretical simulations for ORR, the initial HEPs (mainly composed of W-P and Pd-P) hydride with MOH (enrichment of Fe/Co/Ni, while Pd and W atoms alternatively doped on the subsurface) with (100) terminated surface were constructed. Notice that this is a simplified approach as the modeling of the exact reconstructed HEP structure is largely hindered by its complexity, the lack of precise tools to determine it, and its probably dynamic evolution during the oxygen redox reactions.

For all the models, a 20 Å vacuum space was set on the z-axis to guarantee full relaxation. The ΔG calculations of each elementary step were based on the standard hydrogen electrode model.[40]

4.4 Results and discussion

4.4.1 Design principles of HEP

A primary challenge in developing bifunctional catalysts for OER/ORR is ensuring the availability of proper catalytic sites. As illustrated in **Scheme 1**, an effective catalyst typically provides surface sites that strongly adsorb reactants and intermediates but only weakly bind to the products, thereby promoting high efficiency in driving the forward reaction. In contrast, this type of catalyst often shows much lower efficiency for the reverse reaction. The opposite is true for catalysts that favor strong adsorption of the products. HEMs offer a promising solution to this challenge. These materials combine a vast array of different active sites, providing a continuum of adsorption energies. This unique feature enables HEMs to efficiently catalyze both OER and ORR, making them highly effective as bifunctional oxygen catalysts.

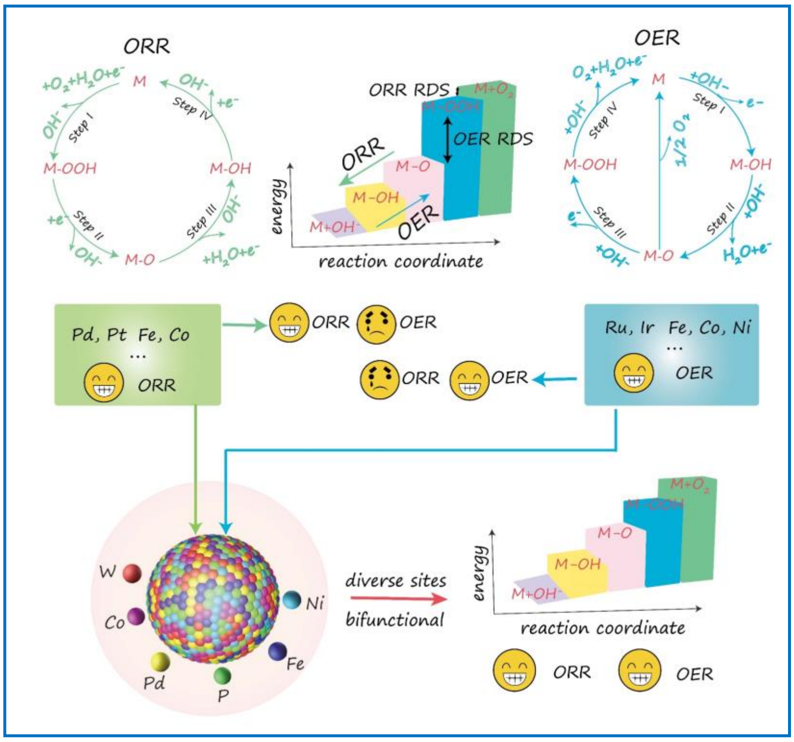

Scheme 1 Schematic illustration of the design principles of FeCoNiPdWP HEPs as bifunctional oxygen catalysts in an alkaline electrolyte.

Transition metal phosphides have attracted substantial attention due to their metallic character and associated high electrical conductivity, as well as their abundant reserves, cost-effectiveness, and stability.[41-45] The higher electronegativity of phosphorus than transition metals triggers electron delocalization and leads to partially positively charged metal and negatively charged phosphorus, where transition metals could serve as the OH^- acceptor to modulate the binding ability for OER/ORR. From the electronic band structure perspective, the presence of phosphorous modifies the electronic energy levels and d_c, increasing the density-of-states near the E_F,[46] which signifies abundant charge carriers similar to the noble metals for the OER/ORR process, thus frequently improving electrocatalytic performance.[47-49] In addition, the covalent nature of the metal-phosphorus bond promotes the durability and long-term stability of the electrocatalysts. Indeed, the hybridization of d metal orbitals with the p orbital of P to form metal-phosphorus bonds has been demonstrated to be beneficial in boosting ORR performance.[43] Therefore, the rational design and engineering of HEPs for ZAB applications is a worthy endeavor.

Based on our previous study, the combination of 3d/4d/5d metals significantly modulates the electronic state and surface electron density, altering the bond strength between the metal and oxygen species, which allows adjusting the adsorption/ desorption ability of intermediates and products.[18,50,51] The d orbitals of 5d metals are more extended and have higher energy and spatial coverage compared to those of 3d/4d metals. When 5d metals combine with 3d metals, hybrid orbitals are formed, adjusting the electron distribution and orbital overlap, thereby potentially providing more active sites and enhancing catalytic activity. The high electronegativity of the 5d metals allows for the regulation of the electron-filling states of the 3d/4d metals, optimizing the surface electronic structure of the catalysts. In addition, 5d metals provide strong electronic attraction and create new coordination environments, stabilizing reaction intermediates, and reducing poisoning. Thus, W, a 5d metal with a unique orbital filling state was incorporated into the HEP catalyst.

In terms of the 3d transition metals, Fe, Co, and Ni were selected as well-established effective OER active sites based on their cost-effectiveness, the theoretically calculated volcano graph curves between η and intrinsic catalytic activity,[52-56] and their rich valence state transitions, abundant electronic configuration, and adjustable spin state, which could effectively regulate the binding energy and modulate the spin flipping of the oxygen intermediates.[57,58] On the other hand, while a large number of excellent ORR catalysts have been reported, the most effective catalysts are still based on Pt and Pd. Therefore, Pd was incorporated into the HEP to promote ORR performance.[59,60] Besides, Pd easily forms alloys with other transition metals,[61] facilitating the HEP formation. Notice also that within an HEM, the amount of Pd is minimized compared with catalysts based on elemental Pd or binary Pd-based alloys. Overall, FeCoNiPdWP HEPs are expected to simultaneously provide superior OER and ORR performance with expectable W-modulated Fe/Co/Ni as the OER active sites and Pd as the ORR active sites, making them a potentially ideal cathode material in ZABs.

4.4.2 HEP synthesis and characterization

FeCoNiPdWP HEPs and the related reference quaternary metal phosphides (FeCoNiPdP, FeCoPdWP, CoNiPdWP, FeNiPdWP, and FeCoNiWP) were synthesized using a heating-up colloidal synthesis approach (**Figure 1**) using a mixture of ODE and OAM as the solvent. TPP was selected as a low-cost, safe, and stable phosphorus source.[62-64] Metal acetylacetonates and carbonyls were used as metal precursors. The reaction temperature was set to 290 °C. At this temperature, the phosphorus-oxygen bonds in TPP molecules are cleaved, releasing phosphorous atoms that react with the metal precursors to yield the HEP. **Figures 2-7** show the results from the characterisation of the reference quaternary metal phosphides.

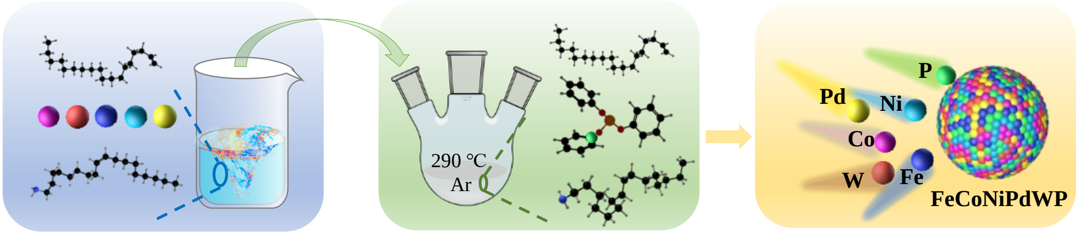

Figure 1. Scheme of the synthesis approach used to produce FeCoNiPdWP HEPs.

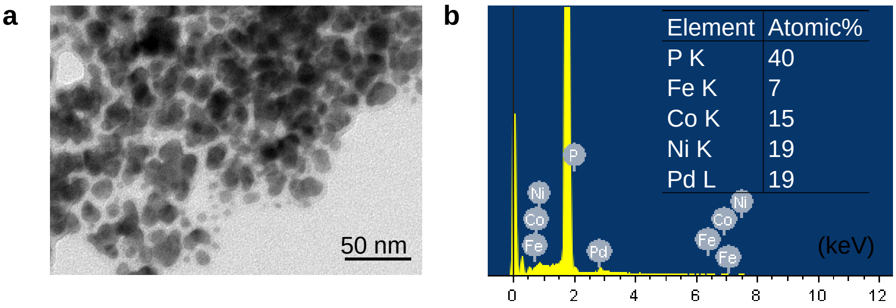

Element	Atomic%
P K	40
Fe K	7
Co K	15
Ni K	19
Pd L	19

Figure 2. (a) TEM image, and (b) EDS spectra. The inset shows the elemental composition of the FeCoNiPdP.

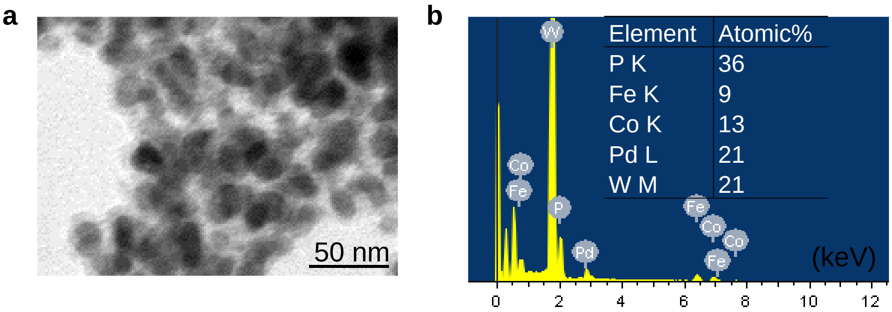

Element	Atomic%
P K	36
Fe K	9
Co K	13
Pd L	21
W M	21

Figure 3. (a) TEM image, and (b) EDS spectra. The inset shows the elemental composition of the FeCoPdWP.

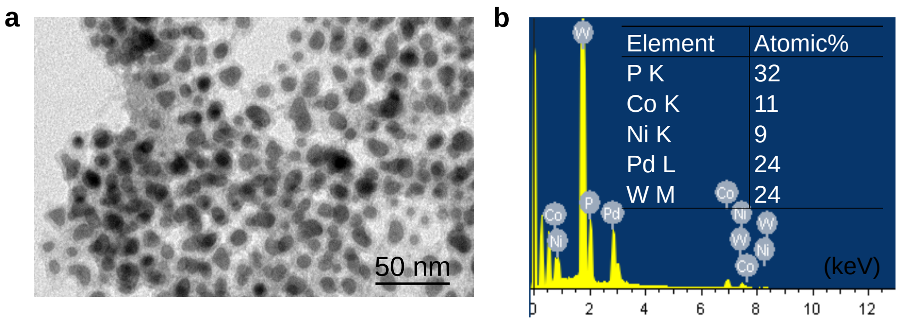

Element	Atomic%
P K	32
Co K	11
Ni K	9
Pd L	24
W M	24

Figure 4. (a) TEM image, and (b) EDS spectra. The inset shows the elemental composition of the CoNiPdWP.

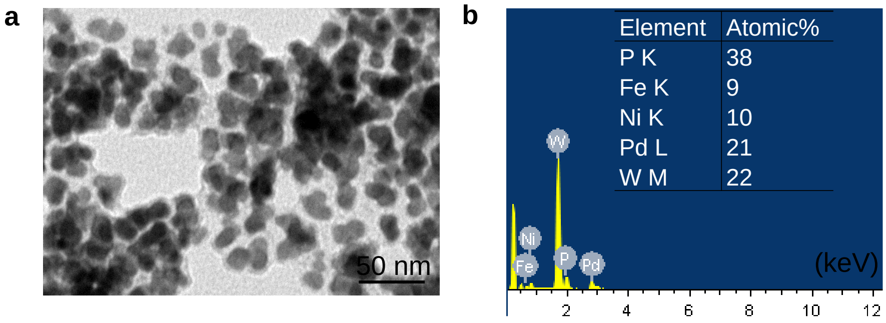

Element	Atomic%
P K	38
Fe K	9
Ni K	10
Pd L	21
W M	22

Figure 5. (a) TEM image, and (b) EDS spectra. The inset shows the elemental composition of the FeNiPdWP.

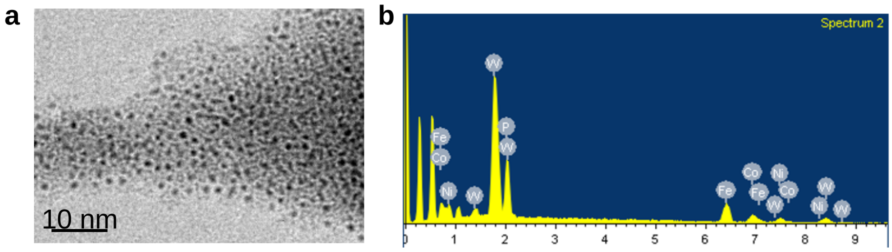

Figure 6. (a) TEM image, and (b) EDS spectra. The inset shows the elemental composition of the FeCoNiWP.

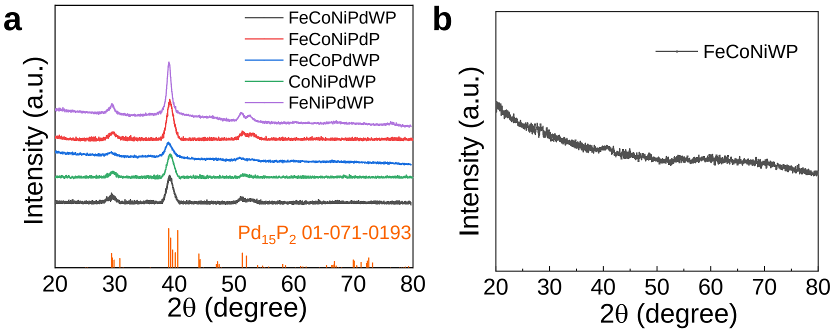

Figure 7. XRD pattern of (a) FeCoNiPdWP, FeCoNiPdP, FeCoPdWP, CoNiPdWP, and FeNiPdWP, and (b) FeCoNiWP.

Figure 2-6 show the TEM images, EDS spectra, and the EDS elemental composition of FeCoNiPdP, FeCoPdWP, CoNiPdWP, FeNiPdWP, and FeCoNiWP. TEM images show the average particle size of the quaternary metal phosphides containing Pd to be ca. 10-20 nm while the Pd-free FeCoNiWP NPs show a significantly smaller average size of ~2 nm. This different particle size can be related to the role played by Pd in the formation of the initial nuclei where the different elements are subsequently incorporated. XRD patterns of FeCoNiPdP, FeCoPdWP, CoNiPdWP, and FeNiPdWP show the Pd-based materials to present a good crystallinity (**Figure 7a**). The main peaks around 30^o, 40^o, 51^o, and 52^o match the $Pd_{15}P_2$ rhombohedral phase (JCPDS 01-071-0193). This is consistent with Pd-P forming the initial crystal seed and the other metals gradually incorporating during the synthesis process. The less intense XRD peaks within the $Pd_{15}P_2$ reference pattern are not observed due to the lattice distortions associated with the replacement of Pd with the different metals (Fe, Co, Ni, W). In contrast, XRD analysis shows the Pd-free sample, FeCoNiWP, to be mostly amorphous (**Figure 7b**), further confirming the essential role played by Pd in the formation of the nanocrystals.

TEM images show the FeCoNiPdWP HEP NPs to have an average size of 20 nm (**Figure 8a**). AC-HRTEM analysis confirmed their high crystallinity (**Figure 8b,c**). XRD pattern determined the particles to have the $Pd_{15}P_2$ rhombohedral phase (JCPDS 01-071-0193) (Figure 7a). GPA shows a random distribution of distortions induced by tensile and compressive stresses attributed to the different atomic radii and electronegativity of the constituent elements (**Figure 8d**). HAADF-STEM micrographs combined with EDS compositional maps show a homogeneous distribution of the different elements within the HEP NPs (**Figure 8e-g**). The TEM-EDS metal ratios are consistent with those obtained from ICP-OES: Fe/Co/Ni/Pd/W = 15.7/19.8/20.3/30.6/13.6 (**Figure 8h**).

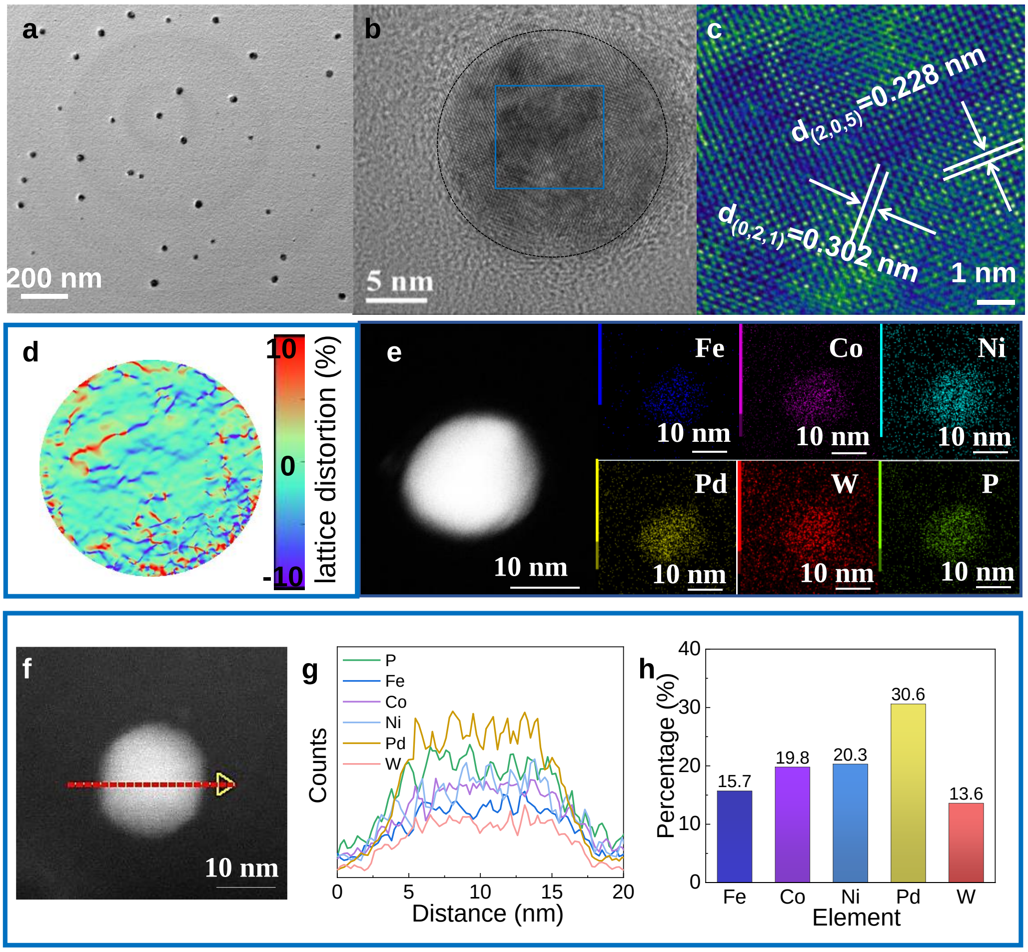

Figure 8. (b) TEM image. (c) AC-HRTEM image. (d) Magnified AC-HRTEM image and lattice distance analysis of the blue square in (c). Two crystal planes with lattice distances of 0.228 and 0.302 nm are indexed to the (205) and (021) crystal planes of the $Pd_{15}P_2$ rhombohedral phase, respectively. (e) GPA analysis. (f) HAADF-STEM micrograph and EDS compositional maps. (g) HAADF-STEM micrograph and (h) line scanning profiles. (i) Metal ratios obtained using ICP-OES.

4.4.3 OER catalytic performance

The OER activity of the materials supported on GC was evaluated by LSV in 1.0 M KOH. The LSV curves display a small bump in the potential range of 1.3-1.4 V vs. RHE associated with the oxidation of the transition metals. FeCoNiPdWP shows the best OER catalytic performance with outstanding low η of 227 mV at 10 mA cm^{-2}, 250 mV at 50 mA cm^{-2}, and 258 mV at 100 mA cm^{-2} (**Figure 9**). These values are well below those measured for RuO_2, PdP_x (**Figure 10**), and the quaternary phosphides, which η at 10/100 mA cm^{-2} follows the trend FeCoNiPdWP < FeCoNiPdP < FeNiPdWP < FeCoPdWP < FeCoNiWP < CoNiPdWP < RuO_2 < PdP_x (**Figure 11**).

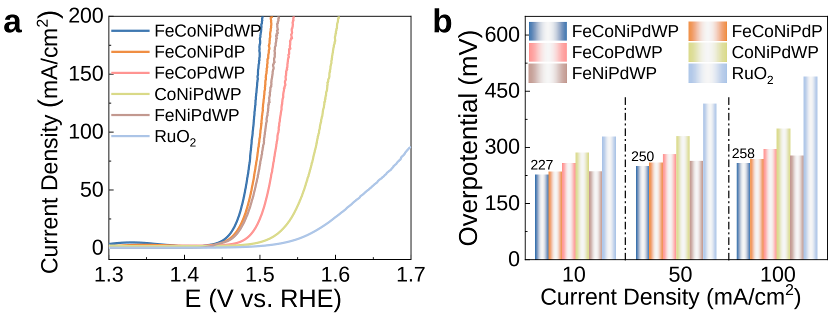

Figure 9. OER performance on GC electrodes with a loading of 0.5 mg cm^{-2}. (a) LSV curves at 5 mV s^{-1}. (b) η at different current densities.

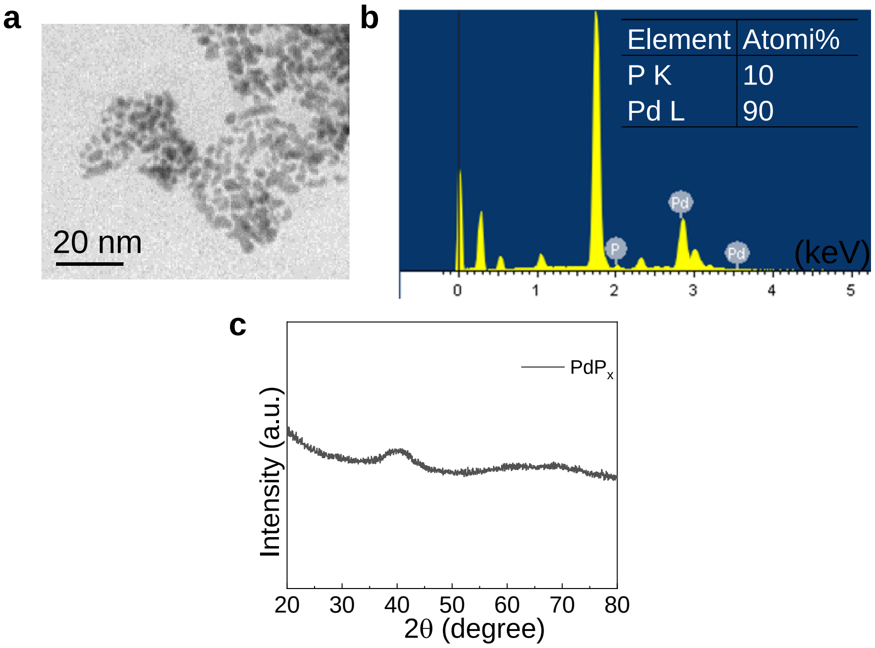

Figure 10. (a) TEM image, (b) EDS spectra. The inset shows the elemental composition. (c) XRD pattern of the PdP$_x$.

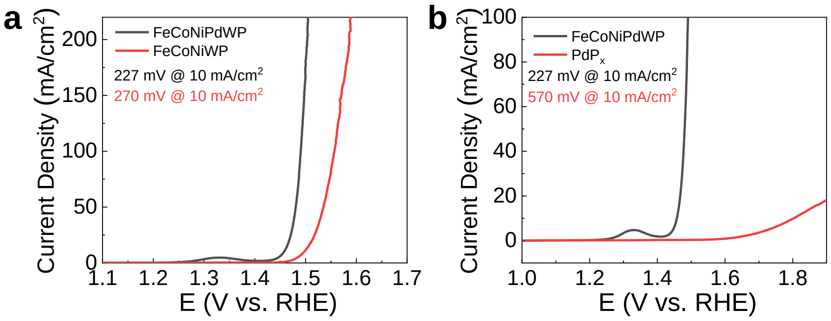

Figure 11. (a) OER LSV curves of FeCoNiPdWP and FeCoNiWP. (b) OER LSV curves of FeCoNiPdWP and PdP$_x$.

FeCoNiPdWP also shows the smallest Tafel slope (33 mV dec^{-1}), well below that of the other metal phosphides (37-59 mV dec^{-1}) and RuO_2 (75 mV dec^{-1}), demonstrating especially favorable OER kinetics (**Figure 12**). CV curves at different scan rates (**Figure 13 a-e**) and the derived C_{dl} values (**Figure 13f**) show that all the quaternary and quinary phosphide catalysts have a similar ECSA, higher than that of PdP_x (**Figure 14**). Normalization of the OER current densities by the ECSA values implies that FeCoNiPdWP has a higher intrinsic activity per active site (**Figure 15**). EIS analysis confirms FeCoNiPdWP to display the smallest OER charge transfer impedance thus the most favorable reaction kinetics (**Figure 16** and **Table 1**).

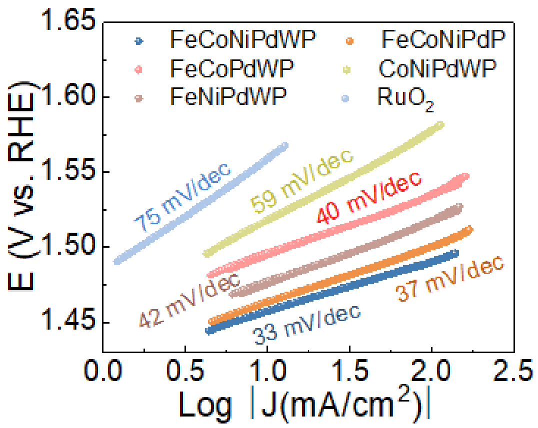

Figure 12. Tafel fitting plots calculated from the LSV curves for different catalysts, the open circles are measured data and the long solid lines are fitted data.

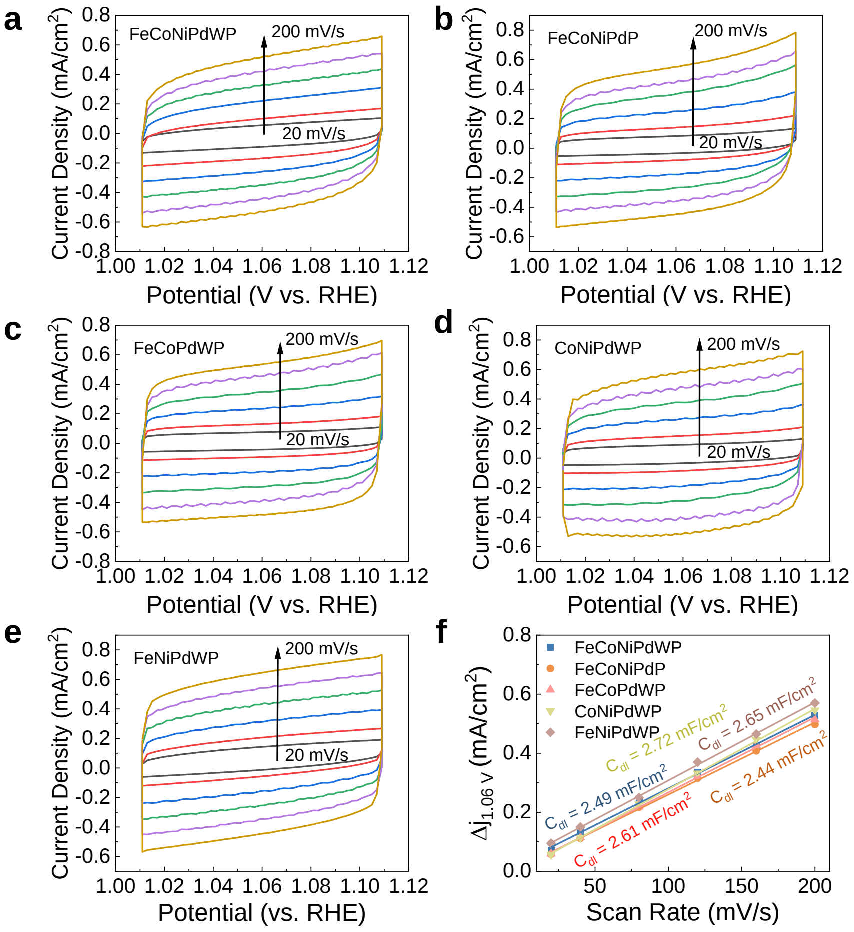

Figure 13. CV curves of (a) FeCoNiPdWP, (b) FeCoNiPdP, (c) FeCoPdWP, (d) CoNiPdWP, and (e) FeNiPdWP at different scan rates from 20 to 200 mV s^{-1} for fitting and calculating the C_{dl} values in (f).

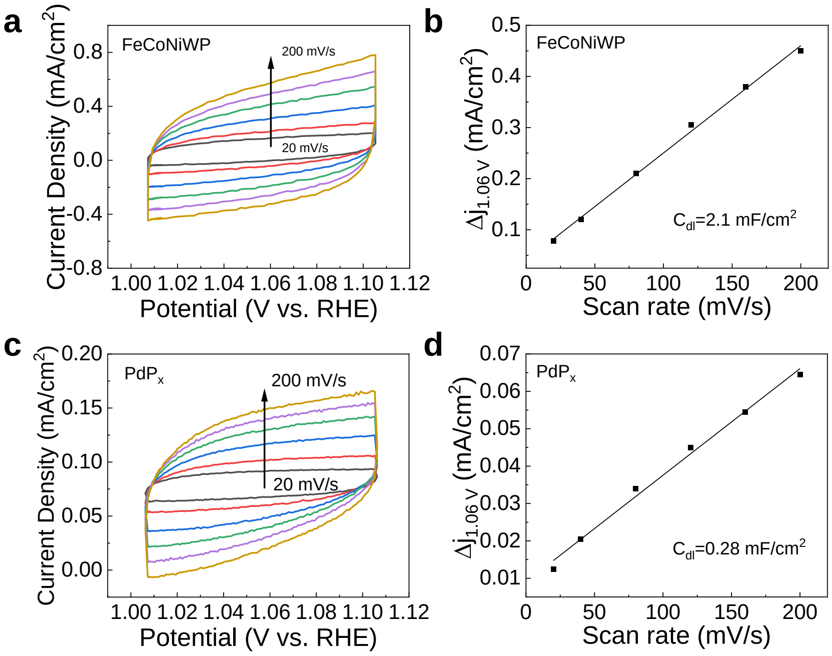

Figure 14. CV curves of (a) FeCoNiWP and (c) PdP_x at different scan rates from 20 to 200 mV/s. C_{dl} values of (b) FeCoNiWP and (d) PdP_x.

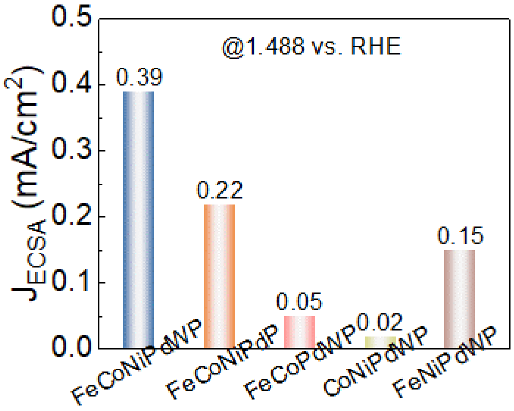

Figure 15. Current density normalized by ECSA at 1.488 vs. RHE for different catalysts.

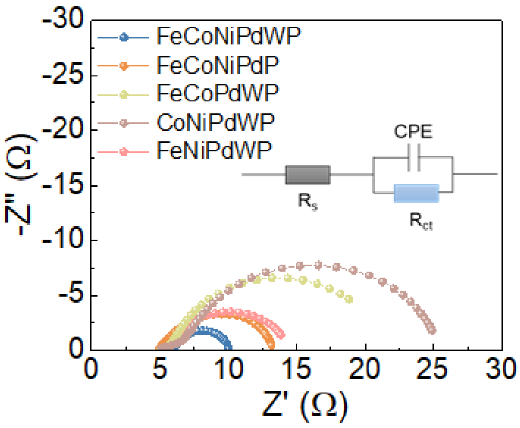

Figure 16. Nyquist plot of the EIS spectra of the different catalysts at 1.5 V vs. RHE. The inset shows the equivalent circuit model used to fit the experimental data, CPE represents the C_{dl} at the electrode-electrolyte interphase.

Table 1. Parameters obtained from the fitting of the EIS spectra using the equivalent circuit.

Catalysts	R_s (Ω)	R_{ct} (Ω)
FeCoNiPdWP	5.34	3.96
FeCoNiPdP	4.91	7.92
FeCoPdWP	4.92	14.64
CoNiPdWP	4.81	18.47
FeNiPdWP	4.95	8.27

Overall, FeCoNiPdWP HEPs show superior OER performance when compared not only with the reference materials tested here but also with previously reported catalysts supported on GCE, as shown in **Figure 17** and **Table 2**.[4,65-97] Besides, FeCoNiPdWP shows excellent stability with a continuously applied potential of 1.46 V vs. RHE for 120 h resulting in just a 3% decrease in current density as determined by CA measurements (**Figure 18**), well below the current density decay obtained from the quaternary metal phosphides (**Figure 19**).

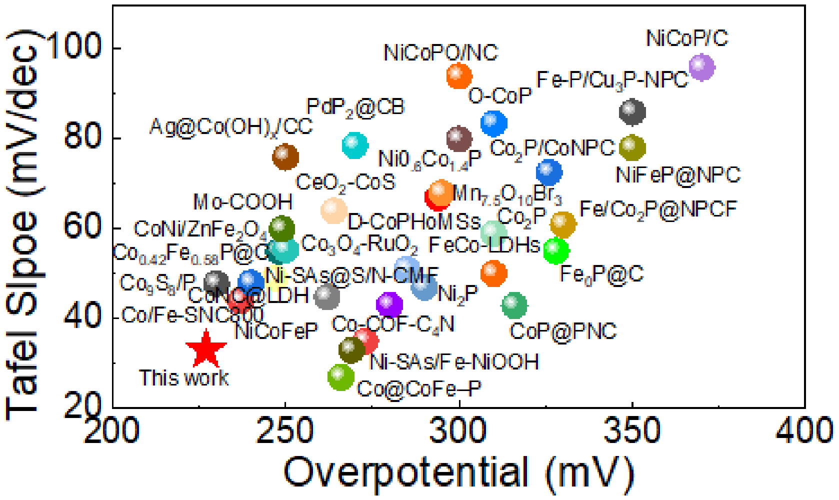

Figure 17. Comparisons of the OER performance of FeCoNiPdWP with other recently reported catalysts on GCE.

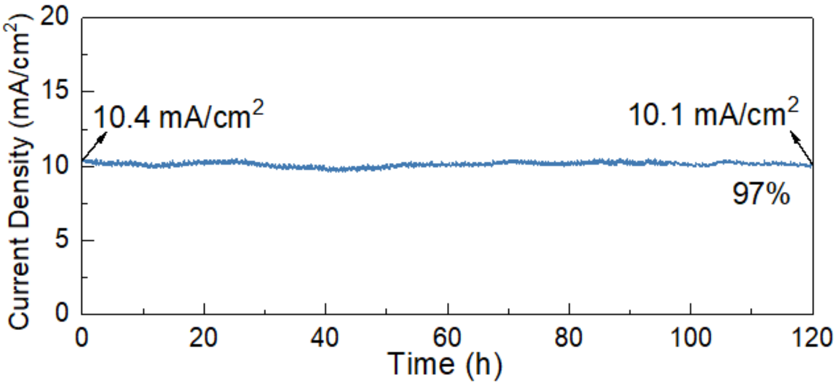

Figure 18. CA curve of FeCoNiPdWP at 1.46 V vs. RHE.

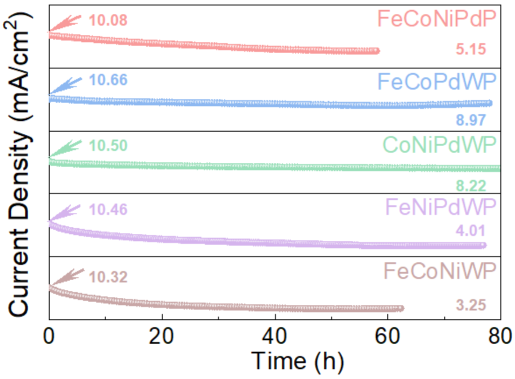

Figure 19. OER stability test of FeCoNiPdP, FeCoPdWP, CoNiPdWP, FeNiPdWP, and FeCoNiWP with CA technique.

Table 2. OER performance comparison of FeCoNiPdWP in 1 M KOH with recently reported catalysts on GCE.

Catalyst	*η@10 mA cm^{-2} (mV)*	*Tafel slope (mV dec^{-1})*	*Stability (h)*	*References*
Fe–P/Cu_3P-NPC	350	86	5.56	*Small*, **2023**, 2301985
NiCoFeP	273	35	2000 cycles	*Small*, **2023**, 1802442
Co_2P/CoNPC	326	72.6	8.33	*Adv. Mater.*, **2020**, 32, 2003649
CoP@PNC	316	42.9	10000 cycles	*Energy Storage. Mater.*, **2020**, 28, 27-36
NiCoP/C	370	96	10	*Angew. Chem. Int. Ed.*, **2017**, 56, 3897-3900
FeCo/Co_2P @NPCF	330	61	1000 cycles	*Adv. Energy Mater.*, **2020**, 10, 1903854
PdP_2@CB	270	78.6	-	*Angew. Chem. Int. Ed.*, **2018**, 57, 14862 -14867
$Ni_{0.6}Co_{1.4}P$	300	80	10	*Adv. Funct. Mater.*, **2018**, 28, 1706008
NiFeP@NPC	350	78	20	*Appl Catal B-environ*, **2019**, 254, 292-299
Co_2P	310	50	10	*ACS Energy Lett.*, **2016**, 1, 169-174
Ni_2P	290	47	10	*Energy Environ. Sci.*, **2015**, 8, 2347-2351
Co@CoFe–P	266	26.94	1000 cycles/12	*Energy Environ. Sci.*, **2022**, 15, 727-739
D-CoPHoMSs	294	67	10	*Angew. Chem. Int. Ed.*, **2021**, 133, 7002
NiCoPO/NC	300	94	10	*Nano Energy*, **2020**, 69, 104453
$Co_{0.42}Fe_{0.58}P$@C	262	44.8	20	*Adv. Energy Mater.*, **2022**, 12, 2202394
Fe_0P@C	328	55.1	-	*Adv. Energy Mater.*, **2022**, 12, 2202394
O-CoP	310	83.5	15	*Adv. Funct. Mater.*, **2020**, 30, 1905252
Co-COF-C_4N	280	43	-	*Appl Catal B-environ*, **2023**, 325, 122366
CoNi/Zn(Fe,Al,Cr)$_2O_4$	248	54.7	100	*Adv. Energy Mater.*, **2023**, 2303450
Co_3O_4-RuO_2-HS	250	55.4	24	*Adv. Funct. Mater.*, **2022**, 32, 2203206
CeO_2-$CoS_{1.97}$	264	64	50	*Adv. Mater.*, **2021**, 33, 2102593
$Mn_{7.5}O_{10}Br_3$	295	68	500	*Nat. Commun.*, **2022**,

				13, 2294
Ag@Co(OH)x/CC	250	76	11	*Angew. Chem. Int. Ed.*, **2020**, 59, 7245-7250
$LiCoO_{1.8}Cl_{0.2}$	270	55	50	*Nat. Catal.*, **2021**, 4, 212
Co/Fe-SNC800	240	48	25	*Energy Environ. Sci.*, **2023**, 16, 1685-1696
CoFe-LDHs	310	59	24	*Nat. Commun.*, **2019**, 10, 1711
Ni SAs/Fe-NiOOH	269	33	11	*Appl Catal B-environ*, **2021**, 297, 120451
Mo-CoOOH	249	60	36	*J. Mater. Chem. A*, **2022**, 10, 6242-6250
Ni SAs@S/N-CMF	285	51	60	*Adv. Mater.*, **2022**, 34, e2203442
$Ni_{0.9}Fe_{0.1}$-MOF	230	-	150	*Nat. Energy*, **2022**, 5, 881
Ru-Co/ELCO	247	49	200	*Angew. Chem. Int. Ed. Engl.*, **2022**, 61, e202205946
$Ni_{0.8}Fe_{0.2}$ NSs	230	-	-	*ChemCatChem*, **2019**, 11, 6002
Co_9S_8/P	230	47.8	-	*Chem. Eng. J.*, **2020**, 381, 122683
WC_x-FeNi	237	44	100	*Nat. Mater.*, **2021**, 20, 1240
CoNC@LDH	240	48	1.38	*Adv. Mater.*, **2021**, 33, 2008606
FeCoNiPdWP	***227***	***33***	***120***	*This work*

NPC: N-, and P- doped carbons, C: Carbon, NPCF: N,P- co doped carbon nanofiber, CB: Carbon black, NC: Nitrogen-doped carbon, @C: @Carbon-cage-encapsulate, HS: Hollow sphere, SNC: S,N- co doped carbon, LDHs: Layered double hydroxides, SAs: Single atoms, S/N-CMF: S/N- Doped carbon macroporous fibers, LCO: Layered $LiCoO_2$, NSs: Nanosheets, @LDH: @Layered double hydroxide.

4.4.4 HEP reconstruction during OER

The high-resolution XPS spectra of FeCoNiPdWP HEPs before and after OER operation are displayed in **Figure 20,21**. Before OER, FeCoNiPdWP displays both M-P and M-O surface chemical environments, the latter originated during sample storage, transportation, and manipulation.[98,99] After long-term OER, surface metals show a single oxidation state, Fe^{3+}, Co^{2+}, Ni^{3+}, Pd^{2+}, and W^{6+}, with no M-P chemical environment. Besides, no P is detected at the surface of the HEP NPs. Additionally, the hydroxide (OOH) contribution to the O 1s XPS spectrum becomes dominant, which is attributed to the formation of a metal (oxy)hydroxide surface.

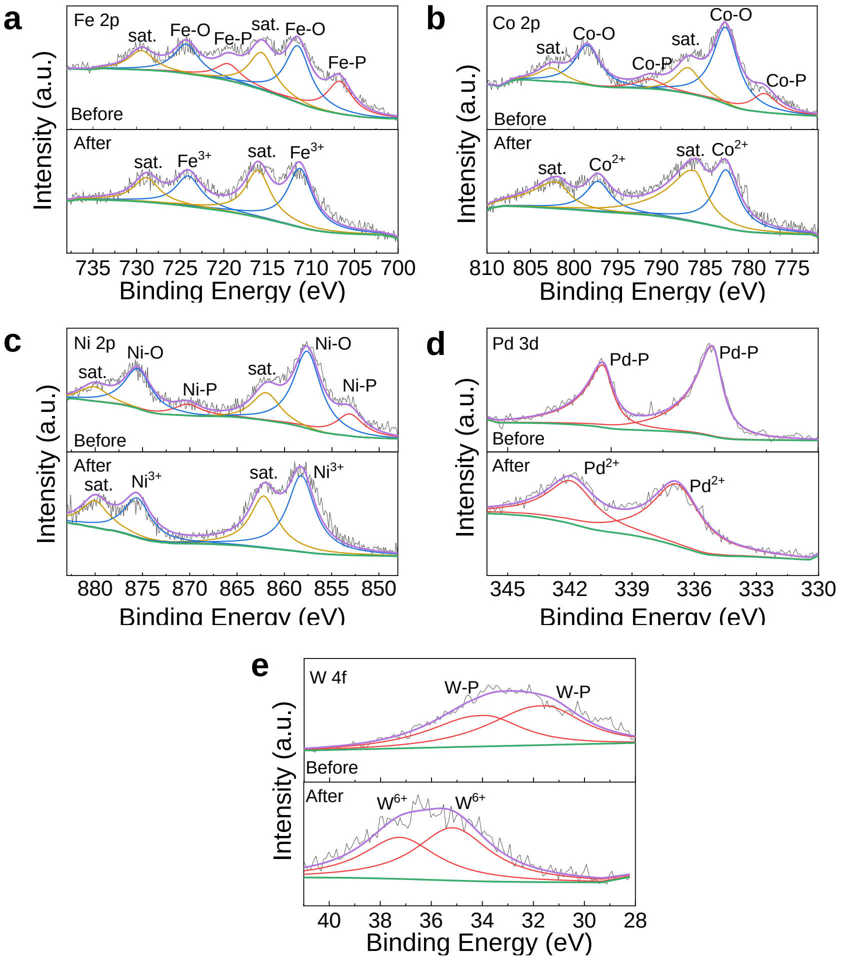

Figure 20. High-resolution (a) Fe 2p, (b) Co 2p, (c) Ni 2p, (d) Pd 3d, and (e) W 4f XPS spectra of FeCoNiPdWP before (upward) and after (downward) OER stability test.

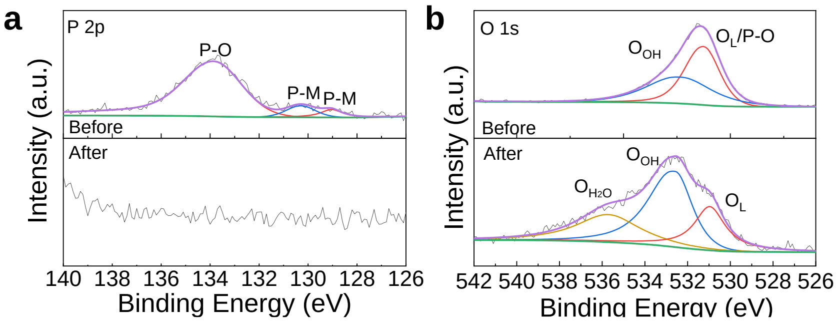

Figure 21. High-resolution (a) P 2p, and (b) O 1s XPS spectra of FeCoNiPdWP before (upward) and after (downward) OER stability test.

XRD analysis of FeCoNiPdWP after the OER stability test revealed that the crystalline $Pd_{15}P_2$ rhombohedral phase disappeared during OER operation (**Figure 22**). Besides, EDS spectra (**Figure 23,24**) show that the P amount strongly decreased from 29% to 3% after OER. *In situ* Raman spectroscopy was used to explore the evolution of HEP with the applied potential (**Figure 25**). The spectra show Raman peaks at around 300 cm^{-1}, and 400-700 cm^{-1}, whose intensity increases with the applied voltage. This observation is related to the formation of layered Fe/Co/Ni (oxy)hydroxides.[100,101] Thus, overall, XPS, XRD, and Raman results are consistent with the HEP being reconstructed into a high entropy oxyhydroxide (HEOOH) in OER conditions.

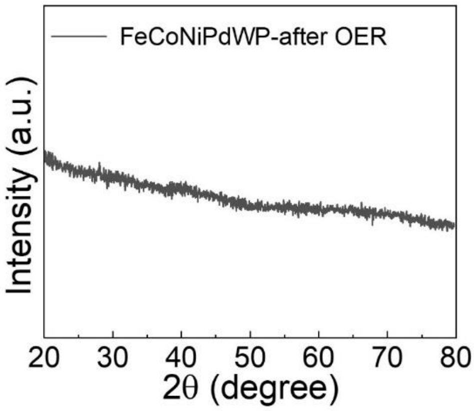

Figure 22. XRD pattern of FeCoNiPdWP after OER stability test.

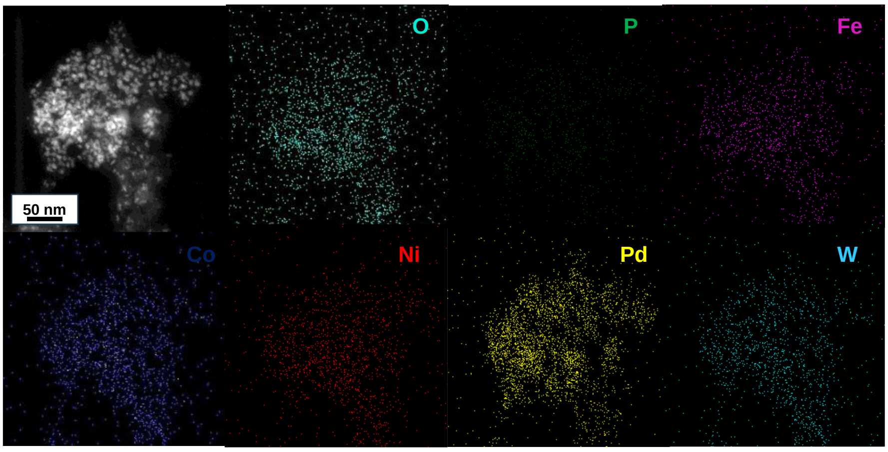

Figure 23. HAADF STEM micrograph and EDS compositional maps for each element of FeCoNiPdWP after OER stability test.

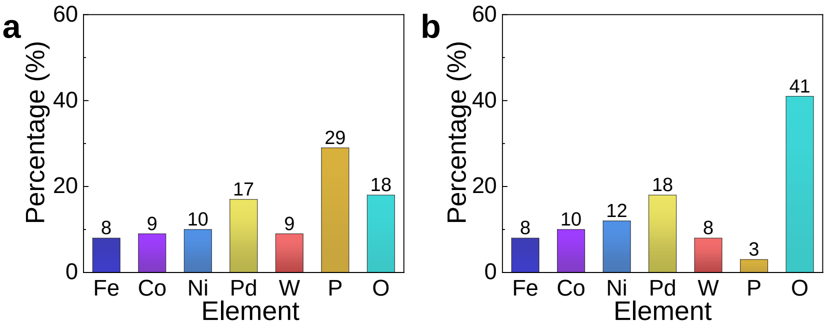

Figure 24. Elemental composition from EDS spectra of FeCoNiPdWP HEPs (a) before the OER test, and (b) after the OER test.

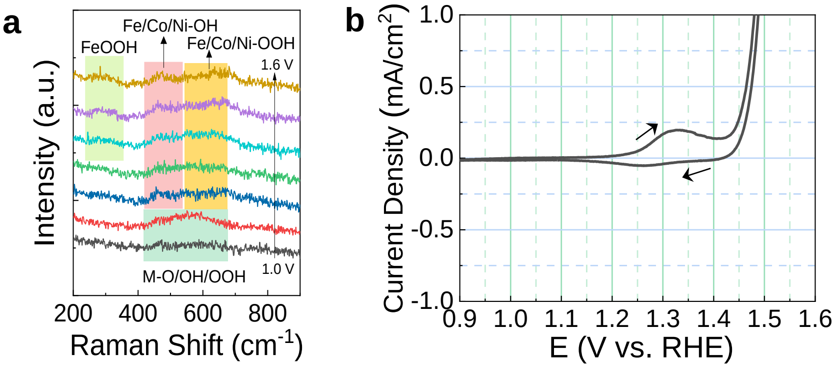

Figure 25. (a) *In situ* Raman spectra taken at Raman shift range of 200-900 cm^{-1}. The vertical arrows mark the two most prominent vibrations and their assignment to vibrations of the Fe/Co/Ni-OH and Fe/Co/Ni-OOH. The Raman spectra was taken at a potential that is shown as vertical line in the CV curves. (b) CV curves with the scan rate of 5 mV s^{-1} in 1 M KOH of FeCoNiPdWP. The black arrows mark the scan direction.

XAS on the Fe, Co, Ni K-edge was used to gain an understanding of the FeCoNiPdWP atomic structure and the reconstruction process taking place during OER for the as-prepared HEP NPs, the fresh electrode, and the electrode with the completed reconstruction process. XANES analysis of the reconstructed samples revealed significant increases in the oxidation states of the metals during OER operation, with Fe increasing from 3.0 to 3.1, Co from 1.4 to 3.3, and Ni from 2.0 to 3.8 (**Figure 26** and **Table 3**). Fe, Co, and Ni in oxidation states above three have been shown to facilitate water oxidation.[102-107] Thus, the high Fe, Co, and Ni average oxidation states during the OER support the hypothesis that these three elements or their multimetallic neighbouring sites function as OER active sites.

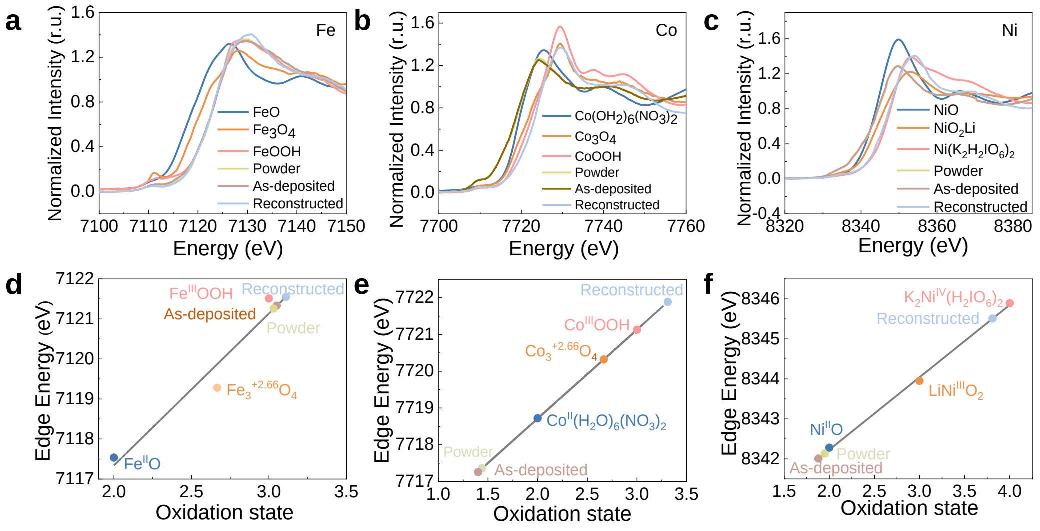

Figure 26. XAS characterization of HEPs. (a)-(c) Fe (a), Co (b), and Ni (c) XANES plots of the as-prepared powders, the as-deposited films, and reconstructed films, freeze-quenched at 1.53 V vs. RHE after 2 h OER operation. (d)-(f) Metal oxidation states of Fe (d), Co (e), and Ni (f) from the XANES. To quantify differences in the edge positions, the K-edge energy was calculated using the integral method,[108] and the obtained values are plotted here as symbols. A linear regression including the three iron/cobalt/nickel oxide references was used to derive the oxidation states of the HEPs before and during the OER.

Table 3. Oxidation states from XANES. Bulk oxidation states determined from K-edge XANES data.

K-edge	Before OER	*Reconstructed*
Fe	3.0	3.1
Co	1.4	3.3
Ni	2.0	3.8

To gain insight into the local structure of Fe/Co/Ni, the EXAFS data and k^3- weighted EXAFS spectra were simulated, as shown in **Figure 27,28**. For all the 3d metals, models of layers with edge-sharing [MO_6] octahedra were applied to simulate the EXAFS spectra (see **Table 4** for fitting parameters). The model comprises three shells: (i) for the M-O bond of the [MO_6] octahedra (1.87-2.02 Å), (ii) for the M-M distance of two adjacent [MO_6] octahedra (2.81-2.98 Å), and (iii) a second, larger M-O distance (3.40-3.43 Å). This model is consistent with the FeCoNi oxyhydroxide structure or their deprotonated, oxidized, and potassium-intercalated relatives that have recently been proposed to form during OER.[107] For Fe, two M-O bond distances (1.89 and 2.02 Å) were required, likely due to the presence of a Jahn-Teller distortion caused by the unevenly occupied t_{2g} orbital of [$Fe^{III}O_6$]. The presence of two different M-O bond lengths automatically leads to two different Fe-M bond distances as well, which were taken into account in the simulation. The short M-O bond distances (1.87-1.89 Å) are consistent with the high oxidation states extracted from the XANES data (**Table 4**). Overall, results from XAS analyses reveal that, during OER, FeCoNiPdWP is fully reconstructed into layers of edge-sharing [MO_6] octahedra with 3d metal oxidation states above three. These motifs are consistent with highly oxidized oxyhydroxides and related structures that are frequently observed during and after the OER.[107, 109-111]

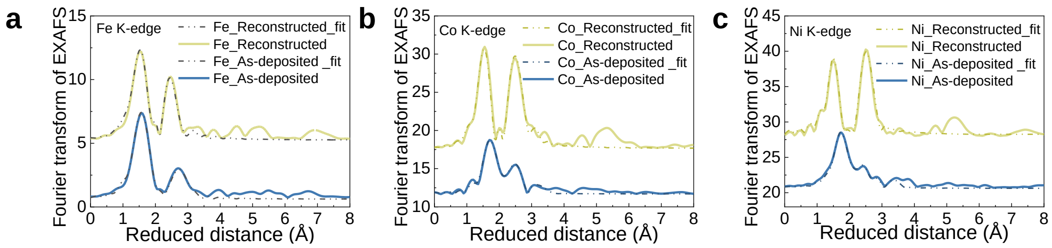

Figure 27. (a)-(c) Fe (g), Co (h), and Ni (i) EXAFS spectra and simulations. The data at the bottom/up show the as-prepared/reconstructed electrodes.

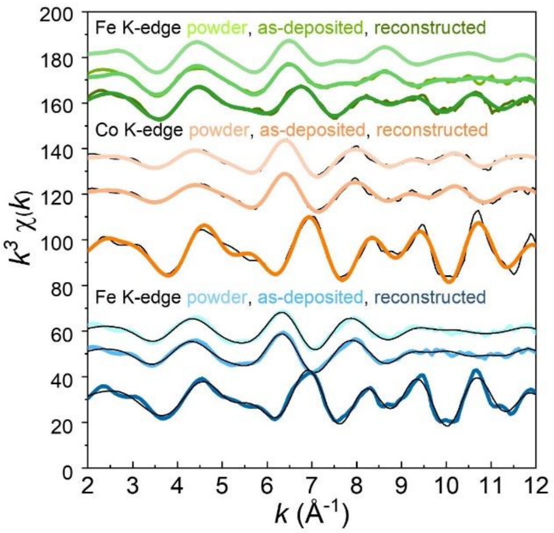

Figure 28. k^3-weighted EXAFS spectra of the Fe, Co, Ni K-edge of the as-prepared powder, the as-deposited film, and reconstructured *in situ* freeze-quenched at 1.53 V vs. RHE after 2 h OER operation. Simulations are shown as black lines.

Table 4. EXAFS simulations. Tables with the parameters used to simulate the Fe (a), Co (b), Ni (c) K-edge EXAFS data of the as-prepared powder, the as-deposited film, and reconstructed sample by *in situ* freeze-quenching at 1.53 V vs. RHE after 2 h OER operation. R_f represents the fit error sm in % in the range 0-3.5 Å. N the population of the shell at distance between two atoms (R_d). The Debye-Waller factors were fixed in order to diminish the number of variables in the fits. The amplitude reduction factor was 0.7, 0.8, and 0.9 for Fe, Co, and Ni, respectively. Italic numbers refer to restraint fits with a fixed number of summed-up shell population (Fe *in situ* sample); bold number refers to a constraint shell population (Co *in situ* sample). The metal-phosphide and metal-metal distances are consistent with the structure of JCPDS 01-071-0193 $Pd_{15}P_2$. A metal-oxide and additional metal-metal shell has been added for a layered oxyhydroxide structure and is described in the main text. The errors of the fit parameters correspond to the 68 %, 1-sigma, confidence intervals coming from the covariance matrix of the Levenberg-Marquardt fit.

(a) Fe

Powder

SHELL	*N*	ERROR	R_D [Å]	ERROR [Å]	*Σ* [Å]
FE-O	3.9	0.4	1.94	0.01	0.050
FE-P	1.5	0.3	2.25	0.01	0.050
FE-FE	1.4	0.6	2.66	0.02	0.050
FE-FE	1.7	0.7	2.87	0.02	0.050
FE-P	3.9	0.9	3.22	0.02	0.050
$R_F = 9.8$					

As-deposited

SHELL	*N*	ERROR	R_D [Å]	ERROR [Å]	*Σ* [Å]
FE-O	3.5	0.4	1.93	0.01	0.050
FE-P	1.7	0.3	2.25	0.01	0.050
FE-FE	1.2	0.6	2.66	0.02	0.050
FE-FE	1.5	0.7	2.86	0.02	0.050
FE-P	3.6	0.9	3.21	0.02	0.050
$R_F = 9.1$					

Reconstructured

SHELL	*N*	ERROR	R_D [Å]	ERROR [Å]	*Σ* [Å]

FE-O	*3.2*	*0.8*	1.89	0.03	0.050
FE-O	*2.8*		2.02	0.04	0.050
FE-FE	2.2	0.8	2.85	0.03	0.050
FE-FE	0.8	0.7	2.98	0.09	0.050
FE-O	3.0	1.7	3.43	0.05	0.050

$R_{\mathrm{F}} = 9.4$

(b) Co

Powder

SHELL	N	ERROR	R_D [Å]	ERROR [Å]	Σ [Å]
CO-O	2.7	0.7	2.03	0.02	0.050
CO-P	1.0	0.5	2.26	0.03	0.050
CO-CO	0.9	0.3	2.55	0.02	0.050
CO-CO	1.0	0.3	2.97	0.03	0.050
CO-P	1.5	0.7	3.33	0.04	0.050

$R_{\mathrm{F}} = 11.3$

As-deposited

SHELL	N	ERROR	R_D [Å]	ERROR [Å]	Σ [Å]
CO-O	2.8	0.7	2.03	0.02	0.050
CO-P	1.1	0.5	2.25	0.03	0.050
CO-CO	1.0	0.3	2.56	0.02	0.050
CO-CO	1.0	0.3	2.97	0.03	0.050
CO-P	1.4	0.7	3.34	0.04	0.050

$R_{\mathrm{F}} = 11.5$

Reconstructured

SHELL	N	ERROR	R_D [Å]	ERROR [Å]	Σ [Å]
CO-O	6		1.89	0.01	0.050
CO-CO	4.3	0.2	2.82	0.01	0.050
CO-O	4.2	1.3	3.40	0.02	0.050

$R_{\mathrm{F}} = 9.2$

(c) Ni

Powder

SHELL	N	ERROR	R_D [Å]	ERROR [Å]	Σ [Å]
NI-O	2.5	0.5	2.03	0.02	0.050
NI-P	1.4	0.3	2.29	0.02	0.050
NI-NI	0.6	0.2	2.56	0.02	0.050

NI-NI	0.3	0.2	2.92	0.05	0.050
NI-P	1.0	0.5	3.22	0.04	0.050
$R_F = 16.5$					

As-deposited

SHELL	N	ERROR	R_D [Å]	ERROR [Å]	Σ [Å]
NI-O	2.6	0.5	2.02	0.02	0.050
NI-P	1.4	0.3	2.29	0.02	0.050
NI-NI	0.7	0.2	2.55	0.02	0.050
NI-NI	0.3	0.2	2.92	0.04	0.050
NI-P	1.1	0.5	3.21	0.03	0.050
$R_F = 16.5$					

Reconstructured

SHELL	N	ERROR	R_D [Å]	ERROR [Å]	Σ [Å]
NI-O	4.0	0.3	1.88	0.01	0.050
NI-NI	3.3	0.2	2.81	0.01	0.050
NI-O	2.6	1.1	3.41	0.03	0.050
$R_F = 10.4$					

4.4.5 HEP element roles in OER

DFT calculations were carried out to identify the roles of individual metal sites and their synergistic effects in the FeCoNiPdWP HEPs reconstructed during the OER, denoted as FeCoNiPdWOOH (**Figure 29**), and the reference reconstructed quaternary compounds (**Figure 30-35**). As shown in **Figure 36a**, all the reconstructed models have the E_F within a band of states, indicating a metallic conductivity. The total DOS (TDOS) of FeCoNiPdWOOH is greater than that of the reference compounds at around E_F, pointing to a higher electron transport rate. The PDOS of each element in the FeCoNiPdWOOH model is displayed in **Figure 36b**. Notably, the O 2p orbitals have a strong overlap with the different metal elements, pointing at an efficient p-d orbital coupling and self-complementary effect.[112] The Ni-3d and Co-3d orbitals are close to E_F, pointing to high electrochemical activity with strong electron depletion capability. The Fe-3d orbital shows e_g-t_{2g} splitting with a strong overlap with the W 5d orbitals, implying a high degree of W 5d-Fe 3d orbital coupling and electron exchange between these two metals.[113,114] The center of the Pd-4d band is located well below the E_F, lower than the other metal sites, indicating an electron-rich characteristic. Consistently, the charge density difference (CDD) analysis revealed that Pd sites exhibit electron accumulation (**Figure 30b**) orbitals cover a wide energy range, from -10.0 eV to E_F.

Overall, Fe-3d, Co-3d, Ni-3d, Pd-4d, W-5d, and O-2p orbitals cross the E_F and show a significant covalent interaction between metal and O bands, which boosts the site-to-site electron transfer and might be one of the reasons for the outstanding OER performance of the reconstructed HEOOH. Meanwhile, the d_c of FeCoNiPdWOOH is higher than that of the quaternary metal oxyhydroxides and the electronic structure balance involves charge transfer between all the different elements (**Figure 36c**).

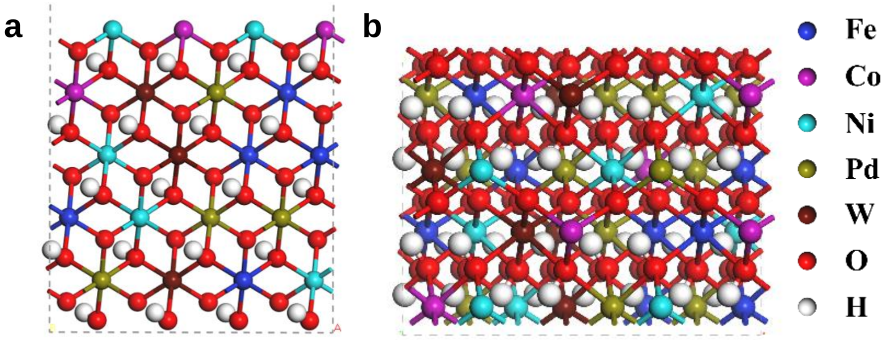

Figure 29. Optimal theoretical model of FeCoNiPdWOOH. (a) side view, (b) top view.

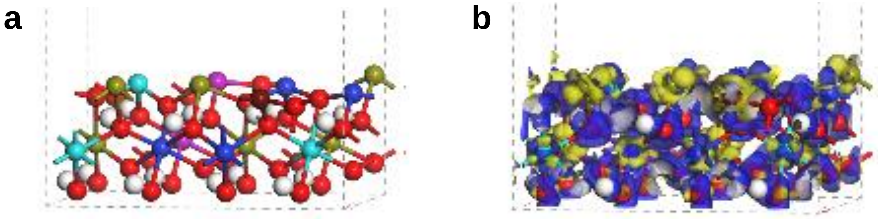

Figure 30. (a) Optimal theoretical model of FeCoNiPdWOOH and (b) CDD of FeCoNiPdWOOH surfaces. Blue and yellow contours represent electron accumulation and depletion.

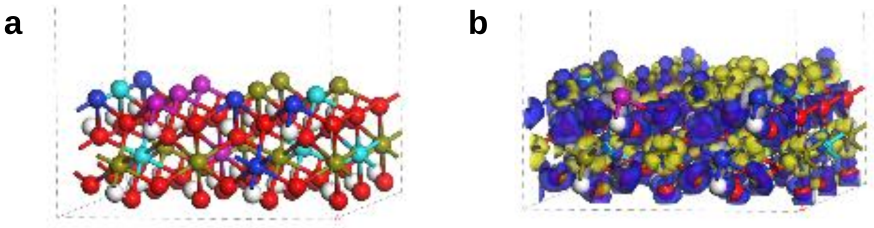

Figure 31. (a) Optimal theoretical model of FeCoNiPdOOH and (b) CDD of FeCoNiPdOOH surfaces. Blue and yellow contours represent electron accumulation and depletion.

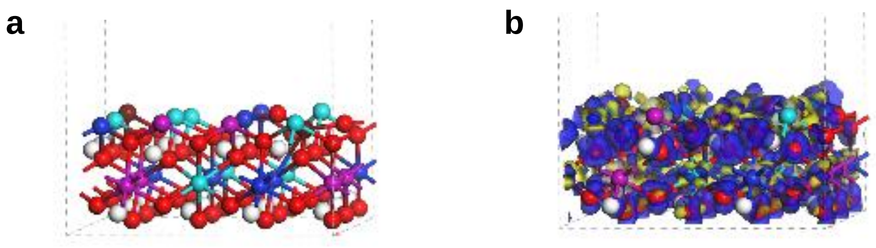

Figure 32. (a) Optimal theoretical model of FeCoNiWOOH and (b) CDD of FeCoNiWOOH surfaces. Blue and yellow contours represent electron accumulation and depletion.

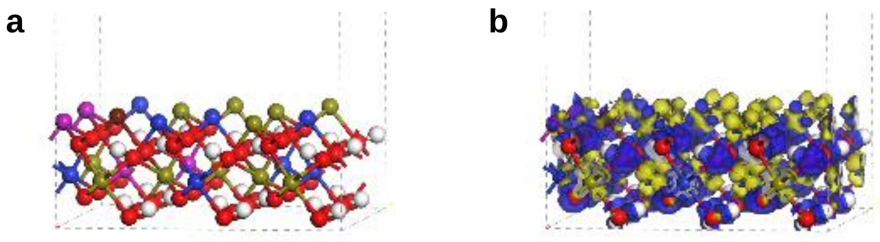

Figure 33. (a) Optimal theoretical model of FeCoPdWOOH and (b) CDD of FeCoPdWOOH surfaces. Blue and yellow contours represent electron accumulation and depletion.

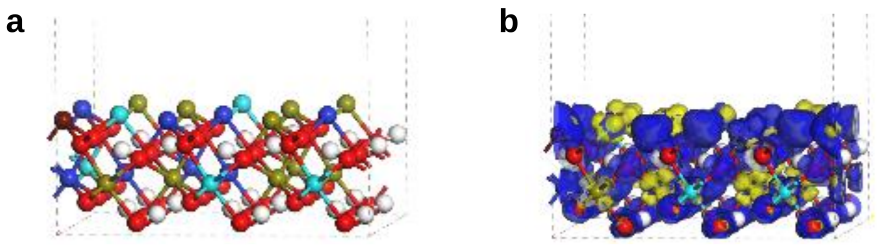

Figure 34. (a) Optimal theoretical model of FeNiPdWOOH and (b) CDD of FeNiPdWOOH surfaces. Blue and yellow contours represent electron accumulation and depletion.

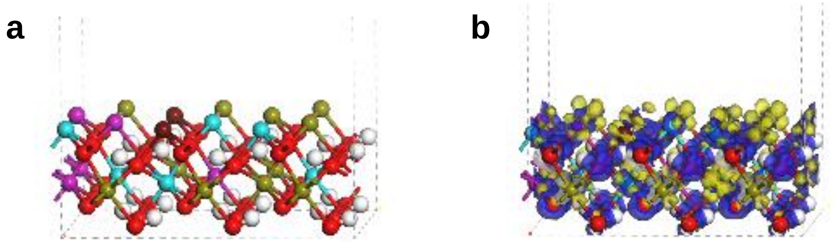

Figure 35. (a) Optimal theoretical model of CoNiPdWOOH and (b) CDD of CoNiPdWOOH surfaces. Blue and yellow contours represent electron accumulation

and depletion.

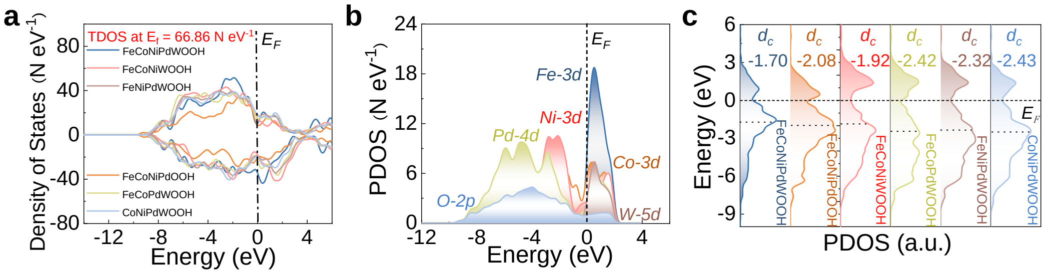

Figure 36. DFT calculation results. (a) TDOS of FeCoNiPdWOOH, FeCoNiPdOOH, FeCoNiWOOH, FeCoPdWOOH, FeNiPdWOOH, and CoNiPdWOOH. (b) PDOS of FeCoNiPdWOOH. (c) Electronic DOS of the d-band for the metal atoms in various models.

PDOS analysis was used to evaluate the adsorption behaviors over different sites. For the reactant OH^- species, during the initial adsorption process, s/p bands were down-shifted (**Figure 37**), indicating electron transfer from the surface sites to OH^- to stabilize adsorbed *OH. The improved adsorption capability favored the weakening of O-H bonds in *OH, thus triggering the subsequent dissociation processes. Compared with Fe, Co, and W sites, stronger p-d orbital couplings between the OH* and Ni/Pd sites were observed, which points to a more stable adsorption of OH* on the Ni/Pd sites within FeCoNiPdWOOH. This was experimentally demonstrated by the methanol probe molecule test of FeCoNiPdWP and FeCoNiWP in 1 M KOH and 1 M methanol, concluding that the presence of Pd significantly promoted the adsorption of OH^- species (**Figure 38**). CDD results also showed that Ni sites presented noticeable electron depletion with OH^- adsorption, demonstrating charge transfer during the adsorbing process (**Figure 39**). The ICOHP provides the number of bonded electrons between the selected metal and O atoms in the active *OH and the corresponding bonding strength. Notably, the ICOHPs of Ni and Pd are larger than those of Fe/Co/W, demonstrating stronger OH adsorption in the formers (**Figure 40**).

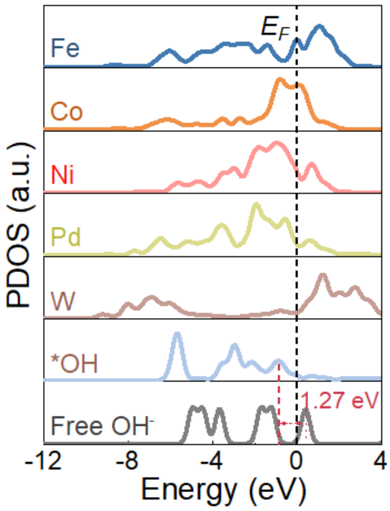

Figure 37. PDOS for OH adsorption at various active sites for FeCoNiPdWOOH.

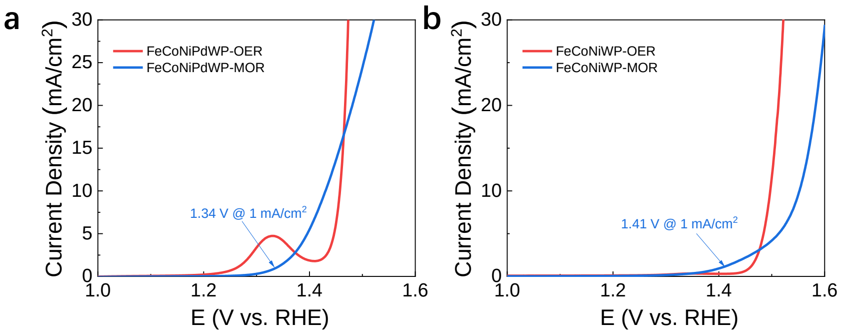

Figure 38. The OER and methanol oxidation reaction (MOR) LSV curves of (a) FeCoNiPdWP and (b) FeCoNiWP.

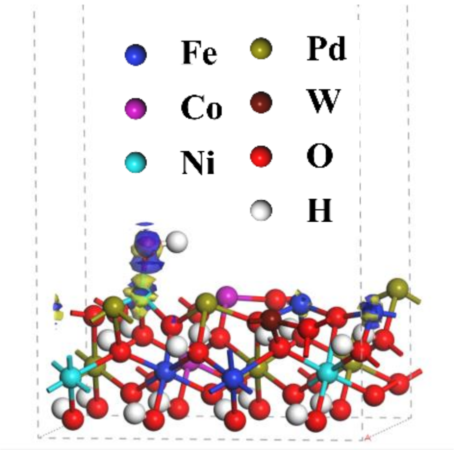

Figure 39. CDD of OH adsorption on Ni sites over the FeCoNiPdWOOH surface. Blue and yellow contours represent electron accumulation and depletion, where the isosurface is set to 0.05 e Å^{-3}.

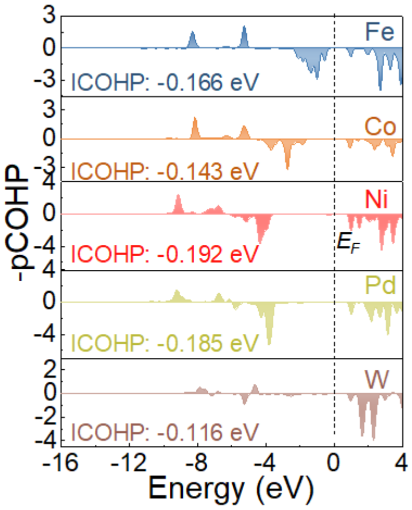

Figure 40. COHP bonding analysis of M-O interactions (M in the surface site over FeCoNiPdWOOH and O in adsorbed OH) for FeCoNiPdWOOH.

Gibbs free energies were calculated considering various potential metal active sites to reveal the energy barriers of adsorption/desorption of key intermediates. As shown in **Figure 41**, the energy barriers for each step among various active sites were quite different. For the Fe/Co/Ni sites in the FeCoNiPdWOOH model, the third step (formation of *OOH from *O with OH^- in the electrolyte) exhibited the largest barrier. On the other hand, for Pd and W sites, the energy barriers values slightly increased at the second step and first step, respectively. Accordingly, Fe/Co/Ni active sites exhibited lower η than those of Pd and W sites, respectively, under the equilibrium potential (1.23 eV, **Figure 42**). Thus, in FeCoNiPdWOOH, activity was associated with Fe/Co/Ni active sites, and the third reaction step was the RDS during the four-electron transfer process. To visualize the electronic environment during the reaction coordinates of OER, the PDOS of the most stable binding of key intermediates (*OH, *O, *OOH, and *O_2) is plotted in **Figure 43**. The s components of O-2p orbitals facilitated the electron transfer of sequential adsorbed intermediates. From the initial OH species to the final product O_2, the consecutive upshifting of the s orbitals demonstrates efficient electron transfer with low barriers for intermediate transformation, which is consistent with the highly efficient OER reaction trend.

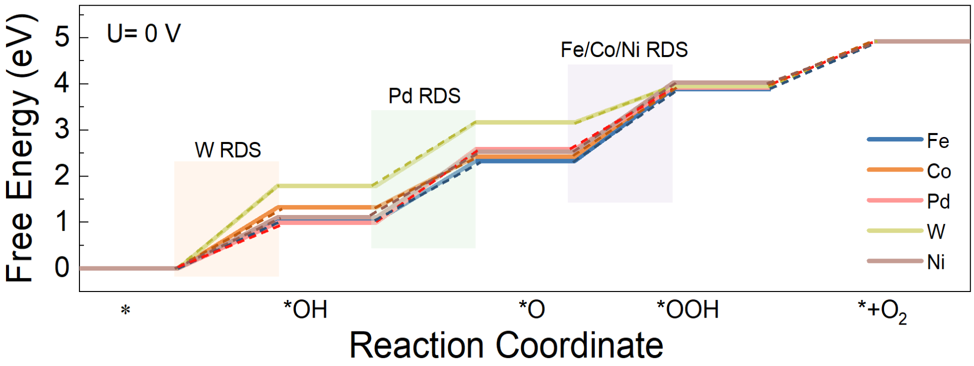

Figure 41. Standard free energy diagram of the OER process at 0 V of FeCoNiPdWOOH for various active sites.

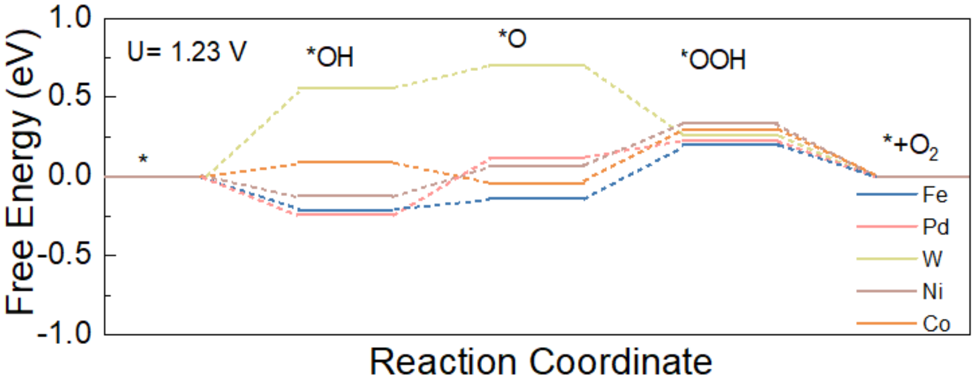

Figure 42. Standard free energy diagram of the OER process at 1.23 V of FeCoNiPdWOOH for various active sites.

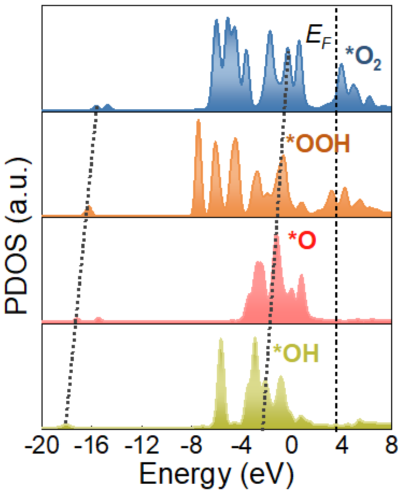

Figure 43. PDOS of key intermediates over Ni sites in FeCoNiPdWOOH.

Notably, all of the Fe, Co, and Ni sites on the FeCoNiPdWOOH model showed smaller energy barriers than within the other models, demonstrating the significant effect of all the elements in the reconstructed sample (**Figure 44**). Consequently, Fe/Co/Ni are identified as the main active sites for OER, which is consistent with the experimental results. In particular, the strong and positive effect of Pd was further demonstrated by DFT calculations over FeCoNiPdWOOH and Pd-free FeCoNiWOOH models. Pd benefits the electron transfer (**Figure 45,46**), optimization of adsorption configuration (**Figure 47**), and electron interaction between the oxygen intermediates (**Figure 48**). Overall, the synergistic effect of the multiple metal atoms, materialized through an efficient p-d orbital coupling and moderate d_c, optimized the adsorption/desorption of OER intermediates to promote OER kinetics.

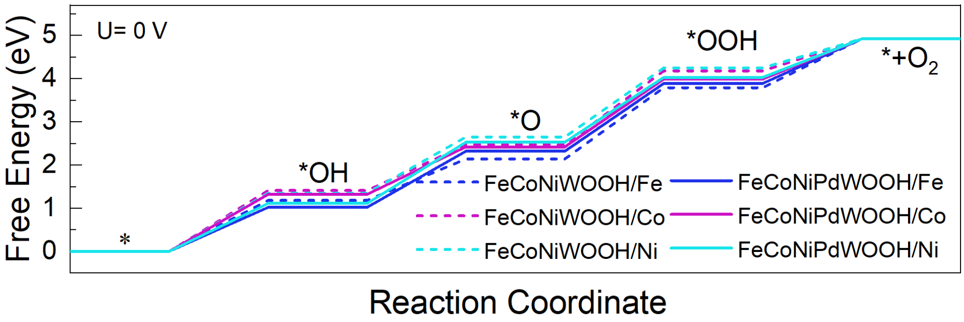

Figure 44. Standard free energy diagram of the OER process at 0 V of various active sites on the different surface-reconstructed samples.

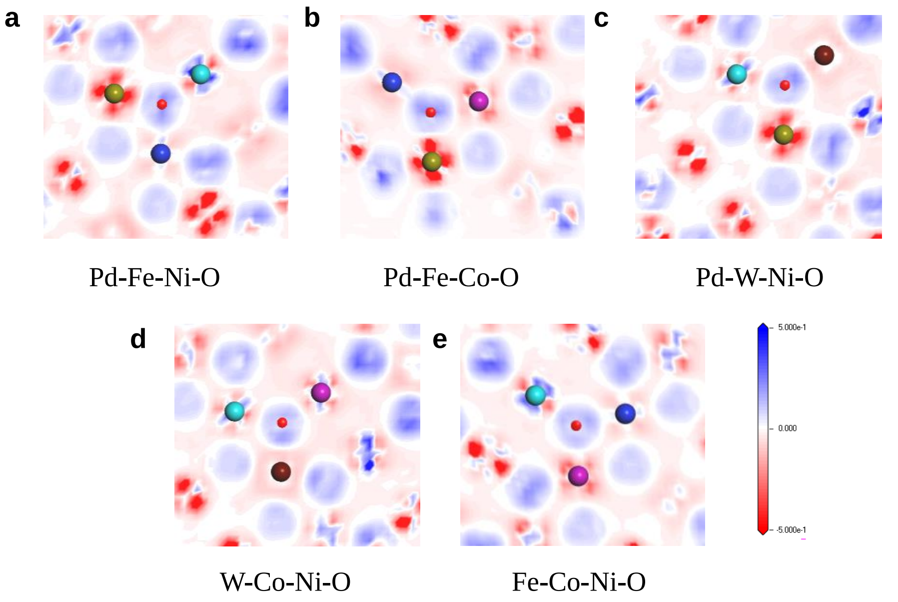

Pd-Fe-Ni-O

Pd-Fe-Co-O

Pd-W-Ni-O

W-Co-Ni-O

Fe-Co-Ni-O

Figure 45. 2D CDD of various M-O configurations in FeCoNiPdWOOH. (a) Pd-Fe-

Ni-O, (b) Pd-Fe-Co-O, (c) Pd-W-Ni-O, (d) W-Co-Ni-O, and (e) Fe-Co-Ni-O. Blue and red contours represent electron accumulation and depletion.

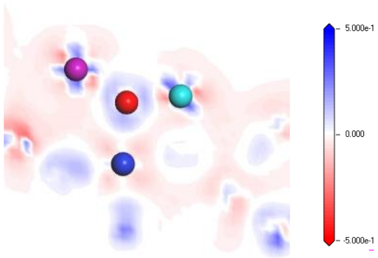

Fe-Co-Ni-O

Figure 46. 2D CDD of Fe-Co-Ni-O configurations in FeCoNiWOOH. Blue and red contours represent electron accumulation and depletion.

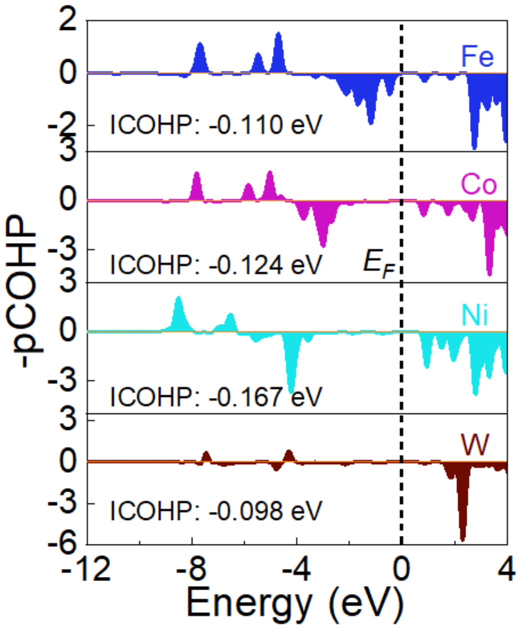

Figure 47. pCOHP bonding analysis of M-O interactions (M in the surface site over FeCoNiWOOH and O in adsorbed OH).

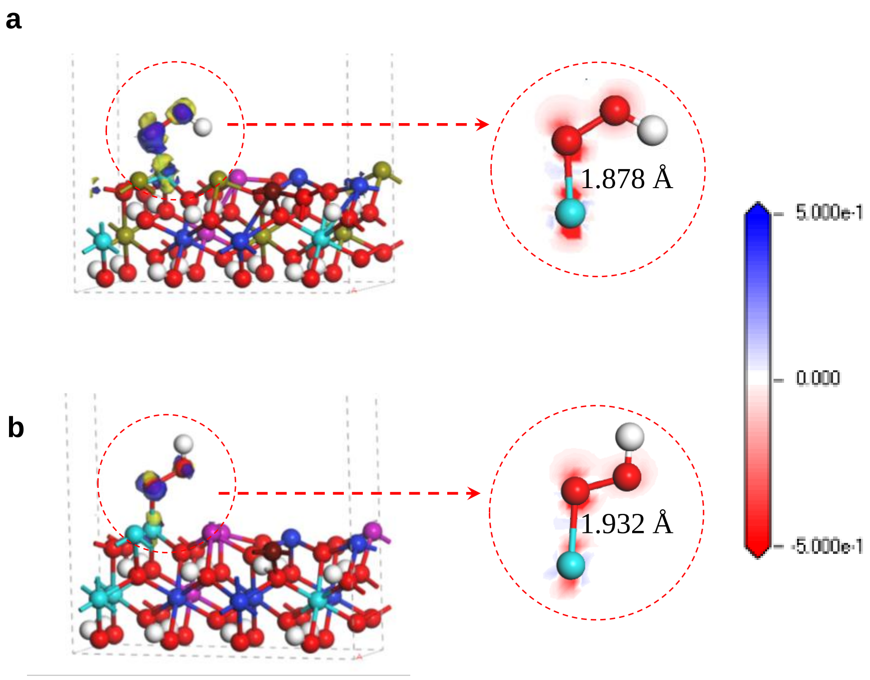

Figure 48. Adsorption configurations and charge analysis of OOH intermediates over (a) FeCoNiPdWOOH and (b) FeCoNiWOOH (b) surfaces. Blue and yellow (in 3D mode) / red (in 2D mode) contours represent electron accumulation and depletion.

2D CDD results show that Pd-containing M-O configurations (M=metal site; O=oxygen from the reconstructed HEOOH) within FeCoNiPdWOOH display more efficient site-to-site electron transfer than the Pd-free ones (**Figure 45,46**). The ICOHP values of the metal sites in FeCoNiPdWOOH are all larger than those of the Pd-free FeCoNiWOOH model (**Figure 47**), indicating the presence of Pd to optimize the adsorption configuration. As shown in **Figure 48**, the bond length of Ni-*OOH in FeCoNiPdWOOH (1.878 Å) is smaller than in FeCoNiWOOH (1.932 Å), indicating a stronger electronic interaction. The calculated CDD results suggest that *OOH adsorption on the FeCoNiPdWOOH surface resulted in a stronger local charge redistribution over the active sites than that of FeCoNiWOOH, causing more electron migration from the surface to the adsorbed *OOH species (supported by quantitative Mulliken charge analysis).

In summary, the FeCoNiPdWOOH reconstructed from FeCoNiPdW HEP is highly active towards OER. In the reconstructed phase, Ni and Pd are favorable for the initial hydroxide adsorption, facilitating the subsequent electron transfer reaction steps. Subsequently, Fe/Co/Ni as the main active sites having favorable OER reaction intermediate adsorption energies, due to their electronic modification by Pd and W. Furthermore, XAS revealed unusually high oxidation states of Fe (+3.1), Co (+3.3), and Ni (+3.8) during the OER, which is crucial to promote the OER reaction.[103-107]

4.4.6 ORR catalytic performance

HEPs were further evaluated towards the ORR in 0.1 M KOH using a RRDE. A large cathodic peak is observed when the electrolyte is saturated with O_2 compared with Ar, indicating a notable ORR electrochemical activity for the FeCoNiPdWP (**Figure 49a**). **Figure 49b** and **Figure 50,51** show the LSV curves with various rotation speeds in the range 400-2500 rpm for the different metal phosphides and a commercial Pd/C reference catalyst. As shown in **Figure 52**, the limiting diffusion current density for the metal phosphides complies with the trend of FeCoNiPdWP (5.37 mA cm^{-2}) > CoNiPdWP (4.37 mA cm^{-2}) > FeCoPdWP (2.77 mA cm^{-2}) > FeCoNiPdP (2.08 mA cm^{-2}) > FeNiPdWP (1.67 mA cm^{-2}). The $E_{1/2}$, extracted from the LSV curves at 1600 rpm, of the different metal phosphides follow the same trend as the limiting diffusion current density, with FeCoNiPdWP showing the highest value at 0.81 V. This value is very close to that obtained for Pd/C, at 0.82 V. When LSV curves are normalized to the quantity of Pd, FeCoNiPdWP and commercial Pd/C catalysts show similar $E_{1/2}$ but FeCoNiPdWP is characterized by a significantly higher current density (**Figure 53**). Overall, FeCoNiPdWP exhibits excellent ORR activity, matching that of Pd/C and state-of-the-art ORR catalysts, as shown in **Figure 54** and **Table 5**.[14,65,67,69,91,115-126] Besides, FeCoNiPdWP displays superior ORR stability with just a slight performance degradation after 5000 cycles (**Figure 55a**), implying much more stable cycling performance than the quaternary metal phosphides (**Figure 55 b-f**).

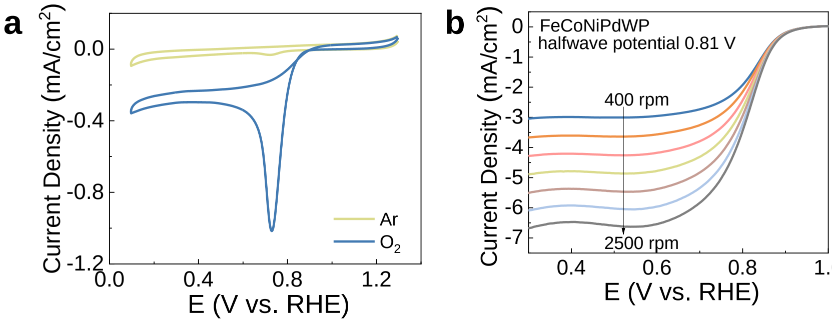

Figure 49. ORR performance. (a) CV curves measured in Ar and O_2 saturated electrolytes of FeCoNiPdWP. (b) LSV curves of FeCoNiPdWP at different rotation

speeds in the range 400–2500 rpm.

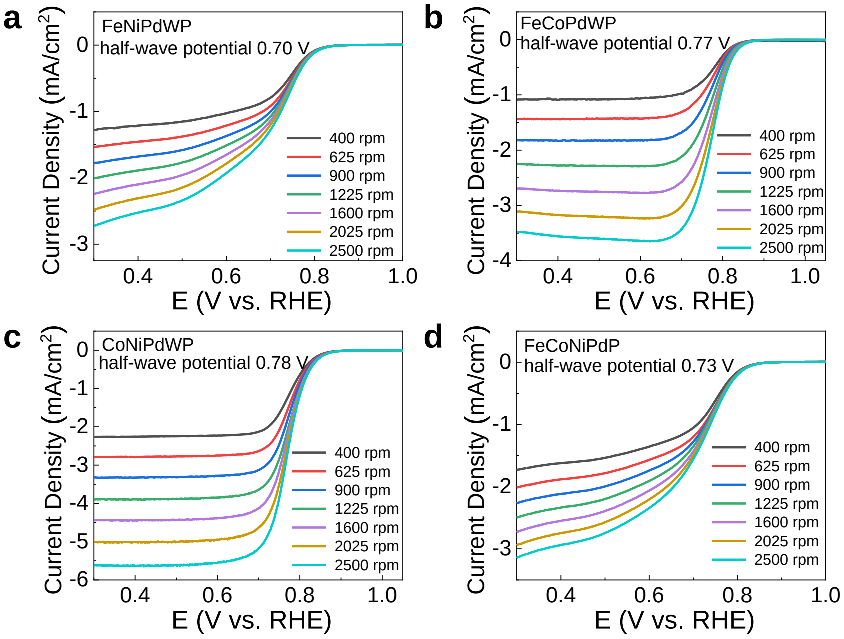

Figure 50. LSV curves at the scan rate of 10 mV s^{-1} of ORR with different rotation speeds from 400 to 2500 rpm by using RRDE electrode with the catalysts of (a) FeNiPdWP, (b) FeCoPdWP, (c) CoNiPdWP, and (d) FeCoNiPdP.

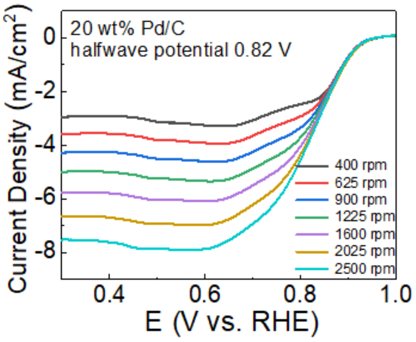

Figure 51. LSV curves at the scan rate of 10 mV s^{-1} of ORR with different rotation speeds from 400 to 2500 rpm by using RRDE electrode with the catalysts of Pd/C.

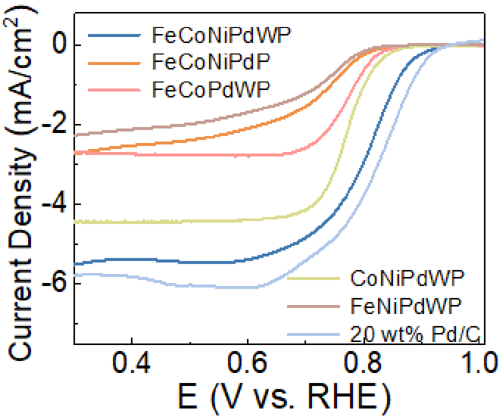

Figure 52. LSV curves at 1600 rpm for different metal phosphides and Pd/C catalysts.

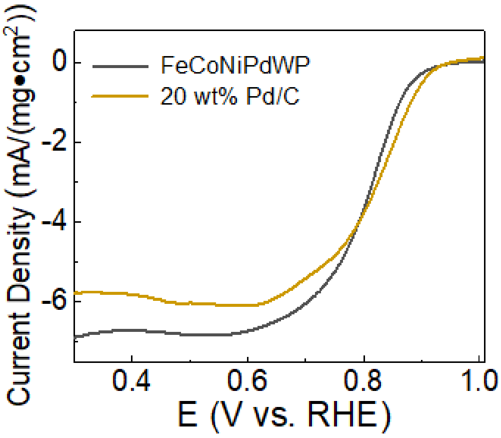

Figure 53. LSV curves at 1600 rpm normalized to the quality of Pd for the FeCoNiPdWP and commercial Pd/C catalysts.

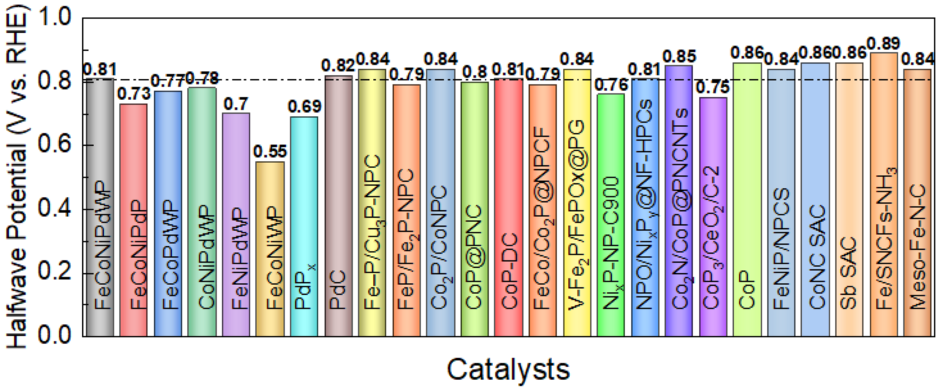

Figure 54. $E_{1/2}$ comparison between metal phosphides and Pd/C catalysts prepared in this work and recently reported state-of-the-art ORR catalysts.

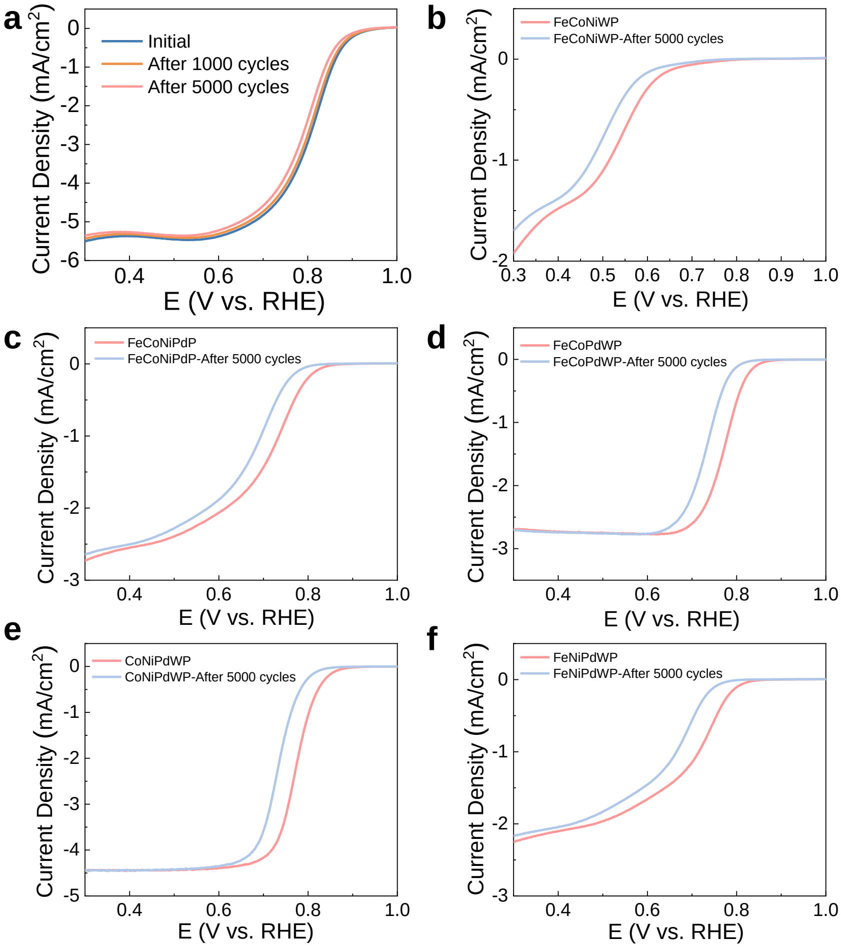

Figure 55. ORR stability test of (a) FeCoNiPdWP, (b) FeCoNiWP, (c) FeCoNiPdP, (d) FeCoPdWP, (e) CoNiPdWP, and (f) FeNiPdWP with different CV cycles.

4.4.7 HEP reconstruction during ORR

After the ORR stability test, the XRD main peak of HEPs is still visible, but it exhibits a broader half-width, indicating a loss of crystallinity or a reduction of the size of the HEP crystal domains during the ORR (**Figure 56**). High-resolution XPS spectra of FeCoNiPdWP HEPs after long-term ORR are displayed in **Figure 57**. The W 5d and Pd 5d XPS spectra display a unique contribution assigned to W-P and Pd-P chemical environments. On the other hand, the Fe 3d, Co 3d, and Ni 3d spectra display two coordination environments, M-P and M-O(H). Besides, as shown in **Figure 58**, the O 1s XPS spectrum displays two peaks, which are indexed to O-P bond and OOH, and the P 2p XPS spectrum shows two coordination environments, P-O and P-M. Besides, XPS spectra also show that during the ORR, the Fe, Co, and Ni metal ratios at the FeCoNiPdWP surface slightly increase (**Figure 59**). Additionally, the amount of P at the surface significantly decreases, from 16.5% to 11.0%, while that of oxygen increases, from 15.1% to 27.2%. EDS analysis confirms that the overall P content decreases after ORR, while that of O increases, and the overall content of the different metals remains mostly unchanged (**Figure 60**). Thus, a slight enrichment of the surface with the 3d elements, Fe, Co, and Ni, is inferred, which is again related to the higher affinity of these elements for oxygen and OH^- groups. Nevertheless, this enrichment is less abrupt than that obtained in the more oxidizing OER conditions. Besides, the lower applied voltages also result in a less oxidized HEP surface where Pd and W maintain the phosphide chemical environment. Within its experimental error, EDS elemental maps show that all the metals, P and O are homogeneously distributed at the particle level after the ORR reaction (**Figure 61**). However, AC-HRTEM single particle analyses reveal highly crystalline HEP cores surrounded by about 2 nm amorphous shells. The crystalline cores with a lattice distance of 2.39 Å match the (211) crystal plane of the rhombohedral $Pd_{15}P_2$ phase, corresponding to the main XRD peak at $2\theta = 39^\circ$ (**Figure 62**). According to XPS data, the amorphous shells are enriched with Fe, Co, and Ni in a hydroxide or oxyhydroxide chemical environment while also containing notable concentrations of W-P and Pd-P. The higher oxidation resistance of W-P and Pd-P during the ORR process is attributed to their stronger bond with shorter bond lengths, as calculated by DFT (**Figure 63**). Additionally, W and Pd exhibit greater stability due to more negative standard enthalpies [127-129] and possess much larger standard redox electrode potentials compared to Fe, Co, and Ni.

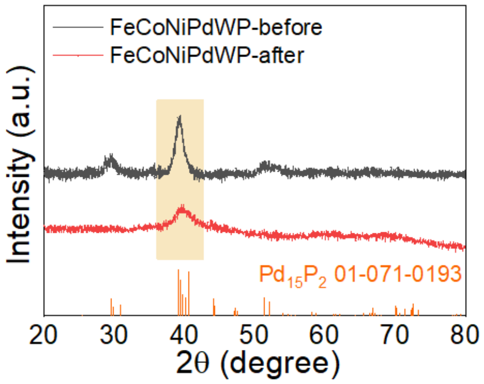

Figure 56. XRD pattern of FeCoNiPdWP before and after ORR stability measurement.

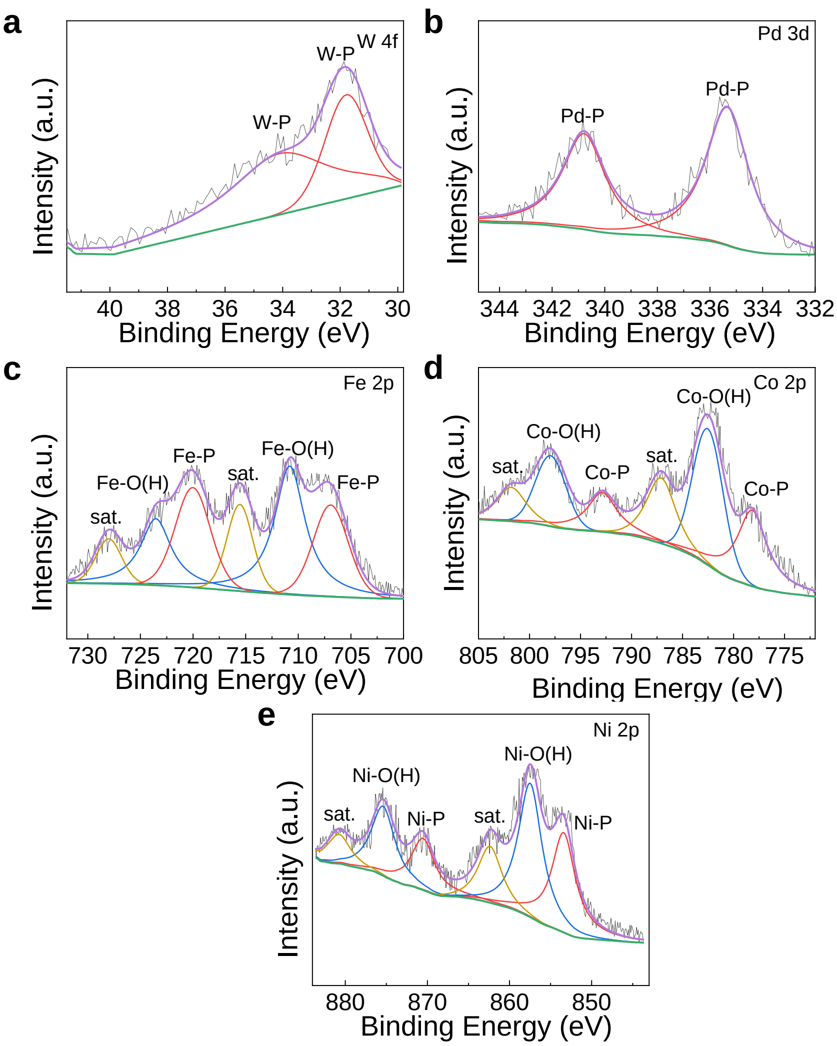

Figure 57. High-resolution (a) W 4f, (b) Pd 3d, (c) Fe 2p, (d) Co 2p, and (e) Ni 2p XPS spectra for FeCoNiPdWP after ORR stability test.

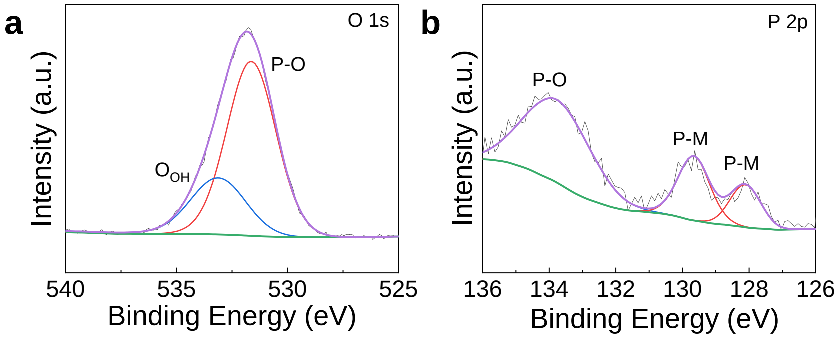

Figure 58. High-resolution (a) O 1s, and (b) P 2p XPS spectra for FeCoNiPdWP after ORR stability test.

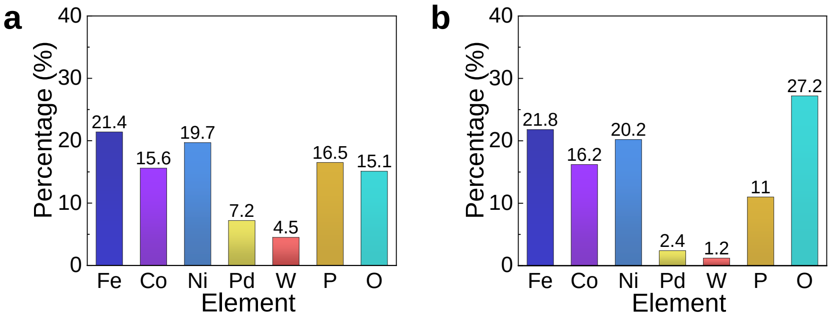

Figure 59. Elemental composition from XPS spectra of FeCoNiPdWP HEPs surface (a) before the ORR test, and (b) after the ORR test.

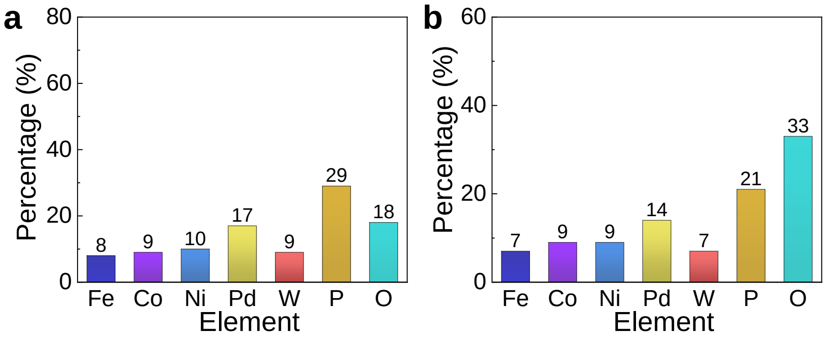

Figure 60. Elemental composition from EDS spectra of FeCoNiPdWP HEPs (a) before the ORR test, and (b) after the ORR test.

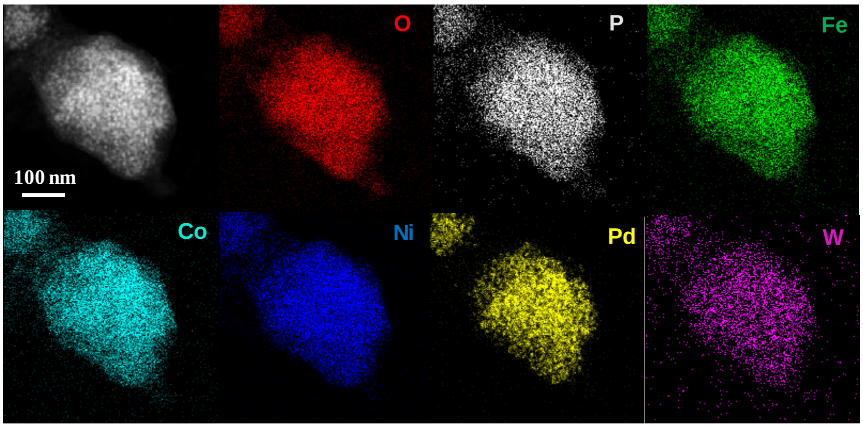

Figure 61. HAADF STEM micrograph and EDS compositional maps for each element of FeCoNiPdWP after ORR stability test.

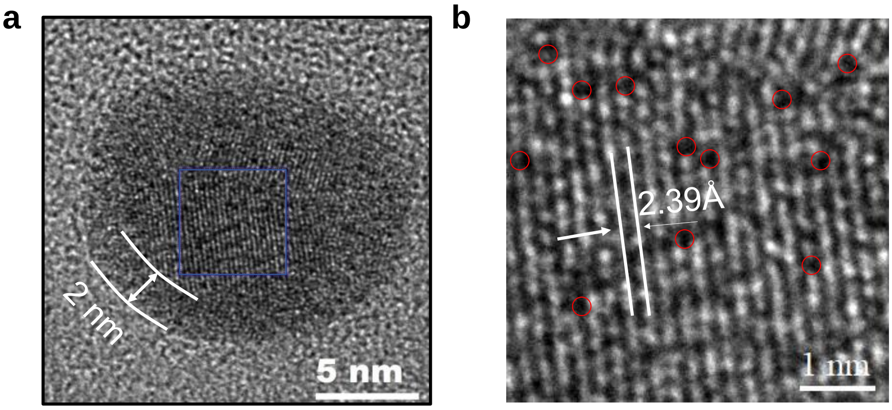

Figure 62. (a) AC-HRTEM image of a single NP of FeCoNiPdWP after ORR stability test. (b) The magnified image of the blue square in (a). The red circles mean the lattice defects after stability test. The lattice distance of 2.39 Å matches the (211) crystal plane of the rhombohedral $Pd_{15}P_2$ phase.

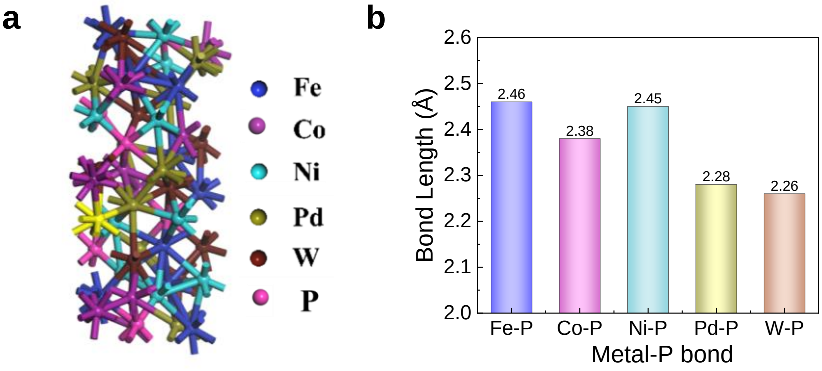

Figure 63. (a) The optimized model of FeCoNiPdWP. (b) The metal-P bond length.

4.4.8 HEP element roles in ORR

Electrochemical measurements were first used to investigate the different element roles in FeCoNiPdWP HEP for ORR. Without Pd, FeCoNiWP displays a very weak catalytic ability (**Figure 64 a,b**), demonstrating the key role played by Pd as an active ORR site. Besides, the $E_{1/2}$ of PdP_x is also relatively low, at 0.69 V (**Figure 65 a,b**). Thus, while Pd serves as the active site, it does not exhibit high catalytic ability within a PdP_x environment. This reinforces the importance of other metals-Fe, Co, Ni, and W-in enhancing and stimulating the catalytic ability of Pd sites within the phosphide environment. An ORR n over 3.9 is obtained for FeCoNiPdWP, CoNiPdWP, FeCoPdWP, PdP_x, and Pd/C, implying a 4-electron pathway (**Figure 64c, 65c and 66a**) at 0.5 V vs. RHE, where a stable limiting diffusion current density is measured. In contrast, FeCoNiPdP, FeNiPdWP, and FeCoNiWP are characterized by smaller n values, in the range 3.6-3.8, indicating the coexistence of the 4 electron and 2 electron pathways. The H_2O_2 yields further confirm the pathway assignment (**Figure 64d, 65d and 66b**). These results point at Pd, Co, and W as collectively assuming a more fundamental role in fine-tuning the reaction pathway, thereby amplifying the ORR performance of FeCoNiPdWP HEPs compared with the quaternary metal phosphides.

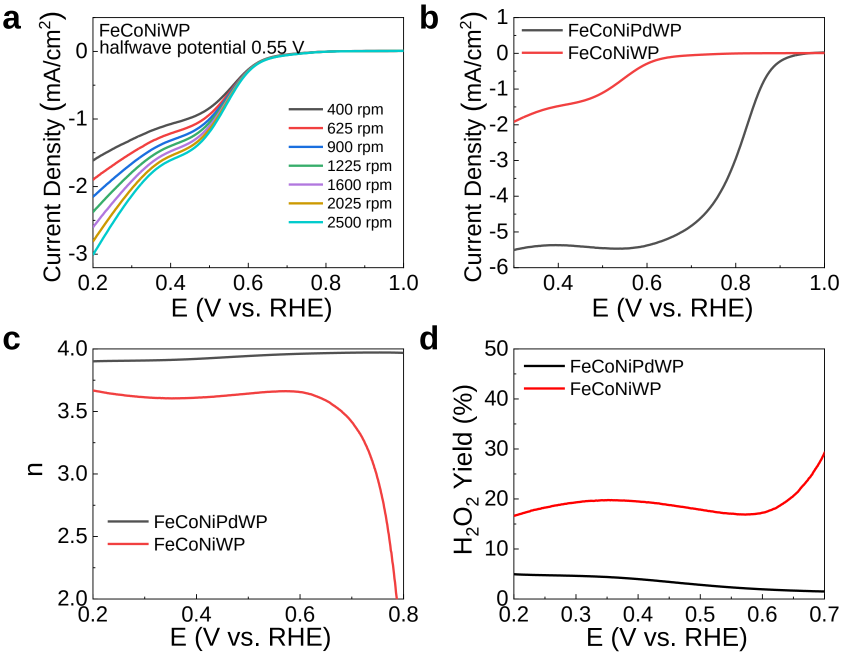

Figure 64. ORR performance. (a) LSV curves of FeCoNiWP at different rotation speeds from 400-2500 rpm. (b) LSV curves at 1600 rpm for FeCoNiWP and FeCoNiPdWP. (c) The calculated n and (d) H_2O_2 yield of FeCoNiWP and FeCoNiPdWP.

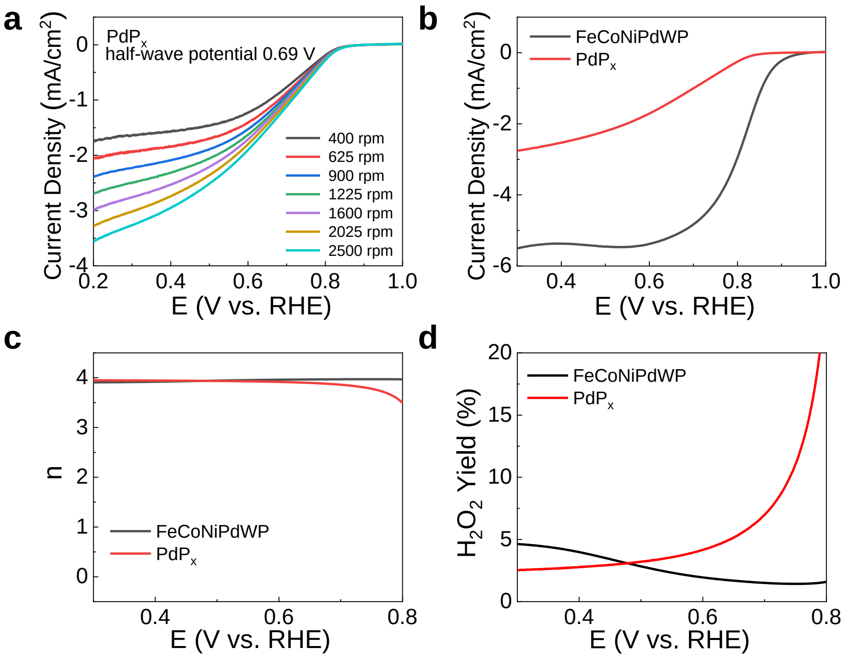

Figure 65. ORR performance. (a) LSV curves of PdP$_x$ at different rotation speeds from 400-2500 rpm. (b) LSV curves at 1600 rpm for PdP$_x$ and FeCoNiPdWP. (c) The calculated n and (d) H_2O_2 yield of PdP$_x$ and FeCoNiPdWP.

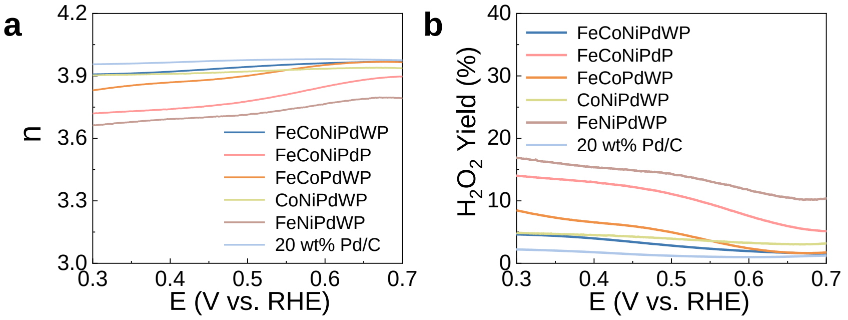

Figure 66. (a) The calculated n and (b) H_2O_2 yield of metal phosphides and Pd/C catalysts in the potential range from 0.3-0.7 V vs. RHE.

DFT calculations were further used to gain an understanding of the catalytic mechanism and element roles in the reconstructed HEPs during ORR. The reconstructed HEP model was built considering the experimental results, i.e. a HEP core with a ~2 nm shell rich in Fe, Co, and Ni in a hydroxide environment and Pd and W in a phosphide environment. We denote this reconstructed HEP as FeCoNiPdWPOH (**Figure 67**). In the PDOS spectra, the good overlap between different metal elements-d orbitals and with the O-p orbitals implies possible p-p/p-d/d-d orbital coupling, which might further promote electron transfer efficiency (**Figure 68**). Pd-4d orbitals not only show a deep position as an electron reservoir but also cover the d-orbitals of other metal sites, resulting in an efficient d-d coupling effect. This guaranteed the stable valence state of the reconstructed sample during the ORR. Although the W-5d orbitals are mostly located above the E_F, there is an evident peak near the E_F that offers a high probability of losing electrons. The Ni-3d orbitals are occupied near the E_F, which supports a high electroactivity. A strong overlap between Co-3d and Ni-3d orbitals promoted efficient electron transfer between Ni and Co sites. Fe-3d orbitals exhibited an obvious e_g–t_{2g} splitting of 3.42 eV, which provides potential efficient d-d orbital coupling between Fe and other metals. Meanwhile, the good overlap of the O-p orbitals with different metal elements implied possible p-p and p-d orbital coupling, which might further promote electron transfer efficiency.

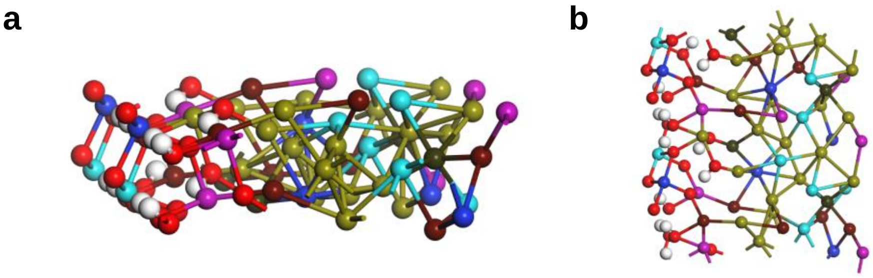

Figure 67. The proposed FeCoNiPdWPOH models. (a) Side view and (b) top view.

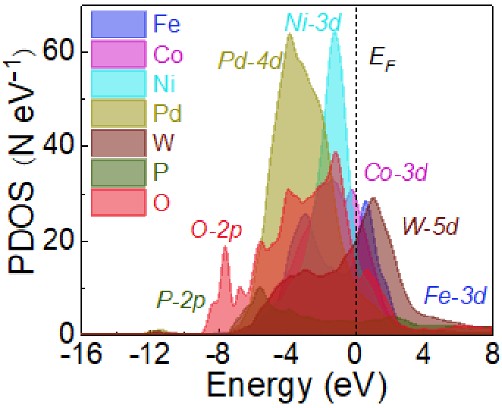

Figure 68. PDOS of FeCoNiPdWPOH.

The site-dependent PDOS of individual metal components located within or at the surface of the FeCoNiPdWPOH was also taken into consideration to appreciate their roles in the enhancement of ORR activity (**Figure 69a**). From the reconstructed

FeCoNiPdWPOH interior to the surface, the e_g-t_{2g} splitting of Fe-3d orbitals gradually decreased. The alleviated e_g-t_{2g} splitting could lead to higher valence states over the surface but also reduce the energy barrier of electron transfer from the electrocatalysts to the adsorbates to improve the ORR performance. Co sites displayed a site-independent electronic structure from the interior to the surface, which could endow the stable adsorption of intermediates and initial electroactive features during the ORR (**Figure 69b**). On the other hand, the Ni-3d and Pd-4d bands gradually approach the E_F from FeCoNiPdWPOH interior to the surface, suggesting improved electroactivity of the surface metal sites (**Figure 69c,d**). In contrast, the W-5d orbitals demonstrated an upshifting trend away from E_F, leading to decreasing valence states (**Figure 69e**). This compensation of the PDOS trend, facilitated by the W-5d orbitals, contributes to the high electroactivity of the Pd/Ni/Co/Fe surface sites.

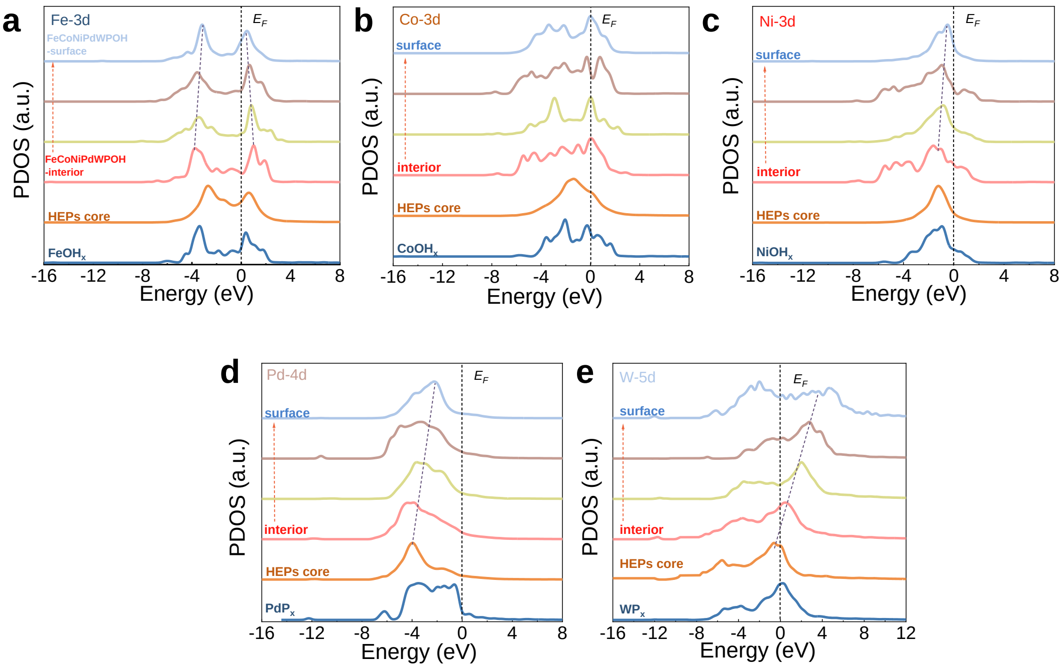

Figure 69. DFT calculations for ORR. (a)-(e) Site-dependent PDOSs of Fe, Co, Ni, Pd, and W sites in the FeCoNiPdWPOH structure.

The ORR Gibbs energy barrier at various metal sites in FeCoNiPdWPOH was also calculated. As shown in **Figure 70** and **Figure 71**, notably, among all of the various metal sites, Pd sites displayed the smallest energy barrier with just a 0.20 eV of the RDS for the conversion from *OOH to O*. Thus, Pd sites show the most thermodynamically favorable process, which is consistent with the experimental results.

In addition, the PDOS of key ORR intermediates displayed a gradual downshifting of the O-p orbitals, indicating the reduction trends and highly efficient intermediate conversions for FeCoNiPdWPOH (**Figure 72**).

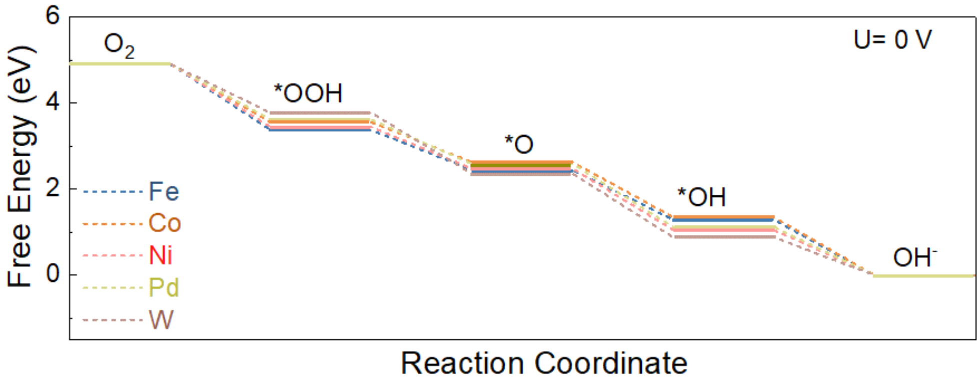

Figure 70. Standard free energy diagram of the ORR process at 0 V of various active sites on the surface-reconstructed samples.

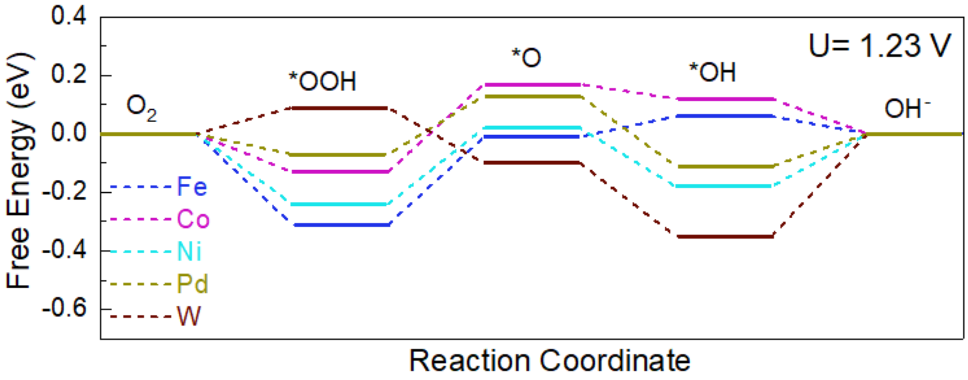

Figure 71. Standard free energy diagram of the ORR process at 1.23 V of various active sites on the surface-reconstructed samples.

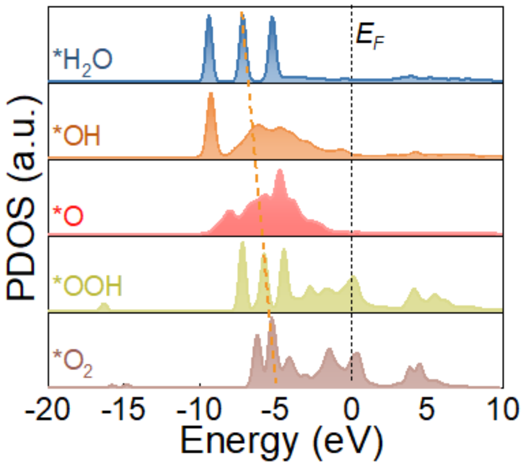

Figure 72. PDOS of key intermediates over Pd sites in FeCoNiPdWPOH.

O_2 adsorption results in strong local charge redistribution over the Pd active sites, causing electron migration from the surface to the adsorbed *O_2 species (**Figure 73**). The PDOS for adsorbed O_2 is down-shifted compared with that of the free O_2 (**Figure 74**), further revealing the strong interaction between the Pd sites and O_2. Besides, the final product H_2O could easily escape from the surface of FeCoNiPdWPOH (**Figure 75**). The adsorption and desorption ability of the oxygen intermediates for Pd sites can be modulated by the introduction of other metals, as determined by the optimum dc values (**Figure 76**).

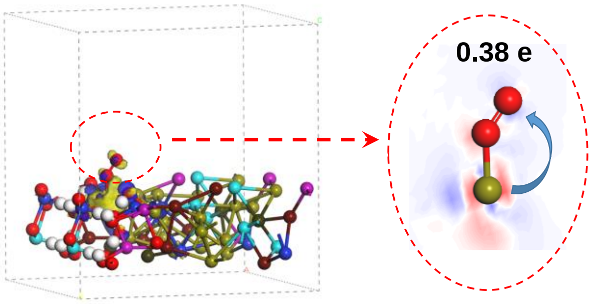

Figure 73. CDD analysis in the constructed FeCoNiPdWPOH model containing an O_2 molecule adsorbed at the Pd site. Blue and yellow (in 3D mode)/red (in 2D mode) contours represent the regions of electron accumulation and depletion, where the isosurfaces are set to 0.05 e Å^{-3}.

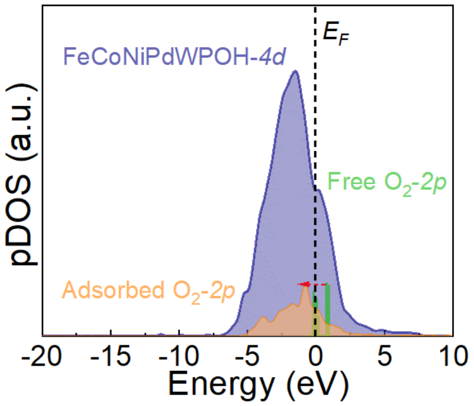

Figure 74. PDOS for a free (green) and adsorbed (orange) O_2 molecule (2p levels) on the surface of FeCoNiPdWPOH model.

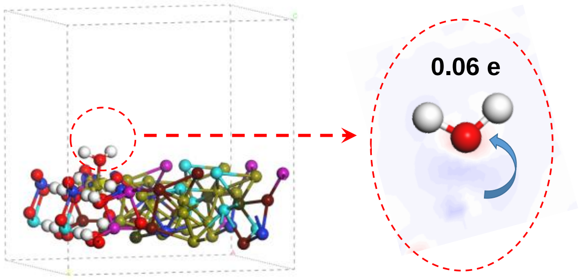

Figure 75. CDD analysis in the constructed FeCoNiPdWPOH model containing an H_2O molecule adsorbed at the Pd site. Blue and yellow (in 3D mode)/red (in 2D mode) contours represent the regions of electron accumulation and depletion, where the isosurfaces are set to 0.05 e Å^{-3}.

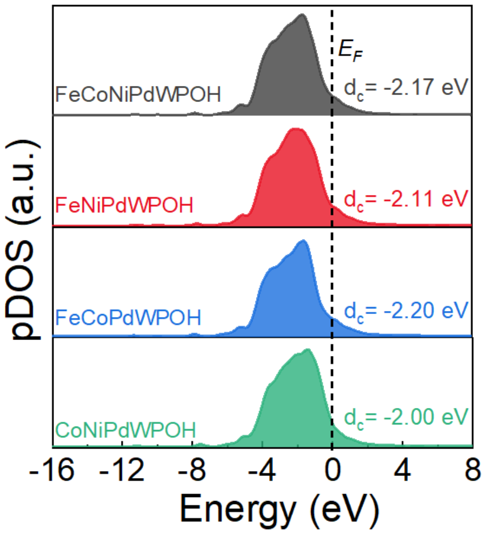

Figure 76. The PDOS of FeCoNiPdWPOH, FeNiPdWPOH, FeCoPdWPOH, and CoNiPdWPOH models. The d_c energy level is also shown.

Overall, FeCoNiPdWP shows excellent ORR performance with large limiting current density, high $E_{1/2}$, four electron-transfer pathways, and long-term cycling performance. In FeCoNiPdWP, Pd was found to be the most active element among the five metals within the reconstructed FeCoNiPdWPOH leading to the excellent ORR catalytic performance. The strong d-d orbital coupling of different elements, especially Pd, Co, and W, fine-tunes ORR electron transfer pathways and the surface electron modulation of Pd with other metal elements decreases the energy barrier during the ORR.

4.4.9 HEPs as bifunctional oxygen catalysts

A key performance parameter to evaluate the oxygen bifunctional catalytic performance is the E_{gap}. A smaller E_{gap} value implies a better bifunctional performance, thus enabling ZABs with higher charge/discharge energy efficiency. Due to the excellent OER and ORR performance, the reconstructed FeCoNiPdWP shows an extremely low E_{gap} value of 0.65 V in 0.1 M KOH, much lower than the combination of the benchmark OER and ORR catalysts, Pd/C and RuO_2, resulting in an E_{gap} of 0.75 V (**Figure 77a**). Besides, the FeCoNiPdWP exhibits an outstanding low bifunctional E_{gap} compared with state-of-the-art bifunctional oxygen catalysts, as shown in **Figure 77b** and **Table 6**.[4, 65, 67, 69,90, 121, 122, 124, 125, 130-134] The remarkable dual functionality of the reconstructed FeCoNiPdWP in both OER and ORR can be attributed to the distinct contributions and cooperative interactions of each metal involved. While OER and ORR typically necessitate varying strengths in binding with the oxygen intermediates, the distinctive roles played by each element within the reconstructed FeCoNiPdWP transcend these conventional constraints. In the OER process, Fe, Co, and Ni emerge as the primary active sites, whereas in ORR, Pd takes on the leading role, complemented by the involvement of Co and W in modulating the electron transfer pathway. The different metal elements play distinctive roles in OER and ORR, respectively, and their synergistic interaction maximizes the performance of the resulting HEM.

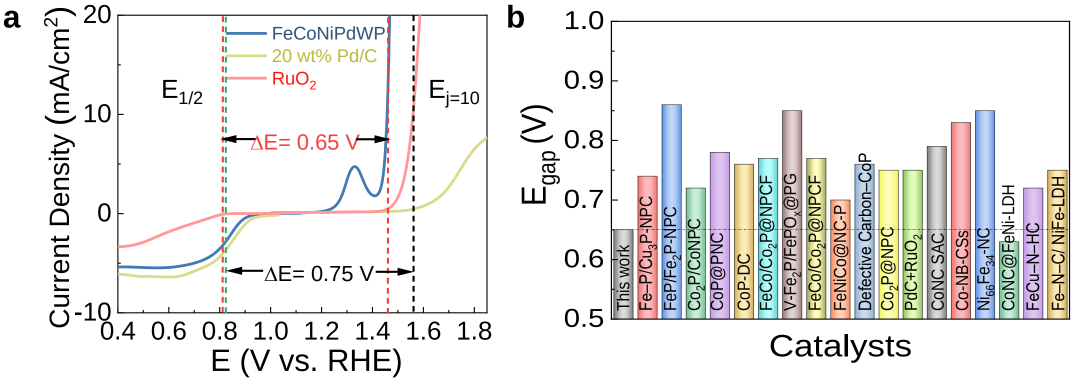

Figure 77. Oxygen bifunctional properties. (a) ORR/OER bifunctional LSV curves of different electrodes. (b) Comparison of the E_{gap} values of FeCoNiPdWP and other state-of-the-art bifunctional oxygen catalysts.

Table 6. E_{gap} comparison of FeCoNiPdWP with recently reported excellent bifunctional oxygen catalysts.

Catalyst	E_{gap} (V)	Ref.
Fe–P/Cu_3P-NPC	0.74	*Small*, **2023**, 2301985
FeP/Fe_2P-NPC	0.86	*Small*, **2023**, 2301985
Co_2P/CoNPC	0.72	*Adv. Mater.*, **2020**, 32, 2003649
CoP@PNC	0.78	*Energy Storage Mater.*, **2020**, 28, 27–36
CoP-DC	0.76	*Adv. Energy Mater.*, **2018**, 8, 1703623
FeCo/Co_2P@ NPCF	0.77	*Adv. Energy Mater.*, **2020**, 10, 1903854
V-Fe_2P/$FePO_x$@PG	0.85	*Appl. Catal. B-environ.*, **2023**, 331, 122674
FeNiCo@NC-P	0.70	*Adv. Funct. Mater.*, **2020**, 30, 1908167
Defective Carbon–CoP	0.76	*Adv. Energy Mater.*, **2018**, 8, 1703623
Co_2P@NPC	0.75	*Energy Environ. Mater.*, **2022**, 5, 515-523
CoNC SAC	0.79	*Sci. Adv.*, **2022**, 8, eabn5091
Co-NB-CSs	0.83	*ACS Nano*, **2018**, 12, 1894–1901
$Ni_{66}Fe_{34}$-NC	0.85	*Appl. Catal. Environ.*, **2020**, 274, 119091

CoNC@FeNi-LDH	0.63	*Adv. Mater.*, **2021**, 33, 2008606
FeCu–N–HC	0.72	*Adv. Funct. Mater.*, **2021**, 31, 2006533
Fe–N–C/NiFe-LDH	0.75	*Energy Environ. Sci.*, **2016**, 9, 2020
PdC+RuO_2	***0.75***	***This work***
FeCoNiPdWP	***0.65***	***This work***

4.4.10 ZAB performance

FeCoNiPdWP was then used as the oxygen cathode in aqueous rechargeable ZABs. Reference ZABs were also assembled with a combination of 20 wt% Pt/C and RuO_2 (Pt/C&RuO_2) as the cathode. **Figure 78a** shows a schematic of the ZAB architecture. As shown in **Figure 78b**, the ZAB with the FeCoNiPdWP-based air cathode exhibits an OCP of 1.60 V, which is 96.4% of the theoretical limit (1.66 V) and higher than that of the reference Pt/C&RuO_2-based ZAB at 1.56 V. The high OCP values could light a red-screen LED, proving its potential for practical application. The peak power density of the FeCoNiPdWP HEPs-based ZAB is 123 mW cm^{-2}, significantly above that of the Pt/C&RuO_2-based ZAB at 111 mW cm^{-2} (**Figure 78c**). The specific capacity and energy density of the FeCoNiPdWP-based ZAB are 886 mA h gZn^{-1} and 1063.2 mW h gZn^{-1} at a current density of 8 mA cm^{-2}, higher than those of the Pt/C&RuO_2-based ZAB at 793 mA h gZn^{-1} and 911.9 mWh gZn^{-1} (**Figure 78d**). The higher specific capacity and energy density are directly attributed to the improved ORR performance of the FeCoNiPdWP-based air cathode, which is the primary factor limiting the discharge process. The FeCoNiPdWP-based ZAB not only excels in performance compared with the reference ZAB tested here but also stands out when compared with state-of-the-art ZABs (**Table 7**).[14, 65, 67, 69, 116, 118, 111, 112, 132, 135-145]

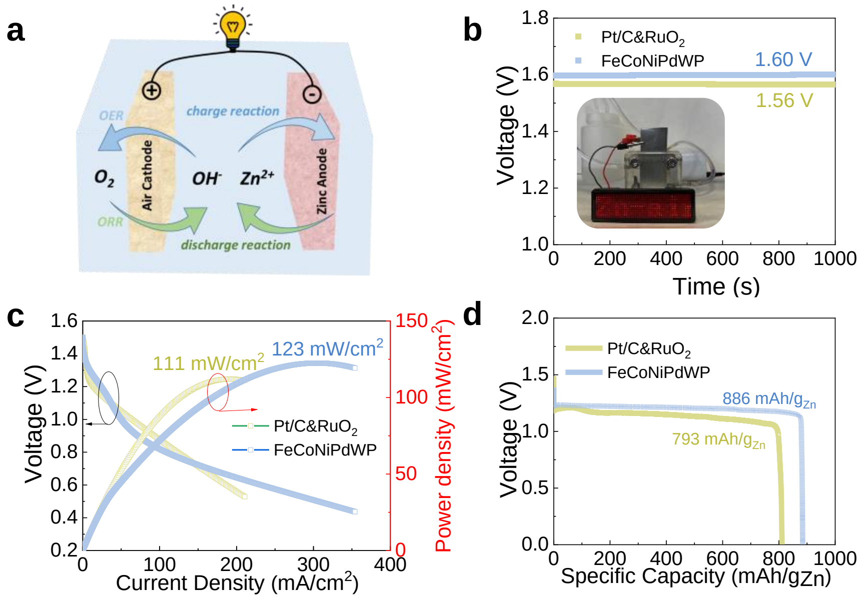

Figure 78. (a) ZAB schematic diagram. (b) OCP measurements, (c) power density plots, and (d) specific capacity comparisons between a FeCoNiPdWP- and a Pt/C&RuO_2-based ZAB. Photograph of a red LED screen powered by a FeCoNiPdWP-based ZAB is also shown in (b).

Table 7. Comparison of the ZAB performances obtained using state-of-the-art air cathodes.

Catalyst & Reference	OCP (V)	Peak power density (mW cm^{-2})	Specific capacity (mAh g_{Zn}^{-1}) @ (mA cm^{-2})	Cycling durability (h) @ (mA cm^{-2})	Ref.
Fe–P/Cu_3P-NPC	1.39	70.8	815@ 10	81@2; 27@5	*Small*, **2023**, 2301985
Co_2P/CoNPC	1.43	116	-	60@10	*Adv. Mater.*, **2020**, 32, 2003649
CoP@PNC	-	138.57	730.5@10	175@30	*Energy Storage Mater.*, **2020**, 28, 27-36
FeCo/Co_2P@NPCF	1.44	154	-	107@10	*Adv. Energy Mater.*, **2020**, 10, 1903854

V-Fe$_2$P/FePO$_x$@PG	1.42	137	642.7@5	600@5	*Appl. Catal. B-environ.*, **2023**, 331, 122674
Co$_2$N/CoP@PNCNTs	1.07	-	823.8	150@10	*Small*, **2022**, 18, 2108094
CoP$_3$/CeO$_2$/C-2	1.34	150	767.7@5	120@5	*Appl. Catal. B-environ.*, **2023**, 321, 122029
FeNiP/NPCS	1.51	163	783.5@10	180@10	*Chem. Eng. J.*, **2020**, 389, 124408
CoP-NC@NFP	1.44	93	-	200@2	*Chem. Eng. J.*, **2022**, 428, 131115
Co/Co$_x$M$_y$ +Pt/C	1.43	125	-	166.7@10	*Small*, **2019**, 15, 1901518
CoP$_x$@CNS	1.40	110	-	130@5	*Angew. Chem. Int. Ed.*, **2020**, 59, 21360-21366
FeNiCo@NC-P	1.36	112	807@10	130@10	*Adv. Funct. Mater.*, **2020**, 30, 1908167
Co-SAs@NC	1.46	105.3	897@20	85@10	*Angew. Chem. Int. Ed.*, **2019**, 58, 5359
Co/Co–N–C	1.41	132	-	330@10	*Adv. Mater.*,**2019**, 31, 1901666
Fe/OES	1.51	186.8	807@5	130@5	*Angew. Chem. Int. Ed.*, **2020**, 132, 7454
Fe–N–C–rich pyrolysis free COF network	1.41	145	784@5	300@5	*Sci. Adv.*, **2019**, 5, eaaw2322

Ni$_x$Fe$_{100x}$-NC	1.44	140	765@10	334@10	*Appl. Catal. B,* **2020**, 274, 119091
Fe-N-C/N-OMC	-	113	711@10	66@10	*Appl. Catal. B,* **2021**, 280, 119411
Fe-Nx-C	1.49	96.4	641@5	300@5	*Adv. Funct. Mater.,* **2019**, 29, 1808872
TMB@NiNC	1.47	107	765.6@10	222@10	*Adv. Energy Mater.,* **2023**, **13**, 2203002
FeCo/FeCoNi@NC NTs-HF	1.48	156.2	783@5	240@5	*Appl. Catal., B,* **2019**, 254, 26-36
NiFeLDH/CFP	-	93.9	800@25	333@5	*Adv. Mater.,* **2022**, 32, 1908488
CuCo$_2$S$_4$ NSs@N-CNFs	1.46	232	896@25	100@5	*Adv. Sci.,* **2019**, 6, 1900628
Co-NiO NFs	1.45	93	830@5	110@2	*Appl. Catal. B,* **2019**, 250, 71-77
2019FeN$_4$CB	1.44	177	800	220@10	*J Energy Chem.,* **2020**, 66, 514-524
FeCoNiPdWP	***1.60***	***123***	***886@8***	***700@8***	***This work***

The rate performance of the FeCoNiPdWP-based ZAB was further evaluated. As shown in **Figure 79,80**, the FeCoNiPdWP-based ZAB exhibits stable charge-discharge curves at the current density of 2-18 mA cm^{-2}, with an energy efficiency in the range of 70-50%.

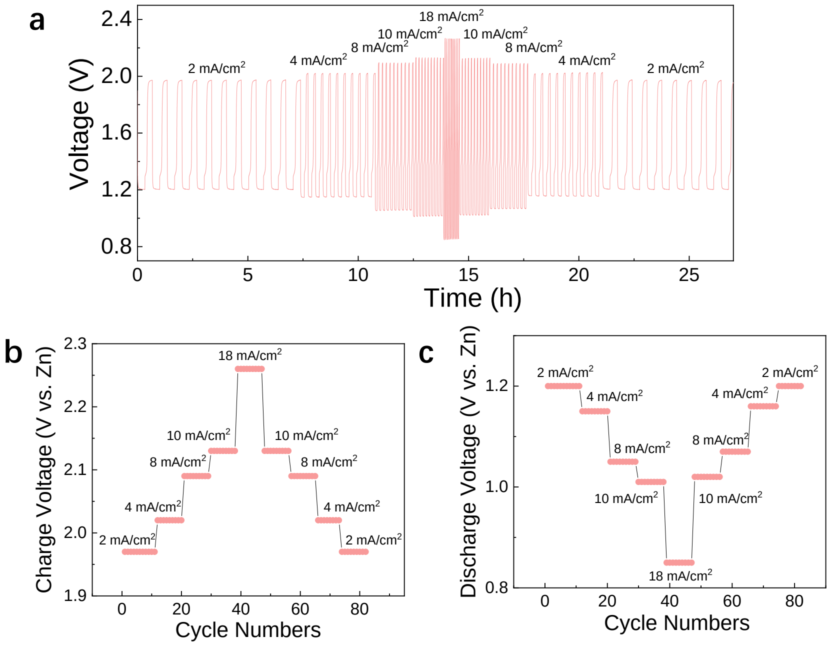

Figure 79. Rate performance of FeCoNiPdWP-based ZABs. (a) Chare-discharge curves, (b) charge voltage, and (c) discharge voltage at different current rates.

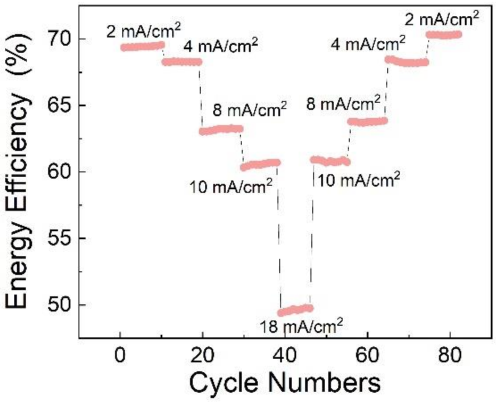

Figure 80. Energy efficiency of FeCoNiPdWP-based ZABs at different current rates.

The long-term stability of the ZABs was also measured with continuous charge/discharge cycles at a current density of 8 mA cm^{-2}. As shown in **Figure 81a**, the FeCoNiPdW-based ZAB can be stable over 700 h, i.e. 1 month, of continuous cycling (over 2000 cycles). In contrast, the Pt/C&RuO$_2$-based ZAB is stable for just about 100 h, i.e. 300 cycles. **Figure 81b** shows the enlarged galvanostatic discharge-charge cycles of FeCoNiPdWP HEPs-based ZABs at the specific cycles at 1st, 200th, 500th, 1000th, and 2000th cycles. The initial charging/discharging potential gap is 1.0 V. With continuous cycling, the potential gap is decreased to 0.97 V at 200 cycles, and it remains in the range of 0.95-0.96 V after 1000-2000 cycles, further proving its good stability.

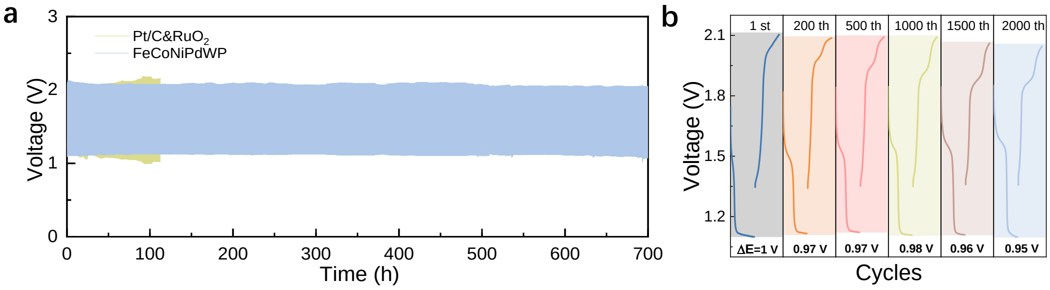

Figure 81. (a) Galvanostatic discharge–charge curves with 10 min discharge and 10 min charge cycles at a current density of 8 mA cm^{-2} of FeCoNiPdWP- and Pt/C&RuO_2-based ZABs. (b) Enlarged galvanostatic discharge-charge cycles at the specific cycles (1st, 200th, 500th, 1000th, 1500th, and 2000th) for 20 min of the FeCoNiPdWP-based ZAB.

4.5 Conclusions

FeCoNiPdWP HEP NPs were synthesized using a mild colloidal method and tested as bifunctional OER/ORR catalysts. These HEPs demonstrated exceptional OER performance, with a low η of 227 mV at 10 mA cm^{-2} and a Tafel slope of 33 mV dec^{-1}. The outstanding OER performance is attributed to a reconstructed FeCoNiPdWOOH surface rich in high-oxidation state Fe, Co, and Ni (Fe = 3.1; Co = 3.3; Ni = 3.8) as main active sites, Pd aiding in OH^- adsorption, and W optimizing oxygen intermediate adsorption via electronic structure modulation. For ORR, FeCoNiPdWP HEPs show a $E_{1/2}$ of 0.81 V and efficient four-electron transfer pathways. During ORR, the surface of the HEP was also slightly enriched in Fe, Co, and Ni and reconstructed into a FeCoNiPdWPOH, with Fe/Co/Ni found as oxyhydroxides but with Pd and W maintaining the phosphide chemical environment as observed by XPS analysis. This unique FeCoNiPdWPOH surface, together with the active role of Pd and the influence of Co and W in modulating the electron transfer pathways, significantly enhances the ORR performance. Overall, each element within FeCoNiPdWP HEPs plays a crucial role in enhancing both OER and ORR performances. The combination of all these elements playing distinctive roles and the switchable active sites in redox reactions transcends the usual constraints of bifunctional catalysts, which generally excel in only one of these reactions. As a result, FeCoNiPdWP shows an extremely low E_{gap} value of 0.65 V and FeCoNiPdWP-based ZABs exhibit outstanding performance and stability for over 700 h. This work provides a platform to understand the different surface reconstruction behaviors of HEP catalysts and the distinct element roles in OER and ORR reactions, which paves the way for designing advanced bifunctional oxygen catalysis, potentially based on HEMs.

4.6 References

[1] X. Zhu, C. Hu, R. Amal, L. Dai and X. Lu, *Energy Environ Sci*, **2020**, 13, 4536-4563.

[2] J. N. Liu, C. X. Zhao, D. Ren, J. Wang, R. Zhang, S. H. Wang, C. Zhao, B. Q. Li and Q. Zhang, *Adv Mater*, **2022**, 34, e2109407.

[3] W. Niu, Z. Li, K. Marcus, L. Zhou, Y. Li, R. Ye, K. Liang and Y. Yang, *Adv Energy Mater*, **2018**, 8, 1701642.

[4] C. X. Zhao, J. N. Liu, J. Wang, D. Ren, J. Yu, X. Chen, B. Q. Li and Q. Zhang, *Adv Mater*, **2021**, 33, e2008606.

[5] T. Binninger and M. L. Doublet, *Energy Environ Sci*, **2022**, 15, 2519-2528.

[6] J. Chen, M. Aliasgar, F. B. Zamudio, T. Zhang, Y. Zhao, X. Lian, L. Wen, H. Yang, W. Sun, S. M. Kozlov, W. Chen and L. Wang, *Nat Commun*, **2023**, 14, 1711.

[7] M. Liu, Z. Zhao, X. Duan and Y. Huang, *Adv Mater*, **2019**, 31, e1802234.

[8] J. Zhang, J. Lian, Q. Jiang and G. Wang, *Chemical Engineering Journal*, **2022**, 439, 135634.

[9] C. Tang, H. S. Wang, H. F. Wang, Q. Zhang, G. L. Tian, J. Q. Nie and F. Wei, *Adv Mater*, **2015**, 27, 4516-4522.

[10] L. Gui, Z. Wang, K. Zhang, B. He, Y. Liu, W. Zhou, J. Xu, Q. Wang and L. Zhao, *Appl Catal B*, **2020**, 266, 118656.

[11] C. Li, M. Wu and R. Liu, *Appl Catal B*, **2019**, 244, 150-158.

[12] J. Zhang, T. Wang, D. Pohl, B. Rellinghaus, R. Dong, S. Liu, X. Zhuang and X. Feng, *Angew Chem Int Ed*, **2016**, 55, 6702-6707.

[13] X. Jia, Y. Zhao, G. Chen, L. Shang, R. Shi, X. Kang, G. I. N. Waterhouse, L. Z. Wu, C. H. Tung and T. Zhang, *Adv Energy Mater*, **2016**, 6, 1502585.

[14] J. Li, Y. Kang, Z. Lei and P. Liu, *Appl Catal B*, **2023**, 321, 122029.

[15] L. Yang, X. Zeng, D. Wang and D. Cao, *Energy Storage Mater*, **2018**, 12, 277-283.

[16] B. Q. Li, C. X. Zhao, S. Chen, J. N. Liu, X. Chen, L. Song and Q. Zhang, *Adv Mater*, **2019**, 31, e1900592.

[17] Y. Zhang, H. Jiang, Y. Lin, H. Liu, Q. He, C. Wu, T. Duan and L. Song, *Adv Mater Interfaces*, **2018**, 5, 1800392.

[18] Y. Mei, Y. Feng, C. Zhang, Y. Zhang, Q. Qi and J. Hu, *ACS Catal*, **2022**, 12, 10808-10817.

[19] J. Kwon, S. Sun, S. Choi, K. Lee, S. Jo, K. Park, Y. K. Kim, H. B. Park, H. Y. Park, J. H. Jang, H. Han, U. Paik and T. Song, *Adv Mater*, **2023**, 35, e2300091.

[20] H. Zhu, S. Sun, J. Hao, Z. Zhuang, S. Zhang, T. Wang, Q. Kang, S. Lu, X. Wang, F. Lai, T. Liu, G. Gao, M. Du and D. Wang, *Energy Environ Sci*, **2023**, 16, 619-628.

[21] T. A. A. Batchelor, J. K. Pedersen, S. H. Winther, I. E. Castelli, K. W. Jacobsen and J. Rossmeisl, *Joule*, **2019**, 3, 834-845.

[22] Y. Chida, T. Tomimori, T. Ebata, N. Taguchi, T. Ioroi, K. Hayashi, N. Todoroki and T. Wadayama, *Nat Commun*, **2023**, 14, 4492.

[23] A. Ostovari Moghaddam, A. Cabot and E. A. Trofimov, *Int J Refract Met H*, **2021**, 97, 105504.

[24] R. He, L. Yang, Y. Zhang, D. Jiang, S. Lee, S. Horta, Z. Liang, X. Lu, A. O. Moghaddam, J. Li, M. Ibanez, Y. Xu, Y. Zhou and A. Cabot, *Adv Mater*, **2023**, 35, e2303719.

[25] R. He, L. Yang, Y. Zhang, X. Wang, S. Lee, T. Zhang, L. Li, Z. Liang, J. Chen, J. Li, A. Ostovari Moghaddam, J. Llorca, M. Ibáñez, J. Arbiol, Y. Xu and A. Cabot, *Energy Storage Mater*, **2023**, 58, 287-298.

[26] L. Yang, R. He, X. Wang, T. Yang, T. Zhang, Y. Zuo, X. Lu, Z. Liang, J. Li, J. Arbiol, P. R. Martínez-Alanis, X. Qi and A. Cabot, *Nano Energy*, **2023**, 115, 108714.

[27] L. Gao, X. Cui, C. D. Sewell, J. Li and Z. Lin, *Chem Soc Rev*, **2021**, 50, 8428-8469.

[28] M. Wilke, G. M. Partzsch, R. Bernhardt, D. Lattard, *Chem. Geol.* **2004**, 213, 71.

[29] H. Dau, P. Liebisch, M. Haumann, Anal. Bioanal. *Chem.* **2003**, 376, 562.

[30] J. J. Rehr, R. C. Albers, *Rev. Mod. Phys.* **2000**, 72, 621.

[31] A. Ankudinov, B. Ravel, Phys. Rev. B - Condens. *Matter Mater. Phys.* **1998**, 58, 7565.

[32] M. Risch, V. Khare, I. Zaharleva, L. Gerencser, P. Chernev, H. Dau, *J. Am. Chem. Soc.* **2009**, 131, 6936.

[33] M. Risch, F. Ringleb, M. Kohlhoff, P. Bogdanoff, P. Chernev, I. Zaharieva, H. Dau, *Energy Environ. Sci.* **2015**, 8, 661.

[34] J. N. Hausmann, S. Mebs, K. Laun, I. Zebger, H. Dau, P. W. Menezes, M. Driess, *Energy Environ. Sci*. **2020**, 13, 3607.

[35] J. N. Hausmann, R. A. Khalaniya, C. Das, I. Remy-Speckmann, S. Berendts, A. V. Shevelkov, M. Driess, P. W. Menezes, *Chem. Commun.* **2021**, 57, 2184.

[36] J. N. Hausmann, S. Mebs, H. Dau, M. Driess, P. W. Menezes, *Adv. Mater.* **2022**, 34, 2207494.

[37] J. N. Hausmann, B. Traynor, R. J.Myers, M. Driess, P. W. Menezes, *ACS Energy Lett.* **2021**, 6, 3567−35713.

[38] J. C. Stewart, D. S. Matthew, J. P. Chris, J. H. Phil, I. J. P. Matt, R. Keith, C. P. Mike, Z Krist-Cryst. *Mater.* **2005**, 220, 567–570.

[39] J. P. Perdew, K. Burke, M. Ernzerhof, *Phys. Rev. Lett.* **1996**, 77, 3865–3868.

[40] J. K. Nørskov, J. Rossmeisl, A. Logadottir, L. Lindqvist, J. R. Kitchin, T. Bligaard, H. Jónsson, *J. Phys. Chem. B* **2004**, 108, 17886–17892.

[41] J. Liu, S. Wang, K. Kravchyk, M. Ibáñez, F. Krumeich, R. Widmer, D. Nasiou, M. Meyns, J. Llorca, J. Arbiol, M. V. Kovalenko and A. Cabot, *J Mater Chem A*, **2018**, 6, 10958-10966.

[42] M. I. Diez-Garcia, G. Montana-Mora, M. Botifoll, A. Cabot, J. Arbiol, M. Qamar and J. R. Morante, *ACS Appl Energy Mater*, **2023**, 6, 5690-5699.

[43] J. Liu, X. Yu, R. Du, C. Zhang, T. Zhang, J. Llorca, J. Arbiol, Y. Wang, M. Meyns and A. Cabot, *Appl Catal B*, **2019**, 256, 117846.

[44] X. Wang, L. Yang, C. Xing, X. Han, R. Du, R. He, P. Guardia, J. Arbiol and A. Cabot, *Nanomaterials*, **2022**, 12, 1098.

[45] J. Liu, Z. Wang, J. David, J. Llorca, J. Li, X. Yu, A. Shavel, J. Arbiol, M. Meyns and A. Cabot, *J Mater Chem A*, **2018**, 6, 11453-11462.

[46] N. Khodayar, A. Noori, M. S. Rahmanifar, M. Moloudi, N. Hassani, M. Neek-Amal, M. F. El-Kady, N. B. Mohamed, X. Xia, Y. Zhang, R. B. Kaner and M. F. Mousavi, *Energy Environ Sci*, **2024**, 17, 5200-5215.

[47] D. Lai, Q. Kang, F. Gao and Q. Lu, *J Mater Chem A*, **2021**, 9, 17913-17922.

[48] Y. Li, Z. Dong and L. Jiao, *Adv Energy Mater*, **2019**, 10, 1902104.

[49] Y. Shi, M. Li, Y. Yu and B. Zhang, *Energy Environ Sci*, **2020**, 13, 4564-4582.

[50] H. Li, C. Zhang, W. Xiang, M. A. Amin, J. Na, S. Wang, J. Yu and Y. Yamauchi, *Chem Eng J*, **2023**, 452, 139104.

[51] G. Ke, F. Duan, B. Liu, X. Liu, J. Wen, B. Jia, X. Liu, H. He and Y. Zhou, *J Alloys and Compd*, **2023**, 934, 167883.

[52] K. Kim, K. Min, Y. Go, Y. Lee, S. E. Shim, D. Lim and S.-H. Baeck, *Appl Catal B*, **2022**, 315, 121501.

[53] Z. Wang, J. Ang, J. Liu, X. Y. D. Ma, J. Kong, Y. Zhang, T. Yan and X. Lu, *Appl Catal B*, **2020**, 263, 118344.

[54] W.-W. Tian, J.-T. Ren and Z.-Y. Yuan, *Appl Catal B*, **2022**, 317, 121764.

[55] Z. Li, M. Chen, L. Zhang, R. Xing, J. Hu, X. Huang, C. Zhou, Y. Zhou, T. Wågberg and G. Hu, *J Mater Chem A*, **2023**, 11, 2155-2167.

[56] C. He, L. Yang, X. Peng, S. Liu, J. Wang, C. Dong, D. Du, L. Li, L. Bu and X.

Huang, *ACS Nano*, **2023**, 17, 5861-5870.

[57] L. Yang, R. He, M. Botifoll, Y. Zhang, Y. Ding, C. Di, C. He, Y. Xu, L. Balcells, J. Arbiol, Y. Zhou and A. Cabot, *Adv. Mater*, **2024**, 36, e2400572.

[58] L. Wu, T. Guo and T. Li, *iScience*, **2021**, 24, 102398.

[59] H. Xie, S. Chen, J. Liang, T. Wang, Z. Hou, H. L. Wang, G. Chai and Q. Li, *Adv Funct Mater*, **2021**, 31, 2100883.

[60] F. Lin, F. Lv, Q. Zhang, H. Luo, K. Wang, J. Zhou, W. Zhang, W. Zhang, D. Wang, L. Gu and S. Guo, *Adv Mater*, **2022**, 34, e2202084.

[61] T. Wang, A. Chutia, D. J. L. Brett, P. R. Shearing, G. He, G. Chai and I. P. Parkin, *Energy Environ Sci*, **2021**, 14, 2639-2669.

[62] S. Wang, Y. Xie, K. Shi, W. Zhou, Z. Xing, K. Pan and A. Cabot, *ACS Sustain Chem Eng*, **2020**, 8, 5920-5926.

[63] J. Liu, Z. Luo, J. Li, X. Yu, J. Llorca, D. Nasiou, J. Arbiol, M. Meyns and A. Cabot, *Appl Catal B*, **2019**, 242, 258-266.

[64] J. Liu, M. Meyns, T. Zhang, J. Arbiol, A. Cabot and A. Shavel, *Chem Mater*, **2018**, 30, 1799-1807.

[65] X. Yang, F. Wang, Z. Jing, M. Chen, B. Wang, L. Wang, G. Qu, Y. Kong and L. Xu, *Small*, **2023**, 19, e2301985.

[66] Y. Guo, J. Tang, Z. Wang, Y. Sugahara and Y. Yamauchi, *Small*, **2018**, 14, e1802442.

[67] H. Liu, J. Guan, S. Yang, Y. Yu, R. Shao, Z. Zhang, M. Dou, F. Wang and Q. Xu, *Adv Mater*, **2020**, 32, e2003649.

[68] P. He, X. Y. Yu and X. W. Lou, *Angew Chem Int Ed*, **2017**, 56, 3897-3900.

[69] Q. Shi, Q. Liu, Y. Ma, Z. Fang, Z. Liang, G. Shao, B. Tang, W. Yang, L. Qin and X. Fang, *Adv Energy Mater*, **2020**, 10, 1903854.

[70] F. Luo, Q. Zhang, X. Yu, S. Xiao, Y. Ling, H. Hu, L. Guo, Z. Yang, L. Huang, W. Cai and H. Cheng, *Angew Chem Int Ed*, **2018**, 57, 14862-14867.

[71] B. Qiu, L. Cai, Y. Wang, Z. Lin, Y. Zuo, M. Wang and Y. Chai, *Adv Funct Mater*, **2018**, 28, 1706008.

[72] J. Wang and F. Ciucci, *Appl Catal B*, **2019**, 254, 292-299.

[73] C. Wang, W. Chen, D. Yuan, S. Qian, D. Cai, J. Jiang and S. Zhang, *Nano Energy*, **2020**, 69, 104453.

[74] Y. Deng, Y. Cao, Y. Xia, X. Xi, Y. Wang, W. Jiang, D. Yang, A. Dong and T. Li, *Adv Energy Mater*, **2022**, 12, 2202394.

[75] G. Zhou, M. Li, Y. Li, H. Dong, D. Sun, X. Liu, L. Xu, Z. Tian and Y. Tang, *Adv Funct Mater*, **2019**, 30, 1905252.

[76] R. Zhang, W. Liu, F.-M. Zhang, Z.-D. Yang, G. Zhang and X. C. Zeng, *Appl Catal B*, **2023**, 325, 122366.

[77] Y. Chen, J. Xu, M. Jiang, L. Wang, R. Ma, Y. Chen, Z. H. Xie, P. Munroe, F. Hu, L. Li and S. Peng, *Adv Energy Mater*, **2023**, 14, 2303450.

[78] Y. Gao, D. Zheng, Q. Li, W. Xiao, T. Ma, Y. Fu, Z. Wu and L. Wang, *Adv Funct Mater*, **2022**, 32, 2203206.

[79] T. Dai, X. Zhang, M. Sun, B. Huang, N. Zhang, P. Da, R. Yang, Z. He, W. Wang, P. Xi and C. H. Yan, *Adv Mater*, **2021**, 33, e2102593.

[80] S. Pan, H. Li, D. Liu, R. Huang, X. Pan, D. Ren, J. Li, M. Shakouri, Q. Zhang, M. Wang, C. Wei, L. Mai, B. Zhang, Y. Zhao, Z. Wang, M. Graetzel and X. Zhang, *Nat Commun*, **2022**, 13, 2294.

[81] Z. Zhang, X. Li, C. Zhong, N. Zhao, Y. Deng, X. Han and W. Hu, *Angew Chem Int Ed*, **2020**, 59, 7245-7250.

[82] J. Wang, S.-J. Kim, J. Liu, Y. Gao, S. Choi, J. Han, H. Shin, S. Jo, J. Kim, F. Ciucci, H. Kim, Q. Li, W. Yang, X. Long, S. Yang, S.-P. Cho, K. H. Chae, M. G. Kim, H. Kim and J. Lim, *Nature Catal*, **2021**, 4, 212-222.

[83] C. Chen, M. Sun, F. Zhang, H. Li, M. Sun, P. Fang, T. Song, W. Chen, J. Dong, B. Rosen, P. Chen, B. Huang and Y. Li, *Energy Environ Sci*, **2023**, 16, 1685-1696.

[84] P. Li, M. Wang, X. Duan, L. Zheng, X. Cheng, Y. Zhang, Y. Kuang, Y. Li, Q. Ma, Z. Feng, W. Liu and X. Sun, *Nat Commun*, **2019**, 10, 1711.

[85] H. Liu, X. Xu, H. Xu, S. Wang, Z. Niu, Q. Jia, L. Yang, R. Cao, L. Zheng and D. Cao, *Appl Catal B*, **2021**, 297, 120451.

[86] L. Tang, L. Yu, C. Ma, Y. Song, Y. Tu, Y. Zhang, X. Bo and D. Deng, *J Mater Chem A*, **2022**, 10, 6242-6250.

[87] Y. Zhao, Y. Guo, X. F. Lu, D. Luan, X. Gu and X. W. D. Lou, *Adv Mater*, **2022**, 34, e2203442.

[88] S. Zhao, C. Tan, C.-T. He, P. An, F. Xie, S. Jiang, Y. Zhu, K.-H. Wu, B. Zhang, H. Li, J. Zhang, Y. Chen, S. Liu, J. Dong and Z. Tang, *Nat Energy*, **2020**, 5, 881-890.

[89] R. Yang, L. An, Y. Zhang, N. Zhang, T. Dai and P. Xi, *ChemCatChem*, **2019**, 11, 6002-6007.

[90] S. Li, B. Chen, Y. Wang, M. Y. Ye, P. A. van Aken, C. Cheng and A. Thomas, *Nat Mater*, **2021**, 20, 1240-1247.

[91] Y. Li, Y. Liu, Q. Qian, G. Wang and G. Zhang, *Energy Storage Mater*, **2020**, 28, 27-36.

[92] A. Dutta, A. K. Samantara, S. K. Dutta, B. K. Jena and N. Pradhan, *ACS Energy Lett*, **2016**, 1, 169-174.

[93] L.-A. Stern, L. Feng, F. Song and X. Hu, *Energy Environ Sci*, **2015**, 8, 2347-2351.

[94] Y. Zhao, N. Dongfang, C. A. Triana, C. Huang, R. Erni, W. Wan, J. Li, D. Stoian, L. Pan, P. Zhang, J. Lan, M. Iannuzzi and G. R. Patzke, *Energy Environ Sci*, **2022**, 15, 727-739.

[95] P. Hou, D. Li, N. Yang, J. Wan, C. Zhang, X. Zhang, H. Jiang, Q. Zhang, L. Gu and D. Wang, *Angew Chem Int Ed*, **2021**, 60, 6926-6931.

[96] X. Zheng, J. Yang, Z. Xu, Q. Wang, J. Wu, E. Zhang, S. Dou, W. Sun, D. Wang and Y. Li, *Angew Chem Int Ed*, **2022**, 61, e202205946.

[97] W. Li, Y. Li, H. Fu, G. Yang, Q. Zhang, S. Chen and F. Peng, *Chem Eng J*, **2020**, 381, 122683.

[98] J. Duan, S. Chen, A. Vasileff and S. Z. Qiao, *ACS Nano*, **2016**, 10, 8738-8745.

[99] G. Zhang, G. Wang, Y. Liu, H. Liu, J. Qu and J. Li, *J Am Chem Soc*, **2016**, 138, 14686-14693.

[100] B. S. Yeo and A. T. Bell, *J Phys Chem C*, **2012**, 116, 8394-8400.

[101] D. L. A. de Faria, S. Venâncio Silva and M. T. de Oliveira, *J Raman Spectrosc*, **1997**, 28, 873-878.

[102] R. Beltrán-Suito, P. W. Menezes and M. Driess, *J Mater Chem A*, **2019**, **7**, 15749-15756.

[103] H. N. Nong, L. J. Falling, A. Bergmann, M. Klingenhof, H. P. Tran, C. Spori, R. Mom, J. Timoshenko, G. Zichittella, A. Knop-Gericke, S. Piccinin, J. Perez-Ramirez, B. R. Cuenya, R. Schlogl, P. Strasser, D. Teschner and T. E. Jones, *Nature*, **2020**, 587, 408-413.

[104] L. Reith, J. N. Hausmann, S. Mebs, I. Mondal, H. Dau, M. Driess and P. W. Menezes, *Adv Energy Mater*, **2023**, 13, 2203886.

[105] M. Gorlin, J. Ferreira de Araujo, H. Schmies, D. Bernsmeier, S. Dresp, M. Gliech, Z. Jusys, P. Chernev, R. Kraehnert, H. Dau and P. Strasser, *J Am Chem Soc*, **2017**, 139, 2070-2082.

[106] J. N. Hausmann, S. Mebs, K. Laun, I. Zebger, H. Dau, P. W. Menezes and M. Driess, *Energy Environ Sci*, **2020**, 13, 3607-3619.

[107] F. Dionigi, Z. Zeng, I. Sinev, T. Merzdorf, S. Deshpande, M. B. Lopez, S. Kunze, I. Zegkinoglou, H. Sarodnik, D. Fan, A. Bergmann, J. Drnec, J. F. Araujo, M. Gliech, D. Teschner, J. Zhu, W. X. Li, J. Greeley, B. R. Cuenya and P. Strasser, *Nat Commun*, **2020**, 11, 2522.

[108] R. D. L. Smith, C. Pasquini, S. Loos, P. Chernev, K. Klingan, P. Kubella, M. R. Mohammadi, D. Gonzalez-Flores and H. Dau, *Nat Commun*, **2017**, 8, 2022.

[109] R. D. L. Smith, C. Pasquini, S. Loos, P. Chernev, K. Klingan, P. Kubella, M. R. Mohammadi, D. González-Flores and H. Dau, *Energy Environ Sci*, **2018**, 11, 2476-2485.

[110] M. Risch, K. Klingan, J. Heidkamp, D. Ehrenberg, P. Chernev, I. Zaharieva and H. Dau, *Chem Commun*, **2011**, 47, 11912-11914.

[111] J. N. Hausmann, R. A. Khalaniya, C. Das, I. Remy-Speckmann, S. Berendts, A. V. Shevelkov, M. Driess and P. W. Menezes, *Chem Commun*, **2021**, 57, 2184-2187.

[112] H. Li, M. Sun, Y. Pan, J. Xiong, H. Du, Y. Yu, S. Feng, Z. Li, J. Lai, B. Huang

and L. Wang, *Appl Catal B*, **2022**, 312, 121431.

[113] J. Li, L. Zheng, B. Huang, Y. Hu, L. An, Y. Yao, M. Lu, J. Jin, N. Zhang and P. J. S. Xi, *small*, **2022**, 18, 2204723.

[114] B. Bao, Y. Liu, M. Sun, B. Huang, Y. Hu, P. Da, D. Ji, P. Xi and C. H. J. S. Yan, *small*, **2022**, 18, 2201131.

[115] R. He, T. Lu, N. Xu, G. Liu, Y. Zhang and J. Qiao, *Chem Eng J*, **2023**, 461, 141843.

[116] C. Yao, J. Li, Z. Zhang, C. Gou, Z. Zhang, G. Pan and J. Zhang, *Small*, **2022**, 18, e2108094.

[117] H. Li, Q. Li, P. Wen, T. B. Williams, S. Adhikari, C. Dun, C. Lu, D. Itanze, L. Jiang, D. L. Carroll, G. L. Donati, P. M. Lundin, Y. Qiu and S. M. Geyer, *Adv Mater*, **2018**, 30, 1705796.

[118] J.-T. Ren, Y.-S. Wang, L. Chen, L.-J. Gao, W.-W. Tian and Z.-Y. Yuan, *Chem Eng J*, **2020**, 389, 124408.

[119] T. Wang, X. Cao, H. Qin, L. Shang, S. Zheng, F. Fang and L. Jiao, *Angew Chem Int Ed*, **2021**, 60, 21237-21241.

[120] Y. Wang, J. Liu, T. Lu, R. He, N. Xu and J. Qiao, *Appl Catal B*, **2023**, 321, 122674.

[121] Q. P. Ngo, T. T. Nguyen, M. Singh, R. Balaji, N. H. Kim and J. H. Lee, *Appl Catal B*, **2023**, 331, 122674.

[122] D. Ren, J. Ying, M. Xiao, Y. P. Deng, J. Ou, J. Zhu, G. Liu, Y. Pei, S. Li, A. M. Jauhar, H. Jin, S. Wang, D. Su, A. Yu and Z. Chen, *Adv Funct Mater*, **2019**, 30, 1908167.

[123] L. Yang, X. Zhang, L. Yu, J. Hou, Z. Zhou and R. Lv, *Adv Mater*, **2022**, 34, e2105410.

[124] Y. Lin, L. Yang, Y. Zhang, H. Jiang, Z. Xiao, C. Wu, G. Zhang, J. Jiang and L. Song, *Adv Energy Mater*, **2018**, 8, 1703623.

[125] C-X Zhao, J-N Liu, J. Wang, C. Wang, X. Guo, X-Y. Li, X. Chen, L. Song, B-Q. Li, and Q. Zhang, *Sci Adv*, **2022**, 8, eabn5091.

[126] Y. Zhou, Y. Yu, D. Ma, A. C. Foucher, L. Xiong, J. Zhang, E. A. Stach, Q. Yue and Y. Kang, *ACS Catal*, **2020**, 11, 74-81.

[127] Z. You and I.-H. Jung, *Mater Trans B*, **2020**, 51, 3108-3129.

[128] R. Ganesan, A. T. Dinsdale and H. Ipser, *Intermetallics*, **2011**, 19, 927-933.

[129] S. Boone and O. J. Kleppa, *J Chem Thermodynamics*, **1991**, 23, 1147-1151.

[130] Q. Shi, Q. Liu, Y. Zheng, Y. Dong, L. Wang, H. Liu and W. Yang, *Energy Environ Mater*, **2021**, 5, 515-523.

[131] Y. Guo, P. Yuan, J. Zhang, Y. Hu, I. S. Amiinu, X. Wang, J. Zhou, H. Xia, Z. Song, Q. Xu and S. Mu, *ACS Nano*, **2018**, 12, 1894-1901.

[132] M. Ma, A. Kumar, D. Wang, Y. Wang, Y. Jia, Y. Zhang, G. Zhang, Z. Yan and X. Sun, *Appl Catal B*, **2020**, 274, 119091.

[133] H. Sun, M. Wang, S. Zhang, S. Liu, X. Shen, T. Qian, X. Niu, J. Xiong and C. Yan, *Adv Funct Mater*, **2020**, 31, 2006533.

[134] S. Dresp, F. Luo, R. Schmack, S. Kühl, M. Gliech and P. Strasser, *Energy Environ Sci*, **2016**, 9, 2020-2024.

[135] E. Vijayakumar, S. Ramakrishnan, C. Sathiskumar, D. J. Yoo, J. Balamurugan, H. S. Noh, D. Kwon, Y. H. Kim and H. Lee, *Chem Eng J*, **2022**, 428, 13115.

[136] J. Chen, C. Fan, X. Hu, C. Wang, Z. Huang, G. Fu, J. M. Lee and Y. Tang, *Small*, **2019**, 15, e1901518.

[137] P. Yu, L. Wang, F. Sun, Y. Xie, X. Liu, J. Ma, X. Wang, C. Tian, J. Li and H. Fu, *Adv Mater*, **2019**, 31, e1901666.

[138] P. Peng, L. Shi, F. Huo, C. Mi, X. Wu, S. Zhang, and Z. Xiang, *Sci Adv*, **2019**, 5, eaaw 2322.

[139] J. Han, H. Bao, J.-Q. Wang, L. Zheng, S. Sun, Z. L. Wang and C. Sun, *Appl Catal B*, **2021**, 280, 1194.

[140] J. Han, X. Meng, L. Lu, J. Bian, Z. Li and C. Sun, *Adv Funct Mater*, **2019**, 29, 1828872.

[141] M. Moloudi, A. Noori, M. S. Rahmanifar, Y. Shabangoli, M. F. El-Kady, N. B. Mohamed, R. B. Kaner and M. F. Mousavi, *Adv Energy Mater*, **2022**, 13, 2203002.

[142] Z. Wang, J. Ang, B. Zhang, Y. Zhang, X. Y. D. Ma, T. Yan, J. Liu, B. Che, Y. Huang and X. Lu, *Appl Catal B*, **2019**, 254, 26-36.

[143] Z. Pan, H. Chen, J. Yang, Y. Ma, Q. Zhang, Z. Kou, X. Ding, Y. Pang, L. Zhang, Q. Gu, C. Yan and J. Wang, *Adv Sci*, **2019**, 6, 1900628.

[144] J. Qian, X. Guo, T. Wang, P. Liu, H. Zhang and D. Gao, *Appl Catal B*, **2019**, 250, 71-77.

[145] X. Zhao, X. Li, Z. Bi, Y. Wang, H. Zhang, X. Zhou, Q. Wang, Y. Zhou, H. Wang and G. Hu, *J Energy Chem*, **2022**, 66, 514-524.

Results and discussion

The rapid development of energy storage technologies is crucial for the widespread adoption of renewable energy sources. Among these technologies, ZABs stand out due to their high energy density, low cost, safety, and environmental friendliness, making them a promising candidate for future energy storage systems. However, the practical application of ZABs is hindered by the slow kinetics of the ORR and OER at the air cathode, which limits their charging and discharging efficiency and long-term stability. To address this challenge, the development of efficient, stable, and cost-effective bifunctional catalysts is key.

In recent years, HEMs have emerged as highly promising catalysts for OER and ORR due to their quasi-continuous distribution of surface energy levels and the extensive flexibility they offer in tuning surface compositions. These properties are crucial for optimizing the adsorption energies of reactants, intermediates, and products involved in the redox processes. In this thesis, I detail the progress I have made beyond the state-of-the-art catalysts on the design and engineering a variety of HEM cathode catalysts for ZAB. Studies show that incorporating 3d transition metals such as Fe, Co, and Ni with 4d and 5d elements can effectively tune the electronic structure of HEMs, optimizing oxygen intermediate adsorption and enhancing catalytic performance in oxygen redox process. Furthermore, the lattice distortions and electronic synergy in HEMs improve their catalytic activity and stability in alkaline environments.

In Chapter 2, I introduce Cr and Cu based on the MnFeCoNi system to form CrMnFeCoNi and CuMnFeCoNi HEA through a low-temperature solution-based approach, Many lattice distortions and dislocations are existed in the HEA NP. Due to different oxidation states, atom r, Cr and Cu generate different local charge unbalance and an associated electric field affecting the atomic organization, leading to different morphology and different extent of the lattice distortions. The twin structure is observed in CrMnFeCoNi HEA NPs. The alloy composition, particularly the introduction of Cr, reduces the energy barrier for the RDS of OER, while lattice distortions and twinned defects enhance the catalytic properties by adjusting the d_c position. The synergy between the elements in CrMnFeCoNi provides both structural stability and optimal electron transfer for efficient catalytic reactions.

Considering that lattice distortions modulated electronic state will produce a positive effect in catalyst redox process. Therefore, in Chapter 3, I introduce Mo and W atoms with greater differences in atomic r and electronegativity compared with Fe/Co/Ni to enlarge the electron modulation effect. Meanwhile, catalyst reconstruction is a common phenomenon in electrocatalytic processes, where the initial structure of the catalyst undergoes significant changes under operating conditions, often leading to a restructured phase that represents the true active catalytic species. Studying catalyst reconstruction is of great importance because the post-reconstruction structure can exhibit different electronic, structural, and surface properties compared to the original catalyst, which directly influences the catalytic performance. Understanding these transformations helps to reveal the actual active sites responsible for catalytic activity, enabling the design of more efficient and stable catalysts.

In Chapter 3, I focus on the synthesis of FeCoNiMoW HEAs by introducing 4d Mo and 5d W in FeCoNi ternary alloy through a low-temperature solution-based approach. In FeCoNiMoW HEA, the addition of 4d/5d elements (Mo/W) plays a crucial role in enhancing catalytic activity. The wider electronic bandwidths of these elements allow better hybridization with oxygen intermediates, lowering the Gibbs free energy barrier and improving OER kinetics. The electron modulation is beneficial for the OER performance, however, the modulation is too strong to modulate the ORR energy barrier, thus leading to a normal ORR performance. The lattice distortions and high configurational entropy contribute to enhanced structural stability, making FeCoNiMoW a robust material for extended use in ZABs.

Designing bifunctional catalysts for both the OER and ORR is inherently challenging due to the reversible nature of these processes. In each step of these reactions, the Gibbs free energy must be overcome, and the optimal binding energies for intermediates in one reaction (e.g., OER) may be detrimental to the other (e.g., ORR). To rationally design bifunctional OER-ORR HEM catalysts, the electronic structure of the catalyst should be carefully tuned to provide optimal intermediate binding energies for both reactions. The key is to create a surface environment where the adsorption of intermediates is neither too weak (which would hinder OER) nor too strong (which would slow ORR), striking a balance that minimizes the energy barriers for both reactions. Additionally, due to the intricate interactions between these elements in HEM catalysts, the specific contribution of each element to the catalytic activity, electronic structure, and stability of the alloy remains difficult to pinpoint.

In Chapter 4, I design and synthesize the 3d-4d-5d bifunctional catalyst FeCoNiPdWP HEPs through a low-temperature solution-based approach. The HEPs have a uniformly distributed size of 10 nm, which increases the specific surface area for the reaction. The catalyst has surface reconstruction behavior during both OER and ORR processes. For OER, HEPs are reconstructed into high entropy oxyhydroxide phases enriched in high-oxidation state Fe, Co, and Ni. This reconstructed surface play a crucial role in providing real active sites for oxygen oxidation. Additionally, the element-specific contributions of HEPs are discussed. Fe/Co/Ni serves as the main active sites for OER to facilitate oxygen intermediate adsorption and desorption. Pd aids in OH^- adsorption, improving OER performance. During ORR, Pd and W maintain the phosphide environment, while Fe, Co, and Ni are oxidated into hydroxide. Pd influences electron transfer pathways and stabilizes the catalytic structure. W optimizes the adsorption of oxygen intermediates by modulating the electronic structure, enhancing ORR efficiency. The ability of the catalyst to form different active surfaces during OER and ORR enables it to function efficiently in both reactions. This switch ability transcends the usual limitations of bifunctional catalysts, which often excel in only one reaction.

Overall, the design strategy relies on carefully balancing the roles of each element to ensure both OER and ORR are catalyzed effectively, resulting in exceptional performance in OER, ORR, and ZABs. This approach offers a platform for understanding surface reconstruction in HEMs and designing advanced bifunctional catalysts.

Conclusions

This thesis presents a comprehensive study on the rational design of HEMs with homogeneous nanostructures, tailored for OER/ORR and ZABs, synthesized via low-temperature colloid-based methods. These nanomaterials are thoroughly examined across multiple dimensions, including crystal phase, morphology, surface state, electrochemical properties, and battery performance. Detailed attention is given to the strategic selection of elements in the design process, the impact of lattice distortions arising from diverse atomic configurations on electronic modulation, and the surface reconstruction behavior. Furthermore, the specific roles of individual metal elements within the HEMs during catalytic reactions are critically analyzed. Collectively, the chapters demonstrate how HEMs can significantly enhance catalytic performance, underscoring their potential in energy-related applications.

The thesis has mainly reached the following conclusions:

In Chapter 2, I develop a low-temperature colloid method for CrMnFeCoNi and CuMnFeCoNi HEAs, along with quaternary and ternary alloys. Among these, CrMnFeCoNi exhibits outstanding catalytic performance for both OER and ORR, outperforming CuMnFeCoNi, quaternary alloys, and commercial RuO_2 and Pt/C catalysts. DFT calculations show that Cr incorporation into the MnFeCoNi structure lowers energy barriers for OER and improved ORR reaction kinetics. With a small E_{gap}, CrMnFeCoNi serves as an efficient bifunctional catalyst in air cathode for ZABs, demonstrating high power density, specific capacity, and excellent long-term cycling stability.

In Chapter 3, I introduce 4d Mo and 5d W into 3d FeCoNi ternary alloy to synthesize the FeCoNiMoW HEA by a low-temperature solution-based method, which exhibits a highly distorted lattice and strong electronic coupling effects. The FeCoNiMoW HEA demonstrates excellent catalytic performance for OER with low η and is an efficient bifunctional oxygen catalyst with a small E_{gap} of 0.75 V, outperforming Pt/C and RuO_2. DFT calculations identified Ni as the active site, with strong interactions between Ni and oxygen intermediates, which is enhanced by Mo and W. The FeCoNiMoW-based ZAB shows high power density, specific capacity, and exceptional long-term cycling stability, even in flexible applications suitable for wearable devices. This study highlights the role of 4d/5d metals in tuning electronic structures for improved catalytic activity.

In Chapter 4, FeCoNiPdWP HEPs is synthesized with homogeneous nanostructure via a mild colloidal method and demonstrate exceptional bifunctional catalytic performance for both OER and ORR. The HEPs achieve a low η of 227 mV at 10 mA cm^{-2} for OER, with a Tafel slope of 33 mV dec^{-1}, attributed to a reconstructed FeCoNiPdWOOH surface enriched with high-oxidation-state Fe, Co, and Ni as the main active sites. Pd facilitates OH^- adsorption, while W modulates the adsorption of oxygen intermediates by altering the electronic structure. For ORR, the HEPs display a $E_{1/2}$ of 0.81 V and efficient four-electron transfer pathways. The ORR performance is enhanced by surface reconstruction into FeCoNiPdWPOH, where Pd is the main active site, Pd and W maintain their phosphide chemical environments while Fe, Co, and Ni form active oxyhydroxides. As a result, the FeCoNiPdWP HEPs achieve an extremely low E_{gap} of 0.65 V, making them highly effective as bifunctional catalysts. When applied in ZABs, FeCoNiPdWP-based ZABs show exceptional performance, with over 700 h of stability during continuous cycling. This work provides insights into the unique surface reconstruction behaviors and roles of individual elements in enhancing OER and ORR, paving the way for the design of next-generation bifunctional catalysts based on HEMs.

Future work

Future research in ZABs should focus on overcoming the key challenges associated with developing flexible and portable versions for integration into next-generation wearable devices, such as cell phones, electronic skins, and intelligent bracelets. However, achieving the flexibility and performance required for such applications will necessitate advances in several critical areas.

One important direction is the development of all-solid-state or QSS electrolytes. These electrolytes should exhibit high ionic conductivity while maintaining excellent mechanical strength and flexibility. Achieving a balance between ionic mobility and mechanical robustness will be essential to ensure both efficient charge transport and structural integrity under the mechanical stresses associated with wearable electronics. Additionally, research into new solid-state electrolyte materials, such as GPEs or hybrid organic-inorganic systems, could help achieve this balance, enabling ZABs to operate reliably in flexible and deformable configurations.

The integration of flexible current collectors and air electrodes is another vital aspect of future ZAB development. Conventional ZABs often rely on rigid metal components, which are incompatible with flexible devices. Future research should explore advanced materials, such as flexible carbon-based materials (e.g., CC, graphene, or carbon nanotubes) or conductive polymers, as current collectors to enable high conductivity while maintaining mechanical flexibility. At the same time, the development of binder-free, self-supported air electrodes with high catalytic activity for both OER and ORR will be critical for enhancing the efficiency and longevity of flexible ZABs. These electrodes should be lightweight, mechanically robust, and capable of withstanding repeated bending and stretching without performance degradation.

Another promising area of research is improving the air management systems in ZABs. Because air cathodes rely on oxygen from the atmosphere, effective air diffusion and water management become even more critical in flexible ZABs, where space and form factors are constrained. Research into advanced GDL and moisture management systems could help optimize air flow and prevent flooding or drying of the air electrodes during operation, ensuring consistent battery performance.

Finally, addressing the recyclability and sustainability of flexible ZABs is essential for their commercialization. Investigating environmentally friendly and low-cost materials for air electrodes and electrolytes, as well as developing efficient recycling processes for zinc and other battery components, will contribute to the environmental sustainability and economic viability of future ZAB technologies.

In summary, future research on flexible ZABs should focus on the development of advanced materials for solid-state electrolytes, flexible current collectors, and self-supported air electrodes, as well as improving air management systems, and sustainability. By addressing these challenges, ZABs could become a transformative energy storage solution for wearable and portable electronic devices.

Curriculum vitae

Personal Details

First Name: Ren **Family name**: He
Gender: Male **Birth day**: 07/01/1994
Phone: +8618830272877 **E-mail**: heren940107@gmail.com
Google scholar: https://scholar.google.com.hk/citations?hl

Education

2021-2024: PhD in Nano Science, faculty of Physics, Barcelona university, Spain

2023.06 Institute of Science and Technology, Austria

2019-2019: MSc in Optical Engineering, faculty of Physics, Adelaide University, Australia

2017-2020: MSc in Optical Engineering, faculty of Physics, Heibei University, China

2012-2016: BSc in Optical Information Science and Technology, faculty of Physics, Shenyang Ligong University, China

Honors & Awards

Hebei University Excellent Graduate Student	2020
The National Scholarship	2020
Hebei University First-class Academic Scholarship	2020
Academic exchange student between Hebei University and Adelaide University	2019
Hebei University Second-class Academic Scholarship	2019
Hebei University Third-class Academic Scholarship	2018

CV Summary

Scientific contributions, relevance, leadership, and supervision

My research interests focus on energy storage technologies including the design and synthesis of nanomaterials, metal-air batteries, anodic valorization alternatives to water oxidation; and their underpinning materials science, and mechanical engineering. Over the period from 2021 to 2024, I have contributed to the publication of a total of **fifteen articles**, resulting in an ***h*-index of 10**, and a **citation** count of **343** (Google Scholar). Below, I offer a brief summary of my scientific trajectory.

My academic career began in 2017 at ***Heibei University***, China, and ***Adelaide University***, Australia, where I pursued my Master degree in optical engineering. I focused on the research of thin crystalline silicon solar cells integrated with industrial production. In 2018, our team successfully developed 120 μm-thick multi-crystalline silicon solar cells with a high efficiency of 19.13%, a first in industrial production at that time (***IEEE Journal of Photovoltaics, 2019,1492-1496***). This breakthrough provided a feasible solution for reducing the cost of silicon solar cells. Following this achievement, I collaborated closely with ***Lightway Green New Energy Co., Ltd and Yingli Co., Ltd, two leading photovoltaic companies in China.*** I was actively involved in discussions and the development of thin silicon solar production lines, gaining extensive experience in both industrial production and laboratory research. Additionally, ***I contributed to the formulation of rules and inspection standards for***

China's photovoltaic thin silicon solar cells as the youngest researcher in the field. During my Master period, I published two first-authored papers and secured one patent.

After completing the Master study, I embarked on a doctoral path at the ***Catalonia Institute for Energy Research (IREC)*** from 2021 to 2024, as part of the Spain project, “COMBENERGY”. Under the mentorship of **Dr. Andreu Cabot,** I delved deeper into the development of ***energy materials, including the design, synthesis, and characterization of nanomaterials for optimizing energy catalysis processes.*** In 2023; I received funding through the Horizon Europe Project “HEALING BAT”, where I explored materials for next-generation self-healing mechanisms to self-repair batteries.

During my PhD, **I introduced aqueous zinc-air batteries and flexible zinc-air battery assembly** to my research group for the first time. **I also established a zinc-air battery test workstation**, effectively integrated electrochemical catalysis and devices. This initiative **filled the gap in electrocatalytic production applications and expanded the research scope,** leading to new project opportunities for IREC. Additionally, it facilitated collaborations with universities in China, such as Jinan University.

To identify a more efficient, promising, and cost-effective transition metal electrocatalyst platform, I pioneered the synthesis of **nano-scale high entropy alloys using a colloidal method at low temperatures** within my research group. The high entropy alloys achieved excellent oxygen catalytic performance and robust zinc-air batteries, with results published in top journals such as ***Adv. Mater., 2023, 2303719, Adv. Mater. 2024, 2400572, Energy Storage Mater., 2023, 287-298, and Energy Environ. Sci. 2024, 17, 7193-7208.*** **The research on high entropy materials has also opened new collaboration opportunities for our group**, including partnerships with South Ural State University (Russia), Freie Universität Berlin (Germany), the National Centre for Nuclear Research (Poland), and the University of Helsinki (Finland).

Additionally, I independently **designed test models** for zinc-air batteries and various *in situ* testing setups and **gained hands-on experience in various *in situ* measurements and analysis,** such as *in situ* Raman, synchrotron *in situ* FTIR, and synchrotron *in situ* XAS.

I have guided one master's student and three undergraduate students in materials synthesis & electrochemical testing and successfully guided them to complete their degrees.

I have extensive experience in cooperation with enterprises and universities/institutes, such as Peaking University, Hebei University, Nanjing University, Zhejiang Ocean University, Chengdu University, Zhengzhou University, Anhui University in **China**, Pennsylvania State University in the **US**, Institute of Science and Technology Austria in **Austria**, Helmholtz-Zentrum Berlin für Materialien und Energie institute in **Germany**, National Centre for Nuclear Research in **Poland**, University of Limerick in **Ireland**, Institut de Ciència de Materials de Barcelona (ICMAB-CSIC), Catalan Institute of Nanoscience and Nanotechnology (ICN2), and Abla synchrotron center in **Spain**.

Publications as the First/Co-First/Corresponding Author

1. **R. He[#],** L. L. Yang[#], Y. Zhang, X. Wang, S. Lee, T. Zhang, L. X. Li, Z. F. Liang, J. W. Chen, J. S. Li, A. O. Moghaddam, J. Llorca, M. Ibáñez, J. Arbiol, Y. Xu, A. Cabot, A CrMnFeCoNi high entropy alloy boosting oxygen evolution/reduction reactions and zinc-air battery performance, ***Energy Storage Mater.***, 2023, 287-298.
2. **R. He**, L. L. Yang, Y. Zhang, D. C. Jiang, S. Lee, S. Horta, Z. F. Liang, X. Lu, A. O. Moghaddam, J. S. Li, M. Ibáñez, Y. Xu, Y. T. Zhou, A. Cabot, A 3d-4d-5d High Entropy Alloy as a Bifunctional Oxygen Catalyst for Robust Aqueous Zinc-Air Batteries, ***Adv. Mater.***, 2023, 2303719.
3. **R. He**[#], S. Q. Wang[#], L. L. Yang[#], S. Horta, Y. Ding, C. Di, X. S. Zhang, Y. Xu, M. Ibáñezd, Y. T. Zhou, S. Mebs, H. Dau, J. N. Hausmann, W. Y. Huo, P. W. Menezes, and Andreu Cabot, Active site switching on high entropy phosphides as bifunctional oxygen electrocatalysts for rechargeable/robust Zn-Air battery, ***Energy Environ. Sci.,*** 2024, 17, 7193-7208.
4. L. L. Yang[#]**, R. He[#]**, M. Botifoll, Y. C. Zhang, Y. Ding, C. Di, C. S. He, Y Xu, J. Arbiol, Y. T. Zhou, A. Cabot, Enhanced oxygen evolution and zinc-air battery performance via electronic spin modulation in heterostructured catalysts, ***Adv. Mater.*** 2024, 2400572.
5. G. L. Gao, Y. Y. Yu, G/ Zhu, B. W. Sun, **R. He***, A. Cabot*, Z. X. Sun*, High entropy alloy electrocatalysts**, *J Energy Chem***, 2024, 335–364.
6. L. L. Yang, **R. He*,** J. L. Chai, X. Q. Qi, Q. Xue, X. Y. Bi, J. Yu, Z. X. Sun, L. Xia, K. W. Wang, N. Kapuria, J. S. Li, A. O. Moghaddam, A. Cabot*, Synthesis strategies for high entropy nanoparticles, ***Adv. Mater.,*** 2024, 2412337.
7. **R. He**, J. W. Chen, D. Y. Wei, Z. P. Huang, D. Y. Song, Y. Xu, Thin multicrystalline silicon solar cells with high mechanical strength and less light-induced degradation, ***IEEE J. Photovolt.***, 2019, 1492-1496.
8. **R. He**, Y. Y. Li, J. X. Chen, X. L. Zhao, H. Tang, L. N. Zhang, Y. J. Shen, F. Li, L. Yang, D. Y. Wei, Three-point and four-point mechanical bending test modelling and application in solar cells, ***Chinese Physical Soc.***, 2019, 68, 20.

Congresses

- **(Oral presentation)** China Renewable Energy Academic Conference, Beijing, China (2018)
- (**Oral presentation**)14th China SoG Silicon and PV Power Conference, Xi An, China (2019)
- (**Poster presentation**) International Summer School on Sustainable Materials for Renewable Energy Applications, Barcelona, Spain (2022)
- ALBA II Symposium, Madrid, Sapin (2024)
- (**Poster presentation**) Battery 2030$^+$:Sustainable Batteries of the Future, Grenoble, France (2024)

- (**Poster presentation**) Catalysis, from understanding to applications, Albi, France (2024)

Main Projects and Roles

During my PhD period, I started to write proposals and there are three projects proposed as the proposer and main researcher.

- **ALBA Synchrotron project** “Fourier transform infrared microscopy of dual-atom catalysts for robust zinc-air battery with/without an external magnetic field” (2023097841). The main researcher.
- **ALBA Synchrotron project** “Fourier transform infrared microscopy of the FeCoNiMoWSe high entropy selenide for robust zinc air battery with/without an external magnetic field” (2023097840). The proposer.
- **ALBA Synchrotron project** “X-ray absorption fine spectroscopy of dual atom catalysts” (2023097832). The main researcher.

Technological or Transfer Merits

As the first originator, one patent for invention has been authorized.

- CN109802009A “A manufacturing method of ultra-thin double-sided crystalline silicon solar cells”, **Ren He**, Jingwei Chen, Jianhui Chen, Zhiping Huang, Dengyuan Song, Yin Xu.

Publications

Collection of Publications Presented in This Thesis

Energy Storage Materials 58 (2023) 287–298

Contents lists available at ScienceDirect

Energy Storage Materials

journal homepage: www.elsevier.com/locate/ensm

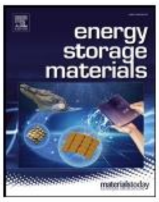

A CrMnFeCoNi high entropy alloy boosting oxygen evolution/reduction reactions and zinc-air battery performance

Ren He[a,b,#], Linlin Yang[a,b,#], Yu Zhang[c], Xiang Wang[a,b], Seungho Lee[d], Ting Zhang[e], Lingxiao Li[f], Zhifu Liang[a,e], Jingwei Chen[g], Junshan Li[h], Ahmad Ostovari Moghaddam[i], Jordi Llorca[j], Maria Ibáñez[d], Jordi Arbiol[e,k], Ying Xu[g,*], Andreu Cabot[a,k,*]

[a] *Catalonia Energy Research Institute – IREC, Sant Adria de Besòs, 08930 Barcelona, Spain*
[b] *Department of nanoscience, Universitat de Barcelona, 08028 Barcelona, Spain*
[c] *Department of Materials Science and Engineering, Pennsylvania State University, University Park, Pennsylvania 16802, United States*
[d] *IST Austria, Am Campus 1, 3400 Klosterneuburg, Austria*
[e] *Catalan Institute of Nanoscience and Nanotechnology (ICN2), CSIC, BIST, Campus UAB, Bellaterra, 08193 Catalonia, Spain*
[f] *School of Mechanical and Power Engineering, Zhengzhou University, Henan, 450001, Zhengzhou, China*
[g] *Hebei Key Lab of Optic-electronic Information and Materials, College of Physics Science and Technology, Hebei University, Baoding 071002, China*
[h] *Institute of Advanced Study, Chengdu University, Chengdu 610106, China*
[i] *Department of Materials Science, Physical and Chemical Properties of Materials, South Ural State University, 76 Lenin Ave, Chelyabinsk, 454080, Russia*
[j] *Institute of Energy Technologies, Department of Chemical Engineering and Barcelona, Research Center in Multiscale Science and Engineering, Universitat Politècnica de Catalunya, EEBE, 08019 Barcelona, Spain*
[k] *ICREA, Pg. Lluis Companys 23, 08010 Barcelona, Catalonia, Spain*

ARTICLE INFO

Keywords:
High entropy alloy
Oxygen evolution reaction
Oxygen reduction reaction
Zinc-air battery
Aqueous battery

ABSTRACT

The development of cost-effective, high-activity and stable bifunctional catalysts for the oxygen reduction and evolution reactions (ORR/OER) is essential for zinc–air batteries (ZABs) to reach the market. Such catalysts must contain multiple adsorption/reaction sites to cope with the high demands of reversible oxygen electrodes. Herein, we propose a high entropy alloy (HEA) based on relatively abundant elements as a bifunctional ORR/OER catalyst. More specifically, we detail the synthesis of a CrMnFeCoNi HEA through a low-temperature solution-based approach. Such HEA displays superior OER performance with an overpotential of 265 mV at a current density of 10 mA/cm^2, and a 37.9 mV/dec Tafel slope, well above the properties of a standard commercial catalyst based on RuO_2. This high performance is partially explained by the presence of twinned defects, the incidence of large lattice distortions, and the electronic synergy between the different components, being Cr key to decreasing the energy barrier of the OER rate-determining step. CrMnFeCoNi also displays superior ORR performance with a half-potential of 0.78 V and an onset potential of 0.88 V, comparable with commercial Pt/C. The potential gap (Egap) between the OER overpotential and the ORR half-potential of CrMnFeCoNi is just 0.734 V. Taking advantage of these outstanding properties, ZABs are assembled using the CrMnFeCoNi HEA as air cathode and a zinc foil as the anode. The assembled cells provide an open-circuit voltage of 1.489 V, i.e. 90% of its theoretical limit (1.66 V), a peak power density of 116.5 mW/cm^2, and a specific capacity of 836 mAh/g that stays stable for more than 10 days of continuous cycling, i.e. 720 cycles @ 8 mA/cm^2 and 16.6 days of continuous cycling, i.e. 1200 cycles @ 5 mA/cm^2.

1. Introduction

Oxygen electrocatalysts play a fundamental role in several energy conversion and storage technologies [1,2]. Oxygen catalysts are required to facilitate the oxygen evolution reaction (OER) at the anode of water electrolyzers [3,4], the oxygen reduction reaction (ORR) at the cathode of fuel cells [5,6], and both OER and ORR at the cathode of rechargeable metal-air batteries, among others [7]. A particularly

---

* Corresponding authors.
E-mail addresses: xuying@hbu.edu.cn (Y. Xu), acabot@irec.cat (A. Cabot).
[#] These authors contributed equally to this work.

https://doi.org/10.1016/j.ensm.2023.03.022
Received 31 October 2022; Received in revised form 7 March 2023; Accepted 19 March 2023

interesting case in the latter field is that of rechargeable aqueous zinc-air batteries (ZABs) [8,9]. While ZABs offer appealing advantages over competing technologies, such as high specific energy (1,218 Wh/kg) [10], safety [11], potential for low cost [12], and suitability for smart-grid energy storage, their cost-effectiveness relies on finding a durable and low-cost bifunctional OER/ORR catalyst that enables an energy-efficient charge/discharge process [13,14]. In this direction, despite the huge efforts dedicated, the most effective oxygen catalysts proposed to date are usually based on noble metals [15–17], which hinders the large-scale practical application of this battery technology.

A particular limitation of the OER and especially ORR is their sluggish reaction kinetics associated with complex multiple-step processes that involve the transference of 4 electrons and several intermediates. Besides, a major difficulty in developing bifunctional oxygen catalysts as ZABs cathode is the difference in binding strengths of the OER and ORR intermediates. Thus, high-performance OER catalysts are not necessarily suitable for ORR and vice versa. Generally, complex functional systems such as the reversible dual oxygen oxidation and reduction processes require equally elaborated catalysts to provide the multiple surface sites required for the adsorption, activation, and reaction of the several involved species [18–29].

High entropy alloys (HEAs) are solid solutions of five or more elements with high thermodynamic and kinetic stability associated with the high activation energy for atomic diffusion [30]. This hampered diffusion is related to lattice distortions associated with the different sizes of the atoms within the HEA. Such lattice distortions play also a notable role in defining the HEA electronic structure, thus leading to unique structural, physical, and chemical properties [31]. HEAs have recently attracted increasing attention in several areas, particularly in catalysis [32–34]. In the catalysis field, HEAs offer advantages in terms of stability, diversity of adsorption/reaction sites, and design and engineering flexibility [35,36]. Owing to their intricate composition, HEAs contain diverse active sites. Besides, the interaction between the different atoms within the HEA may result in favorable synergistic effects [37]. Additionally, such complex compositions provide additional degrees of freedom to fine-tune the material structural, electronic, and catalytic properties [38]. Thus, overall, HEAs are highly promising candidates as bifunctional oxygen catalysts compared with elemental particles and binary or ternary alloys that are generally optimized for a single oxygen reaction due to the limited degrees of freedom available for their design and engineering.

Despite the high potential of HEAs as multifunctional catalysts and the significant efforts devoted to the production of HEA-based oxygen electrocatalysts, the developed catalysts have usually targeted just a single oxygen reaction, either OER or ORR. At the same time, little work has been done on the application of no-noble metal HEA bifunctional electrocatalysts in ZABs. A notable exception is a work by Qiu et al. detailing a dealloying method to synthesize the bifunctional electrocatalysts AlFeCoNiCr that provides a specific capacity of 799.8 mAh/g [39].

The most studied HEAs are based on 3d transition metals. As a representative HEA, CrMnFeCoNi can be synthesized by sputtering [40], arc-melting [41], and plasma sintering [42], which involve either high temperatures or expensive and low production throughput equipment, that do not meet the demands for cost-efficiency. Besides, most previous works on this material have focused on studying the crystal formation mechanism [43,44], mechanical strength [45,46], anti-radiation performance [47,48], and corrosion resistance [49,50].

Here, we detail the synthesis of the noble metal-free CrMnFeCoNi HEA using a solution-based approach. The final composition was optimized after screening several combinations of elements based on the system Mn-Fe-Co-Ni. Cr or Cu was afterward introduced into the optimized quaternary composition to further tune its morphology, lattice and electronic structure, and overall catalytic properties. The resulting HEAs were tested both for OER and ORR, and as bifunctional OER/ORR catalysts within reversible ZABs. The outstanding performances obtained, well above state-of-the-art commercial catalysts, are rationalized using density functional theory (DFT) calculations.

2. Materials and methods

2.1 Chemicals

Manganese(II) acetylacetonate (Mn(acac)$_2$), nickel(II) acetylacetonate (Ni(acac)$_2$), cobalt(II) acetylacetonate (Co(acac)$_2$), iron(II) acetylacetonate (Fe(acac)$_2$), copper(II) acetylacetonate (Cu(acac)$_2$), chromium(III) acetylacetonate (Cr(acac)$_3$), oleylamine (OAm, >70 %) and D(+)-glucose (99.5 %) were bought from Sigma-Aldrich. Methanol (99 %), cyclohexane (99 %), potassium hydroxide (87 %), (1-hexadecyl) trimethylammonium chloride (CTAC, 96 %), and Nafion solution (5 wt %) were supplied by Alfa Aesar. Ethanol (96 %) and isopropanol (99.7 %) were purchased from Solvech. All chemicals were used as received without further purification. Deionized (DI) water (≥18.2 MΩ/cm) was obtained by an ultra-pure purification system (Aqua Solutions).

2.2 Preparation of MnFeCoNi, CrMnFeCoNi, and CuMnFeCoNi particles

All syntheses were carried out using standard vacuum/argon Schlenk lines. In a typical preparation of MnFeCoNi particles, 240 mg glucose and 400 mg CTAC were dissolved in 10 mL OAm, followed by ultrasonication for 2 h. Then, 0.1 mmol Mn(acac)$_2$, Fe(acac)$_2$, Co(acac)$_2$, and Ni(acac)$_2$ were added into the mixture, followed by ultrasonication for 2 h and magnetic stirring for 30 min to form a homogeneous solution. The mixture was then vacuumed for 1 h at 90 °C to remove oxygen and low boinging point impurities. Then the temperature was increased to 260 °C in an argon atmosphere and the mixture was allowed to react for 2 h. Afterward, the flask was allowed to cool down to 200 °C by removing the heating mantle and then cooled rapidly down to room temperature with a water bath. The black product was collected by centrifugation and washed three times with a cyclohexane/ethanol mixture. CrMnFeCoNi and CuMnFeCoNi particles were produced following the exact same procedure but adding 0.1 mmol of the additional metal precursor (Cr(acac)$_3$ or Cu(acac)$_2$) in the initial reaction mixture.

2.3 Electrochemical measurements

All the electrochemical measurements were carried out on a Chi760E electrochemical workstation (Shanghai Chenhua, China) at room temperature using a standard three-electrode setup system with iR compensation. A platinum grid, a glassy carbon electrode (GCE) with a 5 mm diameter, and a Hg/HgO electrode were used as the counter electrode, working electrode, and reference electrode, respectively. To prepare the working electrode, 4 mg catalyst, 2 mg carbon black, and 30 μL 5 wt% Nafion solution were added to 750 μL isopropanol and 220 μL deionized water. The obtained solution was sonicated for 1 h to obtain a homogeneous catalyst ink. 5 μL of the mixture solution was dropped on the GCE electrode and dried before the electrochemical tests.

For OER, linear sweep voltammetry (LSV) measurements were conducted in 1.0 M KOH at room temperature with a scan rate of 5 mV/s. Electrochemical impedance spectroscopy (EIS) measurements were recorded under alternating current voltage with frequencies from 0.01 to 10^5 Hz. The electrochemical active surface area (ECSA) of the catalyst was estimated using the following equation:

$$\mathrm{ECSA} = C_{dl}/C_s$$

where C_{dl} and C_s represent the double-layer capacitance and specific capacitance, respectively. The C_{dl} value was measured from cyclic voltammetry (CV) curves at different scan rates (20, 40, 80, 120, 160, 200 mV/s) within the non-faradaic potential range of 0.91–1.01 V vs. RHE, and by plotting $j = (j_p - j_n)/2$ at 0.96 V vs. RHE as a function of the scan rate, j_p and j_n represent the current density in positive scan and negative scan at 0.96 V, respectively. The slope of the linear fit corresponds to the C_{dl} value. *In situ* Raman spectra were collected by a Raman microscope (iHR320 monochromator, HORIBA) using an *in situ* Raman cell. The excitation source was a frequency-doubled Nd: YAG laser, emitting 532 nm laser, and the spectra were collected using a grating of 1800 lines/mm. The electrode was first subjected to chronoamperometry measurements at a particular applied voltage (1.1-1.6 V vs. RHE) for 5 min, then we started acquiring Raman spectra while keep running the chronoamperometry measurements.

The ORR was conducted in 0.1 M KOH. A rotating ring disk electrode (RRDE) was used as the substrate for the working electrode. Before tests, O_2 was flowed through the electrolyte for about 30 min to achieve an O_2-saturated solution. CV curves were measured in O_2-saturated or Ar-saturated 0.1 M KOH solution with a scan rate of 10 mV/s. LSV tests were conducted in O_2-saturated 0.1 M KOH at different rotation rates with a sweep rate of 10 mV/s at room temperature.

The electron transfer number (n) was determined by the Koutecky-Levich equation:

$$\frac{1}{J} = \frac{1}{J_L} + \frac{1}{J_K} = \frac{1}{B\omega^{\frac{1}{2}}} + \frac{1}{J_K}$$

$$\mathrm{B} = 0.62\mathrm{nF}C_0 D_0^{\frac{2}{3}} V^{-\frac{1}{6}}$$

where J, J_K, and J_L are the measured, kinetic and limiting current density, respectively, ω is the angular velocity of the disk, n is the overall number of electrons transferred in oxygen reduction, F is the Faraday constant (96485 $C \cdot mol^{-1}$), C_0 is the bulk concentration of O_2 (1.2×10^{-6} $mol \cdot cm^{-3}$), D_0 is the diffusion coefficient of O_2 in 0.1 M KOH (1.9×10^{-5} $cm^2 \cdot s^{-1}$), and V is the kinematic viscosity of the electrolyte (0.01 $cm^2 \cdot s^{-1}$), and k is the electron transfer rate constant.

The hydrogen peroxide yield (H_2O_2 %) was determined by the following equation:

$$H_2O_2(\%) = 200 \times \frac{\frac{I_r}{N}}{I_d + \frac{I_r}{N}}$$

Here, I_r is the ring current, I_d is the disk current, and N is the H_2O_2 collection coefficient.

2.4 Zinc-air batteries (ZAB) measurements

10 mg catalyst was dispersed in 1 mL solution containing 750 µL isopropyl alcohol, 220 µL deionized water, and 30 µL 5 wt% Nafion solution. Then, the ink was sprayed on the hydrophobic carbon paper uniformly with a mass loading of 0.5 mg/cm^2. This carbon paper was used as the air cathode while a polished Zn foil was used as the anode. The two electrodes were assembled into a ZAB, while a 6 M KOH and 0.2 M zinc acetate aqueous solution was used as the electrolyte.

Solid flexible ZABs based on the HEA catalyst were produced using an electrolyte gel. The PVA-KOH-H_2O gel was prepared as follows: 2 g PVA was dissolved in 16 mL deionized water at 98 °C under magnetic stirring. Then 2 g KOH dissolved in 4 mL deionized water was introduced until the liquid turned viscous and pale-yellow. After that, the gel was introduced into the container and frozen for 2 hours, then thawed at room temperature. ZABs were assembled following a stack-type cell configuration. The air electrode was fabricated by dropping 50 µL catalyst ink on a clean carbon paper and then dried at room temperature for 24 h. The polished Zn plate electrode was used as the anode, and the PVA-KOH-H_2O gel was used as the electrolyte.

Charge–discharge polarization curves and open circuit voltage measurements were determined utilizing an electrochemical workstation (Chi760E, Chenhua). The galvanostatic test was performed using a Neware BTS4008 battery test system at room temperature. The specific capacities were determined using the galvanostatic discharge profiles standardized to the consumed mass of Zn.

3. Results and discussion

3.1. Catalyst structural and chemical characterization

As schematized in Fig. 1a, ternary and quaternary particles within the Mn-Fe-Co-Ni system, and CrMnFeCoNi and CuMnFeCoNi alloys were produced from the simultaneous reduction of the metal salts at 260 °C in the presence of OAm as a solvent and reducing agent, glucose as an additional reducing agent, and CTAC as a surfactant.

The ternary alloys, FeCoNi, MnFeNi, MnCoNi, and MnFeCo were initially produced to determine the possible range of reaction parameters and as a reference for electrochemical measurements. The results from their composition and structural analysis are shown in the Supporting Information (SI), in Figs. S1 and S2. All the ternary alloys show an amorphous or weak crystalline phase.

According to inductively coupled plasma optical emission spectroscopy (ICP-OES) analysis, the quaternary MnFeCoNi particles were characterized by a metal ratio of Mn:Fe:Co:Ni = 28:29:19:24 (Fig. S3a). As displayed in Fig. S3b, the X-ray diffraction (XRD) pattern shows the MnFeCoNi alloy to be characterized by a face-centered cubic (FCC) structure with a lattice constant of 3.543 Å, resembling that of cubic CoNi (3.530 Å). As observed by transmission electron microscopy (TEM) analysis, MnFeCoNi particles showed a large dispersion in size and morphology (Fig. S3c). The high-resolution TEM (HRTEM) micrograph shown in Fig. S3d displays a cubic crystal phase in agreement with XRD analysis with a lattice fringe distance of 0.211 nm along the (111) zone axis, which is similar to that of CoNi phase (0.204 nm). As shown in Fig. S3d, no significant lattice distortions were observed in the MnFeCoNi quaternary alloy.

Cr was introduced into the MnFeCoNi system to form the CrMnFeCoNi quinary alloy. Fig. 1b shows a representative TEM image of the produced CrMnFeCoNi particles that display an average size of 170 nm and octahedral morphology. Energy dispersive spectroscopy (EDS) composition maps show a homogeneous distribution of Cr, Mn, Fe, Co, and Ni within each particle. XRD peaks of CrMnFeCoNi were detected at 43.60°, 50.85° and 74.39°, as shown in Fig. 1c, pointing at an FCC structure, resembling that of the cubic FeCoNi phase, but with a lattice constant of 3.559 Å. The slightly larger lattice constant measured, compared with that of the FeCoNi phase (3.545 Å), is consistent with the slightly larger atomic radius of Cr and Mn compared with Fe, Co, and Ni (see details in Table S1). ICP-OES showed the Cr:Mn:Fe:Co:Ni ratio to be 12:24:31:16:17 (Fig. 1d).

The mixing entropy of CrMnFeCoNi was calculated to be 1.55R, where R is the gas constant [51]. According to the entropy concept, HEAs are quantitatively defined as having a configurational entropy larger than 1.5R in their random solution state, Therefore, taking into account the single crystal phase observed, the large atomic percentage of each element, and the high entropy calculated, the CrMnFeCoNi produced here is probed to be a HEA.

Unlike the quaternary compounds, CrMnFeCoNi HEAs were characterized by a large density of defects, including lattice distortions and dislocations. As observed in the representative HRTEM image shown in Fig. 1e, the region marked by a yellow square and amplified in Fig. 1f shows a large number of dislocations indicated by T-shape symbols. The red-squared area in Fig. 1g shows a twin structure with an interface composed of a (111) coherent boundary (Fig. 1g). The lattice fringes observed here have double hump shape dislocations. The fast Fourier transformation (FFT) of this region is shown in Fig. 1h. The two overlapping patterns from the two observed crystallites are indicated by the indexation of the FCC phases with two different colors. For the growth of the CrMnFeCoNi HEA FCC structure, the segregation of metal atoms on the (111) crystallographic plane proceeds with a twin fault packing sequence (-'A-B-C'-D-'C-B-A'), where A, B, and C represent different kinds of atomic stacking sites, in which the twin faulted plane "D" separates the twinned lattice "-C-B-A".

CuMnFeCoNi particles were produced by introducing Cu instead of

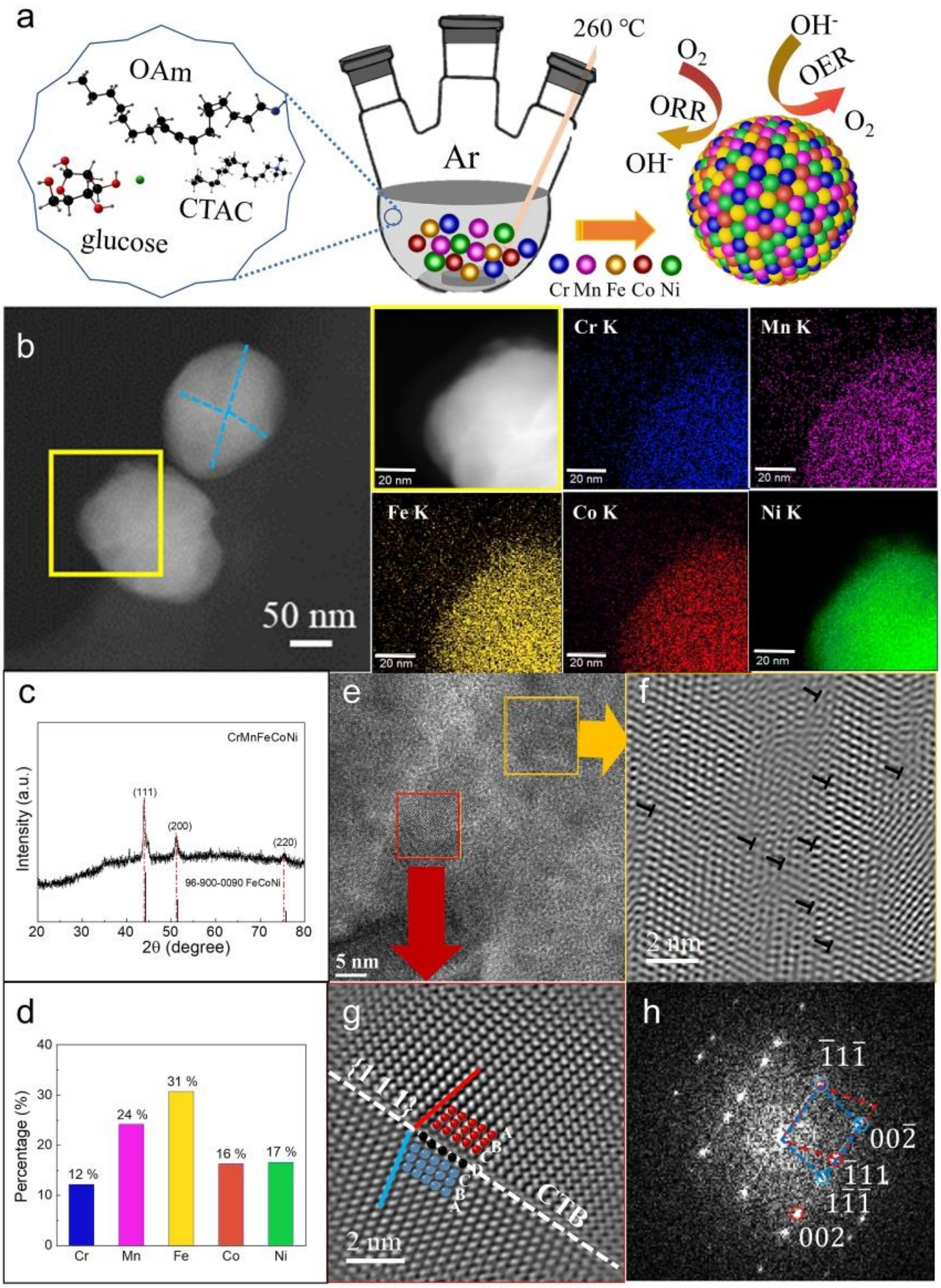

Fig. 1. CrMnFeCoNi structural and chemical characterization. (a) Schematic diagram of a high-entropy alloy synthesis process. (b) TEM image and EDS chemical composition maps. (c) XRD pattern and (d) ICP-OES composition of a CrMnFeCoNi HEAs. (e) HRTEM image of CrMnFeCoNi particles. (f) HRTEM image of the magnified right yellow square in (e). (g) HRTEM image of the magnified red square in (e). (h) Fast Fourier transformation of (g).

Cr into the quaternary MnFeCoNi system. ICP-OES analysis showed the CuMnFeCoNi particles to have a metal ratio Cu:Mn:Fe:Co:Ni of 21:20:16:21:22 (Fig. S4a). Their XRD pattern (Fig. S4b) showed the CuMnFeCoNi particles to be characterized by an FCC structure with a lattice constant of 3.54 Å, resembling that of the cubic CuNi phase (3.60 Å). The mixing entropy of CuMnFeCoNi was calculated to be 1.60R, thus confirming this alloy as a HEA. CuMnFeCoNi particles displayed a non-uniform geometry and a broad size distribution centered at around 120 nm (Fig. S4c). All the particles contained the five elements according to EDS maps (Fig. S4c). HRTEM micrographs displayed numerous lattice dislocations with a lattice fringe distance of 0.206 nm along the (111) zone axis, which is similar to the 0.208 nm of CuNi (Fig. S4d).

Overall, it was experimentally observed that when Cr or Cu was introduced into the MnFeCoNi system, a significant change in the crystal structure took place, distorting the lattice and creating dislocations and particularly twins. We associate this distortion with the slightly different atomic radius, electronegativity, and oxidation state of Cr and Cu. Particularly, electronic differences between the several distinct atoms generate a local charge unbalance and an associated electric field that affects the atomic organization and particle morphology [52], which could explain the lattice dislocations and twin structures observed by HRTEM.

The high-resolution Cr 2p, Mn 2p, Fe 2p, Co 2p, and Ni 2p X-ray photoelectron spectroscopy (XPS) spectra of the MnFeCoNi, CrMnFeCoNi, and CuMnFeCoNi particles are shown in Fig. 2. All elements display two chemical states, a metallic component assigned to the particle core and an oxidized component associated with the formation of a thin oxide layer at the particle surface. As shown in Fig. 2a, the Mn 2p XPS spectrum of MnFeCoNi displays a doublet at 638.36 eV (Mn $2p_{3/2}$) assigned to Mn^0 and a second doublet at 642.48 eV (Mn $2p_{3/2}$) assigned to Mn^{4+}. The Fe 2p XPS spectrum of MnFeCoNi displays a doublet at 706.79 eV (Fe $2p_{3/2}$) assigned to Fe^0 and a second doublet at 710.22 eV (Fe $2p_{3/2}$) assigned to Fe^{3+}, accompanied by two satellite peaks (Fig. 2b). The Co 2p XPS spectrum (Fig. 2c) displays a Co^0 valence state at 777.88 eV (Co $2p_{3/2}$), and a Co^{2+} state at 781.81 eV (Co $2p_{3/2}$). The Ni 2p XPS spectrum of MnFeCoNi shows two doublets, assigned to Ni^0 at 852.84 eV (Ni $2p_{3/2}$), and Ni^{2+} at 856.45 eV (Ni $2p_{3/2}$), and two satellite peaks (Fig. 2d). For the CrMnFeCoNi HEA, the Cr 2p XPS spectrum displays two chemical states, Cr^0 at 574.38 eV (Cr $2p_{3/2}$) and Cr^{3+} at 576.56 eV (Cr $2p_{3/2}$) (Fig. 2e). In comparison with the MnFeCoNi quaternary alloy, the introduction of Cr significantly changed the local chemical environment of the different elements. When introducing Cr, the Co 2p electronic states shifted to lower binding energies, which implies some electron transfer towards this element [53]. Meanwhile, the binding energy of Mn 2p, Fe 2p, and Ni 2p electrons were positively shifted, implying electron transfer from these elements to the surrounding atoms. The detailed peak positions obtained from the fitting of the spectra are shown in Table S2. For the CuMnFeCoNi HEA, the Cu 2p XPS spectrum displays two chemical states, Cu^0 at 932.47 eV (Cu $2p_{3/2}$) and Cu^{2+} at 934.50 eV (Cu $2p_{3/2}$) (Fig. 2e). In comparison with the MnFeCoNi quaternary alloy, in the CuMnFeCoNi HEA, the Mn 2p and Co 2p electronic states shifted to lower binding energies, while Fe 2p and Ni 2p shifted to higher binding energies, indicating that Mn and Co attract electrons, while Fe and Ni lose them. Fig. 2f, Fig. S5 and S6 show the slices of the electron density difference of CrMnFeCoNi and CuMnFeCoNi obtained from DFT calculations, which further indicates the interaction of electrons in each atom of the HEAs.

3.2. Electrocatalytic OER performance

LSV in 1.0 M KOH electrolyte was initially used to evaluate the OER activity of the catalysts. Fig. S7a shows the LSV curves of the four ternary alloys based on Mn, Fe, Co, and Ni. The overpotential at 10 mA/cm^2 of FeCoNi, MnFeNi, MnCoNi, and MnFeCo particles was 295 mV, 323 mV, 345 mV, and 331 mV, respectively (Fig. S7b). As shown in Figs. S7c and S7d, among the ternary compounds, FeCoNi displays the smallest Tafel slope and charge transfer resistance, as measured by EIS. We generally observed the performance of the ternary alloys containing Fe to be better than that of MnCoNi, indicating that Fe plays an essential role in the OER. The LSV curve of the MnFeCoNi alloy is displayed in Fig. 3a. It shows that the combination of the four elements results in an even lower overpotential, 282 mV, at 10 mA/cm^2.

Subsequently, we tested the performance of the HEAs obtained by adding Cr or Cu into the Mn-Fe-Co-Ni precursor solution. These two

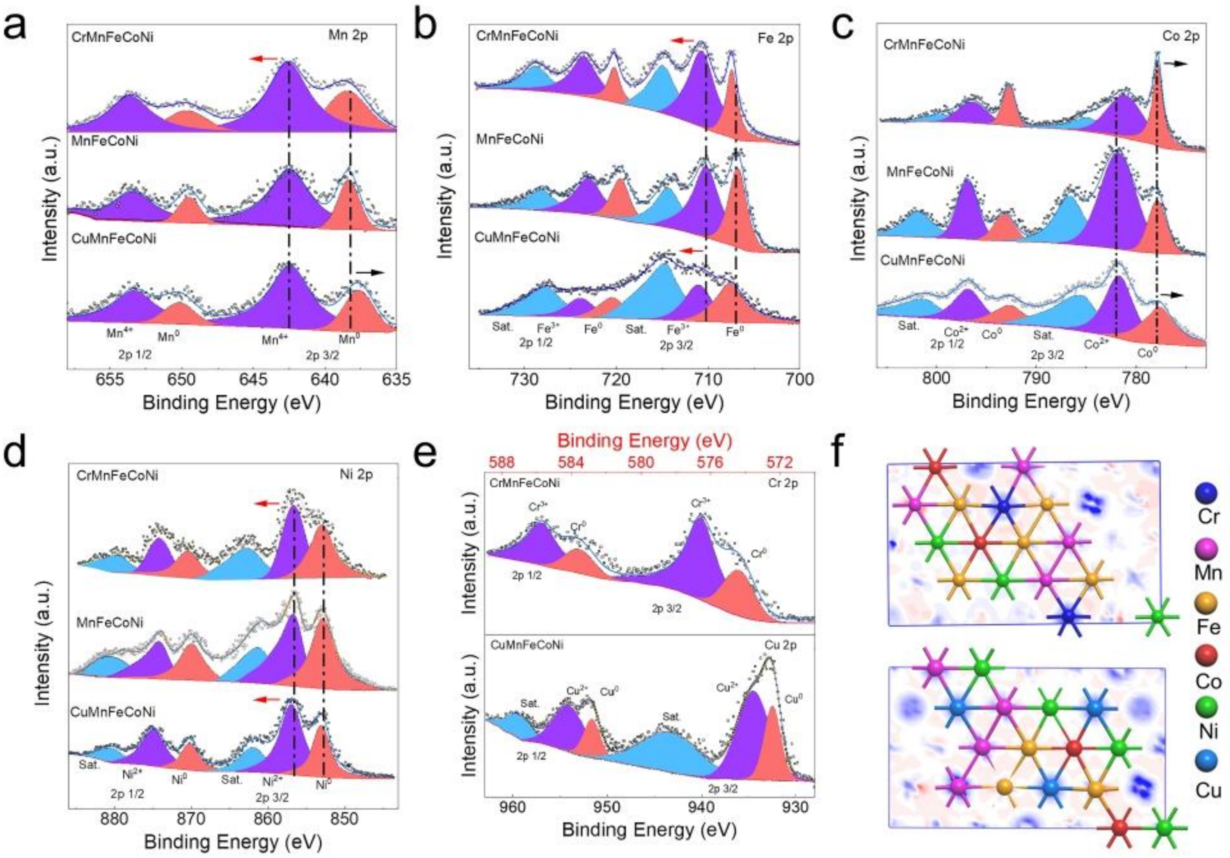

Fig. 2. High resolution (a) Mn 2p, (b) Fe 2p, (c) Co 2p, (d) Ni 2p, and (e) Cr 2p and Cu 2p XPS spectra of MnFeCoNi, CrMnFeCoNi, and CuMnFeCoNi particles. (f) Slices of electron density difference of CrMnFeCoNi and CuMnFeCoNi. The contour around the atoms represents electron accumulation (red) or electron depletion (blue).

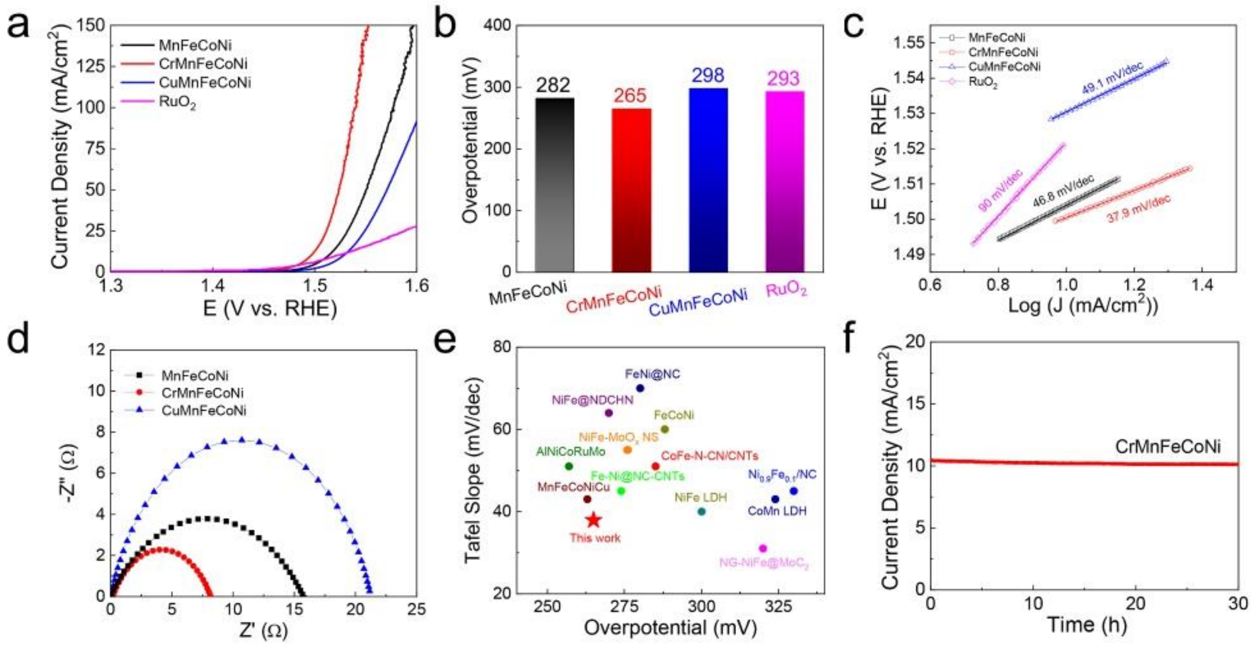

Fig. 3. OER performance. (a) LSV curves, (b) overpotential at 10 mA/cm^2, and (c) Tafel slopes of CrMnFeCoNi, MnFeCoNi, CuMnFeCoNi, and RuO$_2$ electrodes. (d) EIS spectra of CrMnFeCoNi, MnFeCoNi, and CuMnFeCoNi electrodes. (e) Comparisons of the OER performance of CrMnFeCoNi with recently reported catalysts. (f) Chronoamperometric curves of CrMnFeCoNi HEA during OER.

additional elements were selected taking into account their low cost, high abundance, non-toxic nature, and potential OER and ORR performance [54–57]. Fig. 3a shows the LSV curves obtained from CrMnFeCoNi, CuMnFeCoNi, and a commercial RuO$_2$ catalyst used as a reference. As displayed in Fig. 3b, CrMnFeCoNi displays the best OER performance with an overpotential at 10 mA/cm^2 of 265 mV, well below that of MnFeCoNi (282 mV), CuMnFeCoNi (298 mV), and RuO$_2$ (293 mV). The Tafel slopes calculated from LSV curves are displayed in Fig. 3c. CrMnFeCoNi is characterized by the fastest OER kinetics, with the smallest Tafel slope at 37.9 mV/dec, significantly below that of MnFeCoNi (46.8 mV/dec), CuMnFeCoNi (49.1 mV/dec), and RuO$_2$ (90 mV/dec). CrMnFeCoNi also displayed the smallest charge transfer resistance among the tested electrocatalysts, as measured by EIS (Fig. 3d). On the other hand, similar C_{dl} and thus ECSA were obtained for all the catalysts, as analyzed through CV at different scan rates (Fig. S8). Thus, the higher catalytic performance of CrMnFeCoNi needs to be attributed to an intrinsically higher activity of its active sites rather than to a higher surface area [58]. Overall, CrMnFeCoNi showed an improved OER performance over the tested materials and most previously reported alloy catalysts, as shown in Fig. 3e and Table S3.

The CrMnFeCoNi stability under OER conditions was analyzed using chronoamperometry. As shown in Fig. 3f, after a 30 h measurement at 1.5 V vs. RHE, 99 % of the initial current density was maintained. Besides, after long-term OER, the composition of the HEA, as measured by ICP-OES analysis, was relatively similar to the original one, with an atomic ratio Cr:Mn:Fe:Co:Ni = 17:21:26:17:19 (Fig. S9). The metal content in the electrolyte after long-term OER was also analyzed and it is displayed in Table S4. After a 30 h reaction, negligible amounts of metal were dissolved in the KOH electrolyte, which indicates HEAs to be very stable and resistant to alkaline corrosion. The high stability of HEAs is generally associated with a high entropy effect [59]. XRD analysis showed the crystal structure of the materials to be maintained (Fig. S10). Besides, HRTEM characterization confirmed that, after the OER stability test, CrMnFeCoNi conserved the cubic FeCoNi phase in the particle core, while a thin amorphous layer attributed to the metal (oxyhydr)oxide had formed on their surface (Fig. S11).

In situ Raman spectroscopy was used to determine the evolution of CrMnFeCoNi (Fig. S12). While no Raman signal was obtained from CrMnFeCoNi at the open circuit potential (OCP), as the potential increased to 1.1 and 1.2 V vs. RHE, two peaks at 452 and 479 cm^{-1} were observed. These two peaks were indexed as the A_{1g} stretching $Ni(OH)_2$ [60] and FeOH asymmetric stretching [61] Raman modes, respectively. With the potential further increasing to 1.3-1.6 V, i.e. above 1.23 V vs. RHE, three additional peaks at 524, 562, and 609 cm^{-1} were detected and indexed as the FeOOH [62], A_{1g} stretching of NiOOH [62], and E_g of FeOOH [63] Raman modes, respectively. Overall, *in situ* Raman data showed that CrMnFeCoNi was first transformed to metal hydroxide and then to metal oxyhydroxide under OER conditions. XPS characterization of the materials after long-term OER showed the surface of the CrMnFeCoNi particles to be completely oxidized (Fig. S13), further verifying the evolution of the catalysts.

3.3. Electrocatalytic ORR performance

Towards obtaining a high-performance bifunctional catalyst, the two HEAs and the quaternary catalyst, CrMnFeCoNi, CuMnFeCONi, and MnFeCoNi, were further characterized towards the ORR in 0.1 M KOH using an RRDE electrode. Fig. 4a shows the CV curves measured from CrMnFeCoNi both in Ar and O$_2$ saturated electrolytes. Beyond the non-Faradic current characteristic of a double-layer charge-discharge, no obvious electrochemical feature was obtained for the CrMnFeCoNi catalyst within an Ar-saturated electrolyte. In contrast, a noticeable cathodic peak was observed when the electrolyte was saturated with O$_2$, pointing at a good electrocatalytic activity toward ORR.

Fig. 4b shows the LSV curves measured with a rotation speed of 1600 rpm from CrMnFeCoNi, CuMnFeCONi, MnFeCoNi, and a commercial Pt/C catalyst. Among the quaternary and quinary alloys, the CrMnFeCoNi electrode provided the highest current densities, comparable with those of Pt/C. Fig. 4c shows the LSV curves obtained from the CrMnFeCoNi electrode at different rotation speeds in the range from 400 rpm to 2500 rpm. At 1600 rpm, the half-wave potential of the CrMnFeCoNi electrode was 0.78 V, and its onset potential was 0.88 V. From the LSV data, the kinetics of the CrMnFeCoNi electrode was investigated using the Koutecky-Levich plots of the inverse current density with the square root of the rotation speed (Fig. 4d). The excellent linearity of the plots indicates a first-order reaction kinetics with the oxygen concentration

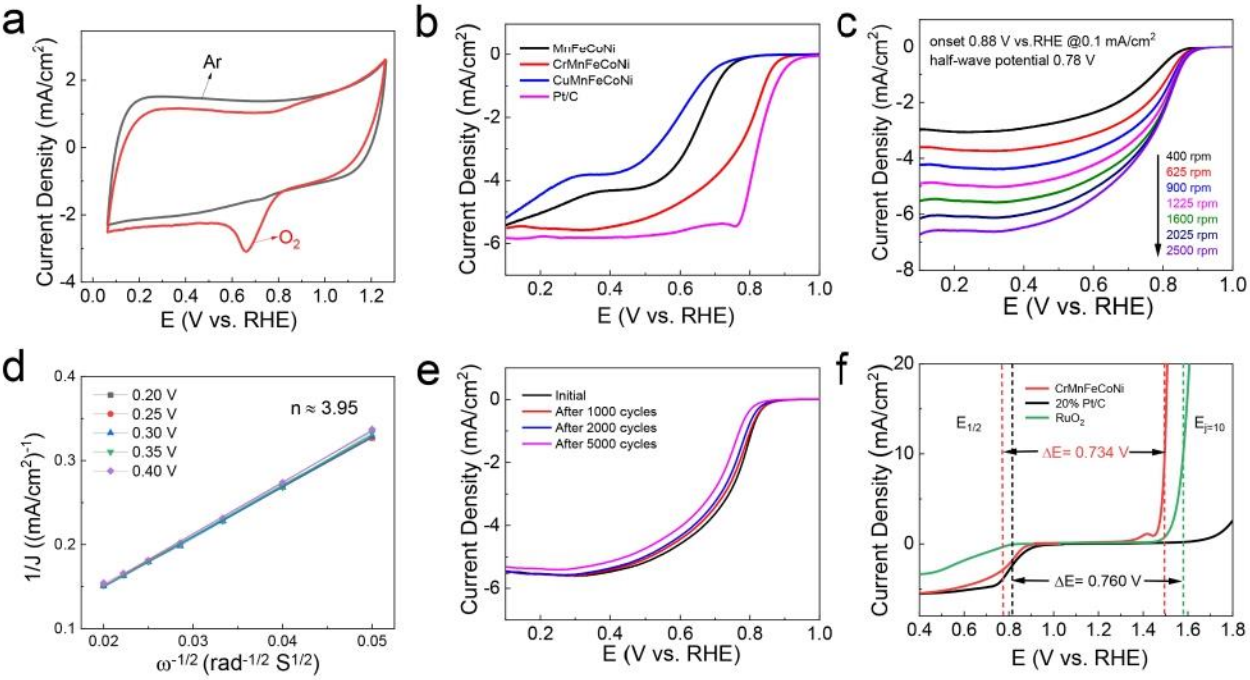

Fig. 4. ORR and bifunctional catalytic performance of the CrMnFeCoNi electrode. (a) CV curves measured in Ar and O_2 saturated electrolytes. (b) ORR polarization curves of different electrodes. (c) LSV curves with different rotation rates. (d) Koutecky-Levich plots. (e) LSV curves before and after stability tests of 1000, 2000, and 5000 cycles. (f) ORR/OER bifunctional LSV curves of different electrodes.

[64]. The overlapping of the curves obtained at different voltages pointed to a potential-independent electron transfer number for ORR, which was estimated at 3.95. Thus, CrMnFeCoNi electrodes showed high selectivity toward a total oxygen reduction dominated by a one-step 4-electron oxygen reduction pathway. This result was corroborated by analyzing the H_2O_2 yield. As determined by RRDE tests, the H_2O_2 average selectivity of the CrMnFeCoNi electrode was just 0.2 % (Fig. S14), confirming the dominant 4-electron ORR pathway [65]. Fig. 4e displays the LSV curves measured from the CrMnFeCoNi electrode before and after 1000, 2000, and 5000 CV cycles. LSV curves showed no significant variation in the maximum current density and the onset potential, demonstrating the excellent stability of the CrMnFeCoNi electrode.

The first quantitative measurement of the potential performance of the bifunctional catalyst towards oxygen reactions was evaluated from the potential gap (E_{gap}) between the overpotential for OER and the half-wave potential for ORR [66]. As shown in Fig. 4f, CrMnFeCoNi electrodes exhibit an outstanding low E_{gap} value of 0.734 V in 0.1 M KOH, well below that of Pt/C and RuO_2 (0.760 V) and most state-of-the-art ORR and OER bifunctional electrocatalysts reported recently (Table S5).

3.4. DFT calculations

DFT calculations were used to evaluate the Gibbs free energy for each of the four OER elementary steps [67] on the MnFeCoNi (111), CrMnFeCoNi (111), and CuMnFeCoNi (111) surfaces:

$$H_2O + * \rightarrow *OH + H^+ + e^- \quad (1)$$

$$*OH + H_2O \rightarrow *O + H_2O + H^+ + e^- \quad (2)$$

$$*O + H_2O \rightarrow *OOH + H^+ + e^- \quad (3)$$

$$*OOH + H_2O \rightarrow * + O_2 + H_2O + H^+ + e^- \quad (4)$$

A 15 Å vacuum layer in the z-direction was considered between the slab and its periodic images. During structural optimizations of the (111) surface models, a 3×3×1 γ-point centered k-point grid for Brillouin zone was used. All the atomic layers were allowed to fully relax. Fig. 5a, Fig. S15 and Fig. S16 show the relaxed molecular configuration of the four fundamental steps of the OER/ORR for CrMnFeCoNi, CuMnFeCoNi, and MnFeCoNi. Fig. 5b shows the Gibbs free energies calculated for the three materials. For OER, the *O reaction with the electrolyte to generate *OOH is the reaction-determining step (RDS) as it is the one involving the largest energy barrier [68]. CrMnFeCoNi displayed a significantly lower energy barrier for the OER RDS step (1.48 eV) compared with MnFeCoNi (1.74 eV), and CuMnFeCoNi (1.95 eV). For ORR, Fig. 5c shows a plot of the free energy of the oxygen intermediates for the associative mechanism at both 0 V and 1.23 V vs. RHE. Comparing the free energy diagram at 0 V and 1.23 V, two uphill steps appear, the O* to OH* and especially the OH* to H_2O, which is considered the RDS for ORR. According to DFT results, CrMnFeCoNi displayed the smallest RDS energy step, 0.28 eV, when compared with MnFeCoNi, 0.65 eV, and CuMnFeCoNi, 0.80 eV. The lower OER/ORR energy barriers are consistent with the best OER and ORR performance experimentally obtained with CrMnFeCoNi. The larger OER/ORR energy barriers obtained for CuMnFeCoNi are also consistent with experimental evidence showing that Cu deteriorated the OER and ORR performances.

Beyond composition, the experimentally-observed lattice distortions can notably impact the physical and chemical properties of the HEA. HEAs are already often characterized by severe strain associated with atomic size mismatches, which potentially affect the binding modes of intermediates as well as the catalytic selectivity [69]. Lattice distortion in HEAs can promote a higher density of active electrons around the Fermi level, resulting in faster electron transfer [70]. Furthermore, twinning is demonstrated to be an effective way of enhancing the performance of metallic catalysts [71].

The adsorption properties of CrMnFeCoNi and CuMnFeCoNi with/without lattice distortions were analyzed using the d band center as a descriptor of the adsorbate-metal interaction. The higher the d band center energy, i.e. the closer to the Fermi level, the stronger the binding between the metal atoms and the intermediates. According to the Sabatier principle, a moderate adsorption value usually gives rise to the

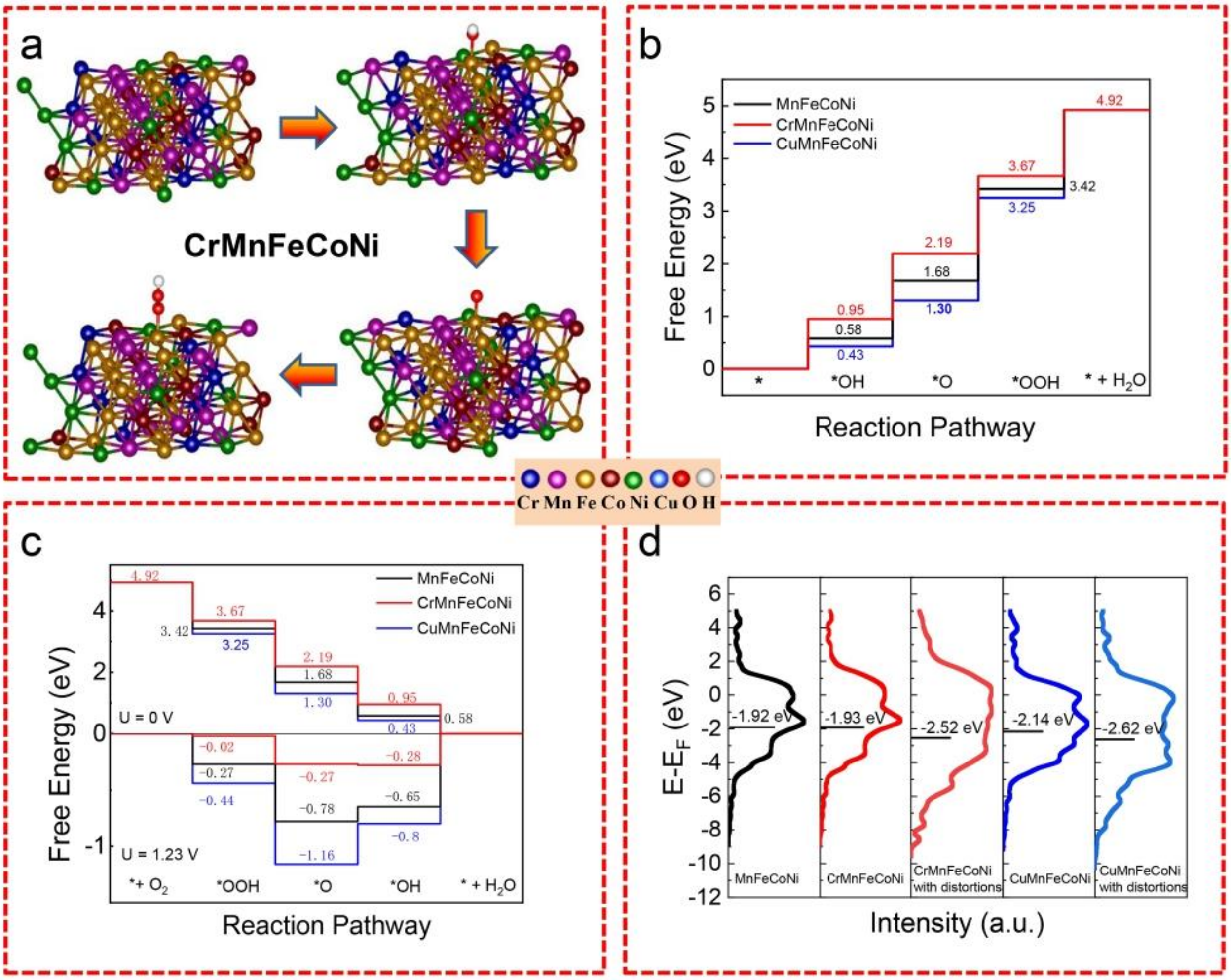

Fig. 5. (a) Relaxed atomic configuration of the four fundamental steps of OER/ORR for the CrMnFeCoNi structure. (b-c) Gibbs free energy change diagrams of the OER/ORR process. (d) D band spectra of MnFeCoNi, CrMnFeCoNi, and CuMnFeCoNi with/without lattice distortions. The black lines represent the corresponding d-band center position.

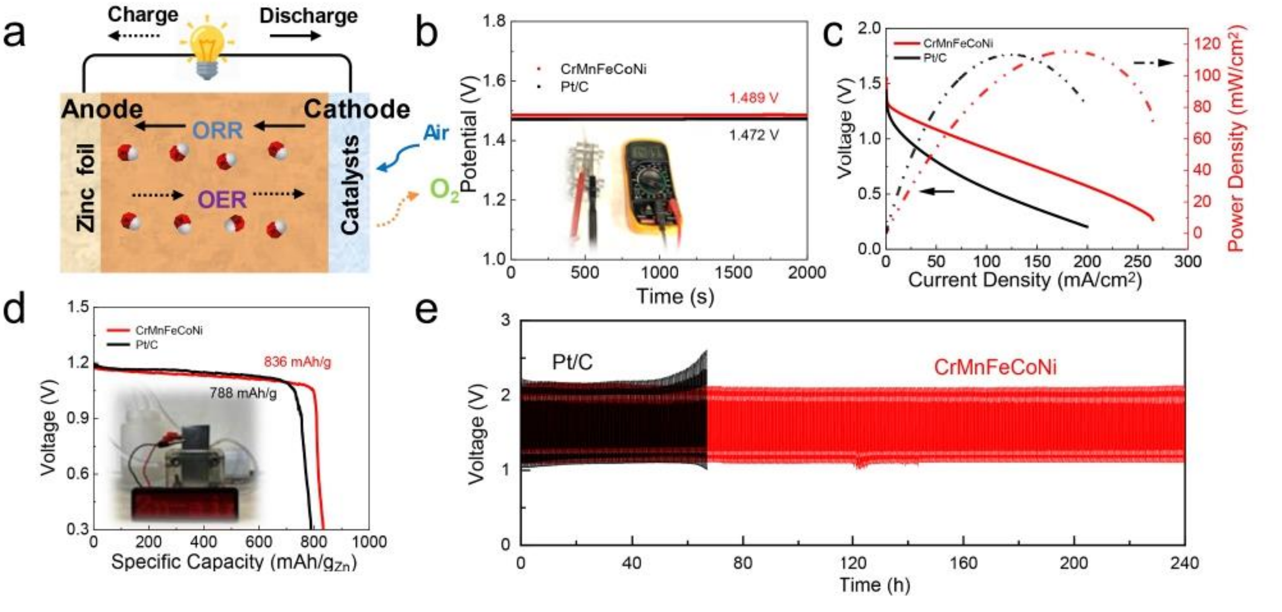

Fig. 6. (a) ZAB schematic diagram. (b) OCV measurements and photograph of the assembled ZAB. (c) Power density plots. (d) Specific capacity comparisons between a CrMnFeCoNi- and a Pt/C-based ZAB. A photograph of a red LED screen powered by a CrMnFeCoNi-based ZAB is also shown. (e) Galvanostatic discharge-charge curves with 10 min discharge and 10 min charge cycles at a current density of 8 mA/cm^2.

highest catalytic activity. As displayed with black lines in Fig. 5d, the d band center of CrMnFeCoNi and CuMnFeCoNi with distortions is downward displaced when compared with those calculated without distortions, indicating a weaker interaction between metal atoms and intermediates in the distorted lattices. The d band center value of MnFeCoNi, CrMnFeCoNi with lattice distortions, and CuMnFeCoNi with lattice distortions are -1.92 eV,-2.52 eV, and -2.62 eV, respectively. Interestingly, the reduced binding energies can facilitate the final reaction step, the release of O_2, which energy barrier is comparable to that of the RDS in CrMnFeCoNi.

3.5. Zinc-air batteries

Owing to the excellent OER and ORR activity of the CrMnFeCoNi HEA, this catalyst was tested as the oxygen electrode in reversible ZABs. ZABs were assembled using the CrMnFeCoNi HEA as the air cathode and zinc foil as the anode (Fig. 6a, see additional details in the Materials and methods section). A 20 wt% Pt/C was also tested as a reference air cathode. As shown in Fig. 6b, the ZAB based on a CrMnFeCoNi cathode exhibited an open-circuit voltage (OCV) of 1.489 V, i.e. 90% of its theoretical limit (1.66 V) [11], slightly above that of the Pt/C-based ZAB (1.472 V). The peak power density of the CrMnFeCoNi-based ZAB was 116.5 mW/cm^2, slightly higher than that of the Pt/C ZAB (114.1 mW/cm^2, Fig. 6c). Besides, at a current density of 8 mA/cm^2, the CrMnFeCoNi-based ZAB delivered a specific capacity of 836 mAh/g, significantly larger than that of the Pt/C ZAB, 788 mAh/g (Fig. 6d). A comparison of the outstanding performance of the CrMnFeCoNi-based ZAB with previously reported devices is provided in Table S6. As shown in Fig. 6d, the CrMnFeCoNi-based ZAB can power a 1.4 V red LED screen. Most important, as shown in Fig. 6e, the CrMnFeCoNi-based ZAB is not only characterized by a lower charge–discharge overpotential, i.e. a higher energy efficiency, compared with the Pt/C-based ZAB, but also much higher durability. Unlike the Pt/C-based ZAB with an obvious overpotential increase after 60 h of charging/discharging cycles, the CrMnFeCoNi-based ZAB exhibits a negligible variation in voltage even after 240 h, i.e. 10 days and 720 cycles, of continuous operation with charge/discharge cycles at a current density of 8 mA/cm^2, which suggests outstanding long-term durability. The stability of CrMnFeCoNi-based ZAB operating at different current densities was also investigated. As shown in Fig. S17 and S18, the CrMnFeCoNi-based ZAB exhibits excellent durability even after 400 h (1200 cycles) and 240 h (720 cycles) of continuous charge/discharge operation at a current density of 5 mA/cm^2 and 12 mA/cm^2, further proving its excellent stability.

Flexible ZABs based on a CrMnFeCoNi oxygen catalyst were also assembled using a gel electrolyte (see details in the Materials and methods section). Fig. 7a shows the structure diagram of the flexible solid ZABs, where a polished Zn plate is used as the anode, a hydrophilic carbon paper with catalysts is used as the cathode, and the PVA-KOH-H_2O gel is used as the electrolyte. CrMnFeCoNi-based ZABs could light a red LED while bent at different angles, proving their flexibility upon operation (Fig. 7b). The solid CrMnFeCoNi-based ZAB displayed a

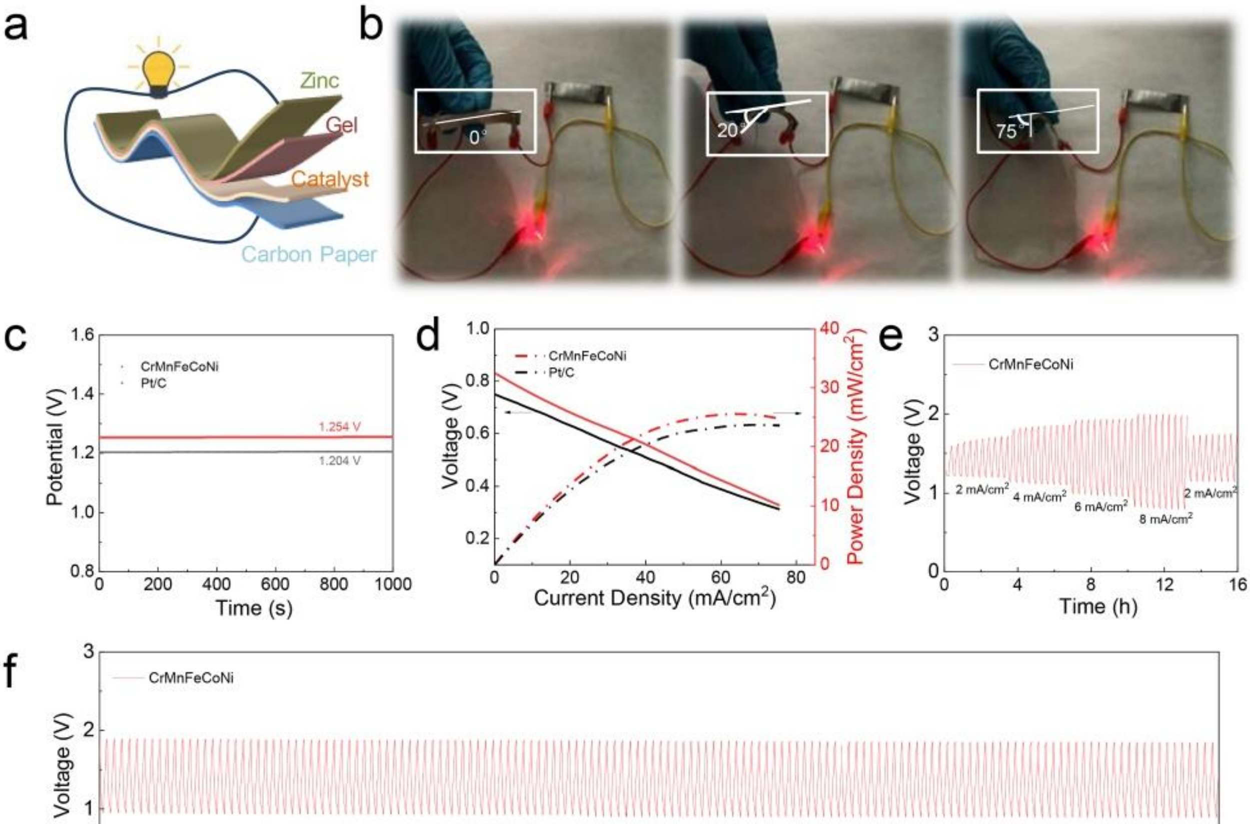

Fig. 7. (a) Solid and flexible ZAB schematic diagram. (b) Optical images of a red LED lighted by a CrMnFeCoNi-based ZABs while bended at differnt angles. (c) OCV measurements, and (d) power density plots of a CrMnFeCoNi- and a Pt/C-based flexible ZAB. (e) Galvanostatic discharge-charge curves of a CrMnFeCoNi-based ZAB with 10 min discharge and 10 min charge cycles at a current density of 2, 4, 6, and 8 mA/cm^2. (f) Galvanostatic discharge-charge curves of a CrMnFeCoNi-based ZAB with 10 min discharge and 10 min charge cycles at a current density of 5 mA/cm^2.

higher OCV value of 1.254 V than that of Pt/C-based ZAB of 1.204 V (Fig. 7c). The peak power density of the solid CrMnFeCoNi-based ZAB was 25.5 mW/cm^2, higher than the 23.7 mW/cm^2 of the Pt/C-based ZAB (Fig. 7d). As shown in Fig. 7e, the solid CrMnFeCoNi-based ZAB exhibits good stability at the current densities of 2, 4, 6, and 8 mA/cm^2 with continuous cycling. Long-time charge-discharge cycling is shown in Fig. 7f. The solid CrMnFeCoNi-based ZAB was stable for 50 h of continuous 10 min discharge and 10 min charge cycles, i.e. 150 cycles, at a current density of 5 mA/cm^2.

4. Conclusion

In summary, we detailed a solution-based synthetic procedure to produce CrMnFeCoNi and CuMnFeCoNi HEAs, the MnFeCoNi quaternary alloy, and the different ternary alloys at a moderate reaction temperature. The CrMnFeCoNi HEA, characterized by a strongly distorted lattice and modulated surface electronic states, showed an outstanding OER and ORR catalytic performance, significantly above that of quaternary alloys, CuMnFeCoNi, and commercial RuO$_2$ and Pt/C catalysts. DFT calculations showed the incorporation of Cr within the quaternary MnFeCoNi and the defective HEA structure to reduce the energy barrier for the generation of *OOH from *O and the release of O$_2$, respectively, which were identified as the RDS of the OER process. DFT calculations also showed the CrMnFeCoNi to present more favorable ORR intermediate energy steps. Owing to the small E$_{gap}$ value between the overpotential for OER and the half-wave potential for ORR of CrMnFeCoNi, 0.734 V, this HEA was used bifunctional catalyst at the air cathode of a rechargeable ZAB. The CrMnFeCoNi-based ZAB showed an OCV of 1.489 V, a peak power density of 116.5 mW/cm^2, and a specific capacity of 836 mAh/g at a current density of 8 mA/cm^2. Besides, CrMnFeCoNi-based ZABs displayed excellent stability for more than 240 h and 400 h of continuous charge/discharge cycling at a current density of 8 mA/cm^2 and 5 mA/cm^2.

Supporting Information

Supporting Information is available from the Online Library or from the author.

CRediT authorship contribution statement

Ren He: Investigation, Conceptualization, Methodology, Validation, Visualization, Writing – original draft. **Linlin Yang:** Conceptualization, Validation, Visualization, Writing – original draft. **Yu Zhang:** Formal analysis, Visualization, Investigation. **Xiang Wang:** Formal analysis. **Seungho Lee:** Formal analysis. **Ting Zhang:** Formal analysis. **Lingxiao Li:** Software. **Zhifu Liang:** Investigation. **Jingwei Chen:** Software. **Junshan Li:** Formal analysis. **Ahmad Ostovari Moghaddam:** Formal analysis. **Jordi Llorca:** Formal analysis. **Maria Ibáñez:** Formal analysis. **Jordi Arbiol:** Formal analysis. **Ying Xu:** Software, Formal analysis, Resources. **Andreu Cabot:** Supervision, Funding acquisition, Project administration, Writing – review & editing.

Declaration of Competing Interest

The authors declare no conflict of interest.

Data availability

Data will be made available on request.

Acknowledgments

The authors thank the support from the project COMBENERGY, PID2019-105490RB-C32, from the Spanish Ministerio de Ciencia e Innovación. The authors acknowledge funding from Generalitat de Catalunya 2021 SGR 01581 and 2021 SGR 00457. ICN2 acknowledges the Severo Ochoa program from Spanish MINECO (Grant No. SEV-2017-0706). IREC and ICN2 are funded by the CERCA Programme from the Generalitat de Catalunya. ICN2 is supported by the Severo Ochoa program from Spanish MCIN / AEI (Grant No.: CEX2021-001214-S). ICN2 acknowledges funding from Generalitat de Catalunya 2017 SGR 327. This study was supported by MCIN with funding from European Union NextGenerationEU (PRTR-C17.I1) and Generalitat de Catalunya. The authors thank the support from the project NANOGEN (PID2020-116093RB-C43), funded by MCIN/ AEI/10.13039/501100011033/ and by "ERDF A way of making Europe", by the "European Union". Part of the present work has been performed in the frameworks of Universitat de Barcelona Nanoscience PhD program. This research was supported by the Scientific Service Units (SSU) of IST Austria through resources provided by Electron Microscopy Facility (EMF). S. Lee. and M. Ibáñez acknowledge funding by IST Austria and the Werner Siemens Foundation. J. Llorca is a Serra Húnter Fellow and is grateful to ICREA Academia program and projects MICINN/FEDER PID2021-124572OB-C31 and GC 2017 SGR 128. L. L.Yang thanks the China Scholarship Council (CSC) for the scholarship support (202008130132). Z. F. Liang acknowledges funding from MINECO SO-FPT PhD grant (SEV-2013-0295-17-1). J. W. Chen and Y. Xu thank the support from The Key Research and Development Program of Hebei Province (No. 20314305D) and the cooperative scientific research project of the "Chunhui Program" of the Ministry of Education (2018-7). This work was supported by the Natural Science Foundation of Sichuan province (NSFSC) and funded by the Science and Technology Department of Sichuan Province (2022NSFSC1229).

Supplementary materials

Supplementary material associated with this article can be found, in the online version, at doi:10.1016/j.ensm.2023.03.022.

References

[1] B. Wei, Z. Fu, D. Legut, T.C. Germann, S. Du, H. Zhang, J.S. Francisco, R. Zhang, Rational design of highly stable and active mxene-based bifunctional ORR/OER double-atom catalysts, Adv. Mater. 33 (2021), e2102595.

[2] J. Yan, Y. Wang, Y. Zhang, S. Xia, J. Yu, B. Ding, Direct magnetic reinforcement of electrocatalytic ORR/OER with electromagnetic induction of magnetic catalysts, Adv. Mater. 33 (2021), e2007525.

[3] Y. Wang, X. Li, M. Zhang, J. Zhang, Z. Chen, X. Zheng, Z. Tian, N. Zhao, X. Han, K. Zaghib, Y. Wang, Y. Deng, W. Hu, Highly active and durable single-atom tungsten-doped $iS_{0.5}Se_{0.5}$ nanosheet @ $NiS_{0.5}Se_{0.5}$ nanorod heterostructures for water splitting, Adv. Mater. (2022), e2107053.

[4] H. Song, J. Yu, Z. Tang, B. Yang, S. Lu, Halogen-doped carbon dots on amorphous cobalt phosphide as robust electrocatalysts for overall water splitting, Adv. Energy Mater. (2022), 2102573.

[5] L. Gong, X.Y.E. Chng, Y. Du, S. Xi, B.S. Yeo, Enhanced catalysis of the electrochemical oxygen evolution reaction by iron(iii) ions adsorbed on amorphous cobalt oxide, ACS Catal. 8 (2017) 807–814.

[6] Y. Chen, S. Ji, S. Zhao, W. Chen, J. Dong, W.C. Cheong, R. Shen, X. Wen, L. Zheng, A.I. Rykov, S. Cai, H. Tang, Z. Zhuang, C. Chen, Q. Peng, D. Wang, Y. Li, Enhanced oxygen reduction with single-atomic-site iron catalysts for a zinc-air battery and hydrogen-air fuel cell, Nat. Commun. 9 (2018), 5422, https://doi.org/10.1038/s41467-018-07850-2.

[7] H. Li, Q. Li, P. Wen, T.B. Williams, S. Adhikari, C. Dun, C. Lu, D. Itanze, L. Jiang, D. L. Carroll, G.L. Donati, P.M. Lundin, Y. Qiu, S.M. Geyer, Colloidal cobalt phosphide nanocrystals as trifunctional electrocatalysts for overall water splitting powered by a zinc-air battery, Adv. Mater. 30 (2018), 1705796.

[8] S. Chen, T. Wang, L. Ma, B. Zhou, J. Wu, D. Zhu, Y. Y. Li, J. Fan, C. Zhi, Aqueous rechargeable zinc air batteries operated at −110°C, Chem, (2022) 10.1016/j.chempr.2022.10.028.

[9] T. Gu, D. Zhang, Y. Yang, C. Peng, D. Xue, C. Zhi, M. Zhu, J. Liu, Dual-sites coordination engineering of single atom catalysts for full-temperature adaptive flexible ultralong-life solid-state zn−air batteries, Adv. Funct. Mater. (2022), 2212299.

[10] J. Han, X. Meng, L. Lu, J. Bian, Z. Li, C. Sun, Single-atom Fe-N_x-C as an efficient electrocatalyst for zinc-air batteries, Adv. Funct. Mater. 29 (2019), 1808872.

[11] J. Fu, Z.P. Cano, M.G. Park, A. Yu, M. Fowler, Z. Chen, Electrically rechargeable zinc-air batteries: progress, challenges, and perspectives, Adv. Mater. 29 (2017), 1604685.

[12] P. Tan, B. Chen, H. Xu, H. Zhang, W. Cai, M. Ni, M. Liu, Z. Shao, Flexible Zn– and Li–air batteries: recent advances, challenges, and future perspectives, Energy Environ. Sci. 10 (2017) 2056–2080.

[13] Z. Li, W. Niu, Z. Yang, N. Zaman, W. Samarakoon, M. Wang, A. Kara, M. Lucero, M. V. Vyas, H. Cao, H. Zhou, G.E. Sterbinsky, Z. Feng, Y. Du, Y. Yang, Stabilizing atomic Pt with trapped interstitial F in Alloyed PtCo nanosheets for high-performance zinc-air batteries, Energy Environ. Sci. 13 (2020) 884–895.

[14] Y. Tian, X. Liu, L. Xu, D. Yuan, Y. Dou, J. Qiu, H. Li, J. Ma, Y. Wang, D. Su, S. Zhang, Engineering crystallinity and oxygen vacancies of Co(II) oxide nanosheets for high performance and robust rechargeable Zn–Air batteries, Adv. Funct. Mater. 31 (2021), 2101239.

[15] L. Zhuang, Y. Jia, H. Liu, X. Wang, R.K. Hocking, H. Liu, J. Chen, L. Ge, L. Zhang, M. Li, C.L. Dong, Y.C. Huang, S. Shen, D. Yang, Z. Zhu, X. Yao, Defect-induced Pt-Co-Se coordinated sites with highly asymmetrical electronic distribution for boosting oxygen-involving electrocatalysis, Adv. Mater. 31 (2019), e1805581.

[16] Y. Chang, P. Zhai, J. Hou, J. Zhao, J. Gao, Excellent HER and OER catalyzing performance of se-vacancies in defects-engineered PtSe$_2$: from simulation to experiment, Adv. Energy Mater. 12 (2021), 2102359.

[17] W. Zhang, J. Chang, G. Wang, Z. Li, M. Wang, Y. Zhu, B. Li, H. Zhou, G. Wang, M. Gu, Z. Feng, Y. Yang, Surface oxygenation induced strong interaction between Pd catalyst and functional support for zinc-air batteries, Energy Environ. Sci. (2022) 157–1584.

[18] Y. Lin, H. Cui, C. Liu, R. Li, S. Wang, G. Qu, Z. Wei, Y. Yang, Y. Wang, Z. Tang, H. Li, H. Zhang, C. Zhi, H. Lv, A covalent organic framework as a long-life and high-rate anode suitable for both aqueous acidic and alkaline batteries, Angew Chem. Int. Ed. (2023), e202218745.

[19] X. Wang, X. Han, R. Du, Z. Liang, Y. Zuo, P. Guardia, J. Li, J. Llorca, J. Arbiol, R. Zheng, A. Cabot, Unveiling the role of counter-anions in amorphous transition metal-based oxygen evolution electrocatalysts, Appl. Catal. B-environ. 320 (2023), 121988.

[20] R. Du, K. Xiao, B. Li, X. Han, C. Zhang, X. Wang, Y. Zuo, P. Guardia, J. Li, J. Chen, J. Arbiol, A. Cabot, Controlled oxygen doping in highly dispersed Ni-loaded g-C$_3$N$_4$ nanotubes for efficient photocatalytic H$_2$O$_2$ production, Chem. Eng. J. 441 (2022), 135999.

[21] X. Wang, J. Li, Q. Xue, X. Han, C. Xing, Z. Liang, P. Guardia, Y. Zuo, R. Du, L. Balcells, J. Arbiol, J. Llorca, X. Qi, A. Cabot, Sulfate-decorated amorphous-crystalline cobalt-iron oxide nanosheets to enhance O-O coupling in the oxygen evolution reaction, ACS Nano 17 (2023) 825–836.

[22] S. Chen, X. Liang, S. Hu, X. Li, G. Zhang, S. Wang, L. Ma, C.L. Wu, C. Zhi, J. A. Zapien, Inducing Fe 3d electron delocalization and spin-state transition of FeN$_4$ species boosts oxygen reduction reaction for wearable zinc-air battery, Nanomicro Lett. 15 (2023) 47.

[23] S.S. Shinde, C.H. Lee, J.-Y. Jung, N.K. Wagh, S.-H. Kim, D.-H. Kim, C. Lin, S.U. Lee, J.-H. Lee, Unveiling dual-linkage 3D hexaiminobenzene metal–organic frameworks towards long-lasting advanced reversible zn–air batteries, Energy Environ. Sci. 12 (2019) 727–738.

[24] T. Berestok, J. Chacon-Borrero, J. Li, P. Guardia, A. Cabot, Crystalline magnetic gels and aerogels combining large surface areas and magnetic moments, Langmuir (2023), https://doi.org/10.1021/acs.langmuir.2c03372.

[25] M. Li, D. Yang, J.J. Biendicho, X. Han, C. Zhang, K. Liu, J. Diao, J. Li, J. Wang, M. Heggen, R.E. Dunin-Borkowski, J. Wang, G. Henkelman, J.R. Morante, J. Arbiol, S.L. Chou, A. Cabot, Enhanced polysulfide conversion with highly conductive and electrocatalytic iodine-doped bismuth selenide nanosheets in lithium-sulfur batteries, Adv. Funct. Mater. 32 (2022), 2200529.

[26] C. Zhang, B. Fei, D. Yang, H. Zhan, J. Wang, J. Diao, J. Li, G. Henkelman, D. Cai, J. J. Biendicho, J.R. Morante, A. Cabot, Robust lithium–sulfur batteries enabled by highly conductive WSe$_2$-based superlattices with tunable interlayer space, Adv. Funct. Mater. 32 (2022), 2201322.

[27] D. Yang, Z. Liang, P. Tang, C. Zhang, M. Tang, Q. Li, J.J. Biendicho, J. Li, M. Heggen, R.E. Dunin-Borkowski, M. Xu, J. Llorca, J. Arbiol, J.R. Morante, S. L. Chou, A. Cabot, A high conductivity 1d π-d conjugated metal-organic framework with efficient polysulfide trapping-diffusion-catalysis in lithium-sulfur batteries, Adv. Mater. 34 (2022), e2108835.

[28] X. Wang, X. Han, R. Du, C. Xing, X. Qi, Z. Liang, P. Guardia, J. Arbiol, A. Cabot, J. Li, Cobalt molybdenum nitride-based nanosheets for seawater splitting, ACS Appl. Mater. Interfaces 14 (2022) 41924–41933.

[29] D. Yang, M. Li, X. Zheng, X. Han, C. Zhang, J. Jacas Biendicho, J. Llorca, J. Wang, H. Hao, J. Li, G. Henkelman, J. Arbiol, J.R. Morante, D. Mitlin, S. Chou, A. Cabot, Phase engineering of defective copper selenide toward robust lithium-sulfur batteries, ACS Nano 16 (2022) 11102–11114.

[30] Q. Ding, Y. Zhang, X. Chen, X. Fu, D. Chen, S. Chen, L. Gu, F. Wei, H. Bei, Y. Gao, M. Wen, J. Li, Z. Zhang, T. Zhu, R.O. Ritchie, Q. Yu, Tuning element distribution, structure and properties by composition in high-entropy alloys, Nature 574 (2019) 223–227.

[31] M.-H. Tsai, Physical properties of high entropy alloys, Entropy 15 (2013) 5338–5345.

[32] D.B. Miracle, O.N. Senkov, A critical review of high entropy alloys and related concepts, Acta Mater. 122 (2017) 448–511.

[33] A. Ostovari Moghaddam, A. Cabot, E.A. Trofimov, Does the pathway for development of next generation nuclear materials straightly go through high-entropy materials? Int. J. Refract. Hard Met. 97 (2021), 105504.

[34] M.-H. Tsai, J.-W. Yeh, High-entropy alloys: a critical review, Mater. Res. Lett. 2 (2014) 107–123.

[35] N. Kumar Katiyar, K. Biswas, J.-W. Yeh, S. Sharma, C. Sekhar Tiwary, A perspective on the catalysis using the high entropy alloys, Nano Energy, 88 (2021) 106261.

[36] C.S. Tiwary, P. Pandey, S. Sarkar, R. Das, S. Samal, K. Biswas, K. Chattopadhyay, Five decades of research on the development of eutectic as engineering materials, Prog. Mater. Sci. 123 (2022), 100793.

[37] G.M. Tomboc, T. Kwon, J. Joo, K. Lee, High entropy alloy electrocatalysts: a critical assessment of fabrication and performance, J. Mater. Chem. A 8 (2020) 14844–14862.

[38] M. Fu, X. Ma, K. Zhao, X. Li, D. Su, High-entropy materials for energy-related applications, iScience 24 (2021), 102177.

[39] G. Fang, J. Gao, J. Lv, H. Jia, H. Li, W. Liu, G. Xie, Z. Chen, Y. Huang, Q. Yuan, X. Liu, X. Lin, S. Sun, H.-J. Qiu, Multi-component nanoporous alloy/(oxy) hydroxide for bifunctional oxygen electrocatalysis and rechargeable zn-air batteries, Appl. Catal. B-Environ. 268 (2020), 118431.

[40] L. Zendejas Medina, L. Riekehr, U. Jansson, Phase formation in magnetron sputtered CrMnFeCoNi high entropy alloy, Surf. Coat. Technol. 403 (2020), 126323.

[41] T. Lindner, M. Löbel, E. Saborowski, L.-M. Rymer, T. Lampke, Wear and corrosion behaviour of supersaturated surface layers in the high-entropy alloy Systems CrMnFeCoNi and CrFeCoNi, Crystals 10 (2020) 110.

[42] Z. Li, S. Zhao, S.M. Alotaibi, Y. Liu, B. Wang, M.A. Meyers, Adiabatic shear localization in the CrMnFeCoNi High-Entropy Alloy, Acta Mater. 151 (2018) 424–431.

[43] Z. Li, K.G. Pradeep, Y. Deng, D. Raabe, C.C. Tasan, Metastable high-entropy dual-phase alloys overcome the strength-ductility trade-off, Nature 534 (2016) 227–230.

[44] B. Cantor, I.T.H. Chang, P. Knight, A.J.B. Vincent, Microstructural Development in Equiatomic Multicomponent Alloys, Mater. Sci. Eng. A 375-377 (2004) 213–218.

[45] H. Cheng, W. Chen, X. Liu, Q. Tang, Y. Xie, P. Dai, Effect of Ti and C additions on the microstructure and mechanical properties of the FeCoCrNiMn high-entropy alloy, Mater. Sci. Eng. A 719 (2018) 192–198.

[46] S. Xiang, J. Li, H. Luan, A. Amar, S. Lu, K. Li, L. Zhang, X. Liu, G. Le, X. Wang, F. Qu, W. Zhang, D. Wang, Q. Li, Effects of process parameters on microstructures and tensile properties of laser melting deposited crmnfeconi high entropy alloys, Mater. Sci. Eng A, 743 (2019) 412–417.

[47] F. Granberg, K. Nordlund, M.W. Ullah, K. Jin, C. Lu, H. Bei, L.M. Wang, F. Djurabekova, W.J. Weber, Y. Zhang, Mechanism of radiation damage reduction in equiatomic multicomponent single phase alloys, Phys. Rev. Lett. 116 (2016), 135504.

[48] C. Lu, L. Niu, N. Chen, K. Jin, T. Yang, P. Xiu, Y. Zhang, F. Gao, H. Bei, S. Shi, M. R. He, I.M. Robertson, W.J. Weber, L. Wang, Enhancing radiation tolerance by controlling defect mobility and migration pathways in multicomponent single-phase alloys, Nat. Commun. 7 (2016) 13564.

[49] Y. Tian, C. Lu, Y. Shen, X. Feng, Microstructure and corrosion property of CrMnFeCoNi high entropy alloy coating on Q235 substrate via mechanical alloying method, Surf. Interfaces 15 (2019) 135–140.

[50] C. Wang, J. Yu, Y. Yu, Y. Zhao, Y. Zhang, X. Han, Comparison of the corrosion and passivity behavior between CrMnFeCoNi and CrFeCoNi coatings prepared by argon arc cladding, J. Mater. Res. Technol. 9 (2020) 8482–8496.

[51] Z.P. Lu, H. Wang, M.W. Chen, I. Baker, J.W. Yeh, C.T. Liu, T.G. Nieh, An assessment on the future development of high-entropy alloys: summary from a recent workshop, Intermetallics 66 (2015) 67–76.

[52] K. Zhang, G. Zhang, J. Qu, H. Liu, Zinc substitution-induced subtle lattice distortion mediates the active center of cobalt diselenide electrocatalysts for enhanced oxygen evolution, Small 16 (2020), e1907001.

[53] F.A. Stevie, C.L. Donley, Introduction to X-Ray photoelectron spectroscopy, J. Vacuum Sci. Technol. A 38 (2020).

[54] Q. Zhou, Z. Zhang, J. Cai, B. Liu, Y. Zhang, X. Gong, X. Sui, A. Yu, L. Zhao, Z. Wang, Z. Chen, Template-guided synthesis of Co nanoparticles embedded in hollow nitrogen doped carbon tubes as a highly efficient catalyst for rechargeable Zn-Air Batteries, Nano Energy 71 (2020), 104592.

[55] E. Luo, H. Zhang, X. Wang, L. Gao, L. Gong, T. Zhao, Z. Jin, J. Ge, Z. Jiang, C. Liu, W. Xing, Single-atom Cr-N$_4$ sites designed for durable oxygen reduction catalysis in acid media, Angew Chem. Int. Ed. 58 (2019) 12469–12475.

[56] J. Su, R. Ge, K. Jiang, Y. Dong, F. Hao, Z. Tian, G. Chen, L. Chen, Assembling ultrasmall copper-doped ruthenium oxide nanocrystals into hollow porous polyhedra: highly robust electrocatalysts for oxygen evolution in acidic media, Adv. Mater. (2018), e1801351.

[57] H. Wu, H. Li, X. Zhao, Q. Liu, J. Wang, J. Xiao, S. Xie, R. Si, F. Yang, S. Miao, X. Guo, G. Wang, X. Bao, Highly doped and exposed Cu(i)–N active sites within graphene towards efficient oxygen reduction for zinc–air batteries, Energy Environ. Sci. 9 (2016) 3736–3745.

[58] H.-J. Qiu, G. Fang, J. Gao, Y. Wen, J. Lv, H. Li, G. Xie, X. Liu, S. Sun, Noble metal-free nanoporous high-entropy alloys as highly efficient electrocatalysts for oxygen evolution reaction, ACS Mater. Lett. 1 (2019) 526–533.

[59] J.W. Yeh, S.K. Chen, S.J. Lin, J.-Y. Gan, T.-S. Chin, C.-H. Tsau, T.-T. Shun, S.-Y. Chang, Microstructure characterization of Al$_x$CoCrCuFeNi high-entropy alloy system with multiprincipal elements, Adv. Eng. Mater. 6 (2004), 299–230.

[60] J. Li, L. Jiang, S. He, L. Wei, R. Zhou, J. Zhang, D. Yuan, S.P. Jiang, Heterostructured Ni(OH)$_2$/Ni$_3$S$_2$ supported on Ni foam as highly efficient and durable bifunctional electrodes for overall water electrolysis, Energ. Fuels 33 (2019) 12052–12062.

[61] J.H. Kwon, L.D. Wilson, R. Sammynaiken, Synthesis and characterization of magnetite and activated carbon binary composites, Synth. Met. 197 (2014) 8–17.

[62] L. Bai, S. lee, X. Hu, Spectroscopic and electrokinetic evidence for a bifunctional mechanism of the oxygen evolution reaction, Angew Chem. Int. Ed. 60 (2021) 3095–3103.

[63] M. Sendova, B.D. Hosterman, A. Grebe, In-situ isothermal micro-raman spectroscopy reveals the activation energy of dehydration in α-FeOOH, J. Raman Spectrosc. 48 (2017) 618–622.

[64] J. Liu, X. Yu, R. Du, C. Zhang, T. Zhang, J. Llorca, J. Arbiol, Y. Wang, M. Meyns, A. Cabot, Chromium phosphide CrP as highly active and stable electrocatalysts for oxygen electroreduction in alkaline media, Appl. Catal. B-environ. 256 (2019), 117846.

[65] H. Tan, Y. Li, J. Kim, T. Takei, Z. Wang, X. Xu, J. Wang, Y. Bando, Y.M. Kang, J. Tang, Y. Yamauchi, Sub-50 nm iron-nitrogen-doped hollow carbon sphere-encapsulated iron carbide nanoparticles as efficient oxygen reduction catalysts, Adv. Sci. 5 (2018), 1800120.

[66] X. Zheng, X. Cao, K. Zeng, J. Yan, Z. Sun, M.H. Rummeli, R. Yang, A self-jet vapor-phase growth of 3D FeNi@NCNT clusters as efficient oxygen electrocatalysts for zinc-air batteries, Small 17 (2021), e2006183.

[67] J. Du, F. Li, L. Sun, Metal-organic frameworks and their derivatives as electrocatalysts for the oxygen evolution reaction, Chem. Soc. Rev. 50 (2021) 2663–2695.

[68] J. Lee, A. Kumar, T. Yang, X. Liu, A.R. Jadhav, G.H. Park, Y. Hwang, J. Yu, C.T. K. Nguyen, Y. Liu, S. Ajmal, M.G. Kim, H. Lee, Stabilizing the OOH* intermediate via pre-adsorbed surface oxygen of a single ru atom-bimetallic alloy for ultralow overpotential oxygen generation, Energy Environ. Sci. 13 (2020) 5152–5164.

[69] M. Luo, S. Guo, Strain-controlled electrocatalysis on multimetallic nanomaterials, Nat. Rev. Mater. 2 (2017), 17059.

[70] K. Chen, S. Kim, R. Rajendiran, K. Prabakar, G. Li, Z. Shi, C. Jeong, J. Kang, O.L. Li, Enhancing ORR/OER active sites through lattice distortion of fe-enriched $FeNi_3$ intermetallic nanoparticles doped n-doped carbon for high-performance rechargeable zn-air battery, J. Colloid Interface Sci. 582 (2021) 977–990.

[71] C.L. Huang, K. Sasaki, D. Senthil Raja, C.T. Hsieh, Y.J. Wu, J.T. Su, C.C. Cheng, P. Y. Cheng, S.H. Lin, Y. Choi, S.Y. Lu, twinning enhances efficiencies of metallic catalysts toward electrolytic water splitting, Adv. Energy Mater. 11 (2021), 2101827.

RESEARCH ARTICLE

ADVANCED MATERIALS
www.advmat.de

A 3d-4d-5d High Entropy Alloy as a Bifunctional Oxygen Catalyst for Robust Aqueous Zinc–Air Batteries

Ren He, Linlin Yang, Yu Zhang, Daochuan Jiang, Seungho Lee, Sharona Horta, Zhifu Liang, Xuan Lu, Ahmad Ostovari Moghaddam, Junshan Li, Maria Ibáñez, Ying Xu, Yingtang Zhou, and Andreu Cabot**

High entropy alloys (HEAs) are highly suitable candidate catalysts for oxygen evolution and reduction reactions (OER/ORR) as they offer numerous parameters for optimizing the electronic structure and catalytic sites. Herein, FeCoNiMoW HEA nanoparticles are synthesized using a solution-based low-temperature approach. Such FeCoNiMoW nanoparticles show high entropy properties, subtle lattice distortions, and modulated electronic structure, leading to superior OER performance with an overpotential of 233 mV at 10 mA cm^{-2} and 276 mV at 100 mA cm^{-2}. Density functional theory calculations reveal the electronic structures of the FeCoNiMoW active sites with an optimized d-band center position that enables suitable adsorption of OOH* intermediates and reduces the Gibbs free energy barrier in the OER process. Aqueous zinc–air batteries (ZABs) based on this HEA demonstrate a high open circuit potential of 1.59 V, a peak power density of 116.9 mW cm^{-2}, a specific capacity of 857 mAh g$_{Zn}$$^{-1}$, and excellent stability for over 660 h of continuous charge–discharge cycles. Flexible and solid ZABs are also assembled and tested, displaying excellent charge–discharge performance at different bending angles. This work shows the significance of 4d/5d metal-modulated electronic structure and optimized adsorption ability to improve the performance of OER/ORR, ZABs, and beyond.

1. Introduction

Aqueous zinc–air batteries (ZABs), offering considerable energy density at a low cost as well as minimal safety concerns and environmental impact, are deemed to be a key component in the future energy storage mix, particularly for the integration of renewables and the transport sector.[1] The main advantages but also limitations of secondary ZABs come from their unique air cathode, which requires highly active, stable, and cost-effective materials able to catalyze the oxygen evolution and oxygen reduction reactions (OER/ORR).[2] Currently, to speed up the sluggish kinetics of the oxygen reactions, state-of-the-art electrocatalysts are based on IrO_2/RuO_2 for OER and Pt for ORR, which compromises the cost-effectiveness of ZABs.[3] Besides their scarcity and high cost, these noble metals are also characterized by moderate long-term stability thus further hindering their practical application. In this

---

R. He, L. Yang, Z. Liang, X. Lu, A. Cabot
Catalonia Energy Research Institute – IREC
Sant Adrià de Besòs 08930, Barcelona, Spain
E-mail: acabot@irec.cat

R. He, L. Yang
Departament d'Enginyeria Electrònica i Biomèdica
Universitat de Barcelona
08028 Barcelona, Spain

Y. Zhang
Department of Materials Science and Engineering
Pennsylvania State University
University Park, PA 16802, USA

The ORCID identification number(s) for the author(s) of this article can be found under https://doi.org/10.1002/adma.202303719

DOI: 10.1002/adma.202303719

D. Jiang
School of Materials Science and Engineering
Anhui University
230601 Hefei, China

S. Lee, S. Horta, M. Ibáñez
Institute of Science and Technology Austria (ISTA)
3400, Am Campus 1 Klosterneuburg, Austria

A. Ostovari Moghaddam
South Ural State University
454080, 76 Lenin Av Chelyabinsk, Russia

J. Li
Institute of Advanced Study
Chengdu University
610106 Chengdu, China

Y. Xu
Hebei Key Lab of Optic-electronic Information and Materials
College of Physics Science and Technology
Hebei University
071002 Baoding, China

scenario, alloys based on more abundant 3d metals such as Fe, Co, and Ni, are widely investigated as alternative oxygen catalysts aiming at finding materials providing optimum binding energies for OER and ORR intermediates.[4] While alloying allows tuning of the electronic properties, the main drawbacks of conventional binary and ternary compositions based on Fe, Co, and Ni are their poor corrosion resistance and moderate catalytic stability associated with their large miscibility gap.[5]

In contrast to 3d orbitals, 4d and 5d orbitals have a larger spatial extent allowing stronger hybridization with neighboring ligand orbitals. Thus the electronic bandwidths in 4d/5d metal are considerably larger than in 3d metals, which allows a wider range of adjustment of the electronic structure.[6] Besides, 4d/5d metals have additional orbital degrees of freedom to tailor the electronic band structure and the adsorption and desorption energy of the intermediates. Recently, 4d and 5d high-valence metals, such as Mo and W, have been demonstrated effective in modulating the electronic structure of catalysts, which could adjust the adsorption and desorption performance of the oxygen intermediates and extend durability.[5,7] Lu et al. showed the presence of Mo within a PtFeMo alloy to alleviate the adsorption energy of the intermediate on the surface of the Pt active site thus promoting ORR performance.[8] Xu et al. successfully incorporated Mo into Co-MOF to promote catalyst stability and OER performance.[9] Besides, Zhang et al. incorporated W^{6+} into amorphous FeCo oxyhydroxide gels to achieve near-optimal *OH adsorption energies for OER intermediates.[10]

High entropy alloys (HEAs), which are solid solutions of five or more elements with high thermodynamic and kinetic stability, hold great promise as bifunctional catalysts owing to their high configurational entropy, distorted atomic arrangement, altered electronic densities, and potentially strong synergistic effects to optimize the adsorption energies and electrical conductivity.[11] The high configurational entropy associated with the mixing of several different elements in similar proportions stabilizes the solid solutions and improves their corrosion resistance. Besides, the lattice distortions related to the different atomic sizes of the combined elements result in significant variations in the electronic structure of the alloy. HEAs also offer numerous additional degrees of freedom to fine-tune the material structural, electronic, and catalytic properties.[12] Overall, the design and engineering of HEA is a powerful strategy to optimize the surface adsorption properties, catalytic active centers, electronic structures,[13] and consequently the OER and ORR catalytic activity and ZAB performance.[14]

Beyond composition, the performance of an electrocatalyst strongly depends on its architectural parameters. To maximize activity, the transport of both electrons and reactant/product and the catalyst/electrolyte interphase area must be maximized. Despite the multiple advantages of HEAs, the synthesis of nanostructured HEAs remains a major challenge.[15] HEAs are generally produced in the form of bulk solids using high-temperature processes or thin films using low throughput vacuum-based technologies, which do not meet the demands of large-scale applications requiring huge 3D surfaces. Besides, while some HEAs have been applied in the electrochemistry field, most of them are based on costly and scarce noble metals.[16]

Herein, noble-metal-free nano-structured HEAs are synthesized using a simple colloidal-based approach at a low temperature and used in aqueous and flexible ZABs. Specifically, transition metals from the 3d series, including Fe, Co, and Ni, along with the 4d metal Mo and 5d metal W, were chosen for synthesizing ternary, quaternary, and quinary compositions. Fe, Co, and Ni exhibit inherent activity in both the OER and ORR. Furthermore, their alloys have been demonstrated to function as bifunctional oxygen catalysts, making them ideal candidates as the primary metal constituents. 4d Mo and 5d W, exhibiting noble metal-like behavior without toxicity, were selected to be introduced within FeCoNi 3d ternary alloys to form FeCoNiMo and FeCoNiW quaternary alloys, and FeCoNiMoW HEAs in the form of nanoparticles. The high entropy properties, lattice distortions, and electron modulations of FeCoNiMoW are thoroughly investigated and discussed. Besides, FeCoNiMoW is explored as OER/ORR bifunctional oxygen catalysts, and in situRaman spectroscopy is used to track its evolution during the OER. The excellent performances obtained are rationalized with the use of density functional theory (DFT) calculations of the electronic synergy, d-band position, and adsorption energy of the oxygen intermediates. Additionally, robust aqueous and flexible ZABs containing FeCoNiMoW-based cathodes are produced and investigated.

2. Results and Discussion

Ternary alloy FeCoNi, quaternary alloys FeCoNiMo and FeCoNiW, and FeCoNiMoW HEA nanoparticles were synthesized through a colloidal synthesis method as described in the Experimental Section, Supporting Information and schematized in **Figure 1**a. Briefly, the nanoparticles were produced in an oxygen-free atmosphere from the simultaneous reduction of the corresponding metal salts at 260 °C in the presence of oleylamine (OAm) as the solvent and reducing agent, glucose as an additional reducing agent, and (1-hexadecyl)trimethylammonium (CTAC) as surfactant.

The results from the elemental composition and crystal structure analyses of the ternary alloy (FeCoNi) and the quaternary alloys (FeCoNiMo and FeCoNiW) are displayed in the Supporting Information (Figures S1–S4, Supporting Information). As shown from the scanning electron microscopy (SEM) energy-dispersive X-ray spectroscopy (EDS) data, the three samples show relatively similar amounts of different metals. According to the X-ray diffraction (XRD) pattern, FeCoNi shows good crystallinity with the cubic Fm-3m FeCoNi phase and a lattice constant of 3.537 Å. With the introduction of Mo or W, FeCoNiMo and FeCoNiW still exhibit the FeCoNi phase, with wider XRD peaks slightly shifted to lower angles due to the relatively large atomic radius of Mo and W.

Y. Zhou
Zhejiang Key Laboratory of Petrochemical Environmental Pollution Control,National Engineering Research Center for Marine Aquaculture
Marine Science and Technology College
Zhejiang Ocean University
Zhoushan, Zhejiang Province 316004, China
E-mail: zhouyingtang@zjou.edu.cn
A. Cabot
ICREA
Pg. Lluis Companys 23, Barcelona, Catalonia 08010, Spain

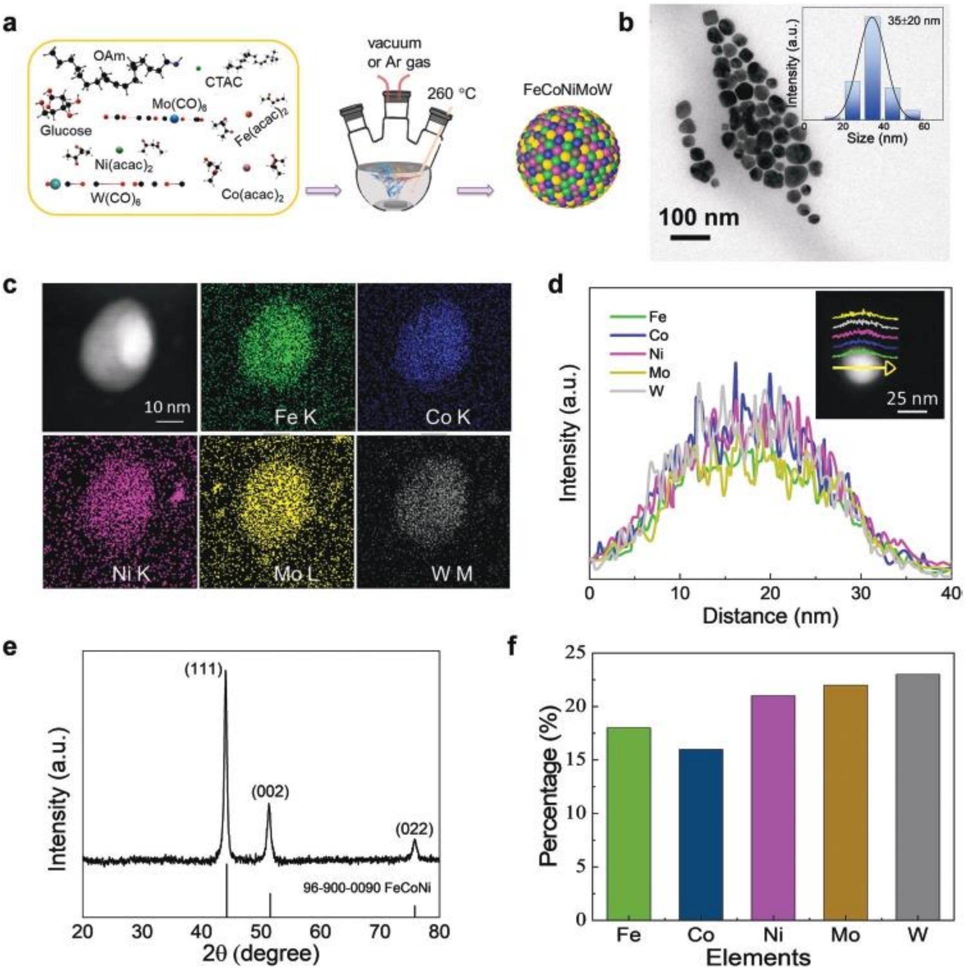

Figure 1. Synthesis process and characteristics of the FeCoNiMoW nanoparticles. a) Schematic diagram of the colloidal synthesis process used to produce FeCoNiMoW nanoparticles. b) TEM micrograph and size distribution histogram (inset). c) High-angle annular dark field scanning TEM (HAADF STEM) micrograph and EDS compositional maps for each element. d) Compositional line profile for each element. e) XRD pattern. f) ICP-OES composition.

Figure 1b shows a representative transmission electron microscope (TEM) image of the FeCoNiMoW particles displaying an average size of 35 ± 20 nm. TEM-EDS composition maps and line scanning profiles demonstrate a homogeneous distribution of the five elements within each particle and a relatively uniform composition from particle to particle with moderate atomic percentage deviations from particle to particle (Figure 1c,d; Figure S5, Supporting Information). Surrounding the particles, a large concentration of oxygen is detected and associated with the presence of oxygen-containing species/ligands adsorbed/bonded to the particle surface and potentially a metal oxide layer formed at the particle surface. The XRD pattern of FeCoNiMoW displays a face-centered cubic (FCC) structure, resembling that of the cubic FeCoNi phase (Figure 1e). The lattice constant was calculated at 3.552 Å, that is, slightly larger than that of FeCoNi (3.545 Å), which is again consistent with the slightly larger atomic radius of Mo and W compared with Fe, Co, and Ni. The overall elemental ratio of FeCoNiMoW was determined by inductively coupled plasma optical emission spectroscopy (ICP-OES) at Fe:Co:Ni:Mo:W = 18:16:21:22:23 (Figure 1f).

According to the measured metal content, the mixing entropy of FeCoNiMoW was calculated using Equation (1).[17]

$$\Delta S_{mix} = -R\sum_{i=1}^{n} c_i ln c_i \tag{1}$$

where R is the gas constant, and c_i is the atomic percentage of each component. FeCoNiMoW particles were characterized by a mixing entropy of 1.60 R, which demonstrates its HEA character.[18] The mixing entropy of FeCoNiMo and FeCoNiW was calculated at 1.37 R, proving its middle entropy properties. The valence electron concentration (VEC) plays a decisive role in determining the crystal solid solution in HEAs.[17b] In particular, a large VEC (≥8) favors the formation of FCC-type solid solutions, while a small VEC (<6.87) favors the formation of (BCC) phases.[17a] The VEC of the ternary, quaternary, and quinary alloys was calculated using Equation (2).[17a]

$$\mathrm{VEC} = \sum_{i=1}^{n} C_i VEC_i \tag{2}$$

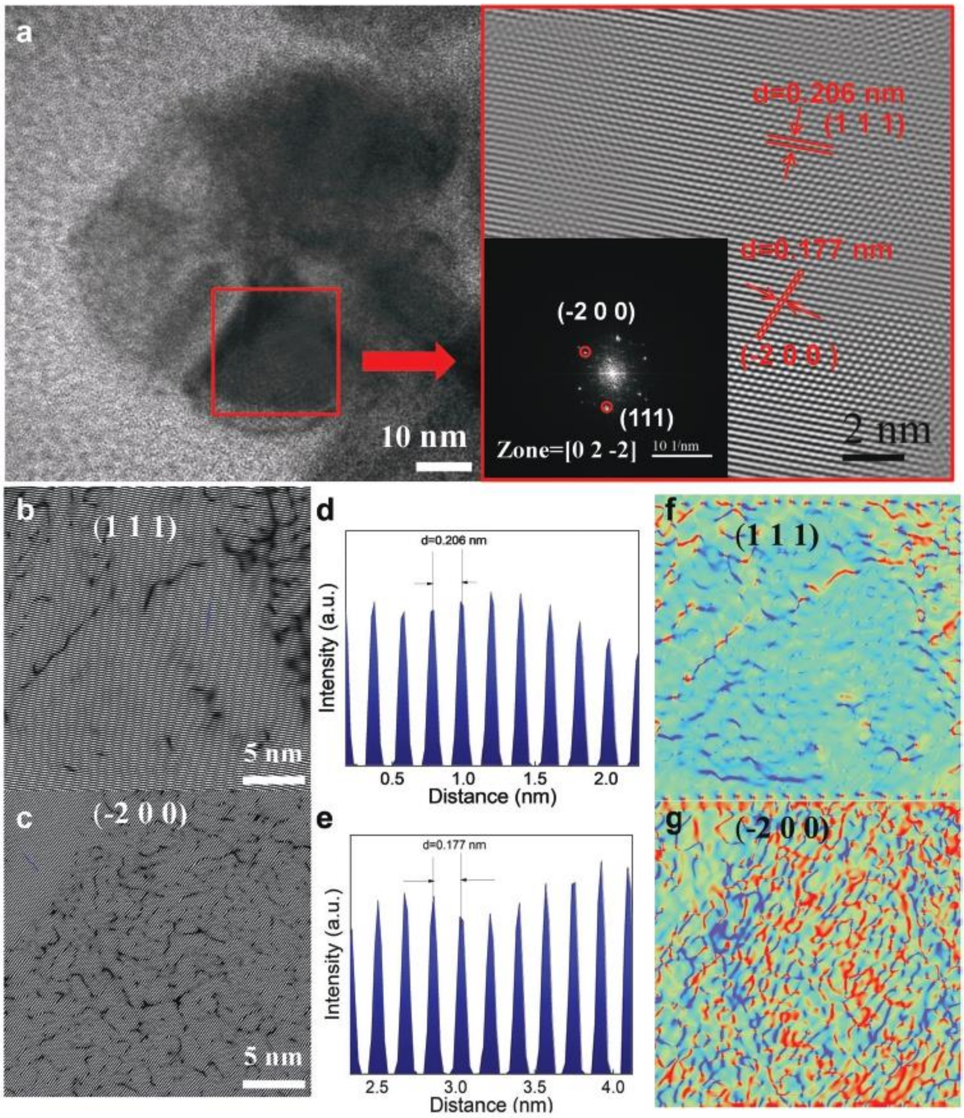

Figure 2. Lattice distortion analysis. a) HRTEM micrograph and magnified image of the red square. Inset is the corresponding SAED pattern. b,c) IFFT patterns of crystal planes (111) and (−200) of the FeCoNiMoW nanoparticles. d,e) Lattice distance plots along the blue lines in (b) and (c), respectively. f,g) Lattice distortion distribution maps of the crystal planes (111) and (−200) zone axis of the FeCoNiMoW nanoparticles based on GPA analysis.

where VEC_i is the VEC of each element. The VEC, atomic radii, and Pauling electronegativity of each of the different elements are shown in Table S1 (Supporting Information). From these values, FeCoNi, FeCoNiMo, FeCoNiW, and FeCoNiMoW were calculated to be characterized by VEC values of 9.12, 8.16, 8.17, and 7.68, respectively, which satisfy the statistical law for the formation of the FCC phase, consistently with the measured XRD patterns. The calculated VEC and ΔS_{mix} of the different alloys are summarized in Table S2 (Supporting Information).

A representative high-resolution TEM (HRTEM) micrograph of one of the FeCoNiMoW nanoparticles and its selected area electron diffraction (SAED) pattern are shown in **Figure 2**a. Figure 2b,c shows the inverse fast Fourier transform (IFFT) lattice fringes of spot (1 1 1) and (−2 0 0) from the SAED pattern of the FeCoNiMoW nanoparticle. As regular fringes, without lattice distortion, we selected those having the FeCoNi lattice spacing, that is, 0.206 and 0.177 nm for the (1 1 1) and (−2 0 0) planes, respectively (Figure 2d,e). A geometric phase analysis (GPA) was carried out to image the internal distortions and strain distribution of the FeCoNiMoW nanoparticles. Figure 2f,g exhibits the quantitative lattice distortions maps and Figure S6 (Supporting Information) displays the internal strain maps of (1 1 1) and (−2 0 0) zone axis in the FeCoNiMoW nanoparticle. A large number of lattice distortions and drastic internal tensile and compressive stresses are ubiquitously observed inside the HEA nanoparticle, which can be reasonably attributed to the different atomic radius and electronegativity of the constituent elements, Fe, Co, Ni, Mo, and W.

The atomic size difference (δ) and the local atomic distortion (α) were used to evaluate the lattice distortion within the HEA

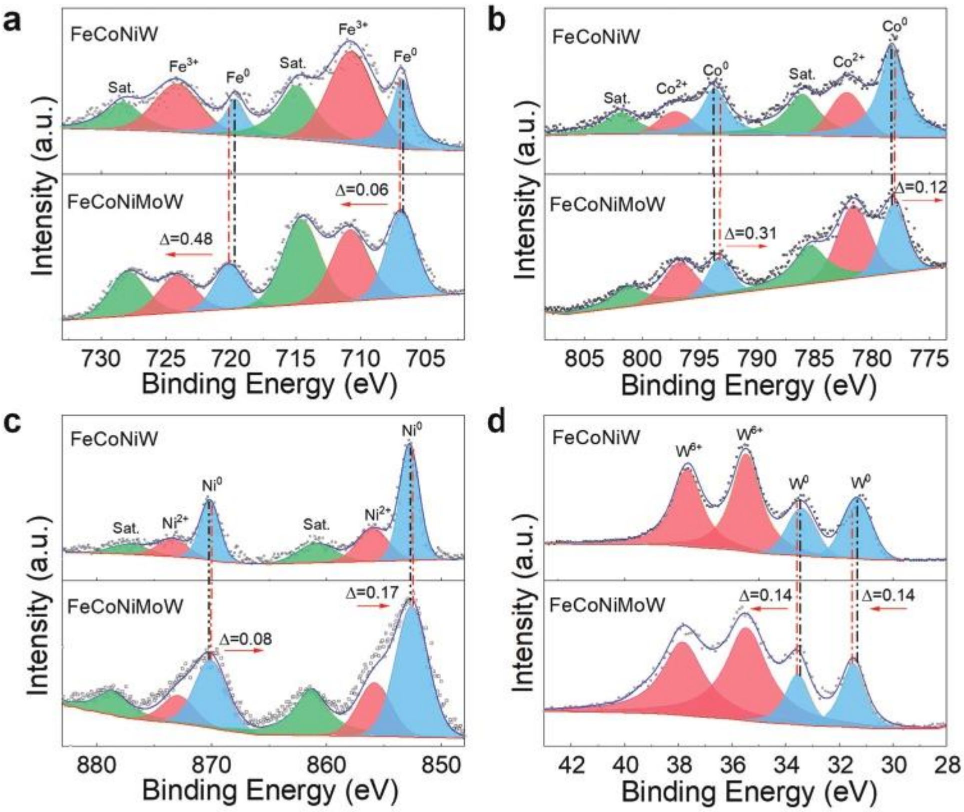

Figure 3. Surface electronic state analysis. High-resolution a) Fe 2p, b) Co 2p, c) Ni 2p, and d) W 4f XPS spectra of FeCoNiW (upper spectra) and FeCoNiMoW (bottom spectra).

particles. δ and α were calculated using Equations (3) and (4), respectively.[19]

$$\delta = 100\sqrt{\sum_{i=1}^{n} c_i(1 - ri/\bar{r})^2} \tag{3}$$

$$\alpha = \sum_{j \geq i}^{n} \frac{C_i C_j \left| r_i + r_j - 2\bar{r} \right|}{2\bar{r}} \tag{4}$$

where C_i and C_j represent the atomic percentages, r_i and r_j are the atomic radius, and $\bar{r}$ is the average atomic radius calculated using Equation (5).[19]

$$\bar{r} = \sum_{i}^{n} C_i r_i \tag{5}$$

The calculated α and δ of the different alloys are included in Table S2 (Supporting Information). FeCoNiMoW shows the largest atomic size difference between the five elements. Besides, FeCoNiMoW shows an α value of 0.78%, higher than that of the other alloys, for example, FeCoNi at 0.05%. These large atomic size differences and local atomic distortions, in large part related to the presence of Mo and W, explain the obvious lattice distortions experimental observed in the FeCoNiMoW HEA nanoparticles.

X-ray photoelectron spectroscopy (XPS) analyses were used to investigate the metal valences and electronic distribution within the HEA surface. The high-resolution Fe 2p, Co 2p, Ni 2p, and W 4f XPS spectra of FeCoNiW and FeCoNiMoW nanoparticles are shown in **Figure 3**. Additionally, the high-resolution Mo 3d XPS spectrum of FeCoNiMoW is displayed in Figure S7 (Supporting Information). The high-resolution Fe 2p, Co 2p, Ni 2p, and Mo 3d XPS spectra of the FeCoNiMo nanoparticles are shown in Figure S8 (Supporting Information). The detailed information on the peaks and metal content are summarized in Tables S3–S5 (Supporting Information). Besides the satellite peaks, all the spectra display two doublets for each of the elements, which are associated with two different chemical states; a metallic component assigned to the particle core and an oxidized component related to the presence of a thin oxide layer at the particle surface. For the FeCoNiMoW HEA, the Fe 2p spectrum displays a doublet at 706.87 eV (Fe $2p_{3/2}$) assigned to Fe^0 and a second doublet at 710.79 eV (Fe $2p_{3/2}$) assigned to a Fe^{3+} chemical environment (Figure 3a).[20] Co displays a Co^0 valence state at 778.12 eV (Co $2p_{3/2}$), and a Co^{2+} state at 781.61 eV (Co $2p_{3/2}$) (Figure 3b).[20] The Ni 2p spectrum shows a doublet assigned to Ni^0 at 852.60 eV (Ni $2p_{3/2}$) and another one to Ni^{2+} at 855.82 eV (Ni $2p_{3/2}$) (Figure 3c).[20] The W 4f spectrum also displays two chemical states, W^0 at 31.47 eV (W $4f_{7/2}$) and W^{6+} at 35.45 eV (W $4f_{7/2}$) (Figure 3d).[20] Finally, the Mo 3d spectrum also displays two chemical states, Mo^0 at 227.59 eV (Mo $3d_{5/2}$) and Mo^{6+} at 232.68 eV (Mo $3d_{5/2}$) (Figure S7, Supporting Information).[20]

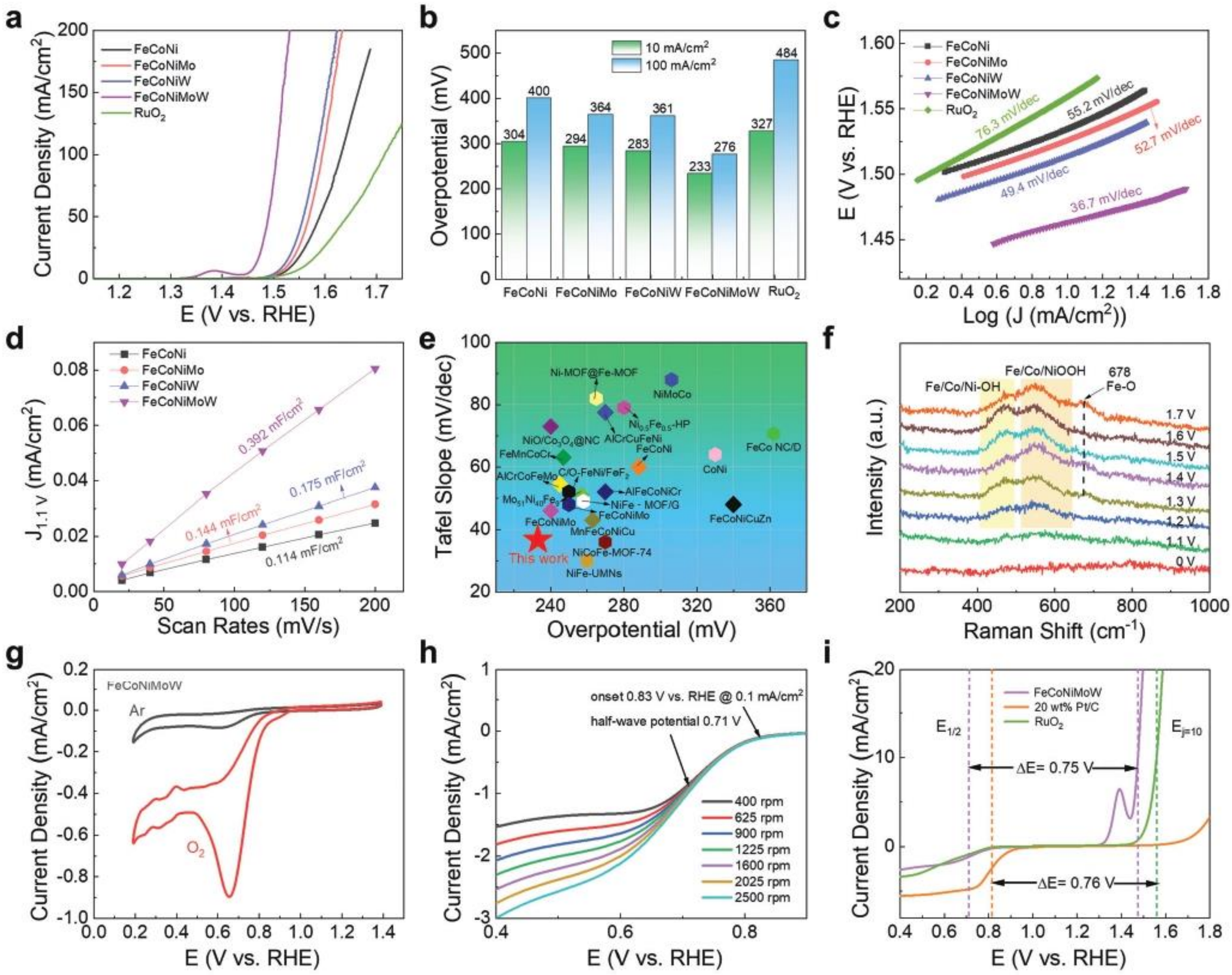

Figure 4. Electrocatalytic OER and ORR performance. a) LSV curves measured in 1.0 м KOH electrolyte. b) OER overpotential comparison at 10 and 100 mA cm^{-2}. c) Tafel slopes. d) C_{dl} plots obtained from CV curves. e) Comparisons of the OER performance of FeCoNiMoW with other recently reported catalysts. f) In situ Raman spectra of FeCoNiMoW at different applied potentials. g) CV curves measured in Ar and O_2 saturated 0.1 м KOH electrolytes. h) LSV curves at different rotation speeds in the range from 400 to 2500 rpm. i) ORR/OER bifunctional LSV curves of different electrodes measured in 0.1 м KOH electrolyte.

Compared with the FeCoNiW and FeCoNiMo quaternary alloys, the binding energy of each element within FeCoNiMoW appears slightly shifted (Tables S3,S4, Supporting Information). Specifically, the Co 2p and Ni 2p electronic states shift to lower binding energies, implying a higher electron density. On the other hand, the binding energies of the Fe 2p are positively shifted, implying a lower electron density. The Mo 3d spectrum shifts to lower binding energies when introducing W into FeCoNiMo while the W 4f spectrum shifts to higher binding energies when introducing Mo into FeCoNiW. These shifts are in part consistent with the different electronegativity of the elements: Fe < Co < Ni << Mo < W (Table S1, Supporting Information) but are probably also influenced by a shift of the Fermi level used as zero energy reference to plot the XPS data. In any case, the presence of the 4d and 5d high valence elements, Mo and W, clearly affects the electronic distribution within the FeCoNiMoW HEA. In terms of composition, XPS analyses (Table S5, Supporting Information) show the surface of the HEA to be slightly Fe-rich and Mo-poor compared with the overall HEA composition obtained by ICP (Figure 1f). The variation in surface composition observed may have arisen from the differential oxidation of the various metals during the partial oxidation of the HEA surface when exposed to air.[21]

Linear sweep voltammetry (LSV) in 1 м KOH electrolyte was used for a preliminary evaluation of the OER activities of electrodes based on FeCoNi, FeCoNiMo, FeCoNiW, FeCoNiMoW, and a commercial RuO_2 catalyst used as a reference (**Figure 4**a, see the Experimental Section, Supporting Information for details). FeCoNiMoW displays the best OER performance with a low overpotential of 233 mV at 10 mA cm^{-2}, well below that of FeCoNi (304 mV), FeCoNiMo (294 mV), FeCoNiW (283 mV), and RuO_2 (327 mV) (Figure 4b). Even at a higher current density of 100 mA cm^{-2}, FeCoNiMoW displays an exceptionally low overpotential of 276 mV, significantly below that of FeCoNi (400 mV), FeCoNiMo (364 mV), FeCoNiW (361 mV), and RuO_2

(484 mV). The Tafel slopes calculated from LSV curves and the chronoamperometry (CA) data are displayed in Figure 4c and Figures S9–S12 (Supporting Information). FeCoNiMoW shows the smallest Tafel slope among the tested catalysts, at 36.7 mV dec^{-1} from the LSV curves and 52.73 mV dec^{-1} using CA data, thus reflecting the fastest OER kinetics. The Tafel slope obtained from the CA data is higher than that of the LSV curves as it has a lower contribution of the double-layer charging and the catalyst's self-oxidation current.[22] This result was further verified using electrochemical impedance spectroscopy (EIS). Figure S13 (Supporting Information) shows the Nyquist plot of the EIS spectra of the different electrodes at 1.5 V versus RHE and the equivalent circuit used for the fittings. The fitting results are listed in Table S6 (Supporting Information). The electrode based on FeCoNiMoW displays the smallest charge transfer resistance among the tested electrocatalysts, consistent with its fastest reaction kinetics. Besides, the electrochemical active surface area was determined from the double-layer capacitance (C_{dl}) calculated using cyclic voltammetry (CV) scans in a non-Faradaic region (Figure S14, Supporting Information). As shown in Figure 4d, FeCoNiMoW shows the largest C_{dl} value among the tested catalysts, indicating the largest active surface area. Overall, FeCoNiMoW displayed excellent OER performance when compared not only with the reference materials here tested but also with previously reported catalysts, as shown in Figure 4e and Table S7 (Supporting Information).

The structural evolution of FeCoNiMoW during the OER was investigated using in situ Raman spectroscopy. A fixed voltage in the range from 0 to 1.7 V versus RHE was applied to the electrode and the CA was measured for 5 min, then the Raman spectra started to be acquired while maintaining the CA measurement running at the set voltage. The Raman spectra were obtained with an acquisition time of 20 s and the accumulation of 8 spectra in the range of 200–1000 cm^{-1}. Figure S15 (Supporting Information) displays an image of the in situ cell coupled with the Raman system and the electrochemical workstation. Figure S16 (Supporting Information) displays the in situ Raman spectra measured for the FeCoNi electrode. A wide peak at ≈450 cm^{-1} is attributed to Ni and potentially also Fe and/or Co hydroxides, as all these metal hydroxides have Raman modes at a similar position (425 cm^{-1} for $Fe(OH)_2$,[23] 452 cm^{-1} for $Ni(OH)_2$,[24] 473 cm^{-1} for $Co(OH)_2$[25]). These hydroxides are the common intermediate formed at the first OER step. The peaks at ≈530–560 cm^{-1} with wide shoulders could be related to the metal oxyhydroxide (538 cm^{-1} for CoOOH,[26] 543 cm^{-1} for FeOOH,[27] and 556 cm^{-1} for NiOOH[28]), which are the common intermediates during the OER at the third step. Besides, as CA progresses, the intensity of the metal hydroxide peak decreases while the intensity of the metal oxyhydroxide peaks increases, proving the surface evolution from hydroxide to oxyhydroxide during the OER. Similar results are obtained for the FeCoNiMo electrode (Figure S17, Supporting Information). At 1.3 V versus RHE, the broadband at ≈420–485 cm^{-1} should be related to the presence of the different Fe/Co/Ni hydroxides, and the wide peak at ≈550 cm^{-1} is attributed to the Fe/Co/Ni metal oxyhydroxide. The in situ Raman spectra of the FeCoNiMoW electrode are shown in Figure 4f. Already at 1.2 V versus RHE, that is, at a slightly lower voltage than the ternary and quaternary alloys, the Raman peaks associated with metal hydroxide and oxyhydroxide were clearly observed. Besides, at 1.3 V versus RHE, a new Raman peak at 678 cm^{-1} is attributed to the Fe–O stretching mode in iron oxide.[29] The observation of the hydroxide Raman peaks at lower potential indicates that Fe/Co/Ni sites in FeCoNiMoW are more active than in FeCoNiMo and FeCoNi. We will return to the discussion on active sites when presenting the results of DFT calculations below.

The stability of FeCoNiMoW under OER conditions was analyzed using CA. As shown in Figure S18 (Supporting Information), the FeCoNiMoW-based electrode shows a current density decrease of 7.5% after 100 h of continuous operation at 1.47 V versus RHE. At higher current densities, the FeCoNiMoW electrode maintained 88.8% of the initial current after 115 h at 1.49 V versus RHE (50 mA cm^{-2}, Figure S19, Supporting Information) and 83.7% after 104 h at 1.51 V versus RHE (100 mA cm^{-2}, Figure S20, Supporting Information). The reduction in current density at higher operation voltages is in large part related to the generation of numerous bubbles, which caused the catalysts to slightly peel off from the carbon paper support. To determine a possible metal leaching during OER, the metal composition of the KOH electrolyte and the metal content reduction of FeCoNiMoW after 20, 50, and 100 h long-term OER tests were analyzed by inductively coupled plasma mass spectrometry (ICP-MS). As shown in Tables S8 and S9 (Supporting Information), small metal amounts, especially of Fe, Ni, and Co, were detected in the KOH, representing a minor HEA compositional change. Interestingly the leaching of Ni but particularly Mo and W was accentuated under ORR conditions, up to 12% for Mo after 50 h ORR, while that of Fe and Co was slightly higher under OER operation.

XPS characterization of the FeCoNiMoW HEAs after long-term OER measurements shows the surface of FeCoNiMoW to be completely oxidized (Figure S21, Supporting Information). The O 1s spectrum displays at least three contributions at 530.0, 532.3, and 533.9 eV, which are assigned to oxygen within a metal oxide chemical environment, and additional O—H and O—O bonds that could be associated with adsorbed oxygen-containing species and/or the formation of a hydroxide or oxyhydroxide surface layer.[30] XRD analysis shows the FeCoNiMoW crystal phase does not change after the OER process. However, the XRD peak intensity decreased after long-term OER, which we correlate with the formation of an amorphous oxide or oxyhydroxide surface layer (Figure S22, Supporting Information). From the width of the XRD peaks, the HEA crystal domain size before and after OER measurements is 13.8 and 12.7 nm, implying the growth of an additional ≈0.5 nm-thick amorphous oxide/oxyhydroxide shell on the particle surface. Notice the small crystal domain size obtained from the fitting of the XRD patterns is notably influenced by the highly distorted lattice, which contributes to the XRD peak broadening. HRTEM images of FeCoNiMoW HEAs after the stability test further confirmed the existence of an amorphous layer on the surface, while the crystal core still displays the cubic FeCoNi phase (Figure S23, Supporting Information).

FeCoNiMoW was further tested as an ORR electrocatalyst in 0.1 м KOH using a rotating ring-disk electrode. Figure 4g shows the CV curves measured from electrolytes saturated in Ar and O_2. Beyond the characteristic double-layer charge–discharge profile, no obvious ORR cathodic peak is obtained for the FeCoNiMoW catalyst within an Ar-saturated electrolyte. In contrast, a large cathodic peak is observed when the electrolyte is saturated with

O_2, pointing at a notable ORR electrochemical activity. Figure 4h shows the LSV curves obtained from FeCoNiMoW at different rotation speeds in the range from 400 to 2500 rpm. At 1600 rpm, the half-wave potential of FeCoNiMoW is 0.71 V and its onset potential is 0.83 V. The CV and LSV curves with rotation speeds in the range from 400 to 2500 rpm of FeCoNi, FeCoNiMo, and FeCoNiW are shown in Figure S24 (Supporting Information). Besides, Figure S25 (Supporting Information) shows the LSV curves at 1600 rpm and the electron transfer number of the different alloys. Among the tested alloys, FeCoNiMoW shows the highest current density, largest onset and half-wave potentials, and highest electron transfer number, proving an enhanced ORR performance with the HEA formation. In the same measurement conditions, the 20 wt.% Pt/C catalyst showed slightly higher half-wave and onset potentials, at 0.82 and 0.95 V, respectively (Figure S26, Supporting Information). The Pt/C catalyst also shows an electron transfer number of 3.95 at 0.5 V versus RHE indicating a direct $4e^-$ pathway. On the other hand, FeCoNiMoW shows an electron transfer number of 3.12 at 0.5 V versus RHE, indicating that ORR does not follow either the $2e^-$ or $4e^-$ pathway (Figure S27, Supporting Information). For FeCoNiMoW, the average electron transfer number calculated by Koutecky–Levich (K–L) plots is 2.66 (Figure S28, Supporting Information), consistent with the coexistence of both the $2e^-$ and $4e^-$ ORR pathways. As shown in Figure S27b (Supporting Information), FeCoNiMoW shows a higher ring disk current density than Pt/C, indicating a relatively higher yield of H_2O_2. The H_2O_2 average selectivity of the FeCoNiMoW electrode is calculated to be 27% at 0.5 V versus RHE (Figure S27c, Supporting Information), further confirming the existence of a $2e^-$ pathway during the ORR. FeCoNiMoW shows good stability under ORR conditions with 5000 cycles and long-term CA measurements with 92% current density retention for 65 h (Figure S29, Supporting Information) without modifying its morphology, crystal phase, and composition (Figures S30,S31, Tables S8,S9, Supporting Information).

Overall, a key performance parameter of a bifunctional oxygen catalyst is the potential gap (E_{gap}) between the OER overpotential at 10 mA cm^{-2} ($E_{\mathrm{j}} = 10$) and the ORR half-wave potential ($E_{1/2}$). Compared with the noble metal-based RuO_2 and Pt/C couple with an E_{gap} of 0.76 V in 0.1 м KOH, the FeCoNiMoW electrode exhibits a slightly improved performance with an E_{gap} of 0.75 V (Figure 4i).

DFT was used to calculate the orbital hybridization overpotential and Gibbs energy barrier to gain inside from the active sites, electronic structure, and catalytic ability of the catalysts during the OER. The DFT models of the FeCoNi, FeCoNiMo, and FeCoNiMoW particles were constructed based on the experimental results of the structural and chemical analysis of the HEA and are shown in Figures S32–S34 (Supporting Information).

The first OER step is the H_2O adsorption on the catalytic surface. The H_2O adsorption energy for different active sites in FeCoNiMoW is shown in **Figure 5**a. The Ni atoms on the FeCoNiMoW surface show the largest H_2O adsorption energy. Generally, the d-band center is an indicator of the binding strength between the metal active center and reactants/intermediates/products. The closer the d-band center level is to the Fermi level, the stronger the adsorption ability.[31] The partial density of states of Ni atoms is displayed in Figure 5b. Compared with FeCoNi and FeCoNiMo, within FeCoNiMoW the d-band center of Ni is shifted to higher energy, which strengthens the adsorption of intermediate species, thus enabling higher reaction rates.

The electron localization function (ELF) was employed to visualize the chemical bond between Ni active sites of different catalysts and OOH* intermediate species. As shown in Figure 5c, the lengths of the Ni—O bond for FeCoNi, FeCoNiMo, and FeCoNiMoW are 1.85, 1.82, and 1.71 Å, respectively, proving their covalent nature. Besides, the Ni—O bond length for FeCoNiMoW is the shortest among the three catalysts, implying that Ni atoms in FeCoNiMoW provide the largest bond strength with O in OOH*, which is consistent with the d-band center analysis.

The crystal orbital Hamilton population (COHP) of Ni—O bond analysis, which is the density of states weighted by the corresponding Hamiltonian matrix element, was further used to analyze the strength and nature of the bonding states of FeCoNi, FeCoNiMo, and FeCoNiMoW. As shown in Figure 5d, the calculated absolute integrated COHP value of FeCoNi, FeCoNiMo, and FeCoNiMoW are 2.453, 2.677, and 2.985 eV, respectively, implying more Ni metal active sites bonding with O atoms in the FeCoNiMoW.[32]

The electrons in the d orbital of Ni atoms in FeCoNiMoW are hybridized with the p orbital of the O atom in H_2O, forming bonding and anti-bonding orbitals. Since the d-band center in FeCoNiMoW is closer to the Fermi level than in the other catalysts, the anti-bonding orbital of FeCoNiMoW is higher, then the occupation degree of electrons on the antibonding orbital is reduced and that of the bonding orbital is larger. The diagram of the hybridizing between FeCoNi and FeCoNiMoW catalysts and O atoms is shown in Figure 5e.

The catalytic activity of each atom within FeCoNi, FeCoNiMo, and FeCoNiMoW was further investigated. Figure 5f shows a volcano-shaped curve where the *x*-axis is the difference in Gibbs free energy between OH* and O*, and the *y*-axis is the theoretical overpotential during OER. As observed in the graph, the Ni active sites in FeCoNiMoW have the lowest overpotential and a moderate Gibbs free energy difference, which is consistent with Ni being the active site and FeCoNiMoW being the most active OER catalyst. Besides, Fe in FeCoNiMoW shows a larger overpotential than Ni, demonstrating Ni sites are much more efficient than Fe, which is consistent with the adsorption energies of H_2O on different active sites obtained by DFT and the appearance of the NiOOH fingerprint in the in situ Raman spectra.

The free energy step diagram of the OER process is shown in Figure 5g. Regardless of whether the applied voltage is 0 or 1.23 V, the Gibbs free energy barrier of the OER potential determination step (PDS) that needs to be overcome is smaller for FeCoNiMoW than for FeCoNi and FeCoNiMo, thus the OER is more favorable to occur in the former. Specifically, when the applied voltage is 0 V, the positive Gibbs free energy changes of the PDS for FeCoNi, FeCoNiMo, and FeCoNiMoW are 1.87, 1.81, and 1.65 eV, respectively. In addition, the catalytic OER efficiencies of FeCoNi, FeCoNiMo, and FeCoNiMoW show a trend of FeCoNi < FeCoNiMo < FeCoNiMoW, and the theoretical overpotential (η_{OER}) are 0.64, 0.58, and 0.42 eV, respectively, which is consistent with the experimental results, indicating that the introduction of 4d Mo and 5d W atoms improves the overall activity of the catalyst. Overall, the proposed OER mechanism on FeCoNiMoW is depicted in Figure S35 (Supporting Information).

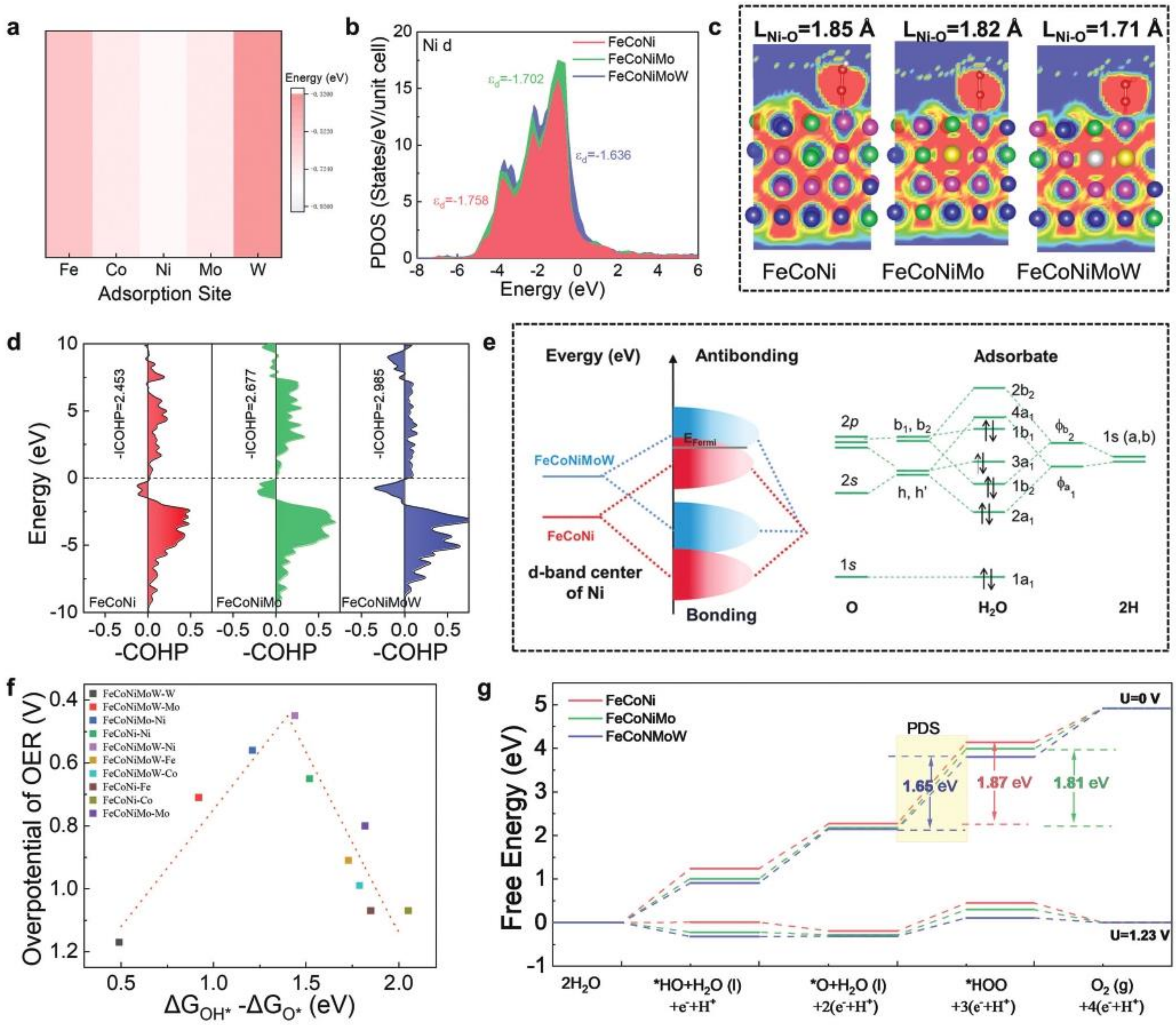

Figure 5. DFT calculations. a) Adsorption energy between different active sites in FeCoNiMoW and H_2O molecules. b) d-band center position of Ni atoms in FeCoNi, FeCoNiMo, and FeCoNiMoW. c) ELF calculations and d) COHP analysis of Ni—O bond for FeCoNi, FeCoNiMo, and FeCoNiMoW. e) Diagram of the hybridizing between catalysts of FeCoNi and FeCoNiMoW and O atoms of H_2O molecule. f) OER catalytic activity of each atom for FeCoNi, FeCoNiMo, and FeCoNiMoW. g) Free energy step diagram during the OER process of FeCoNi, FeCoNiMo, and FeCoNiMoW.

The free energy step diagram of the ORR process is shown in Figure S36 (Supporting Information). There are two PDS, the O_2 molecule transfer to *HOO at the first step, and *O transfer to *HO at the third step. For the first step, the Gibbs free energy barrier of the FeCoNiMoW is 0.11 eV, which is smaller than that of FeCoNi at 0.45 eV and FeCoNiMo at 0.30 eV. The third step involves no energy barrier for the FeCoNiMoW catalyst, while in FeCoNi and FeCoNiMo energy barriers of 0.20 and 0.06 eV, respectively, need to be overcome. Therefore, DFT calculations show the catalytic ORR performance should follow the trend FeCoNi < FeCoNiMo < FeCoNiMoW, which is consistent with the experimental data.

Ab initio molecular dynamics simulations using a canonical ensemble with a Nosé–Hoover heat bath scheme were employed to investigate the thermal stability of the FeCoNiMoW.[33] As shown in Figure S37 (Supporting Information). the free energy of the FeCoNiMoW fluctuates in a narrow range in all cases at 300, 500, and 700 K, indicating that the FeCoNiMoW structure is thermally stable during the OER/ORR process, which is consistent with the long-term catalytic stability for OER/ORR.

We further evaluated the impact of the observed partial surface oxidation of the HEA on OER and ORR using DFT calculations using a model consisting of 5% oxygen doping into the surface of FeCoNiMoW (Figure S38, Supporting Information). Our results show that the presence of oxygen increases the adsorption energy of water and reduces that of oxygen on the various metal elements (Figure S39, Supporting Information). Thus, partial oxidation of FeCoNiMoW enhances OER performance but degrades ORR

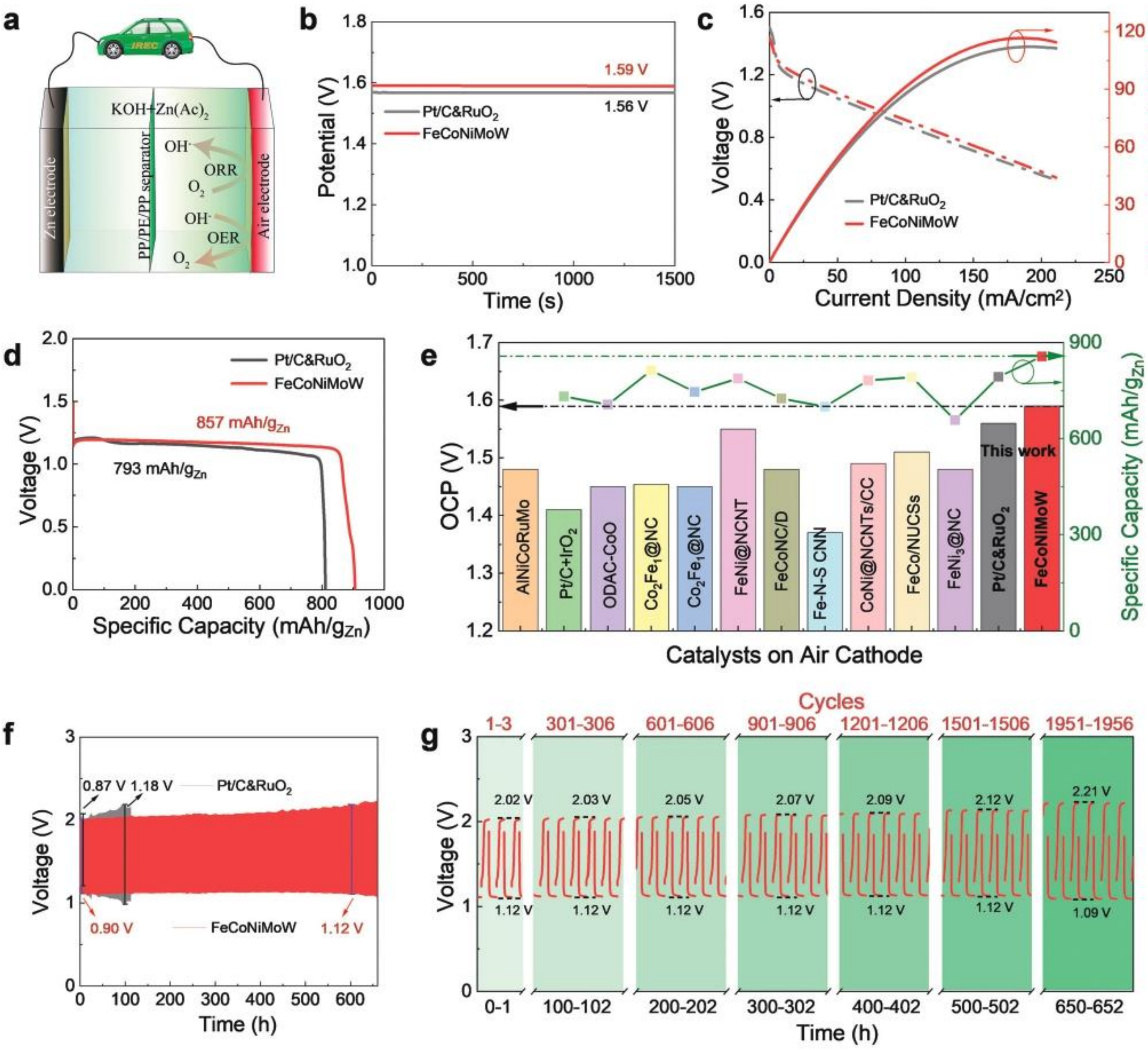

Figure 6. Aqueous reversible ZABs performance. a) ZAB schematic diagram. b) OCP, c) power density plots, and d) specific capacity curves of a FeCoNiMoW- and a Pt/C and RuO_2-based ZAB. e) Comparison of OCP and specific capacity of FeCoNiMoW-based ZAB with state-of-the-art ZABs. f) Galvanostatic discharge–charge curves with 10 min discharge and 10 min charge cycles at a current density of 8 mA cm^{-2}. g) Enlarged galvanostatic discharge–charge cycles at the specific cycling time of the FeCoNiMoW-based ZAB.

performance. As shown in Figure S40 (Supporting Information), after introducing 5% oxygen doping, the d-band of Ni shifts from −1.636 to −1.582 eV for FeCoNiMoW, −1.702 to −1.686 eV for FeCoNiMo, −1.758 to −1.705 eV for FeCoNi. While the presence of oxygen on the surface of the alloy clearly alters adsorption energies and electronic properties, the overall trends observed with the pure metal surfaces, in terms of the role of each element and the comparative performance of the different alloys, remain unchanged and consistent with the experimental results.

Since catalysts restructure during the OER/ORR process, DFT calculations were further performed based on the alloy model reconstructed with OH. The reconstructed models of FeCoNiOH, FeCoNiMoOH, and FeCoNiMoWOH are shown in Figures S41–S43 (Supporting Information). Figure S44 (Supporting Information) shows the detailed analysis of the adsorption energy, d-band center analysis, ELF, COHP, the catalytic ability of different active sites, and the free energy step diagram for all the catalysts. Compared with the precatalyst metal models, all the reconstructed catalysts show improved performances and the same trends both among the different elements, with Ni as the most active site, and the different materials, with FeCoNiMoW outperforming FeCoNiMo and FeCoNi.

FeCoNiMoW was used as the oxygen cathode in aqueous ZABs. The 20 wt.% Pt/C and RuO_2 couple were used to produce reference ZABs. **Figure 6**a shows a schematic of the ZAB architecture, with a polished 0.5 mm-thick Zn plate as the anode, a polypropylene (PP)/ polyethylene(PE)/PP three-layer composite film as the separator, hydrophilic carbon paper with the catalyst as the cathode, and a KOH and zinc acetate solution as the electrolyte (see the Experimental Section, Supporting Information for details). The ZAB containing the FeCoNiMoW-based air cathode can light a red LED screen (Figure S45, Supporting Information) and exhibits an open-circuit potential (OCP) of 1.59 V, that is, 95.8% of the theoretical limit (1.66 V),[34] significantly above that of the Pt/C and RuO_2-based ZAB (1.56 V) (Figure 6b). The peak power density of the FeCoNiMoW-based ZAB was 116.9 mW cm^{-2}, sensible above that of the Pt/C and RuO_2-based ZAB at 112.4 mW cm^{-2} (Figure 6c). Besides, at a current density of 8 mA cm^{-2}, the FeCoNiMoW-based ZAB delivered a specific capacity of 857 mAh $g_{Zn}{}^{-1}$, also well above that of the Pt/C and RuO_2 ZAB (793 mAh $g_{Zn}{}^{-1}$) (Figure 6d). Overall, the FeCoNiMoW-based ZAB displayed an outstanding OCP and specific capacity compared not only with the reference Pt/C and RuO_2 ZAB but also with previously reported devices (Figure 6e, Table S10, Supporting Information).

As shown in Figure 6f, the FeCoNiMoW-based ZAB is not only characterized by a lower charge–discharge potential, implying a higher energy efficiency, compared with the Pt/C and RuO_2-based ZAB, but also much higher durability. Unlike the Pt/C and RuO_2-based ZAB with an obvious potential gap increase of 35.6% from 0.87 to 1.18 V after just 100 h of charging/discharging cycles at 8 mA cm^{-2}, the FeCoNiMoW-based ZAB exhibits a much lower voltage variation, ≈24.4% from 0.90 to 1.12 V, even after 660 h (≈28 days) of continuous cycling, that is, after ≈2000 charge/discharge cycles at 8 mA cm^{-2}. Figure 6g exhibits the enlarged cycles at the specific time of 0–1, 100–102, 200–202, 300–302, 400–402, 500–502, and 650–652 h of the FeCoNiMoW-based ZAB. The charging and discharging potentials at the first cycle are 2.02 and 1.12 V, respectively, that is, the discharging–charging potential gap was 0.90 V. The potential gap increased 5.5% to 0.95 V at the 900th cycle, 11.1% to 1 V at the 1500th cycle, and 24.4% to 1.12 V at the 1950th cycle. The corresponding voltaic efficiency (discharge end voltage divided by charge end voltage) slightly decreases from the initial 55.4% to 54.1% at the 900th cycle, 52.8% at the 1500th cycle, and 49.3% at the 1950th cycle, indicating an excellent rechargeability and stability (Figure S46, Supporting Information). Furthermore, Figure S47 (Supporting Information) shows the charge/discharge curves at the specific cycles, first, 100th, 500th, 1000th, 1500th, and 1950th of the FeCoNiMoW-based ZAB, showing a minor evolution, further proving the outstanding long-term durability of the battery. SEM characterization of the Zn anode shows urchin-shaped ZnO structures at the anode surface after long-term charging/discharging in both the Pt/C and RuO_2-based and FeCoNiMoW-based ZABs, which could explain the slight deterioration of the ZAB performance (Figure S48, Supporting Information).

Besides capacity, flexibility and miniaturization potential are two additional battery characteristics frequently targeted in the field of energy storage. Thus, we also manufactured and tested prototypes of solid and flexible ZABs based on a gel electrolyte and the FeCoNiMoW catalyst. **Figure 7**a shows a schematic of the ZAB architecture, where a polished 0.08 mm-thick Zn foil is used as the anode, a PP/PE/PP three-layer composite film as the separator, a hydrophilic carbon paper with the catalysts is used as the cathode, and a poly(vinyl alcohol) (PVA)-KOH-gel as the electrolyte (see the Experimental Section, Supporting Information for details). A reference ZAB was produced using the combination of Pt/C and RuO_2 catalysts. The solid FeCoNiMoW-based ZAB displayed a higher OCP, at 1.34 V than the Pt/C and RuO_2-based ZAB, at 1.30 V. As shown in Figure 7b, two ZABs in series were able to light a green LED bulb (2.2 V). The peak power density of the solid FeCoNiMoW-based ZAB was 42.05 mW cm^{-2}, slightly above the 40.12 mW cm^{-2} obtained for the Pt/C and RuO_2-based ZAB (Figure 7c), and comparable with state-of-the-art solid ZABs (Table S11, Supporting Information). The charge-discharge curves at different current densities and the corresponding voltaic efficiency in each cycle of the FeCoNiMoW-based ZAB are displayed in Figure 7d. The average voltaic efficiency at 2, 4, 6, and 8 mA cm^{-2} is 80.67%, 71.63%, 64.61%, and 58.86%, respectively, demonstrating a notable rate performance. On the other hand, the average voltaic efficiency at 2 mA cm^{-2} increases to 86.43% after undergoing several charging and discharging processes at different current densities, from 2 to 8 mA cm^{-2}. Galvanostatic discharge–charge measurements for 5 h at bending angles of 0, 30°, 50°, and 70° are shown in Figure 7e. Notably, the battery maintains constant charging (1.88 V) and discharging (0.86 V) platforms at 5 mA cm^{-2} during and after bending, suggesting that the technology has potential in flexible electronics and wearable markets. Finally, Figure 7e also shows that the FeCoNiMoW-based ZAB could maintain a good cycling performance even after 30 h of operation. In contrast, the Pt/C and RuO_2-based ZAB failed after ≈9 h (Figure S49, Supporting Information).

3. Conclusion

A solution-based synthetic procedure to produce a FeCoNiMoW HEA at a low reaction temperature was detailed. With the introduction of 4d Mo and 5d W into 3d FeCoNi, FeCoNiMoW was characterized by an extensively distorted lattice, and synergistic electronic coupling effects, which resulted in an outstanding OER catalytic performance with a low overpotential of 233 mV at 10 mA cm^{-2} and 276 mV at 100 mA cm^{-2}. Besides, FeCoNiMoW was demonstrated to be an efficient bifunctional oxygen catalyst with a low E_{gap} value of 0.75 V, even a little better than commercial noble catalysts of Pt/C and RuO_2 (0.76 V). DFT calculations showed the Ni atoms in FeCoNiMoW as the active sites to react with the oxygen intermediates. FeCoNiMoW had the highest d-band center energy and shortest Ni—O bond, proving its strongest interaction ability with oxygen intermediates. Much more d orbital of Ni atoms in FeCoNiMoW is hybridized with 2p orbital of O atoms in H_2O in the bonding states due to 3d metal FeCoNi combined with 4d Mo atom and 5d W atom, which is the reason for the highest active ability of FeCoNiMoW compared with FeCoNi and FeCoNiMo. Overall, combining experimental results and DFT calculations, Fe, Co, and especially Ni are shown to be the OER and ORR active sites, while Mo and W play a role in adjusting the electronic structure of the alloy and its individual elements. The 3d-4d-5d FeCoNiMoW-based ZAB showed an OCP of 1.59 V, 95.8% of its theoretical limit, a peak power density of 116.90 mW cm^{-2}, and a specific capacity of 857 mAh $g_{Zn}{}^{-1}$ at a current density of 8 mA cm^{-2}, which displayed excellent stability

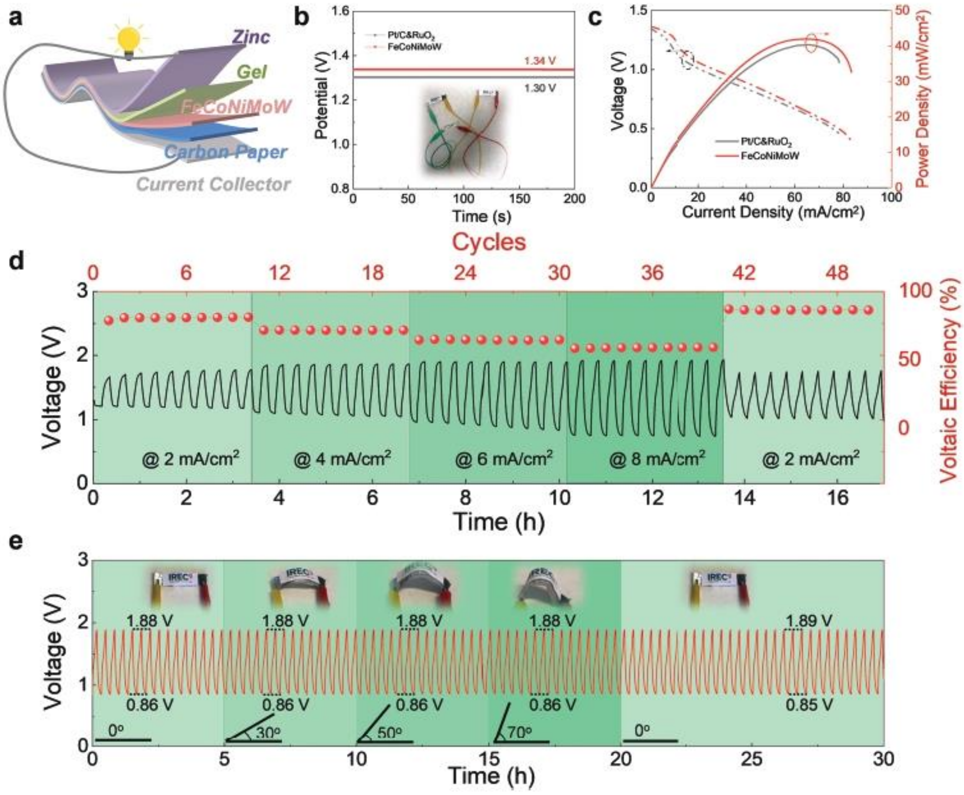

Figure 7. Solid and flexible ZAB performance. a) Solid ZAB schematic diagram. b) OCP measurements. The inset shows an optical image of a green LED bulb (2.2 V) lighted with two FeCoNiMoW-based ZABs. c) Power density plots of a FeCoNiMoW- and a Pt/C and RuO_2-based ZAB. d) Galvanostatic discharge–charge curves of a FeCoNiMoW-based ZAB with 10 min discharge and 10 min charge cycles at a current density of 2, 4, 6, and 8 mA cm^{-2}. e) Galvanostatic discharge–charge curves with 10 min discharge and 10 min charge cycles at a current density of 5 mA cm^{-2} of the FeCoNiMoW-based ZAB with different bending angles.

for more than 660 h of continuous charge/discharge cycling. Furthermore, the 3d-4d-5d FeCoNiMoW also had outstanding catalytic performance in flexible ZABs, which could retain good performance at different bending angles, thus having the potential to be integrated into wearable devices as electrical power. This work has significance for 4d/5d high-valence metal modulated electronic structure and optimized the adsorption ability of the oxygen intermediates.

Supporting Information

Supporting Information is available from the Wiley Online Library or from the author.

Acknowledgements

The authors acknowledge funding from Generalitat de Catalunya 2021 SGR 01581; the project COMBENERGY, PID2019-105490RB-C32, from the Spanish Ministerio de Ciencia e Innovación; the National Natural Science Foundation of China (22102002); the Anhui Provincial Natural Science Foundation (2108085QE192); Zhejiang Province key research and development project (2023C01191); the Foundation of State Key Laboratory of High-efficiency Utilization of Coal and Green Chemical Engineering (GrantNo.2022-K31); and The Key Research and Development Program of Hebei Province (20314305D). IREC is funded by the CERCA Programme from the Generalitat de Catalunya. L.L.Y. thanks the China Scholarship Council (CSC) for the scholarship support (202008130132). This research was supported by the Scientific Service Units (SSU) of ISTA (Institute of Science and Technology Austria) through resources provided by the Electron Microscopy Facility (EMF). S.L., S.H., and M.I. acknowledge funding by ISTA and the Werner Siemens.

Conflict of Interest

The authors declare no conflict of interest.

Author Contributions

Conceptualization was done by R.H., L.Y., and A.C. Methodology was dealt with by R.H. Investigation was done by R.H. and L.Y. Visualization was done by R.H., L.Y., Y.Z., D.J., S.L., S.H., Z.L., X.L., A.O.M., J.L., M.I., Y.X., and Y.Z. The software was dealt with by Y.Z. Supervision was done by A.C. R.H. and L.Y. wrote the original draft. A.C. wrote the review and did the editing.

Data Availability Statement

The data that support the findings of this study are available from the corresponding author upon reasonable request.

Keywords

electrocatalysis, high entropy alloys, oxygen cathode, oxygen evolution reaction, oxygen reduction reactions, zinc–air batteries

Received: April 20, 2023
Revised: July 17, 2023

---

[1] a) X. Zhu, C. Hu, R. Amal, L. Dai, X. Lu, *Energy Environ. Sci.* **2020**, *13*, 4536; b) M. Yang, X. Shu, W. Pan, J. Zhang, *Small* **2021**, *17*, 2006773.

[2] a) Q. Liu, L. Wang, H. Fu, *J. Mater. Chem. A* **2023**, *11*, 4400; b) G. Yasin, S. Ali, S. Ibraheem, A. Kumar, M. Tabish, M. A. Mushtaq, S. Ajmal, M. Arif, M. A. Khan, A. Saad, L. Qiao, W. Zhao, *ACS Catal.* **2023**, *13*, 2313; c) X. Zhao, J. Chen, Z. Bi, S. Chen, L. Feng, X. Zhou, H. Zhang, Y. Zhou, T. Wagberg, G. Hu, *Adv. Sci.* **2023**, *10*, e2205889.

[3] a) D. Böhm, M. Beetz, M. Schuster, K. Peters, A. G. Hufnagel, M. Döblinger, B. Böller, T. Bein, D. Fattakhova-Rohlfing, *Adv. Funct. Mater.* **2019**, *30*, 1906670; b) L. Zhang, H. Jang, H. Liu, M. G. Kim, D. Yang, S. Liu, X. Liu, J. Cho, *Angew. Chem., Int. Ed.* **2021**, *60*, 18821; c) M. Liu, Z. Zhao, X. Duan, Y. Huang, *Adv. Mater.* **2019**, *31*, 1802234.

[4] a) K. Kim, K. Min, Y. Go, Y. Lee, S. E. Shim, D. Lim, S.-H. Baeck, *Appl. Catal., B* **2022**, *315*, 121501; b) Z. Wang, J. Ang, J. Liu, X. Y. D. Ma, J. Kong, Y. Zhang, T. Yan, X. Lu, *Appl. Catal., B* **2020**, *263*, 118344; c) W.-W. Tian, J.-T. Ren, Z.-Y. Yuan, *Appl. Catal., B* **2022**, *317*, 121764; d) Z. Li, M. Chen, L. Zhang, R. Xing, J. Hu, X. Huang, C. Zhou, Y. Zhou, T. Wågberg, G. Hu, *J. Mater. Chem. A* **2023**, *11*, 2155; e) X. Wang, X. Han, R. Du, C. Xing, X. Qi, Z. Liang, P. Guardia, J. Arbiol, A. Cabot, J. Li, *ACS Appl. Mater. Interfaces* **2022**, *14*, 41924; f) R. Du, K. Xiao, B. Li, X. Han, C. Zhang, X. Wang, Y. Zuo, P. Guardia, J. Li, J. Chen, J. Arbiol, A. Cabot, *Chem. Eng. J.* **2022**, *441*, 135999; g) X. Wang, J. Li, Q. Xue, X. Han, C. Xing, Z. Liang, P. Guardia, Y. Zuo, R. Du, L. Balcells, J. Arbiol, J. Llorca, X. Qi, A. Cabot, *ACS Nano* **2023**, *17*, 825; h) X. Wang, X. Han, R. Du, Z. Liang, Y. Zuo, P. Guardia, J. Li, J. Llorca, J. Arbiol, R. Zheng, A. Cabot, *Appl. Catal., B* **2023**, *320*, 121988.

[5] Y. Mei, Y. Feng, C. Zhang, Y. Zhang, Q. Qi, J. Hu, *ACS Catal.* **2022**, *12*, 10808.

[6] B. J. Kim, J. Yu, H. Koh, I. Nagai, S. I. Ikeda, S. J. Oh, C. Kim, *Phys. Rev. Lett.* **2006**, *97*, 106401.

[7] a) J. Zhang, K. Wang, L. Fan, H. Liu, H. Zhu, S. Yan, *J. Alloys Compd.* **2023**, *933*, 167613; b) G. Ke, F. Duan, B. Liu, X. Liu, J. Wen, B. Jia, X. Liu, H. He, Y. Zhou, *J. Alloys Compd.* **2023**, *934*, 167883; c) H. Li, C. Zhang, W. Xiang, M. A. Amin, J. Na, S. Wang, J. Yu, Y. Yamauchi, *Chem. Eng. J.* **2023**, *452*, 139104.

[8] J. Lu, L. Luo, S. Yin, S. W. Hasan, P. Tsiakaras, *ACS Sustainable Chem. Eng.* **2019**, *7*, 16209.

[9] Y. T. Xu, Z. M. Ye, J. W. Ye, L. M. Cao, R. K. Huang, J. X. Wu, D. D. Zhou, X. F. Zhang, C. T. He, J. P. Zhang, X. M. Chen, *Angew. Chem., Int. Ed.* **2019**, *58*, 139.

[10] M. Yuan, J. Chen, Y. Bai, Z. Liu, J. Zhang, T. Zhao, Q. Shi, S. Li, X. Wang, G. Zhang, *Chem. Sci.* **2021**, *12*, 6048.

[11] a) X. Huang, G. Yang, S. Li, H. Wang, Y. Cao, F. Peng, H. Yu, *J. Energy Chem.* **2022**, *68*, 721; b) G. Yan, H. Tan, Y. Wang, Y. Li, *Appl. Surf. Sci.* **2019**, *489*, 519; c) H. Wu, Z. Li, Z. Wang, Y. Ma, S. Huang, F. Ding, F. Li, Q. Zhai, Y. Ren, X. Zheng, Y. Yang, S. Tang, Y. Deng, X. Meng, *Appl. Catal., B* **2023**, *325*, 122356; d) D. Feng, Y. Dong, P. Nie, L. Zhang, Z.-A. Qiao, *Chem. Eng. J.* **2022**, *430*, 132883; e) A. Ostovari Moghaddam, A. Cabot, E. A. Trofimov, *Int. J. Refract. Met. Hard Mater.* **2021**, 97; f) Z. Jin, J. Lyu, K. Hu, Z. Chen, G. Xie, X. Liu, X. Lin, H. J. Qiu, *Small* **2022**, *18*, 2107207; g) T. Yu, Y. Zhang, Y. Hu, K. Hu, X. Lin, G. Xie, X. Liu, K. M. Reddy, Y. Ito, H.-J. Qiu, *ACS Mater. Lett.* **2021**, *4*, 181; h) Z. Jin, X. Zhou, Y. Hu, X. Tang, K. Hu, K. M. Reddy, X. Lin, H. J. Qiu, *Chem. Sci.* **2022**, *13*, 12056; i) R. He, L. Yang, Y. Zhang, X. Wang, S. Lee, T. Zhang, L. Li, Z. Liang, J. Chen, J. Li, A. Ostovari Moghaddam, J. Llorca, M. Ibáñez, J. Arbiol, Y. Xu, A. Cabot, *Energy Storage Mater.* **2023**, *58*, 287.

[12] a) Q. Ding, Y. Zhang, X. Chen, X. Fu, D. Chen, S. Chen, L. Gu, F. Wei, H. Bei, Y. Gao, M. Wen, J. Li, Z. Zhang, T. Zhu, R. O. Ritchie, Q. Yu, *Nature* **2019**, *574*, 223; b) H. Li, J. Lai, Z. Li, L. Wang, *Adv. Funct. Mater.* **2021**, *31*, 2106715; c) W. J. Liu, Z. Xu, D. Zhao, X. Q. Pan, H. C. Li, X. Hu, Z. Y. Fan, W. K. Wang, G. H. Zhao, S. Jin, G. W. Huber, H. Q. Yu, *Nat. Commun.* **2020**, *11*, 265; d) W. Ling, H. Wang, Z. Chen, Z. Ji, J. Wang, J. Wei, Y. Huang, *Adv. Funct. Mater.* **2020**, *31*, 2006855.

[13] K. Zhang, G. Zhang, J. Qu, H. Liu, *Small* **2020**, *16*, 1907001.

[14] a) M. A. Ahsan, A. R. Puente Santiago, Y. Hong, N. Zhang, M. Cano, E. Rodriguez-Castellon, L. Echegoyen, S. T. Sreenivasan, J. C. Noveron, *J. Am. Chem. Soc.* **2020**, *142*, 14688; b) Z. Xia, S. Guo, *Chem. Soc. Rev.* **2019**, *48*, 3265.

[15] H. Zhou, F. Yu, Y. Liu, J. Sun, Z. Zhu, R. He, J. Bao, W. A. Goddard, S. Chen, Z. Ren, *Energy Environ. Sci.* **2017**, *10*, 1487.

[16] a) M. W. Glasscott, A. D. Pendergast, S. Goines, A. R. Bishop, A. T. Hoang, C. Renault, J. E. Dick, *Nat. Commun.* **2019**, *10*, 2650; b) D. Zhang, H. Zhao, X. Wu, Y. Deng, Z. Wang, Y. Han, H. Li, Y. Shi, X. Chen, S. Li, J. Lai, B. Huang, L. Wang, *Adv. Funct. Mater.* **2020**, *31*, 2006939; c) Z. Chen, J. Wen, C. Wang, X. Kang, *Small* **2022**, *18*, 2204255; d) P. Zhang, X. Hui, Y. Nie, R. Wang, C. Wang, Z. Zhang, L. Yin, *Small* **2023**, *19*, e2206742.

[17] a) S. Guo, C. T. Liu, *Prog. Nat. Sci.* **2011**, *21*, 433; b) A. Ostovari Moghaddam, R. Fereidonnejad, A. Cabot, *J. Alloys Compd.* **2023**, *960*, 170802.

[18] Z. P. Lu, H. Wang, M. W. Chen, I. Baker, J. W. Yeh, C. T. Liu, T. G. Nieh, *Intermetallics* **2015**, *66*, 67.

[19] Z. Wang, W. Qiu, Y. Yang, C. T. Liu, *Intermetallics* **2015**, *64*, 63.

[20] J. Chastain, R. C. King Jr, *Tech. News - Perkin-Elmer Corp., Opt. Group* **1992**, *40*, 221.

[21] R. Nafria, A. Genc, M. Ibanez, J. Arbiol, P. R. de la Piscina, N. Homs, A. Cabot, *Langmuir* **2016**, *32*, 2267.

[22] S. Anantharaj, S. Noda, M. Driess, P. W. Menezes, *ACS Energy Lett.* **2021**, *6*, 1607.

[23] N. Boucherit, A. Hugot-Le Goff, S. Joiret, *Corros. Sci.* **1991**, *32*, 497.

[24] D. S. Hall, D. J. Lockwood, C. Bock, B. R. MacDougall, *Proc. Math Phys. Eng. Sci.* **2015**, *471*, 20140792.

[25] D. Shi, L. Zhang, N. Zhang, Y. W. Zhang, Z. G. Yu, H. Gong, *Nanoscale* **2018**, *10*, 10554.

[26] Y. Zhang, H. Guo, P. Yuan, K. Pang, B. Cao, X. Wu, L. Zheng, R. Song, *J. Power Sources* **2019**, *442*, 227252.

[27] V. Ciobotă, W. Salama, N. Tarcea, P. Rösch, M. E. Aref, R. Gaupp, J. Popp, *J. Raman Spectrosc.* **2012**, *43*, 405.

[28] B. S. Yeo, A. T. Bell, *J. Phys. Chem.* **2012**, *116*, 8394.

[29] a) X. Yin, H. Li, L. Han, J. Meng, J. Lu, Q. Song, *Small* **2021**, *17*, 2008056; b) Y. Sang, G. Ding, Z. Guo, Y. Xue, G. Li, R. Zhang, *J. Alloys Compd.* **2022**, *919*, 165855.

[30] D. Zhou, S. Wang, Y. Jia, X. Xiong, H. Yang, S. Liu, J. Tang, J. Zhang, D. Liu, L. Zheng, Y. Kuang, X. Sun, B. Liu, *Angew. Chem., Int. Ed.* **2019**, *58*, 736.

[31] E. Santos, W. Schmickler, *ChemPhysChem* **2006**, *7*, 2282.

[32] M. Ha, A. Hajibabaei, D. Y. Kim, A. N. Singh, J. Yun, C. W. Myung, K. S. Kim, *Adv. Energy Mater.* **2022**, *12*, 2201497.

[33] N. Wang, H. Gong, Z. Sun, C. Shen, B. Li, H. Xiao, X. Zu, D. Tang, Z. Yin, X. Wu, H. Zhang, L. Qiao, *ACS App. Energy Mater.* **2021**, *4*, 12163.

[34] J. Fu, Z. P. Cano, M. G. Park, A. Yu, M. Fowler, Z. Chen, *Adv. Mater.* **2017**, *29*, 1604685.

Energy &
Environmental
Science

ROYAL SOCIETY
OF CHEMISTRY

PAPER

View Article Online
View Journal

Cite this: DOI: 10.1039/d4ee01912a

Active site switching on high entropy phosphides as bifunctional oxygen electrocatalysts for rechargeable/robust Zn–air battery†

Ren He,‡[ab] Shiqi Wang,‡[c] Linlin Yang,‡[ab] Sharona Horta,[d] Yang Ding,[ef] Chong Di,[e] Xuesong Zhang,[g] Ying Xu,[e] Maria Ibáñez,[d] Yingtang Zhou,[h] Stefan Mebs,[i] Holger Dau,[i] Jan Niklas Hausmann,*[j] Wenyi Huo,*[kl] Prashanth W. Menezes*[jm] and Andreu Cabot*[an]

High-entropy materials (HEMs) offer a quasi-continuous spectrum of active sites and have generated great expectations in fields such as electrocatalysis and energy storage. Despite their potential, the complex composition and associated surface phenomena of HEMs pose challenges to their rational design and development. In this context, we have synthesized FeCoNiPdWP high entropy phosphide (HEP) nanoparticles using a low-temperature colloidal method, and explored their application as bifunctional electrocatalysts for the oxygen evolution and reduction reactions (OER/ORR). Our analysis provides a detailed understanding of the individual roles and transformations of each element during OER/ORR operation. Notably, the HEPs exhibit an exceptionally low OER overpotential of 227 mV at 10 mA cm^{-2}, attributed to the reconstructed HEP surface into a FeCoNiPdW high entropy oxyhydroxide with high oxidation states of Fe, Co, and Ni serving as the active sites. Additionally, Pd and W play crucial roles in modulating the electronic structure to optimize the adsorption energy of oxygen intermediates. For the ORR, Pd emerges as the most active component. In the reconstructed catalyst, the strong d–d orbital coupling of especially Pd, Co, and W fine-tunes ORR electron transfer pathways, delivering an ORR half-wave potential of 0.81 V with a pure four-electron reduction mechanism. The practicality of these HEPs catalysts is showcased through the assembly of aqueous zinc–air batteries. These batteries demonstrate a superior specific capacity of 886 mA h g$_{\mathrm{Zn}}^{-1}$ and maintain excellent stability over more than 700 hours of continuous operation. Overall, this study not only elucidates the role of each element in HEMs but also establishes a foundational framework for the design and development of next-generation bifunctional oxygen catalysts, broadening the potential applications of these complex materials in advanced energy systems.

Received 1st May 2024,
Accepted 21st August 2024

DOI: 10.1039/d4ee01912a

rsc.li/ees

---

[a] *Catalonia Energy Research Institute – IREC, Sant Adria de Besòs, 08930 Barcelona, Spain. E-mail: acabot@irec.cat*
[b] *Enginyeria Electrònica i Biomèdica Facultat de Física, Universitat de Barcelona, 08028 Barcelona, Spain*
[c] *Jiangsu Key Laboratory of Advanced Metallic Materials, Southeast University, Nanjing 211189, China*
[d] *Institute of Science and Technology Austria, Am Campus 1, 3400 Klosterneuburg, Austria*
[e] *Hebei Key Lab of Optic-electronic Information and Materials, College of Physics Science and Technology, Hebei University, Baoding 071002, China*
[f] *Songshan lake materials laboratory, Dongguan 523820, China*
[g] *Institut de Ciència de Materials de Barcelona (ICMAB-CSIC), Campus de la UAB, 08193 Bellaterra, Spain*
[h] *National Engineering Research Center for Marine Aquaculture, Marine Science and Technology College, Zhejiang Ocean University, Zhoushan, Zhejiang Province 316004, China*
[i] *Department of Physics, Freie Universität Berlin, Arnimallee 14, 14195 Berlin, Germany*
[j] *Materials Chemistry Group for Thin Film Catalysis – CatLab, Helmholtz-Zentrum Berlin für Materialien und Energie, Albert-Einstein-Str. 15, 12489 Berlin, Germany. E-mail: niklas.hausmann@helmholtz-berlin.de, prashanth.menezes@mailbox.tu-berlin.de*
[k] *College of Mechanical and Electrical Engineering, Nanjing Forestry University, Nanjing 210037, China. E-mail: wyhuo@njfu.edu.cn*
[l] *NOMATEN Centre of Excellence, National Centre for Nuclear Research, Otwock 05-400, Poland*
[m] *Department of Chemistry, Technische Universität Berlin, Straße des 17 Juni 135, Sekr. C2, 10623 Berlin, Germany*
[n] *ICREA, Pg. Lluis Companys 23, 08010 Barcelona, Catalonia, Spain*

† Electronic supplementary information (ESI) available. See DOI: **https://doi.org/10.1039/d4ee01912a**

‡ These authors contributed equally to this work.

Broader context

Rechargeable zinc–oxygen batteries represent a cutting-edge technology with promising applications ranging from large-scale stationary energy storage for renewable energy integration to powering electric vehicles and small-scale wearable devices. However, their performance is limited by the slow kinetics of oxygen redox reactions at the oxygen cathode, which significantly restricts their practical utility. To address these challenges, there is a pressing need for a new generation of oxygen redox catalysts. High entropy materials are emerging as powerful bifunctional oxygen electrocatalysts due to their quasi-continuous distribution of surface energy levels and the extensive flexibility they offer in tuning surface compositions. These properties are crucial for optimizing the adsorption energies of reactants, intermediates, and products involved in the redox processes. In this study, we present a solution-based synthesis route for producing FeCoNiPdWP nanoparticles, and demonstrate them to show outstanding combined performance in both oxygen reduction and evolution reactions. Besides, we have conducted a thorough investigation into the specific roles that each metal element plays in the redox process. Additionally, these high entropy phosphide nanoparticles are integrated as the air cathode in rechargeable zinc–air batteries, resulting in devices that exhibit unprecedented performance and stability.

1. Introduction

Rechargeable aqueous zinc–air batteries (ZABs) are recognized for their exceptional energy densities, inherent safety, sustainability, and potential for cost-effectiveness across various applications, including electric vehicles and large-scale stationary energy storage systems.[1] However, the performance of ZABs strongly relies on the activity, stability, and cost of the oxygen catalyst used at the cathode side to boost the oxygen evolution and reduction reactions (OER, ORR) during battery charging and discharging, respectively.[2–4]

For decades, significant efforts have been directed toward developing high-performance bifunctional oxygen electrocatalysts. Traditionally, a physical mixture of noble metal catalysts, *e.g.* Pt/C for ORR and Ir/C for OER, has been used to accelerate the kinetics of the two reactions. Despite their relative effectiveness, the high cost, the scarcity of these noble metals, and the need to double the catalyst amount—since each material facilitates only one type of reaction—pose substantial barriers to the commercial viability of ZABs.[5–8] To address this limitation, alternative bifunctional oxygen catalysts based on layered double hydroxides,[9] perovskites,[10] metallic alloys,[11] sulfides,[12] nitrides,[13] phosphides,[14] and their composites[15–17] are intensively investigated.

Electrocatalysts based on high-entropy materials (HEMs) have emerged as particularly promising due to their vast compositional versatility and the ability to finely tune their surface properties to optimize performance. Their complex composition and a huge amount of different potential surface configurations also result in quasi-continuous surface energy levels able to suit the adsorption of reactants, intermediates, and products, facilitating enhanced catalytic activities across various reactions.[18–23] The diverse range of surface sites provided by HEMs makes them ideal for catalyzing complex reactions and especially valuable as bifunctional catalysts. Despite these advantages, achieving a single HEM that excels in both OER and ORR remains a formidable challenge, primarily due to the divergent pathways and distinct intermediate adsorption energies required by these reactions.[24,25]

The vast range of potential HEM compositions makes trial-and-error processes hopeless to optimize them as dual-functional catalysts. Thus, to avoid a futile odyssey across the boundless expanse of HEMs, an educated selection of the HEMs characteristics leading to optimized catalytic performance is fundamental. This rational design must be supported by reliable structure–activity relationships and precise information on the distinct roles of each element in the OER and ORR mechanisms. However, gathering this information is especially difficult for HEMs having hundreds of thousands of possible atomic configurations. Besides, further complications arise with inevitable surface reconstructions caused by the strongly alkaline reaction conditions used.[26,27] Therefore, it is essential to delve into the catalyst reconstruction and explore the unique contributions of each metal involved. This approach is crucial for a holistic comprehension of the intricate dynamics at play within HEMs during catalysis.

Herein, FeCoNiPdWP high entropy phosphide (HEP) nanoparticles are synthesized using a mild colloidal method. Subsequently, their OER and ORR performance is compared with a series of control phosphides and commercial reference catalysts. To gain deeper insights into the oxygen redox reaction mechanisms, the distinct roles played by each metal in HEPs are analyzed using electrochemical measurements, X-ray absorption spectroscopy (XAS), and density functional theory (DFT) calculations. Furthermore, the HEP surface reconstruction and the real active species are explored and identified. Last, rechargeable ZABs based on FeCoNiPdWP HEPs bifunctional oxygen catalysts as the air cathodes are assembled and tested.

2. Results and discussion

2.1 Design principles of HEP

A primary challenge in developing bifunctional catalysts for OER/ORR is ensuring the availability of proper catalytic sites. As illustrated in Scheme 1, an effective catalyst typically provides surface sites that strongly adsorb reactants and intermediates but only weakly bind to the products, thereby promoting high efficiency in driving the forward reaction. In contrast, this type of catalyst often shows much lower efficiency for the reverse reaction. The opposite is true for catalysts that favor strong adsorption of the products. HEMs offer a promising solution to this challenge. These materials combine a vast array of different active sites, providing a continuum of adsorption energies. This unique feature enables HEMs to efficiently catalyze both OER and ORR, making them highly effective as bifunctional oxygen catalysts.

Transition metal phosphides have attracted substantial attention due to their metallic character and associated high electrical conductivity, as well as their abundant reserves, cost-effectiveness, and stability.[28–32] The higher electronegativity of

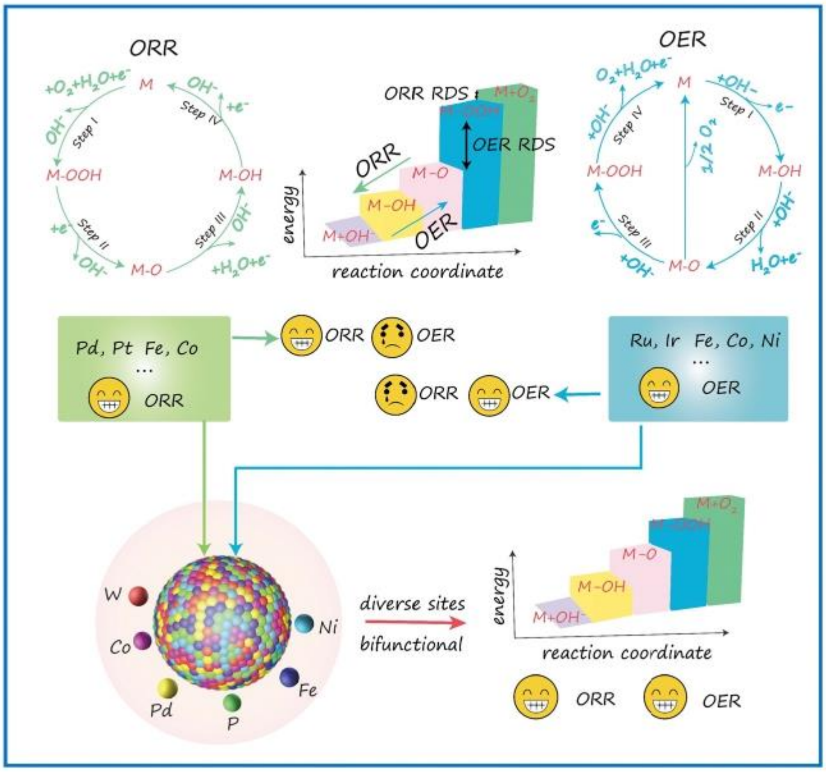

Scheme 1 Schematic illustration of the design principles of FeCoNiPdWP HEPs as bifunctional oxygen catalysts in an alkaline electrolyte.

phosphorus than transition metals triggers electron delocalization and leads to partially positively charged metal and negatively charged phosphorus, where transition metals could serve as the OH^- acceptor to modulate the binding ability for OER/ORR. From the electronic band structure perspective, the presence of phosphorous modifies the electronic energy levels and d-band center, increasing the density-of-states near the Fermi level,[33] which signifies abundant charge carriers similar to the noble metals for the OER/ORR process, thus frequently improving electrocatalytic performance.[34–36] In addition, the covalent nature of the metal–phosphorus bond promotes the durability and long-term stability of the electrocatalysts. Indeed, the hybridization of d metal orbitals with the p orbital of P to form metal–phosphorus bonds has been demonstrated to be beneficial in boosting ORR performance.[30] Therefore, the rational design and engineering of HEPs for ZAB applications is a worthy endeavor.

Based on our previous study, the combination of 3d/4d/5d metals significantly modulates the electronic state and surface electron density, altering the bond strength between the metal and oxygen species, which allows adjusting the adsorption/desorption ability of intermediates and products.[18,37,38] The d orbitals of 5d metals are more extended and have higher energy and spatial coverage compared to those of 3d/4d metals. When 5d metals combine with 3d metals, hybrid orbitals are formed, adjusting the electron distribution and orbital overlap, thereby potentially providing more active sites and enhancing catalytic activity. The high electronegativity of the 5d metals allows for the regulation of the electron-filling states of the 3d/4d metals, optimizing the surface electronic structure of the catalysts. In addition, 5d metals provide strong electronic attraction and create new coordination environments, stabilizing reaction intermediates, and reducing poisoning. Thus, W, a 5d metal with a unique orbital filling state was incorporated into the HEP catalyst.

In terms of the 3d transition metals, Fe, Co, and Ni were selected as well-established effective OER active sites based on their cost-effectiveness, the theoretically calculated volcano graph curves between overpotential and intrinsic catalytic activity,[39–43] and their rich valence state transitions, abundant electronic configuration, and adjustable spin state, which could effectively regulate the binding energy and modulate the spin flipping of the oxygen intermediates.[44,45] On the other hand, while a large number of excellent ORR catalysts have been reported, the most effective catalysts are still based on Pt and Pd. Therefore, Pd was incorporated into the HEP to promote ORR performance.[46,47] Besides, Pd easily forms alloys with other transition metals,[48] facilitating the HEP formation. Notice also that within an HEM, the amount of Pd is minimized compared with catalysts based on elemental Pd or binary Pd-based alloys. Overall, FeCoNiPdWP HEPs are expected to simultaneously provide superior OER and ORR performance with expectable W-modulated Fe/Co/Ni as the OER active sites and Pd as the ORR active sites, making them a potentially ideal cathode material in ZABs.

2.2 HEP synthesis and characterization

FeCoNiPdWP HEPs and the related reference quaternary metal phosphides (FeCoNiPdP, FeCoPdWP, CoNiPdWP, FeNiPdWP, and FeCoNiWP) were synthesized using a heating-up colloidal synthesis approach (Fig. 1a) using a mixture of 1-octadecene and oleylamine as the solvent (see details in the experimental section in the ESI†). Triphenyl phosphite was selected as a low-cost, safe, and stable phosphorus source.[49–51] Metal acetylacetonates and carbonyls were used as metal precursors. The reaction temperature was set to 290 °C. At this temperature, the phosphorus–oxygen bonds in triphenyl phosphite molecules are cleaved, releasing phosphorous atoms that react with the metal precursors to yield the HEP. Fig. S1–S6 (ESI†) show the results from the characterisation of the reference quaternary metal phosphides.

Transmission electron microscope (TEM) images show the FeCoNiPdWP HEP nanoparticles to have an average size of 20 nm (Fig. 1b). Spherical aberration-corrected high-resolution TEM (AC-HRTEM) analysis confirmed their high crystallinity (Fig. 1c and d). X-Ray diffraction (XRD) pattern determined the particles to have the $Pd_{15}P_2$ rhombohedral phase (JCPDS 01-071-0193) (Fig. S6a, ESI†). Geometric phase analysis (GPA) shows a random distribution of distortions induced by tensile and compressive stresses attributed to the different atomic

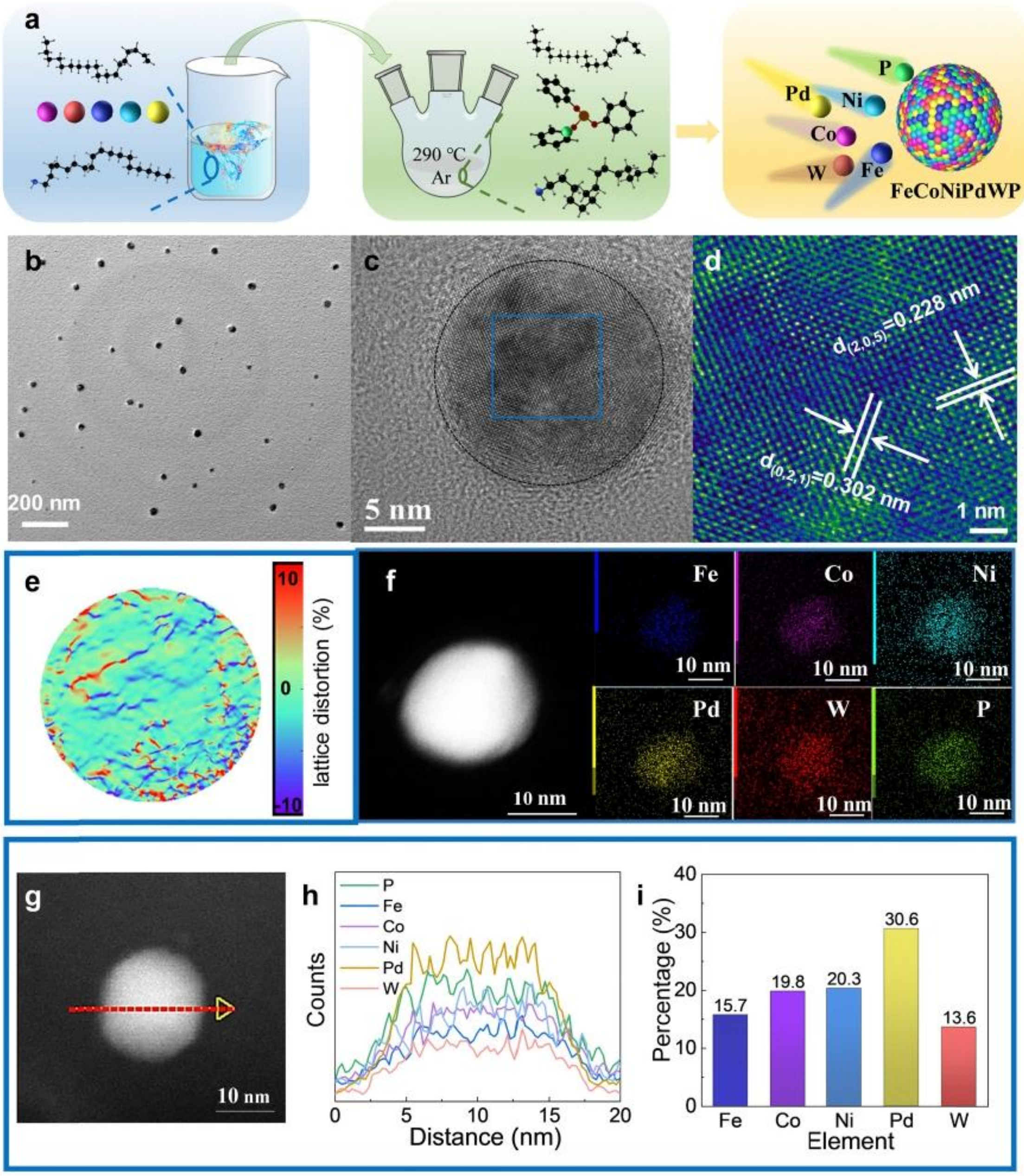

Fig. 1 Chemical and structural characterization of FeCoNiPdWP nanoparticles. (a) Scheme of the synthesis approach used to produce FeCoNiPdWP HEPs. (b) TEM image. (c) AC-HRTEM image. (d) Magnified AC-HRTEM image and lattice distance analysis of the blue square in (c). Two crystal planes with lattice distances of 0.228 and 0.302 nm are indexed to the (205) and (021) crystal planes of the $Pd_{15}P_2$ rhombohedral phase, respectively. (e) GPA analysis. (f) HAADF-STEM micrograph and EDS compositional maps. (g) HAADF-STEM micrograph and (h) line scanning profiles. (i) Metal ratios obtained using ICP-OES.

radii and electronegativity of the constituent elements (Fig. 1e). High-angle annular dark field scanning TEM (HAADF-STEM) micrographs combined with energy-dispersive X-ray spectroscopy (EDS) compositional maps show a homogeneous distribution of the different elements within the HEP nanoparticles (Fig. 1f–h). The TEM-EDS metal ratios are consistent with those obtained from inductively coupled plasma optical emission spectroscopy (ICP-OES): Fe/Co/Ni/Pd/W = 15.7/19.8/20.3/30.6/13.6 (Fig. 1i).

2.3 OER

2.3.1 OER catalytic performance. The OER activity of the materials supported on glassy carbon (GC) was evaluated by linear sweep voltammetry (LSV) in 1.0 M KOH (see the experimental section in the ESI† for electrode preparation and OER test details). The LSV curves display a small bump in the potential range of 1.3–1.4 V *vs.* RHE associated with the oxidation of the transition metals. FeCoNiPdWP shows the best OER catalytic performance with outstanding low overpotentials of 227 mV at 10 mA cm^{-2}, 250 mV at 50 mA cm^{-2}, and 258 mV at 100 mA cm^{-2} (Fig. 2a and b). These values are well below those measured for RuO$_2$, PdP$_x$ (Fig. S7, ESI†), and the quaternary phosphides, which overpotential at 10/100 mA cm^{-2} follows the trend FeCoNiPdWP < FeCoNiPdP < FeNiPdWP < FeCoPdWP < FeCoNiWP < CoNiPdWP < RuO$_2$ < PdP$_x$ (Fig. S8, ESI†).

FeCoNiPdWP also shows the smallest Tafel slope (33 mV dec^{-1}), well below that of the other metal phosphides (37–59 mV dec^{-1}) and RuO$_2$ (75 mV dec^{-1}), demonstrating especially favorable OER kinetics (Fig. 2c). Cyclic voltammetry (CV) curves at different scan rates (Fig. S9, ESI†) and the derived double-layer capacitance (C_{dl}) values (Fig. 2d) show that all the quaternary and quinary phosphide catalysts have a similar electrochemical active surface area (ECSA), higher than that of PdP$_x$ (Fig. S10, ESI†). Normalization of the OER current densities by the ECSA values implies that FeCoNiPdWP has a higher intrinsic activity per active site (Fig. 2e). Electrochemical impedance spectroscopy (EIS) analysis confirms FeCoNiPdWP to display the smallest OER charge transfer impedance thus the most favorable reaction kinetics (Fig. 2f and Table S1, ESI†).

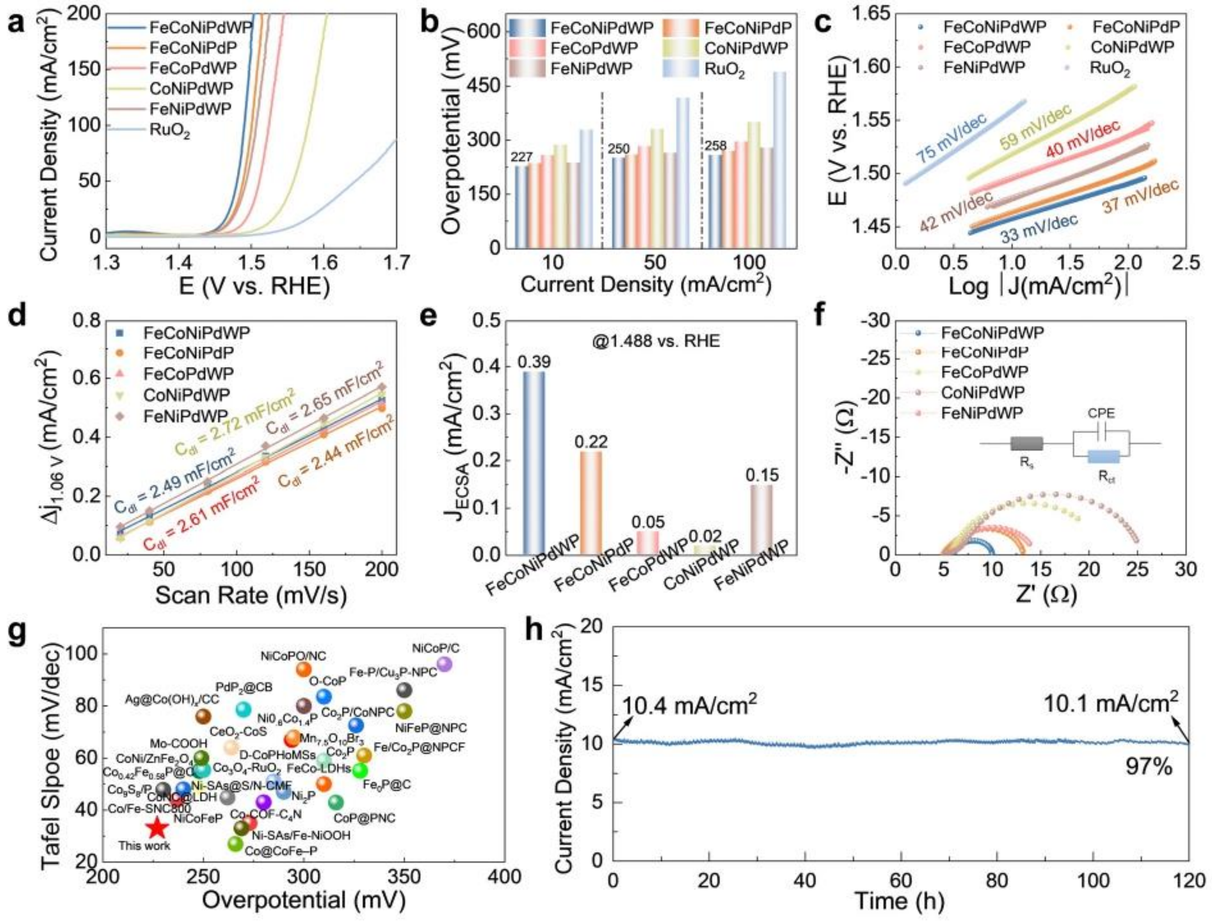

Fig. 2 OER performance on GC electrodes with a loading of 0.5 mg cm^{-2}. (a) LSV curves at 5 mV s^{-1}. (b) Overpotential at different current densities. (c) Tafel fitting plots calculated from the LSV curves in (a), the open circles are measured data and the long solid lines are fitted data. (d) C_{dl} values calculated from the CV curves in Fig. S9 (ESI†). (e) Current density normalized by ECSA at 1.488 *vs.* RHE. (f) Nyquist plot of the EIS spectra of the different catalysts at 1.5 V *vs.* RHE. The inset shows the equivalent circuit model used to fit the experimental data (Table S1, ESI†), where R_s is the internal resistance of the cell, R_{ct} is the charge-transfer resistance, and CPE represents the double-layer capacitance at the electrode–electrolyte interphase. (g) Comparisons of the OER performance of FeCoNiPdWP with other recently reported catalysts on GC. (h) CA curve of FeCoNiPdWP at 1.46 V *vs.* RHE.

Overall, FeCoNiPdWP HEPs show superior OER performance when compared not only with the reference materials tested here but also with previously reported catalysts supported on GC, as shown in Fig. 2g and Table S2 (ESI†).[4,52–84] Besides, FeCoNiPdWP shows excellent stability with a continuously applied potential of 1.46 V *vs.* RHE for 120 h resulting in just a 3% decrease in current density as determined by chronoamperometry (CA) measurements (Fig. 2h), well below the current density decay obtained from the quaternary metal phosphides (Fig. S11, ESI†)

2.3.2 HEP reconstruction during OER. The high-resolution X-ray photoelectron spectroscopy (XPS) spectra of FeCoNiPdWP HEPs before and after OER operation are displayed in Fig. S12 and S13 (ESI†). Before OER, FeCoNiPdWP displays both M–P and M–O surface chemical environments, the latter originated during sample storage, transportation, and manipulation.[85,86] After long-term OER, surface metals show a single oxidation state, Fe^{3+}, Co^{2+}, Ni^{3+}, Pd^{2+}, and W^{6+}, with no M–P chemical environment. Besides, no P is detected at the surface of the HEP nanoparticles. Additionally, the hydroxide (O_{OH}) contribution to the O 1s XPS spectrum becomes dominant, which is attributed to the formation of a metal (oxy)hydroxide surface.

XRD analysis of FeCoNiPdWP after the OER stability test revealed that the crystalline $Pd_{15}P_2$ rhombohedral phase disappeared during OER operation (Fig. S14, ESI†). Besides, EDS spectra (Fig. S15 and S16, ESI†) show that the P amount strongly decreased from 29% to 3% after OER. *In situ* Raman spectroscopy was used to explore the evolution of HEP with the applied potential (Fig. S17, ESI†). The spectra show Raman peaks at around 300 cm^{-1}, and 400–700 cm^{-1}, whose intensity increases with the applied voltage. This observation is related to the formation of layered Fe/Co/Ni (oxy)hydroxides.[87,88] Thus, overall, XPS, XRD, and Raman results are consistent with the HEP being reconstructed into a high entropy oxyhydroxide (HEOOH) in OER conditions.

XAS on the Fe, Co, Ni K-edge was used to gain an understanding of the FeCoNiPdWP atomic structure and the reconstruction process taking place during OER for the as-prepared HEP nanoparticles, the fresh electrode, and the electrode with the completed reconstruction process. X-ray absorption near edge spectroscopy (XANES) analysis of the reconstructed samples revealed significant increases in the oxidation states of the metals during OER operation, with Fe increasing from 3.0 to

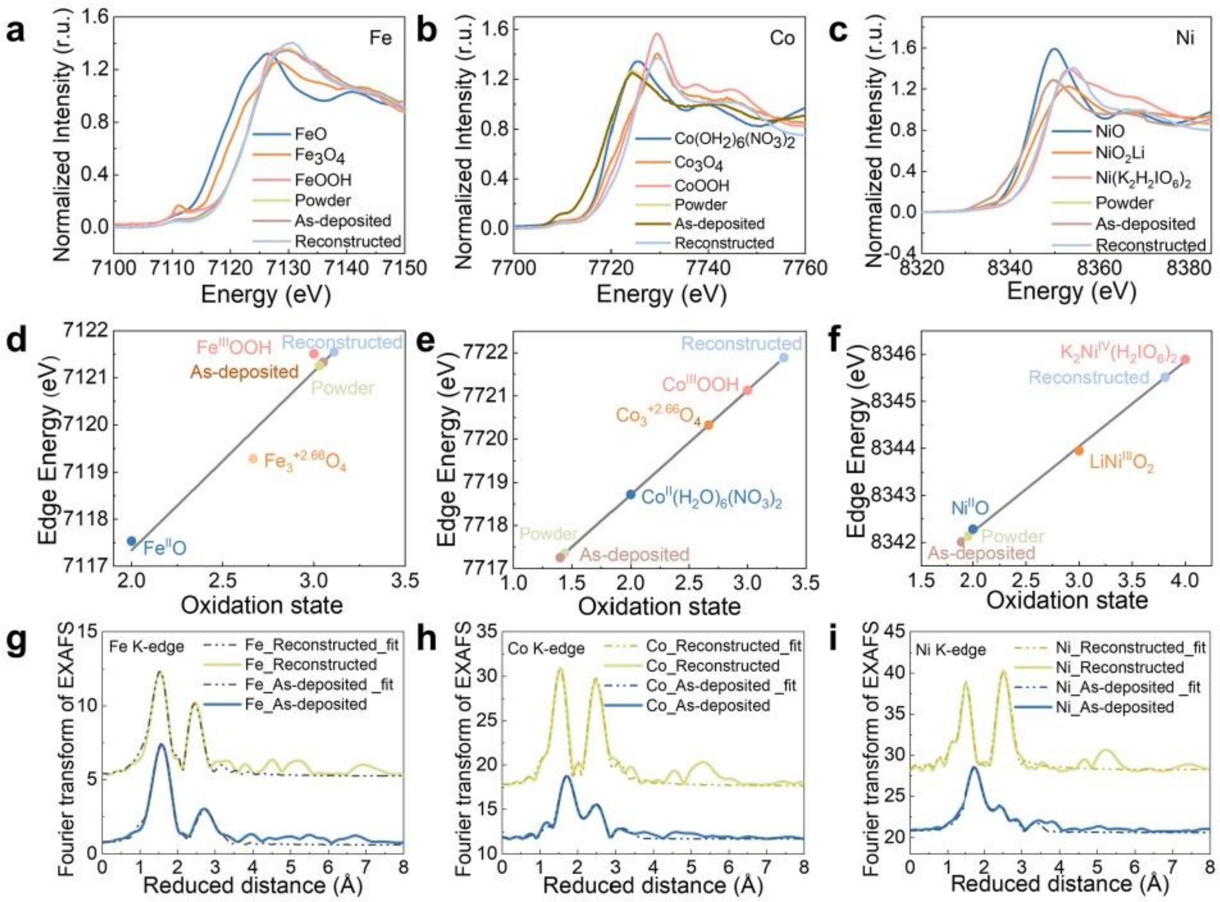

Fig. 3 XAS characterization of HEPs. (a)–(c) Fe (a), Co (b), and Ni (c) XANES plots of the as-prepared powders, the as-deposited films, and reconstructed films, freeze-quenched at 1.53 V *vs.* RHE after 2 h OER operation. (d)–(f) Metal oxidation states of Fe (d), Co (e), and Ni (f) from the XANES. To quantify differences in the edge positions, the K-edge energy was calculated using the integral method,[95] and the obtained values are plotted here as symbols. A linear regression including the three iron/cobalt/nickel oxide references was used to derive the oxidation states of the HEPs before and during the OER. (g)–(i) Fe (g), Co (h), and Ni (i) EXAFS spectra (Fig. S18, ESI†) and simulations (Table S4 for the simulation parameters, ESI†). The data at the bottom/up show the as-prepared/reconstructed electrodes.

3.1, Co from 1.4 to 3.3, and Ni from 2.0 to 3.8 (Fig. 3a–f and Table S3, ESI†). Fe, Co, and Ni in oxidation states above three have been shown to facilitate water oxidation.[89–94] Thus, the high Fe, Co, and Ni average oxidation states during the OER support the hypothesis that these three elements or their multimetallic neighbouring sites function as OER active sites.

To gain insight into the local structure of Fe/Co/Ni, the extended X-ray absorption fine structure (EXAFS) data and k^3-weighted EXAFS spectra were simulated, as shown in Fig. 3g–i and Fig. S18 (ESI†). For all the 3d metals, models of layers with edge-sharing [MO_6] octahedra were applied to simulate the EXAFS spectra (see Table S4 for fitting parameters, ESI†). The model comprises three shells: (i) for the M–O bond of the [MO_6] octahedra (1.87–2.02 Å), (ii) for the M–M distance of two adjacent [MO_6] octahedra (2.81–2.98 Å), and (iii) a second, larger M–O distance (3.40–3.43 Å). This model is consistent with the FeCoNi oxyhydroxide structure or their deprotonated, oxidized, and potassium-intercalated relatives that have recently been proposed to form during OER.[94] For Fe, two M–O bond distances (1.89 and 2.02 Å) were required, likely due to the presence of a Jahn–Teller distortion caused by the unevenly occupied t_{2g} orbital of [$Fe^{III}O_6$]. The presence of two different M–O bond lengths automatically leads to two different Fe–M bond distances as well, which were taken into account in the simulation. The short M–O bond distances (1.87–1.89 Å) are consistent with the high oxidation states extracted from the XANES data (Table S4, ESI†). Overall, results from XAS analyses reveal that, during OER, FeCoNiPdWP is fully reconstructed into layers of edge-sharing [MO_6] octahedra with 3d metal oxidation states above three. These motifs are consistent with highly oxidized oxyhydroxides and related structures that are frequently observed during and after the OER.[94,96–98]

2.3.3 HEP element roles in OER.

DFT calculations were carried out to identify the roles of individual metal sites and their synergistic effects in the FeCoNiPdWP HEPs reconstructed during the OER, denoted as FeCoNiPdWOOH (Fig. S19, ESI†), and the reference reconstructed quaternary compounds (Fig. S20–S25, ESI†). As shown in Fig. 4a, all the reconstructed models have the Fermi level (E_F) within a band of states, indicating a metallic conductivity. The total density of state (TDOS) of FeCoNiPdWOOH is greater than that of the reference compounds at around E_F, pointing to a higher electron transport rate. The projected DOS (PDOSs) of each element in the FeCoNiPdWOOH model is displayed in Fig. 4b. Notably, the O 2p orbitals have a strong overlap with the different metal elements, pointing at an efficient p–d orbital coupling and self-complementary effect.[99] The Ni-3d and Co-3d orbitals are close to E_F, pointing to high electrochemical activity with strong electron depletion capability. The Fe-3d orbital shows e_g–t_{2g} splitting with a strong overlap with the W 5d orbitals, implying a high degree of W 5d–Fe 3d orbital coupling and electron exchange between these two metals.[100,101] The center of the Pd-4d band is located well below the E_F, lower than the other metal sites, indicating an electron-rich characteristic. Consistently, the charge density difference (CDD) analysis revealed that Pd sites exhibit electron accumulation (Fig. S20b, ESI†). In addition, Pd-4d orbitals cover a wide energy range, from −10.0 eV to E_F. Overall, Fe-3d, Co-3d, Ni-3d, Pd-4d, W-5d, and O-2p orbitals cross the E_F and show a significant covalent interaction between metal and O bands, which boosts the site-to-site electron transfer and might be one of the reasons for the outstanding OER performance of the reconstructed HEOOH. Meanwhile, the d-band center (d_c) of FeCoNiPdWOOH is higher than that of the quaternary metal oxyhydroxides and the electronic structure balance involves charge transfer between all the different elements (Fig. 4c).

PDOS analysis was used to evaluate the adsorption behaviors over different sites. For the reactant OH^- species, during the initial adsorption process, s/p bands were down-shifted (Fig. 4d), indicating electron transfer from the surface sites to OH^- to stabilize adsorbed *OH. The improved adsorption capability favored the weakening of O–H bonds in *OH, thus triggering the subsequent dissociation processes. Compared with Fe, Co, and W sites, stronger p–d orbital couplings between the OH* and Ni/Pd sites were observed, which points to a more stable adsorption of OH* on the Ni/Pd sites within FeCoNiPdWOOH. This was experimentally demonstrated by the methanol probe molecule test of FeCoNiPdWP and FeCoNiWP in 1 M KOH and 1 M methanol, concluding that the presence of Pd significantly promoted the adsorption of OH^- species (Fig. S26, ESI†). CDD results also showed that Ni sites presented noticeable electron depletion with OH^- adsorption, demonstrating charge transfer during the adsorbing process (Fig. S27, ESI†). The integral projected crystal orbital Hamilton population value (ICOHP) provides the number of bonded electrons between the selected metal and O atoms in the active *OH and the corresponding bonding strength. Notably, the ICOHPs of Ni and Pd are larger than those of Fe/Co/W, demonstrating stronger OH adsorption in the formers (Fig. 4e).

Gibbs free energies were calculated considering various potential metal active sites to reveal the energy barriers of adsorption/desorption of key intermediates. As shown in Fig. 4f, the energy barriers (ΔG) for each step among various active sites were quite different. For the Fe/Co/Ni sites in the FeCoNiPdWOOH model, the third step (formation of *OOH from *O with OH^- in the electrolyte) exhibited the largest barrier. On the other hand, for Pd and W sites, the ΔG values slightly increased at the second step and first step, respectively. Accordingly, Fe/Co/Ni active sites exhibited lower overpotentials than those of Pd and W sites, respectively, under the equilibrium potential (1.23 eV, Fig. S28, ESI†). Thus, in FeCoNiPdWOOH, activity was associated with Fe/Co/Ni active sites, and the third reaction step was the rate-determining step (RDS) during the four-electron transfer process. To visualize the electronic environment during the reaction coordinates of OER, the PDOS of the most stable binding of key intermediates (*OH, *O, *OOH, and *O_2) is plotted in Fig. 4g. The σ components of O-2p orbitals facilitated the electron transfer of sequential adsorbed intermediates. From the initial OH species to the final product O_2, the consecutive upshifting of the σ orbitals demonstrates efficient electron transfer with low barriers for intermediate transformation, which is consistent with the highly efficient OER reaction trend.

Notably, all of the Fe, Co, and Ni sites on the FeCoNiPdWOOH model showed smaller energy barriers than within the other models, demonstrating the significant effect of all the

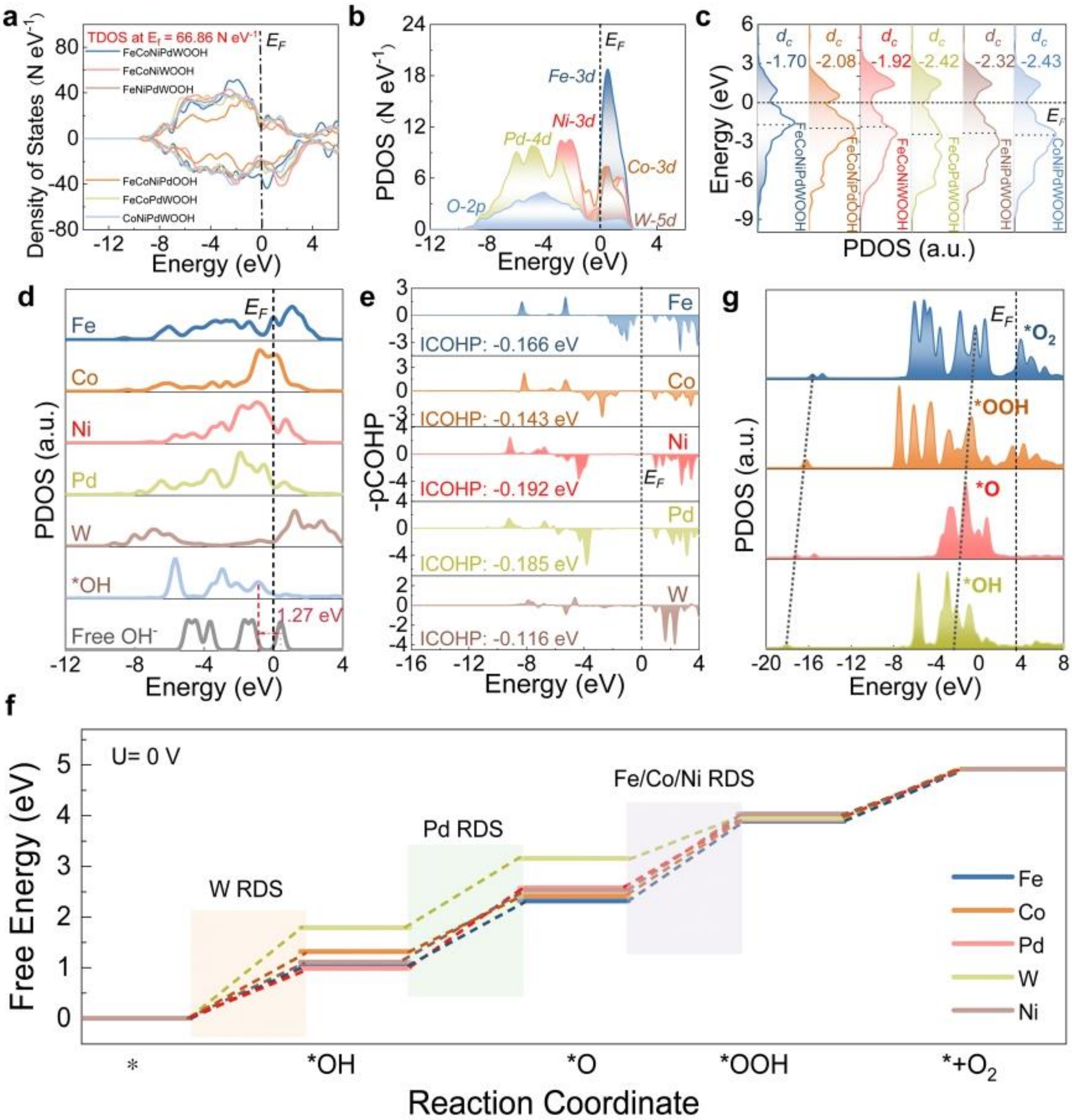

Fig. 4 DFT calculation results. (a) TDOS of FeCoNiPdWOOH, FeCoNiPdOOH, FeCoNiWOOH, FeCoPdWOOH, FeNiPdWOOH, and CoNiPdWOOH. (b) PDOS of FeCoNiPdWOOH. (c) Electronic density of states of the d-band for the metal atoms in various models. (d) PDOS for OH adsorption at various active sites. (e) COHP bonding analysis of M–O interactions (M in the surface site over FeCoNiPdWOOH and O in adsorbed OH). (f) Standard free energy diagram of the OER process at 0 V of FeCoNiPdWOOH for various active sites. (g) PDOS of key intermediates over Ni sites in FeCoNiPdWOOH.

elements in the reconstructed sample (Fig. S29, ESI†). Consequently, Fe/Co/Ni are identified as the main active sites for OER, which is consistent with the experimental results. In particular, the strong and positive effect of Pd was further demonstrated by DFT calculations over FeCoNiPdWOOH and Pd-free FeCoNiWOOH models. Pd benefits the electron transfer (Fig. S30 and S31, ESI†), optimization of adsorption configuration (Fig. S32, ESI†), and electron interaction between the oxygen intermediates (Fig. S33, ESI†). Overall, the synergistic effect of the multiple metal atoms, materialized through an efficient p–d orbital coupling and moderate d-band center, optimized the adsorption/desorption of OER intermediates to promote OER kinetics.

In summary, the FeCoNiPdWOOH reconstructed from FeCoNiPdW HEP is highly active towards OER. In the reconstructed phase, Ni and Pd are favorable for the initial hydroxide adsorption, facilitating the subsequent electron transfer reaction steps. Subsequently, Fe/Co/Ni as the main active sites having favorable OER reaction intermediate adsorption energies, due to their electronic modification by Pd and W. Furthermore, XAS revealed unusually high oxidation states of Fe (+3.1), Co (+3.3), and Ni (+3.8) during the OER, which is crucial to promote the OER reaction.[90–94]

2.4 ORR

2.4.1 ORR catalytic performance. HEPs were further evaluated towards the ORR in 0.1 M KOH using a rotating ring-disk electrode (RRDE). A large cathodic peak is observed when the electrolyte is saturated with O_2 compared with Ar, indicating a notable ORR electrochemical activity for the FeCoNiPdWP (Fig. 5a). Fig. 5b and Fig. S34 and S35 (ESI†) show the LSV curves with various rotation speeds in the range 400–2500 rpm for the different metal phosphides and a commercial Pd/C reference catalyst. As shown in Fig. 5c, the limiting diffusion current density for the metal phosphides complies with the trend of FeCoNiPdWP (5.37 mA cm^{-2}) > CoNiPdWP (4.37 mA cm^{-2}) > FeCoPdWP (2.77 mA cm^{-2}) > FeCoNiPdP (2.08 mA cm^{-2}) > FeNiPdWP (1.67 mA cm^{-2}). The half-wave potentials, extracted from the LSV curves at 1600 rpm, of the different metal phosphides follow the same trend as the limiting diffusion current density, with FeCoNiPdWP showing the highest value at 0.81 V. This value is very close to that obtained for Pd/C, at 0.82 V. When LSV curves are normalized to the quantity of Pd, FeCoNiPdWP and commercial Pd/C catalysts show similar half-wave potentials but FeCoNiPdWP is characterized by a significantly higher current density (Fig. S36, ESI†). Overall, FeCoNiPdWP exhibits excellent ORR activity, matching that of Pd/C and state-of-the-art ORR catalysts, as shown in Fig. 5d and Table S5 (ESI†).[14,52,54,56,78,102–113] Besides, FeCoNiPdWP displays superior ORR stability with just a slight performance degradation after 5000 cycles (Fig. 5e), implying much more stable cycling performance than the quaternary metal phosphides (Fig. S37, ESI†).

2.4.2 HEP reconstruction during ORR. After the ORR stability test, the XRD main peak of HEPs is still visible, but it exhibits a broader half-width, indicating a loss of crystallinity or a reduction of the size of the HEP crystal domains during the ORR (Fig. S38, ESI†). High-resolution XPS spectra of FeCoNiPdWP HEPs after long-term ORR are displayed in Fig. S39 (ESI†). The W 5d and Pd 5d XPS spectra display a unique contribution assigned to W–P and Pd–P chemical environments. On the other hand, the Fe 3d, Co 3d, and Ni 3d spectra display two coordination environments, M–P and M–O(H). Besides, as shown in Fig. S40 (ESI†), the O 1s XPS spectrum displays two peaks, which are indexed to O–P bond and O_{OH}, and the P 2p XPS spectrum shows two coordination environments, P–O and P–M. Besides, XPS spectra also show that during the ORR, the Fe, Co, and Ni metal ratios at the FeCoNiPdWP surface slightly increase (Fig. S41, ESI†). Additionally, the amount of P at the surface significantly decreases, from 16.5% to 11.0%, while that of oxygen increases, from 15.1% to 27.2%. EDS analysis confirms that the overall P content decreases after ORR, while that of O increases, and the overall content of the different metals remains mostly unchanged (Fig. S42, ESI†). Thus, a slight enrichment of the surface with the 3d elements, Fe, Co, and Ni, is inferred, which is again related to the higher affinity of these elements for oxygen and OH^- groups. Nevertheless, this enrichment is less abrupt than that obtained in the more oxidizing OER conditions. Besides, the lower applied voltages also result in a less oxidized HEP surface where Pd and W maintain the phosphide chemical environment. Within its experimental error, EDS elemental maps show that all the metals, P and O are homogeneously distributed at the particle level after the ORR reaction (Fig. S43, ESI†). However, AC-HRTEM single particle analyses reveal highly crystalline HEP cores surrounded by about 2 nm amorphous shells. The crystalline cores with a lattice distance of 2.39 Å match the (211) crystal plane of the rhombohedral $Pd_{15}P_2$ phase, corresponding to the main XRD peak at $2\theta = 39°$ (Fig. S44, ESI†). According to XPS data, the amorphous shells are enriched with Fe, Co, and Ni in a hydroxide or

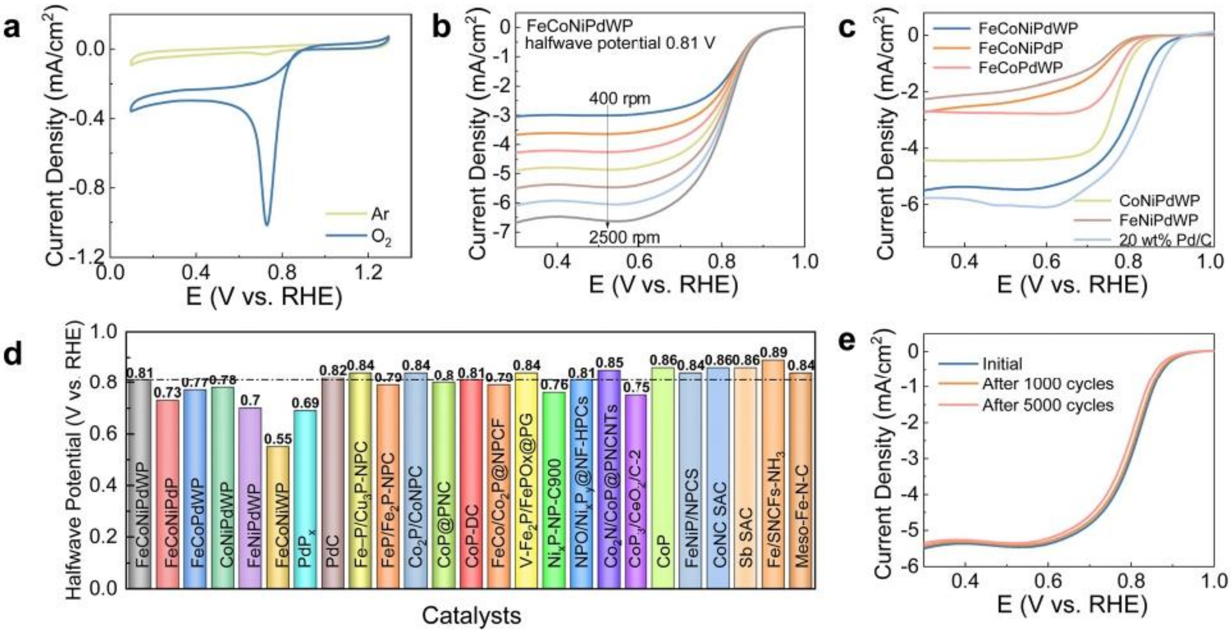

Fig. 5 ORR performance. (a) CV curves measured in Ar and O_2 saturated electrolytes of FeCoNiPdWP. (b) LSV curves of FeCoNiPdWP at different rotation speeds in the range 400–2500 rpm. (c) LSV curves at 1600 rpm for different metal phosphides and Pd/C catalysts. (d) Half-wave potential comparison between metal phosphides and Pd/C catalysts prepared in this work and recently reported state-of-the-art ORR catalysts. (e) Stability of FeCoNiPdWP HEPs during 5000 cycles.

oxyhydroxide chemical environment while also containing notable concentrations of W–P and Pd–P. The higher oxidation resistance of W–P and Pd–P during the ORR process is attributed to their stronger bond with shorter bond lengths, as calculated by DFT (Fig. S45, ESI†). Additionally, W and Pd exhibit greater stability due to more negative standard enthalpies[114–116] and possess much larger standard redox electrode potentials compared to Fe, Co, and Ni.

2.4.3 HEP element roles in ORR. Electrochemical measurements were first used to investigate the different element roles in FeCoNiPdWP HEP for ORR. Without Pd, FeCoNiWP displays a very weak catalytic ability (Fig. S46a and b, ESI†), demonstrating the key role played by Pd as an active ORR site. Besides, the half-wave potential of PdP_x is also relatively low, at 0.69 V (Fig. S47a and b, ESI†). Thus, while Pd serves as the active site, it doesn't exhibit high catalytic ability within a PdP_x environment. This reinforces the importance of other metals–Fe, Co, Ni, and W-in enhancing and stimulating the catalytic ability of Pd sites within the phosphide environment.

An ORR electron transfer number (n) over 3.9 is obtained for FeCoNiPdWP, CoNiPdWP, FeCoPdWP, PdP_x, and Pd/C, implying a 4 electron pathway (Fig. S46c, S47c and S48a, ESI†) at 0.5 V *vs.* RHE, where a stable limiting diffusion current density is measured. In contrast, FeCoNiPdP, FeNiPdWP, and FeCoNiWP are characterized by smaller n values, in the range 3.6–3.8, indicating the coexistence of the 4 electron and 2 electron pathways. The hydrogen peroxide (H_2O_2) yields further confirm the pathway assignment (Fig. S46d, S47d and S48b, ESI†). These results point at Pd, Co, and W as collectively assuming a more fundamental role in fine-tuning the reaction pathway, thereby amplifying the ORR performance of FeCoNiPdWP HEPs compared with the quaternary metal phosphides.

DFT calculations were further used to gain an understanding of the catalytic mechanism and element roles in the reconstructed HEPs during ORR. The reconstructed HEP model was built considering the experimental results, *i.e.* a HEP core with a $\sim$2 nm shell rich in Fe, Co, and Ni in a hydroxide environment and Pd and W in a phosphide environment. We denote this reconstructed HEP as FeCoNiPdWPOH (Fig. S49, ESI†). In the PDOS spectra, the good overlap between different metal elements-d orbitals and with the O-p orbitals implies possible p–p/p–d/d–d orbital coupling, which might further promote electron transfer efficiency (Fig. S50, ESI†).

The site-dependent PDOS of individual metal components located within or at the surface of the FeCoNiPdWPOH was also taken into consideration to appreciate their roles in the enhancement of ORR activity (Fig. 6a). From the reconstructed FeCoNiPdWPOH interior to the surface, the e_g–t_{2g} splitting of Fe-3d orbitals gradually decreased. The alleviated e_g–t_{2g} splitting could lead to higher valence states over the surface but also reduce the energy barrier of electron transfer from the electrocatalysts to the adsorbates to improve the ORR performance. Co sites displayed a site-independent electronic structure from the interior to the surface, which could endow the stable adsorption of intermediates and initial electroactive features during the ORR (Fig. 6b). On the other hand, the Ni-3d and Pd-4d bands gradually approach the E_F from FeCoNiPdWPOH interior to the surface, suggesting improved electroactivity of the surface metal sites (Fig. 6c and d). In contrast, the W-5d orbitals demonstrated an upshifting trend away from E_F, leading to decreasing valence states (Fig. 6e). This compensation of the PDOS trend, facilitated by the W-5d orbitals, contributes to the high electroactivity of the Pd/Ni/Co/Fe surface sites.

The ORR Gibbs energy barrier at various metal sites in FeCoNiPdWPOH was also calculated. As shown in Fig. 6f and Fig. S51 (ESI†), notably, among all of the various metal sites, Pd sites displayed the smallest energy barrier with just a 0.20 eV of the RDS for the conversion from *OOH to O*. Thus, Pd sites show the most thermodynamically favorable process, which is consistent with the experimental results. In addition, the PDOS of key ORR intermediates displayed a gradual downshifting of the O-p orbitals, indicating the reduction trends and highly efficient intermediate conversions for FeCoNiPdWPOH (Fig. 6g).

O_2 adsorption results in strong local charge redistribution over the Pd active sites, causing electron migration from the surface to the adsorbed $*O_2$ species (Fig. S52, ESI†). The PDOS for adsorbed O_2 is down-shifted compared with that of the free O_2 (Fig. S53, ESI†), further revealing the strong interaction between the Pd sites and O_2. Besides, the final product H_2O could easily escape from the surface of FeCoNiPdWPOH (Fig. S54, ESI†). The adsorption and desorption ability of the oxygen intermediates for Pd sites can be modulated by the introduction of other metals, as determined by the optimum d_c values (Fig. S55, ESI†).

Overall, FeCoNiPdWP shows excellent ORR performance with large limiting current density, high half-wave potentials, four electron-transfer pathways, and long-term cycling performance. In FeCoNiPdWP, Pd was found to be the most active element among the five metals within the reconstructed FeCoNiPdWPOH leading to the excellent ORR catalytic performance. The strong d–d orbital coupling of different elements, especially Pd, Co, and W, fine-tunes ORR electron transfer pathways and the surface electron modulation of Pd with other metal elements decreases the energy barrier during the ORR.

2.5 HEP as bifunctional oxygen catalysts

A key performance parameter to evaluate the oxygen bifunctional catalytic performance is the potential gap (E_{gap}) between the OER overpotential at 10 mA cm^{-2} (E_j = 10) and the ORR half-wave potential ($E_{1/2}$). A smaller E_{gap} value implies a better bifunctional performance, thus enabling ZABs with higher charge/discharge energy efficiency. Due to the excellent OER and ORR performance, the reconstructed FeCoNiPdWP shows an extremely low E_{gap} value of 0.65 V in 0.1 M KOH, much lower than the combination of the benchmark OER and ORR catalysts, Pd/C and RuO_2, resulting in an E_{gap} of 0.75 V (Fig. 7a). Besides, the FeCoNiPdWP exhibits an outstanding low bifunctional E_{gap} compared with state-of-the-art bifunctional oxygen catalysts, as shown in Fig. 7b and Table S6 (ESI†).[4,52,54,56,78,108,109,111,112,117–121] The remarkable dual functionality of the reconstructed FeCoNiPdWP in both OER and ORR can be attributed to the distinct contributions and cooperative interactions of each metal involved. While OER and ORR typically

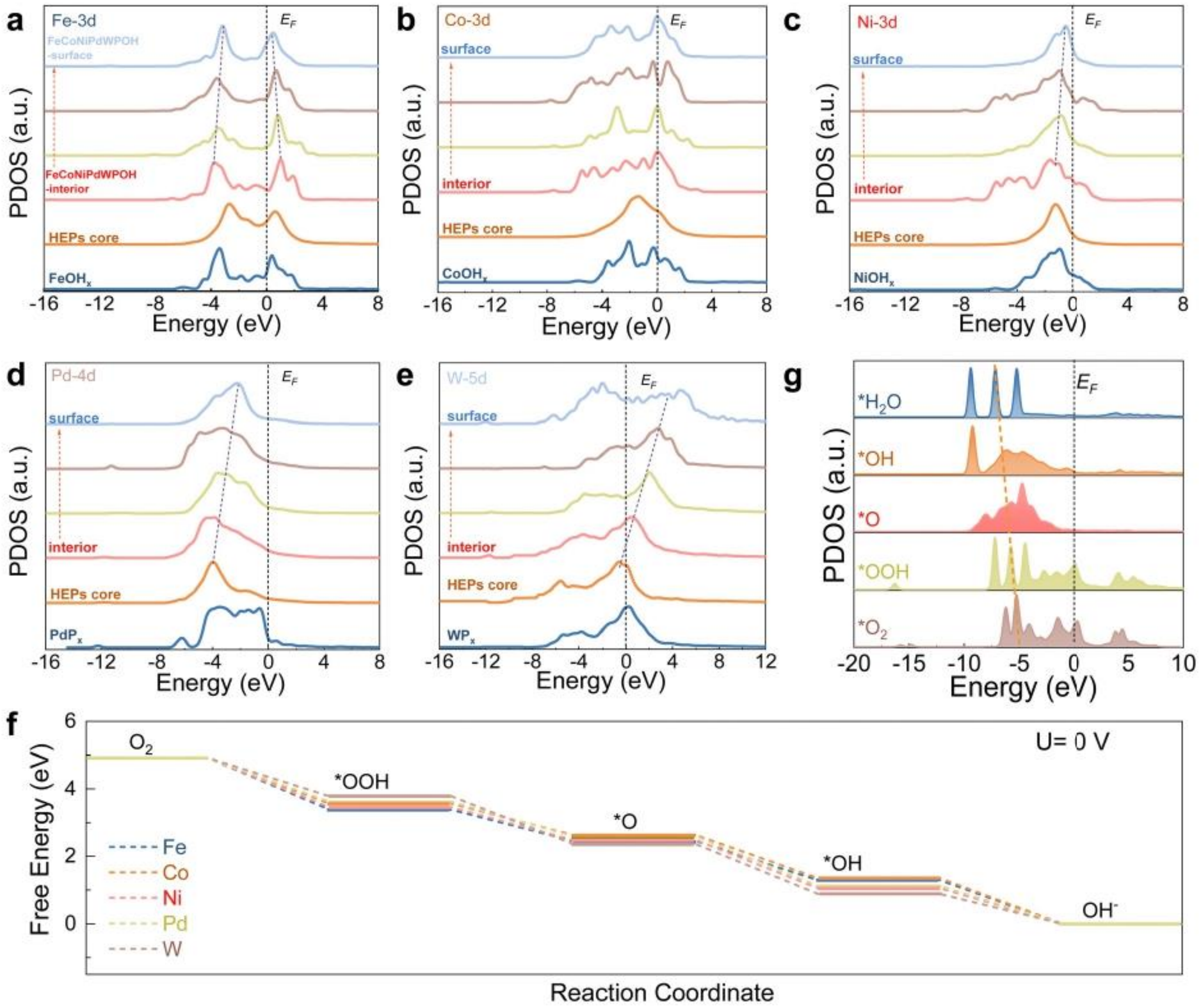

Fig. 6 DFT calculations for ORR. (a)–(e) Site-dependent PDOSs of Fe, Co, Ni, Pd, and W sites in the FeCoNiPdWPOH structure. (f) Standard free energy diagram of the ORR process at 0 V of various active sites on the surface-reconstructed samples. (g) PDOS of key intermediates over Pd sites in FeCoNiPdWPOH.

necessitate varying strengths in binding with the oxygen intermediates, the distinctive roles played by each element within the reconstructed FeCoNiPdWP transcend these conventional constraints. In the OER process, Fe, Co, and Ni emerge as the primary active sites, whereas in ORR, Pd takes on the leading role, complemented by the involvement of Co and W in modulating the electron transfer pathway. The different metal elements play distinctive roles in OER and ORR, respectively, and their synergistic interaction maximizes the performance of the resulting HEM.

2.6 ZAB performance

FeCoNiPdWP was then used as the oxygen cathode in aqueous rechargeable ZABs. Reference ZABs were also assembled with a combination of 20 wt% Pt/C and RuO_2 (Pt/C&RuO_2) as the cathode. Fig. 7c shows a schematic of the ZAB architecture. As shown in Fig. 7d, the ZAB with the FeCoNiPdWP-based air cathode exhibits an open-circuit potential (OCP) of 1.60 V, which is 96.4% of the theoretical limit (1.66 V) and higher than that of the reference Pt/C&RuO_2-based ZAB at 1.56 V. The high OCP values could light a red-screen LED, proving its potential for practical application. The peak power density of the FeCoNiPdWP HEPs-based ZAB is 123 mW cm^{-2}, significantly above that of the Pt/C&RuO_2-based ZAB at 111 mW cm^{-2} (Fig. 7e). The specific capacity and energy density of the FeCoNiPdWP-based ZAB are 886 mA h g_{Zn}^{-1} and 1063.2 mW h g_{Zn}^{-1} at a current density of 8 mA cm^{-2}, higher than those of the Pt/C&RuO_2-based ZAB at 793 mA h g_{Zn}^{-1} and 911.9 mW h g_{Zn}^{-1} (Fig. 7f). The higher specific capacity and energy density are directly attributed to the improved ORR performance of the FeCoNiPdWP-based air cathode, which is the primary factor limiting the discharge process. The FeCoNiPdWP-based ZAB not only excels in performance compared with the reference ZAB tested here but also stands out when compared with state-of-the-art ZABs (Table S7, ESI†).[14,52,54,56,103,105,108,109,119,122–132]

The rate performance of the FeCoNiPdWP-based ZAB was further evaluated. As shown in Fig. S56 and S57 (ESI†), the FeCoNiPdWP-based ZAB exhibits stable charge–discharge curves at the current density of 2–18 mA cm^{-2}, with an energy efficiency in the range of 70–50%.

The long-term stability of the ZABs was also measured with continuous charge/discharge cycles at a current density

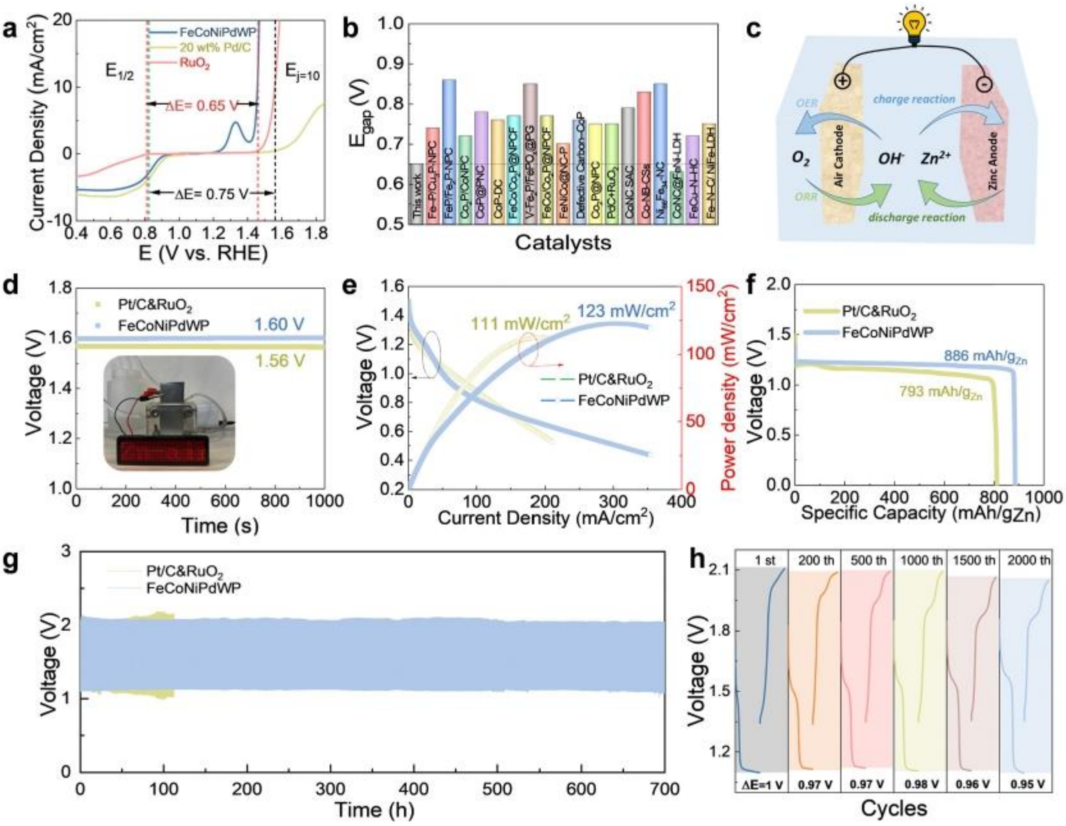

Fig. 7 Oxygen bifunctional properties and ZAB performance. (a) ORR/OER bifunctional LSV curves of different electrodes. (b) Comparison of the E_{gap} values of FeCoNiPdWP and other state-of-the-art bifunctional oxygen catalysts. (c) ZAB schematic diagram. (d) OCP measurements, (e) power density plots, and (f) specific capacity comparisons between a FeCoNiPdWP- and a Pt/C&RuO$_2$-based ZAB. Photograph of a red LED screen powered by a FeCoNiPdWP-based ZAB is also shown in (d). (g) Galvanostatic discharge–charge curves with 10 min discharge and 10 min charge cycles at a current density of 8 mA cm^{-2} of FeCoNiPdWP- and Pt/C&RuO$_2$-based ZABs. (h) Enlarged galvanostatic discharge–charge cycles at the specific cycles (1st, 200th, 500th, 1000th, 1500th, and 2000th) for 20 min of the FeCoNiPdWP-based ZAB.

of 8 mA cm^{-2}. As shown in Fig. 7g, the FeCoNiPdW-based ZAB can be stable over 700 h, *i.e.* 1 month, of continuous cycling (over 2000 cycles). In contrast, the Pt/C&RuO$_2$-based ZAB is stable for just about 100 h, *i.e.* 300 cycles. Fig. 7h shows the enlarged galvanostatic discharge–charge cycles of FeCoNiPdWP HEPs-based ZABs at the specific cycles at 1st, 200th, 500th, 1000th, and 2000th cycles. The initial charging/discharging potential gap is 1.0 V. With continuous cycling, the potential gap is decreased to 0.97 V at 200 cycles, and it remains in the range of 0.95–0.96 V after 1000–2000 cycles, further proving its good stability.

3. Conclusion

FeCoNiPdWP HEP nanoparticles were synthesized using a mild colloidal method and tested as bifunctional OER/ORR catalysts. These HEPs demonstrated exceptional OER performance, with a low overpotential of 227 mV at 10 mA cm^{-2} and a Tafel slope of 33 mV dec^{-1}. The outstanding OER performance is attributed to a reconstructed FeCoNiPdWOOH surface rich in high-oxidation-state Fe, Co, and Ni (Fe = 3.1; Co = 3.3; Ni = 3.8) as main active sites, Pd aiding in OH$^-$ adsorption, and W optimizing oxygen intermediate adsorption *via* electronic structure modulation. For ORR, FeCoNiPdWP HEPs show a half-wave potential of 0.81 V and efficient four-electron transfer pathways. During ORR, the surface of the HEP was also slightly enriched in Fe, Co, and Ni and reconstructed into a FeCoNiPdWPOH, with Fe/Co/Ni found as oxyhydroxides but with Pd and W maintaining the phosphide chemical environment as observed by XPS analysis. This unique FeCoNiPdWPOH surface, together with the active role of Pd and the influence of Co and W in modulating the electron transfer pathways, significantly enhances the ORR performance. Overall, each element within FeCoNiPdWP HEPs plays a crucial role in enhancing both OER and ORR performances. The combination of all these elements playing distinctive roles and the switchable active sites in redox reactions transcends the usual constraints of bifunctional catalysts, which generally excel in only one of these reactions. As a result, FeCoNiPdWP shows an extremely low E_{gap} value of 0.65 V and FeCoNiPdWP-based ZABs exhibit outstanding performance and stability for over 700 h. This work provides a platform to understand the different surface reconstruction behaviors of HEP catalysts and the distinct element roles in OER and ORR reactions, which paves the way for designing advanced bifunctional oxygen catalysis, potentially based on HEMs.

Author contributions

Ren He (data curation: lead; formal analysis: lead; investigation: lead; methodology: lead; resources: lead; validation: lead; visualization: lead; writing – original draft: lead). Shiqi Wang (data curation: equal; software: lead; visualization: equal; writing – original draft: equal). Linlin Yang (data curation: equal; formal analysis: equal; validation: equal; writing – original draft: lead). Sharona Horta (formal analysis: equal; investigation: equal; resources: equal). Yang Ding (formal analysis: supporting; investigation: supporting). Chong Di (data curation: supporting; visualization: supporting). Xuesong Zhang (data curation: supporting; formal analysis: supporting). Ying Xu (data curation: supporting; resources: supporting). Maria Ibáñez (formal analysis: supporting; resources: supporting). Yingtang Zhou (formal analysis: supporting; validation: supporting). Stefan Mebs (formal analysis: supporting; investigation: supporting). Holger Dau (formal analysis: supporting; visualization: supporting). Jan Niklas Hausmann (data curation: equal; formal analysis: equal; writing – original draft: equal). Wenyi Huo (formal analysis: equal; software: lead; writing – original draft: equal; writing – review & editing: equal; supervision: equal). Prashanth W. Menezes (data curation: equal; formal analysis: equal; resources: equal; writing – original draft: equal). Andreu Cabot (conceptualization: lead; funding acquisition: lead; project administration: lead; resources: lead; writing – review & editing: lead).

Data availability

The data that support the findings of this study are available from the corresponding author upon reasonable request.

Conflicts of interest

There are no conflicts to declare.

Acknowledgements

This work was financially supported by the SyDEC at project from the Spanish MCIN/AEI/FEDER (PID2022-136883OB-C22) and Generalitat de Catalunya 2021SGR01581. J. N. H. and P. W. M. acknowledge support from the German Federal Ministry of Education and Research in the framework of the project "Catlab" (03EW0015A/B). L. Yang thanks the China Scholarship Council (CSC) for the scholarship support (202008130132). This work was supported by the European Union Horizon 2020 research and innovation program (No. 857470) and the European Regional Development Fund *via* the Foundation for Polish Science International Research Agenda PLUS program (No. MAB PLUS/2018/8). The publication was created within the framework of the project of the Minister of Science and Higher Education, Poland "Support for the activities of Centres of Excellence established in Poland under Horizon 2020" under contract no. MEiN/2023/DIR/3795. H. D. and S. M. thank the German Federal Ministry of Education and Research (BMBF) for supporting the Live-XAS project (05K22KE1) and the Deutsche Forschungsgemeinschaft (DFG, German Research Foundation) for support under Germany's Excellence Strategy – EXC 2008/1 – 390540038 – UniSysCat. The authors thank the Helmholtz-Zentrum Berlin (HZB) for beamtime allocation at the KMC-3 synchrotron beamline of the BESSY synchrotron in Berlin-Adlershof and Dr Ivo Zizak as well as Dr Michael Haumann for technical support.

Notes and references

1 X. Zhu, C. Hu, R. Amal, L. Dai and X. Lu, *Energy Environ. Sci.*, 2020, **13**, 4536–4563.

2 J. N. Liu, C. X. Zhao, D. Ren, J. Wang, R. Zhang, S. H. Wang, C. Zhao, B. Q. Li and Q. Zhang, *Adv. Mater.*, 2022, **34**, e2109407.

3 W. Niu, Z. Li, K. Marcus, L. Zhou, Y. Li, R. Ye, K. Liang and Y. Yang, *Adv. Energy Mater.*, 2018, **8**, 1701642.

4 C. X. Zhao, J. N. Liu, J. Wang, D. Ren, J. Yu, X. Chen, B. Q. Li and Q. Zhang, *Adv. Mater.*, 2021, **33**, e2008606.

5 T. Binninger and M. L. Doublet, *Energy Environ. Sci.*, 2022, **15**, 2519–2528.

6 J. Chen, M. Aliasgar, F. B. Zamudio, T. Zhang, Y. Zhao, X. Lian, L. Wen, H. Yang, W. Sun, S. M. Kozlov, W. Chen and L. Wang, *Nat. Commun.*, 2023, **14**, 1711.

7 M. Liu, Z. Zhao, X. Duan and Y. Huang, *Adv. Mater.*, 2019, **31**, e1802234.

8 J. Zhang, J. Lian, Q. Jiang and G. Wang, *Chem. Eng. J.*, 2022, **439**, 135634.

9 C. Tang, H. S. Wang, H. F. Wang, Q. Zhang, G. L. Tian, J. Q. Nie and F. Wei, *Adv. Mater.*, 2015, **27**, 4516–4522.

10 L. Gui, Z. Wang, K. Zhang, B. He, Y. Liu, W. Zhou, J. Xu, Q. Wang and L. Zhao, *Appl. Catal., B*, 2020, **266**, 118656.

11 C. Li, M. Wu and R. Liu, *Appl. Catal., B*, 2019, **244**, 150–158.

12 J. Zhang, T. Wang, D. Pohl, B. Rellinghaus, R. Dong, S. Liu, X. Zhuang and X. Feng, *Angew. Chem., Int. Ed.*, 2016, **55**, 6702–6707.

13 X. Jia, Y. Zhao, G. Chen, L. Shang, R. Shi, X. Kang, G. I. N. Waterhouse, L. Z. Wu, C. H. Tung and T. Zhang, *Adv. Energy Mater.*, 2016, **6**, 1502585.

14 J. Li, Y. Kang, Z. Lei and P. Liu, *Appl. Catal., B*, 2023, **321**, 122029.

15 L. Yang, X. Zeng, D. Wang and D. Cao, *Energy Storage Mater.*, 2018, **12**, 277–283.

16 B. Q. Li, C. X. Zhao, S. Chen, J. N. Liu, X. Chen, L. Song and Q. Zhang, *Adv. Mater.*, 2019, **31**, e1900592.

17 Y. Zhang, H. Jiang, Y. Lin, H. Liu, Q. He, C. Wu, T. Duan and L. Song, *Adv. Mater. Interfaces*, 2018, **5**, 1800392.

18 Y. Mei, Y. Feng, C. Zhang, Y. Zhang, Q. Qi and J. Hu, *ACS Catal.*, 2022, **12**, 10808–10817.

19 J. Kwon, S. Sun, S. Choi, K. Lee, S. Jo, K. Park, Y. K. Kim, H. B. Park, H. Y. Park, J. H. Jang, H. Han, U. Paik and T. Song, *Adv. Mater.*, 2023, **35**, e2300091.

20 H. Zhu, S. Sun, J. Hao, Z. Zhuang, S. Zhang, T. Wang, Q. Kang, S. Lu, X. Wang, F. Lai, T. Liu, G. Gao, M. Du and D. Wang, *Energy Environ. Sci.*, 2023, **16**, 619–628.

21 T. A. A. Batchelor, J. K. Pedersen, S. H. Winther, I. E. Castelli, K. W. Jacobsen and J. Rossmeisl, *Joule*, 2019, **3**, 834–845.

22 Y. Chida, T. Tomimori, T. Ebata, N. Taguchi, T. Ioroi, K. Hayashi, N. Todoroki and T. Wadayama, *Nat. Commun.*, 2023, **14**, 4492.

23 A. Ostovari Moghaddam, A. Cabot and E. A. Trofimov, *Int. J. Refract. Met. Hard Mater.*, 2021, **97**, 105504.

24 R. He, L. Yang, Y. Zhang, D. Jiang, S. Lee, S. Horta, Z. Liang, X. Lu, A. O. Moghaddam, J. Li, M. Ibanez, Y. Xu, Y. Zhou and A. Cabot, *Adv. Mater.*, 2023, **35**, e2303719.

25 R. He, L. Yang, Y. Zhang, X. Wang, S. Lee, T. Zhang, L. Li, Z. Liang, J. Chen, J. Li, A. Ostovari Moghaddam, J. Llorca, M. Ibáñez, J. Arbiol, Y. Xu and A. Cabot, *Energy Storage Mater.*, 2023, **58**, 287–298.

26 L. Yang, R. He, X. Wang, T. Yang, T. Zhang, Y. Zuo, X. Lu, Z. Liang, J. Li, J. Arbiol, P. R. Martínez-Alanis, X. Qi and A. Cabot, *Nano Energy*, 2023, **115**, 108714.

27 L. Gao, X. Cui, C. D. Sewell, J. Li and Z. Lin, *Chem. Soc. Rev.*, 2021, **50**, 8428–8469.

28 J. Liu, S. Wang, K. Kravchyk, M. Ibáñez, F. Krumeich, R. Widmer, D. Nasiou, M. Meyns, J. Llorca, J. Arbiol, M. V. Kovalenko and A. Cabot, *J. Mater. Chem. A*, 2018, **6**, 10958–10966.

29 M. I. Diez-Garcia, G. Montana-Mora, M. Botifoll, A. Cabot, J. Arbiol, M. Qamar and J. R. Morante, *ACS Appl. Energy Mater.*, 2023, **6**, 5690–5699.

30 J. Liu, X. Yu, R. Du, C. Zhang, T. Zhang, J. Llorca, J. Arbiol, Y. Wang, M. Meyns and A. Cabot, *Appl. Catal., B*, 2019, **256**, 117846.

31 X. Wang, L. Yang, C. Xing, X. Han, R. Du, R. He, P. Guardia, J. Arbiol and A. Cabot, *Nanomaterials*, 2022, **12**, 1098.

32 J. Liu, Z. Wang, J. David, J. Llorca, J. Li, X. Yu, A. Shavel, J. Arbiol, M. Meyns and A. Cabot, *J. Mater. Chem. A*, 2018, **6**, 11453–11462.

33 N. Khodayar, A. Noori, M. S. Rahmanifar, M. Moloudi, N. Hassani, M. Neek-Amal, M. F. El-Kady, N. B. Mohamed, X. Xia, Y. Zhang, R. B. Kaner and M. F. Mousavi, *Energy Environ. Sci.*, 2024, **17**, 5200–5215.

34 D. Lai, Q. Kang, F. Gao and Q. Lu, *J. Mater. Chem. A*, 2021, **9**, 17913–17922.

35 Y. Li, Z. Dong and L. Jiao, *Adv. Energy Mater.*, 2019, **10**, 1902104.

36 Y. Shi, M. Li, Y. Yu and B. Zhang, *Energy Environ. Sci.*, 2020, **13**, 4564–4582.

37 H. Li, C. Zhang, W. Xiang, M. A. Amin, J. Na, S. Wang, J. Yu and Y. Yamauchi, *Chem. Eng. J.*, 2023, **452**, 139104.

38 G. Ke, F. Duan, B. Liu, X. Liu, J. Wen, B. Jia, X. Liu, H. He and Y. Zhou, *J. Alloys Compd.*, 2023, **934**, 167883.

39 K. Kim, K. Min, Y. Go, Y. Lee, S. E. Shim, D. Lim and S.-H. Baeck, *Appl. Catal., B*, 2022, **315**, 121501.

40 Z. Wang, J. Ang, J. Liu, X. Y. D. Ma, J. Kong, Y. Zhang, T. Yan and X. Lu, *Appl. Catal., B*, 2020, **263**, 118344.

41 W.-W. Tian, J.-T. Ren and Z.-Y. Yuan, *Appl. Catal., B*, 2022, **317**, 121764.

42 Z. Li, M. Chen, L. Zhang, R. Xing, J. Hu, X. Huang, C. Zhou, Y. Zhou, T. Wågberg and G. Hu, *J. Mater. Chem. A*, 2023, **11**, 2155–2167.

43 C. He, L. Yang, X. Peng, S. Liu, J. Wang, C. Dong, D. Du, L. Li, L. Bu and X. Huang, *ACS Nano*, 2023, **17**, 5861–5870.

44 L. Yang, R. He, M. Botifoll, Y. Zhang, Y. Ding, C. Di, C. He, Y. Xu, L. Balcells, J. Arbiol, Y. Zhou and A. Cabot, *Adv. Mater.*, 2024, **36**, e2400572.

45 L. Wu, T. Guo and T. Li, *iScience*, 2021, **24**, 102398.

46 H. Xie, S. Chen, J. Liang, T. Wang, Z. Hou, H. L. Wang, G. Chai and Q. Li, *Adv. Funct. Mater.*, 2021, **31**, 2100883.

47 F. Lin, F. Lv, Q. Zhang, H. Luo, K. Wang, J. Zhou, W. Zhang, W. Zhang, D. Wang, L. Gu and S. Guo, *Adv. Mater.*, 2022, **34**, e2202084.

48 T. Wang, A. Chutia, D. J. L. Brett, P. R. Shearing, G. He, G. Chai and I. P. Parkin, *Energy Environ. Sci.*, 2021, **14**, 2639–2669.

49 S. Wang, Y. Xie, K. Shi, W. Zhou, Z. Xing, K. Pan and A. Cabot, *ACS Sustainable Chem. Eng.*, 2020, **8**, 5920–5926.

50 J. Liu, Z. Luo, J. Li, X. Yu, J. Llorca, D. Nasiou, J. Arbiol, M. Meyns and A. Cabot, *Appl. Catal., B*, 2019, **242**, 258–266.

51 J. Liu, M. Meyns, T. Zhang, J. Arbiol, A. Cabot and A. Shavel, *Chem. Mater.*, 2018, **30**, 1799–1807.

52 X. Yang, F. Wang, Z. Jing, M. Chen, B. Wang, L. Wang, G. Qu, Y. Kong and L. Xu, *Small*, 2023, **19**, e2301985.

53 Y. Guo, J. Tang, Z. Wang, Y. Sugahara and Y. Yamauchi, *Small*, 2018, **14**, e1802442.

54 H. Liu, J. Guan, S. Yang, Y. Yu, R. Shao, Z. Zhang, M. Dou, F. Wang and Q. Xu, *Adv. Mater.*, 2020, **32**, e2003649.

55 P. He, X. Y. Yu and X. W. Lou, *Angew. Chem., Int. Ed.*, 2017, **56**, 3897–3900.

56 Q. Shi, Q. Liu, Y. Ma, Z. Fang, Z. Liang, G. Shao, B. Tang, W. Yang, L. Qin and X. Fang, *Adv. Energy Mater.*, 2020, **10**, 1903854.

57 F. Luo, Q. Zhang, X. Yu, S. Xiao, Y. Ling, H. Hu, L. Guo, Z. Yang, L. Huang, W. Cai and H. Cheng, *Angew. Chem., Int. Ed.*, 2018, **57**, 14862–14867.

58 B. Qiu, L. Cai, Y. Wang, Z. Lin, Y. Zuo, M. Wang and Y. Chai, *Adv. Funct. Mater.*, 2018, **28**, 1706008.

59 J. Wang and F. Ciucci, *Appl. Catal., B*, 2019, **254**, 292–299.

60 C. Wang, W. Chen, D. Yuan, S. Qian, D. Cai, J. Jiang and S. Zhang, *Nano Energy*, 2020, **69**, 104453.

61 Y. Deng, Y. Cao, Y. Xia, X. Xi, Y. Wang, W. Jiang, D. Yang, A. Dong and T. Li, *Adv. Energy Mater.*, 2022, **12**, 2202394.

62 G. Zhou, M. Li, Y. Li, H. Dong, D. Sun, X. Liu, L. Xu, Z. Tian and Y. Tang, *Adv. Funct. Mater.*, 2019, **30**, 1905252.

63 R. Zhang, W. Liu, F.-M. Zhang, Z.-D. Yang, G. Zhang and X. C. Zeng, *Appl. Catal., B*, 2023, **325**, 122366.

64 Y. Chen, J. Xu, M. Jiang, L. Wang, R. Ma, Y. Chen, Z. H. Xie, P. Munroe, F. Hu, L. Li and S. Peng, *Adv. Energy Mater.*, 2023, **14**, 2303450.

65 Y. Gao, D. Zheng, Q. Li, W. Xiao, T. Ma, Y. Fu, Z. Wu and L. Wang, *Adv. Funct. Mater.*, 2022, **32**, 2203206.

66 T. Dai, X. Zhang, M. Sun, B. Huang, N. Zhang, P. Da, R. Yang, Z. He, W. Wang, P. Xi and C. H. Yan, *Adv. Mater.*, 2021, **33**, e2102593.

67 S. Pan, H. Li, D. Liu, R. Huang, X. Pan, D. Ren, J. Li, M. Shakouri, Q. Zhang, M. Wang, C. Wei, L. Mai, B. Zhang, Y. Zhao, Z. Wang, M. Graetzel and X. Zhang, *Nat. Commun.*, 2022, **13**, 2294.

68 Z. Zhang, X. Li, C. Zhong, N. Zhao, Y. Deng, X. Han and W. Hu, *Angew. Chem., Int. Ed.*, 2020, **59**, 7245–7250.

69 J. Wang, S.-J. Kim, J. Liu, Y. Gao, S. Choi, J. Han, H. Shin, S. Jo, J. Kim, F. Ciucci, H. Kim, Q. Li, W. Yang, X. Long, S. Yang, S.-P. Cho, K. H. Chae, M. G. Kim, H. Kim and J. Lim, *Nat. Catal.*, 2021, **4**, 212–222.

70 C. Chen, M. Sun, F. Zhang, H. Li, M. Sun, P. Fang, T. Song, W. Chen, J. Dong, B. Rosen, P. Chen, B. Huang and Y. Li, *Energy Environ. Sci.*, 2023, **16**, 1685–1696.

71 P. Li, M. Wang, X. Duan, L. Zheng, X. Cheng, Y. Zhang, Y. Kuang, Y. Li, Q. Ma, Z. Feng, W. Liu and X. Sun, *Nat. Commun.*, 2019, **10**, 1711.

72 H. Liu, X. Xu, H. Xu, S. Wang, Z. Niu, Q. Jia, L. Yang, R. Cao, L. Zheng and D. Cao, *Appl. Catal., B*, 2021, **297**, 120451.

73 L. Tang, L. Yu, C. Ma, Y. Song, Y. Tu, Y. Zhang, X. Bo and D. Deng, *J. Mater. Chem. A*, 2022, **10**, 6242–6250.

74 Y. Zhao, Y. Guo, X. F. Lu, D. Luan, X. Gu and X. W. D. Lou, *Adv. Mater.*, 2022, **34**, e2203442.

75 S. Zhao, C. Tan, C.-T. He, P. An, F. Xie, S. Jiang, Y. Zhu, K.-H. Wu, B. Zhang, H. Li, J. Zhang, Y. Chen, S. Liu, J. Dong and Z. Tang, *Nat. Energy*, 2020, **5**, 881–890.

76 R. Yang, L. An, Y. Zhang, N. Zhang, T. Dai and P. Xi, *ChemCatChem*, 2019, **11**, 6002–6007.

77 S. Li, B. Chen, Y. Wang, M. Y. Ye, P. A. van Aken, C. Cheng and A. Thomas, *Nat. Mater.*, 2021, **20**, 1240–1247.

78 Y. Li, Y. Liu, Q. Qian, G. Wang and G. Zhang, *Energy Storage Mater.*, 2020, **28**, 27–36.

79 A. Dutta, A. K. Samantara, S. K. Dutta, B. K. Jena and N. Pradhan, *ACS Energy Lett.*, 2016, **1**, 169–174.

80 L.-A. Stern, L. Feng, F. Song and X. Hu, *Energy Environ. Sci.*, 2015, **8**, 2347–2351.

81 Y. Zhao, N. Dongfang, C. A. Triana, C. Huang, R. Erni, W. Wan, J. Li, D. Stoian, L. Pan, P. Zhang, J. Lan, M. Iannuzzi and G. R. Patzke, *Energy Environ. Sci.*, 2022, **15**, 727–739.

82 P. Hou, D. Li, N. Yang, J. Wan, C. Zhang, X. Zhang, H. Jiang, Q. Zhang, L. Gu and D. Wang, *Angew. Chem., Int. Ed.*, 2021, **60**, 6926–6931.

83 X. Zheng, J. Yang, Z. Xu, Q. Wang, J. Wu, E. Zhang, S. Dou, W. Sun, D. Wang and Y. Li, *Angew. Chem., Int. Ed.*, 2022, **61**, e202205946.

84 W. Li, Y. Li, H. Fu, G. Yang, Q. Zhang, S. Chen and F. Peng, *Chem. Eng. J.*, 2020, **381**, 122683.

85 J. Duan, S. Chen, A. Vasileff and S. Z. Qiao, *ACS Nano*, 2016, **10**, 8738–8745.

86 G. Zhang, G. Wang, Y. Liu, H. Liu, J. Qu and J. Li, *J. Am. Chem. Soc.*, 2016, **138**, 14686–14693.

87 B. S. Yeo and A. T. Bell, *J. Phys. Chem. C*, 2012, **116**, 8394–8400.

88 D. L. A. de Faria, S. Venâncio Silva and M. T. de Oliveira, *J. Raman Spectrosc.*, 1997, **28**, 873–878.

89 R. Beltrán-Suito, P. W. Menezes and M. Driess, *J. Mater. Chem. A*, 2019, **7**, 15749–15756.

90 H. N. Nong, L. J. Falling, A. Bergmann, M. Klingenhof, H. P. Tran, C. Spori, R. Mom, J. Timoshenko, G. Zichittella, A. Knop-Gericke, S. Piccinin, J. Perez-Ramirez, B. R. Cuenya, R. Schlogl, P. Strasser, D. Teschner and T. E. Jones, *Nature*, 2020, **587**, 408–413.

91 L. Reith, J. N. Hausmann, S. Mebs, I. Mondal, H. Dau, M. Driess and P. W. Menezes, *Adv. Energy Mater.*, 2023, **13**, 2203886.

92 M. Gorlin, J. Ferreira de Araujo, H. Schmies, D. Bernsmeier, S. Dresp, M. Gliech, Z. Jusys, P. Chernev, R. Kraehnert, H. Dau and P. Strasser, *J. Am. Chem. Soc.*, 2017, **139**, 2070–2082.

93 J. N. Hausmann, S. Mebs, K. Laun, I. Zebger, H. Dau, P. W. Menezes and M. Driess, *Energy Environ. Sci.*, 2020, **13**, 3607–3619.

94 F. Dionigi, Z. Zeng, I. Sinev, T. Merzdorf, S. Deshpande, M. B. Lopez, S. Kunze, I. Zegkinoglou, H. Sarodnik, D. Fan, A. Bergmann, J. Drnec, J. F. Araujo, M. Gliech, D. Teschner, J. Zhu, W. X. Li, J. Greeley, B. R. Cuenya and P. Strasser, *Nat. Commun.*, 2020, **11**, 2522.

95 J. N. Hausmann, R. A. Khalaniya, C. Das, I. Remy-Speckmann, S. Berendts, A. V. Shevelkov, M. Driess and P. W. Menezes, *Chem. Commun.*, 2021, **57**, 2184–2187.

96 R. D. L. Smith, C. Pasquini, S. Loos, P. Chernev, K. Klingan, P. Kubella, M. R. Mohammadi, D. Gonzalez-Flores and H. Dau, *Nat. Commun.*, 2017, **8**, 2022.

97 R. D. L. Smith, C. Pasquini, S. Loos, P. Chernev, K. Klingan, P. Kubella, M. R. Mohammadi, D. González-Flores and H. Dau, *Energy Environ. Sci.*, 2018, **11**, 2476–2485.

98 M. Risch, K. Klingan, J. Heidkamp, D. Ehrenberg, P. Chernev, I. Zaharieva and H. Dau, *Chem. Commun.*, 2011, **47**, 11912–11914.

99 H. Li, M. Sun, Y. Pan, J. Xiong, H. Du, Y. Yu, S. Feng, Z. Li, J. Lai, B. Huang and L. Wang, *Appl. Catal., B*, 2022, **312**, 121431.

100 J. Li, L. Zheng, B. Huang, Y. Hu, L. An, Y. Yao, M. Lu, J. Jin, N. Zhang and P. J. S. Xi, *Small*, 2022, **18**, 2204723.

101 B. Bao, Y. Liu, M. Sun, B. Huang, Y. Hu, P. Da, D. Ji, P. Xi and C. H. J. S. Yan, *Small*, 2022, **18**, 2201131.

102 R. He, T. Lu, N. Xu, G. Liu, Y. Zhang and J. Qiao, *Chem. Eng. J.*, 2023, **461**, 141843.

103 C. Yao, J. Li, Z. Zhang, C. Gou, Z. Zhang, G. Pan and J. Zhang, *Small*, 2022, **18**, e2108094.

104 H. Li, Q. Li, P. Wen, T. B. Williams, S. Adhikari, C. Dun, C. Lu, D. Itanze, L. Jiang, D. L. Carroll, G. L. Donati, P. M. Lundin, Y. Qiu and S. M. Geyer, *Adv. Mater.*, 2018, **30**, 1705796.

105 J.-T. Ren, Y.-S. Wang, L. Chen, L.-J. Gao, W.-W. Tian and Z.-Y. Yuan, *Chem. Eng. J.*, 2020, **389**, 124408.

106 T. Wang, X. Cao, H. Qin, L. Shang, S. Zheng, F. Fang and L. Jiao, *Angew. Chem., Int. Ed.*, 2021, **60**, 21237–21241.

107 Y. Wang, J. Liu, T. Lu, R. He, N. Xu and J. Qiao, *Appl. Catal., B*, 2023, **321**, 122674.

108 Q. P. Ngo, T. T. Nguyen, M. Singh, R. Balaji, N. H. Kim and J. H. Lee, *Appl. Catal., B*, 2023, **331**, 122674.

109 D. Ren, J. Ying, M. Xiao, Y. P. Deng, J. Ou, J. Zhu, G. Liu, Y. Pei, S. Li, A. M. Jauhar, H. Jin, S. Wang, D. Su, A. Yu and Z. Chen, *Adv. Funct. Mater.*, 2019, **30**, 1908167.

110 L. Yang, X. Zhang, L. Yu, J. Hou, Z. Zhou and R. Lv, *Adv. Mater.*, 2022, **34**, e2105410.
111 Y. Lin, L. Yang, Y. Zhang, H. Jiang, Z. Xiao, C. Wu, G. Zhang, J. Jiang and L. Song, *Adv. Energy Mater.*, 2018, **8**, 1703623.
112 C.-X. Zhao, J.-N. Liu, J. Wang, C. Wang, X. Guo, X.-Y. Li, X. Chen, L. Song, B.-Q. Li and Q. Zhang, *Sci. Adv.*, 2022, **8**, eabn5091.
113 Y. Zhou, Y. Yu, D. Ma, A. C. Foucher, L. Xiong, J. Zhang, E. A. Stach, Q. Yue and Y. Kang, *ACS Catal.*, 2020, **11**, 74–81.
114 Z. You and I.-H. Jung, *Metall. Mater. Trans. B*, 2020, **51**, 3108–3129.
115 R. Ganesan, A. T. Dinsdale and H. Ipser, *Intermetallics*, 2011, **19**, 927–933.
116 S. Boone and O. J. Kleppa, *J. Chem. Thermodyn.*, 1991, **23**, 1147–1151.
117 Q. Shi, Q. Liu, Y. Zheng, Y. Dong, L. Wang, H. Liu and W. Yang, *Energy Environ. Mater.*, 2021, **5**, 515–523.
118 Y. Guo, P. Yuan, J. Zhang, Y. Hu, I. S. Amiinu, X. Wang, J. Zhou, H. Xia, Z. Song, Q. Xu and S. Mu, *ACS Nano*, 2018, **12**, 1894–1901.
119 M. Ma, A. Kumar, D. Wang, Y. Wang, Y. Jia, Y. Zhang, G. Zhang, Z. Yan and X. Sun, *Appl. Catal., B*, 2020, **274**, 119091.
120 H. Sun, M. Wang, S. Zhang, S. Liu, X. Shen, T. Qian, X. Niu, J. Xiong and C. Yan, *Adv. Funct. Mater.*, 2020, **31**, 2006533.
121 S. Dresp, F. Luo, R. Schmack, S. Kühl, M. Gliech and P. Strasser, *Energy Environ. Sci.*, 2016, **9**, 2020–2024.
122 E. Vijayakumar, S. Ramakrishnan, C. Sathiskumar, D. J. Yoo, J. Balamurugan, H. S. Noh, D. Kwon, Y. H. Kim and H. Lee, *Chem. Eng. J.*, 2022, **428**, 13115.
123 J. Chen, C. Fan, X. Hu, C. Wang, Z. Huang, G. Fu, J. M. Lee and Y. Tang, *Small*, 2019, **15**, e1901518.
124 P. Yu, L. Wang, F. Sun, Y. Xie, X. Liu, J. Ma, X. Wang, C. Tian, J. Li and H. Fu, *Adv. Mater.*, 2019, **31**, e1901666.
125 P. Peng, L. Shi, F. Huo, C. Mi, X. Wu, S. Zhang and Z. Xiang, *Sci. Adv.*, 2019, **5**, eaaw2322.
126 J. Han, H. Bao, J.-Q. Wang, L. Zheng, S. Sun, Z. L. Wang and C. Sun, *Appl. Catal., B*, 2021, **280**, 1194.
127 J. Han, X. Meng, L. Lu, J. Bian, Z. Li and C. Sun, *Adv. Funct. Mater.*, 2019, **29**, 1828872.
128 M. Moloudi, A. Noori, M. S. Rahmanifar, Y. Shabangoli, M. F. El-Kady, N. B. Mohamed, R. B. Kaner and M. F. Mousavi, *Adv. Energy Mater.*, 2022, **13**, 2203002.
129 Z. Wang, J. Ang, B. Zhang, Y. Zhang, X. Y. D. Ma, T. Yan, J. Liu, B. Che, Y. Huang and X. Lu, *Appl. Catal., B*, 2019, **254**, 26–36.
130 Z. Pan, H. Chen, J. Yang, Y. Ma, Q. Zhang, Z. Kou, X. Ding, Y. Pang, L. Zhang, Q. Gu, C. Yan and J. Wang, *Adv. Sci.*, 2019, **6**, 1900628.
131 J. Qian, X. Guo, T. Wang, P. Liu, H. Zhang and D. Gao, *Appl. Catal., B*, 2019, **250**, 71–77.
132 X. Zhao, X. Li, Z. Bi, Y. Wang, H. Zhang, X. Zhou, Q. Wang, Y. Zhou, H. Wang and G. Hu, *J. Energy Chem.*, 2022, **66**, 514–524.